Revealing Structure-Activity Relationships and Mechanisms of Action in Novel Metal-Based Antibacterial Scaffolds

Çağrı Özsan

Doctor of Philosophy

University of York

Chemistry

July 2026

Abstract

This thesis explores novel metal-based chemical spaces as potential antibacterial scaffolds, elucidates their modes of action and structure-activity relationships (SAR). In Chapter 2, a class of non-toxic, Gram-positive-acting platinum-based antibacterial agents with high activity was explored. SAR studies revealed that the simplest scaffold exhibited the strongest antibacterial activity. Mode of action studies demonstrated a multifaceted mechanism of the lead compound **Pt1**, including visible morphological changes in bacterial DNA through DNA breaks and fragmentation, and oxidative stress through hydroxyl radical formation. In line with the multi-target mechanism, no resistance development to **Pt1** was observed. Finally, we demonstrate the *in vivo* activity of **Pt1**, which significantly reduced the bacterial load in a murine *S. aureus* skin infection model. In Chapter 3, a one-pot, three-component combinatorial strategy for generating a library of 1440 piano-stool iridium(III) cyclopentadienyl (Cp) Schiff base complexes as potential antibacterial agents was described. Biological screening conducted using a Direct-to-Biology (D2B) approach revealed pronounced activity against the Gram-positive bacterium *Staphylococcus aureus*, particularly for biphenyl-substituted Cp (**Cp2**) complexes. A subset of the compounds exhibits potent and selective antibacterial activity with moderate mammalian cell toxicity. The selected lead compound **Ir15** exhibited low-micromolar activity against a panel of Gram-positive pathogens, limited haemolysis, and moderate cytotoxicity. Initial mechanistic studies indicate that **Ir15** acts via a membrane-associated mechanism and induces changes in nucleoid morphology. Chapter 4 summarises collaborative and supervised research contributions to expand the metal-based antibacterial chemical space and to mode of action studies of novel scaffolds. SuFEx click chemistry generated 192 pyridyl-triazole ligands and 576 iridium(III) complexes, revealing Cp- and ligand-dependent antibacterial activity. Furthermore, macrocyclic lactams, ruthenium(II) and iridium(III) Schiff base complexes, copper(I) photosensitisers, and rhenium(V) dioxo complexes were evaluated as potential antibacterial scaffolds. Several metal complexes showed low-micromolar activity against Gram-positive bacteria, distinct cellular effects and, in some cases, light-enhanced activity.

Table of Contents

Abstract *2*

Table of Contents *3*

List of Tables *7*

List of Figures *11*

Acknowledgments *29*

Author's Declaration *34*

Chapter 1: Introduction *37*

1.1 Bacteria **37**

1.2 Bacteria size and morphology **37**

1.3 Gram-positive and Gram-negative bacteria **38**

1.3.1 The Gram-negative cell envelope 38

1.3.2 The Gram-positive cell envelope 40

1.4 Antibacterial therapy: Antibiotics **41**

1.4.1 Modern antibiotics 41

1.4.2 Golden age of antibiotics 42

1.4.3 Semi-synthetic antibiotics 43

1.4.4 Synthetic antibiotics 44

1.5 Antimicrobial resistance **45**

1.5.1 Antibacterial resistance mechanism 45

1.5.2 Resistance to last-resort antibiotics and a declining antibiotic pipeline 47

1.6 Metals in medicine: A general introduction **48**

1.7 Community for Open Antimicrobial Drug Discovery (CO-ADD) **49**

1.8 Metal complexes as novel antibiotics **49**

1.8.1 Rhenium complexes 50

1.8.2 Ruthenium complexes 59

1.8.3 Manganese complexes 67

1.8.4 Bismuth, Gallium and Silver Complexes 70

1.8.5 Other metal complexes 77

1.9 Aims and objectives **79**

Chapter 2: A Platinum Butterfly Effect: Small Changes Turn an Anticancer Drug into a Non-toxic Metalloantibiotic with In Vivo Efficacy *80*

2.1 Introduction **80**

2.1.1 Cisplatin and the rise of inorganic medicinal chemistry 80

2.1.2 Mechanism of action of cisplatin 80

2.2 Platinum compounds as antibacterials **82**

2.2.1 Siderophore conjugation to increase bacterial uptake 85

2.3 Aims and Objectives 92

2.4 Results and Discussion 93

2.4.1 Synthesis of Pt(COD-R)Cl_2 complexes 93

2.4.2 Biological characterisation of Pt(COD-R)Cl_2 complexes 96

2.4.3 Structure and activity relationship (SAR) of this compound class 101

2.4.4 Mode of action studies of Pt1 and Pt8 103

2.4.5 Advanced biological evaluation of Pt1 122

2.4.6 Stability of the lead complexes 126

2.5 Summary, conclusions and outlook 130

Chapter 3: Unlocking Iridium Chemical Space for Antibiotic Discovery through One-Pot Combinatorial Synthesis in a Direct-to-Biology Approach 133

3.1 Introduction 133

3.1.1 Iridium Complexes as Antibacterial Scaffolds 133

3.1.2 Combinatorial Chemistry 138

3.1.3 Direct-2-Biology (D2B) Approach 144

3.2 Aims and Objectives 146

3.3 Results and Discussion 146

3.3.1 Combinatorial synthesis of Ir(III) Cp library 146

3.3.2 LC-MS characterisation of the combinatorial library 149

3.3.3 Single-dose response biological activity of the combinatorial library 150

3.3.4 Dose-response biological activity of selected complexes 160

3.3.5 Batch synthesis of selected complexes 162

3.3.6 Antibacterial activity of lead complexes: Hit validation 164

3.3.7 Haemolytic and cytotoxic properties of lead complexes 168

3.3.8 Stability of Ir15 170

3.3.9 Preliminary Mode of action studies 175

3.4 Antifungal Activity of IrCp Library 183

3.4.1 Introduction 183

3.4.2 Single-dose response biological activity of the combinatorial library 185

3.4.3 Batch syntheses of selected complexes 188

3.4.4 Antifungal activity of lead complexes: Hit validation 189

3.4.5 Haemolytic and cytotoxic properties of lead complexes 190

3.4.6 Summary, conclusion and outlook 191

Chapter 4: Additional Research Contributions and Supervised Research Projects 196

4.1 Expanding Iridium Chemical Space for Antibiotic Discovery through High-Throughput Click Chemistry in a Direct-to-Biology Approach 196

4.1.1 Introduction 196

4.1.2 Results and Discussion 198

4.2 Combinatorial Synthesis and Direct-to-Biology Antibacterial Evaluation of Ruthenium(II) and Iridium(III) N^O-Schiff-Base Complexes and Their Initial Mode of Action Studies 216
4.2.1 Biological characterisation of the lead compounds 216
4.2.2 Evaluation of the initial mode of action 217
4.2.3 Summary, conclusion and outlook 223

4.3 Copper(I) Photosensitisers for Antimicrobial Photodynamic Therapy: from Solution Studies to Silica-Immobilised Composite Materials 225
4.3.1 Introduction 225
4.3.2 Results and disccussion 227

4.4 Supervised Research Projects 232
4.4.1 Synthesis and evaluation of antibacterial activity of bis(diphosphine) rhenium (v) dioxo complexes 232

Chapter 5: Summary, conclusions and Future Work 235

Chapter 6: Experimental 245

6.1 Compounds preparative techniques 245
6.1.1 Chapter 2 245
6.1.2 Chapter 3, and 4 245

6.2 Instrument details and methods for compound characterization 245
6.2.1 Chapter 2 245
6.2.2 Chapter 3 and 4 245

6.3 Synthesis Procedures 247
6.3.1 Chapter 2: A Platinum Butterfly Effect: Small Changes Turn an Anticancer Drug into a Non-toxic Metalloantibiotic with In Vivo Efficacy 247
6.3.2 Unlocking Iridium Chemical Space for Antibiotic Discovery through One-Pot Combinatorial Synthesis in a Direct-to-Biology Approach 252
6.3.3 Additional Research Contributions and Supervised Research Projects 258
6.3.4 Sythesis of rhenium complexes 265

6.4 X-ray crystallography 270

6.5 LC-MS processing (Chapter 3 and 4) 277

6.6 Stability testing of lead compounds 277
6.6.1 Determination of Pt1 and Pt8 stability (Chapter 1) 277
6.6.2 Determination of Ir15 stability (Chapter 2) 278

6.7 Biological Testing 278
6.7.1 Antibacterial Testing 278
6.7.2 Checkerboard Assay: Determination of Synergy with Clinically-relevant Antibiotics (Chapter 2) 281
6.7.3 Checkerboard Assay: Determination of Synergy with Clinically-relevant Antibiotics (Chapter 3) 281
6.7.4 Postantibiotic effect (Chapter 2) 282
6.7.5 Resistance Induction[453] (Chapter 2) 282

6.7.6 Cytotoxicity Testing of Compounds 282
6.7.7 Mode of Action Studies (Chapter 2, 3, and 4) 285
6.7.8 Murine *In Vivo* Infection Model (Chapter 2)[470] 291

List of Abbreviations 293

Chapter 7: Appendix 295

7.1 NMR Spectra 295

7.2 Mass spectra 354

Chapter 8: Bibliography 393

List of Tables

Table 1. Antibacterial activity of the synthesised complexes. MICs (μM) of synthesised PtCOD complexes against MRSA – methicillin-resistant *S. aureus* COL ; clinical isolate MSSA – methicillin-susceptible *S. aureus*; *B.subtilis* MW168 – *Bacillus subtilis*. Vancomycin for Gram-positive and Polymyxin B for Gram-negative were used as positive controls, and the MICs were given in μg/mL. 97
Table 2. Antibacterial activity of COD ligand and Pt precursor against *S. aureus* CCUG 62707 and *E. coli* NCTC 13476. 98
Table 3. Antibacterial activity of the lead complexes (Pt1 and Pt8) against expanded Gram-positive panel. MSSA ATCC 29213; MRSA NRS 100, S119, 129, 186, 191, 192, 193, 194, 198, and vancomycin-resistant *S.aureus* (VRSA) VRS 1, 4 and 12. 99
Table 4. Heamolytic activity of the synthesized complexes against human Red Blood Cells. MHC – minimum heamolytic concentration was determined by eye and HC_{50} values..... 100
Table 5. Cytotoxicity of the lead compounds in Vero and HEK293T cells. For Vero cells, CC_{50} values were given after 72 hours of incubation. For HEK293T cells after 24 and 48 hours of incubation..... 101
Table 6. DMSO-normalized cytotoxicity of the lead compounds in HEK293T cells. 101
Table 7. Antibiogram of *S. aureus* ATCC 29213 grown in the presence of sub-inhibitory concentrations of Pt1/levofloxacin for a period of 36 days..... 124
Table 8. *In vitro* post-antibiotic effect (PAE) of **Pt1** at different concentrations. 124
Table 9. MIC values of building blocks against *S. aureus* CCUG 62707. 161
Table 10. Selected 19 compounds from the single-dose biological assays. %Conv. is the conversion percentage determined by LC-MS. MIC values are given in μM and determined against *S. aureus* CCUG 62707 and *E.coli* NCTC 13476. PMBN was used as an outer membrane permeabilizer at a sublethal concentration (10 μg/mL). Cytotoxicity was determined against Human Embryonic Kidney cells (HEK293T) and is given as CC_{50}. Therapeutic index (TI) is given as the ratio of CC_{50} and MIC against S. aureus. Experiments were repeated as three biological replicates in triplicate..... 164
Table 11. Antibacterial activity of **Ir15** against Gram-positive panel, *S. aureus* CCUG 62707, MRSA (JE2), *S. aureus* (SH1000), *S. epidermidis* TU3298, and *Bacillus subtilis* MW168, *Enterococcus feacium* CUG 19434, and *Enterococcus faecalis* CCUG 19916T; Gram-negative panel, *Escherichia coli* NCTC 134376, *A. baumannii* AB5075. *indicates the presence of sublethal coa ncentration (10 μg/mL) of PMBN, outer membraan ne permeabilizer. Control is positive control antibiotic Vancomycin (VCM) for Gram-positive, Polymyxin B (PMB) for Gram-

negative. MIC values were given in μM. Experiments were repeated as three biological replicas as triplicates. 167
Table 12. Antibacterial activity of **Ir14** against Gram-positive panel, *S. aureus* CCUG 62707, *E. feacium* CUG 19434, and *E. faecalis* CCUG 19916T. 168
Table 13. MIC and MBC values of **Ir14** and **Ir15** against *S. aureus*..... 168
Table 14. Cytotoxicity of **Ir14** and **Ir15** against HEK293T and human red blood cells. CC_{50} , HC_{10}, and HC_{50} values were given in μM. 168
Table 15. MIC values of **Ir15** against *S. aureus* CCUG 62707, bacteria inoculated immediately, and after 24 hours. 170
Table 16. Absorbance at 320 nm changes of **Ir15** in different solvents. 172
Table 17. UV_{254} peak area changes of **Ir15** in different solvents. 175
Table 18. MIC values of **Ir15** in MH and glucose-defined M9 media against *S. aureus*..... 179
Table 19. MIC values of **Ir15** in MH, 150 mM tiron, 40 mM thiourea, and 150 mM tiron and 40 mM Thiourea. H_2O_2 was used positive control for thiourea. MIC values were given in μM for Ir15, and % for H_2O_2. 181
Table 20. Selected 4 compounds from the single-dose biological assays. %Conv. is the conversion percentage determined by LC-MS. % Growth inhibition is given as the ratio of OD_{600} of the drug-free control and the treated replicas with corresponding compounds at 100 μM. % Cell viability was measured in the presence of 50 μM of corresponding compounds against HEK293T cells. 186
Table 21. Antifungal activity of **IrCp1 K7**, **L7**, **B7**, B8 against *C. albicans* ATCC 90028 and *A. fumigatus* A1160. MIC values were given in μM. Experiments were repeated as three biological replicates and triplicates. 189
Table 22. Cytotoxicity of **IrCp1K7**, **IrCp1L7**, **IrCp1B7**, and IrCp1B8 against HEK293T and human red blood cells(hRBC). CC_{50} and HC_{50} values were given in μM. Therapeutic index (TI) is given as the ratio of CC_{50} and MIC against A. fumigatus. Experiments were repeated as three biological replicas as triplicates. 190
Table 23. Antibacterial activity and cytotoxicity of **IrCp4M23Y2** against Gram-positive panel, *S. aureus* CCUG 62707, MRSA (JE2), and *B. subtilis* MW168, and HEK293T. The positive control was the antibiotic Vancomycin (VCM); MIC values were reported in μM. Experiments were repeated as three biological replicates and three technical replicates. n.d : no data. 212
Table 24. Viability of *S. aureus* CCUG 62707 and E. coli after treatment with 100 μM of the corresponding compounds. Vancomycin (VCM) and Polymyxin B (PMB) were used as positive controls; Experiments were repeated as two biological replicates and two technical replicates. n.d : no data. ..... **Error! Bookmark not defined.**
Table 25. Minimum Inhibitory Concentration (MIC) and toxicity data for the lead compounds against a selection of bacterial strains. Antibacterial activity is

displayed as μM. The positive controls are the antibiotics Vancomycin (VCM) for Gram-positive and polymyxin B (PMB) for Gram-negative. MIC values were given in μM. PMBN: polymyxin B nonapeptide (10 μg / mL); CC_{50} and crude toxicity in HEK293T cells at 50 μM, the error recorded is the standard deviation; HC_{10} – 10% hemolytic concentration in human red blood cells; TI – therapeutic index, determined by dividing the lowest value between CC_{50} and the lowest MIC value for each compound against *S. aureus.* MIC determined with n = 3 across two biological replicates. 217
Table 26. MIC values of **IrCp-B5**, **RuCy-J3**, **Actinomycin D** and Vancomycin (VCM) in *S. aureus* in the presence of 0, 50, 125, 250, and 500 μg/mL Calf-Thymus (CT) DNA. 221
Table 27. Median MIC values of hit compounds in *B. subtilis* in MH, 10 mM tiron, 40 mM thiourea, and 10 mM tiron and 40 mM Thiourea. H_2O_2 was used as a positive control for thiourea. MIC values are given in μM for **IrCp-B5** and **RuCy-J3**, % for H_2O_2, and ug/mL for control antibiotics. 222
Table 28. Minimum inhibitory concentrations (MICs, μM) of the Copper(I) photosensitisers against MRSA and *E. coli* under dark conditions and after 405 nm irradiation (10 min, 250 mW/LED). The phototoxicity index (PTI = MIC_{dark}/MIC_{light}) quantifies the light-driven enhancement of activity. CC_{50}: concentration at which 50% of HEK293T cells are not viable (mean ± standard deviation). HC_{10}: concentration at which 10% haemolysis is observed in human red blood cells. 228
Table 29. MIC values of the ligands of the most promising copper(I) complexes. 228
Table 30. Copper(I) complexes immobilised on SiO_2 and their activity against methicillin-resistant *Staphylococcus aureus* (MRSA). Minimum inhibitory concentration (MIC) values (mg / mL) of Copper(I)@SiO_2 composite materials against MRSA under dark conditions and after 405 nm irradiation (10 min, 250 mW/LED). 230
Table 31. Copper loading in silica-immobilised samples quantified by ICP-OES (Cu mg/g, measured at 324.754 nm)..... 231
Table 32. Minimum Inhibitory Concentration (MIC) of rhenium complexes against selected bacterial strains. The positive controls are the antibiotics Vancomycin (VCM) for Gram-positive and polymyxin B (PMB) for Gram-negative. MIC values were given in μM. n.d.: no data..... 233
Table 33. Cytotoxicity evaluation of the rhenium complexes. HC_{10} was determined in hRBC; CC_{50} was determined in HEK293T cells; they were given in μM. TI is the ratio of the CC_{50} value against HEK293T cells and MIC values against MRSA..... 234
Table 34. Flow gradient for LC-MS method. 246
Table 35. Flow gradient for LC-MS method (7 minutes method). 246
Table 36. Crystal data and structure refinement for **IrCp1K7**. 271

Table 37. Bond lengths for **IrCp1K7.** 272
Table 38. Crystal data and structure refinement for **IrCp1L7**..... 272
Table 39. Bond lengths for **IrCp1L7**. 273
Table 40. Crystal data and structure refinement for **IrCp1B7**. 274
Table 41. Bond lengths for **IrCp1B7**. 275
Table 42. Crystal data and structure refinement for **IrCp1B8**. 276
Table 43. Bond lengths for **IrCp1B8**. 276
Table 44. *Bacillus subtilis* strains used in mode of action assays for. mgfp= monomeric green-fluorescent protein. 286

List of Figures

Figure 1. Common bacterial morphologies. Cocci (upper panel), bacilli (middle panel), and spiral (lower panel) bacteria. The figure was created with Biorender.com. 37
Figure 2. Depiction of Gram-negative cell envelope (upper) and the generalized structure of Lipopolysaccharide (LPS) (lower). LP or LPP:Lipoprotein[12]. Figure was created with Biorender.com. 39
Figure 3. Depiction of Gram-positive cell envelope. CAP: covalently attached protein. 41
Figure 4. The timeline of antibiotic classes, showing the decade in which each entered clinical use. The antibiotics were highlighted by source: green = actinomycetes, blue = other bacteria, purple = fungi, and orange = synthetic. * Indicates that compound synthesis was inspired by a natural product. VRE = vancomycin-resistant enterococci, vancomycin-resistant *S. aureus* (VRSA).[23] The figure was made with BioRender.com 43
Figure 5. Structure of hetero-tri-nuclear FC-PNA, M=Fe, and RC-PNA, M=Ru. 50
Figure 6. Rhenium(I) complexes bearing bioconjugated tridentate pyridyl-1,2,3-triazole macrocycles. The triazole moiety was modified with different groups (A-F) 52
Figure 7. Reported light-activated rhenium bisquinoline tricarbonyl complexes (Re2–Re4) by Frei and co-workers. 53
Figure 8. The most promising rhenium diimine complexes among 57 compounds investigated by Fabio Zobi's group. The counterion was omitted in the paper. 55
Figure 9. Rhenium(v) complexes bearing bis(disphosphine) ligands were reported by Cooper and co-workers. 57
Figure 10. Rhenium(v) complexes bearing diimine ligands reported by the Zobi and co-workers. 57
Figure 11. Rhenium complexes reported by Mendes and co-workers. To assess the effect of clotrimazole (Ctz), they also synthesised and subsequently tested the bromine analogue. 58
Figure 12. Dinuclear Ru(II) polypyridiyl complexes reported by Collins and Keene. **Ru1** is the most active compound against a panel of bacteria.[123] **Ru2** is the representative compound that was reported by the same group to investigate the effect of the labile chloride ligand.[126] The counterion was omitted in the paper. ...60
Figure 13. Ruthenium (II) complexes reported by the Thomas group. The counterion was omitted in the paper. 61
Figure 14. Heterobifunctional ruthenium complex (**Ru7**), a metal-based protein-targeted photosensitizer reported by Jeannine Hess's group. The NDM-1-bound part was highlighted in green, and the linker was highlighted in blue. **Ru8** is the

control photosynthesizer without the targeting group.[130] N1 is NDM-1 inhibitor 4-(3-amino-phenyl) dipicolinic acid.[138] 63
Figure 15. The design of RuBTIs (ruthenium-based bacterial type IIA topoisomerase inhibitors) and control compounds reported by Hess and co-workers. Gepotidacin has three main domains: a DNA-intercalating unit, LHS (highlighted in yellow), a protein-binding motif, RHS (highlighted in purple), and a linker. The design of the **Ru9** and **Ru10** was inspired by gepotidacin. Control compounds: **L1** & **L2** for the ligand, C1 without any targeting vector, **C2** with only a DNA-intercalating vector, and **C3** with only the protein-binding motif..... 65
Figure 16. Mn-CORM reported by the Schatzschneider group. 67
Figure 17. Mn complexes, reported by the Schatzschneider group. 70
Figure 18. Selected Ga complexes utilised as antibacterial agents..... 72
Figure 19. Structure of Bismuth subcritate (CBS). 74
Figure 20. Selected metal complexes with different metal centres. 78
Figure 21. Cisplatin uptake is governed by both passive diffusion and carrier-mediated transport via several membrane-associated transporters. Once inside, relatively lower intercellular chloride concentration governs the aquation reaction of Cisplatin. It forms covalent bonds between the platinum centre and the N7 position of purine bases in DNA. This primarily leads to 1,2- and 1,3-intrastrand crosslinks. The resulting cisplatin-DNA adducts distort the DNA structure and trigger multiple cellular responses, including inhibition of replication and transcription, cell-cycle arrest, activation of DNA repair pathways, and ultimately apoptosis. The figure was created with BioRender. 81
Figure 22. The monofunctional Pt(II) complexes investigated by Lippard and co-workers. 83
Figure 23. Antibacterial mono- and binuclear Pt(II) and Pd(II) complexes with 2,5-bis(2-thienyl)-1,3,4-thiadiazole (DTBTA) ligand..... 84
Figure 24. Reported luminescent complexes against Gram positive bacteria..... 85
Figure 25. SACs that get advanced to preclinical/clinical studies. Cefiderocol was approved by FDA in 2019. The linker group was highlighted in red, siderophore motif in blue. 87
Figure 26. Chemical structures of L-, D-Ent-Pt(IV) conjugates and Pt (IV)-Alkyne reported by Nolan and co-workers. Stereocenters are designated with red asterisks. The Pt(IV) cargos are shown in blue..... 89
Figure 27. Chemical structures of L-, D-Ent-oxPt(IV) conjugates reported by Nolan and co-workers. Stereocenters are designated with red asterisks. The Pt(IV) cargos are shown in blue..... 90
Figure 28. Previously reported **platinum**(II) COD complexes. **Pt1** is the parent complex. The designation **Pt1** was retained for consistency, as this compound is referred to by the same label throughout **Chapter 2** and forms part of the

series **Pt2–Pt10**. Other examples from the previously published paper were numbered sequentially. 91
Figure 29. Reaction scheme for double-bond-modified COD ligands and their corresponding Pt(II) complexes. (A) I: Br_2, DCM, 30 mins, r.t., 77%; II: DBU, DMF, overnight, 80°C, 21%; III: $RB(OH)_2$, $Pd(PPh_3)_4$, Na_2CO_3, Dioxane:H_2O, 4 h, reflux, 28-41%; IV:K_2PtCl_4, EtOH:H_2O, 1 h, MW, 90°C, 12-55%. (B) Reaction scheme for allylic position-modified Pt(II) complexes. I: t-butylhydroperoxide, CuCl, AcOH, 52 h, reflux, 7%; II: K_2PtCl_4, H_2O:RCH_2OH, 1 h, MW, 90°C, 7-13%. 96
Figure 30. Determination of optimal stressor concentrations (indicated in bold) of Pt1, Pt8, and CisPt. 104
Figure 31. Bacterial cytological profiling of *B. subtilis* bSS82, constitutively expressing GFP from the *PrpsD* promoter, stained with Nile red (membrane) and DAPI (DNA). Cultures were treated with Pt1 (3.125 µM), Pt8 (25 µM), and CisPt (100 µM) for 30 and 60 min, respectively. (A) Phase contrast and fluorescence microscopy images. Scale bar 2 µm. (B-C) Quantification of nucleoid compaction measured as a ratio of the whole cell area vs the area occupied by the DAPI-stained nucleoid (B) and DAPI fluorescence intensity (C). Grey lines indicate the median. Graphs show pooled data from three biological replicates. See Figure 33 for cell populations divided by individual replicates. Significance was tested with nested t-tests (p values: *≤0.5, **≤0.01, ***≤0.001). 107
Figure 32. Quantification of membrane stress measured as percent of *B. subtilis* bSS82 cells with Nile red foci. Error bars show standard deviation of three biological replicates. No statistically significant changes were observed (p≤0.05). For statistical analysis, the Mann-Whitney (unpaired, nonparametric) test was used. 108
Figure 33. Quantification of nucleoid compaction (A) and DAPI fluorescence intensity (B) corresponding to Figure 31, separated into individual biological replicates..... 109
Figure 34. Cell length measured from BCP images. Grey lines indicate the median. Significance was tested with nested t-tests (p value: * ≤ 0.5). 109
Figure 35. Localisation of RecA-GFP (*B. subtilis* UG10) after treatment with Pt1 (3.125 µM), Pt8 (25 µM), and CisPt (100 µM). Mitomycin C (MitoC, 0.05 µg/mL) was used as a positive control. (A) Phase contrast and fluorescence microscopy images. Scale bar 2 µm. (B) Quantification of microscopy images. Cells with distinct RecA foci were counted and expressed relative to the number of total cells. A minimum of 50 cells were counted per condition per replicate. Error bars show the standard deviation of at least three biological replicates..... 111
Figure 36. Single-molecule imaging of YOYO-1-labeled λ-DNA. (A) Fluorescence microscopy images of λ phage DNA exposed to the different lead compounds.

DMSO was included as negative control. Scale bar 5 µm. (B) DNA strand length distribution measured from microscopy images (pooled from three biological replicates). 112
Figure 37. Effects on membrane integrity. (A) Propidium Iodide staining of *B. subtilis* 168CA (pore formation assay). 0.23 µM nisin was used as a positive control. Note the different scales at 30 and 60 min. (B) $DiSC_3(5)$) assay in *B. subtilis* 168CA (membrane depolarization assay). 0.53 µM gramicidin was used as positive control. (C) Locasization of MinD-GFP in B. subtilis TB35 (Pxyl-gfp-minD). Localization of MinD depends on the membrane potential. 100 µM CCCP were used as positive control. All assays were performed after treatment with 3.125 µM Pt1 and 25 µM Pt8. Scale bar 2 µm. 114
Figure 38. Fluorescence overlays of *B. subtilis* MW10 (Pxyl-gfp-mreB). Cultures were treated with 3.12 µM Pt1, 25 µM Pt8, or 0.67 µM vancomycin for 30 and 60 min. Images show overlays of two consecutive images captured from the same cells in a 30-second interval. Images were false-colored in blue and orange with overlapping signal appearing white. Distinct blue and orange spots indicate movement of MreB foci. Entirely white images indicate a stop of MreB moility (vancomycin control). Scale bar 2 µm. 115
Figure 39. Localization of FtsZ in *B. subtilis* 2020 (Pxyl-gfp-ftsZ). Cultures were treated with 3.12 µM Pt1, 25 µM Pt8, or 100 µM CCCP (**carbonyl cyanide m-chlorophenyl hydrazone**) for 30 and 60 min. Scale bar 2 µm. 116
Figure 40. Localization of RpoC-GFP (*B. subtilis* 1048). Cultures were treated with 3.12 µM Pt1, 25 µM Pt8, or 1.2 µM rifampicin (Rif) for 30 and 60 min. Scale bar 2 µm. 117
Figure 41. Localization of RpsB-GFP (*B. subtilis* 1049). Cultures were treated with 3.12 µM Pt1, 25 µM Pt8, or 1.2 µM rifampicin (Rif) for 30 and 60 min. Scale bar 2 µm. 118
Figure 42. MinD translation induction assay. TB35 (Pxyl-minD-gfp) was grown without xylose, thus not expressing GFP-MinD. In log phase, cells were simultaneously induced with 0.1% xylose and treated with 3.125 µM Pt1, 25 µM Pt8, or 309.5 µM (100 µg/ml) chloramphenicol (CHL). Images were taken after 60 min of induction/treatment. Scale bar 2 µm. 119
Figure 43. Compound uptake and ROS play a role in the increased potency of Pt1 compared to Pt8. (A) Percent Pt content of MRSA cell lysate after 60 min treatment with Pt1, Pt8, and CisPt. (B) MIC fold changes (increase) in the presence of ROS scavengers compared to regular medium without scavengers). Error bars represent standard deviation of at least three biological replicates. (C) Mode of action model based on phenotypic analysis of *B. subtilis*. Both Pt compounds damage DNA, causing DNA strand breaks and fragmentation, resulting in nucleoid compaction

and reduced DAPI staining. Pt1 additionally generates ROS, mainly hydroxyl radicals, further increasing its potency through multimodal cell damage, e.g., on the cell membrane. 121
Figure 44. Compound uptake across lysis (cytosolic content) and pellet (bacterial membrane) after 60 min incubation with Pt1, Pt8, and CisPt. Pt content was measured with ICP-MS. 122
Figure 45. Resistance development and *in vivo* efficacy of Pt1. (A) Growth pattern of *S. aureus* ATCC 29213 grown in the presence of Pt1 and levofloxacin at 0.5x MIC for 36 days. (B) Reduced bacterial load in an in vivo skin infection model in mice. Fusidic acid (FA) was used as a positive control. 125
Figure 46. ^{1}H-NMR of Pt1 in DMSO-d_6 immediately after being dissolved (A), after being incubated at 37°C for 24 h (B), and 48 h (C). 127
Figure 47. ^{195}Pt-NMR of Pt1 in DMSO-d_6 immediately after being dissolved (A), after incubated at 37°C for 24 h (B), and 48 h (C). 128
Figure 48. ^{1}H-NMR of Pt1 in DMSO-d_6 at immediately after being dissolved (A), after added 10% D_2O (B) and incubated at 37°C for 24 h (C)..... 129
Figure 49. ^{1}H-NMR of Pt8 in DMSO-d_6 at immediately after being dissolved (A), after added 10% D_2O (B) and incubated at 37°C for 24 h (C). 129
Figure 50. Iridium NHC complex with SO_3 (28) charged moiety reported by Simpson and coworkers. 134
Figure 51. General structure of α-amino acid bearing iridium(III) Cp complexes. 15 examples were reported. 134
Figure 52. Iridium(III) Cp*/Cp biguanide complexes reported by Sadler and co-workers. 137
Figure 53. 1,2-diaminoalkane moiety-bearing iridium(III) Cp complexes (cis- and trans- isomers). 138
Figure 54. The Combinatorial iridium methodology. a) Heteroleptic iridium(III) complexes pioneered and investigated by Bernhard and co-workers. b) Vilar's group recently expanded this approach. 140
Figure 55. Hit manganese(I) tricarbonyl complexes selected from the combinatorial library of 420. The lead complex (Mn15) was highlighted with the red square. Counterion is TFA or triflate, omitted for the clarity in the paper. 143
Figure 57. D2B-HTC PhABit screening platform developed by GSK. Direct-to-biology high-throughput chemistry (D2B-HTC) enables the synthesis and screening of photoreactive fragments, termed PhotoAffinity Bits (PhABits), without intermediate purification. Amine-containing fragments are coupled with a diazirine-bearing N-hydroxysuccinimide ester in 384-well plates over 24 h to generate amide-linked photoreactive fragments. Following quenching of the remaining activated ester, the crude reaction mixtures are incubated with the

target protein, exemplified here by human carbonic anhydrase I (CAI), and irradiated with UV light at 302 nm for 10 min. Photoactivation of the diazirine group releases nitrogen and generates reactive intermediates that can covalently crosslink fragments to nearby protein residues. Intact-protein liquid chromatography-mass spectrometry (LC-MS) is subsequently used to detect protein-fragment adducts through the corresponding increase in protein mass, accounting for nitrogen loss, and to quantify crosslinking yields for hit identification. Created in https://BioRender.com. 145
Figure 58. (**A**) General reaction scheme for the combinatorial synthesis of iridium scaffolds. (**B**) Selected building block library consisting of 15 picolinaldehydes, 24 amines, and 4 Cp*/Cp derivatives. Counterion is chloride. 149
Figure 59. Purity of the metal complex libraries determined as LC-MS peak area percentages at 254 nm (top left: **Cp1**; top right: **Cp2**; bottom left: **Cp3**; bottom right: **Cp4**). Compound peaks were automatically identified based on the target ion mass, and the corresponding UV signals were integrated using custom Python scripts (see Experimental section for details). Reported conversions represent the combined signal of the parent ion (M^+) and the MeCN adduct $(M + MeCN)^{2+}$. The colour scale represents LC-MS-derived conversion percentages, ranging from red for low conversion through pale shades for intermediate conversion to dark blue for high conversion. The value within each circle indicates the conversion percentage for the corresponding aldehyde-amine combination. 152
Figure 60. LC-MS Based conversion distribution of the building blocks. (**A**) Conversion distribution of compounds across cyclopentadiene moieties. (**B**) Conversion distribution of compounds across aldehyde moieties (**C**) Conversion distribution of compounds across amine moieties. 153
Figure 61. Single-dose biological characterisation of the combinatorial library against *S. aureus* CCUG 62707 (top left: **Cp1**; top right: **Cp2**; bottom left: **Cp3**; bottom right: **Cp4**). Filled circles indicate measurable antibacterial activity at both 50 µM and 12.5 µM. Small white circles denote compounds that are active only at 50 µM, while empty circles indicate no detectable activity against *S. aureus* under the tested conditions. The colour intensity corresponds to the single dose cytotoxic activity against HEK293T cells. The circle size is proportional to viability of HEK293T cells. 156
Figure 62. Activity distribution of the building blocks. (**A**) Antibacterial activity distribution of compounds across cyclopentadiene moieties against *S. aureus* at 50 µM (red) and 12.5 µM (blue), and HEK293T cell viability at 50 µM. (**B**) Antibacterial activity distribution of compounds across aldehyde moieties against *S. aureus* at 50 µM (red) and 12.5 µM (blue), and HEK293T cell viability at 50 µM. (**C**) Antibacterial activity distribution of compounds across amine moieties

against *S. aureus* at 50 μM (red) and 12.5 μM (blue), and HEK293T cell viability at 50 μM. 157
Figure 63. % of active compounds by Cp building block (OD_{600}<0.1). 158
Figure 64. % of active compounds by aldehyde building blocks (OD_{600}<0.1). 158
Figure 65. % of active compounds by amine building blocks (OD_{600}<0.1)..... 159
Figure 66. Mean HEK293T viabilities based on the Cp building blocks. 159
Figure 67. Mean HEK293T viabilities based on the aldehyde building blocks. 159
Figure 68. Mean HEK293T viabilities based on the amine building blocks. 160
Figure 69. Selection of lead compounds from the initial screening library for dose-response biological characterisation. A total of 19 compounds were selected based on their antibacterial activity against *S. aureus* at 12.5 μM. Compounds were further filtered to retain those maintaining >50% single-dose (50 μM) viability in HEK293T cells. Hit compounds are shown in boxes. Counterion, chloride, was omitted for clarity. 163
Figure 70. Processed LC-MS spectrum for **Ir14** (crude). The lower graph is UV trace at 254 nm, and the upper trace is extracted ion chromatography for the target mass of the complex. 165
Figure 71. Processed LC-MS spectrum for **Ir14** (crude). The lower graph is UV trace at 254 nm, and the upper trace is extracted ion chromatography for the **[(M–Cl)+ MeCN]$^{2+}$** ion of the complex. 165
Figure 72. Processed LC-MS spectrum for **Ir15** (crude). The lower graph is UV trace at 254 nm, and the upper trace is extracted ion chromatography for the target mass of the complex. 166
Figure 73. Processed LC-MS spectrum for **Ir15** (crude). The lower graph is UV trace at 254 nm, and the upper trace is extracted ion chromatography for the [(M–Cl)+ MeCN]$^{2+}$ ion of the complex. 166
Figure 74. Dose-response plots of Ir14 and Ir15 against HEK293T cells. 169
Figure 75. Dose-response heamolysis plots of Ir14 and Ir15 against hRBC. 169
Figure 76. Stability of the hit compound, Ir15. The absorbance was measured at 300 and 37°C. 172
Figure 77. LC-MS spectra of Ir15 in H_2O at t_{15}. Rt :3.22 shows the mass of the parent complex. 173
Figure 78. LC-MS spectra of Ir15 in H_2O at t_{15}, Rt :4.09 shoes the two dimeric IrCp species 173
Figure 79. LC-MS spectra of Ir15 in H_2O:DMSO at t_{53}. R_t :3.22 shows the mass of the parent complex. 174
Figure 80. LC-MS spectra of Ir15 in PBS at t_{53}. R_t :3.22 shows the mass of the parent complex. 174

Figure 81. LC-MS stability of Ir15. The peak area for each time point was calculated with Python script and plotted against time in hours. 175
Figure 82. Initial mode of action of **Ir15**, hit compound. (**A**) Bacterial cytological profiling of *B. subtilis* bSS82, constitutively expressing GFP from the PrpsD promoter, stained with Nile red (membrane) and DAPI (DNA) after 30 and 60 minutes of incubation. (**B**) Propidium Iodide staining of *B. subtilis* 168CA (pore formation assay). 1.6 µg/mL nisin was used as a positive control. (**C**) $DiSC_3(5)$) assay in *B. subtilis* 168CA (membrane depolarizstion assay). 1 µg/mL gramicidin was used as positive control. **(D**) Localization of MinD-GFP in *B. subtilis* TB35 (Pxyl-gfp-minD). Localization of MinD depends on the membrane potential. 10 µg/mL gramicidin was used as positive control. All assays were performed after treatment with 4.25 µM Ir15. Scale bar 2 µm. 175
Figure 83. Determination of optimal stressor concentrations (OSC) (indicated in bold) of Ir15. 176
Figure 84. MIC values of Ir15 (left) and Actinomycin D (right) in the presence of 0, 50, 125, 250, and 500 µg/mL CT DNA. Compound concentrations ranged from 0.78 to 100 µM (0.63–80.91 µg/mL). 178
Figure 85. Fluorescence competitive EtBr displacement assay for Ir15 (left) and Actinomycin D (right) at 30th minute time point. EtBr:CT DNA ratio is 1:0.8 179
Figure 86. Checkerboard assay against *S. aureus* CCUG 62707 with clinically relevant antibiotics, vancomycin (**A**), kanamycin (**B**), ciprofloxacin(**C**), and chloramphenicol (**D**) (one out of three biological replica is shown). Concentration values were given in µg/mL. 180
Figure 87. $DisC_3(5)$ membrane depolarisation assay in the presence of thiourea in *B. subtilis* 168CA. 182
Figure 88. Synergy assay of Ir15 with thiourea against *B. subtilis* 168CA. Concentration values were given in µg/mL. 182
Figure 89. Synergy assay of Ir15 with thiourea against *S. aureus* CCUG 62707. Concentration values were given in µg/mL. 182
Figure 90. Selected complexes with antifungal activity. 184
Figure 91. Single-dose biological characterisation of the IrCp1 combinatorial library against *A.fumigatus*. Compounds are arranged according to their aldehyde building block (A–O, x-axis) and amine building block (1–24, y-axis). Each cell represents the percentage growth inhibition relative to the untreated control. Growth inhibition values were normalised to a scale of 0–100%. The colour intensity corresponds to the antifungal activity. 187
Figure 92. Purified lead compounds for dose-response antifungal testing and single X-ray diffraction structures of IrCp1K7, IrCp1B7, IrCp1L7, and IrCp1B8

thermal ellipsoids are shown at a probability level of 50% (hydrogen atoms have been omitted for clarity). 188
Figure 93. Building blocks used to generate a library of 96 **Tz-1-P** ligands and a library of 96 **Tz-4-MP** ligands. 199
Figure 94. The conversion rates for the library of 96 **Tz-1-P** ligands. Compound peaks were automatically identified based on the target ion mass, and the corresponding UV signals were integrated using custom Python scripts. The colour scale represents the percentage values shown in each well, with darker blue indicating higher values, pale colours indicating intermediate values, and darker red indicating lower values. 200
Figure 95. The conversion rates for the library of 96 **Tz-4-MP** ligands. Compound peaks were automatically identified based on the target ion mass, and the corresponding UV signals were integrated using custom Python scripts. The colour scale represents the percentage values shown in each well, with darker blue indicating higher values, pale colours indicating intermediate values, and darker red indicating lower values. 201
Figure 96. The conversion rate of the library of 288 **Tz-1-P**-based iridium **Cp2** complexes. It was determined from LC-MS peak area percentages at 254 nm. Compound peaks were automatically identified based on the target ion mass, and the corresponding UV signals were integrated using custom Python scripts. Reported conversions represent the combined signal of the parent ion (M^+) and the MeCN adduct $(M + MeCN)^{2+}$. The colour scale represents the percentage values shown in each well, with darker blue indicating higher values, pale colours indicating intermediate values, and darker red indicating lower values. 203
Figure 97. The conversion rate of the library of 288 **Tz-1-P**-based iridium **Cp3** complexes. It was determined from LC-MS peak area percentages at 254 nm. Compound peaks were automatically identified based on the target ion mass, and the corresponding UV signals were integrated using custom Python scripts. Reported conversions represent the combined signal of the parent ion (M^+) and the MeCN adduct $(M + MeCN)^{2+}$. The colour scale represents the percentage values shown in each well, with darker blue indicating higher values, pale colours indicating intermediate values, and darker red indicating lower values. 203
Figure 98. The conversion rate of the library of 288 **Tz-1-P**-based iridium **Cp4** complexes. It was determined from LC-MS peak area percentages at 254 nm. Compound peaks were automatically identified based on the target ion mass, and the corresponding UV signals were integrated using custom Python scripts. Reported conversions represent the combined signal of the parent ion (M^+) and the MeCN adduct $(M + MeCN)^{2+}$. The colour scale represents the percentage values

shown in each well, with darker blue indicating higher values, pale colours indicating intermediate values, and darker red indicating lower values. 203
Figure 99. The conversion rate of the library of 288 **Tz-4-MP**-based iridium complexes. It was determined from LC-MS peak area percentages at 254 nm (right: **Cp2**; middle: **Cp3**; left: **Cp4**). Compound peaks were automatically identified based on the target ion mass, and the corresponding UV signals were integrated using custom Python scripts. Reported conversions represent the combined signal of the parent ion (M^+) and the MeCN adduct $(M + MeCN)^{2+}$. The colour scale represents the percentage values shown in each well, with darker blue indicating higher values, pale colours indicating intermediate values, and darker red indicating lower values. 204
Figure 100. Single-dose biological characterisation of the combinatorial library against *S. aureus* CCUG 62707. The top part shows **Tz-1-P** complexes classified by their Cp scaffold. The bottom part shows **Tz-4-MP** complexes classified by their Cp scaffold. Filled circles indicate measurable antibacterial activity at both 50 μM and 12.5 μM. Small white circles denote compounds that are active only at 50 μM, while empty circles indicate no detectable activity against *S. aureus* under the tested conditions. The colour intensity corresponds to the single-dose cytotoxic activity against HEK293T cells. The circle size is proportional to the viability of HEK293T cells. 208
Figure 101. Selected lead complexes for batch synthesis and hit validation. Counterion is chloride. 211
Figure 102. The selected complexes from the library of 176 complexes for hit validation studies. 216
Figure 103. Determination of optimal stressor concentrations (OSC) (indicated in bold) of IrCpB5 and RuCyJ3. 218
Figure 104. Initial mode of action of IrCp-B5 and RuCy-J3, hit compounds. (**A**) Bacterial cytological profiling of *B. subtilis* bSS82, constitutively expressing GFP from the PrpsD promoter, stained with Nile red (membrane) and DAPI (DNA) after 30 and 60 minutes of incubation. (**B**) Propidium Iodide staining of *B. subtilis* 168CA (pore formation assay). 1.6 μg/mL nisin was used as positive control. (**C**) $DiSC_3(5)$ assay in B. subtilis 168CA (membrane depolarization assay). 1 μg/mL gramicidin was used as a positive control. (**D**) Localisation of MinD-GFP in *B. subtilis* TB35 (Pxyl-gfp-minD). Localisation of MinD depends on the membrane potential. 10 μg/mL gramicidin was used as a positive control. All assays were performed after treatment with 1.56 μM of hit compounds. Scale bar 2 μm. 219
Figure 105. ICP-OES analysis of cellular uptake and distribution of complexes IrCp-B5 and RuCy-J3. Results are represented as the mass of specific metal present within cellular fractions after 60 mins of treatment with complexes of

interest. Lysate, Debris and Wash represent the cell cytosol, cell membrane and the first wash with Tris/EDTA buffer, respectively. Error bars represent the standard deviation of 3 replicates. 220
Figure 106. Fluorescence competitive EtBr displacement assay for Actinomycin-D, IrCp-B5, **RuCy-J3**. 222
Figure 107. (**A**) An exemplary checkerboard assay evaluating the synergistic behaviour of IrCp-B5 against B. subtilis in the presence of different concentrations of the ROS scavenger thiourea. Biological activity is displayed as OD_{600}, with values <0.1 indicating no significant bacterial growth. (**B**) $DiSC_3(5)$ assay in *B. subtilis* 168CA (membrane depolarisation assay) in the presence of 40 mM thiourea. 1 µg/mL gramicidin was used as a positive control. 223
Figure 108. Overview of the investigated Copper(I) complexes and their abbreviations. With phen = 1,10-phenanthroline, neo = neocuproine, bcp = bathocuproine, $bcpSO_3$ = bathocuproine-5,6-disulfonate disodium salt, biipo = 16H-benzo-[4′,5′]-isoquinolino-[2′,1′,:1,2]-imidazo-[4,5-f]-[1,10]-phenanthrolin-16-one, POP = bis[(2-diphenylphosphino)phenyl] ether, xant = xantphos. 227
Figure 109. Rhenium(v) complexes synthesised by the supervised bachelor student. 232
Figure 110. ^{1}H NMR spectrum of **COD-Br$_2$** in $CDCl_3$ 295
Figure 111. ^{1}H NMR spectrum of **COD-Br$_2$** in $CDCl_3$ 296
Figure 112. ^{1}H NMR spectrum of **COD-Br** in $CDCl_3$ 296
Figure 113. ^{13}C NMR spectrum of **COD-Br** in $CDCl_3$. 297
Figure 114. ^{1}H NMR spectrum of **27** in $CDCl_3$. 297
Figure 115. ^{13}C NMR spectrum of **27** in $CDCl_3$. 298
Figure 116. ^{1}H NMR spectrum of 23 in $CDCl_3$. 298
Figure 117. ^{13}C NMR spectrum of **23** in $CDCl_3$. 299
Figure 118. ^{1}H NMR spectrum of **24** in $CDCl_3$. 300
Figure 119. ^{13}C NMR spectrum of **24** in $CDCl_3$. 300
Figure 120. ^{1}H NMR spectrum of **25** in $CDCl_3$. 301
Figure 121. ^{13}C NMR spectrum of **25** in $CDCl_3$. 301
Figure 122. ^{1}H NMR spectrum of **26** in $CDCl_3$. 302
Figure 123. ^{13}C NMR spectrum of **26** in $CDCl_3$. 302
Figure 124. ^{1}H NMR spectrum of **Pt2** in $CDCl_3$ 303
Figure 131. ^{13}C NMR spectrum of **Pt2** in $CDCl_3$ 303
Figure 132. ^{195}Pt NMR spectrum of **Pt2** in DMSO-d_6. 304
Figure 133. ^{1}H NMR spectrum of **Pt3** in acetone-d6. 304
Figure 134. ^{1}H NMR spectrum of **Pt4** in $CDCl_3$ 305
Figure 135. ^{13}C NMR spectrum of **Pt4** in $CDCl_3$ 305
Figure 136. ^{195}Pt NMR spectrum of **Pt4** in $CDCl_3$ 306

Figure 137. ^{1}H NMR spectrum of **Pt5** in CD_2Cl_2. 306
Figure 138. ^{13}C NMR spectrum of **Pt5** in $CDCl_3$. 307
Figure 139. ^{195}Pt NMR spectrum of **Pt5** in acetone-d*6*. 307
Figure 140. ^{1}H NMR spectrum of **Pt6** in $CDCl_3$. 308
Figure 141. ^{13}C NMR spectrum of **Pt6** in $CDCl_3$. 308
Figure 142. ^{195}Pt NMR spectrum of **Pt6** in $CDCl_3$. 309
Figure 143. ^{1}H NMR spectrum of **Pt7** in $CDCl_3$. 309
Figure 144. ^{13}C NMR spectrum of **Pt7** in $CDCl_3$. 310
Figure 145. ^{195}Pt NMR spectrum of **Pt7** in $CDCl_3$. 310
Figure 146. ^{1}H NMR spectrum of **Pt8** in $CDCl_3$. 311
Figure 147. ^{13}C NMR spectrum of **Pt8** in $CDCl_3$. 311
Figure 148. ^{195}Pt NMR spectrum of **Pt8** in $CDCl_3$. 312
Figure 149. ^{1}H NMR spectrum of **Pt9** in $CDCl_3$. 312
Figure 150. ^{13}C NMR spectrum of **Pt9** in $CDCl_3$. 313
Figure 151. ^{195}Pt NMR spectrum of **Pt9** in $CDCl_3$. 313
Figure 152. ^{1}H NMR spectrum of **Pt10** in $CDCl_3$. 314
Figure 153. ^{13}C NMR spectrum of **Pt10** in $CDCl_3$. 314
Figure 154. ^{195}Pt NMR spectrum of **Pt10** in $CDCl_3$. 315
Figure 155. ^{1}H NMR spectrum of **Cp2** in $CDCl_3$. 315
Figure 156. ^{13}C NMR spectrum of **Cp2** in $CDCl_3$. 316
Figure 157. ^{1}H NMR spectrum of **Cp3** in $CDCl_3$. 316
Figure 158. ^{13}C NMR spectrum of **Cp3** in $CDCl_3$. 317
Figure 159. ^{1}H NMR of **IrCp2** in $CDCl_3$. 317
Figure 160. ^{13}C NMR of **IrCp2** in $CDCl_3$. 318
Figure 161. ^{1}H NMR of **IrCp3** in $CDCl_3$. 318
Figure 162. ^{13}C NMR of **IrCp3** in $CDCl_3$. 319
Figure 163. ^{19}F NMR of **IrCp3** in $CDCl_3$. 319
Figure 164. ^{1}H NMR of **IrCp4** in $CDCl_3$. 320
Figure 165. ^{13}C NMR of **IrCp4** in $CDCl_3$. 320
Figure 166. ^{1}H NMR of **Ir9** in DMSO-d_6. 321
Figure 167. ^{13}C NMR of **Ir9** in DMSO-d_6. 321
Figure 168. ^{19}F NMR of **Ir9** in DMSO-d_6. 322
Figure 169. ^{1}H NMR of **Ir14** in DMSO-d_6. 322
Figure 170. ^{13}C NMR of **Ir14** in DMSO-d_6. 323
Figure 171. ^{19}F NMR of **Ir14** in DMSO-d_6. 323
Figure 172. ^{1}H NMR of **Ir15** in DMSO-d_6. 324
Figure 173. ^{13}C NMR of **Ir15** in DMSO-d_6. 324
Figure 174. ^{19}F NMR of **Ir15** in DMSO-d_6. 325
Figure 175. ^{1}H NMR of **IrCp1K7** in $CDCl_3$. 325

Figure 176. ^{13}C NMR of **IrCp1K7** in $CDCl_3$. 326
Figure 177. ^{1}H NMR of **IrCp1L7** in $CDCl_3$. 326
Figure 178. ^{13}C NMR of **IrCp1L7** in $CDCl_3$. 327
Figure 179. ^{1}H NMR of **IrCp1B7** in $CDCl_3$. 327
Figure 180. ^{13}C NMR of **IrCp1B7** in $CDCl_3$. 328
Figure 181. ^{1}H NMR of **IrCp1B8** in $CDCl_3$. 328
Figure 182. ^{13}C NMR of **IrCp1B8** in $CDCl_3$. 329
Figure 183. ^{1}H NMR of **$(BimH)_3$** in DMSO-d_6. 330
Figure 184. ^{13}C NMR of **$(BimH)_3$** in DMSO-d_6. 330
Figure 185. ^{1}H NMR of **M23Y3** in $CDCl_3$. 331
Figure 186. ^{13}C NMR of **M23Y3** in $CDCl_3$. 331
Figure 187. ^{1}H NMR of **P3A10** in $CDCl_3$. 332
Figure 188. ^{13}C NMR of **P3A10** in $CDCl_3$. 332
Figure 189. ^{19}F NMR of **P3A10** in $CDCl_3$. 333
Figure 190. ^{1}H NMR of **M23Y2** in $CDCl_3$. 333
Figure 191. ^{13}C NMR of **M23Y2** in $CDCl_3$. 334
Figure 192. ^{1}H NMR of **IrCp3M23Y3** in CD_2Cl_2. 334
Figure 194. ^{1}H NMR of **IrCp3P3A10** in DMSO-d_6. 335
Figure 195. ^{13}C NMR of **IrCp3P3A10** in DMSO-d_6. 335
Figure 196. ^{19}F NMR of **IrCp3P3A10** in $CDCl_3$. 336
Figure 197. ^{1}H NMR of **IrCp4M23Y2** in DMSO-d_6. 336
Figure 198. ^{13}C NMR of **IrCp4M23Y2** in DMSO-d_6. 337
Figure 199. ^{1}H NMR of **$ReIO_2(PPh_3)_2$** in $CDCl_3$. 338
Figure 200. ^{31}P NMR of $ReIO_2(PPh_3)_2$ in $CDCl_3$. 338
Figure 201. ^{1}H NMR of **45** in D_2O. 339
Figure 202. ^{13}C NMR of **45** in D_2O. 339
Figure 203. ^{1}H NMR of **46** in $CDCl_3$. 340
Figure 204. ^{31}P NMR of **46** in $CDCl_3$. 340
Figure 205. ^{1}H NMR of **47** in $CDCl_3$. 341
Figure 206. ^{31}P NMR of **47** in $CDCl_3$. 341
Figure 207. ^{1}H NMR of **48** in $CDCl_3$. 342
Figure 208. ^{31}P NMR of **48** in $CDCl_3$. 342
Figure 209. ^{1}H NMR of **49** in MeOD-d_4. 343
Figure 210. ^{31}P NMR of **4**9 in MeOD-d_4 343
Figure 211. ^{1}H NMR of **50** in DMSO-d_6. 344
Figure 212. ^{31}P NMR of **50** in DMSO-d_6. 344
Figure 213. ^{1}H NMR of **51** in MeOD-d_4. 345
Figure 214. ^{31}P NMR of 51 in MeOD-d_4. 345
Figure 215. ^{1}H NMR of **52** in $CDCl_3$. 346

Figure 216. ^{31}P NMR of **52** in $CDCl_3$. 346
Figure 217. ^{1}H NMR of **53** in $CDCl_3$. 347
Figure 218. ^{31}P NMR of **53** in $CDCl_3$. 347
Figure 219. ^{1}H NMR of **Re34** in DMSO-d_6. 348
Figure 220. ^{13}C NMR of Re34 in DMSO-d_6. 348
Figure 221. ^{31}P NMR of **Re34** in DMSO-d_6. 349
Figure 222. ^{1}H NMR of **Re35** in DMSO-d_6. 349
Figure 223. ^{13}C NMR of **Re35** in DMSO-d_6. 350
Figure 224. ^{31}P NMR of **Re35** in DMSO-d_6. 350
Figure 225. ^{1}H NMR of **Re36** in DMSO-d_6. 351
Figure 226. ^{13}C NMR of **Re36** in DMSO-d_6. 351
Figure 227. ^{31}P NMR of **Re36** in DMSO-d_6. 352
Figure 228. ^{1}H NMR of **Re37** in DMSO-d_6. 352
Figure 229. ^{13}C NMR of **Re37** in DMSO-d_6. 353
Figure 230. ^{31}P NMR of **Re37** in DMSO-d_6. 353
Figure 231. HRMS spectrum of **24** m/z calculated for $C_{14}H_{18}O^+$ 200.1434: found 200.1434 $[M+H]^+$. $[M+H]^+$. 354
Figure 232. HRMS spectrum of **25**. m/z calculated for $C_{15}H_{17}O^+$ 213.1279: found 213.1272 $[M+H]^+$. 355
Figure 233. HRGCMS chromatogram of **26**. HRGCMS: t_R: 10.03 min. 356
Figure 234. HRGCMS spectrum of **26**. m/z calculated for $C_{12}H_{14}O$ 174.1045; found 174.1042 [M]. 357
Figure 235. HRMS spectrum of **Pt2**. m/z calculated for $C_{14}H_{20}Cl_2NPt^+$ 467.0615: found 467.0610 $[M+NH_4]^+$. 358
Figure 236. HRMS spectrum of **Pt3**. m/z calculated for $C_{14}H_{17}ClNPt^+$ 429.0697: found 429.0690 $[M-Cl]^+$. 359
Figure 237. HRMS spectrum of **Pt4**. m/z calculated for $C_{15}H_{20}Cl_2NOPt^+$ 495.0564: found 495.0579 $[M+NH_4]^+$. 360
Figure 238. HRMS spectrum of **Pt5.** HRMS (ES+): m/z calculated for $C_{12}H_{14}ClOPt^+$ 404.0381: found 404.0373 $[M-Cl]^+$. 361
Figure 239. HRMS spectrum of **Pt6**. m/z calculated for $C_{10}H_{20}Cl_2NOPt^+$ 435.0570: found 435.0573 $[M+NH_4]^+$. 361
Figure 240. HRMS spectrum of **Pt7**. m/z calculated for $C_{11}H_{18}Cl_2KOPt^+$ 470.0014: found 470.0011 $[M+K]^+$. 362
Figure 241. HRMS spectrum of **Pt9**. m/z calculated for $C_{15}H_{22}Cl_2NOPt^+$ 497.0721: found 497.0717 $[M+NH_4]^+$ 362
Figure 242. HRMS spectrum of **Pt10**. m/z calculated for $C_{19}H_{30}Cl_2NOPt^+$ 553.1347: found 553.1341 $[M+NH_4]^+$. 363
Figure 243. HRMS spectrum of Cp2. 363

Figure 244. HRMS spectrum of Cp3. 364
Figure 245. HRMS spectrum of Cp4. 364
Figure 246. GCMS total ion chromatogram (TIC) of Cp4. Rt: 5.79 min is desired product. 365
Figure 247. GCMS fragmentation pattern of Rt: 4.89 min, side product homo-coupled 1,1'-bicyclohexyl. 365
Figure 248. GCMS fragmentation pattern of Rt: 5.79 min, the desired product. 366
Figure 249. HRMS of IrCp3. 366
Figure 250. HRMS of Ir9. 367
Figure 251. HRMS of Ir14. 367
Figure 252. HRMS of Ir15. 368
Figure 253. HRMS of IrCp1K7. 368
Figure 254. HRMS of IrCp1L7. 369
Figure 255. HRMS of IrCp1B7. 369
Figure 256. HRMS of IrCp1B8. 370
Figure 257. HRMS of $(BimH)_3$ ligand. 370
Figure 258. HRMS of M23Y3. 371
Figure 259. HRMS of P3A10. 371
Figure 260. HRMS of M23Y2. 372
Figure 261. HRMS of IrCp3M23Y3. 372
Figure 262. HRMS of IrCp3P3A10. 373
Figure 263. HRMS of IrCp4M23Y2. 373
Figure 264. Processed LC-MS spectrum for Ir1 (crude). The lower graph is UV trace at 254 nm, and the upper trace is extracted ion chromatography for the target mass of the complex. 374
Figure 265. Processed LC-MS spectrum for Ir1 (crude). The lower graph is UV trace at 254 nm, and the upper trace is extracted ion chromatography for the $[(M - Cl) + MeCN]^{2+}$ ion of the complex. 374
Figure 266. Processed LC-MS spectrum for Ir2 (crude). The lower graph is UV trace at 254 nm, and the upper trace is extracted ion chromatography for the target mass of the complex. 375
Figure 267. Processed LC-MS spectrum for Ir2 (crude). The lower graph is UV trace at 254 nm, and the upper trace is extracted ion chromatography for the $[(M - Cl) + MeCN]^{2+}$ ion of the complex. 375
Figure 268. Processed LC-MS spectrum for Ir3 (crude). The lower graph is UV trace at 254 nm, and the upper trace is extracted ion chromatography for the target mass of the complex. 376

Figure 269. Processed LC-MS spectrum for Ir3 (crude). The lower graph is UV trace at 254 nm, and the upper trace is extracted ion chromatography for the [(M – Cl)+ MeCN]$^{2+}$ ion of the complex. 376
Figure 270. Processed LC-MS spectrum for Ir4 (crude). The lower graph is UV trace at 254 nm, and the upper trace is extracted ion chromatography for the target mass of the complex. 377
Figure S271. Processed LC-MS spectrum for Ir4 (crude). The lower graph is UV trace at 254 nm, and the upper trace is extracted ion chromatography for the [(M – Cl)+ MeCN]$^{2+}$ ion of the complex. 377
Figure 272. Processed LC-MS spectrum for Ir5 (crude). The lower graph is UV trace at 254 nm, and the upper trace is extracted ion chromatography for the target mass of the complex. 378
Figure 273. Processed LC-MS spectrum for Ir5 (crude). The lower graph is UV trace at 254 nm, and the upper trace is extracted ion chromatography for the [(M – Cl)+ MeCN]$^{2+}$ ion of the complex. 378
Figure 274. Processed LC-MS spectrum for Ir6 (crude). The lower graph is UV trace at 254 nm, and the upper trace is extracted ion chromatography for the target mass of the complex. 379
Figure 275. Processed LC-MS spectrum for Ir6 (crude). The lower graph is UV trace at 254 nm, and the upper trace is extracted ion chromatography for the [(M–Cl)+ MeCN]$^{2+}$ ion of the complex. 379
Figure 276. Processed LC-MS spectrum for Ir7 (crude). The lower graph is UV trace at 254 nm, and the upper trace is extracted ion chromatography for the target mass of the complex. 380
Figure 277. Processed LC-MS spectrum for Ir7 (crude). The lower graph is UV trace at 254 nm, and the upper trace is extracted ion chromatography for the [(M–Cl)+ MeCN]$^{2+}$ ion of the complex. 380
Figure 278. Processed LC-MS spectrum for Ir8 (crude). The lower graph is UV trace at 254 nm, and the upper trace is extracted ion chromatography for the target mass of the complex. 381
Figure 279. Processed LC-MS spectrum for Ir8 (crude). The lower graph is UV trace at 254 nm, and the upper trace is extracted ion chromatography for the [(M–Cl)+ MeCN]$^{2+}$ ion of the complex. 381
Figure 280. Processed LC-MS spectrum for Ir9 (crude). The lower graph is UV trace at 254 nm, and the upper trace is extracted ion chromatography for the target mass of the complex. 382
Figure 281. Processed LC-MS spectrum for Ir9 (crude). The lower graph is UV trace at 254 nm, and the upper trace is extracted ion chromatography for the [(M–Cl)+ MeCN]$^{2+}$ ion of the complex. 382

Figure 282. Processed LC-MS spectrum for Ir10 (crude). The lower graph is UV trace at 254 nm, and the upper trace is extracted ion chromatography for the target mass of the complex. 383
Figure 283. Processed LC-MS spectrum for Ir10 (crude). The lower graph is UV trace at 254 nm, and the upper trace is extracted ion chromatography for the [(M–Cl)+ MeCN]$^{2+}$ ion of the complex. 383
Figure 284. Processed LC-MS spectrum for Ir11 (crude). The lower graph is UV trace at 254 nm, and the upper trace is extracted ion chromatography for the target mass of the complex. 384
Figure 285. Processed LC-MS spectrum for Ir11 (crude). The lower graph is UV trace at 254 nm, and the upper trace is extracted ion chromatography for the [(M–Cl)+ MeCN]$^{2+}$ ion of the complex. 384
Figure 286. Processed LC-MS spectrum for Ir12 (crude). The lower graph is UV trace at 254 nm, and the upper trace is extracted ion chromatography for the target mass of the complex. 385
Figure 287. Processed LC-MS spectrum for Ir12 (crude). The lower graph is UV trace at 254 nm, and the upper trace is extracted ion chromatography for the [(M–Cl)+ MeCN]$^{2+}$ ion of the complex. 385
Figure 288. Processed LC-MS spectrum for Ir13 (crude). The lower graph is UV trace at 254 nm, and the upper trace is extracted ion chromatography for the target mass of the complex. 386
Figure 289. Processed LC-MS spectrum for Ir13 (crude). The lower graph is UV trace at 254 nm, and the upper trace is extracted ion chromatography for the [(M–Cl)+ MeCN]$^{2+}$ ion of the complex. 386
Figure 290. Processed LC-MS spectrum for Ir14 (crude). The lower graph is UV trace at 254 nm, and the upper trace is extracted ion chromatography for the target mass of the complex. 387
Figure 291. Processed LC-MS spectrum for Ir14 (crude). The lower graph is UV trace at 254 nm, and the upper trace is extracted ion chromatography for the [(M–Cl)+ MeCN]$^{2+}$ ion of the complex. 387
Figure 292. Processed LC-MS spectrum for Ir15 (crude). The lower graph is UV trace at 254 nm, and the upper trace is extracted ion chromatography for the target mass of the complex. 388
Figure 293. Processed LC-MS spectrum for Ir15 (crude). The lower graph is UV trace at 254 nm, and the upper trace is extracted ion chromatography for the [(M–Cl)+ MeCN]$^{2+}$ ion of the complex. 388
Figure 294. Processed LC-MS spectrum for Ir16 (crude). The lower graph is UV trace at 254 nm, and the upper trace is extracted ion chromatography for the target mass of the complex. 389

Figure 295. Processed LC-MS spectrum for Ir16 (crude). The lower graph is UV trace at 254 nm, and the upper trace is extracted ion chromatography for the [(M–Cl)+ MeCN]$^{2+}$ ion of the complex. 389
Figure 296. Processed LC-MS spectrum for Ir17 (crude). The lower graph is UV trace at 254 nm, and the upper trace is extracted ion chromatography for the target mass of the complex. 390
Figure 297. Processed LC-MS spectrum for Ir17 (crude). The lower graph is UV trace at 254 nm, and the upper trace is extracted ion chromatography for the [(M–Cl)+ MeCN]$^{2+}$ ion of the complex. 390
Figure 298. Processed LC-MS spectrum for Ir18 (crude). The lower graph is UV trace at 254 nm, and the upper trace is extracted ion chromatography for the target mass of the complex. 391
Figure 299. Processed LC-MS spectrum for Ir18 (crude). The lower graph is UV trace at 254 nm, and the upper trace is extracted ion chromatography for the [(M–Cl)+ MeCN]$^{2+}$ ion of the complex. 391
Figure 300. Processed LC-MS spectrum for Ir19 (crude). The lower graph is UV trace at 254 nm, and the upper trace is extracted ion chromatography for the target mass of the complex. 392
Figure 301. Processed LC-MS spectrum for Ir19 (crude). The lower graph is UV trace at 254 nm, and the upper trace is extracted ion chromatography for the [(M–Cl)+ MeCN]$^{2+}$ ion of the complex. 392

Acknowledgments

Although the last four years were extraordinarily demanding and challenging, both physically and emotionally, they also became the journey of a lifetime. Looking back, I realise that somewhere along the way, I became a different person: more resilient, more compassionate, and more aware of both my strengths and my limits. The path was rarely straightforward; it was full of uncertainty, disappointments, and moments when I thought finishing would not be possible. However, as Rumi has written in the *Divan-e Shams,* "Walk the path, the way will be opened to you". I did not always know where this path would lead, but with every step, even the most uncertain ones, a way forward slowly opened up. Beyond the technical skills I gained, I learned to keep moving forward even when the path seemed impossible, and to continue despite uncertainty, without waiting to feel completely confident. Before thanking everyone who made this journey possible, I would like to thank myself first. Today, I am deeply grateful that, despite the overwhelming noise of insecurity and self-doubt, I chose to listen to the quiet voice within me that kept whispering, "You can do it." It was not always the strongest voice, but it was the one that carried me forward. I would like to believe that the eight-year-old version of me would be very proud of the person I have become. A small reminder to my future self: whenever life gives you another challenge in your path, listen closely to that quiet voice within you. It may be faint beneath the noise of fear and uncertainty, but it has carried you forward before, and it will do so again.

This journey would have been far more challenging, and perhaps even impossible, without the support of many people. First and foremost, I would like to thank my PhD supervisor, **Dr. Angelo Frei**, for his patience, guidance, and support throughout these years. When things did not work as expected, he was always there to help me take a step back, look at the problem from a different perspective, and find a way forward. I am sure that supervising me throughout this PhD was not always easy, and I will always be grateful for the patience, dedication, and care he brought to the role. I could not have asked for a more committed supervisor, and I deeply appreciate everything he has done to guide me through this journey. I have learned a great deal from him, not only about how to become a better scientist, but also about how to appreciate a properly cooked steak. I am sure my former choices for well-done steak caused him a lot of disappointment, but I hope he can now take some pride in my progress, both scientific and culinary. In addition, he greatly helped me overcome my fear of dogs by introducing me to his lovely dog, **Bonnie**. Perhaps I should thank her as well, for giving me a safe and gentle space in which to become more comfortable around dogs. She will always

remain my favourite dog in the world. **Erin** also deserves my heartfelt gratefulness for the many dinners she organised for us and for always being such a warm and generous presence at our group gatherings.

I am very grateful to **Prof. Anne-Kathrin Duhme-Klair** for helping us to settle in York, and for insightful discussions during the TAP meeting and along the way; **Dr. Rianne Lord** for accepting to be my external examiner.

Along the way, I formed friendships that I believe will remain with me for many years to come. My heartfelt thanks go to **Başak** and **Markus** for always supporting me and never allowing me to feel alone; to **Fabian**, for being not only a wonderful friend but also a patient German teacher; and to **Markus** and **Fabian** together, for our Sunday walks, which I miss and hope to have again. I am also deeply grateful to **Mirco** and **Sofia** for their friendships and for all the memorable moments we shared along the way, and to **Robin** for all his incredibly hard work on his bachelor's thesis and for his lovely presence in our group.

During my PhD, one of the things I enjoyed the most was studying the modes of action of the compounds I had synthesised. I can truly say that learning how to investigate their biological mechanisms opened up a whole new world to me.I am very grateful to **Dr. Michaela Wenzel** for our collaboration on mode of action studies and everything I learnt from her during my stay at her laboratory in Sweden. **Dr. Ann-Britt Schäfer** for everything she taught me with great kindness and patience. She was one of the best mentors I have ever had, and I am lucky to have her as a friend.

I also feel very lucky to have had the chance to strengthen my close friendship with **Beril**, whose support and positive energy I have always been able to feel. With her around, it is almost impossible to feel sad, and I am also very grateful for the chance to get to know **Timothée**. I have always enjoyed his company and deeply appreciated his support whenever I needed it. I already miss our Schnitzel dinners, although we will now have to find a new place in Basel, and I am very much looking forward to being closer to both of them.

Relocating to another country in the middle of my PhD was a difficult transition, and adapting to this new chapter was not always easy. However, that move also brought many wonderful people into my life and marked the beginning of friendships for which I will always be grateful. My heartfelt thanks go to **Sara** for her constant support and for always treating me with such kindness and care, even during the moments when I

struggled to offer the same compassion to myself. Her presence has been a source of comfort and strength throughout this journey, and I am deeply grateful to have had her by my side. **Katie**, for introducing me to a new hobby, always being there whenever I need support, and offering reassurance and validation whenever I need it most. I have always appreciated our coffee breaks during and after office hours, and I feel very lucky to work with you. I am very excited to stay as your 'dinosaur' friend. I will always be grateful to **David** for the incredible support he has shown me since the day he joined the group, and I am equally thankful for the many wine-and-cheese evenings he organised. I sincerely hope that, wherever life takes us, my invitation to these evenings will remain valid. **Athi,** for his always supportive presence in the group, whenever I needed assurance, he was always there to help and give me peace of mind. I am pretty certain he will remain in my life as one of the calmest people I have ever met. I am also very thankful to him for all his efforts to train me in cell culture and for all his help along the way. I am feeling very lucky to be able to work with him and have him as my friend. I also feel incredibly lucky to have had the chance to get to know **Aljawharah** and **Ash**. I will always be grateful for their positive energy and for all the wonderful moments we have shared, and I look forward to continuing our friendship for many years to come. A heartfelt thank you to **Stefano** for his supportive presence and all his help with biology experiments; working together was one of the most productive and joyful times of my PhD, which I will always remember fondly, feeling very lucky to have had the chance to work with him and have him as my friend. **Anson**, for his supportive presence and our conversations at the office generally after 7 p.m. **Lukas,** for his kind support and friendship; especially, I will deeply miss our discussions during coffee breaks; **Matthew** for being a very good climbing friend; **Kiera** for her hard work on her master's thesis, and I am very grateful for the supportive presence of **Basma**, **Gustavo**, **Sean** and **Nate**.

Outside of work, I feel very lucky to have had the chance to get to know **Rafael**, and I hope our friendship will continue for many years to come.

I am very grateful to the administrative and technical staff at the University of Bern, **Beatrice Thönen** and **Sandra Zbinden**, for their kind help and for always being there for me with great patience when it comes to my admin problems; I cannot express my appreciation enough. **Dr. Ilche Gjuroski** for all his help with NMR, and the chemical store in the department for their constant help. At the University of York, **Rachel Crooks** for all her help before and after the relocation to York, **Niall Donaldson** for being there whenever I have a problem or questions, regardless of how naïve it was, and his kind

help with ICP-OES; **Karl Heaton** for his help with mass spectrometry, **Ed Bergstrom** for his kind help with LC-MS.

There are also people who have been part of my life long before I began my PhD, and whose support has carried me through this journey in ways that made even the most challenging moments much easier to overcome. **Özkan**, for being an extremely supportive friend and always being there for me whenever I need support; I always wish we were living closer. **Eda**, for being my long-distance soul mate; even though you are thousands of miles away, you have always been within calling distance, and I sincerely hope we will be living closer in the very near future. **Aylin**, for being (maybe) the only friend of mine with whom we haven't offended each other even once, I always feel grateful and lucky to have her friendship, her support whenever I need, and thank you for loving me for who I am; **Ahsen**, for her constant support and friendship, which I have always felt incredibly lucky to have. I still miss the days when we lived so close to each other, and I hope we will be much closer in distance very soon; **Dilara,** for always being such a good listener and a constant source of positive energy. I feel incredibly lucky to have you as my friend, and one of the best parts of moving to the UK was getting to see you more often; **Sultan** for her positive energy and supportive friendship and of course **Hande** hocam for her great former mentorship and current friendship, very lucky to have her. A heartfelt thank you to **Seray** and **Sevgi** for their supportive friendships.

A heartfelt thank you also goes to **Sema**, **Eda**, and **Çağlar**, whose friendship has been part of my life since my primary and high school years. I feel incredibly lucky to have had you by my side while growing up and to still have you in my life today.

I also want to express my deepest gratitude to **Övgü,** whom I very unexpectedly lost during my PhD. If you were still here, we would be celebrating the 17th anniversary of our friendship. I will always be grateful for the years we shared and for having had you in my life, and I miss you deeply every single day. I would like to believe that, wherever you are, you are still watching over me, and I hope that you are proud of me.

Another person I have met during my time in York, and who became so important in my life, I would like to express my heartfelt gratitude to **Samuel**, who supported me whenever I needed him with his constant patience and love. I am feeling very lucky to have him in my life.

Last but not least, none of this would have been possible without my family. Whenever I achieved something, I always felt that it was also their achievement, because their

endless support, encouragement, and belief in me have been behind every step I have taken. Even when I did not believe in myself, they always believed in me. I cannot imagine being the person I am today without my mother, **Nermin**, and my father, **Şükrü.** I have always felt incredibly lucky to be their son. I am equally grateful for my sister, **Hande**, who was my wonderful playmate while we were growing up and has since become an incredible sister whose constant support I can always feel, even without having to ask.

Çağrı Özsan

Author's Declaration

I hereby declare that this thesis is a presentation of original work and I am the sole author. This research was performed under the supervision of Dr. Angelo Frei at the University of Bern, Switzerland (July 2022-March 2024), and at the University of York (April 2024-July 2026). This work has been submitted for any other qualifications or any other university. Any publications that resulted from this work are indicated below and stated in the text to which they correspond. All sources are acknowledged in the Bibliography section as References. The following work was carried out by me or with the assistance and collaboration of other researchers:

Chapter 2:

This chapter was published as the following article: **Özsan, Ç**., Schäfer, AB. *et al.* A platinum butterfly effect: small changes turn an anticancer drug into a non-toxic metalloantibiotic with in vivo efficacy. *npj Antimicrob Resist* **4**, 37 (2026).

I am the the first author of the publication and majority of the manuscript was prepared by me.

- Cytotoxicity testing was done with the help of **Ms.Sofia Fulgencio**
- The training for the mode of action assays was provided by **Dr. Ann-Britt Schäfer** under the supervision of **Assoc. Prof. Michaela Wenzel**
- Some of the biological repetitions of the microscopy experiments were done by **Dr Ann-Britt Schäfer, Dr Rahul Maitra, and Dr Rupa Rani. It is worth noting that I performed each microscopy experiment** at least **2 times**.
- Quantification of mode of action data (except RecA, done by me) was performed by **Dr. Ann-Britt Schäfer**
- Single-molecule DNA assays were performed by **Dr. Obed Akwasi Aning**
- Advanced biological characterisation was done by **Deepanshi Saxena**, and **Dr. Sidharth Chopra**

Chapter 3:

This chapter was published as the following article: **Özsan Ç**. *et al*. Unlocking Iridium Chemical Space for Antibiotic Discovery through One-Pot Combinatorial Synthesis in a Direct-to-Biology Approach. *JACS Au* **6**, ASAP (2026).

I am the the first author of the publication and majority of the manuscript was prepared by me.

- Cytotoxicity profiling was performed with the help of **Dr. Athi Welsh**
- Checkerboard assays and MIC in the glucose-defined medium were performed with the help of **Dr. Stefano Zineddu**
- Some of the MIC assays were done with the help of **Ms Kiera Robinsons**
- Some of the large data analyses were done with the help of **Dr. David Husbands**
- **Antifungal screening** was done by external collaborator.

Chapter 4

- This chapter involves unpublished data.
- The combinatorial synthesis library was prepared by **Dr. David Husbands**
- The single-dose antibacterial screening was done with the help of **Dr. David Husbands**
- The cytotoxicity screening was performed with the help of **Dr. Athi Welsh**

- This chapter partly covers the collaborative projects I have worked on, both with external groups and within our group, that have been published or are currently under review, as follows (in the corresponding part of the chapter, only my contributions are discussed).

1. Dukalksi A., **Özsan Ç**., *et al.* Copper(I) photosensitizers for antimicrobial photodynamic therapy from solution studies to silica-immobilised composite materials. *Dalton trans*., (2026).
2. Zineddu S., Welsh A., **Özsan Ç.**, Husbands D.R., Messori L., Frei A. Synthesis and evaluation of the antibacterial properties of novel N^O Schiff-base Ru(II) and Ir(III) complexes: a combinatorial synthesis approach.*ChemRxiv* (2026). https://doi.org/10.26434/chemrxiv.15005024/v1

- Part of the chapter involves data from the students that I supervised.
- Syntheses of Re complexes were done by **Mr Robin Knüsel** under my supervision at the University of Bern
- Biological screening of the complexes was done with the help of **Mr. Robin Knüsel** under my supervision, and **Ms.Sofia Fulgencio**

Throughout this thesis, compounds are labelled by metal centre and whether they were reported in the literature or investigated in this work. Literature complexes containing metals other than platinum and iridium are labelled with the metal symbol followed by a sequential number, such as **Mn1**, **Mn2**, etc. Where a specific name or designation was used in the original publication, this has been retained.

Platinum and iridium complexes discussed in the literature review are generally labelled with sequential numbers without a metal prefix, such as **1**, **2**, etc. For platinum complexes with a specific name or designation in the original publication, this has been retained. Platinum complexes investigated in this work are labelled **Pt1–Pt10**. Although **Pt1** was previously reported, it was also investigated in this thesis. Therefore, the designation **Pt1** is used in both the literature review and the experimental chapters to maintain consistency.

For the iridium complexes prepared in this work, two labelling systems are used. Crude complexes selected for biological dose-response assays are labelled **Ir1–Ir19**. The remaining library complexes are labelled using the format **IrCp[1–4][aldehyde code][amine number]**. In this notation, **Cp1–Cp4** refers to the cyclopentadienyl core, **A–M** to the aldehyde building block, and **1–24** to the amine building block. For example, **IrCp2A1** refers to the complex prepared from the Cp2 core, aldehyde A and amine 1. This notation identifies the building blocks used for each library complex, while the shorter labels **Ir1–Ir19** are used to simplify the discussion of the selected compounds.

Chapter 1: Introduction

1.1 Bacteria

Bacteria are unicellular prokaryotic microorganisms that lack a membrane-bound nucleus and other membrane-bound organelles. They reproduce mainly by binary fission, and typically possess a peptidoglycan-containing cell envelope.[1] Bacteria play important roles in ecosystems; they contribute to the breakdown of organic matter and are central to the recycling of key elements through biogeochemical cycles, including the carbon and nitrogen cycles.[2] In the human body, bacteria also form a major component of the microbiome. Current estimates suggest that bacterial cells are present in numbers broadly comparable to human cells, with the largest populations found in the gastrointestinal tract, where they contribute to digestion, metabolism, and overall host health.[3,4]

1.2 Bacteria size and morphology

Bacteria vary considerably in size; larger species, such as *Bacillus anthracis*, typically measure approximately 1.0–1.3 µm in width and 3–10 µm in length, whereas smaller bacteria, such as *Francisella tularensis*, are around 0.2 µm wide and 0.2–0.7 µm long. Mycoplasmas are even smaller, with diameters of roughly 0.1–0.2 µm.[1] Bacteria exhibit substantial morphological diversity and are commonly grouped by cell shape, including spherical cocci, rod-shaped bacilli, and spiral or curved forms (**Figure 1**).[5] Additionally, bacteria can also adopt less common morphologies, including star-shaped, pear-shaped, flask-shaped, and branching or dendroid forms.[6]

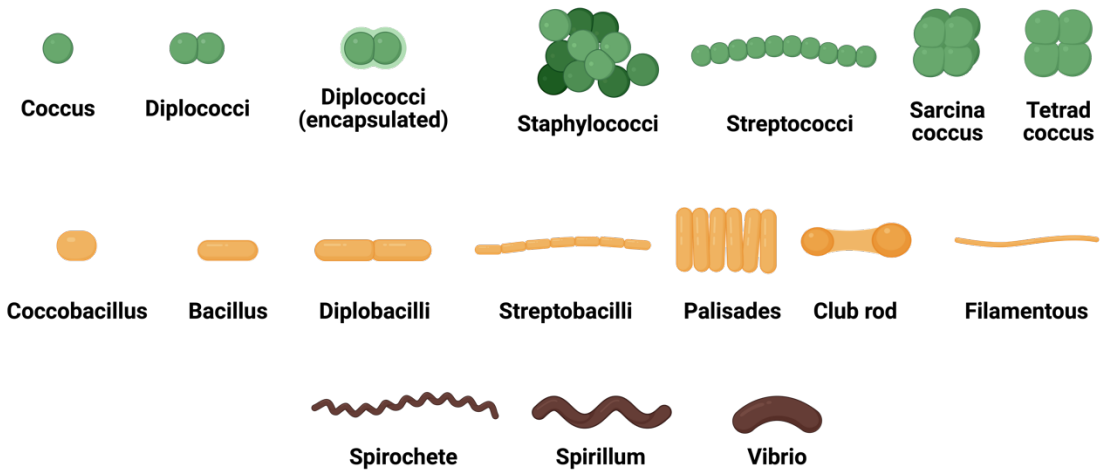


Figure 1. Common bacterial morphologies. Cocci (upper panel), bacilli (middle panel), and spiral (lower panel) bacteria. The figure was created with Biorender.com.

Bacterial cell shape is not arbitrary; it reflects adaptation to different ecological and physiological conditions. These include nutrient acquisition, cell division, surface attachment, dispersal, motility, polar differentiation, predator avoidance, and cellular differentiation. Together, these selective pressures contribute to the evolution of bacterial sizes and shapes that are suited to their specific environments.[7] Notably, bacterial morphology also plays an important role in their pathogenicity.[8,9] For example, the helical morphology of *Helicobacter pylori* together with flagellar motility allows the bacterium to move efficiently through the viscous gastric mucus layer, helping it penetrate or escape the mucin gel environment.[10]

1.3 Gram-positive and Gram-negative bacteria

In 1884, Hans Christian Gram developed a differential staining technique classifying bacteria into two major groups: Gram-positive and Gram-negative. The distinction arises from fundamental differences in cell envelope structure. Gram-positive bacteria retain the crystal violet-iodine complex after ethanol washing and therefore appear purple, whereas Gram-negative bacteria are decolourised during this step and subsequently take up the safranin counterstain and appear pink.[11,12]

1.3.1 The Gram-negative cell envelope

The cell envelope of the Gram-negative bacteria consists of three main substructures: outer membrane, a thin peptidoglycan-based cell wall, and inner cytoplasmic membrane (**Figure 2**). The space between the inner and outer membranes is known as the periplasm, a compartment containing the peptidoglycan layer and numerous proteins involved in nutrient transport, envelope biogenesis, protein folding, and stress responses.[12]

1.3.1.1 The outer membrane

The presence of an outer membrane is a key structural feature that distinguishes Gram-negative bacteria from Gram-positive bacteria.[13] The main function of the outer membrane is to provide a selective barrier for the bacteria. It protects bacteria by limiting the entry of toxic compounds, while still permitting the uptake of necessary nutrients for growth.[12,13] Although the outer membrane has a lipid bilayer, it differs from typical phospholipid-based biological membranes. In the Gram-negative outer membrane, they are mainly confined to the inner leaflet, whereas the outer leaflet is predominantly composed of lipopolysaccharide (LPS). It consists of lipid A, a core oligosaccharide, a glucosamine disaccharide with six or seven acyl chains, and, in many species, an O-antigen, an extended polysaccharide chain (**Figure 2**). An additional function of the outer

membrane is facilitating the interaction of symbiotic or pathogenic bacteria with their host organisms.[12] LPS is one of the most important immunostimulatory components of the Gram-negative outer membrane, and its lipid A region is largely responsible for the endotoxic activity associated with Gram-negative sepsis.[12,14] Additionally, the outer membrane also contains a range of proteins that contribute to its structure and selective permeability. These proteins are broadly divided into lipoproteins and β-barrel outer membrane proteins.

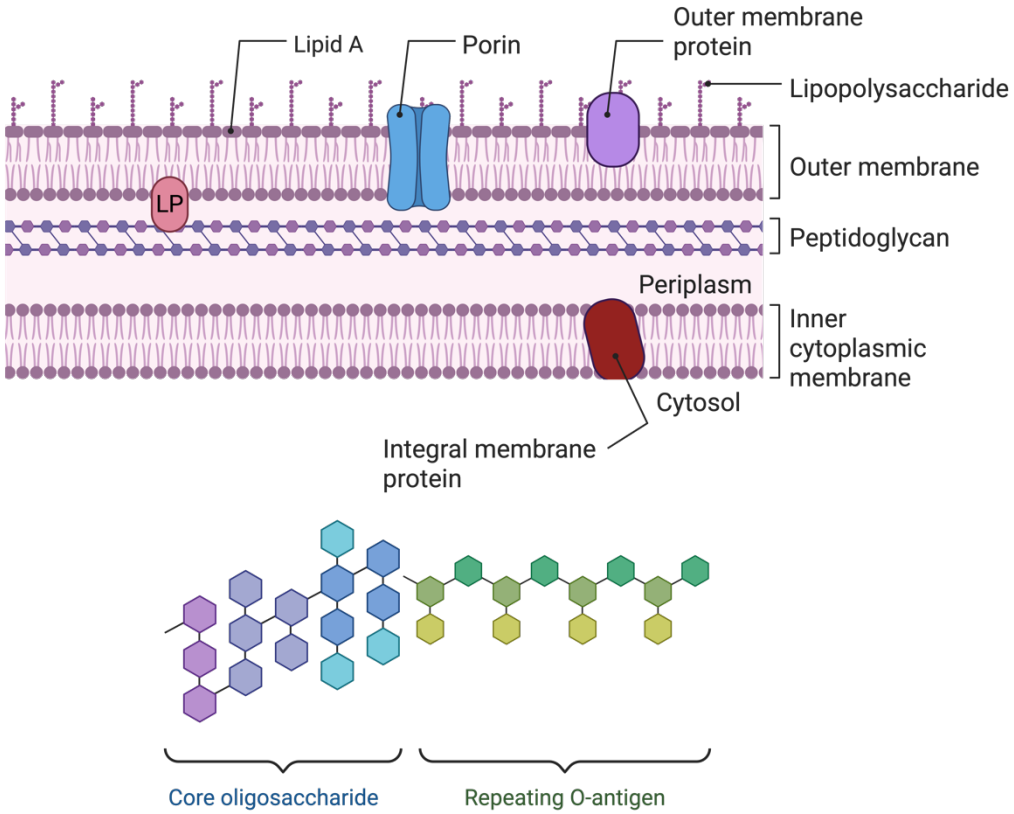


Figure 2. Depiction of Gram-negative cell envelope (upper) and the generalized structure of Lipopolysaccharide (LPS) (lower). LP or LPP:Lipoprotein[12]. Figure was created with Biorender.com.

Lipoproteins are anchored to the membrane through lipid groups attached to an *N*-terminal cysteine residue and are generally associated with the inner leaflet of the outer membrane rather than spanning the membrane.[15] In contrast, most integral outer membrane proteins have a β-barrel structure, in which β-sheets form cylindrical channels across the membrane. A major group of these proteins are porins, such as OmpF and OmpC, which enable the passive diffusion of small hydrophilic molecules, including sugars, amino acids, and ions, across the outer membrane.[16] Other β-barrel proteins are

more selective and facilitate the uptake of specific nutrients, such as maltose, phosphate, iron chelates, or vitamins.[17] Together, these outer membrane proteins allow Gram-negative bacteria to acquire essential nutrients while maintaining the protective barrier function of the outer membrane.[12]

1.3.1.2 The peptidoglycan layer

In Gram-negative bacteria, a thin peptidoglycan layer is located between the outer and inner cytoplasmic membranes. It provides structural support and helps preserve bacterial cell shape. Peptidoglycan is a large, mesh-like polymer composed of repeating disaccharide units of N-acetylglucosamine and N-acetylmuramic acid, which are cross-linked by pentapeptide side chains.[12,18] The resulting peptidoglycan sacculus surrounds the bacterial cell and counteracts the internal turgor pressure of the cytoplasm. Therefore, disruption of peptidoglycan synthesis or integrity can weaken the cell envelope and lead to cell lysis. Braun's lipoprotein, also known as Lpp or murein lipoprotein, anchors the outer membrane to the underlying peptidoglycan layer. Its N-terminal lipid modifications anchor the protein in the outer membrane, thereby forming a structural link between these two compartments of the Gram-negative cell envelope.[12,19]

1.3.1.3 The periplasm

The space between the peptidoglycan layer and the inner cytoplasmic membrane forms an aqueous, protein-rich compartment known as the periplasm. This compartment enables Gram-negative bacteria to localise degradative enzymes, including RNases and alkaline phosphatases, outside the cytoplasm while keeping them contained within the cell envelope.[12,20]

1.3.1.4 The inner cytoplasmic membrane

The bacterial inner membrane is a phospholipid bilayer that surrounds the cytoplasm and serves as the main compartment for many membrane-associated cellular processes. In contrast to eukaryotic cells, which compartmentalise functions within membrane-bound organelles such as mitochondria and the endoplasmic reticulum, bacteria generally lack intracellular organelles. Consequently, processes such as energy production, lipid biosynthesis, protein secretion, nutrient transport, and waste export are primarily carried out at the inner membrane.[12]

1.3.2 The Gram-positive cell envelope

The structure of the Gram-positive cell envelope is substantially different from that of the Gram-negative cell envelope (**Figure 3**). A notable difference is that instead of an outer membrane, Gram-positive bacteria are surrounded by a thick peptidoglycan layer, which

provides structural support and helps the cell resist internal turgor pressure. This thick peptidoglycan layer compensates for the lack of an additional outer membrane barrier. Its function is further supported by the presence of teichoic acid, an anionic polymer composed of repeating units of glycerol phosphate, glucosyl phosphate, or ribitol phosphate. While teichoic acid is covalently linked to the peptidoglycan matrix, another class of polymer, lipoteichoic acid, is anchored to the head groups of membrane lipid.[12,21]

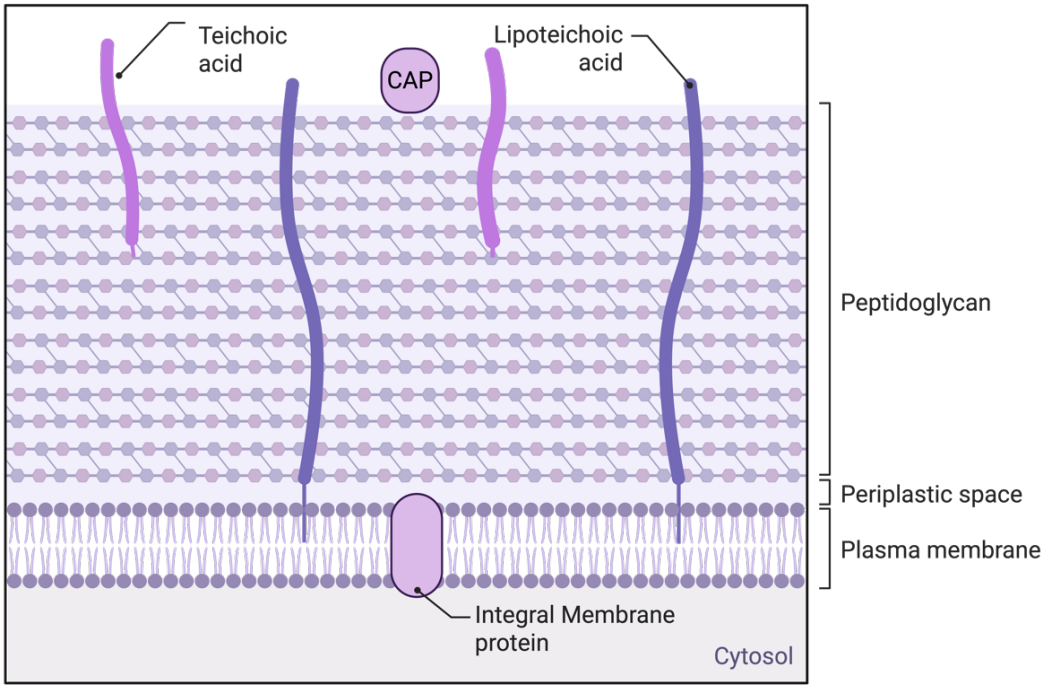


Figure 3. Depiction of Gram-positive cell envelope. CAP: covalently attached protein.

Gram-positive bacteria also have various surface-associated proteins. Because they lack an outer membrane, these proteins must be retained at the cell surface through other mechanisms, such as membrane-spanning helices, lipid anchors, covalent attachment to peptidoglycan, or interactions with teichoic acids. Together, the thick peptidoglycan layer (30-100 nm), teichoic acids, and surface proteins allow Gram-positive bacteria to maintain cell integrity and adapt to different environmental conditions.[12,22]

1.4 Antibacterial therapy: Antibiotics

1.4.1 Modern antibiotics

The development of modern antibacterial chemotherapy began with the arsenic-based prodrugs salvarsan and neo-salvarsan for treating syphilis caused by *Treponema pallidum* (**Figure 4**).[23] Subsequently, a sulfonamide prodrug developed by Gerhard

Domagk and colleagues at Bayer, Prontosil, was established as the first clinically successful systemic antibiotic against a broad range of pathogenic bacteria. The success of Prontosil was overshadowed by the serendipitous discovery of penicillin by Alexander Fleming in 1928.[27] Later, it was developed into a clinically useful antibacterial agent through its extraction, purification, and scale-up by Norman Heatley, Howard Florey, Ernst Chain, and co-workers at the University of Oxford.[28] Its chemical structure was subsequently resolved by Dorothy Hodgkin using X-ray crystallography in 1945.[29] The elucidation of penicillin's structure paved the way for the development of semi-synthetic derivatives to combat penicillin resistance.

Interestingly, the phenomenon of 'antibiosis' between microbes was identified well before the discovery of penicillin, with Louis Pasteur suggesting the presence of heat-stable compounds secreted by bacteria to kill other bacteria.[30] In the late 19th century, this concept was later applied in the clinic using pyocyanase, a crude extract from *Pseudomonas aeruginosa*. Although it was initially thought to act enzymatically, subsequent studies indicated that its activity was more likely due to small-molecule metabolites produced by the bacteria, including the phenazine pyocyanin and alkyl quinolone derivatives.[31]

1.4.2 Golden age of antibiotics

The recognition of microorganisms capable of producing antibacterial compounds, together with the discoveries of penicillin and tyrocidine, encouraged a more systematic exploration of microbes as sources of novel antibiotics.[23] In the late 1930s, Selman Waksman recognised that filamentous Actinomycetales, a group of complex soil-dwelling bacteria, could suppress the growth of other microorganisms.[32] This observation suggested that naturally occurring microbial competition in soil could be exploited to identify antibiotic-producing organisms. They defined antibiotics subsequently as '*a compound made by a microbe to destroy other microbes*'. From 1939 onward, Waksman and co-workers developed systematic agar-based screening methods to examine thousands of microbial isolates for antimicrobial activity.[33] The large scale of this screening approach, reportedly involving more than 10,000 strains, demonstrated the practicality and scalability of microbial discovery platforms and laid the foundation for many subsequent antibiotic discoveries. This study led to the development of many of the major antibiotic classes currently used in the clinic.[34] The success of this approach marked the beginning of the so-called golden age of antibiotic discovery from the 1940s to the 1960s. Streptomycin was particularly important because it was the first effective

antibiotic for tuberculosis and acted by inhibiting bacterial protein synthesis by targeting the 30S ribosomal subunit. In the following decades, microbial screening programs revealed many additional antibiotic classes, including amphenicols from *Streptomyces venezuelae*, tetracyclines from *Streptomyces aureofaciens*, macrolides such as erythromycin from *Saccharopolyspora erythrea*, glycopeptides such as vancomycin from *Amycolatopsis orientalis*, and rifamycins from *Amycolatopsis mediterranei*.[23]

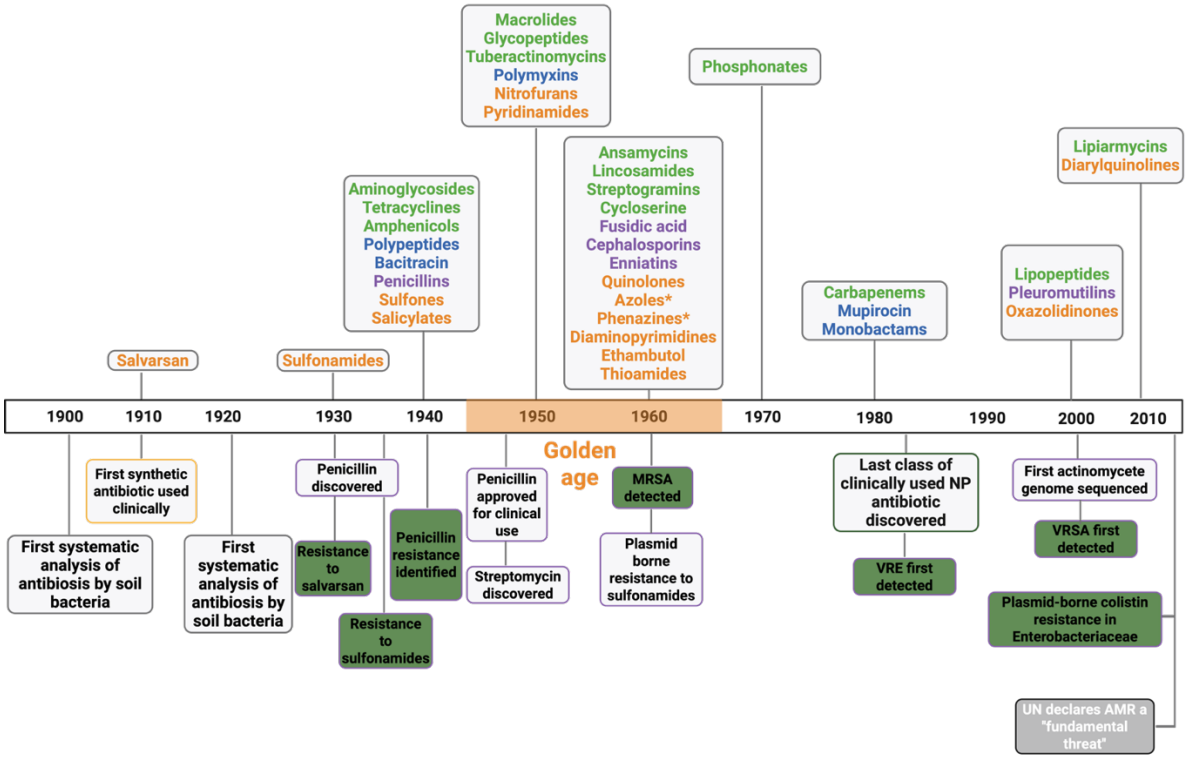


Figure 4. The timeline of antibiotic classes, showing the decade in which each entered clinical use. The antibiotics were highlighted by source: green = actinomycetes, blue = other bacteria, purple = fungi, and orange = synthetic. * Indicates that compound synthesis was inspired by a natural product. VRE = vancomycin-resistant enterococci, vancomycin-resistant *S. aureus* (VRSA).[23] The figure was made with BioRender.com

1.4.3 Semi-synthetic antibiotics

The success of natural product antibiotic discovery laid the foundation for medicinal chemistry, with many of these antibiotics identified using the Waksman platform. However, natural products are shaped by evolutionary selective pressures. Although they are highly adapted to interact with their targets, this does not always translate into

therapeutic potency, as it can lead to unselective toxicity, instability, and poor bioavailability. At the same time, resistance to the antibiotics was becoming increasingly evident. By the mid-1960s, the discovery of new antibiotic scaffolds from natural sources had begun to slow. These limitations shifted antibiotic development toward medicinal chemistry, where established natural scaffolds were systematically modified to improve potency, broaden the antibacterial spectrum, reduce toxicity, and overcome resistance mechanisms.[35] Semi-synthesis, therefore, became an important strategy to optimise these natural scaffolds while enabling the development of patentable derivatives.[34] One early example was the catalytic hydrogenation of streptomycin to dihydrostreptomycin in 1946, which improved chemical stability while retaining comparable antibacterial activity.[36] However, the clinical use of both compounds was later limited due to concerns about ototoxicity.[37]

1.4.4 Synthetic antibiotics

Alongside semi-synthesis, fully synthetic approaches further expanded the antibacterial arsenal by enabling scalable production, structural diversification, and access to novel scaffolds. Chloramphenicol, originally isolated as a natural product from *S. venezuelae*, became the first antibiotic produced by total synthesis, and subsequent chemical modifications yielded derivatives such as thiamphenicol with improved safety profiles. Fully synthetic strategies also contributed to clinically important classes, including nitroimidazoles, diaminopyrimidines, quinolones, oxazolidinones, and synthetic β-lactam derivatives. Notably, the development of fluoroquinolones, carbapenems, monobactams, and linezolid demonstrated how medicinal chemistry could generate antibiotics with improved potency, activity spectra, pharmacological properties, and resistance profiles. Together, natural-product screening, semi-synthesis, and total synthesis laid the groundwork for modern antibacterial drug discovery, offering clinicians a growing array of tools to combat bacterial infections.[34]

Despite significant advances, the pace of the discovery of new, clinically useful classes of antibiotics has slowed considerably since the early 1960s. This decline can be attributed to both scientific and economic challenges. It has become much harder to identify novel antibacterial compounds through natural product screening and the development of synthetic compound libraries. Additionally, antibiotic development has shifted from the discovery of novel compound classes to the synthesis of analogues of pre-existing compounds. Low financial returns, regulatory hurdles, and limited use of new antibiotics to delay the development of resistance have all contributed to reduced

investment in antibacterial discovery. Consequently, the conventional antibacterial pipeline has struggled to produce sufficiently innovative compounds.[38–41]

1.5 Antimicrobial resistance

Antimicrobial resistance (AMR) has emerged as one of the most significant health problems of the 21st century.[42] In 2021, 4.71 million deaths were associated with bacterial AMR, and it was the direct cause of 1.14 millions of those. It is forecasted that from 2025 to 2050, there will be 39.1 million deaths attributable directly to AMR and 169 million deaths associated with it. Additionally, it is estimated that it will be the leading cause of mortality by 2050, with approximately 8.22 million annual deaths.[43] More specifically, its potential to increase up to 2.4 million deaths in high-income countries from 2015 to 2050, and up to 5.2 million deaths in the Western Pacific region between 2023 and 2030, without proper preventative measures.[44,45] Eastern European countries also have a high rate of resistance. For instance, even though the proportion of antibiotics prescribed by family physicians in Turkey dropped from 35% to 25% between 2011 and 2017, the rate of antibiotic resistance was reported as 35%.[46] The driving force of bacterial AMR is attributed to mis-, overuse, or inappropriate use of antibiotics in human and veterinary medicine.[42 47] Although there are many preventive measures and restrictions on antibiotic use in food production, their implementation and regulation are challenging, especially in developing countries with increasing demand for food animals.[42]

1.5.1 Antibacterial resistance mechanism

Although antibiotic resistance became clinically apparent during the modern antibiotic era, resistance itself is not a new phenomenon. The microbial world has long possessed the necessary molecular tools to develop resistance.[35] In 2011, D'Costa and co-workers demonstrated that antibiotic resistance is not of contemporary origin, but instead predates the modern clinical use of antibiotics. They analysed ancient DNA recovered from approximately 30.000-year-old Beringian permafrost sediments using metagenomic analysis. They identified a diverse collection of genes associated with resistance to antibiotic classes, including β-lactams, tetracyclines, and glycopeptides. Interestingly, the study not only detected resistance-associated sequences but also provided structural and functional evidence for an ancient vancomycin-resistance element, VanA.[48] These findings showed that antibiotic resistance determinants existed long before the clinical use of antibiotics and support the idea that resistance is an ancient, naturally occurring feature of microbial ecosystems. This conclusion is consistent with the ancient

evolutionary history of antibiotics themselves, as several antibiotic biosynthetic pathways are thought to have emerged hundreds of millions of years ago.[49]

Bacteria can have intrinsic antibiotic resistance, but they can also acquire resistance through mutations in chromosomal genes or *via* horizontal gene transfer.[50] These mechanisms can be grouped into three major categories: reducing the intracellular concentration of the antibiotic by decreasing uptake[51,52] or increasing efflux[53,54]; altering the drug target by mutation or post-translational modification[55]; and directly inactivating the antibiotic through enzymatic degradation[56] or chemical modification.[57–59]

Gram-negative bacteria are intrinsically less susceptible to toxic compounds due to their additional outer membrane. Hydrophilic compounds enter Gram-negative bacteria primarily through outer membrane porins. Bacteria can limit antibiotic uptake and reduce effective antibiotic concentrations by downregulating porin expression and replacing unselective porins with more selective channels. This decrease in outer-membrane permeability is an important contributor to acquired resistance.[50] For Gram-positive bacteria, the situation is different because they lack an outer membrane and instead possess a thick, exposed peptidoglycan layer. Notably, they can also reduce the effective antibiotic concentration through cell envelope-related mechanisms, including cell wall thickening[60–62], alterations in teichoic acid moieties, and changes in cytoplasmic membrane phospholipid composition[63,64]. Vancomycin resistance in *S. aureus* was associated with a thickened cell wall and an increased abundance of glucosaminyl-muramyl-muropeptides.[61,62] Concurrently, bacteria can decrease the effective concentration of antibiotics by upregulating efflux proteins. These transport proteins export antibiotics from the cell and contribute significantly to intrinsic resistance.[50]

Another major resistance mechanism involves the inactivation of antibiotics through enzymatic cleavage or covalent modification. One of the most infamous mechanisms is the β-lactamases-facilitated degradation of β-lactam antibiotics *via* hydrolysis of the amide bond in the β-lactam ring.[65] β-lactamases are a highly diverse class of enzymes, with 12,741 enzyme entries currently listed in the Beta-lactamase Database.[66] Enzymatic inactivation is not limited to β-lactams; tetracycline-inactivating enzymes, also known as tetracycline destructases.[67,68] These flavin-dependent monooxygenases inactivate tetracycline antibiotics by catalysing oxidative modifications of their scaffolds via regioselective hydroxylation.[69] This modification disrupts the ribosomal binding and therefore inhibits antibacterial activity.[67]

Together with reduced permeability, active efflux, and target modification, enzymatic inactivation highlights the diverse strategies by which bacteria overcome antibiotic pressure. Importantly, these mechanisms are not only molecular adaptations but also have profound clinical consequences as they significantly reduce the effectiveness of antibiotics reserved for difficult-to-treat or multidrug-resistant infections.

1.5.2 Resistance to last-resort antibiotics and a declining antibiotic pipeline

Colistin (Polymyxin E) is considered a last-line drug for treating drug-resistant infections, and the prevalence of colistin resistance varies worldwide, ranging from 3% to 28% in *Acinetobacter baumannii* and 2.5% to 10.5% in *Klebsiella pneumoniae*.[70] Additionally, among the WHO's 2024 priority pathogens, Gram-positive bacteria methicillin-resistant *Staphylococcus aureus* (MRSA) and vancomycin-resistant *Enterococcus faecium* (VRE) were designated as high priority.[71,72] MRSA is particularly concerning due to its multidrug resistance, while VRE presents a serious challenge because of its resistance to vancomycin and other key antimicrobials.[72] Vancomycin has traditionally been designated as a 'last-resort' therapeutic for the treatment of resistant Gram-positive bacterial infections; however, the emergence and spread of vancomycin-resistant strains have increasingly compromised its clinical utility.[73] The emergence of resistance to colistin and vancomycin provides significant evidence for prevailing crises, and developing new antibiotics with novel structures and modes of action presents an opportunity to address it. However, the conventional pipeline for antibacterial drug development, relying on organic medicinal chemistry, has progressed insufficiently. As of February 2025, 90 antibacterial agents containing at least one new therapeutic entity are in clinical development worldwide, comprising both traditional and non-traditional agents. Since 2019, only three small-molecule antibiotics, Lefamulin[74], gepotidacin[75], and zoliflodacin[76], have been approved with novel mechanisms, representing the first new classes since the approval of the tuberculosis drug bedaquiline in 2012. This insufficient progress demonstrates the urgent need to explore novel chemical space and alternative strategies in antibiotic discovery. The near future does not appear to meet the urgent need for novel antibiotics through the existing conventional organic-compound-based antibiotic drug pipeline.

1.6 Metals in medicine: A general introduction

Metal-based compounds began to appear on the medicinal chemistry stage in the 20th century, with semi-metal arsenic-based Salvarsan as the first effective treatment for syphilis[77], mercury-based topical antiseptic mercurochrome, the vaccine preservative thiomersal, and the gold-based Auranofin as the treatment of rheumatoid arthritis[78]. The major milestone in medicinal inorganic chemistry was the discovery of cisplatin, which entered human clinical trials in 1972 and received FDA approval in 1978 for testicular cancer, with approval for advanced ovarian and bladder cancers granted in the same year. Cisplatin also became a backbone treatment for several solid tumours, including lung, bladder, cervical, ovarian, gastric, head and neck cancers, and malignant mesothelioma. Its success led to the development of numerous platinum analogues, of which cisplatin, carboplatin and oxaliplatin are now approved worldwide. Today, platinum-based drugs remain among the most widely used chemotherapeutic agents, with estimates suggesting that nearly half of patients receiving cancer chemotherapy are treated with a platinum-containing drug.[79] Beyond platinum chemotherapy, metal-containing compounds are also clinically established in other areas of medicine: arsenic trioxide is used in acute promyelocytic leukaemia, where arsenic-containing regimens have produced complete remission rates of approximately 70–90% in relapsed disease and survival rates exceeding 90% in clinical-trials[80]; gadolinium-based contrast agents are used in approximately 30–45% of the nearly 40 million MRI procedures performed annually in the United States[81]; and technetium-99m radiopharmaceuticals account for around 80% of nuclear medicine procedures worldwide.[82] Recently, copper histidine was approved as the first treatment for Menkes disease.[83] Notably, several metal-based compounds are also currently being evaluated in human clinical trials. These include ruthenium-based Ruvidar (TLD-1433), currently in phase II clinical trials for photodynamic therapy in non-muscle-invasive bladder cancer[84]; Ferroquine[85], a ferrocene derivative of chloroquine for asymptomatic malaria[86]; gallium maltolate in early phase I for recurrent glioblastoma[87], and manganese-based mangaciclanol[88] as an MRI contrast agent in operational phase II and III trials.

Taken together, these examples demonstrate that metal complexes are clinically validated across several areas of medicine. This broader clinical precedent supports exploring metal complexes as an underinvestigated chemical space to expand antibacterial drug discovery beyond the conventional drug-development pipeline.

1.7 Community for Open Antimicrobial Drug Discovery (CO-ADD)

Upon investigating the structures of recently established antibacterial molecules, it is clear that a significant majority do not conform to traditional medicinal-chemistry structural criteria, such as Lipinski's Rule of Five.[89,90] Under the light of this new trend in medicinal chemistry, it is highly possible that there are numerous types of compounds remaining unexplored as potential antibiotics**.** In 2015, the Community for Open Antimicrobial Drug Discovery (CO-ADD) was launched as an open-access facility for chemists worldwide to submit their compounds, paving the way for the discovery of uncharted chemical space for potential antibiotics. The submitted compounds are evaluated against the key bacterial and fungal pathogens to find novel antibacterial scaffolds.[91] As of 2020, more than 280.000 compounds had been submitted and tested, and among these compounds, a considerable number do not meet the 'usual drug-likeness' properties. One of these types of compound classes is metal complexes. 906 metal complexes with 29 different metals had been submitted. Among these metal complexes, 246 were active against bacterial strains, with minimum inhibitory concentration (MIC) values lower than 16 μg/mL or 10 μM, an extraordinary hit rate of 27%. On the other hand, the purely organic ones tested showed only a 1.6% hit rate. The rate of antibacterial metal compounds without significant cytotoxicity against human cells was 9.9%, more than 10-fold higher than that of the general CO-ADD library (0.87%).[92] This study revealed that not only do metal complexes exhibit high potency against a large panel of bacteria, but, in contrast to the common stereotype, they are not more cytotoxic than purely organic compounds. Together, these findings highlight metal complexes as an underexplored and highly promising class of compounds for the discovery of novel scaffolds to combat antibacterial resistance.

1.8 Metal complexes as novel antibiotics

Metal complexes could be the key to the 'escape from flatland[93] of purely organic molecules with their highly three-dimensional structures, and they can offer higher structural diversity with the number of stereoisomers.[94] Morrison and co-workers analysed the topology of metal complexes and organic compounds, and 77% of the investigated metal compounds were populated in the 3D region, whereas this rate was less than 25% for organic compounds, despite their majority.[95] Since biological systems recognise molecules by their structures, molecular shape is the leading factor in determining biological activity, and structural diversity is a desirable property for targeting different targets.[95,96] Additionally, three-dimensional structural properties lead to higher aqueous solubility and favourable physicochemical properties.[97] In addition to geometric

diversity, metal complexes can offer unique modes of action, such as ligand exchange or release, redox properties, catalytic activity that forms toxic species, and metal exchange that stabilises native protein structures and causes denaturation.[92,94,98] Metal compounds were starting to be present in modern medicinal chemistry in early 20th century (Salvarsan). In 1952, the antibacterial activity of a ruthenium phenanthroline complex against *Staphylococcus heamolyticus* was demonstrated.[99] Since then, reports studying antibacterial activity of metal complexes have increased drastically. In the following section, selected antibacterial metal complexes reported in the literature will be classified and discussed according to their metal centres. It is noted that platinum and iridium complexes used as antibacterials will be discussed in the introductions to **chapters 2** and **3**, respectively.

1.8.1 Rhenium complexes

The Metzler-Nolte and Gasser groups established hetero-trinuclear **FC-PNA** and **Rc-PNA** complexes (**Figure 5** with a peptide nucleic acid (PNA) backbone and an alkyne side chain.[100] The antibacterial potency and mode of action were further investigated by Wenzel and co-workers. These complexes were inactive against Gram-negative bacteria but exhibited potent activity against the Gram-positive pathogens *S. aureus* and *B. subtilis*. **FC-PNA** showed MIC values of 1.4 μM against *B. subtilis* DSM 402, and 1.4–4 μM against various strains of *S. aureus*, including MRSA. Notably**, RC-PNA** has exhibited MIC values of 21 μM against *B. subtilis*, 2.7 μM against *S. aureus*, and 4 μM against MRSA. The more potent derivative **FC-PNA** (**Figure 5**) showed limited solubility in biological media (25 μg/mL). Therefore, cell viabilities across different mammalian cell lines were determined at this concentration and ranged from 55–108%.

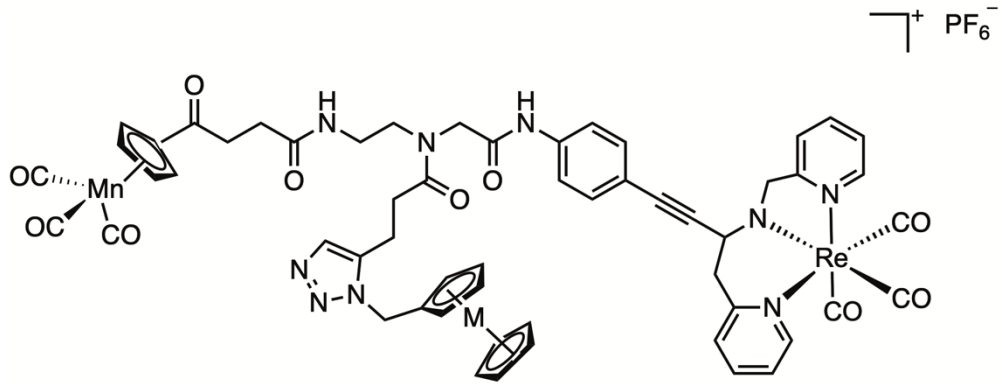


Figure 5. Structure of hetero-tri-nuclear FC-PNA, M=Fe, and RC-PNA, M=Ru.

Subsequently, they investigated the mode of action of the novel trinuclear scaffolds. Antibiotic-induced changes in protein expression can provide valuable insight into

bacterial stress responses. In *B. subtilis*, established proteomic response libraries enable comparison of the profiles of structurally novel compounds with those of antibiotics with known mechanisms of action. Mechanism-specific patterns of marker proteins, known as proteomic signatures, can therefore help to identify the likely cellular target or affected pathway of new antibacterial agents.[101] To gain initial insight into the bacterial target of **FC-PNA** and **Rc-PNA** in *B. subtilis*, global proteome analysis was performed. The proteomic responses to **FC-PNA** and **RC-PNA** treatments exhibited similar patterns, with affected protein expressions grouped into three categories: cell envelope stress, energy metabolism, and general stress response. Upregulation of PspA (phage shock protein A) and NAD synthase (NadE) was attributed to the direct interaction with the membrane. The direct membrane-related mechanism was independently confirmed by high subcellular manganese content in the cellular membrane and by GFP profiling of the membrane-associated protein MinD, which showed membrane depolarisation upon treatment with both compounds. Subsequently, **FC-PNA** and **RC-PNA** treatments reduced cellular ATP content by 50% and 70%, respectively. Notably, oxidative stress increased with **FC-PNA** treatment, whereas **RC-PNA** did not. Taken together, these findings demonstrate that **FC-PNA** has a multimodal antibacterial mode of action. The target is identified as the cytosolic membrane, possibly through anchoring to the phospholipid bilayer and subsequent effects on the functions of multiple membrane-related proteins. Additionally, **RC-PNA** was found to induce oxidative stress in *B. subtilis*. Although it exhibits favourable antibacterial properties with limited cytotoxicity and low-resistance-associated mechanisms, it exhibited limited aqueous solubility, which might hinder its further applications.[102]

As one of the earliest studies in the field of metal-based antibiotics, the same group investigated the structure-activity relationships (SAR) of these rhenium complexes.[103] In the previous study, the ferrocene derivative, **FC-PNA** (**Figure 5**), was demonstrated as more potent than ruthenocene, an effect attributed to oxidative stress induction.[102] Next, they investigated whether the trinuclear structure is necessary for the potent antibacterial activity. When the [(dpa)$Re(CO)_3$] moiety was removed, the dinuclear complex did not exhibit antibacterial activity against any of the strains at concentrations up to 512 µg/mL. The mono-metallic derivative, with only the [(dpa)$Re(CO)_3$] moiety as the organometallic scaffold, demonstrated full antibacterial activity, whereas both ferrocene and $CpMn(CO)_3$ were replaced with phenyl groups. Taken together, these findings show that the ferrocene and $CpMn(CO)_3$ substituents are not required for antibacterial activity. In contrast, the [(dpa)$Re(CO)_3$] moiety appears to be essential. Notably, the alkyne-substituted Re

scaffolds exhibited no antibacterial activity up to 512 µg/mL. This suggests that the antibacterial potency arises from the combination of the [(dpa)Re(CO)$_3$] moiety and the pseudo-peptide backbone.[103]

Subsequently, Noor and co-workers developed rhenium(I) complexes bearing bioconjugated, tridentate pyridyl-1,2,3-triazole macrocycles (**Figure 6**). Although these complexes exhibited stability in the presence of histidine, they did not show promising antibacterial activity against *S. aureus* and *E.coli*. **Re1C** (**Figure 6**) and **Re1E** (**Figure 6**) exhibited only weak antibacterial activity with MIC values of 512 and 256 µg/mL, respectively. Unfortunately, in addition to the low antibacterial potency, the cytotoxicity of these compounds was not evaluated.[104]

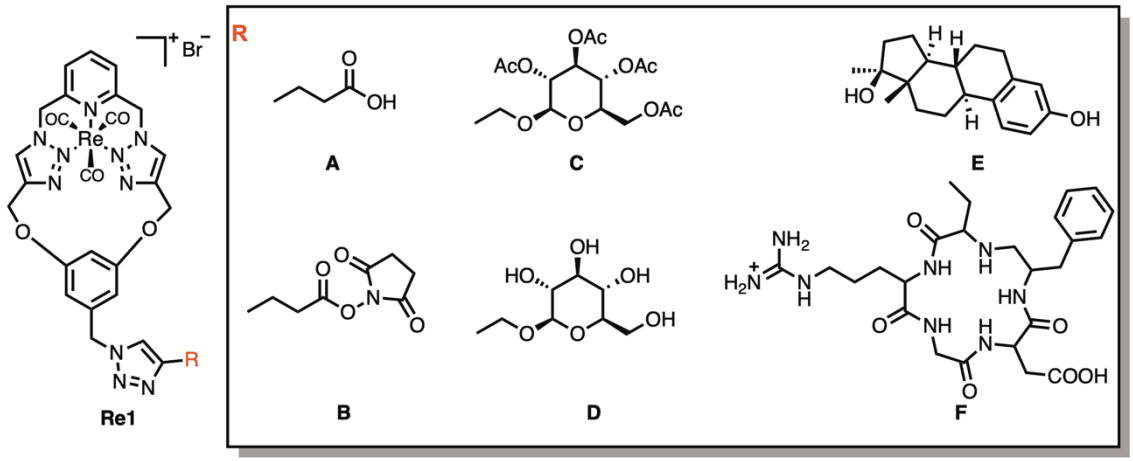
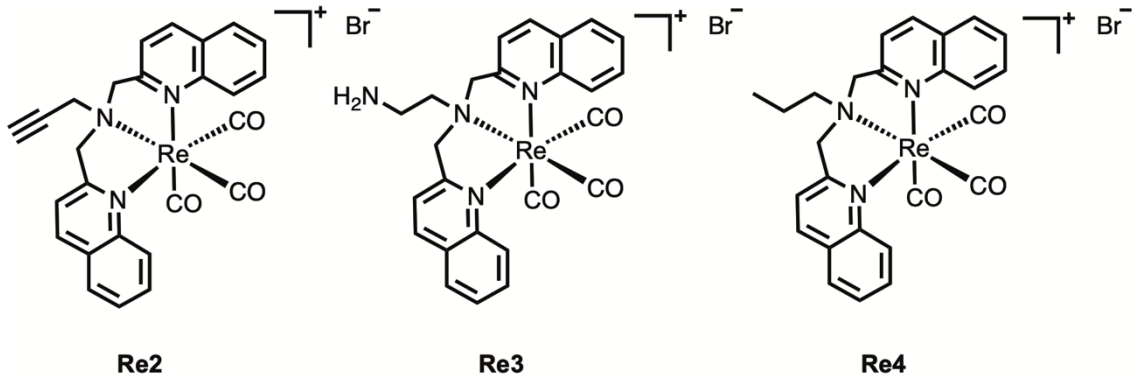


Figure 6. Rhenium(I) complexes bearing bioconjugated tridentate pyridyl-1,2,3-triazole macrocycles. The triazole moiety was modified with different groups (A-F)

Although rhenium complexes bearing macrocyclic moieties did not show promising antibacterial activity, **[(dpa)Re(CO)$_3$]** was previously demonstrated as a promising antibacterial scaffold. Building on these previous findings, Frei and co-workers have investigated the light-activated antibacterial activities of three rhenium complexes (**Figure 7**).



Re2 **Re3** **Re4**

Figure 7. Reported light-activated rhenium bisquinoline tricarbonyl complexes (Re2–Re4) by Frei and co-workers.

The complexes exhibited moderate antibacterial activity, with MIC values of 11.6 μM (**Re2**), 46.2 μM (**Re3**), and 2.9 μM (**Re4**) against *S. aureus* ATCC 25923. Subsequently, the complexes were irradiated at 365 nm for 1 hour. Upon irradiation, the antibacterial potencies of the complexes markedly increased, with MIC values of 0.72–1.45 μM for **Re2**, 5.8–11.6 μM for **Re3**, and 0.36–0.72 μM for **Re4**. Notably, no activity was observed against *E. coli* in the dark up to 93 μM. However, **Re2** exhibited enhanced activity, with an MIC value of 5.8–11.6 μM. In contrast, **Re3** and **Re4** showed only weak activity under the same conditions. As selectivity against bacteria rather than mammalian cells is essential for antibacterial development, the cytotoxicity and hemolytic activity of these rhenium complexes were also investigated. Among the three complexes, **Re2** displayed the most favorable overall biological profile. In the absence of irradiation, **Re2** exhibited moderate cytotoxicity toward human embryonic kidney cells, with a CC_{50} of 59.9 ± 9.2 μM, and no hemolytic activity was detected up to 300 μM. Upon irradiation, cytotoxicity increased, as indicated by a reduced CC_{50} of 19.1 ± 5.7 μM. Nevertheless, under light-irradiated conditions, **Re2** remained more active against bacteria than against mammalian cells, showing approximately 13–26-fold selectivity against *S. aureus* and 1.5–3-fold selectivity against *E. coli*. They also investigated the potency of the compounds against the *E. coli tolC* mutant strain lacking the main multidrug efflux pumps[105], and the *lpxC* mutant strain lacking an enzyme in the biosynthesis of lipid A, which is essential for outer membrane integrity.[106] Under light irradiation, **Re2** exhibited a MIC of 2.9 μM, which is attributed to the compound reaching an effective intracellular concentration in the absence of efflux pump activity. Subsequently, cellular uptake studies with ICP-MS showed that the intracellular accumulation of the rhenium complex is generally correlated with the antibacterial potency. In the *E. coli lpxC* mutant strain, only a small increase in total intracellular accumulation was detected compared with the

wild-type strain. Although the MIC under light irradiation improved from 8–16 μg/mL in the wild-type strain to 1–4 μg/mL in the *lpxC* mutant, the modest change in uptake might not be attributed directly to the difference in MIC values. In contrast, the *tolC* mutant showed a much greater increase in intracellular accumulation, consistent with the improved MIC values. The distribution of rhenium between the lysate and pellet fractions in the *tolC* mutant was also similar to that observed in *S. aureus*, in agreement with their comparable antibacterial susceptibility. Across the *E. coli* mutant strains, increased intracellular concentration of compounds generally coincided with increased membrane-associated compounds. These findings suggest that the rhenium complex can exert activity against *E. coli* both in the dark and upon irradiation, but that in the wild-type strain, *tolC*-mediated efflux prevents sufficient accumulation for the light-independent mechanism to become effective. In addition to the photodynamic action of the compounds, co-administration of the complexes with sublethal concentrations of the membrane-targeting antibiotics polymyxin B and octapeptin C4 resulted in a synergistic increase in antibacterial potency. Given this relatively high toxicity against mammalian cells, it may indicate an additional membrane-related mechanism of action.[107]

The potency of the ***fac*-[Re(CO)$_3$]** scaffold was further demonstrated by Zobi and co-workers. A series (57 complexes) of Re diimine (NN) complexes was investigated as potential antibacterial compounds. Several rhenium(I) complexes (**Figure 8**) exhibited strong activity against *S. aureus* strains, including MRSA. Among these, **Re5** and **Re6** were the most potent against MRSA, with therapeutic index (the ratio of CC_{50} value against control cell line and MIC against target bacteria) values of 47 and 24, respectively. These complexes were active in the low micromolar range, with MIC values down to 0.4 μM. Notably, their activity was reported to be up to 15-fold greater than that of linezolid and approximately 2-fold greater than that of vancomycin. Subsequently, the *in vivo* hepatotoxicity of the most potent compounds (**Figure 8**) was evaluated in transgenic zebrafish embryos with fluorescently labelled livers. Embryos were exposed to 0.5 x MIC, 1 x MIC, and 2 x MIC doses from 72 to 120 h post-fertilisation, and liver damage was evaluated by measuring liver area, liver fluorescence, necrosis, and yolk consumption. Notably, **Re5**, **Re6,** and **Re8** at 8–32x MIC and Re9 at 17x MIC did not exhibit toxicity. In contrast, **Re7** showed cardio- and hepatotoxicity above 25 μM.

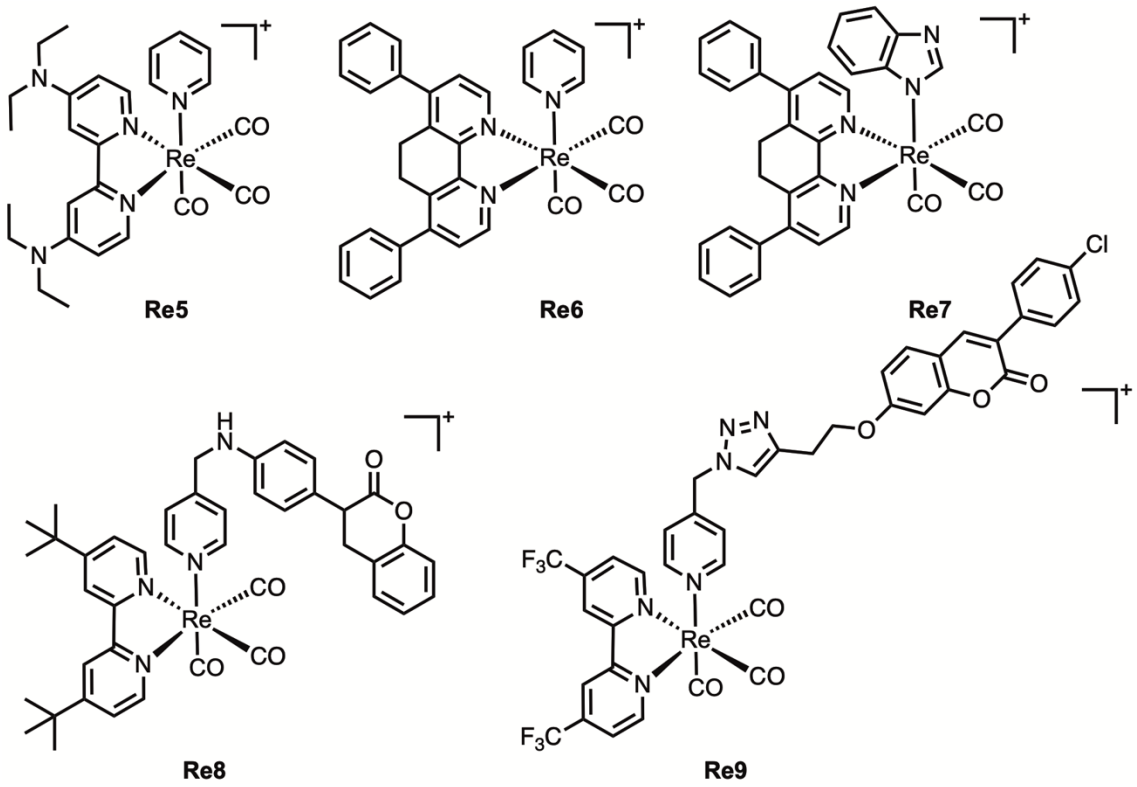


Figure 8. The most promising rhenium diimine complexes among 57 compounds investigated by Fabio Zobi's group. The counterion was omitted in the paper.

Overall, these results suggest that the majority of the selected hit complexes possess a favourable *in vivo* toxicity profile. Additionally, these complexes showed potency against *Candida albicans* and MRSA co-infection model. Taken together, this study reveals rhenium complexes as promising candidates for metallantibiotics, showing potent activity against MRSA and a favourable *in vitro* and *in vivo* toxicity profile. Selected complexes exhibited nanomolar antibacterial activity against MRSA, while most compounds showed limited hepatotoxicity in zebrafish embryos, even at concentrations above their MIC values. In addition, the SAR indicated that cationic complexes bearing lipophilic bidentate ligands were particularly associated with improved antibacterial potency. This may arise from enhanced interactions with the negatively charged bacterial envelope, increased cellular uptake, or improved membrane association. To establish a more comprehensive cytotoxicity profile, these complexes should be further evaluated across multiple cell lines, particularly for nephrotoxicity. In addition, further mode of action studies are required to identify the cellular targets and molecular pathways responsible for the antibacterial activity of this compound class.[108]

In 2022, Cooper and coworkers investigated the antibacterial activity of a new class of rhenium(v) complexes bearing bis(disphosphine) ligands (**Figure 9**) against Gram-

positive and Gram-negative bacteria. Antibacterial studies revealed that Re(v) compounds exhibited various levels of activity. Complexes bearing an acidic moiety exhibited moderate antibacterial potency, with MIC values between 16–32 μg/mL. When the acidic moiety was replaced with an alkyl group, activity increased, but the extent depended on the structure. The alkyne (**Figure 9**, **Re14**) and methyl (**Figure 9**, **Re15**) moieties showed the lowest activity in the alkyl series, with MIC values of 4 and 2 μg/mL, respectively. The rest of the alkyl series showed MIC values lower than 0.25 μg/mL. Subsequently, the cytotoxicity of the compounds was evaluated against HEK293 (Human Embryonic Kidney cell line) cells, and apart from a few exceptions, high antibiotic potency was correlated with high cytotoxicity. **Re11** (**Figure 9**) and **Re14** (**Figure 9**) exhibited favourable cytotoxicity, with a therapeutic index higher than 128.[109] Although this compound class revealed promising compounds, further SAR and modes of action should be investigated.

Building on this, recently, Zobi and co-workers studied the antibacterial potency of oxo-rhenium(v) complexes bearing diimine ligands (**Figure 10**). They revealed that complexes with a bipyridine ligand system (**Re24**–**26**, **Re32, Figure 10**) showed antibacterial activity up to 128 μM. On the other hand, **Re28**–**31** exhibited promising Gram-positive antibacterial activity against MSSA and MRSA, with MIC values of 16,32, 2, and 16 μM, respectively. Complexes exhibited little to no activity against *E. coli*, with a maximum MIC of 64 μM. Subsequently, the cytotoxicity of the complexes was evaluated against L929 cells, revealing that the active complexes were also cytotoxic against mammalian cells. Notably, **Re30** exhibited a therapeutic index of 4.9. Further, the authors investigated *in vivo* toxicity using the *Artemia salina* model, a species of brine shrimp, and demonstrated that even at 4x MIC concentration (8 μM), **Re30** exhibited only 12.9 ± 1.0% mortality. Additionally, **Re30** increased the potency of ampicillin against MRSA; co-administration with 0.5xMIC resulted in a significant growth delay when treated with 0.0625xMIC ampicillin. It was suggested that **Re9** binds resistance-related proteins, based on docking studies.[110] Together, this study further demonstrated the potential of rhenium(v) oxo complexes as antibacterial scaffolds. However, the mechanistic claims for amphicilin potentiation should be further confirmed with wet-lab experiments.

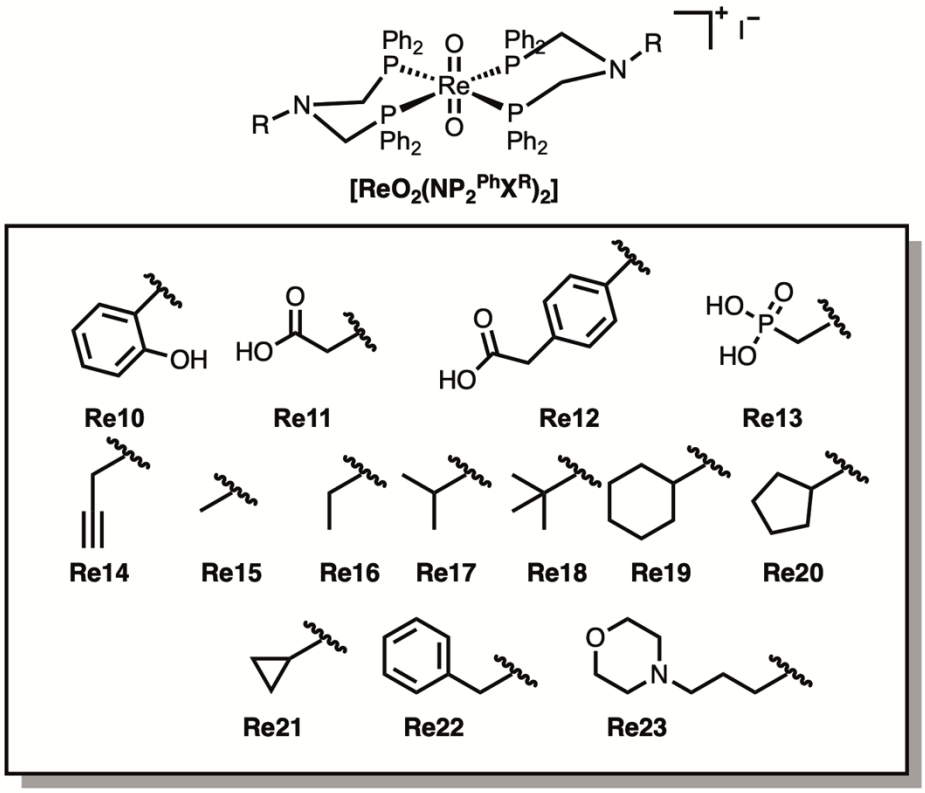


Figure 9. Rhenium(v) complexes bearing bis(disphosphine) ligands were reported by Cooper and co-workers.

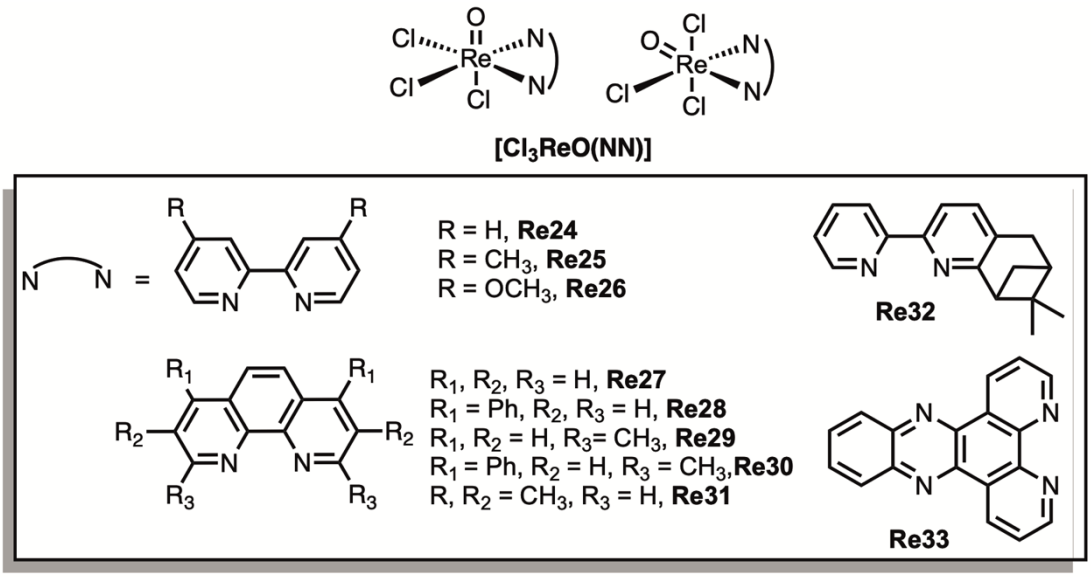


Figure 10. Rhenium(v) complexes bearing diimine ligands reported by the Zobi and co-workers.

Mendes and co-workers established clotrimazole-bearing rhenium (**Figure 11**) and manganese complexes as potential antibacterials. The clotrimazole (Ctz) derivative

exhibited high potency, with a MIC value of 0.5 µg/mL. When the clotrimazole group was replaced with bromine, this change was detrimental to antibacterial activity, and the corresponding analogue did not inhibit the growth of *S. aureus* at concentrations up to 32 µg/mL. The same trend was also observed against the extended Gram-positive panel. The Ctz derivative showed an MIC of 0.25 µg/mL against *B. subtilis* 168CA and MIC values between 0.25 and 2 µg/mL against different *S. aureus* strains and *Enterococcus faecium.*

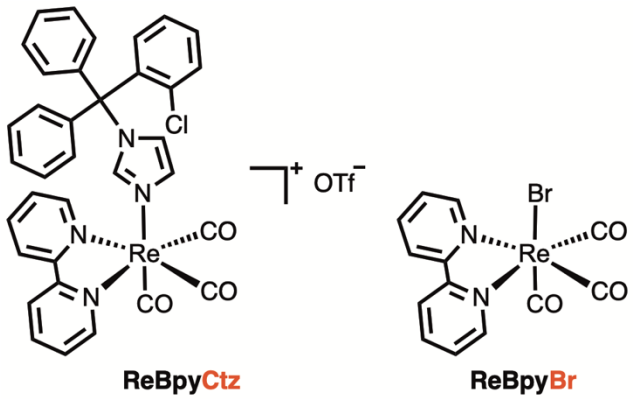


Figure 11. Rhenium complexes reported by Mendes and co-workers. To assess the effect of clotrimazole (Ctz), they also synthesised and subsequently tested the bromine analogue.

The bromine analogue (**ReBpyBr**) did not exhibit antibacterial activity up to 32 µg/mL. However, the enhanced potency associated with Ctz incorporation was not selective to bacteria and was also reflected in cytotoxicity assays in mammalian cells. **ReBpyCtz** (**Figure 11**) showed an IC_{50} value of 1.4 ± 0.4 µM against the HepG2 human hepatic cancer cell line, and 2.0 ± 0.4 µM against the LLC-PK1 porcine kidney cell line. By comparison, **ReBpyBr** (**Figure 11**) showed an IC_{50} value of 31.1 ± 11.0 µM against HepG2 and 16.4 ± 8.3 µM against LLC-PK1. Free Ctz showed IC_{50} values of 29.2 ± 21.9 µM against HepG2 and 11.6 ± 3.2 µM against LLC-PK1. Further, the antibacterial mode of action of these compounds was investigated. Upon the treatment of *S. aureus* with **ReBpyCtz**, the morphology of the cytoplasmic membrane was immediately disturbed. Although severe membrane depolarisation was observed, there were no signs of large pore formation, as demonstrated by the propidium iodide uptake assay. In addition to severe membrane damage, it was demonstrated that **ReBpyCtz** inhibited peptidoglycan synthesis via binding lipid-bound peptidoglycan precursors.

The antibacterial activity of **ReBpyCtz** was shown to involve a sequential process that begins with rapid, efficient insertion into the bacterial membrane, followed by a pleiotropic mechanism. This mechanism includes disruption of the cytoplasmic membrane,

inhibition of peptidoglycan biosynthesis, release of carbon monoxide, and collapse of the membrane potential. Together, these effects result in bacterial killing at substantially lower concentrations than those required for free clotrimazole. Overall, the enhanced antibacterial potency of the **$[Re(CO)_3(L\text{-}L)]^+$** fragment may represent a useful strategy for improving antibacterial potency and addressing resistance in clinically relevant pathogens.[111] Recently, the antibacterial potency of this scaffold was further investigated[112–114] , and our mechanistic studies of rhenium carbonyl scaffolds also revealed a membrane-targeting mechanism.[114]

1.8.2 Ruthenium complexes

Among transition-metal complexes, ruthenium-based compounds have attracted significant attention in medicinal inorganic chemistry. This interest can be attributed to several favourable properties, including their ability to bind nucleic acids and proteins, ligand-exchange kinetics comparable to those of platinum complexes, and iron-mimicking behaviour in biological systems. In addition, ruthenium complexes commonly access Ru(II) and Ru(III) oxidation states and often adopt octahedral geometries, which provide relatively stable coordination environments. The luminescent properties of many Ru(II) complexes also enable the investigation of cellular uptake and localisation using techniques such as confocal microscopy and flow cytometry.[115]

Over the years, various ruthenium complexes have been investigated as potential antibacterial agents.[115–133] Rather than discussing all reported examples in detail, the following section focuses on selected representative complexes that illustrate key SAR, biological activity, and proposed mechanisms of action.

The seminal work by Collins and Keene investigated the antibacterial properties of polypyridylruthenium(II) complexes (**Figure 12**). Kinetically inert mono- and oligonuclear ruthenium(II) complexes, including di-, tri-, and tetra-nuclear complexes, with systematic variation in linker length, rigidity, and polarity. In this series, dinuclear Ru(II) complexes containing phenanthroline ligands connected by long alkyl linkers were particularly active, with MIC values of 1–8 μg/mL against *S. aureus*, 4–16 μg/mL against *E. coli* and 8–128 μg/mL against *P. aeruginosa*. The highest potency against *P. aeruginosa* was demonstrated with the complexes with C_{14} and C_{16} linkers and decreased gradually with the chain length, which was completely lost (>128 μg/mL) with the alkyl linkers shorter than C_7.. The most potent antibacterial activity was observed with the C_{12}–C_{16} alkyl linkers. The increasing chain length was also associated with enhanced hemolytic

activity against human red blood cells. The HC_{50} value (concentration necessary to heamolyse 50% of the cell population) decreased gradually from the complex with the C_7 chain to the C_{16} chain. While the complex with the C_7 chain showed an HC_{50} greater than 1024 µg/mL, the complex with the C_{16} chain showed an HC_{50} of 22 µg/mL. Additionally, the same pattern was observed in cytotoxic activity against THP-1 (a human monocytic leukaemia cell line). While the C_7 complex had an IC_{50} of 400 µg/mL after 24 hours of incubation, the C_{16} complex showed an IC_{50} of 78 µg/mL under the same conditions.[123] Correspondingly, tri- and tetranuclear complexes[123], as well as dinuclear analogues bearing a labile chlorido ligand[126], also exhibited promising antibacterial activity. However, increased linker length was also associated with greater haemolytic activity and moderate cytotoxicity toward THP-1 cells. Despite these toxicity concerns, the complexes showed therapeutic indices of 10–100, depending on the bacterial strain and mammalian cell line used. Together, the highest activity was observed for the dinuclear complex with the longest bridging linker, suggesting that linker length, molecular size and lipophilicity are important contributors to antibacterial potency. The similar activity of the ΔΔ- and ΛΛ-enantiomers indicated that the mode of action is unlikely to depend on highly stereoselective interactions with chiral biological targets, such as proteins.[123,134]

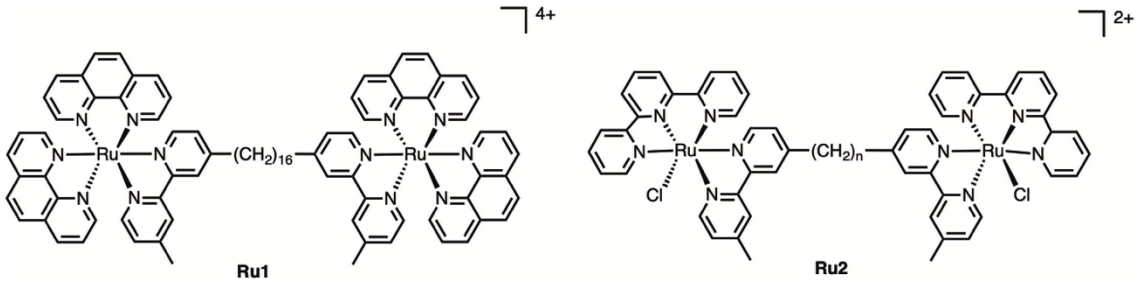


Figure 12. Dinuclear Ru(II) polypyridiyl complexes reported by Collins and Keene. **Ru1** is the most active compound against a panel of bacteria.[123] **Ru2** is the representative compound that was reported by the same group to investigate the effect of the labile chloride ligand.[126] The counterion was omitted in the paper.

Building on these findings, the Thomas group developed novel dinuclear Ru(II) complexes (**Figure 13**) and investigated their antibacterial potency against clinically critical pathogens.

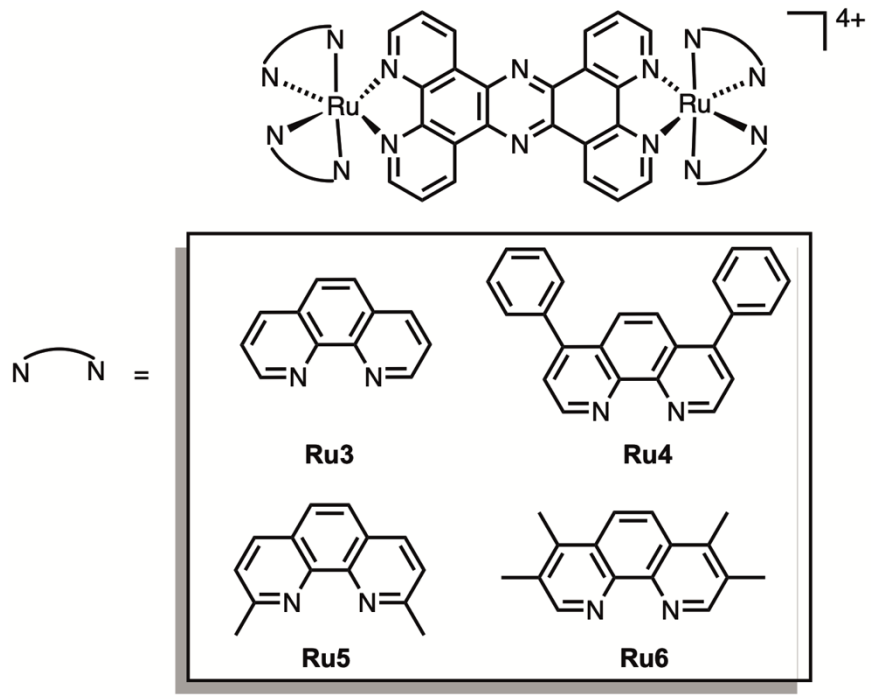


Figure 13. Ruthenium (II) complexes reported by the Thomas group. The counterion was omitted in the paper.

Antibacterial activity of the ruthenium compounds was investigated in both the Glucose-Defined medium (GDMM) and the nutrient-rich MH medium (MH-II). It was revealed that, except for **Ru4**, which had low solubility in aqueous media, antibacterial potency was correlated with lipophilicity. **Ru6** (**Figure 13**) demonstrated the highest potency, with MIC values of 5.6 μM against *E. coli* MH1655 and EC958 and 3.3 μM against *E. faecalis* V583 (in MH). **Ru6** was subsequently assessed for cytotoxicity against HEK293 cells and showed an average IC_{50} value of 135 μM. This corresponded to a minimum therapeutic index of 80. Subsequently, uptake studies in the presence and absence of glucose were performed via ICP-OES to assess the uptake mechanism of **Ru6**.The significant difference in uptake between the two conditions revealed that an energy-requiring active transport mechanism was involved in cellular uptake. Furthermore, the observed discontinuity in uptake in the absence of glucose was attributed to a potential membrane targeting mechanism, as it facilitates the passive diffusion of the compound. Cellular localisation subsequently revealed a rapid uptake of **Ru6** by *E. coli* EC958 within 20 minutes. Initially, it accumulates at cellular membranes and is distributed among cellular compartments. However, in the extended period, it is preferentially located at the cell poles. A similar localisation pattern was also observed by Collins and Keene with the oligonuclear Ru(II) complexes and attributed to localisation within RNA-rich

polysomes.[135] Further investigations with membrane permeability, depolarisation, and direct visualisation of the bacteria with a transmission electron microscope (TEM) further demonstrated that the antibacterial mode of action of **Ru6** involves a membrane-related mechanism. Based on the localisation of the compound in other bacterial compartments, it is highly likely that **Ru6** has a multifaceted mode of action.

Overall, **Ru6** has favourable biological activity, with high potency against bacteria, low cytotoxicity, and a therapeutic index of 80 or higher. Notably, **Ru6** exhibited higher activity against Gram-negative than Gram-positive bacteria, which often show reduced activity against Gram-negative species due to the additional permeability barrier provided by the outer membrane.[133] The same group further demonstrated the *in vivo* potency of this compound class as a theranostic agent against resistant *A. baumannii* infection.[136]

Subsequently, the further biological characterisation of **Ru6** was investigated by the same group. Initially, the compound's potent activity against an extended panel of Gram-negative bacteria was demonstrated. It exhibited MIC values of 1.1–4.2 μM against resistant strains and clinical isolates. Then, the evaluation of resistance in *E. coli* EC958 was performed, and within five weeks of exposure, the compound's MIC increased 4- to 8-fold, indicating the emergence of moderate resistance. Notably, after each treatment, the bacteria were cryopreserved, and upon revival of these stocks, the MIC returned to the wild-type value. This was attributed to the minor resistance formation resulting from increased efflux pump expression or altered membrane permeability, rather than a mutational change. Subsequently, transcriptomic analysis was performed to elucidate the antibacterial mechanism of **Ru6** (**Figure 13**). It revealed that **Ru6** altered the expression of genes associated with damage to the outer and inner membranes and periplasmic stress.[131] The same group further demonstrated the potency of this compound class against UTI-associated pathogens.[119] **Ru6** (**Figure 13**) is currently being advanced through preclinical evaluation by MetalloBio.

Jeannine Hess and coworkers recently established Light-Activated Metal-Dependent Protein Degradation (LAMP-D), a ruthenium-based photocatalytic strategy designed to target New Delhi metallo-β-lactamase 1 (NDM-1), a broad-spectrum metallo-β-lactamase enzyme expressed by Gram-negative bacteria.[130,137]

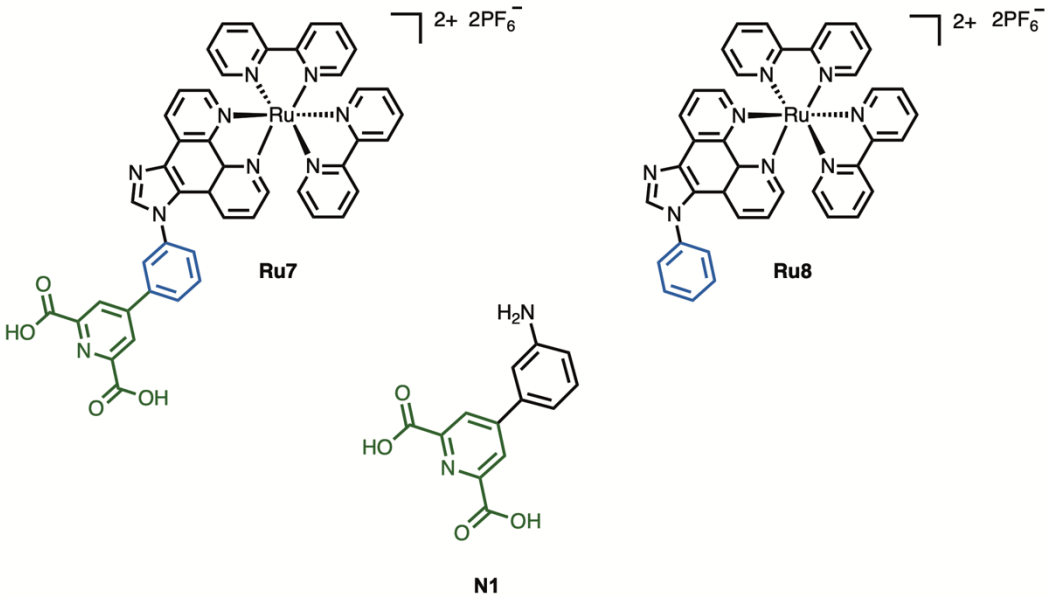


Figure 14. Heterobifunctional ruthenium complex (**Ru7**), a metal-based protein-targeted photosensitizer reported by Jeannine Hess's group. The NDM-1-bound part was highlighted in green, and the linker was highlighted in blue. **Ru8** is the control photosynthesizer without the targeting group.[130] N1 is NDM-1 inhibitor 4-(3-amino-phenyl) dipicolinic acid.[138]

This strategy was inspired by proteolysis-targeting chimaeras (PROTACs), which are bifunctional molecules that bring a protein of interest into proximity with an E3 ubiquitin ligase, leading to ubiquitination and proteasomal degradation.[139] However, because bacteria lack the classical ubiquitin-proteasome system, LAMP-D replaces E3 ligase recruitment with a ruthenium-based photosensitiser that induces light-triggered protein degradation. **N1** (**Figure 14)** was utilised as the targeting vector because it binds the protein of interest (NDM-1) via interactions with the two active-site Zn(II) ions rather than sequestering them.

The inhibitory activity of **Ru7** against NDM-1 was initially compared with that of **N1** and **Ru8**, revealing 100- and 25-fold improvements in potency, respectively. It was revealed that **Ru7** inhibited NDM-1 in the dark, with an IC_{50} of 22 ± 1.5 μM. Upon irradiation, potency increased 30-fold, with an IC_{50} of 0.75 ± 0.054 μM. Notably, the control complex **Ru8** exhibited no *in vitro* enzyme-inhibitory activity. They further demonstrate the activity of the targeted complex by rescuing the β-lactamase antibiotic meropenem using a checkerboard MIC assay against *E. coli* with NDM-1 and a control strain.

It was demonstrated that **Ru7** can inhibit NDM-1 in living bacteria and restore the antibacterial activity of meropenem against *E. coli*. In the dark, treatment with 160 μM **Ru7** increased the meropenem activity 9-fold, whereas light irradiation increased it 53-fold at the same **Ru7** concentration. Notably, **N1** also demonstrated a 43-fold increase

in meropenem potency. Therefore, **Ru7** provided a modest improvement over the free targeting group.

Nevertheless, this work demonstrates the potential of metal complexes as chemical tools to overcome beta-lactamase-mediated antibiotic resistance, one of the most clinically important mechanisms of resistance in Gram-negative bacteria.

Recently, the same group reported the rational design of ruthenium-based bacterial type IIA topoisomerase inhibitors, **Ru9** and **Ru10** (**Figure 15**). Gepotidacin (**Figure 15**) received FDA approval in 2025 for the treatment of uncomplicated urinary tract infections (cUTIs)[140] and is currently under investigation for the oral treatment of uncomplicated urogenital gonorrhoeae (uUGC).[141] Its structure can be divided into three main parts: the left-hand side (LHS) intercalates DNA, the right-hand side binds the hydrophobic protein pocket, and the linker connecting these functional domains.[142] In this design of **Ru9** and **Ru10,** a tris-heteroleptic Ru(II) polypyridyl scaffold with a DNA-binding ddpz ligand, a bpy ligand, and a topoisomerase-binding motif[143] was utilised, inspired by the well-established DNA-binding activity of similar Ru complexes.[144,145]

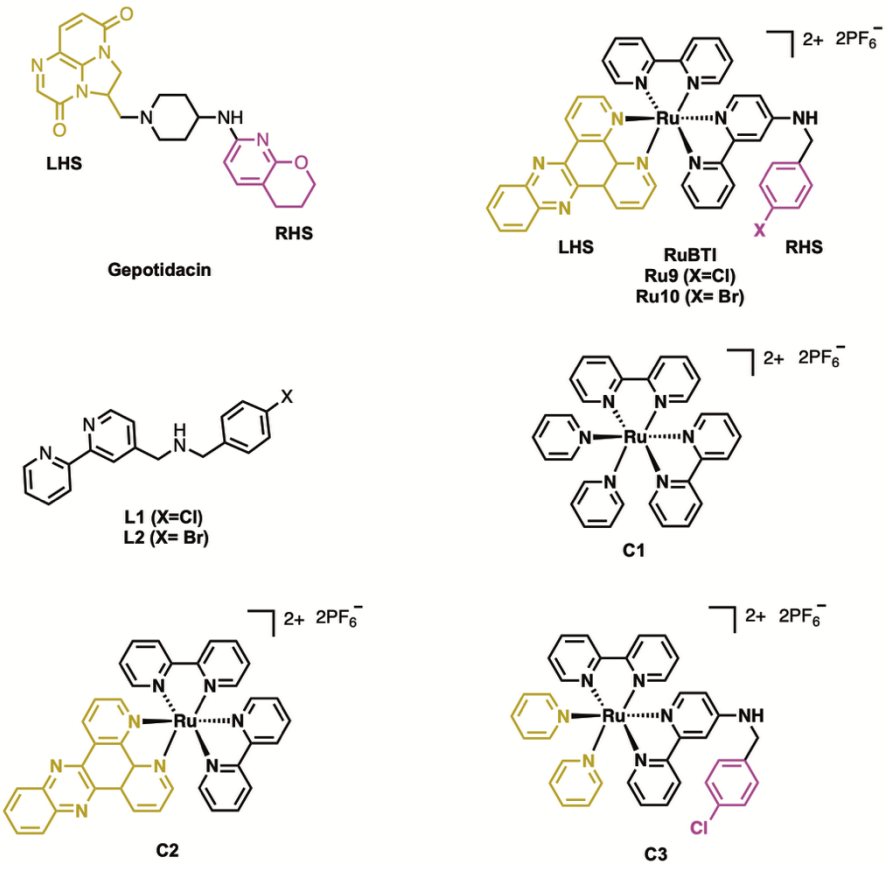


Figure 15. The design of RuBTIs (ruthenium-based bacterial type IIA topoisomerase inhibitors) and control compounds reported by Hess and co-workers. Gepotidacin has three main domains: a DNA-intercalating unit, LHS (highlighted in yellow), a protein-binding motif, RHS (highlighted in purple), and a linker. The design of the **Ru9** and **Ru10** was inspired by gepotidacin. Control compounds: **L1** & **L2** for the ligand, C1 without any targeting vector, **C2** with only a DNA-intercalating vector, and **C3** with only the protein-binding motif.

Initially, the antibacterial potency of the compounds **Ru9** and **Ru10** (**Figure 15**) was evaluated against an expanded panel of *S. aureus* strains, including MRSA. **Ru9** (**Figure 15**) exhibited potent antibacterial activity against the bacterial panel, with MIC values ranging from 6.25–31.3 μM. **Ru10** has MIC values of 1.9–15.6, demonstrating the same range of antibacterial potency, with a slight increase. Relatively higher MIC values against *S. aureus* 1199b were observed, which can be attributed to the overexpression of the NorA efflux pump in the corresponding strain.[146] NorA is one of the major efflux proteins in *S. aureus,* facilitating the active transport of hydrophilic fluoroquinolones from the cell,[147,148] and inhibition of this protein was associated with increased activities of levofloxacin and ciprofloxacin.[149] Notably, none of the control compounds, **L1** and **2** and **C1**–**C3** showed significant antibacterial activity. The antibacterial potencies of **Ru9** and **Ru10** were further demonstrated against clinical isolates of *S. aureus,* including methicillin- and fluoroquinolone-resistant strains. Subsequently, the authors

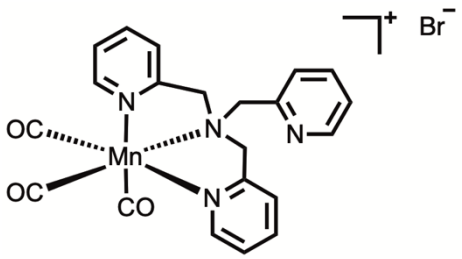
demonstrated the intracellular localisation of the compounds, consistent with a cytoplasmic target. Next, the target engagement of the designed complexes was studied. It revealed that **Ru9** and **Ru10** had strong potency to inhibit *S. aureus* TopoIV, with IC_{50} values of 6.0 μM and 5.0 μM, respectively, and demonstrated potency against *S. aureus* DNA gyrase, with IC_{50} values of 63 and 31 μM, respectively. Subsequently, DNA cleavage assays revealed that **Ru9** and **Ru10** induced single-strand DNA breaks, which were associated with novel bacterial topoisomerase inhibitors. It is one of the first proofs of concept demonstrating that rationally designed metal-based compounds can mimic the mode of action of their organic analogues. Transcriptomic profiling of 120 significantly differentially expressed genes revealed further insights about the antibacterial mode of action of **Ru10**. Several DNA damage-associated genes (*recA*, *lexA*, *uvrA*, *uvrB*, and *uvrC*) and DNA repair genes *polA* and *recN* were upregulated. Consequently, similar transcriptomic profiling was observed with ciprofloxacin treatment, suggesting that DNA damage is the primary contributor to its antibacterial potency. However, **Ru10** appeared to trigger a broader downstream response, underscoring a potentially more pleiotropic mode of action. In addition to DNA SOS response genes, DNA gyrase subunit genes (*gyrA* and *gyrB*) were upregulated, whereas the topoisomerase IV genes (*parC* and *parE*) were downregulated. It also revealed a substantial difference compared to ciprofloxacin-treated cells. This difference might be attributable to differences in binding to DNA gyrase and topoisomerase IV. Notably, along with genes related to the general stress response, including heat shock proteins and chaperones, genes associated with cytosolic membrane charge and lipoteichoic acid synthesis were also upregulated. It indicates that membrane damage might serve as a secondary mechanism contributing to antibacterial potency and potentially as a tolerance mechanism. The authors further investigated resistance induction by isolating *S. aureus* mutants on agar plates containing 5x- and 10x-MIC concentrations of **Ru10**. It revealed that these strains exhibited a 4-fold higher MIC than the wild type. The genomic analysis of the mutant strains demonstrated changes in cell-wall architecture, adhesion, and host interactions rather than mutational alterations in cytoplasmic targets. As a final proof, crystallisation of the ternary complex of **Ru9** and **Ru10** with DNA gyrase and DNA indicated that the binding of these complexes is very similar to that of gepotidacin.[118]

This study demonstrated that rationally designed metal-based compounds recapitulate mechanisms commonly associated with conventional antibiotics and can overcome antibiotic resistance.

1.8.3 Manganese complexes

Manganese is one of the essential trace metals in the metabolism of various organisms, serving as a cofactor for several enzymes involved in phosphorylation, hydrolysis, carbon metabolism, and oxidative stress response.[150,151] Over the years, manganese complexes have been investigated as antibacterial scaffolds with diverse ligand systems, oxidation states, and mechanisms of action.[100,103,111,152–161]

The seminal work by the Schatzschneider group reported a manganese-based photoactivatable CO-releasing molecule (PhotoCORM). CORMs are CO-delivering prodrugs, commonly based on transition-metal carbonyl scaffolds, that enable controlled release of CO under defined conditions and have been widely used to investigate the biological and therapeutic potential of CO.[162] Since the first report of CO-releasing molecules (CORMs) by Motterlini and co-workers in 2002, these compounds have been widely used as chemical tools for the controlled delivery of carbon monoxide. In this study, a relatively dark, stable, tris(2-pyridylmethyl)amine (tpa)-bearing manganese complex (**Figure 16**) was synthesised, and its CO-releasing properties were investigated. Upon irradiation at 365 nm, the UV absorption band of the complex disappeared, and no signal remained within 30 minutes. Subsequently, the CO release was further proven in the presence of myoglobin (Mb).



Mn-CORM

Figure 16. Mn-CORM reported by the Schatzschneider group.

After myoglobin and the compound were co-incubated for 16 hours in the dark, upon irradiation, the absorption bands at 540 and 577 nm, which are correlated with MbCO, increased and the band at 557 nm, which is Mb, disappeared, which was attributed to the release of CO from the complex and transfer to the iron centre of the haem group. The authors demonstrated that all three CO groups were successfully transferred. However, when they decreased the pre-incubation to 1 hour, only 2 equivalents of MbCO per manganese complex formed. It indicates that the third CO requires a different, longer, and more time-consuming mechanism for release. Subsequently, the uptake of the

complex into *E. coli* was investigated by ICP-MS, which revealed that the concentration remained at 10 μM for 20 minutes and increased to 85 μM over 80 minutes. Notably, the compound did not cause bacterial growth inhibition in the dark. Upon irradiation, a slight decrease in absorbance was observed. To verify the compound's efficacy, an *E. coli* culture was exposed to CO gas for an extended period, revealing that the growth inhibition was less effective than that of the compound treatment.[159] Together, the authors synthesised the first Mn-based CORM and proved that it can efficiently release CO upon irradiation and exhibit antibacterial activity.

Subsequently, the same group expanded the study to gain deeper insights into the antibacterial mechanism of action of **Mn-CORM (Figure 16)**. It was hypothesised that the mode of action of CORMs involves binding CO to respiratory oxidases and other heme proteins. To test the inhibitory effect of **Mn-CORM** on the oxidases, *E. coli* EC958 membrane was treated with 200 μM and exposed to a safe amount of UV light, and subsequently transferred to the oxygen electrode chamber. It was demonstrated that **Mn-CORM** markedly reduced the NADH-supported respiration rate 80% and 95% at the 50% and 15% of O_2, respectively. Notably, in the dark, **Mn-CORM** did not inhibit respiratory activity. The effect on the respiratory system was further demonstrated by proteomic profiling of two main terminal oxidases, *cyoA* and *cydA,* which were both downregulated upon treatment with **Mn-CORM**. The authors further investigated the uptake of the complex into *E. coli* EC958 via ICP-MS, and revealed that there was not a significant amount of Mn compared to untreated samples. It was hypothesised that upon entry of the Mn complex, activation and subsequent CO release rapidly export Mn-CORM. As in the previous paper, it was revealed that the CO gas bubbling did not reach the activity level of **Mn-CORM**. It was demonstrated that the Mn scaffold is important for potent activity. Next, the authors investigated a possible synergy between reactive extracellular molecules and **Mn-CORM**. The total growth inhibition of the bacteria with H_2O_2 required 10 mM, whereas this amount was reduced to 4 mM in the cultures containing a subinhibitory concentration of **Mn-CORM**. Additionally, when bacteria were treated with **Mn-CORM** in iron-depleted media, they became substantially more resistant to H_2O_2 (6–10 mM), which was attributed to decreased formation of hydroxyl radicals via the Fenton reaction. Subsequently, it was revealed that Mn-CORM and H_2O_2 upregulate the *spy* protein 14-fold, whereas H_2O_2 alone increases it only 6-fold.[156] Spy, *E. coli* spheroplat protein (*Ecspy*), is a small periplasmic protein that plays an important role in cell envelope stress. The upregulation of this protein indicates increased environmental stress.[163]

It was concluded that **Mn-CORM** induces reactive oxygen species formation in the presence of H_2O_2 through the reaction between the CO-depleted Mn scaffold and H_2O_2. It further demonstrated via hydroxyl radical-specific fluorescence dye and thiourea scavenger assay that Mn-CORM induces hydroxyl radical formation. Subsequently, the Mn-CORM enhanced the doxycycline activity in the resistant strain. In this study, the authors further revealed the mechanism of action of the previously established **Mn-CORM** system. They demonstrated that it has multifaceted action, involving bacterial respiratory chain inhibition and hydroxyl radical formation via reactions between a CO-depleted Mn scaffold and metabolism-driven or exogenous H_2O_2, thereby causing subsequent membrane damage.[156] Although the mechanistic details of the antibacterial activity of **Mn-CORM** were well-proven, a clear picture of membrane damage, perhaps through phenotypic analysis and expansion of the investigation to a wider range of bacteria, would give a clearer picture.

The same group expanded the $Mn(CO)_3$ scaffold library and synthesised complexes with an azole ligand in the axial position (**Figure 17**). The antibacterial potency of the synthesised complexes and the corresponding azole drugs (ketoconazole, miconazole, and clotrimazole) against the Gram-positive and Gram-negative panels was investigated. Except for **Mn2 (Figure 17),** all the complexes exhibited high potency against the Gram-positive panel, with MIC values ranging from 0.625 μM to 10 μM. **Mn2** showed moderate activity, with MIC values between 20 and 40 μM. However, the compounds exhibited much lower potency against Gram-negative bacteria, with **Mn3** showing an MIC of 20 μM and **Mn5** of 40 μM. Notably, the free azole drugs exhibited lower antibacterial potency than their corresponding Mn complexes. Although the complexes exhibited Gram-positive potency, they showed high cytotoxicity against HEK293T cells, with therapeutic indices between 1.1 and 3.7. Notably, free azole drugs showed much higher toxicity, with a TI found as 0.3–0.6.

Taken together, this study appeared as one of the early examples of investigating the $Mn(CO)_3$ scaffold as a potential antibacterial agent, with its selective cytotoxicity remaining open to improvement.

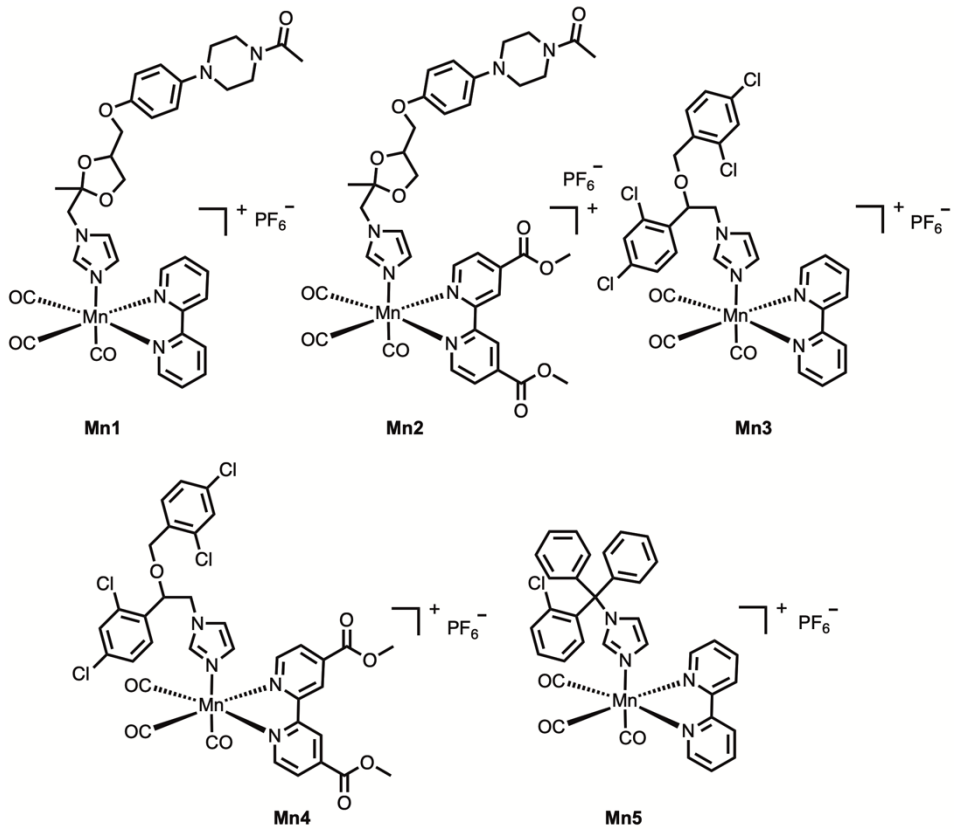


Figure 17. Mn complexes, reported by the Schatzschneider group.

In our group, a combinatorial library of 420 manganase (I) complexes were evaluated as potential antibacterials, and their initial mode of action was revelead.[161] The paper was explained in detail in the introduction of **chapter 3**.

1.8.4 Bismuth, Gallium and Silver Complexes

1.8.4.1 Gallium complexes

As mentioned earlier, metal ions have essential duties in the metabolism of almost all forms of life. One of those metals is iron, which functions as a cofactor for many important enzymes involved in cellular respiration, DNA synthesis, and ROS homeostasis in bacteria.[164,165] Given its importance, bacterial iron metabolism is an attractive target for developing antibacterial strategies. As Fe(III) and Ga(III) have similar ionic radii, bacteria cannot distinguish between them, and Ga(III) could be used to target iron-related pathways. Upon internalisation into bacteria, Ga(III) is incorporated into iron-bound enzymes, and because it cannot be reduced to the 2+ oxidation state of iron under physiological conditions, the intrinsic function of these enzymes is inhibited. $Ga(NO_3)_3$,**Ganite** (**Figure 18**), was approved by the FDA to treat cancer-associated hypercalcemia. Subsequently, Ga(III) complexes were repurposed as antibacterial

agents. In 2007, Koneko and co-workers demonstrated the antibacterial potency of **Ganite** against *Pseudomonas aeruginosa* at concentrations exceeding 1 μM. Additionally, Ganite successfully inhibited biofilm formation. Notably, both antibacterial and biofilm-inhibitory potency could be reversed by iron addition. These results led the authors to investigate the antibacterial mode of action. They demonstrated that Ga uptake interferes with Fe signalling and reduces bacterial Fe uptake. The transcriptomics analysis revealed that Ga induces downregulation of pyoverdine expression, a major transcriptional regulator of Fe uptake, thereby increasing Ga uptake and reducing Fe uptake.[166]

Subsequently, in 2008, gallium desferrioxamine, **Ga-DFO** (**Figure 18**), was investigated and shown to be a potential antibacterial agent against *P. aeruginosa.* **Ga-DFO** exhibited high potency against planktonic *P. aeruginosa*, with a MIC value of 32 μM, whereas DFO itself did not inhibit bacterial growth up to 1 mM. Further, **Ga-DFO** efficiently killed mature biofilms and caused a 3-4 fold log decrease in CFU. Additionally, the synergistic effect of **Ga-DFO** with gentamicin (Gm) was also demonstrated. While Gm alone caused a 2-log decrease, co-treatment with **Ga-DFO** resulted in a 6-log decrease in mature biofilm bacterial count. Subsequently, the *in vivo* efficacy of **Ga-DFO** and Gm combination was investigated by using a rabbit keratitis model. It revealed that **Ga-DFO** + **Gm** reduced the scratch size by 50-60% compared to Gm alone.[167] Taken together, this study revealed a novel gallium complex that can inhibit bacterial growth under challenging conditions, including mature biofilms and *in vivo* settings.

Subsequently, gallium protoporphyrine IX, **GaPPIX** (**Figure 18**), was demonstrated to have promising activity against the Gram-positive panel with MIC values between 0.031 and 0.062 μg/mL, and the Gram-negative panel with MIC values between 4 and 16 μg/mL. Notably, this Ga porphyrin analogue was found to inhibit iron metabolism through heme uptake, unlike free Ga^{3+} ions, which inhibit siderophore-mediated and Fe^{3+} uptake.[168]

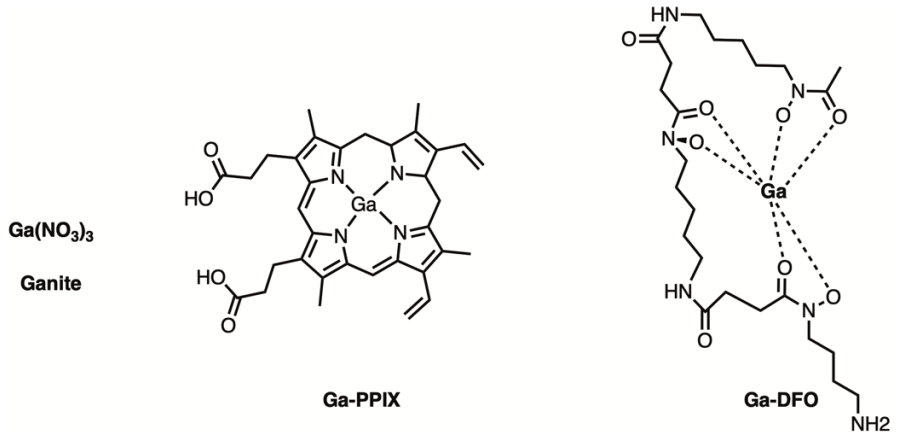


Figure 18. Selected Ga complexes utilised as antibacterial agents.

Building on these findings, a synergistic therapeutic approach using Ga complexes, Gallium protoporphyrin (**GaPP**), and **$Ga(NO_3)_3$** was also investigated. As **$Ga(NO_3)_3$** and porphyrine derivatives inhibit iron metabolism through distinct pathways, it was hypothesised that combining these Ga complexes could enhance inhibition of bacterial growth. While **$Ga(NO_3)_3$** exhibited MIC values of 1–3 μg/mL, and **GaPP** exhibited 4–16 μg/mL against *P. aeruginosa* and *K. pneumoniae*, the combination of them showed MIC values of 0.50 and 0.13 μg/mL against *P. aeruginosa* and *K. pneumoniae*, respectively. Subsequently, this synergistic effect was tested for biofilm inhibition, and at the lowest synergistic concentration (4 ng/mL **GaPP** and 0.5 μg/mL **$Ga(NO_3)_3$**), it achieved over 95% biofilm disruption. *In vivo* efficacy of this combination therapy was also demonstrated in *C. elegans* infection models with *P. aeruginosa* and *K. pneumoniae*. No survival was observed with **$Ga(NO_3)_3$** alone, and **GaPP** showed only 25% and 38% survival against *K. pneumoniae* and *P. aeruginosa*, respectively. On the other hand, the combination of 0.004 μg/mL of **GaPP** and 0.5 μg/mL of **$Ga(NO_3)_3$** exhibited 100% survival in *P. aeruginosa* infection, and the combination of 0.125 μg/mL of **GaPP** and 1 μg/mL of **$Ga(NO_3)_3$** showed 80% survival in *K. pneumoniae*.[169]

Together, **$Ga(NO_3)_3$**, and **GaPP** combination therapy demonstrated promising antibacterial potency *in vitro* and *in vivo*. Additionally, Ga-based compounds reported in the literature were appealing for their efficient antibiofilm activity and growth inhibition against the Gram-negative panel, which is generally considered challenging.

Building on these, gallium complexes began to be utilised in a Trojan-horse approach to target the bacterial iron-acquisition pathway. In 2019, the Boros group established a gallium(III) conjugated ciprofloxacin probe as a theranostic agent. The authors reported the gallium compounds with the highest bacterial potency to date, with MIC values

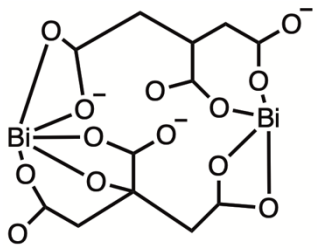
ranging from 0.94 to 12.5 μM. Additionally, a radioactive gallium isotope was used to detect accumulation *in vitro* and *in vivo*. However, there was no activity improvement of ciprofloxacin upon the gallium modification.[170] Subsequently, this approach was expanded to ciprofloxacin-salmochelin conjugate[171] and galbofloxacin.[172]

The same group revealed mechanistic insight into gallium siderophore antibacterial activity. It was demonstrated that ciprofloxacin resistance does not necessarily reduce the efficacy of the Ga siderophore ciprofloxacin probe. Together with a substantial decrease in potency with the iron analogue of this probe, it was revealed that the probe's potency arises from both ciprofloxacin and the gallium scaffold. Transcriptomic analysis following sub-MIC exposure showed that the conjugates retained an expression change profile with ciprofloxacin activity, while also affecting iron acquisition pathways.[173]

Further Ga-based combination therapies[174–176], and complexes with different ligand systems,[177,178] were developed against Gram-positive and Gram-negative bacteria.

1.8.4.2 Bismuth complexes

Bismuth is another metal with a long history of medicinal use for nearly over three centuries in the treatment of syphilis, colitis, wound infections and quartan malaria. Three bismuth drugs: bismuth subsalicylate (**Pepto-Bismol**), colloidal bismuth subcitrate (**CBS**, **De-Nol**), and ranitidine bismuth citrate (**Pylorid**) are commonly utilised in clinics as part of triple therapy with antibiotics and proton pump inhibitors to treat *H. pylori* infections.[179–181] Currently, Pylera, a single capsule with bismuth subcitrate (**Figure 19**), potassium, metronidazole, tetracycline, and omeprazole, is prescribed as the first-line treatment.[179] Bismuth complexes have been appealing for selective toxicity against bacteria, with the low toxicity against human cells attributed to effective binding of Bi to GSH, subsequent compartmentalisation into subcellular vesicles, and removal from the cell.[182] Despite its long clinical use, the mode of action of CBS remained elusive for many years. In 2007, the Sun group investigated the interactions between CBS and proteins in bacteria using proteomic profiling. It was revealed that the expression of eight proteins was altered upon the CBS treatment. They observed a 1.8-fold increase in lipid hydroperoxide expression, indicating bismuth-induced oxidative stress. Additionally, they demonstrated inhibition of certain proteases, and interference with nickel homeostasis contributes to the antibacterial potency of CBS.[183]



CBS

Figure 19. Structure of Bismuth subcritate (CBS).

Later, the same group revealed that CBS disrupts central carbon metabolism and inhibits *H. pylori* energy production.[184] Subsequently, the same group repurposed CBS, demonstrating that it can irreversibly inhibit the activity of metallo-β-lactamases (MBLs), such as New Delhi MBLs, Verona integron-encoded MBLs (VIMs), and imipenemases (IMPs). The inhibition mechanism was revealed by crystallography, which showed that one of the Zn(III) ions in the active side of MBL can be replaced with Bi(III). Additionally, it was demonstrated that CBS can restore the efficacy of meropenem in NDM-1-positive *E. coli* bacteria *in vitro* and *in vivo*. [92,179]

So far, bismuth drugs have been demonstrated to have high-potency antibiofilm activity[185], but the inhibition mechanism has never been understood. Recently, the same group demonstrated that CBS serves as an antibiotic adjuvant to combat biofilm formation by *Burkholderia cepacia*, which exhibits intrinsic resistance to many conventional antibiotics. It was revealed that CBS binds primarily to two terminal oxidases of the electron transport chain, cytochrome bo_3 ubiquinol oxidase (CyoC) and cytochrome *bd*-I ubiquinol oxidase subunit 1 (CydA). As these proteins are primarily responsible for nitric oxide (NO) detoxification in bacteria, the authors hypothesised that CBS leads to NO accumulation in bacteria. NO detection revealed that 40 μg/mL CBS induced substantial accumulation of NO in *B. cepacia*. Additionally, CBS did not significantly induce NO accumulation in *B. cepacia* overexpressing CyoC and CydA, demonstrating that the synergistic bismuth antibiofilm activity depends on the binding of these two oxidases. Additionally, the downstream effect of Bi-dependent NO accumulation was investigated. It is known that during biofilm formation, NO modulates the levels of cyclic diguanylate (c-di-GMP), which induces biofilm formation at high levels and maintains a planktonic state at lower levels.[186–188] It was demonstrated that NO accumulation decreases the level of c-di-GMP by nearly 62% in WT strain. Overall, it was further revealed that CBS can increase the efficacy of conventional antibiotics in combination therapy and inhibit biofilm formation.[189] The favourable selectivity profile of

CBS, together with its increasingly well-understood mechanism of action and its ability to inhibit MBLs and restore β-lactam efficacy, makes this compound class an attractive platform for further development.

Recently, the Sun group investigated the antibiotic adjuvant effect of CBS against *P. aeruginosa*. It was revealed that CBS exhibited synergistic activity with many clinically related antibiotics. Subsequently, the authors elaborated on the study to elucidate the mechanism of action. It was demonstrated that CBS exert its activity through a multifaceted mode of action. The transcriptome analyses revealed that treatment of *P. aeruginosa* with 16 μM CBS for 30 minutes downregulated iron uptake mechanism-related genes. Additionally, ICP-MS analysis showed a decrease in intracellular iron concentration. It was further revealed that treatment with CBS reduced electron transport chain activity by inhibiting NADH dehydrogenases and disrupting the proton-motive force. The efficacy against *P. aeruginosa* was also demonstrated in a mouse lung infection model, as it nearly 4-fold increased the potency of ofloxacin and chloramphenicol treatments.[190]

1.8.4.3 Silver complexes

The history of silver stretches back to the ancient Indian *Ayurvedic system* of medicine, dating back to 5000 A.D.[191] In ancient Greece, the practice of storing water and other beverages in silver bowls was used to prevent mould growth.[192] Medicinal applications of silver have been reported by Avicenna in 980 A.D., who used silver filings as a blood purifier and to treat offensive breath and heart palpitations.[92] Later, in the early 19th century, surgeons used silver wires to suture surgical wounds, and silver leaf was used to treat soldiers' wounds during World War I.[192] In the modern antibiotic era, although silver lost its former popularity, silver sulfadiazine, an Ag^{+}-bound sulfonamide antibiotic, has been approved by the FDA for the topical treatment of burn wounds. However, its clinical efficacy has been increasingly questioned, and subsequently, several comparative studies indicate that silver sulfadiazine does not necessarily confer greater potency than non-silver-based wound treatments. In patients with partial-thickness burns, for instance, polyhexanide/betaine gel produced similar healing times, infection rates, and overall treatment costs to silver sulfadiazine, while being associated with lower reported pain scores.[193] Similarly, a randomised clinical trial comparing Flaminal Forte with Flamazine showed no improvement in average healing time with the silver sulfadiazine formulation; instead, the non-silver treatment was considered more convenient because dressing changes were required less often.[194] These findings are

consistent with a subsequent meta-analysis, which concluded that among the eligible studies assessed, alternative burn treatments outperformed silver sulfadiazine in mean wound-healing time.[195] Overall, while silver sulfadiazine remains an established topical antimicrobial, the available clinical evidence suggests that its advantages over current non-silver approaches are limited.[92]

Although the mechanisms of action of silver-based compounds have only recently begun to be clarified, Ag^+ is generally considered the biologically active silver species. Consequently, the antibacterial activity of these compounds is primarily influenced by how Ag^+ is delivered to the biological environment. [192,196] It has been demonstrated that silver has a multifaceted antibacterial mode of action; specifically, four mechanisms are often invoked: effects on the cell envelope, interactions with DNA, inhibition of certain enzymes and proteins, and oxidative stress.[134] Positively charged silver ions can bind to the negatively charged bacterial membrane, disrupting its integrity.[192] Dibrov and co-workers demonstrated that silver treatment caused the complete collapse of the transmembrane pH gradient and depolarised the membrane of *Vibrio cholerae*.[197] Similar membrane damage and leakage of cytosolic content have also been reported for cationic silver nanoparticles against *S. aureus*, alongside the inhibition of respiratory chain dehydrogenase activity and evidence of impaired DNA integrity and replication.[198] Recently, proteomics profiling and structural studies have begun to identify specific Ag^+ binding proteins. In *E. coli*, it was shown that silver can bind to various proteins involved in bacterial energy metabolism, including those involved in glycolysis and the tricarboxylic acid cycle.[199] These interactions were associated with impaired energy metabolism, suppression of oxidative stress responses, and inhibition of key enzymes, such as glyceraldehyde-3-phosphate dehydrogenase. Crystallographic studies revealed that Ag^+ targets the enzyme's catalytic site and coordinates to Cys149 and His176.[200] Subsequently, Wang and co-workers identified 38 silver-binding proteins in *S. aureus,* with glycolysis being the most affected pathway. It was revealed that Ag^+ inhibits the activity of 6-phosphogluconate dehydrogenase by binding to its catalytic site, His185, thereby causing ATP depletion.[201]

Overall, these studies indicate that Ag^+ exerts antibacterial activity through multiple mechanisms, including disruption of the cell envelope, inhibition of key metabolic enzymes, interference with nucleoid morphology and DNA replication, and perturbation of oxidative-stress responses. This multifaceted mode of action may reduce the

likelihood of resistance development compared with agents that act on a single defined target.

In recent years, silver complexes have been widely investigated in the literature as potential antibacterials. Among the silver complexes investigated as antibacterial agents, N-heterocyclic carbene (NHC) complexes have received particularly wide attention.[202] However, their biological activity is often associated with Ag+ delivery; therefore, they are not considered in detail here.

1.8.5 Other metal complexes

As discussed in the previous section, metal complexes have been widely investigated as potential antibacterial agents. While much of this work has focused on improving biological activity by modifying the ligand environment, the choice of metal centre is equally important in determining antibacterial potency, selectivity, and mechanism of action. In addition to the metal scaffolds discussed above, complexes of several other transition metals have also been explored for their antibacterial properties. To illustrate this broader chemical diversity, selected examples of transition metal complexes are discussed in this section. Back in 2004, Chen and co-workers investigated the antibacterial potency of the tungsten norfloxacin complex, **W1** (**Figure 20**). They demonstrated a slight increase in the zone of inhibition against *E. coli*, *Bacillus dysenteriae*, and *S. aureus*.[203] The Metzler-Nolte and Bandow groups studied the antibacterial activity and cellular uptake of four chromium complexes, **Cr1**–**4** (**Figure 20**), demonstrating moderate activity, with MIC values of around 150 μM.[204] Low and coworkers investigated the antibacterial potency of the copper bidentate dithiocarbazate complexes, **Cu1** (only the general structure was given, **Figure 20**), with various vectors.[205] Rhodium(II) complex, **Rh1** (**Figure 20**), was investigated as a *Streptococcus pneumoniae*-targeting antibacterial agent that acts by interfering with iron metabolism, decreasing the expression of proteins involved in heme uptake and metabolism.[206] Kalaivani and coworkers identified four palladium thiosemicarbazone complexes (**Pd1**–**4**) as promising antibacterials primarily against the Gram-positive panel and determined one of their DNA-binding properties.[207] The Thomas and Elliott groups investigated the antibacterial properties of near-IR-luminescent triazole-based osmium(II) complexes, **Os1**–**6 (Figure 20)**. **Os1** was identified as the hit compound, with an MIC of 32 μg/mL against MRSA.[208]

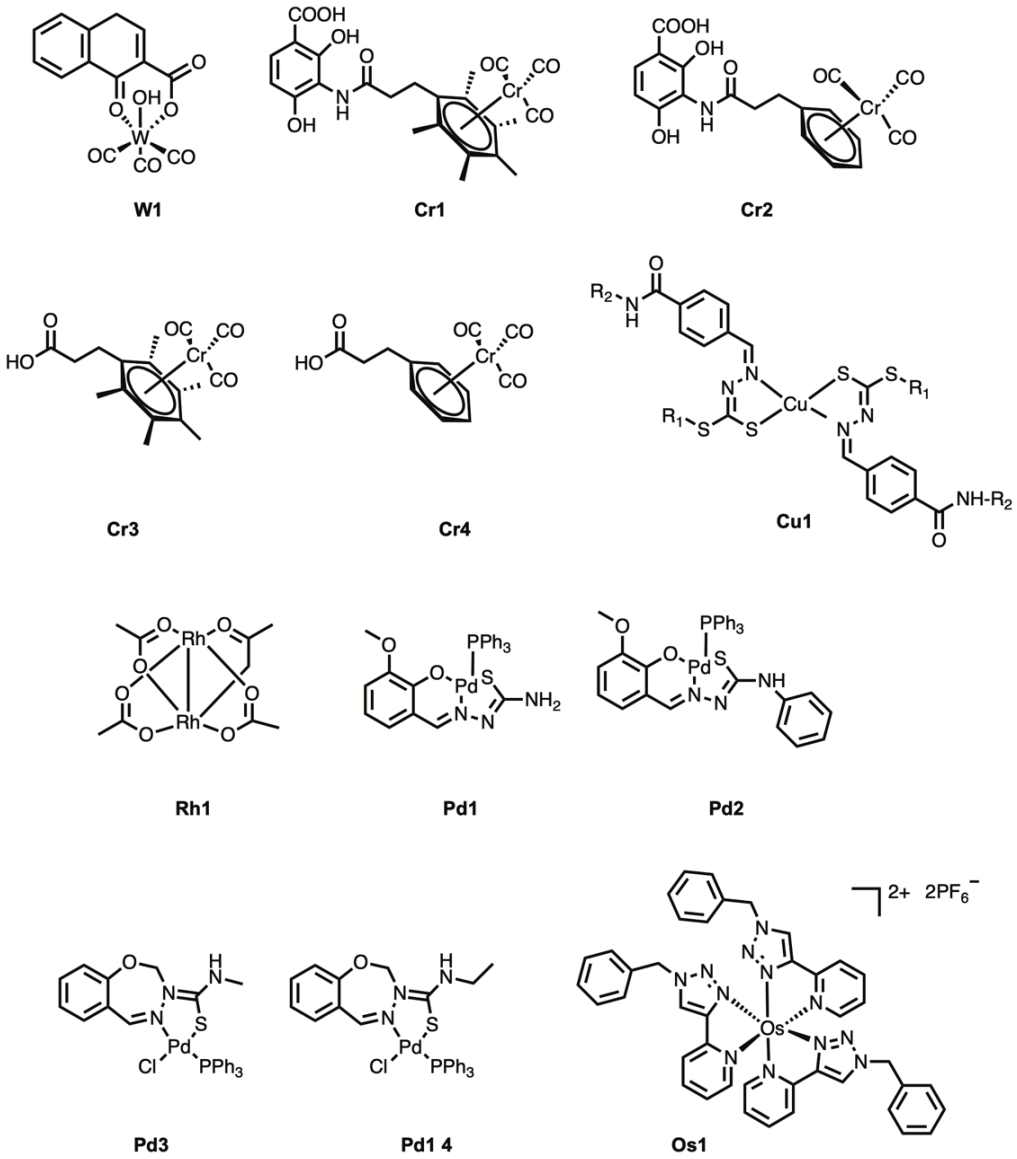


Figure 20. Selected metal complexes with different metal centres.

Metal complexes have emerged as promising antibacterial scaffolds with their favourable structural and biological properties. Several antibacterial complexes with diverse metal centres and ligand systems were reported, demonstrating the broad chemical space available for further investigation. However, many reported studies remain primarily focused on *in vitro* activity evaluation, while detailed modes of action and SAR are less frequently explored. In particular, the systematic screening of large metal-complex libraries, coupled with mechanistic studies to determine how structural features influence bacterial uptake, target engagement and downstream cellular responses, remains underdeveloped.

1.9 Aims and objectives

Antibacterial resistance is one of the major global health challenges of the 21st century, threatening the effective treatment of bacterial infections and putting increasing pressure on healthcare systems worldwide. Despite the urgent need for novel antibiotics, the conventional antibiotic discovery pipeline has not kept pace with the rapid emergence and spread of drug-resistant pathogens. This highlights the need to explore novel chemical spaces and develop workflows that enable rapid, efficient screening of large compound libraries to elucidate structure-activity relationships.

Additionally, understanding the mechanism of action of the identified scaffold paves the way for developing more efficient scaffolds. In this context, metal complexes appear as an attractive platform, offering three-dimensional structures, tunable ligand environments, variable redox properties, and the potential for multifaceted modes of action that are difficult to achieve with conventional organic molecules.

The main aim of the study was to synthesise novel metal scaffolds through conventional and combinatorial approaches to investigate them as potential antibacterial agents, to elucidate their structure-activity relationships, and to study their antibacterial mode of action.

Specifically;

- **Chapter 2** aims to evaluate novel Pt(II) compounds as Gram-positive bacteria-targeting metalloantibiotics and elucidate their SAR and mode of action.
- **Chapter 3** aims to expand the chemical space of antibacterial iridium complexes through combinatorial Schiff-base chemistry and Direct-2-Biology (D2B) approaches
- **Chapter 4** aims to further expand the chemical space of potential antibacterial iridium complexes through SuFFex click chemistry and Direct-2-Biology (D2B) approaches, and to develop novel chemical spaces as potential antibacterial agents. This chapter summarises my contributions to collaborative projects and those of a Bachelor student I supervised.

Chapter 2: A Platinum Butterfly Effect: Small Changes Turn an Anticancer Drug into a Non-toxic Metalloantibiotic with *In Vivo* Efficacy

The work presented in this chapter has been published in the following article: **Özsan, Ç**., Schäfer, AB. *et al.* A platinum butterfly effect: small changes turn an anticancer drug into a non-toxic metalloantibiotic with in vivo efficacy. *npj Antimicrob Resist* **4**, 37 (2026).

2.1 Introduction

2.1.1 Cisplatin and the rise of inorganic medicinal chemistry

The golden age of inorganic medicinal chemistry began with the approval of the first platinum-based chemotherapeutic agent, cisplatin (**CisPt**), in 1978.[209] Although cisplatin was first synthesised by Michele Peyrone in 1844[210] and its chemical structure was elucidated by Alfred Werner in 1893[211], the compound did not attract significant scientific attention until the 1960s, when Rosenberg and colleagues serendipitously discovered that certain electrolysis products of platinum electrodes inhibited cell division of *Escherichia coli*.[212,213] Afterwards, its cytotoxic properties were discovered[214], and by the end of the 1970s it had become a key component in the systemic treatment of germ cell cancers.[215] Today, platinum drugs are still used as a gold-standard first-line chemotherapy against many cancer types.[216,217]

2.1.2 Mechanism of action of cisplatin

Cisplatin uptake is governed by both passive diffusion and carrier-mediated transport through membrane-associated transport proteins (**Figure 21A).** Among these, the copper transporter CTR1 is considered a major mediator of cisplatin uptake in both yeast and mammalian cells.[218] Reduced CTR1 expression or rapid degradation of the transporter after cisplatin exposure lowers intracellular platinum accumulation and contributes to drug resistance[219], whereas elevated CTR1 levels generally correlate with increased cisplatin sensitivity.[220] Other membrane-associated proteins have also been linked to platinum resistance. In particular, overexpression of TMEM205 has been associated with reduced cisplatin susceptibility and may serve as a potential biomarker for platinum resistance.[221] Although Glut1 is not believed to directly transport cisplatin, altered localization of this transporter has likewise been reported to enhance resistant phenotypes.[221,222]

In the bloodstream, the high extracellular chloride concentration, approximately 100 mM, suppresses cisplatin aquation and helps maintain the complex predominantly in its neutral dichlorido form.[223] Following cellular uptake, cisplatin undergoes aquation reactions[224] promoted by the low intracellular chloride concentration (approx. 20 mM), resulting in replacement of the chloride ligands by water molecules and generation of highly reactive platinum species (**Figure 21A**).[223] These activated complexes readily interact with nucleophilic cellular components, particularly thiol-containing proteins[225] and nucleic acids. DNA is considered the principal intracellular target of cisplatin, with platinum preferentially coordinating to the N7 positions of purine bases. This interaction leads to the formation of several types of DNA lesions that interfere with replication and transcription. The predominant adducts are 1,2-intrastrand d(GpG) crosslinks, which account for most lesions (90%), while 1,2-intrastrand d(ApG) adducts are formed less frequently (**Figure 21B**).

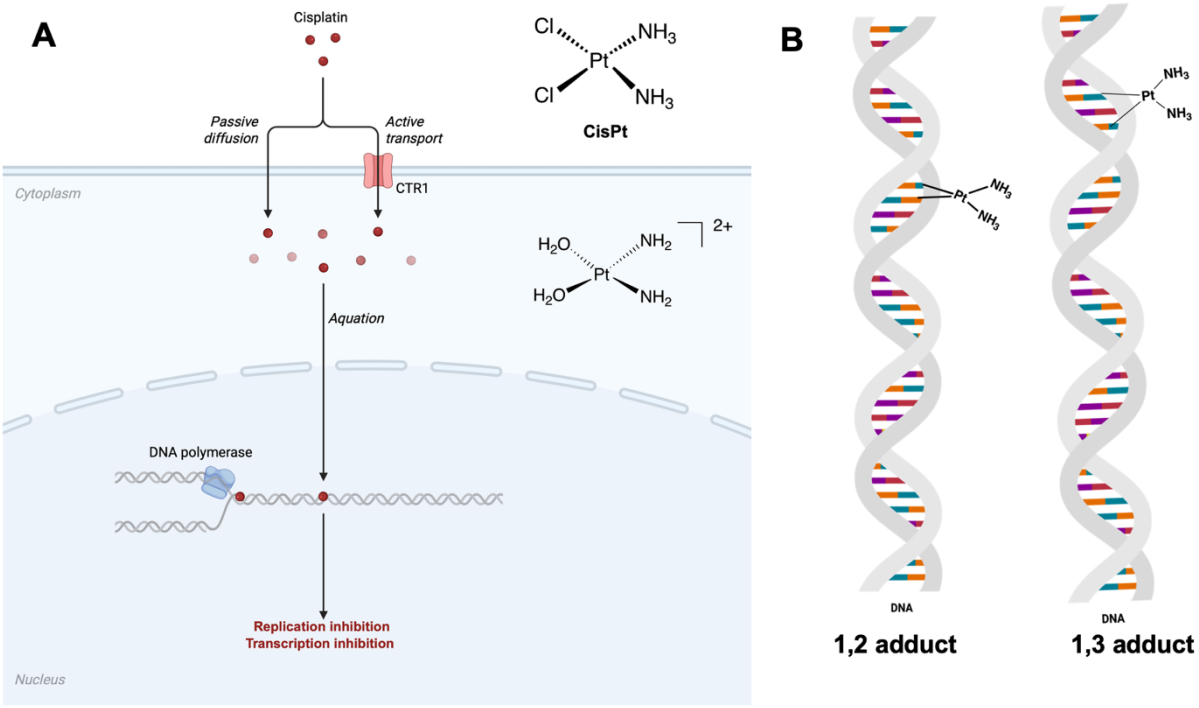


Figure 21. Cisplatin uptake is governed by both passive diffusion and carrier-mediated transport via several membrane-associated transporters. Once inside, relatively lower intercellular chloride concentration governs the aquation reaction of Cisplatin. It forms covalent bonds between the platinum centre and the N7 position of purine bases in DNA. This primarily leads to 1,2- and 1,3-intrastrand crosslinks. The resulting cisplatin-DNA adducts distort the DNA structure and trigger multiple cellular responses, including inhibition of replication and transcription, cell-cycle arrest,

activation of DNA repair pathways, and ultimately apoptosis. The figure was created with BioRender.

The high prevalence of 1,2-intrastrand d(GpG) adducts arises from both the coordination geometry of cisplatin and the intrinsic reactivity of guanine bases within DNA. The proximity of neighbouring guanine bases within 5′-GpG sequences strongly favours formation of short-range intrastrand crosslinks, making these lesions both kinetically preferred and thermodynamically stable. Consequently, 1,2-d(GpG) adducts constitute the dominant class of cisplatin-induced DNA lesions, while 1,2-d(ApG) crosslinks are formed less frequently.[223,226] Importantly, these intrastrand adducts induce pronounced bending and local unwinding of the DNA helix, thereby disrupting replication and transcription processes and promoting recognition by DNA damage response proteins. These structural distortions are considered central to the cytotoxic and anticancer activity of cisplatin. Additional DNA damage includes 1,3-intrastrand d(GpXpG) lesions, interstrand crosslinks, as well as monofunctional and other less cytotoxic adducts, all of which contribute to the overall cytotoxic activity of cisplatin.[226] Accumulation of these DNA lesions ultimately activates multiple cellular stress and apoptotic signaling pathways, which are central to the anticancer activity of cisplatin.[227]

2.2 Platinum compounds as antibacterials

In the CO-ADD study, platinum complexes represented the highest number of active compounds without cytotoxicity.[92] To investigate the mechanism underlying platinum-induced inhibition of bacterial cell division, they examined the effects of cisplatin on λ-lysogenic *E. coli*. In lysogenic bacteria, bacteriophage λ remains integrated within the bacterial genome and viral gene expression is suppressed by the phage repressor protein λcI. Upon DNA damage, activation of the bacterial SOS response leads to formation of activated RecA (RecA*), which promotes cleavage of both the bacterial LexA repressor and the λcI repressor protein. This process derepresses viral genes and initiates the lytic cycle, ultimately resulting in phage production and bacterial lysis.[228] Reslova demonstrated that cisplatin was capable of inducing lysis in λ-lysogenic *E. coli*, suggesting that interference with bacterial DNA was responsible for the observed inhibition of cell division.[229] However, this potential was left untapped as all the focus shifted to cancer research as at that time, the current antibiotics were sufficient to treat existing infections. Until Lippard and co-workers investigated the effect of the monofunctional Pt(II) complexes on the bacterial growth of *E. coli* in 2014, there had been no investigation of Pt complexes as antibacterial agents.[228] Among the tested compounds, CisPt, **1** (**Figure 22**), and phenanthriplatin (**4**) displayed superior

antibacterial activity against *E. coli* over compound **2** and **3** (**Figure 22**). To further evaluate antibacterial activity of the platinum complexes, Lippard and co-workers examined their ability to induce lytic phage in λ-lysogenic *E. coli* W3104 cells. Bacterial cultures were treated with 15 μM of compounds **1**–**4** and incubated for 5 h before being diluted and spotted onto lawns of nonlysogenic *E. coli*. Formation of plaques, indicative of bacteriophage production following induction of the lytic cycle, was observed only for cells treated with CisPt (**1**) and phenanthriplatin (**4**). No plaques were detected for cells treated with compounds **2** or **3**. Control experiments using untreated cells or dilute platinum solutions in the absence of prior bacterial exposure also failed to produce plaques, confirming that phage induction resulted specifically from platinum-mediated cellular damage rather than residual extracellular platinum. These findings further supported the ability of compounds **1** and **4** to induce significant DNA stress responses in bacterial cells.[228]

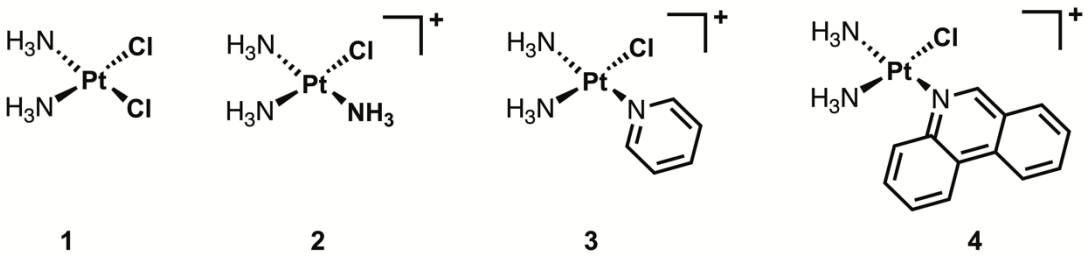
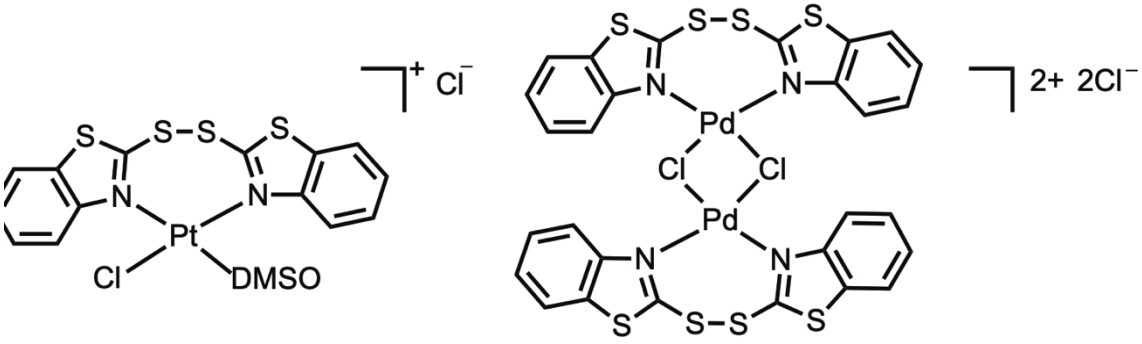


Figure 22. The monofunctional Pt(II) complexes investigated by Lippard and co-workers.

In 2017, Rubino and co-workers synthesised mono and binuclear Pt(II) and Pd(II) complexes with 2,5-bis(2-thienyl)-1,3,4-thiadiazole (DTBTA) and evaluated their antibacterial properties against both Gram-positive (*Kokuria rhizophila*) and Gram-negative (*E. coli*) bacteria. Among the tested compounds, the platinum complex **5** (**Figure 23**), displayed the most significant antibacterial activity with MIC value of 2.5 μM against *K. rhizophila*. Whereas the palladium analogue **6** (**Figure 23**) showed considerably lower potency (MIC = 7.5 μM). In contrast, the compounds demonstrated no activity against *E.coli* up to 20 μM. The corresponding ligand **DTBTA** showed an MIC value of 30 μM against *K. rhizophila* and no antibacterial activity up to 30 μM against *E. coli*.

The enhanced antibacterial effect of the Pt(II) derivative **5** compared with the free ligand was attributed to increased lipophilicity after metal coordination, which may facilitate penetration through the bacterial membrane. Additionally, complex **5** exhibited potent activity cancer cell lines HepG2 (hepatocellular carcinoma) with IC_{50} value of 20.2 ± 1.8 μM and MCF-7 (breast cancer) with IC_{50} value of 4.0 ± 0.2 μM. Although these findings demonstrated promising antibacterial activity of the complex, the low IC_{50} value observed against cancer cells suggests that its activity may arise from broad and potentially unselective cytotoxicity rather than selective antibacterial potency. Importantly, the absence of cytotoxicity data against healthy mammalian cell lines limits evaluation of the compound's therapeutic potential.[230]

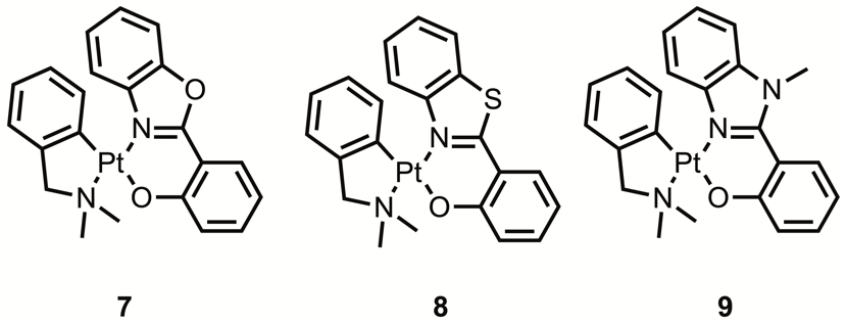


5 **6**

Figure 23. Antibacterial mono- and binuclear Pt(II) and Pd(II) complexes with 2,5-bis(2-thienyl)-1,3,4-thiadiazole (DTBTA) ligand.

Subsequently, Ortega and co-workers reported luminescent Pt(II) complexes with benzothiazole ligand as a potential photodynamic therapy agent against MRSA. They screened the synthesized complexes (**Figure 24**) against Gram-positive resistant strains (vancomycin-resistant *Enterococcus feacium* and MRSA) and Gram-negative (*A. baumannii* and *Pseudomonas aeruginosa*). The complexes did not show significant activity toward Gram-negative bacteria, with MIC values remaining above 100 μM. In contrast, complex **8** demonstrated the highest efficacy against Gram-positive bacterial strains, suggesting that incorporation of the benzothiazole ligand plays an important role in enhancing antibacterial performance under both dark and light-irradiated conditions. Complex **9** exhibited relatively lower antibacterial activity for both dark and irradiated conditions against Gram-positive bacteria, which MIC values of 75 μM. This effect was particularly pronounced against *S. aureus*, where a strong photoinduced antibacterial response was observed after 20 min of exposure to blue light at 420 nm, resulting in an

MIC of 2 μM. The compound achieved a photo-index value (MIC_{dark}/MIC_{light}) of 15, highlighting its considerable light-enhanced antibacterial effect. The cytotoxicity of the compounds was evaluated against the Chinese hamster ovary (CHO) mammalian cell line. Complex **8** exhibited moderate dark toxicity with an IC_{50} value of 59 ± 4 μM with cytotoxic concentrations remaining substantially higher than the MIC values observed against Gram-positive bacteria. In comparison, complex **7** showed slightly higher toxicity toward CHO cells (37 ± 3 μM), while complex **9** displayed the highest mammalian-cell toxicity among the series (13 ± 2 μM). These findings indicate that incorporation of the benzothiazole ligand in complex **8** provides an improved balance between antibacterial efficacy and mammalian-cell compatibility, highlighting its potential as a promising photosensitizer for antibacterial photodynamic therapy.[231]



7 **8** **9**

Figure 24. Reported luminescent complexes against Gram positive bacteria.

Although these Pt(II) benzothiazole complexes demonstrated promising light-enhanced antibacterial activity against Gram-positive resistant strains, their limited efficacy against Gram-negative bacteria highlights a major challenge in antibacterial drug development: inefficient uptake across the outer membrane.

2.2.1 Siderophore conjugation to increase bacterial uptake

This permeability barrier is also an obstacle for many conventional antibiotics, often resulting in poor intracellular accumulation and reduced antibacterial activity. Therefore, strategies to promote bacterial uptake have attracted increasing attention. One such approach is the conjugation of antibacterial agents to siderophores, which exploit bacterial iron-acquisition pathways to facilitate selective transport into bacterial cells. This “Trojan horse” strategy has been widely explored to redirect the activity of antibiotics against resistant Gram-negative pathogens. The name “Trojan horse” derives from the

Greek myth in which soldiers concealed within a wooden horse gained access to the city of Troy, analogous to how bacteria unknowingly import toxic drug conjugates disguised as nutrient sources. In this strategy, antibacterial agents are conjugated to siderophores, iron-chelating molecules secreted by bacteria during iron limitation and subsequently recognized by iron-uptake systems. Because bacteria rely on these molecules to obtain iron, the conjugated cargo can be transported across the outer membrane via receptor-mediated uptake pathways. By exploiting these transport systems, the antibacterial agent can overcome the permeability barriers and, in some cases, evade efflux-associated resistance mechanisms. Once internalized, the active compound is released or activated within the bacterial cell, enabling interaction with intracellular targets and enhancing antibacterial efficacy.[232] In 2019, US Food and Drug Administration (FDA) was approved the first siderophore-antibiotic (SAC) conjugate, cephalosporin-catecholate, cefiderocol (Fetroja®) (**Figure 25)** for the treatment of complex urinary tract infections.[232–234] This first-in-class antibiotic demonstrated potent activity against a broad panel of carbapenem-resistant Gram-negative bacteria.[235] Notably, cefiderocol exhibited high potency across the tested species (MIC below 4 µg/mL), with 97% of Enterobacteriaceae strains, 91% of *Acinetobacter baumannii*, 99% of *Pseudomonas aeruginosa*, and 100% of *Stenotrophomonas maltophilia*. In contrast, other tested antibiotics exhibited more variable, and often substantially lower, growth-inhibition rates. For example, ceftazidime-avibactam retained MIC values below 8 µg/mL against 77% of Enterobacteriaceae strains but showed a markedly reduced ratio of susceptible strains against *P. aeruginosa* (36.3%) and was not applicable to several other species. Similarly, ceftolozane-tazobactam and ciprofloxacin exhibited limited activity against most of the carbapenem-resistant strains tested. Although colistin retains relatively high activity against *A. baumannii* and *P. aeruginosa*, its clinical use is limited by toxicity concerns and the development of resistance. Its broad potency is attributed to the distinctive uptake mechanism utilising an iron transporter and high stability against all classes of carbapenemases.[236] The clinical success of cefiderocol demonstrates that siderophore-mediated uptake can be exploited to overcome the outer-membrane permeability barrier of Gram-negative bacteria. This has encouraged the broader application of the Trojan-horse strategy beyond conventional antibiotic scaffolds. In this context, metal-based compounds are particularly attractive candidates, as many possess favourable biological potency but often exhibit insufficient uptake by Gram-negative bacteria. Building upon these findings, more recent efforts have focused on repurposing platinum-based

anticancer agents as antibacterial therapeutics by improving their intracellular accumulation.

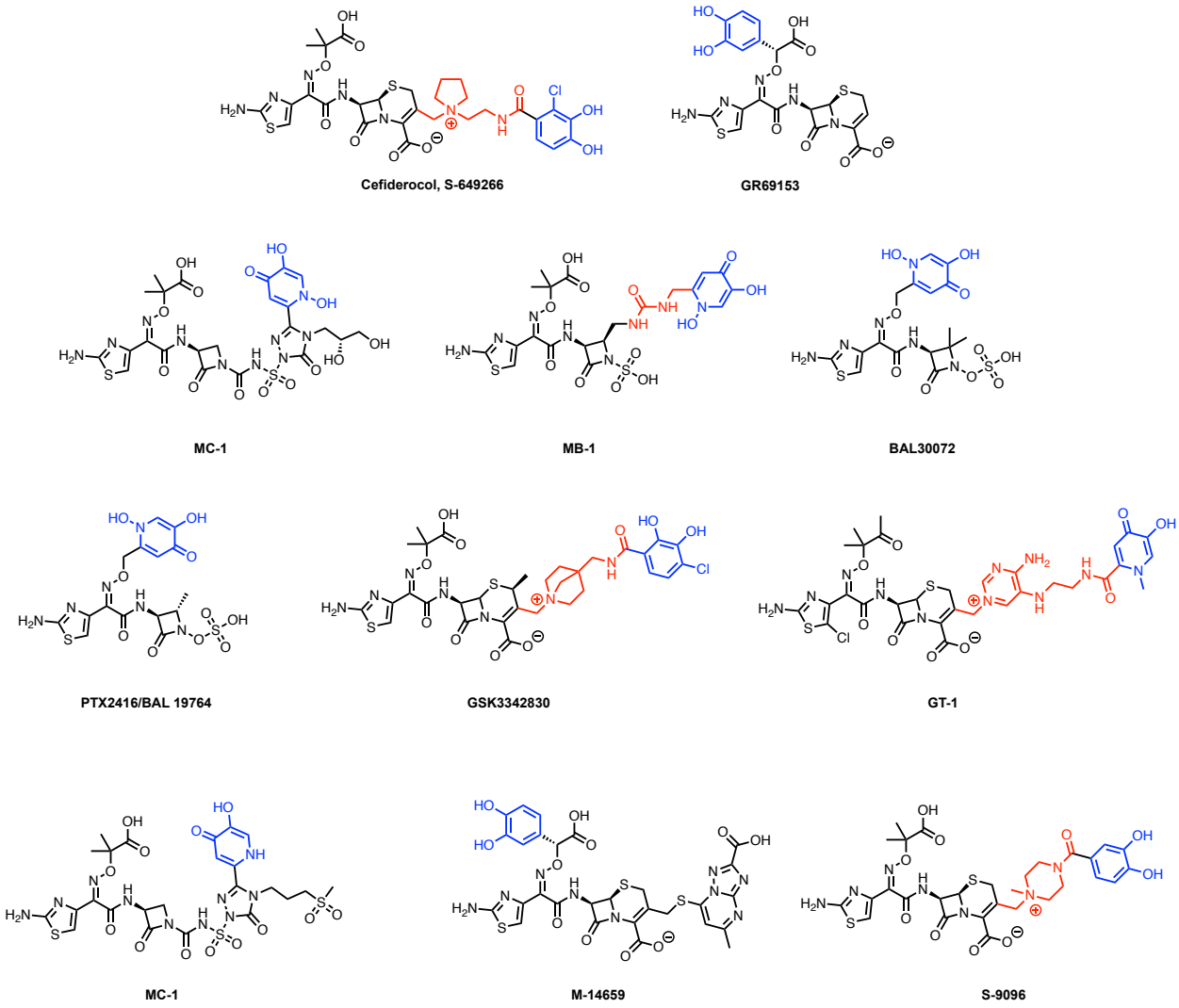


Figure 25. SACs that get advanced to preclinical/clinical studies. Cefiderocol was approved by FDA in 2019. The linker group was highlighted in red, siderophore motif in blue.

In 2022, Nolan and co-workers demonstrated that the anticancer compound cisplatin could be redirected toward *E. coli*, a Gram-negative bacterium, through a "Trojan horse" strategy.[237] In this work, two enterobactin-conjugated Pt(IV) complexes, **L-Ent-Pt(IV)** and **D-Ent-Pt(IV) (Figure 26)**, were reported. The Fe(III)-bound form of the L-conjugate was evaluated in modified M9 medium, which contains low levels of iron (<1 μM), to promote uptake through bacterial iron-acquisition pathways. **L-Ent-Pt(IV)** produced moderate, concentration-dependent growth inhibition in *E. coli* K12 and CFT073, along with pronounced bacterial filamentation, a phenotype commonly associated with platinum-

induced DNA damage and activation of the SOS response.[212,228] Consistent with this mechanism, **L-Ent-Pt(IV)** also induced lytic phage release in lysogenic *E. coli*, supporting DNA damage as a major contributor to its antibacterial effect. Mechanistic studies using transporter mutants demonstrated that the antibacterial activity of **L-Ent-Pt(IV)** depended strongly on the enterobactin uptake pathway. Loss of the outer-membrane receptor FepA or the inner-membrane transporter FepCDG substantially reduced filamentation and cell death, indicating that active siderophore-mediated transport was required for efficient intracellular delivery. These findings demonstrated that active siderophore-mediated transport was required for efficient intracellular delivery. However, efficient uptake alone did not fully determine antibacterial potency, as the activity of the L-enterobactin conjugate was partially limited by enzymatic processing of the siderophore scaffold. The activity of the L-enterobactin conjugate was partially limited by enzymatic processing of the siderophore scaffold. Since bacterial esterases such as Fes can hydrolyse natural L-enterobactin, releasing iron, this process may improve bacterial fitness and partially prevent platinum toxicity. To overcome this limitation, the **D-Ent-Pt(IV)** conjugate was developed as an enantiomer that retains siderophore-mediated uptake while resisting esterase-mediated hydrolysis. **D-Ent-Pt(IV)** displayed substantially improved antibacterial activity, compared with the L-conjugate and cisplatin. ICP-MS analysis further showed that both enterobactin conjugates accumulated in *E. coli* at levels more than tenfold higher than cisplatin or the unconjugated Pt(IV) alkyne complex, while uptake into HEK293T mammalian cells remained comparatively low. These findings demonstrated that enterobactin conjugation can improve bacterial selectivity by exploiting active iron-uptake systems that are absent in mammalian cells.

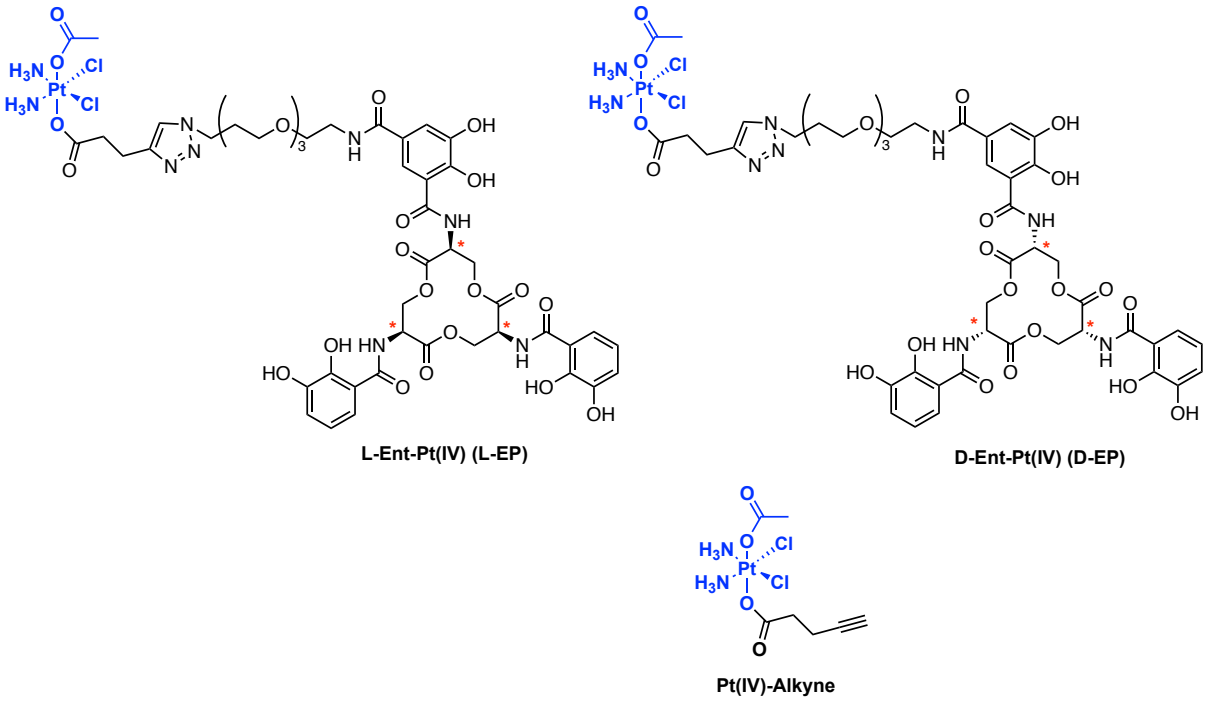


Figure 26. Chemical structures of L-, D-Ent-Pt(IV) conjugates and Pt (IV)-Alkyne reported by Nolan and co-workers. Stereocenters are designated with red asterisks. The Pt(IV) cargos are shown in blue.

The same group further expanded this delivery strategy by replacing the cisplatin payload with an oxaliplatin-based Pt(IV) prodrug, obtaining the enterobactin-oxaliplatin conjugates **L/D-EOP** (**Figure 5**). Similar to the previously reported L/D-EP system, these conjugates were selectively transported into the *E. coli* cytoplasm through the enterobactin uptake machinery, resulting in enhanced platinum accumulation in bacterial cells and reduced uptake by mammalian cells. Both conjugates induced bacterial filamentation and DNA damage responses consistent with platinum-mediated toxicity. Despite successful intracellular delivery, the oxaliplatin-based conjugates exhibited lower antibacterial activity than the corresponding cisplatin derivatives. Comparative analyses suggested that the overall antibacterial efficacy of the enterobactin-Pt(IV) systems correlated strongly with the intrinsic potency of the platinum warhead and its ability to induce DNA damage in *E. coli*. These findings further demonstrated the versatility of siderophore-mediated platinum delivery while highlighting the importance of the Pt cargo in determining antibacterial activity and cellular responses.[238]

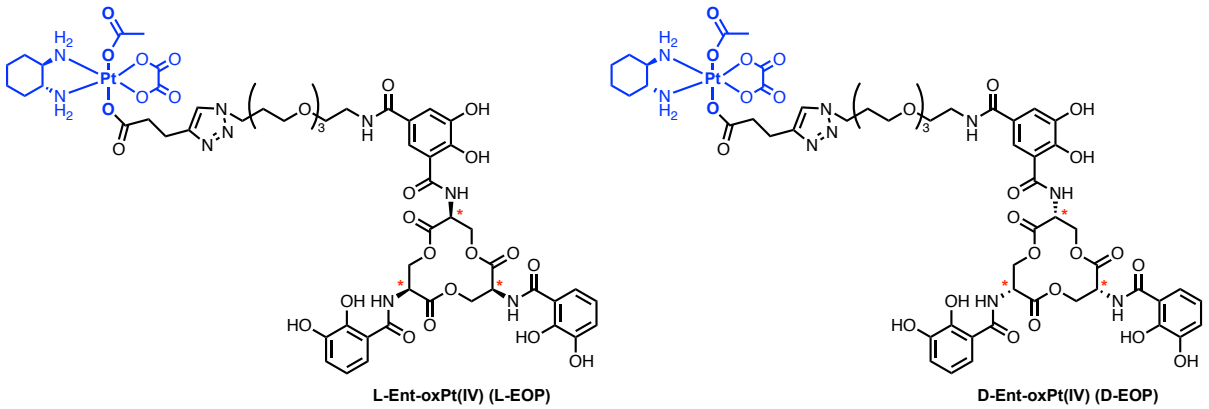


Figure 27. Chemical structures of L-, D-Ent-oxPt(IV) conjugates reported by Nolan and co-workers. Stereocenters are designated with red asterisks. The Pt(IV) cargos are shown in blue.

Taken together, these studies demonstrate that targeted delivery can enhance the accumulation and selectivity of platinum complexes in Gram-negative bacteria. However, the overall antibacterial effects remained relatively modest, with the enterobactin conjugate producing only moderate growth inhibition despite improved intracellular delivery. These findings indicate that enhanced uptake alone is not sufficient to achieve strong antibacterial activity, as the final biological characteristics remains constrained by the intrinsic potency of the platinum cargo. This limitation provides a clear rationale for the discovery of novel platinum complexes with inherent antibacterial activity, rather than relying solely on delivery-based strategies to improve the performance of classical anticancer platinum scaffolds.

In this context, structurally distinct platinum complexes with intrinsic antibacterial activity have attracted an interest. In 2021, Frei *et. al* established 1.5-cyclooctadiene (COD) Pt(II) complexes as a promising antibacterial against Gram-positive bacteria (**Figure 28**). The parent compound **Pt1** (**Figure 28**) exhibited promising antibacterial activity, with an MIC value of 0.625–2.5 μM against *S. aureus* ATCC 43300. **Pt1** showed no significant cytotoxicity up to 100 μM in HEK293 cells, and no haemolytic activity in human Red Blood Cells up to 100 μM. The structure-activity relationship (SAR) of this compound class was also investigated. Substitution of the chloride ligands with iodide ligands, **10** (**Figure *28***), did not significantly affect the antibacterial activity, which remained within the same range as that of the parent compound, nor did it change the cytotoxicity profile. When one of the chloride ligands was substituted with a methyl group, **12** (**Figure 28**), a significant reduction in antibacterial activity was observed, with no inhibition of *S. aureus* growth at concentrations up to 20 μM. Furthermore, compound **10** displayed haemolytic activity in human Red Blood Cells (hRBCs), with an HC_{50} value of 52.11 μM.

The replacement of the Pt centre with Pd, **Pd1** (**Figure 28**) caused haemolytic activity against hRBC. Overall, the substitution of the chloride ligand with aliphatic or aromatic substituents was associated with a significant reduction in Gram-positive antibacterial activity.

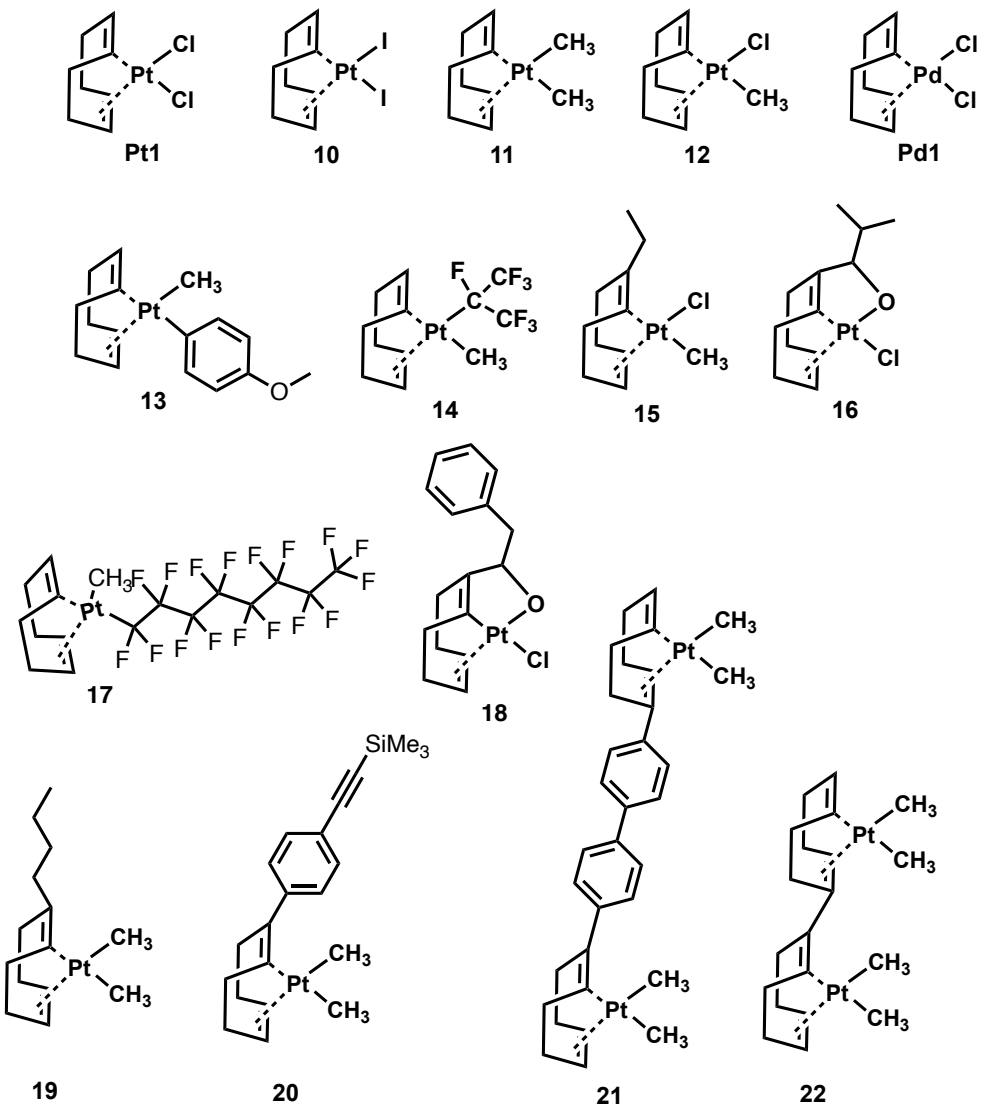


Figure 28. Previously reported **platinum**(II) COD complexes. **Pt1** is the parent complex. The designation **Pt1** was retained for consistency, as this compound is referred to by the same label throughout **Chapter 2** and forms part of the series **Pt2–Pt10**. Other examples from the previously published paper were numbered sequentially.

Pt1 exhibited favourable *in vivo* toxicity in the greater wax moth larvae, *Galleria mellonella*. No toxicity was observed at concentrations up to 0.4 mM, corresponding to approximately 6–7.5 mg/kg.

To obtain preliminary insight into the mode of action of these Pt(II) complexes, their antibacterial activity was assessed against a panel of *E. coli* membrane mutants. To investigate whether these factors contributed to the lack of activity against Gram-negative bacteria, the compounds were tested against *E. coli* ΔtolC and lpxC mutant strains. The ΔtolC mutant lacks a functional outer membrane efflux channel, resulting in impaired efflux activity, whereas the lpxC mutant exhibits defects in lipid A biosynthesis, leading to increased outer membrane permeability.

Despite these alterations, none of the platinum(II) complexes displayed antibacterial activity against either mutant strain at concentrations ranging from 50 to 200 μM. These results suggest that the absence of activity against Gram-negative bacteria cannot be attributed solely to restricted cellular uptake or active efflux and may instead involve additional resistance mechanisms or a lack of suitable intracellular targets.

SAR studies further highlighted the importance of the chloride ligands for antibacterial activity, as substitution with aliphatic or aromatic groups generally resulted in a substantial reduction in potency. Altogether, these findings demonstrated this class of Pt(II) complexes as promising antibacterial candidates with favourable safety profiles and highlight the need for further mechanistic investigations to determine their cellular targets and further biological characterisation.[239]

2.3 Aims and Objectives

The aim of this chapter was to build on the previous study[239] by exploring novel, non-toxic, Gram-positive-targeting platinum-based antibacterial agents with low-micromolar activity. In the previous study, the SAR of this compound class were investigated. Although the importance of chloride ligands and the Pt centre was established, the sole effect of the modification of the cyclooctadiene ring remained unexplored. Therefore, this study initially aimed to gain deeper insight into the SAR of this compound class. Upon the determination of the promising compounds within the series, mechanistic details of the antibacterial potency of the lead compounds were revealed. Subsequently, the advanced biological characterisation of the most promising compound was studied.

2.4 Results and Discussion

2.4.1 Synthesis of Pt(COD-R)Cl_2 complexes

In previous work[239], Pt(COD) complexes bearing halogen ligands have been investigated and identified as promising antibacterial agents against Gram-positive bacteria. To further elucidate their (SAR), novel derivatives of this compound class **Pt 2–10** (**Figure 29**) were synthesised. Given the observed significance of halogen ligands in their promising antibacterial activity, it was aimed to explore modifications to the cyclooctadiene ring. The modifications were performed either at the double bond (**Figure 29A**) or at the allylic position (**Figure 29B**). To enable selective double-bond modification, commercially available 1,5-cyclooctadiene was first treated with Br_2 in DCM. To minimise bromination of the second double bond, Br_2 was diluted in DCM and added dropwise over 30 min, after which the reaction was stopped. The 1,2-vicinal dibromide **COD-Br_2** (**Figure 29**) was obtained following purification by column chromatography. Then, the elimination reaction was performed with dibromo, 1,8-diazabicyclo(5.4.0)undec-7-ene(DBU) in anhydrous DMF under Ar atmosphere and stirred overnight at 80°C. The bromide derivative **COD-Br** (**Figure 29**) was obtained following purification by column chromatography. The desired monobrominated alkene was further characterised by NMR. The appearance of the vinylic proton resonance at 6.01 ppm was consistent with formation of the new double bond following elimination from the vicinal dibromide starting material. The Suzuki-Miyaura cross-coupling reaction was used to functionalize 1,5-cyclooctadiene, proceeding via a palladium-catalysed cycle involving oxidative addition, transmetallation, and reductive elimination.[240] In this work, the brominated cyclooctadiene derivative **COD-Br** (**Figure 29**) acts as the electrophilic coupling partner, while the boronic acid derivatives serve as the nucleophilic coupling component.[241] Taken together, the Suzuki-Miyaura reaction provided an efficient strategy for introducing various substituents onto the COD scaffold under relatively mild conditions (Dioxane:H_2O, reflux for 5 hours). After completion of the reaction, the mixture was diluted with ethyl acetate and the organic layer was separated. This reaction enabled the double-bond modification of the cyclooctadiene ligand and the generation of aromatic-group-substituted COD ligands (Compounds **23**–**26**). The desired ligands were obtained through column chromatography and characterised by NMR and HRMS. The appearance of additional aromatic protons provided apparent evidence for incorporation of the aromatic substituents into the COD scaffold. Additionally, HRMS analysis confirmed the presence of the expected target masses. For compound **25**, the presence of a carbonyl peak at 191.5 ppm in the ^{13}C NMR spectrum provided additional evidence

for product formation. Subsequently, the Pt(II) complexes were synthesised with K_2PtCl_4 and a catalytic amount of $SnCl_2$ in a water and ethanol mixture and stirred for 2 days. The complexes were purified by column chromatography with heptane and ethyl acetate as mobile phase. The presence of the desired compounds was confirmed with NMR spectroscopy (^1H, ^{13}C, and ^{195}Pt) and HRMS. Successful formation of the double bond-modified complexes was confirmed by comparison of the ^1H NMR spectra of the free ligands and their corresponding platinum complexes. Upon coordination, the COD double bonds bind to platinum centre in an η^4 binding mode leading to changes in the electronic environment of the alkene protons and resulting in shifted alkene resonances relative to the free ligands. Complexation also affected the aliphatic proton signals of the COD scaffold. Upon coordination to Pt(II) centre, the aliphatic proton resonances of the COD ring became more dispersed, extending from approximately δ 2.3–2.8 ppm (**Figure 115**) in the free COD-Ph ligand to δ 2.0–3.3 ppm (**Figure 123**) in the complex, and showed a more complex splitting pattern. This could be attributed to restricted conformational flexibility following coordination of both double bonds to the platinum centre, causing the methylene protons to experience different chemical environments. Additionally, changes in the electronic environment and ring geometry upon coordination could affect proton shielding and coupling interactions, contributing to the observed differences in chemical shifts and splitting patterns. Additionally, the purity and identity of the complex was also confirmed with ^{195}Pt NMR.

Allylic position-modified ligands were synthesised via the Kharasch-Sosnovsky reaction. One important feature of this reaction is its high selectivity toward allylic C-H bonds. This selectivity arises from the significant resonance stabilization of allylic radical intermediates. In cyclic dienes such as COD, the reaction proceeds efficiently due to the accessibility of allylic positions adjacent to the double bonds. In the present study, formation of the COD acetate derivative demonstrated that the oxidation proceeded with sufficient selectivity to afford the desired functionalized intermediate for subsequent complexation reactions.[242,243]

After the desired compound, COD acetate derivative, **27** (**Figure 29**), was purified with column chromatography. The desired product was further characterised by NMR spectroscopy (^1H and ^{13}C). Formation of the modified COD ligand was supported by the splitting of the alkene proton resonances into two distinct signals at 5.23 and 5.13 ppm, integrating as 1H and 3H, respectively (**Figure 113**). This change in the alkene proton

environment, together with the presence of a carbonyl peak at 170.3 ppm in the ^{13}C NMR spectrum, is consistent with allylic functionalisation of the COD scaffold (**Figure 114**).

The complexation was performed in presence of an excess of the corresponding alcohol (20 eq.) and water under microwave irradiation. At the beginning, it was aimed to obtain the complex of compound **27** with acetate moiety in EtOH: H_2O. Surprisingly, ^1H NMR analysis of the purified product did not show the expected methyl proton corresponding to the acetyl group. Instead, a terminal CH_3 group was observed at 2.13 ppm, with an integration consistent with the ethoxy-substituted complex. This result indicated that ethanol had likely participated in the reaction, replacing the allylic acetate group during complexation. We therefore obtained ethyl ether bearing Pt(II) complex **Pt6** (**Figure 29**). This unexpected ethanol-mediated substitution prompted us to investigate whether changing the alcohol solvent could provide access to further ether-substituted Pt complexes. Accordingly, the complexation reaction was repeated using different alcohols under analogous conditions. In each case, substitution of the allylic acetate group was observed, affording a series of ether-substituted Pt complexes **Pt7**–**Pt10** (**Figure 29**). A plausible mechanism for this reaction involves an alcohol-mediated solvolysis/substitution reaction. During complexation, coordination of the COD double bonds to Pt(II), together with microwave irradiation, may activate the allylic acetate group for C-OAc bond cleavage. Leaving of acetate would generate a resonance-stabilised allylic intermediate, which is then trapped by the alcohol solvent acting as a nucleophile. Subsequent deprotonation affords the corresponding allylic ether-substituted COD ligand, which remains coordinated to Pt through both alkene units in an η^4-binding mode. The formation of different ether-substituted complexes upon changing the alcohol further supports the involvement of alcohol as the nucleophile in this transformation. All final complexes were purified by silica chromatography and characterised by NMR and mass spectrometry.

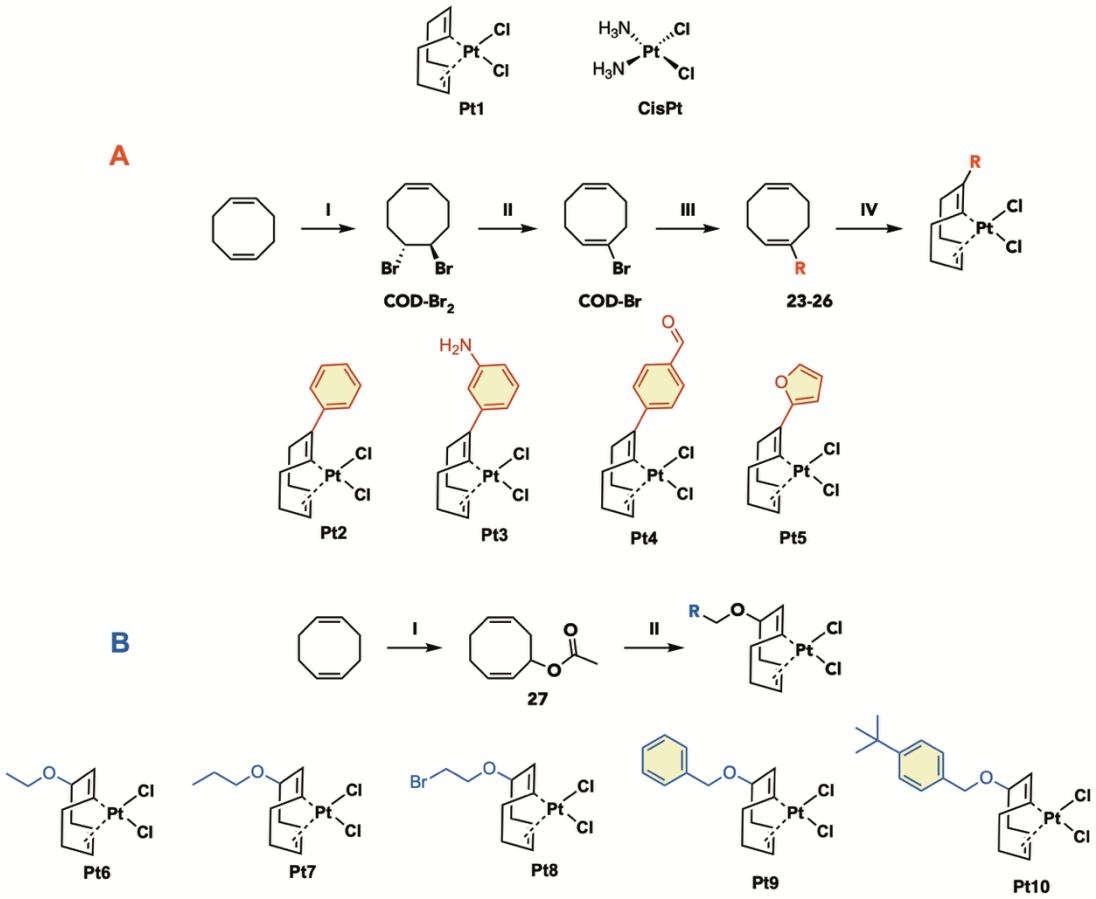


Figure 29. Reaction scheme for double-bond-modified COD ligands and their corresponding Pt(II) complexes. (A) I: Br_2, DCM, 30 mins, r.t., 77%; II: DBU, DMF, overnight, 80°C, 21%; III: $RB(OH)_2$, $Pd(PPh_3)_4$, Na_2CO_3, Dioxane:H_2O, 4 h, reflux, 28-41%; IV:K_2PtCl_4, EtOH:H_2O, 1 h, MW, 90°C, 12-55%. (B) Reaction scheme for allylic position-modified Pt(II) complexes. I: t-butylhydroperoxide, CuCl, AcOH, 52 h, reflux, 7%; II: K_2PtCl_4, H_2O:RCH_2OH, 1 h, MW, 90°C, 7-13%.

2.4.2 Biological characterisation of Pt(COD-R)Cl_2 complexes

2.4.2.1 Antibacterial activity of Pt(COD-R)Cl_2 complexes

To evaluate the antibacterial activity of the complexes, minimum inhibitory concentration (MIC) assay was performed against selected Gram-positive (MRSA, MSSA, and *B. subtilis*) and Gram-negative bacteria (*E. coli*) (**Table 1**). The previously reported **Pt1** was used as reference compound.[239] It was observed that substituting the double bond with benzyl or furan rings (**Pt2-5**) significantly reduced activity against Gram-positive strains. While **Pt2** showed limited activity (MIC 50–100 µM), the other complexes were inactive in this concentration range. In contrast, modifications at the allylic position demonstrated good antibacterial activity (**Pt8**), yet did not exceed the activity of the parent compound **Pt1** (**Table 1**).

Table 1. Antibacterial activity of the synthesised complexes. MICs (μM) of synthesised PtCOD complexes against MRSA – methicillin-resistant *S. aureus* COL ; clinical isolate MSSA – methicillin-susceptible *S. aureus*; *B.subtilis* MW168 – *Bacillus subtilis*. Vancomycin for Gram-positive and Polymyxin B for Gram-negative were used as positive controls, and the MICs were given in μg/mL.

	Minimum Inhibitory Concentration (MIC) [μM]			
	MRSA	**MSSA**	***B. subtilis***	***E.coli***
Pt1	3.125 – 6.25	3.125	6.25	>100
Pt2	50 – 100	100	100	
Pt3	>100	>100	>100	
Pt4	>100	>100	>100	
Pt5	>100	>100	>100	
Pt6	12.5	12.5	100	
Pt7	>100	12.5	50 – 100	
Pt8	12.5	12.5 –25	50	
Pt9	12.5 – 25	6.25	50 – 100	
Pt10	12.5 – 25	12.5	25	
Cisplatin	>100	>100	>100	
Carboplatin	>100	>100	>100	
Oxaliplatin	>100	>100	>100	
Control [μg/mL]	1.25	1.25	<0.312	0.625

No antibacterial activity against *E. coli* was observed for any of the compounds at concentrations up to 100 μM (**Table 1**). To investigate whether the lack of activity was associated with limited permeability across the outer membrane of Gram-negative bacteria, the activity of **Pt1** was additionally evaluated in the presence of a sublethal concentration (10 μg/mL) of polymyxin B nonapeptide (PMBN).[244] It is a derivative of polymyxin B that lacks its terminal aminoacyl residue. Unlike polymyxin B, PMBN lacks intrinsic antibacterial activity, making it a valuable adjuvant in combination therapies. Its ability to permeabilize the outer membrane of Gram-negative bacteria enhances the uptake and efficacy of otherwise membrane-impermeable antibacterial agents.[245] Despite permeabilisation of the outer membrane by PMBN, **Pt1** did not inhibit bacterial growth at concentrations up to 100 μM. These findings suggest that the lack of activity against *E. coli* is not solely due to limited outer membrane permeability and may additionally involve insufficient intracellular target engagement.

The structural similarity of **Pt1** with the anticancer drug CisPt prompted us to re-examine the antibacterial properties of the latter, which had been noted to induce bacterial elongation in the past.[228] In our hands, CisPt**, carboplatin,** and **oxaliplatin** showed no antibacterial activity up to 100 μM against any of the evaluated bacterial strains (**Table 1**). The antibacterial activity of **CisPt** has been investigated several times since the first report by Rosenberg *et al.* However, only moderate activity was observed, and it was lower against Gram-positive than against Gram-negative strains.[246,247]

To confirm whether the observed antibacterial activity originates from the complexes themselves, rather than the ligand (COD) or platinum alone, the antibacterial effects of 1,5-cyclooctadiene and K_2PtCl_4 against *S. aureus* and *E. coli* were examined. Neither of them was found to be active up to 200 μM (**Table 2).**

Table 2. Antibacterial activity of COD ligand and Pt precursor against *S. aureus* CCUG 62707 and *E. coli* NCTC 13476.

	Minimum Inhibitory Concentration (MIC) [μM]	
	S. aureus	***E. coli***
1,5-Cyclooctadiene	>200	>200
K_2PtCl_4	>200	>200

The parent compound **Pt1** as well as **Pt8,** which was the most promising amongst the newly synthesised allylic-modified complexes, were selected as lead compounds for further characterisation. To this end, their antibacterial activity against an extended panel of Gram-positive strains, including a range of MRSA and vancomycin-resistant *S. aureus* (VRSA) strains, was assessed. **Pt1** exhibited nanomolar-range activity against the extended panel of Gram-positive bacteria, while **Pt8** was slightly less active (**Table 3**).

Since **Pt1** has broad and promising activity and **Pt8** has one of the most promising activities among the allylic-modified complexes, they have been selected as lead compounds for further investigations.

Table 3. Antibacterial activity of the lead complexes (Pt1 and Pt8) against expanded Gram-positive panel. MSSA ATCC 29213; MRSA NRS 100, S119, 129, 186, 191, 192, 193, 194, 198, and vancomycin-resistant *S.aureus* (VRSA) VRS 1, 4 and 12.

Minimum Inhibitory Concentration (MIC) [μM]

		Pt1	**Pt8**
MSSA	**ATCC 29213**	0.67	4.02
MRSA	**NRS 100**	0.67 – 1.34	8.04 – 16.1
	NRS 119	0.33 – 0.67	2.01
	NRS 129	0.33 – 0.67	2.01 – 4.02
	NRS 186	0.33 – 0.67	4.02 – 16.1
	NRS 191	0.67	2.01 – 4.02
	NRS 192	0.33 – 0.67	2.01
	NRS 193	0.67	4.02
	NRS 194	0.33 – 0.67	2.01
	NRS 198	0.668	8.04
VRSA	**VRS 1**	0.67 – 1.34	64.3
	VRS 4	0.67 – 1.34	8.04
	VRS 12	0.67 – 1.34	8.04 –16.1

2.4.2.2 Haemolytic and cytotoxic activity of Pt(COD-R)Cl_2 complexes

Selectivity of antibacterial compounds for bacteria over mammalian cells is essential. Therefore, HC_{50} were determined against human Red Blood Cells (RBC). Haemolytic properties of the compounds were investigated with minimum haemolytic concentration (MHC) assay. The absorbance at 540 nm of supernatant of each well has been read by well-plate reader, and the HC_{50} values, which the necessary concentration to haemolyse 50% of the population, were calculated. All tested PtCOD complexes showed HC_{50} values above 200 μM and were thus classified as not haemolytic **(Table 4)**.

Table 4. Heamolytic activity of the synthesized complexes against human Red Blood Cells. MHC – minimum heamolytic concentration was determined by eye and HC_{50} values.

Minimum Haemolytic Concentration [μM]		
	MHC	**HC_{50}**
Pt1	>200	>200
Pt2	100	>200
Pt3	100	>200
Pt4	100	>200
Pt5	>200	>200
Pt6	100	>200
Pt7	100	>200
Pt8	100	>200
Pt9	100–200	>200
Pt10	200	>200

To test cytotoxicity of the lead compounds against mammalian cell lines, 50% inhibitory concentrations (CC_{50}) were determined against African Green Monkey kidney cells (Vero) and Human Embryonic Kidney cells (HEK293T). Neither **Pt1** nor **Pt8** significantly reduced the viability of Vero cells up to the highest tested concentrations (134 μM and 402 μM respectively, **Table 5**). CC_{50} values of **Pt1** (74.1 ± 4.1 μM) and **Pt8** (92.2 ± 3.9 μM) against HEK293T cells after 24 h were comparable to those of **CisPt** (81.6 ± 5.1 μM). However, neither **Pt1** (65.3 ± 2.7 μM) nor **Pt8** (84.8 ±10.1 μM) showed a large increase of toxicity after 48 h, which is in stark contrast to **CisPt** (22.04 ± 3.4 μM, **Table 5).** Notably, **Pt1** and **Pt8** were dissolved in 100% DMSO and cells were treated with these solutions. The apparent cytotoxicity of **Pt1** and **Pt8** is partially attributable to the elevated DMSO concentration, which have exceeded the tolerance limit of the cells under the experimental conditions. Under these circumstances, the CC_{50} values were nevertheless calculated, as the DMSO control was used as the growth control (**Table 7**). After correction for the DMSO effect, the CC_{50} value of **Pt8** increased to >100 μM, while the CC_{50} value of **Pt1** increased to 92.9 ± 1.8 μM (**Table 6**).

Table 5. Cytotoxicity of the lead compounds in Vero and HEK293T cells. For Vero cells, CC_{50} values were given after 72 hours of incubation. For HEK293T cells after 24 and 48 hours of incubation.

Cytotoxicity Assays (Pt1 & Pt8)				
Cell Line		**Pt1**	**Pt8**	**CisPt**
Vero	**72 h**	> 134	> 402	*n.d.*
HEK293T	**24 h**	74.1 ± 4.1	92.2 ± 3.9	81.6 ± 5.1
	48 h	65.3 ± 2.7	84.8 ±10.1	22.04 ± 3.4

Table 6. DMSO-normalized cytotoxicity of the lead compounds in HEK293T cells.

	Cytotoxicity Assays (Pt1 & Pt8)	
	24h	**48h**
Pt1	>100	92.9 ± 1.8
Pt8	>100	>100

Taken together, **Pt1** and **Pt8** show promising antibacterial activity against a broad panel of Gram-positive pathogens, do not cause haemolysis, and exhibit only minor toxicity against mammalian cell lines at concentrations sufficient to elicit antibacterial effects. However, as shown in our previous study[239] **Pt1** lost its antibacterial activity completely in human serum, indicating strong serum interactions and reduced systemic efficacy. Indeed, no *in vivo* activity was observed in a systemic infection model in *Galleria mellonella*. Therefore, this compound class may not be suitable for systemic administration (oral or intravenous). Instead, these compounds appear more suitable for topical applications, where serum binding is less relevant (*vide infra*).

2.4.3 Structure and activity relationship (SAR) of this compound class

In the search for novel classes of antimicrobial agents we have identified platinum cyclooctadiene complexes with promising activity against Gram-positive bacteria and low toxicity against healthy human cells. SAR studies in this and previous work revealed several key insights. The halogen ligands on the platinum centre seem to be crucial as alteration to methyl or hydroxy-containing ligands led to reduced activity and/or increased toxicity.[239] More scope remains to explore the effect of other, potentially bidentate, ligands (in conjunction with the COD) on the antibacterial activity and toxicity of these compounds. Switching the metal center to palladium was shown to result in complete loss of antibacterial properties and significant haemolysis[239], concluded that the platinum is key. Finally, in this work, we explored the synthetically more challenging modifications

of the COD ligand. Initially, we focused on modifications at the double bond to investigate how substitution at this position influences biological activity of this compound class. **Pt2**-**Pt5** were designed to investigate how variations in ligand electronics and steric properties influence the antibacterial activity of the resulting platinum complexes. The selected aromatic substituents were intended to provide a small but representative range of electronically and structurally distinct motifs, rather than to constitute a systematic substituent screening study. Accordingly, a phenyl group (**Pt2**), a meta-substituted aniline derivative (**Pt3**), and a para-benzaldehyde derivative (**Pt4**) were chosen as representative aryl systems bearing functional groups with different electronic characteristics and substitution patterns. This selection enabled us to assess whether both substituent identity and substitution position influence complex formation and/or biological activity. In addition, a furan derivative (**Pt5**) was included as a simple heteroaromatic motif to evaluate whether replacing a phenyl-type aromatic system with a heterocycle alters the behaviour of the complex. it was observed that any modification of the ligand at the double bond position resulted in loss of antibacterial activity in the final platinum compound. Therefore, further double-bond modifications were not pursued. Subsequently, a small series of allylic ether complexes (**Pt6**-**Pt10**) was prepared to explore how variation at the allylic position influences the properties and antibacterial activity of the complexes. Within this series, it was examined the effect of aliphatic chain length (n = 2 for **Pt6** and n = 3 for **Pt7**). The introduction of a bromine containing substituent (**Pt8**) was also investigated. Although the bromine substituent can modulate physicochemical properties and potentially enhance target binding through halogen bonding[248], the C-Br bond is generally weaker than the corresponding C-Cl or C-F bond, making C-Br bond stability an important consideration for further development.[249] Depending on their chemical environment, carbon centres bearing bromine may undergo nucleophilic substitution by biological thiols, including glutathione and protein cysteine residues, potentially inactivating the compound or causing off-target protein modification.[250]Together with aromatic substitution at the allylic position (**Pt9** and **Pt10**), this approach allowed us to probe how steric bulk, lipophilicity, and electronic variation at the allylic position affect the behaviour and biological activity of the resulting platinum complexes. Modification on the allylic COD position maintained some of the antibacterial properties. However, the best modified complex, **Pt8** was still significantly less active than the original hit-compound **Pt1**. Further expansion of these ligand series was not pursued at this time. This was motivated both by the significant synthetic challenges associated with the preparation and purification substituted Pt complexes,

and because the biological results obtained for new derivatives of the present series were not sufficiently promising to justify a more extensive derivatization study at this stage. Both **Pt1** and **Pt8** showed broad activity against a range of clinical isolates of drug-resistant *S. aureus* and low cytotoxicity and haemolysis values.

2.4.4 Mode of action studies of Pt1 and Pt8

Encouraged by these results, it was proceeded to study the modes of action of **Pt1** and **Pt8** in comparison with **CisPt** using phenotypic analysis of the Gram-positive model organism *B. subtilis*. As 1,5-COD ligand did not exhibit an antibacterial potency, it was not included in the mode of action studies. To this end, we first confirmed the MICs against *B. subtilis* 168CA, the background strain of our reporter constructs (**Pt1**: 6.25 µM; **Pt8**: 50 µM). Based on these values, we determined the optimal stressor concentrations (OSCs) in acute shock experiments. The optimal stressor concentration is a concentration that leads to a 50-70% reduction of bacterial growth during mid-exponential phase. It imposes sufficient stress to elicit a clear phenotype without causing excessive cell death or lysis, which would mask the direct effects of the test compound. We determined OSCs of 3.125 µM for **Pt1** and 25 µM for **Pt8** (**Figure 30**). No growth inhibition could be observed with **CisPt** (**Figure 30**), leading to the decision to proceed with the highest tested concentration (100 µM). Both **Pt1** and **Pt8** showed a reproducible delay until the onset of growth inhibition (~30 min for **Pt1** and ~60 min for **Pt8**, **Figure 30**). Hence, we chose 30 and 60 min after antibiotic addition as timepoints for phenotypic analysis experiments.

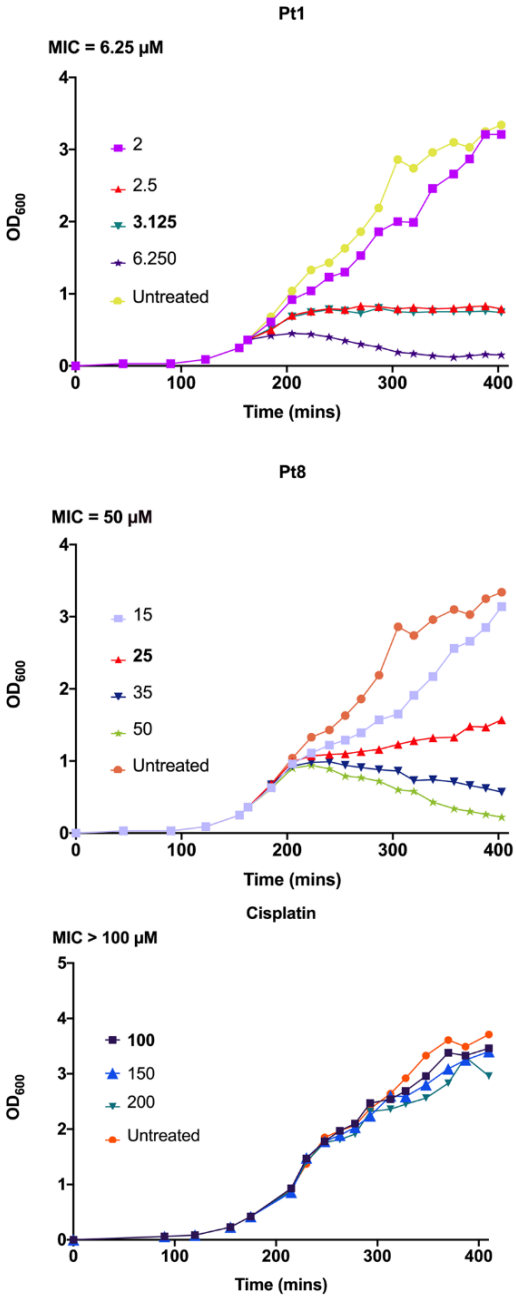


Figure 30. Determination of optimal stressor concentrations (indicated in bold) of Pt1, Pt8, and CisPt.

2.4.4.1 Bacterial cytological profiling

To get an overview of the cellular effects of the compounds, we employed bacterial cytological profiling (BCP). To this end, we used a strain intracellularly expressing green-fluorescent protein (GFP) from the strong, constitutive *PrpsD* promoter (*B. subtilis* bSS82[251]), stained with the membrane dye Nile Red and the DNA dye DAPI (4′,6-

diamidino-2-phenylindole). Nile Red is a lipophilic solvatochromic fluorophore that readily partitions into the hydrophobic region of bacterial phospholipid membranes. While the dye exhibits only weak fluorescence in aqueous environments, its fluorescence intensity increases substantially upon incorporation into the nonpolar lipid phase of the membrane. This pronounced enhancement in fluorescence provides high membrane-to-background contrast, allowing clear visualisation of the bacterial membrane in live cells.[252,253] DAPI (is a fluorescent DNA-binding dye widely used for the visualisation of bacterial and eukaryotic nucleoids. The dye preferentially binds to the minor groove of double-stranded DNA, particularly at adenine-thymine (A-T)-rich regions. In solution, DAPI exhibits relatively weak fluorescence; however, upon binding to DNA, its fluorescence intensity increases substantially due to restricted molecular motion and reduced solvent-mediated quenching.[254] When combined with phase-contrast microscopy, this setup enables simultaneous assessment of cell morphology, cell lysis, pore formation, membrane morphology, and nucleoid morphology in a single assay.[255]

None of the compounds caused apparent differences in overall cell morphology (phase contrast) or compromised membrane integrity (GFP) (**Figure 31A**). Nile Red foci, visible as distinct bright spots along the membrane, were observed in **Pt1**-treated cells. These regions showed stronger fluorescence than the surrounding membrane, resulting in an uneven staining pattern consistent with local changes in membrane organisation and possible membrane stress. However, quantification of the percentage of cells exhibiting Nile red foci did not provide statistically significant support for this observation due to high variability among treated samples (**Figure 32**). These results suggest that membrane damage may be a secondary component of the **Pt1** mode of action that may occur to varying degrees, but it is unlikely to be the primary mechanism of action.

Striking effects of **Pt1** and **Pt8** were observed on the bacterial nucleoid (DAPI), showing visible changes in both nucleoid morphology and fluorescence intensity (**Figure 31A**). In untreated cells, the DNA-rich regions were distributed along the longitudinal axis of the cell, whereas treatment altered their shape and distribution, with the nucleoids appearing more compact after 60 min. When it was quantified these differences, both **Pt1** and **Pt8** as well as **CisPt** showed clear nucleoid compaction after 60 min of treatment (**Figure 31B**). This is indicative of DNA packing defects. Similarly, **Pt1** and **CisPt** caused a significant reduction of the DAPI signal in the same timeframe, **Pt8** showing a similar trend. This phenotype points towards compromised DNA integrity and can indicate DNA fragmentation or other structural changes that decrease the availability of the minor

groove to the DAPI dye (**Figure 31C**). These results gave rise to the hypothesis that **Pt1** and **Pt8** affect the structural integrity of DNA, and consequently nucleoid packing, possibly in a manner similar to **CisPt**. Notably, although it wasn't observed antibacterial activity neither during our initial MIC nor growth curve experiments, we did observe slight growth defects and a mild cell elongation phenotype in *B. subtilis* treated with 100 µM **CisPt** (**Figure 31**). This observation was consistent with previous reports describing filamentation in *E. coli* following DNA damage and the consequent inhibition of cell division.[228,237,238]

2.4.4.2 DNA damage

BCP revealed that **Pt1** and **Pt8** elicited their strongest effect on the bacterial nucleoid, both in terms of nucleoid packing and fluorescence intensity of the DAPI stain (**Figure 31**). A reduced DAPI signal indicates less efficient DNA binding of the dye, suggesting inaccessibility of the minor groove[256] and thus structural changes to the DNA. To confirm whether the compounds induce DNA damage in bacterial cells, the localization of RecA was assessed. RecA is a highly conserved bacterial protein that plays a central role in SOS response to DNA damage and initiates homologous recombination-mediated DNA repair. Following DNA damage or replication-fork arrest, exposed single-stranded DNA promotes the ATP-dependent assembly of RecA into an activated nucleoprotein filament (RecA*). If strand breaks are present, RecA accumulates at the damaged sites, appearing as foci or elongated structures.[257] Since the RecA response is strongest shortly after stress induction[258], we additionally examined a 10 min timepoint in this assay. Indeed, clear RecA accumulations were found on the nucleoids of cells treated with **Pt1**, **Pt8**, and **CisPt**, with the strongest response induced after 10 min and **Pt1** showing the most pronounced effects (**Figure 35**).

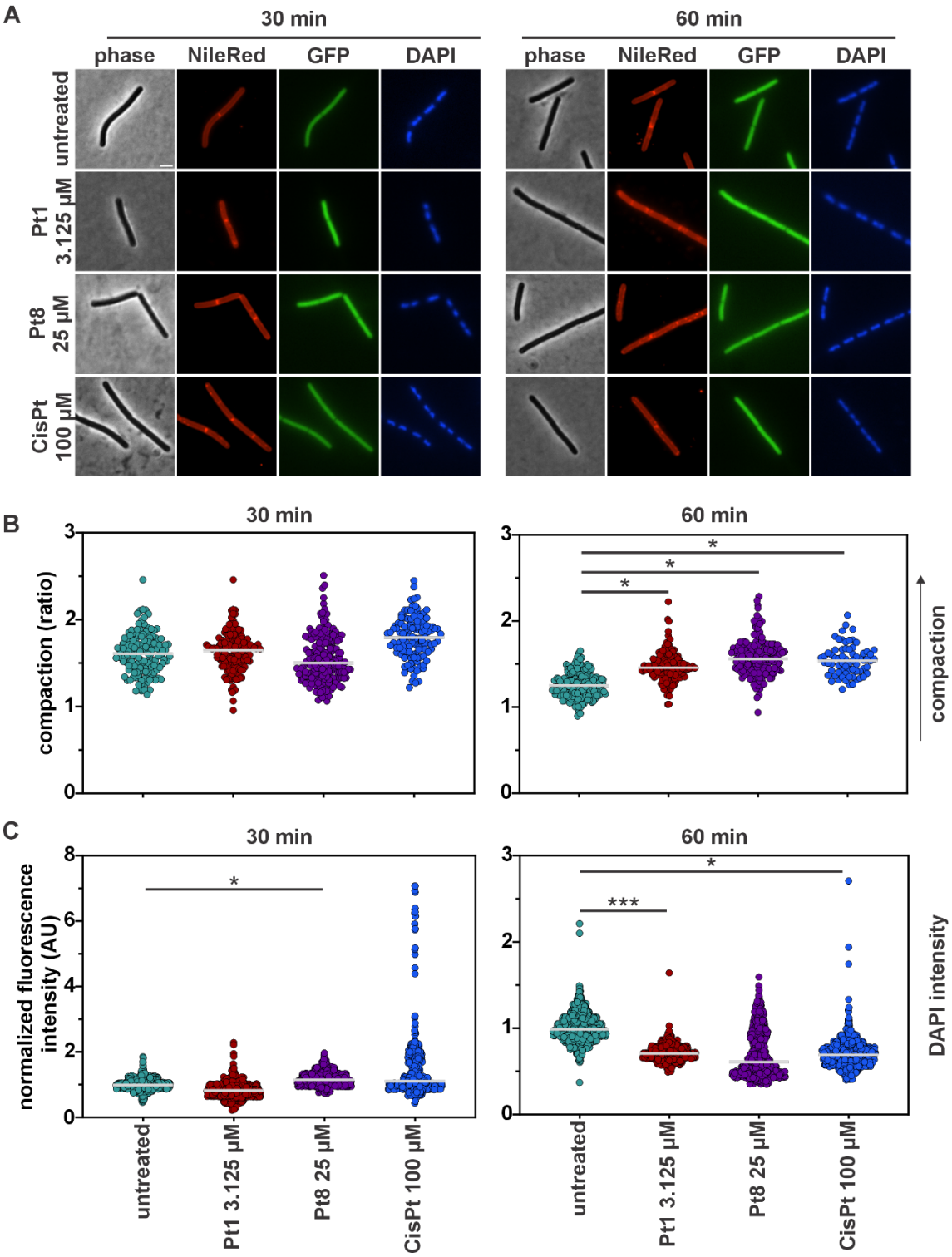


Figure 31. Bacterial cytological profiling of *B. subtilis* bSS82, constitutively expressing GFP from the *PrpsD* promoter, stained with Nile red (membrane) and DAPI (DNA). Cultures were treated with Pt1 (3.125 µM), Pt8 (25 µM), and CisPt (100 µM) for 30 and 60 min, respectively. (A) Phase contrast and fluorescence microscopy images. Scale bar 2 µm. (B-C) Quantification of nucleoid compaction measured as a ratio of the whole cell area vs the area occupied by the DAPI-stained nucleoid (B) and DAPI fluorescence intensity (C). Grey lines indicate the median. Graphs show

pooled data from three biological replicates. See Figure 33 for cell populations divided by individual replicates. Significance was tested with nested t-tests (p values: *≤0.5, **≤0.01, ***≤0.001).

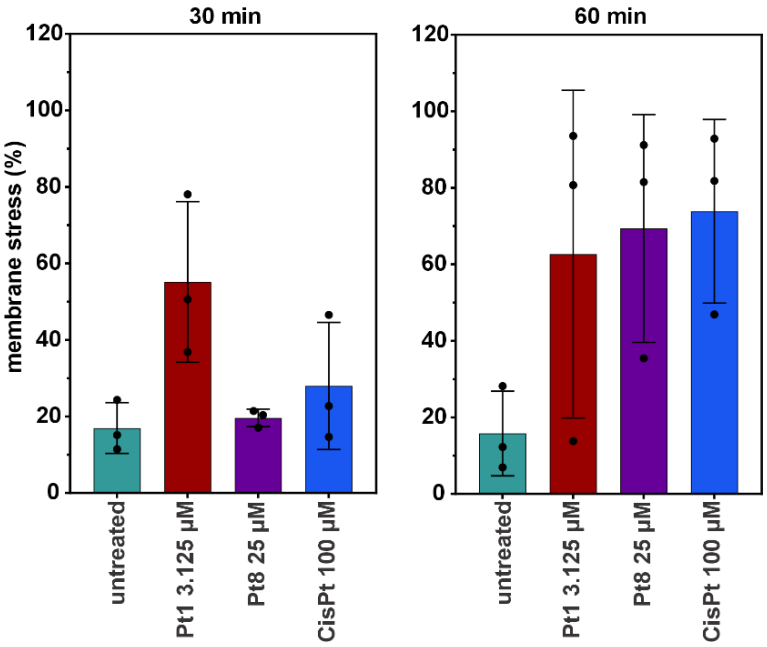


Figure 32. Quantification of membrane stress measured as percent of *B. subtilis* bSS82 cells with Nile red foci. Error bars show standard deviation of three biological replicates. No statistically significant changes were observed (p≤0.05). For statistical analysis, the Mann-Whitney (unpaired, nonparametric) test was used.

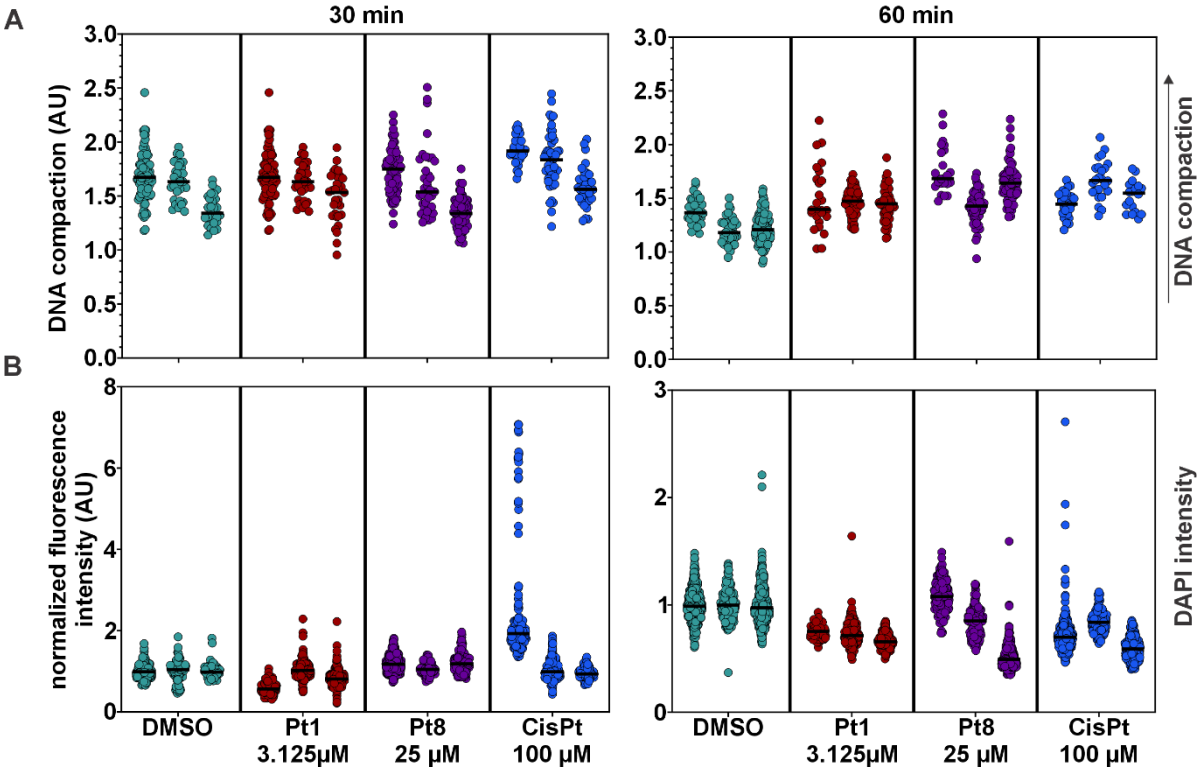


Figure 33. Quantification of nucleoid compaction (A) and DAPI fluorescence intensity (B) corresponding to Figure 31, separated into individual biological replicates.

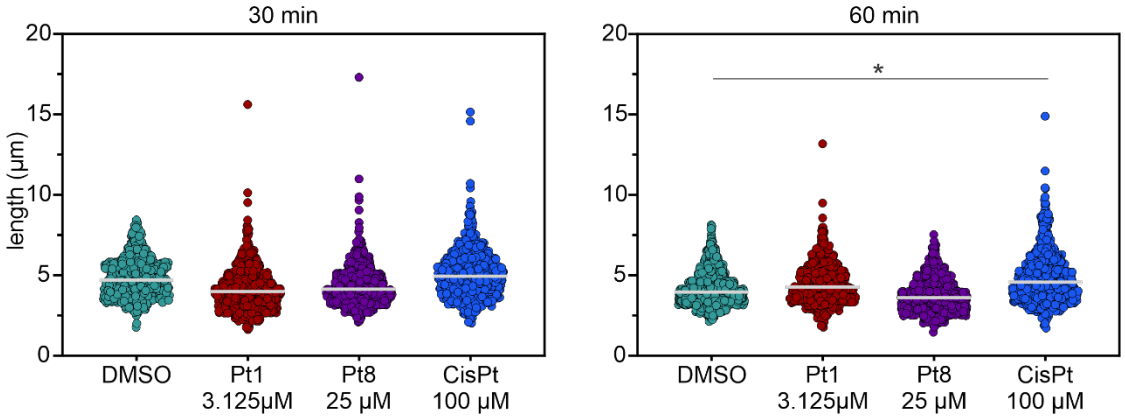


Figure 34. Cell length measured from BCP images. Grey lines indicate the median. Significance was tested with nested t-tests (p value: * ≤ 0.5).

It was wondered whether the compounds directly interact with and damage DNA. To address this, commercially available λ-phage DNA (ʎ-DNA) was incubated with **Pt1**, **Pt8**, and **CisPt**, followed by staining with the DNA dye YOYO-1 and stretching of DNA strands on functionalized glass slides. Samples were then subjected to single-molecule

fluorescence imaging followed by length analysis of individual DNA strands.[259] We observed a clear shift of the DNA molecule length, revealing shorter fragments in samples treated with 3.125 µM **Pt1**, 25 µM **Pt8**, and 100 µM **CisPt** (**Figure 36**). These findings demonstrate that the compounds do indeed directly interact with and damage DNA. The data further shows that both **Pt1** and **Pt8** induce strand breaks, which was expected based on the RecA recruitment results (**Figure 35**). These observations match the known mechanism of **CisPt**, which causes 1,2-intrastrand cross-links of purine bases leading to single strand DNA breaks.[260] Taken together, these results confirm DNA damage as the primary mechanism of **Pt1** and **Pt8**. Interestingly, **Pt1**, which was the most potent antibacterial agent, had the mildest effects on λ-DNA. We wondered whether this observation may be due to the different concentrations, which were based on the OSC determined for *B. subtilis* cultures. Therefore, we additionally tested 25 µM **Pt1** and 3.125 µM **Pt8** to directly compare equimolar concentrations. While an increase of **Pt1** clearly showed stronger DNA fragmentation, the decrease of **Pt8** did not diminish its effect (**Figure 36**). These results suggest that **Pt8** is a more potent DNA-damaging agent.

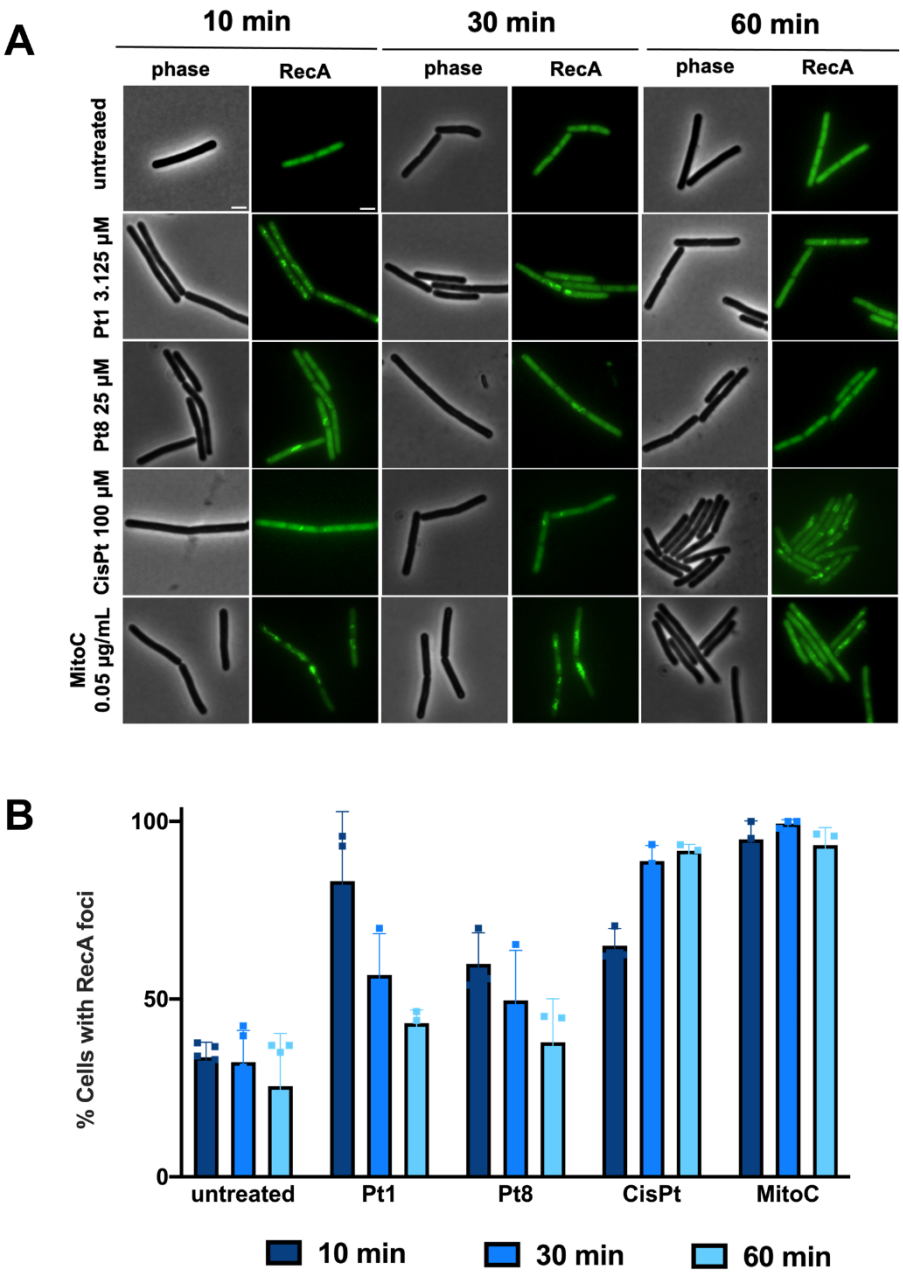


Figure 35. Localisation of RecA-GFP (*B. subtilis* UG10) after treatment with Pt1 (3.125 µM), Pt8 (25 µM), and CisPt (100 µM). Mitomycin C (MitoC, 0.05 µg/mL) was used as a positive control. (A) Phase contrast and fluorescence microscopy images. Scale bar 2 µm. (B) Quantification of microscopy images. Cells with distinct RecA foci were counted and expressed relative to the number of total cells. A minimum of 50 cells were counted per condition per replicate. Error bars show the standard deviation of at least three biological replicates.

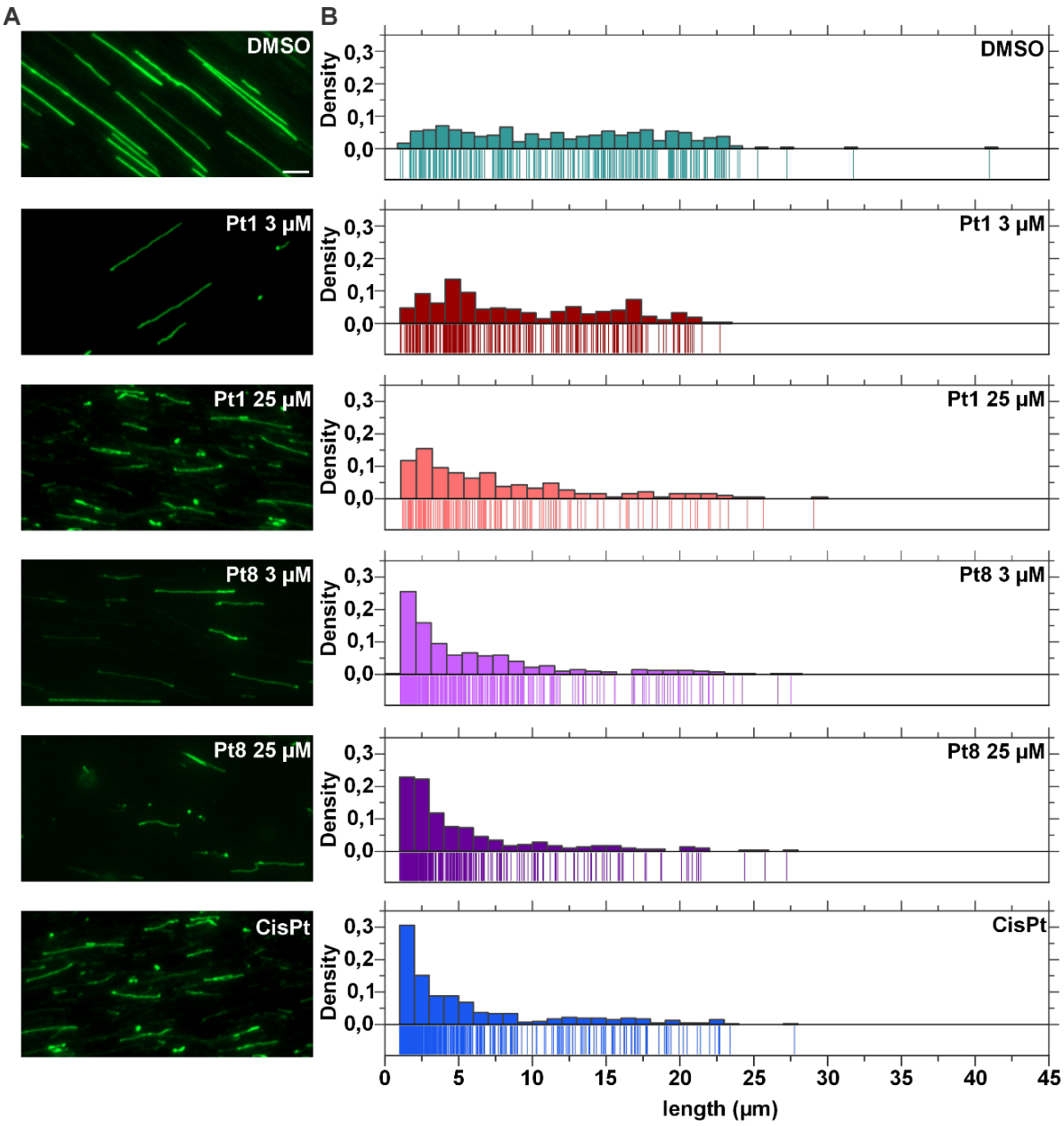


Figure 36. Single-molecule imaging of YOYO-1-labeled λ-DNA. (A) Fluorescence microscopy images of λ phage DNA exposed to the different lead compounds. DMSO was included as negative control. Scale bar 5 µm. (B) DNA strand length distribution measured from microscopy images (pooled from three biological replicates).

2.4.4.3 Cell envelope stress

Nile red stains suggested that **Pt1** could additionally partially act through membrane activity. It was followed up on this lead to explore whether it may allow molecules smaller than GFP to pass the cell membrane.[255] It was first tested the uptake of the membrane-impermeable, red-fluorescent dye propidium iodide (PI). Neither **Pt1** nor **Pt8** showed

increased PI uptake confirming that they do not compromise membrane integrity (**Figure 37A**). Nisin was selected as a positive control for this assay because of its well-established pore-forming mechanism of action. Likewise, no membrane depolarization could be observed when measured with the membrane potentiometric fluorescent dye 3,3'-dipropylthiadicarbocyanine iodide (DiSC(3)5)[261] (**Figure 37B**), showing that no relevant ion translocation is caused by the compounds. Gramicidin is an ion pore that leads to rapid dissipation of the membrane potential and serve as standard positive control in membrane depolarisation assays.[261,262] This finding was independently confirmed by assessing the localization of the cell division regulation protein MinD, which localizes at midcell and cell poles in healthy cells, but delocalizes into membrane-associated clusters upon loss of membrane potential[263] (**Figure 37C**). These results show that neither **Pt1** nor **Pt8** affect membrane integrity.

Despite not being statistically significant, the tendency of **Pt1** and **Pt8** to cause membrane foci was apparent (**Figure 32**). In addition to direct membrane damage, an impairment of cell wall synthesis or cell division can also cause Nile red foci.[255,264]

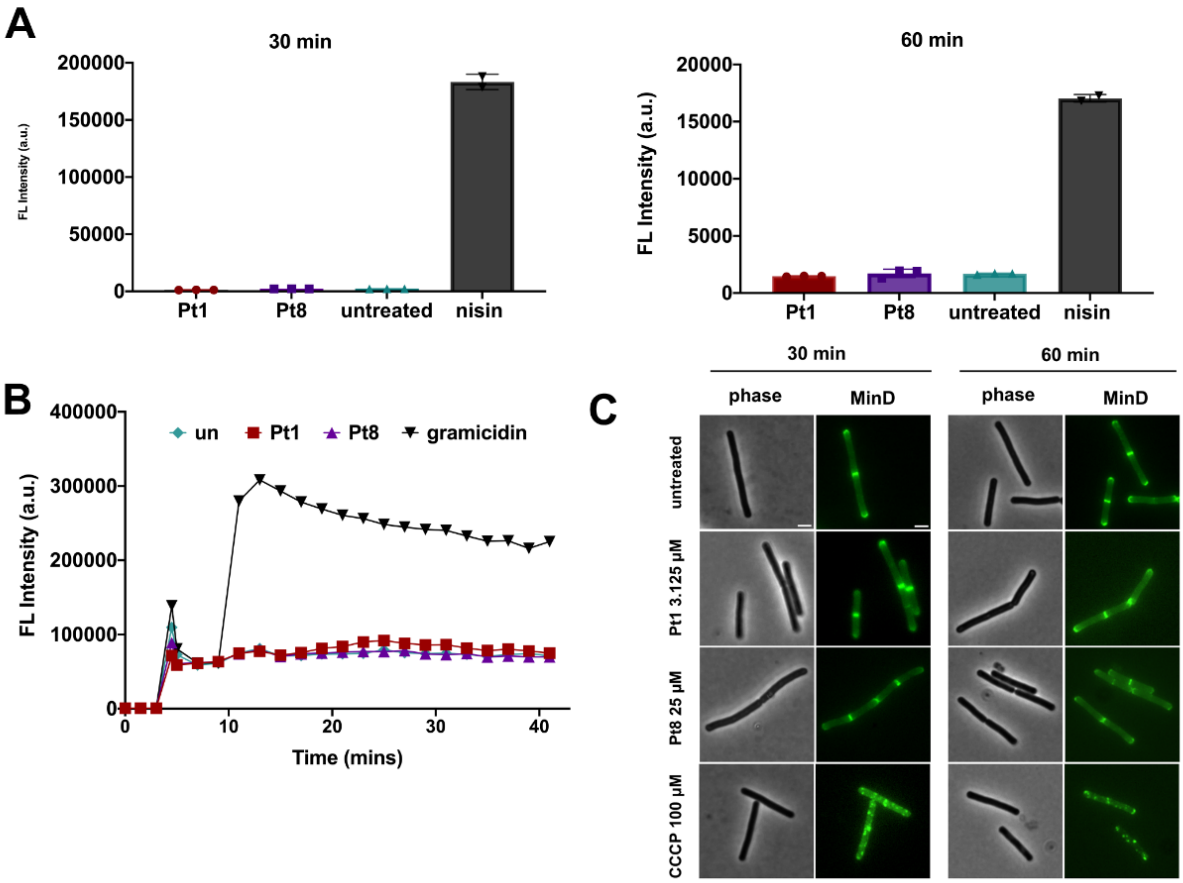


Figure 37. Effects on membrane integrity. (A) Propidium Iodide staining of *B. subtilis* 168CA (pore formation assay). 0.23 µM nisin was used as a positive control. Note the different scales at 30 and 60 min. (B) $DiSC_3(5)$) assay in *B. subtilis* 168CA (membrane depolarization assay). 0.53 µM gramicidin was used as positive control. (C) Locasization of MinD-GFP in B. subtilis TB35 (Pxyl-gfp-minD). Localization of MinD depends on the membrane potential. 100 µM CCCP were used as positive control. All assays were performed after treatment with 3.125 µM Pt1 and 25 µM Pt8. Scale bar 2 µm.

To assess possible effects on these processes, the localization of the proteins MreB and FtsZ were examined. MreB is an actin homologue that moves around the lateral cell axis driving the cell wall elongation machinery forward. This movement stops when cell wall synthesis is impaired, making MreB mobility a reliable reporter for cell wall synthesis inhibition.[255,265,266] However, neither **Pt1** nor **Pt8** affected MreB mobility, showing that they do not inhibit this process (**Figure 38**).

Likewise, the localization of the tubulin homologue FtsZ, the major cell division protein in bacteria[267], remained unaffected demonstrating that the division machinery is not disturbed (**Figure 39**). These results suggest that **Pt1** and **Pt8** do not elicit their antibacterial activity through impairment of cell envelope function.

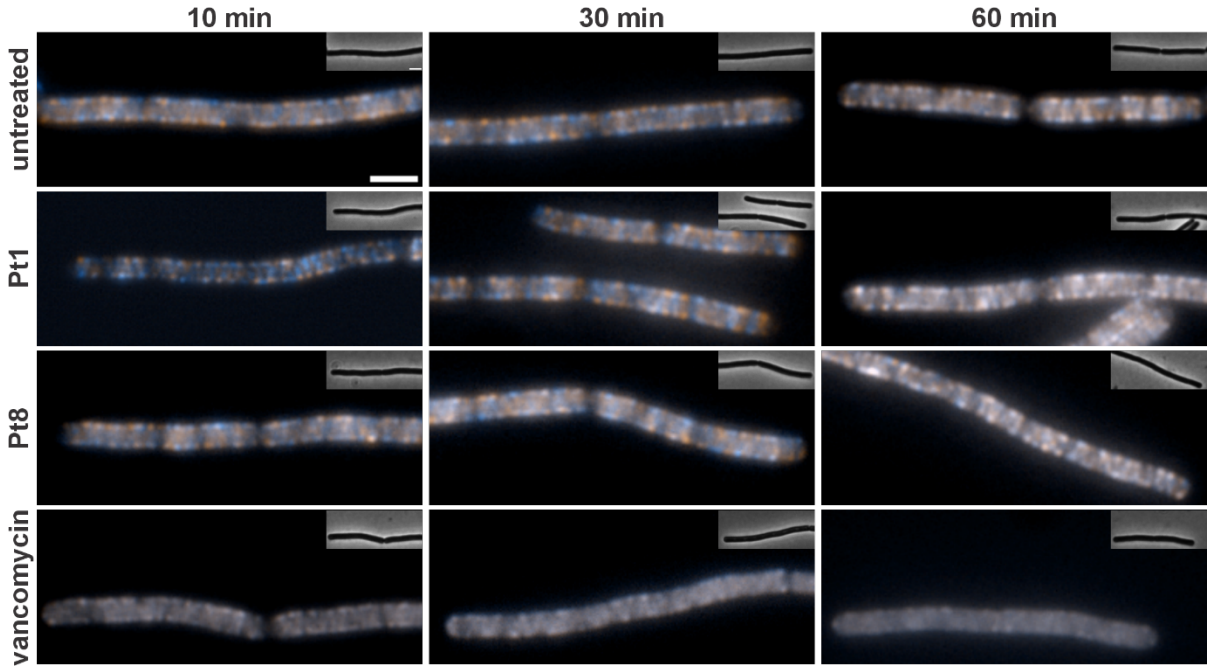


Figure 38. Fluorescence overlays of *B. subtilis* MW10 (Pxyl-gfp-mreB). Cultures were treated with 3.12 µM Pt1, 25 µM Pt8, or 0.67 µM vancomycin for 30 and 60 min. Images show overlays of two consecutive images captured from the same cells in a 30-second interval. Images were false-colored in blue and orange with overlapping signal appearing white. Distinct blue and orange spots indicate movement of MreB foci. Entirely white images indicate a stop of MreB moility (vancomycin control). Scale bar 2 µm.

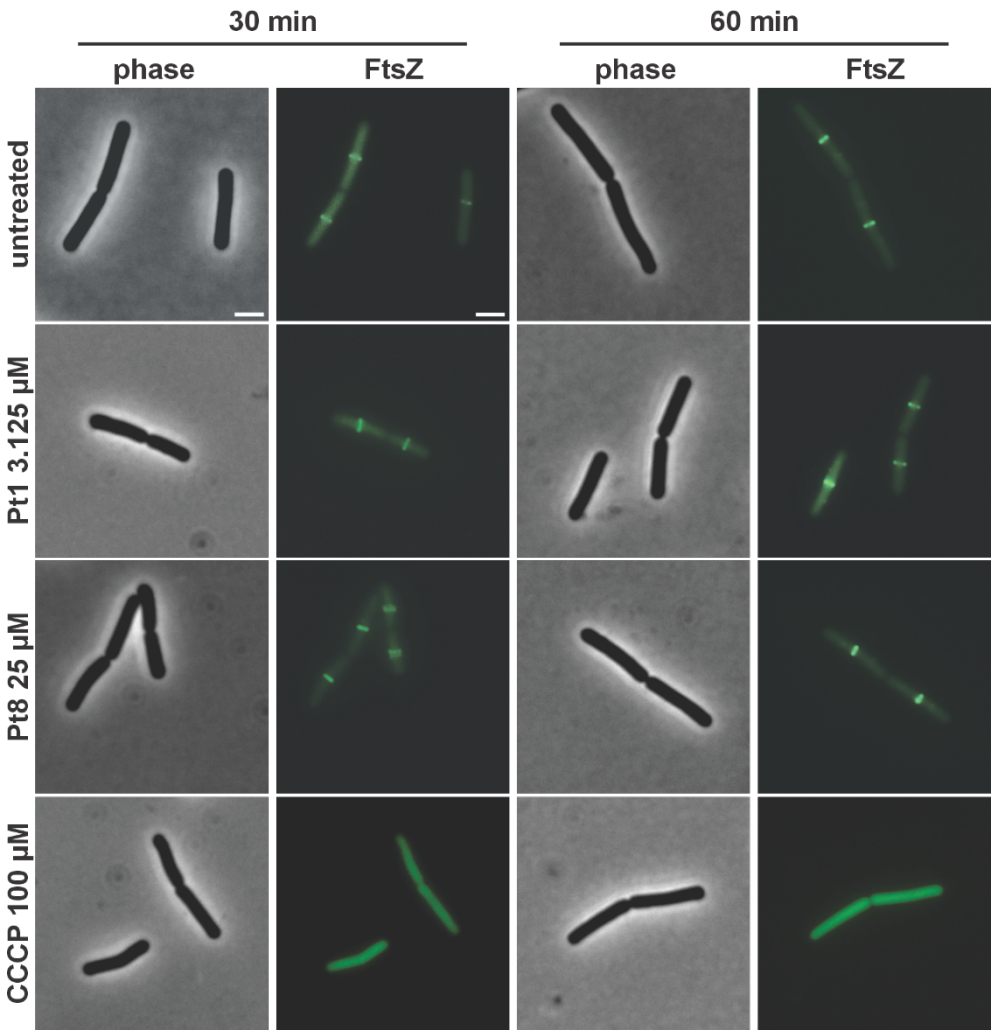


Figure 39. Localization of FtsZ in *B. subtilis* 2020 (Pxyl-gfp-ftsZ). Cultures were treated with 3.12 µM Pt1, 25 µM Pt8, or 100 µM CCCP (**carbonyl cyanide m-chlorophenyl hydrazone**) for 30 and 60 min. Scale bar 2 µm.

2.4.4.4 Effects on transcription and translation

Strong GFP signal in the BCP suggested that the platinum compounds did not interfere with protein expression. However, *PrpsD* is a strong, constitutive promoter and mild effects will not be visible against the background of already accumulated GFP. To determine if the DNA damage response and nucleoid morphology changes induced by **Pt1** and **Pt8** were specific to DNA and did not broadly affect other nucleoid-associated cellular processes, the localisation of the RNA polymerase β′ subunit RpoC and the ribosomal protein RpsB were examined. These proteins have previously been established as reporters for transcriptional and translational inhibition, respectively.[268]

Neither protein showed a distinct phenotype after treatment with **Pt1** and **Pt8**, confirming our notion (**Figure 40 and Figure 41**).

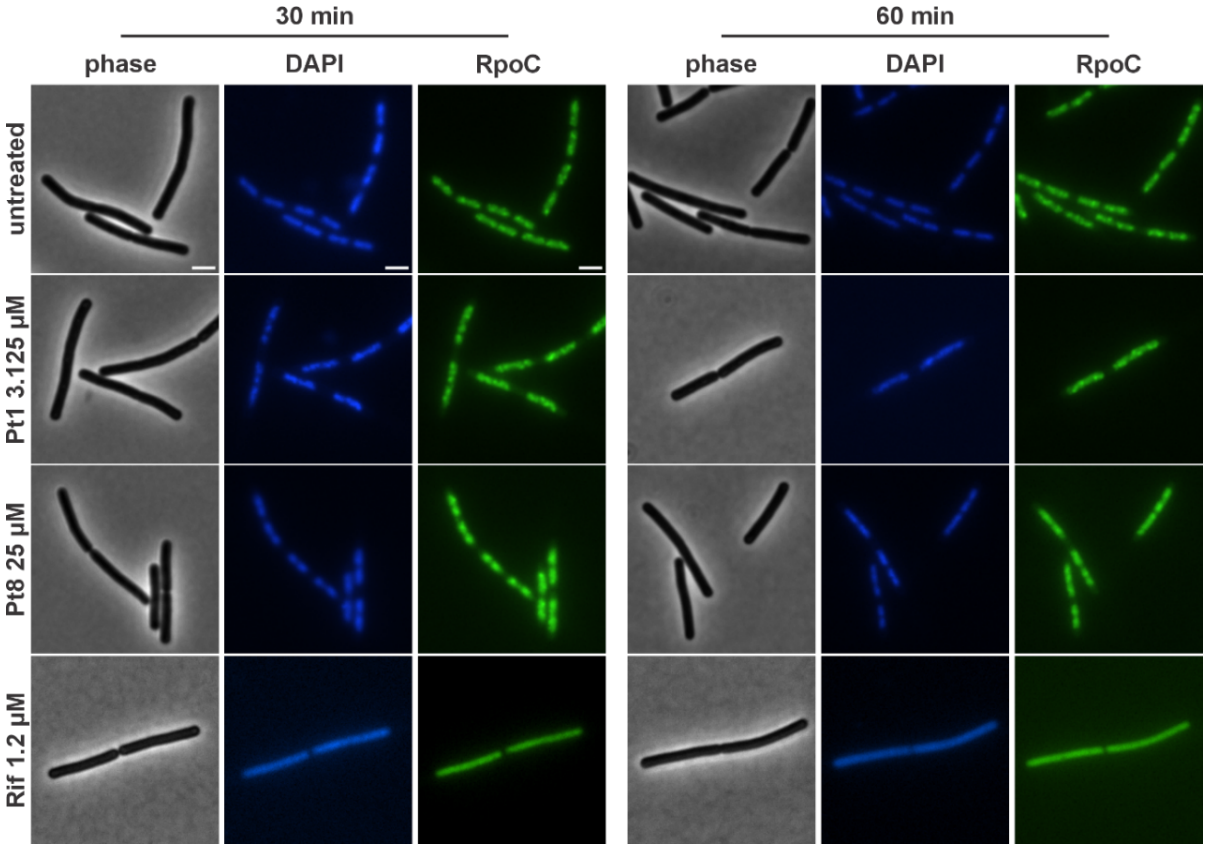


Figure 40. Localization of RpoC-GFP (*B. subtilis* 1048). Cultures were treated with 3.12 µM Pt1, 25 µM Pt8, or 1.2 µM rifampicin (Rif) for 30 and 60 min. Scale bar 2 µm.

We then directly tested their capacity to impair protein production using inducible GFP-MinD as readout. To this end, we added the respective compounds prior to induction of protein expression with xylose. No differences in GFP-MinD expression were observed, demonstrating that protein expression is unaffected by **Pt1** and **Pt8** (**Figure 42**).

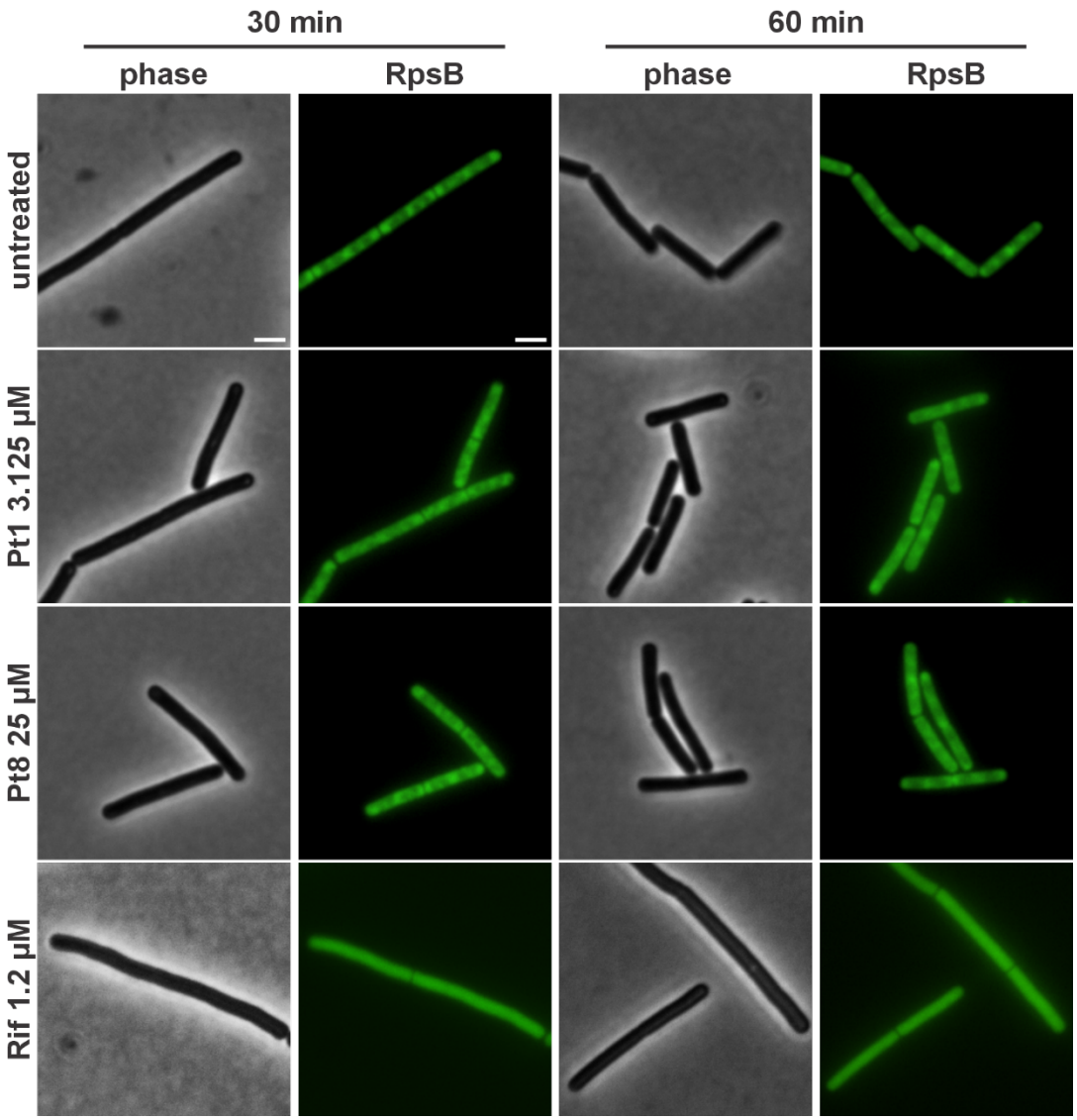


Figure 41. Localization of RpsB-GFP (*B. subtilis* 1049). Cultures were treated with 3.12 µM Pt1, 25 µM Pt8, or 1.2 µM rifampicin (Rif) for 30 and 60 min. Scale bar 2 µm.

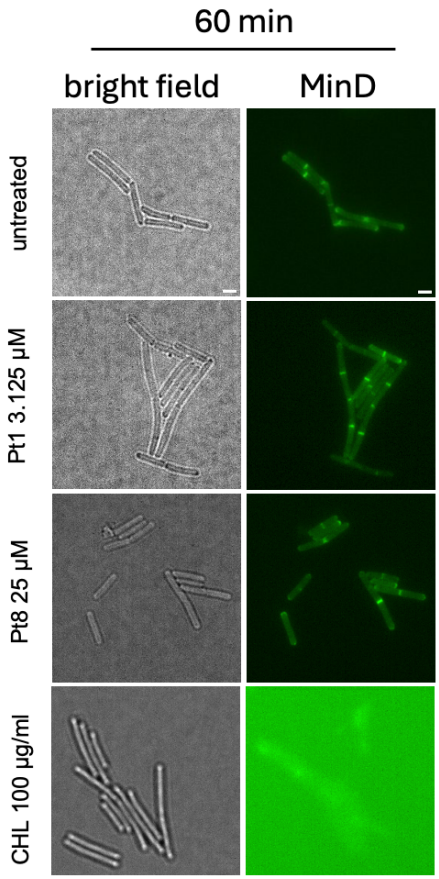


Figure 42. MinD translation induction assay. TB35 (Pxyl-minD-gfp) was grown without xylose, thus not expressing GFP-MinD. In log phase, cells were simultaneously induced with 0.1% xylose and treated with 3.125 µM Pt1, 25 µM Pt8, or 309.5 µM (100 µg/ml) chloramphenicol (CHL). Images were taken after 60 min of induction/treatment. Scale bar 2 µm.

2.4.4.5 Compound uptake

Following the previous observations, we hypothesized that the difference in antibacterial activity between **Pt1** and **Pt8** may be due to less efficient uptake of the latter compared to the former, and that this is likely the reason underlying the poor antibacterial activity of **CisPt** as well. Therefore, bacteria were treated with 584 µg/L (1.56 µM) **Pt1**, 3093 µg/L (6.25 µM) **Pt8** and 30005 µg/L (100 µM) **CisPt** and inductively-coupled plasma mass spectrometry (ICP-MS) was used to assess compound uptake into MRSA based on detection of cellular Pt levels.[269] Indeed, **Pt1** showed much more efficient uptake than **Pt8**, while **CisPt** showed the lowest uptake (**Figure 43A** and **16**). The poor activity of **CisPt** is partially attributed to the inefficient membrane translocation of the compound.

Indeed the group of Nolan has shown that coupling platinum chemotherapeutics to siderophores leads to significant antibacterial activity.[237,238]

Although the uptake percentages differ significantly between the lead compounds and **CisPt**, the absolute amounts of platinum in bacteria after treatment (**Pt1**: 3.5 µg/L, **Pt8**: 4.0 µg/L, **CisPt:** 2.6 µg/L) did not show a marked difference. While the variation in uptake clearly plays an important role in the differences in antibacterial activity, other molecular factors likely contribute as well.

2.4.4.6 Reactive oxygen species

Metal complexes often induce oxidative stress in cells, which can significantly contribute to DNA damage, mostly through generation of hydroxyl radicals. While platinum cannot substitute for iron or copper in a Fenton reaction to create hydroxyl radicals from hydrogen peroxide, it has been shown to increase hydroxyl radical-mediated DNA damage[270] in a system capable of the Fenton reaction. Bacterial cells contain significant amounts of iron and the Fenton reaction is a common source of hydroxyl radicals.[271] Exacerbation of DNA-damaging reactive oxygen species (ROS) in addition to direct DNA-damaging action constitutes a mechanism that could explain the higher antibacterial activity of **Pt1** compared to **Pt8**, in addition to more efficient uptake. To test whether ROS play a role in the activity of the compounds, a scavenger assay was employed. In this modified MIC assay, the activity of a test compound is determined in scavenger-free medium, medium containing the superoxide scavenger tiron, the hydroxyl radical scavenger thiourea, or a mix of both.[258,272] If ROS contribute to antibacterial activity, an increase of the MIC value is expected in medium containing the scavenger specific to the ROS that is generated. Thus, the antibacterial activity of hydrogen peroxide, a hydroxyl radical donor, was not significantly affected by the superoxide scavenger tiron, but in presence of the hydroxyl radical scavenger thiourea, the MIC increased by a factor of 14, and no additive effect was observed when tiron and thiourea were combined (**Figure 43B**). The same trend was observed with **Pt1**, which showed a threefold MIC increase in medium containing tiron, a tenfold increase in the presence of thiourea, and a 13-fold increase in medium containing both scavengers. These results suggest that mostly hydroxyl radicals and to a lesser extent superoxide contribute to the activity of **Pt1**. Importantly, **Pt8** showed no notable MIC increase in the presence of ROS scavengers, confirming our notion that the increased activity of **Pt1** is due to the generation of ROS in addition to direct DNA damage.

Taken together, we propose a mode of action model for this new compound class (**Figure 43**). Both **P1** and **Pt8** directly bind to and damage bacterial DNA, leading to strand breaks and consequently DNA fragmentation. While **Pt8** is the more efficient DNA damaging agent, **Pt1** shows higher antibacterial activity. This seeming conundrum can be explained by (i) more efficient compound uptake, **Pt1** being taken up 50x more efficiently than **CisPt** and 3x more efficiently than **Pt8**, and (ii) by an additional mechanism of **Pt1**, namely the generation of ROS. This multimodal effect of **Pt1** further explain the tendency of **Pt1** to induce Nile red foci, since ROS can also damage membrane lipids[273], likely contributing to the potency of the compound (**Figure 43C**).

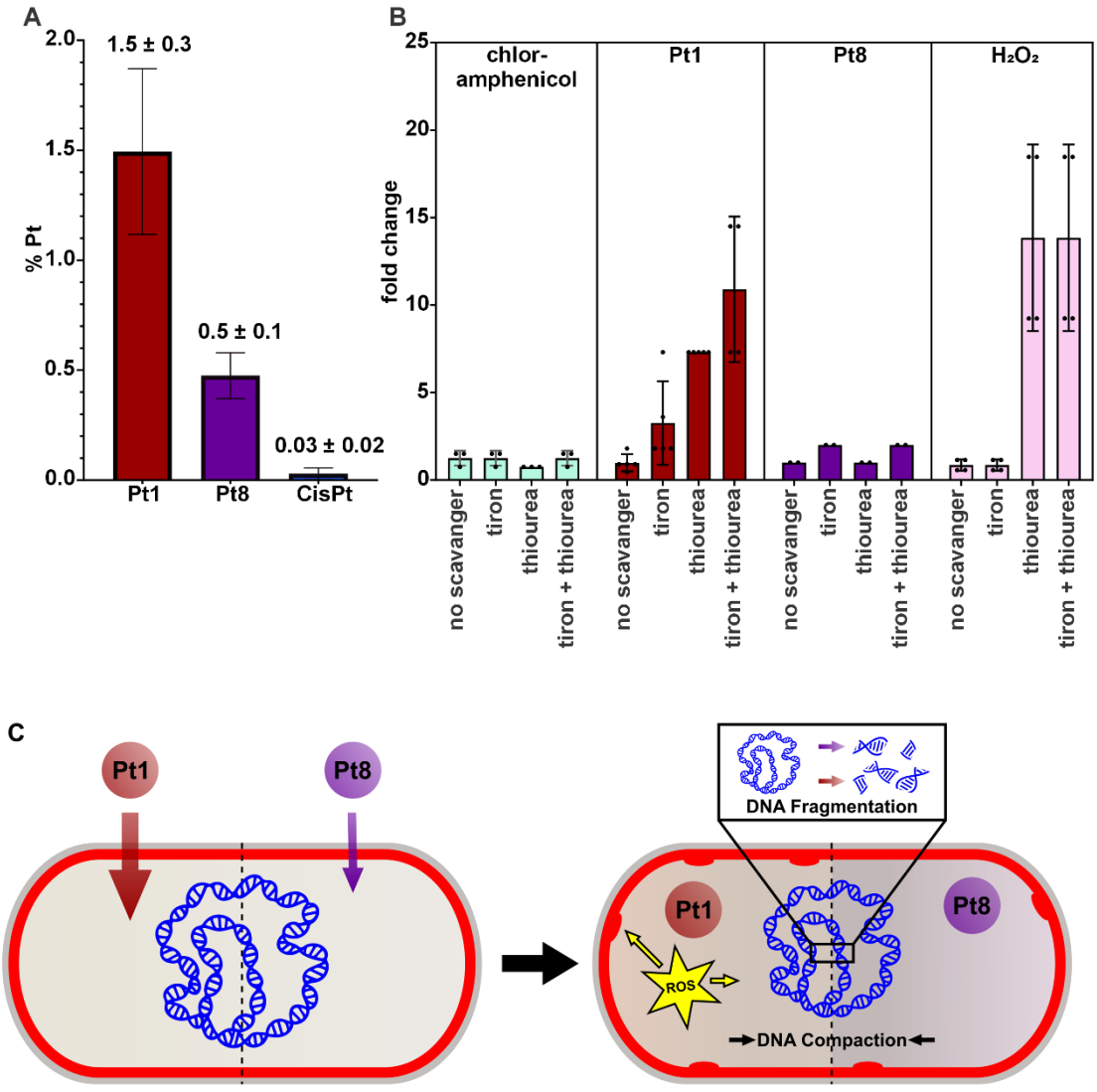


Figure 43. Compound uptake and ROS play a role in the increased potency of Pt1 compared to Pt8. (A) Percent Pt content of MRSA cell lysate after 60 min treatment with Pt1, Pt8, and CisPt.

(B) MIC fold changes (increase) in the presence of ROS scavengers compared to regular medium without scavengers). Error bars represent standard deviation of at least three biological replicates. (C) Mode of action model based on phenotypic analysis of *B. subtilis*. Both Pt compounds damage DNA, causing DNA strand breaks and fragmentation, resulting in nucleoid compaction and reduced DAPI staining. Pt1 additionally generates ROS, mainly hydroxyl radicals, further increasing its potency through multimodal cell damage, e.g., on the cell membrane.

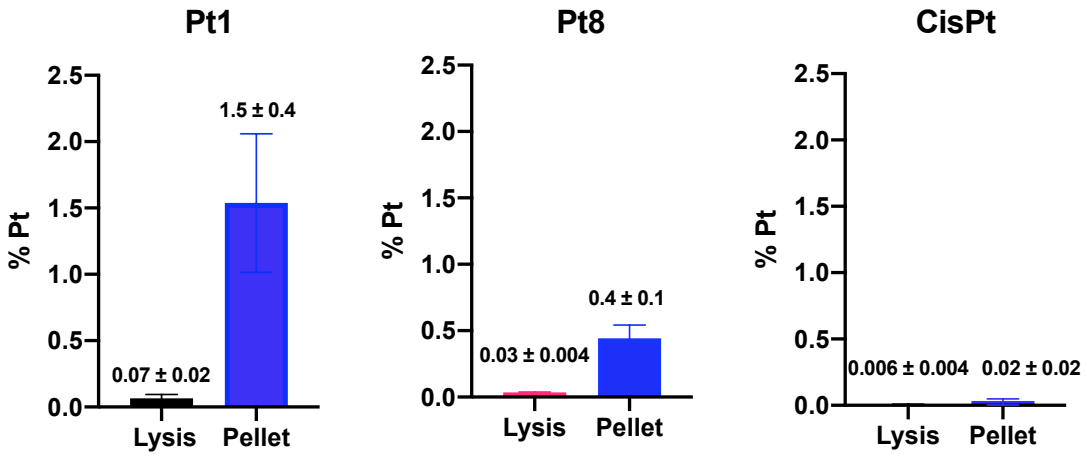


Figure 44. Compound uptake across lysis (cytosolic content) and pellet (bacterial membrane) after 60 min incubation with Pt1, Pt8, and CisPt. Pt content was measured with ICP-MS.

2.4.5 Advanced biological evaluation of Pt1

Amongst all evaluated PtCOD derivatives, **Pt1** displayed the best properties. It showed nano to low micromolar antibacterial activity across a panel of Gram-positive bacteria, displayed low toxicity, both in cell lines and in live *G. mellonella,*[239] and possesses a new mode of action. Furthermore, **Pt1** reduced the fungal load in a *G. mellonella* model of *C. albicans* infection in previous studies.[274] Thus, we further characterized its properties towards *in vivo* applications.

2.4.5.1 Resistance development

We then explored the potential of **Pt1** to induce resistance in *S. aureus* (ATCC 29213), by growing the culture in the presence of compound at ½ MIC for 36 days. Only a minimal increase in the MIC (0.125 to 0.25 µg/mL) was observed over this time period, which is in stark contrast to a 256x fold MIC increase of the antibiotic levofloxacin under the same conditions (**Figure 45A**).

We then used the strain resulting from 36 passages to interrogate whether cross-resistance to other antibiotics could be observed (**Table 7**). As expected, based on the

preceding combination study and the very low resistance, no cross-resistance was observed, further emphasising the unique nature of the mechanism of **Pt1**.

2.4.5.2 Post-antibiotic effect (PAE)

The post-antibiotic effect (PAE) is defined as the continued suppression of bacterial growth following limited exposure to an antibiotic, even after the stress has been removed and the drug concentration has declined below the MIC. Unlike MIC measurements, which describe antibacterial potency under continuous exposure, the PAE provides insight into the persistence of antibacterial activity after limited treatment. This is particularly relevant for compounds that induce lasting cellular damage, as delayed regrowth may reflect the time required for bacteria to recover from disrupted cellular processes, repair antibiotic-induced damage, or restore normal physiological function.[275] The efficacy of **Pt1** in suppressing bacterial growth after a brief exposure to the compound was assessed by studying its post-antibiotic effect (PAE). **Pt1** displayed a PAE of ~5.5 hr compared to the control drugs levofloxacin and vancomycin, which displayed PAEs of 1.5 h and 2.5 h, respectively, at 10x MIC antibacterial activity is not solely dependent on the continuous presence of the compound at inhibitory concentrations. Instead, brief exposure appears to impose cellular stress or damage that delays bacterial recovery and resumption of growth. This is consistent with the proposed multimodal mode of action of **Pt1**, which involves oxidative stress, DNA damage, SOS-response activation as these effects would be expected to require time for repair before normal bacterial proliferation can resume. Therefore, the extended PAE supports the idea that **Pt1** induces persistent intracellular damage rather than acting only through a rapidly reversible growth-inhibitory mechanism.

Table 7. Antibiogram of *S. aureus* ATCC 29213 grown in the presence of sub-inhibitory concentrations of **Pt1**/levofloxacin for a period of 36 days.

	MIC (µg/mL)		
Drug	**36th Passage *S.aureus* ATCC 29213 in the presence of Pt1**	**36th Passage *S.aureus* ATCC 29213 in the presence of Levofloxacin**	***S.aureus* ATCC 29213**
Pt1	0.125	-	0.0625
Ceftazidime	16	8	16
Daptomycin	1	1	1
Gentamycin	0.5	0.25	0.25
Levofloxacin	0.25	32	0.25
Linezolid	2	2	2
Meropenem	0.25	0.125	0.25
Minocycline	0.125	0.125	0.0625
Rifampicin	0.0156	0.0156	0.0156
Vancomycin	1	1	1

Table 8. *In vitro* post-antibiotic effect (PAE) of **Pt1** at different concentrations.

Treatments	**Time for 1 log_{10} increase in bacterial cfu count (h)**	**PAE (h)**
Untreated *S. aureus* ATCC 29213	**~2.5**	**0**
Pt1 1x	**~8**	**~5.5**
Pt1 5x	**~8**	**~5.5**
Pt1 10x	**~8**	**~5.5**
Vancomycin 1x	**~5**	**~2.5**
Vancomycin 5x	**~5**	**~2.5**
Vancomycin 10x	**~5**	**~2.5**
Levofloxacin 1x	**~3**	**~0.5**
Levofloxacin 5x	**~4**	**~1.5**
Levofloxacin 10x	**~4**	**~1.5**

2.4.5.3 *In vivo* skin infection model

Following establishment of a favourable biological profile for **Pt1**, we proceeded to evaluate its efficacy in a topical *S. aureus* skin infection model (**Figure 45B**). To this end, 5–7 weeks-old Swiss mice (22–25 g) were given a superficial wound on the dorsal surface, followed by infection with a bacterial load of ~10^7 CFU/mL. Mice treated with a 2% **Pt1** cream formulation displayed a ~1.9 $\log_{10}$ CFU/g reduction in bacterial load compared to the mice in the vehicle-treated group. Thus, **Pt1** reduced the bacterial load to an extent that is comparable to the established treatment (fusidic acid, ~2.9 $\log_{10}$ CFU/g). This experiment demonstrated the antibacterial *in vivo* efficacy of a platinum-containing compound in a mouse model.

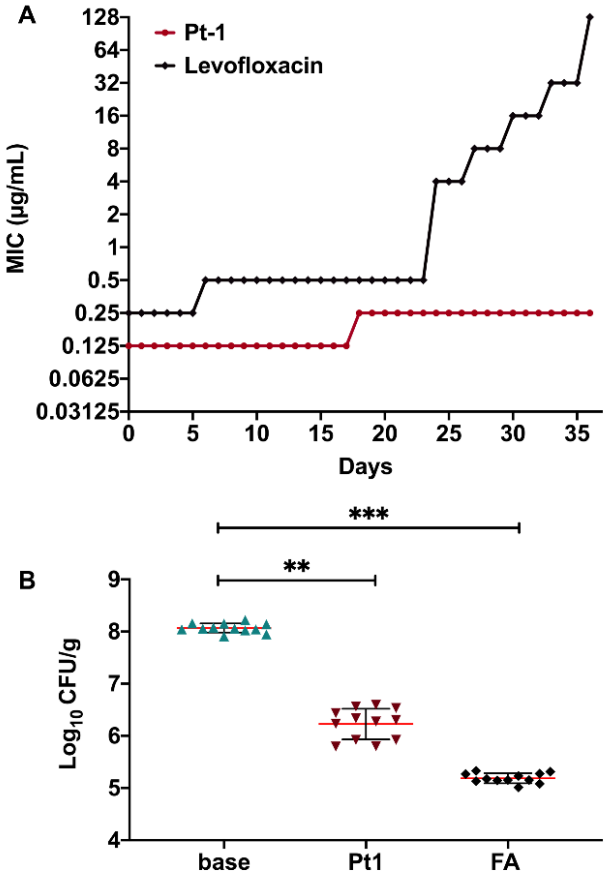


Figure 45. Resistance development and *in vivo* efficacy of Pt1. (A) Growth pattern of *S. aureus* ATCC 29213 grown in the presence of Pt1 and levofloxacin at 0.5x MIC for 36 days. (B) Reduced bacterial load in an in vivo skin infection model in mice. Fusidic acid (FA) was used as a positive control.

2.4.6 Stability of the lead complexes

Demonstrating the stability of the lead compound under biologically relevant conditions is essential to ensure that its biological activity can be attributed to the intact parent complex rather than to decomposition products or released ligands. The stability of **Pt1** was examined by ^{1}H and ^{195}Pt NMR. NMR of approximately 7 mM **Pt1** in DMSO-d_6 was recorded immediately after preparation, and after 24 h and 48 h of incubation at 37 °C (

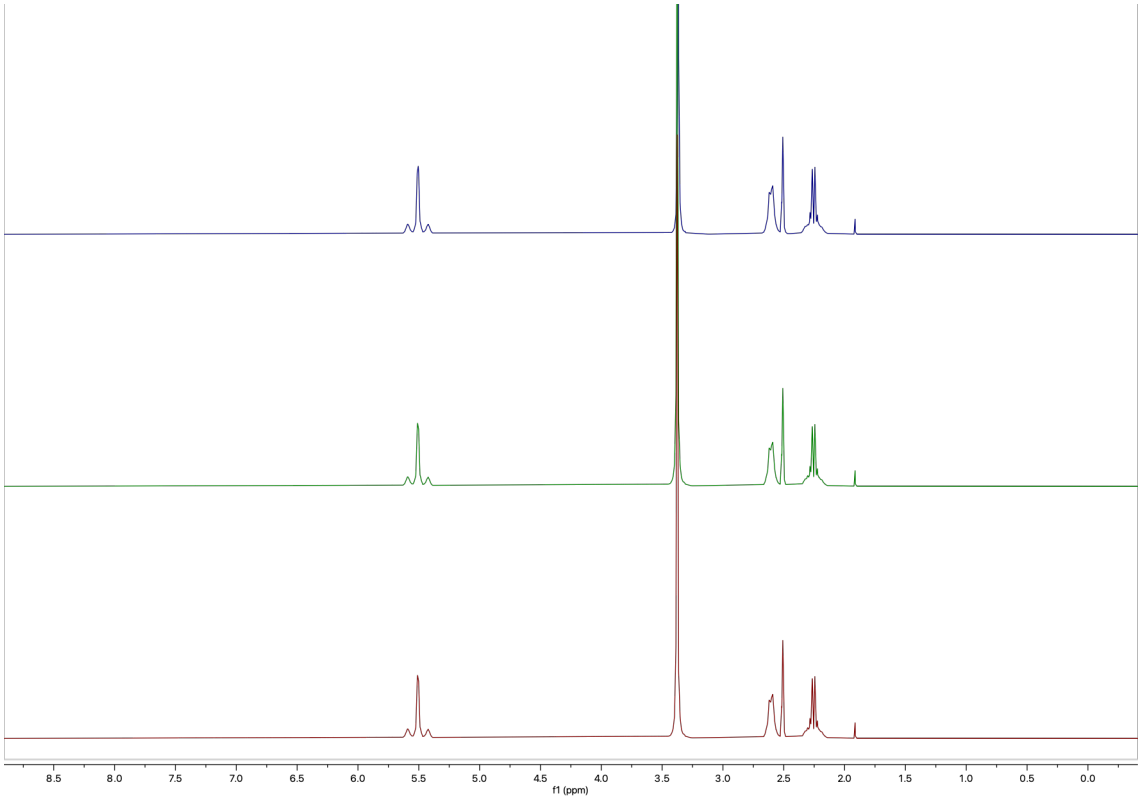


Figure 46 and Figure 47). No differences in the NMR spectra could be identified, suggesting that **Pt1** remains intact for at least 48 h under the tested conditions.

The stability of **Pt1 and Pt8** in aqueous environment were examined by ^{1}H-NMR in the presence of 10% D_2O. No differences in the NMR spectra could be identified, suggesting that **Pt1** and **Pt8** remain intact for at least 24 h under the tested conditions (**Figure 48 and Figure 49**).

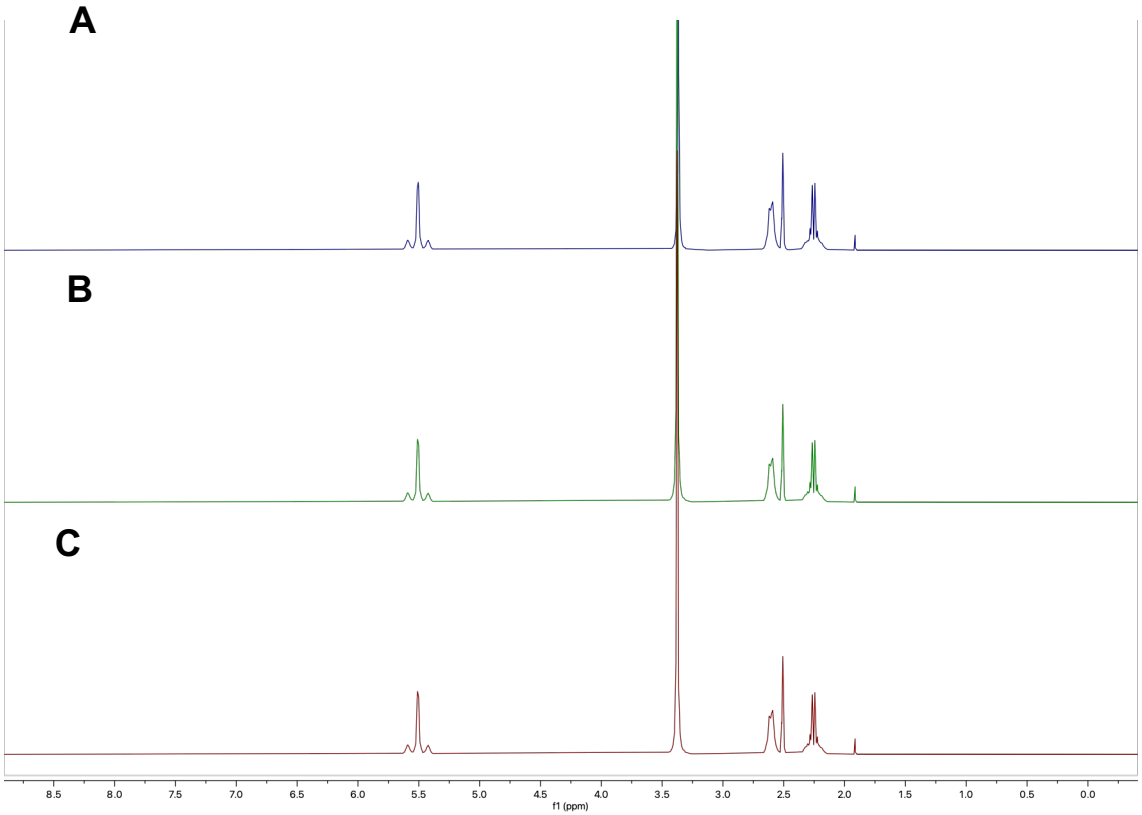


Figure 46. ^{1}H-NMR of Pt1 in DMSO-d_6 immediately after being dissolved (A), after being incubated at 37°C for 24 h (B), and 48 h (C).

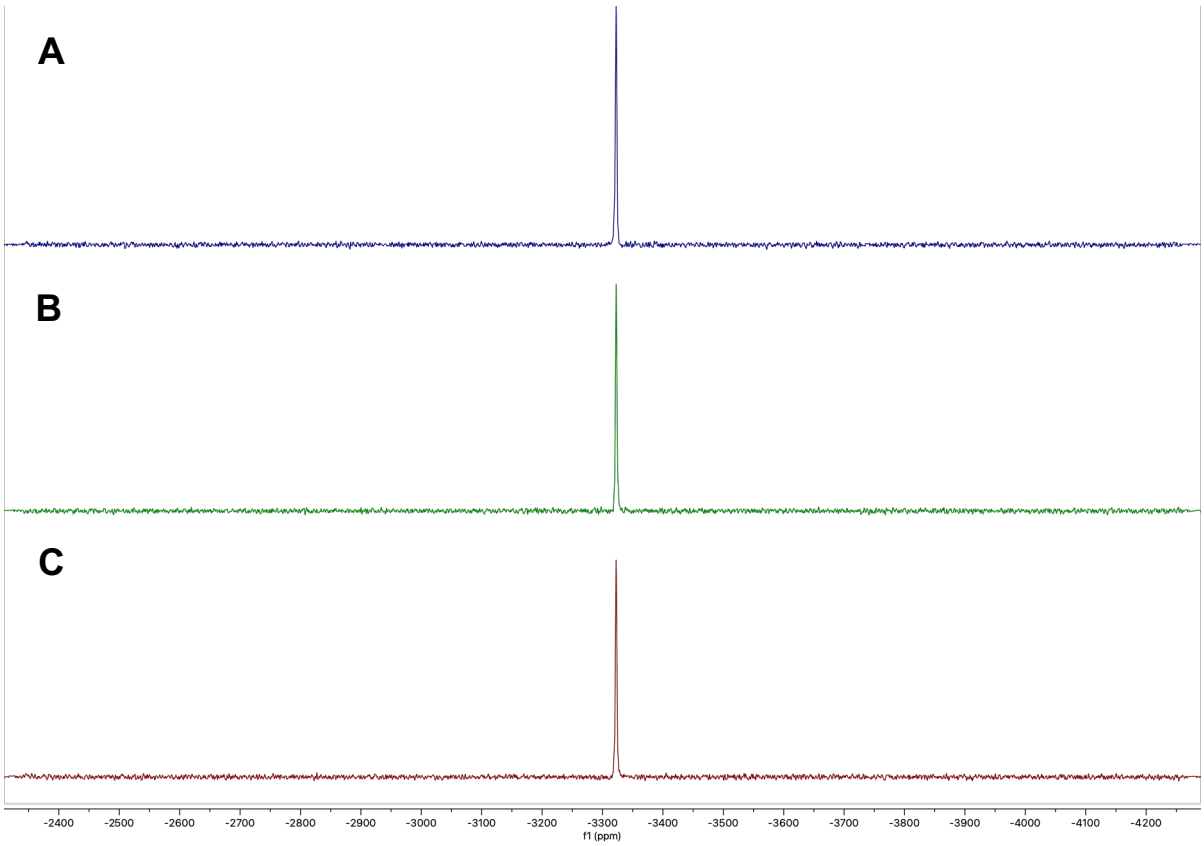


Figure 47. ^{195}Pt-NMR of Pt1 in DMSO-d_6 immediately after being dissolved (A), after incubated at 37°C for 24 h (B), and 48 h (C).

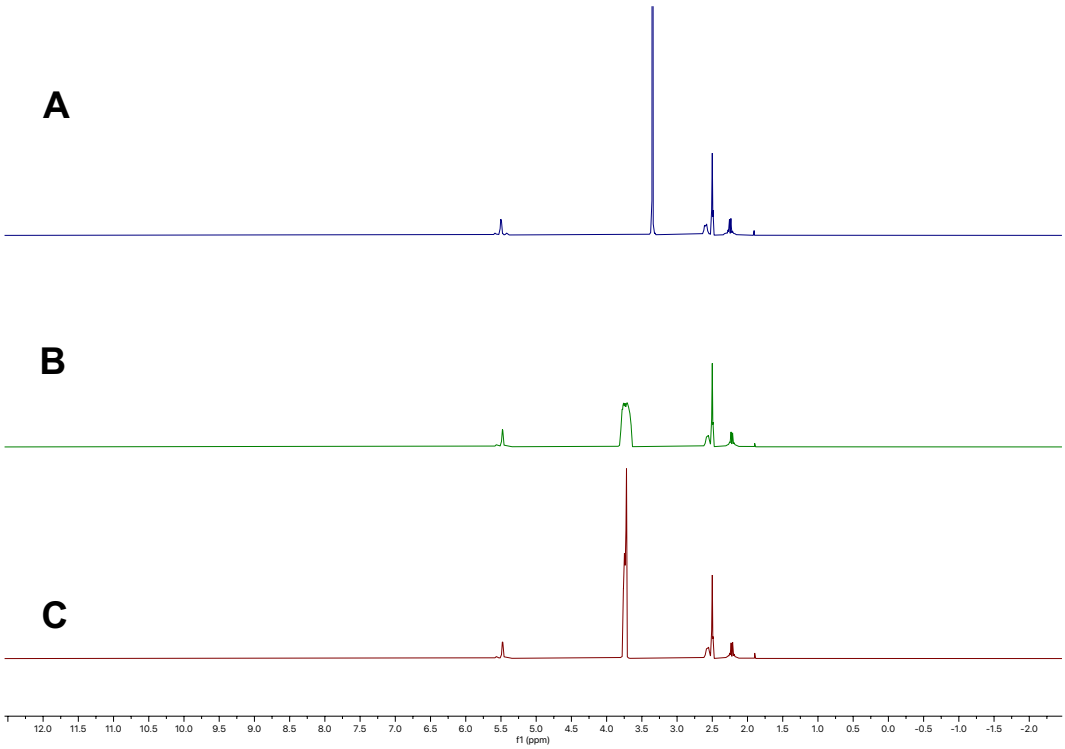


Figure 48. ^{1}H-NMR of Pt1 in DMSO-d_6 at immediately after being dissolved (A), after added 10% D_2O (B) and incubated at 37°C for 24 h (C).

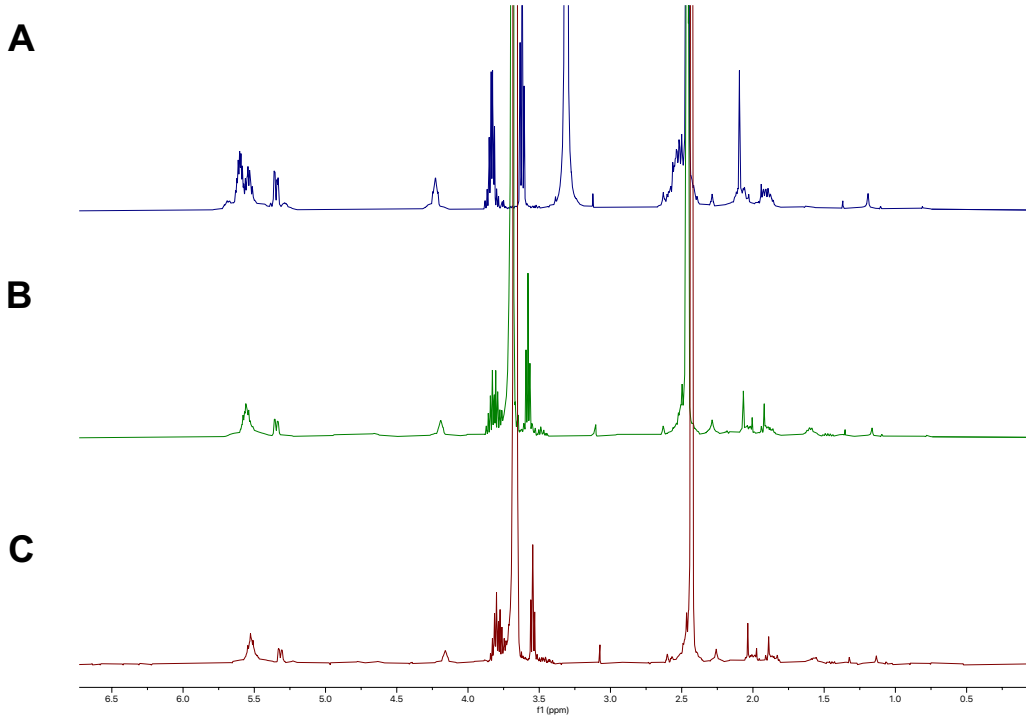


Figure 49. ^{1}H-NMR of Pt8 in DMSO-d_6 at immediately after being dissolved (A), after added 10% D_2O (B) and incubated at 37°C for 24 h (C).

2.5 Summary, conclusions and outlook

In this chapter, a series of platinum cyclooctadiene (COD) complexes was investigated as a potential new class of antibacterial agents targeting Gram-positive pathogens. The lead compounds, **Pt1** and **Pt8**, demonstrated potent antibacterial activity against drug-resistant *S. aureus* strains, while maintaining low toxicity toward healthy human cells and low haemolytic activity. Together with previous work, the present study provided important insights into the structure-activity relationship of this compound class. The halide ligands coordinated to platinum were shown to be essential for activity, as replacement with methyl or hydroxy-containing ligands reduced antibacterial potency and/or increased toxicity. Similarly, substitution of the platinum centre with palladium resulted in complete loss of antibacterial activity and increased haemolysis, highlighting the critical role of platinum in mediating the biological effects of these complexes.[239]

This work further explored chemical modification of the COD ligand to investigate how structural variation influences antibacterial activity. Initial modifications at the double bond position (**Pt2**–**Pt5**) introduced aromatic and heteroaromatic substituents with varying steric and electronic properties. During the SAR studies, modification of the COD ring at the double-bond position with a nitro group was attempted. Although the corresponding ligand was successfully synthesised and purified, subsequent complexation was unsuccessful. It may be attributed to the strong electron-withdrawing nature of the nitro group. Coordination of COD to platinum centre depends on π-donation from the alkene double bonds to the metal centre; therefore, introduction of a nitro substituent at the double-bond position is expected to reduce the electron density of the alkene and weaken its ability to coordinate to platinum. In addition, the nitro group may alter the geometry and electronic properties of the COD scaffold, further disfavouring formation of the desired PtCOD complex. However, all double-bond modifications resulted in complete loss of antibacterial activity, indicating that this region of the ligand scaffold is highly sensitive to substitution. Subsequent modification at the allylic position produced a series of allylic ether complexes (**Pt6**–**Pt10**), allowing investigation of steric bulk, lipophilicity, and electronic effects at this position. Although several compounds retained partial antibacterial activity, none surpassed the original hit compound **Pt1**, with **Pt8** emerging as the most promising derivative of this series. Expansion of these ligand series was not pursued further due to both the considerable synthetic challenges associated with preparing substituted platinum complexes and the limited biological improvements observed.

Mechanistic studies demonstrated that both **Pt1** and **Pt8** primarily target bacterial DNA. Bacterial cytological profiling revealed strong DNA-associated phenotypes, while investigations into membrane integrity, membrane potential, cell wall synthesis, cell division, transcription, and translation showed no significant change in phenotypes. Both **Pt1** and **Pt8** rapidly induced the bacterial SOS response, consistent with DNA damage, and direct DNA fragmentation was confirmed using single-molecule imaging of fluorescently labelled λ-DNA. Interestingly, **Pt8** produced stronger direct DNA fragmentation despite exhibiting lower antibacterial potency than **Pt1**.

Additional studies suggested that the superior antibacterial activity of **Pt1** arises from a multimodal mechanism of action. ICP-MS uptake studies showed that **Pt1** accumulates in bacterial cells substantially more efficiently than **Pt8** and **CisPt**, indicating that membrane translocation is an important determinant of activity. Furthermore, ROS quenching experiments demonstrated that hydroxyl radicals contribute significantly to the antibacterial activity of **Pt1**, whereas **Pt8** activity was unaffected by ROS scavengers. These findings support a model in which **Pt1** combines efficient uptake, direct DNA damage, and ROS generation to exert potent antibacterial activity. This multimodal mechanism likely also contributes to the inability of bacteria to develop high-level resistance over prolonged serial passaging experiments.

Importantly, **Pt1** also demonstrated efficacy *in vivo* in a murine topical *S. aureus* skin infection model, producing a substantial reduction in bacterial burden. These findings establish **Pt1** as a highly promising lead compound with potent activity against clinically relevant antibiotic-resistant pathogens, low mammalian toxicity, and a unique mechanism of action distinct from conventional antibiotics.

Despite these promising results, several limitations remain. Although **Pt1** compares favourably with other recently reported metalloantibiotics in terms of antibacterial potency, its current applicability appears restricted to topical infections, limiting immediate clinical translatability. Future work should therefore focus on improving the physicochemical and pharmacological properties of this compound class to enable systemic administration. While modifications explored in this and previous studies generally reduced antibacterial activity without improving properties such as solubility, additional chemical strategies remain unexplored. Replacement of the halide ligands with alternative bidentate ligands, analogous to those employed in oxaliplatin and carboplatin, may provide improved stability and pharmacological behaviour. As discussed previously, cisplatin undergoes aquation after cellular internalisation,

generating reactive aqua species that contribute to its biological activity. A similar process could therefore be investigated for this class of platinum complexes to determine whether ligand exchange or aquation contributes to their antibacterial potency. Exploration of alternative diene ligands in place of COD may also offer access to more chemically versatile scaffolds. As part of the ligand-modification strategy, norbornadiene was explored as an alternative diene scaffold to COD. However, despite its structural similarity as a strained diene ligand, the corresponding platinum complex could not be obtained under the attempted conditions. Furthermore, development of Pt(IV)-based prodrug systems represents another promising avenue for future investigation.

More broadly, this work highlights bacterial DNA as an underexploited antibacterial target. Only a limited number of clinically used antibiotics directly target bacterial DNA, and few metal-based compounds with selective antibacterial DNA activity have been described. The platinum complexes reported herein represent the first non-cisplatin-based platinum compounds with demonstrated direct DNA-damaging activity, high bacterial selectivity, and *in vivo* efficacy. Altogether, these findings validate platinum-based complexes as a promising platform for the development of a new class of antibacterial agents with a highly attractive biological profile.

Chapter 3: Unlocking Iridium Chemical Space for Antibiotic Discovery through One-Pot Combinatorial Synthesis in a Direct-to-Biology Approach

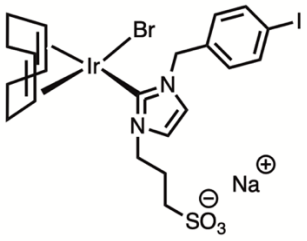
The part of the work presented in this chapter has been published as the following pre-print and currently in peer-review: Özsan Ç., *et al*. Unlocking Iridium Chemical Space for Antibiotic Discovery through One-Pot Combinatorial Synthesis in a Direct-to-Biology Approach. *ChemRxiv*. https://doi.org/10.26434/chemrxiv.15003837/v1

3.1 Introduction

3.1.1 Iridium Complexes as Antibacterial Scaffolds

Discovered by Smithson Tennant in 1803 during studies of platinum ore residues, iridium derives its name from the Greek word *iris* (“rainbow”), a reference to the diverse colours displayed by its salts and coordination compounds.[276] Iridium is a third-row transition metal, and its Ir(III) oxidation state possesses a low-spin $5d^6$ electronic configuration. This configuration is generally associated with kinetically inert metal complexes, which is advantageous for maintaining the original ligands bound while reaching biological targets.[277,278] However, it should be noted that piano-stool iridium complexes undergo hydrolysis in aqueous environments by replacing Cl with water. In particular, electron-donating methyl substituents on the Cp ligand can accelerate this process by increasing electron density at the metal centre, thereby facilitating dissociation of the chloride ligand.[277] Thus, despite their overall kinetic inertness, these complexes exhibit a degree of controlled lability that may be beneficial for biological activity by enabling ligand exchange and activation under physiological conditions. In the aforementioned CO-ADD study, iridium emerged as a promising metal centre, with 33 evaluated complexes of which five exhibited low cytotoxicity and high antimicrobial activity.[274]

Diverse classes of iridium complexes have been investigated as potential antimicrobial agents[279–291]. In 2013, Simpson and co-workers investigated iridium NHC complexes bearing charged moieties (**Figure 50**) and evaluated their activity against a panel of Gram-positive and Gram-negative bacteria as one of the first examples of iridium scaffolds as potential antibacterials. Compound **28** (**Figure 50**) displayed MIC values in the range of 2.5–10 μM. Although promising antimicrobial activity was observed, cytotoxic activity down to 13.4 μM against L-929 Mouse Fibroblast cells remained a major limitation.[279]



28

Figure 50. Iridium NHC complex with SO_3 (**28**) charged moiety reported by Simpson and coworkers.

In parallel, piano-stool Ir(III) systems have been extensively studied due to their water solubility and well-tunable ligand environment. Piano-stool Ir(III) complexes have emerged as a promising class of antibacterial agents, exhibiting potent activity against drug-resistant pathogens such as MRSA, combined with low cytotoxicity, high stability, and reduced propensity for resistance development.[32–45] In 2013, Falkinham and co-workers established α-amino acid bearing Ir(III) Cp complexes (**Figure 51Error! Reference source not found.)** as effective antibacterials against nontuberculous mycobacterium species.[292] They found that the nature of the amino acid substituent clearly influenced antimycobacterial activity. Complexes with hydrophobic L-amino acids exhibited more potent activity than those bearing hydrophilic or *N*-methylated amino acid derivatives. In particular, the L-phenylglycine complex was among the most active derivatives, displaying low MIC values against several mycobacterial strains (8.53–52.9 μM), followed by complexes containing L-proline (18–227 μM), L-phenylalanine (16.6–101.6 μM), L-valine (30.8–110.5 μM), L-leucine (56.5 μM), and L-isoleucine (26.5–56.5 μM).

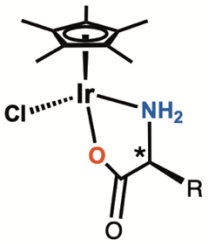


Figure 51. General structure of α-amino acid bearing iridium(III) Cp complexes. 15 examples were reported.

In addition, comparison with the other metal-arene scaffolds indicated that the Cp ring also plays a key role, as strong antimycobacterial activity was mainly associated with Cp

iridium complexes. Therefore, the combination of a hydrophobic L-amino acid with a Cp metal fragment appears to be important for potent antimycobacterial activity.

Sadler and co-workers developed 14 iridium(III) complexes (**Figure 52**) with different cyclopentadienyl derivatives, metformin or an *N*-substituted biguanide, and a halide ligand were synthesised (**Figure 52**). The free biguanide ligands exhibited no antimicrobial activity up to 32 μg/mL, indicating that the iridium Cp scaffold was essential for the activity. Several of the complexes demonstrated selective and notable activity against Gram-positive bacteria, with minimum inhibitory concentrations (MICs) down to 0.5 μM.

The most hydrophilic complexes **29** and **30** (**Figure 52)** were inactive against most of the tested pathogens, with MIC values above 60 μM. In contrast, increasing hydrophobicity through biphenyl substitution on the Cp moiety improved antimicrobial activity, as shown by **34**, which displayed MIC values ranging from 3.2 to 50 μM. Additionally, the halido ligand also influenced the potency of the compounds. Replacement of the chlorido ligand with bromido or iodido analogues enhanced the potency against *K. pneumoniae* but reduced the activity against *E. coli* and *A. baumannii*. The compounds were further tested against the mammalian cell line HEK293 and hRBC to assess the selectivity of their antimicrobial activity. Complexes **35**–**39** displayed favourable selectivity in the Gram-positive panel, including *S. aureus*, *B. subtilis*, *S. pyogenes*, and *S. epidermidis*, with selectivity factors of 4 to >256 based on HEK293 cytotoxicity and 2 to 118 based on haemolytic activity. In contrast, poor selectivity was observed against *E. faecalis*, which was attributed to the weaker activity of the complexes against this strain, which is resistant to several antibiotics.[305] Subsequently, the stability of the active complexes was investigated by storing them in cation-adjusted MH medium at different temperatures (-18, 18, and 42°C), and their MIC values were determined after 1, 4, 8, and 21 days. When compounds **35**–**39** were incubated at 42°C, their MIC values gradually increased, attributable to their decomposition under these conditions. On the other hand, compound **33** showed no change in its MIC value. The investigated complexes were generally stable in broth and exhibited a low tendency to induce resistance, with unchanged MIC values observed for selected compounds after 24 passages against *S. aureus*. Subsequently, they extended their investigation to preliminary mode of action studies. Although the sixth coordination site is labile, no interactions were detected with guanine-containing biomolecules (9-ethylguanine (9-EtG), 5′-guanosine monophosphate (5′-GMP), DNA nucleobase models)

by NMR spectroscopy; with histidine, tryptophan, and leucine by NMR, ESI-MS, and LC-MS. However, L-cysteine reacted readily with the complexes, displacing the biguanide ligand. The authors therefore proposed that the complexes may serve as delivery systems that transport biguanides into bacterial cells, where thiol-containing biomolecules trigger ligand release. The released biguanides may then interfere with endogenous metal ions or metal-dependent enzymes, potentially contributing to the bactericidal activity of complexes **33**–**37 (Figure 52)**. In contrast, sulfonated complexes **38**–**41 (Figure 52)** were mainly bacteriostatic, possibly because the released sulfonyl-biguanide ligands have lower basicity and a different charge state at physiological pH.

It was suggested that these iridium(III) biguanide complexes do not act primarily by binding to DNA, generating ROS, or disrupting the cell envelope, and they likely exert their activity through guanidyl release. Altogether, these findings highlight organoiridium(III) biguanide complexes as promising scaffolds for further development as antimicrobial agents.[278]

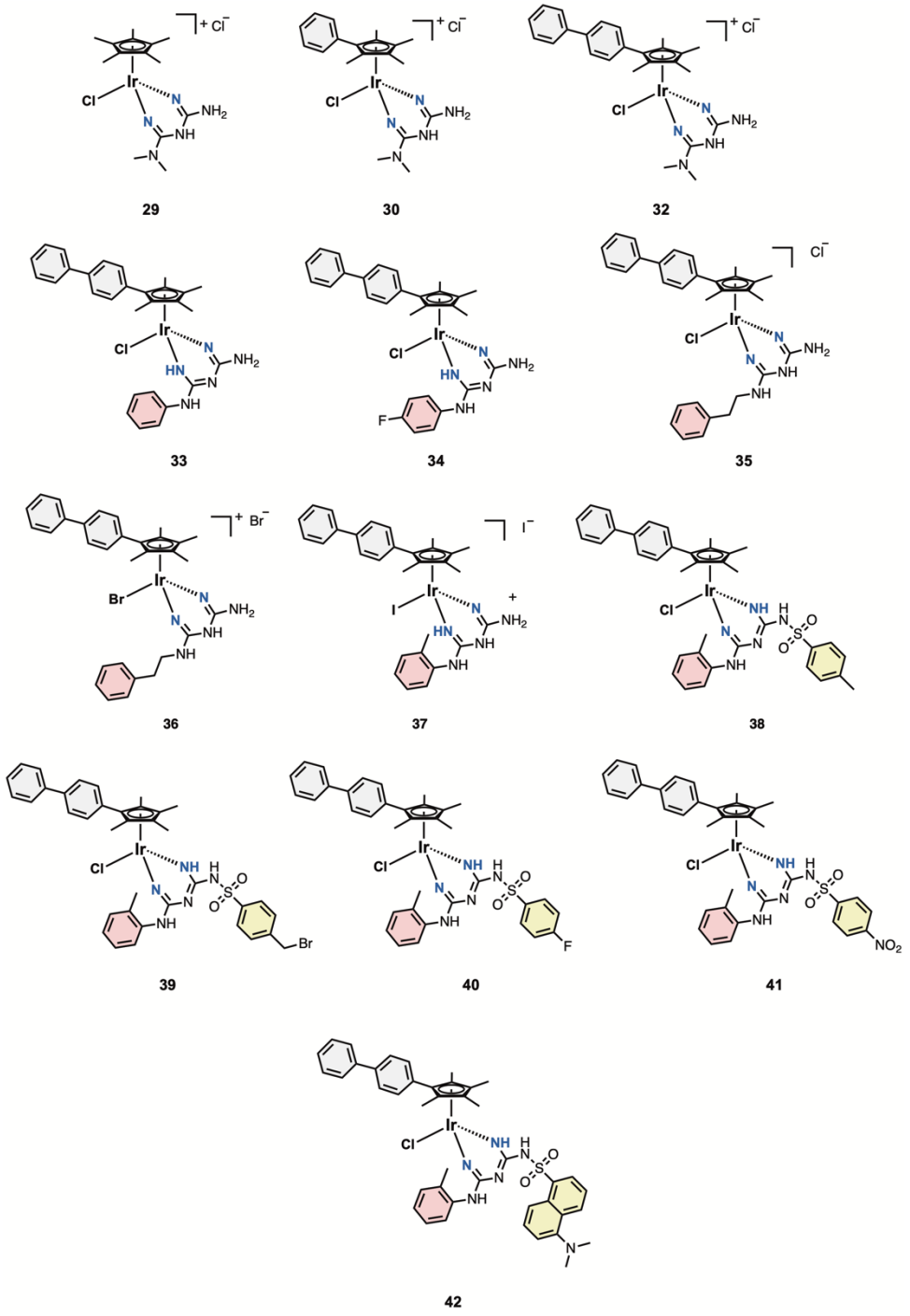


Figure 52. Iridium(III) Cp*/Cp biguanide complexes reported by Sadler and co-workers.

In 2019, 1,2-diaminoalkane moiety-bearing iridium(III) Cp complexes have been reported as potent antibacterial agents against several resistant strains of *S. aureus*. The antibacterial potency of *cis* (**43**, **Figure 53**) and *trans* (**44**, **Figure 53**) isomers was investigated. Notably, the *trans* isomer exhibited no antibacterial potency up to 125 μM,

whereas the lead compound, the *cis* isomer, (**Figure 53**) exhibited minimum inhibitory concentrations (MICs) of 9.8 μM against *S. aureus* and 14.6 μM against MRSA. Subsequently, they investigated the toxicity of the lead compound and observed no haemolytic activity in sheep red blood cells. Additionally, no cytotoxic effects were observed against Vero and HEK293 cells at concentrations at least 50-fold higher than the MIC values. Furthermore, the lead compound exhibited low in vivo cytotoxicity and was evaluated in a mouse model after a single intravenous dose of 2.5 mg/kg. They also performed biodistribution studies by ICP-OES. It showed that iridium was initially present in the bloodstream at levels consistent with the administered dose. By the fourth day, blood iridium levels decreased sharply, while iridium accumulated in the liver and kidneys. By day 14, no iridium was detectable in blood. Iridium was also detected in urine collected over the study period, suggesting that the compound or its metabolites can be cleared from the body. [297]

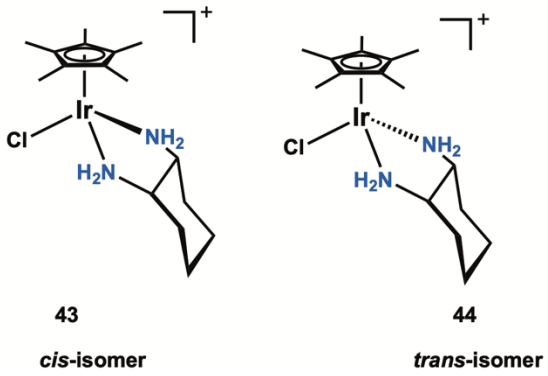


Figure 53. 1,2-diaminoalkane moiety-bearing iridium(III) Cp complexes (cis- and trans- isomers).

3.1.2 Combinatorial Chemistry

While the potential of metal complexes with diverse metal centres and ligand scaffolds as antimicrobial agents has been demonstrated in recent years, most current studies investigate only a small number of compounds at a time. This makes it inefficient and impractical to explore large libraries. Moreover, although promising compounds continue to be identified, our understanding of the relationships between their structure and antimicrobial activity remains limited.[161] Combinatorial chemistry offers a powerful solution by enabling the generation of structurally diverse large chemical libraries through the combination of building blocks using synthetic methodologies that are robust, adaptable, and highly efficient.[306] It has become an important strategy in drug discovery, materials science, and catalysis because it enables the systematic generation and evaluation of large numbers of structurally diverse compounds. When combined with

automation, this approach significantly reduces the time, labour, and cost associated with synthesis and screening.[307] The preparation of small-scale libraries, followed by high-throughput screening, allows many compounds to be assessed rapidly and economically. Integration with DNA-encoded library technologies has further improved the efficiency of hit identification and validation, making combinatorial approaches increasingly valuable in early-stage discovery. In this technology, each compound is attached to a unique DNA barcode that records its synthetic history and enables identification after target-based selection. By coupling split-and-pool synthesis with DNA sequencing-based hit identification, DEL technology enables screening of very large chemical spaces with minimal material, making it a powerful platform for modern drug discovery.[308,309] Recently, the translational potential of DNA-encoded libraries has been demonstrated through their successful application in drug discovery[309–317], with compounds progressing to preclinical and clinical development.[318,319]

In this context, the generation of combinatorial libraries of metal complexes is particularly attractive, as both the metal centre and ligand framework can be systematically varied and optimised. Successful combinatorial chemistry in drug development relies on diverse, modular building blocks that enable efficient access to broad chemical space, thereby increasing the likelihood of identifying active compounds. Concurrently, the synthetic methodology must be robust, scalable, and broadly tolerant of functional groups, while operating under mild conditions. Reactions should proceed with minimal side reactions and require little to no purification, ensuring suitability for high-throughput synthesis, characterisation, and screening.[320]

3.1.2.1 Combinatorial Chemistry in Syntheses of Metal Complexes

Identification of novel biologically active metal complexes through combinatorial chemistry was first demonstrated by Lippard and co-workers in 1998. They pioneered the combinatorial synthesis of metal complexes by preparing a library of 17 platinum-amino acid complexes and evaluating their DNA-binding properties. This screening identified a complex containing an L-lysine moiety, which was subsequently re-synthesised, purified, and validated as a hit with moderate activity in human cervical cancer (HeLa) and human colon cancer (KM12) with CC_{50} value of 59.2 µM and 74 µM, respectively.[321]

3.1.2.2 Combinatorial Iridium Chemistry

Building on these developments, iridium-based scaffolds have emerged as particularly attractive candidates for the discovery of biologically active metal complexes. Iridium

metal scaffolds have accessible oxidation states (+1 and +3) and can coordinate a wide range of donor ligands. These properties make it feasible to efficiently explore diverse chemical spaces by constructing large libraries of iridium complexes. Bernhard and co-workers pioneered combinatorial synthesis of luminescent iridium complexes back in 2004. They developed a diverse library of 100 complexes by combining one neutral, 10 diamine-type and 10 different cyclometalating ligands to an iridium(III) metal centre.[322] Subsequently, they demonstrated the robustness of this approach through expanding it to a library of 1440 complexes by using 60 diverse cyclometallated iridium(iii) dimers, 24 *N^N* ancillary ligands including 1,10 phenanthroline, tetrazoles and pyrazoles derivatives (**Figure 54**, a).[323]

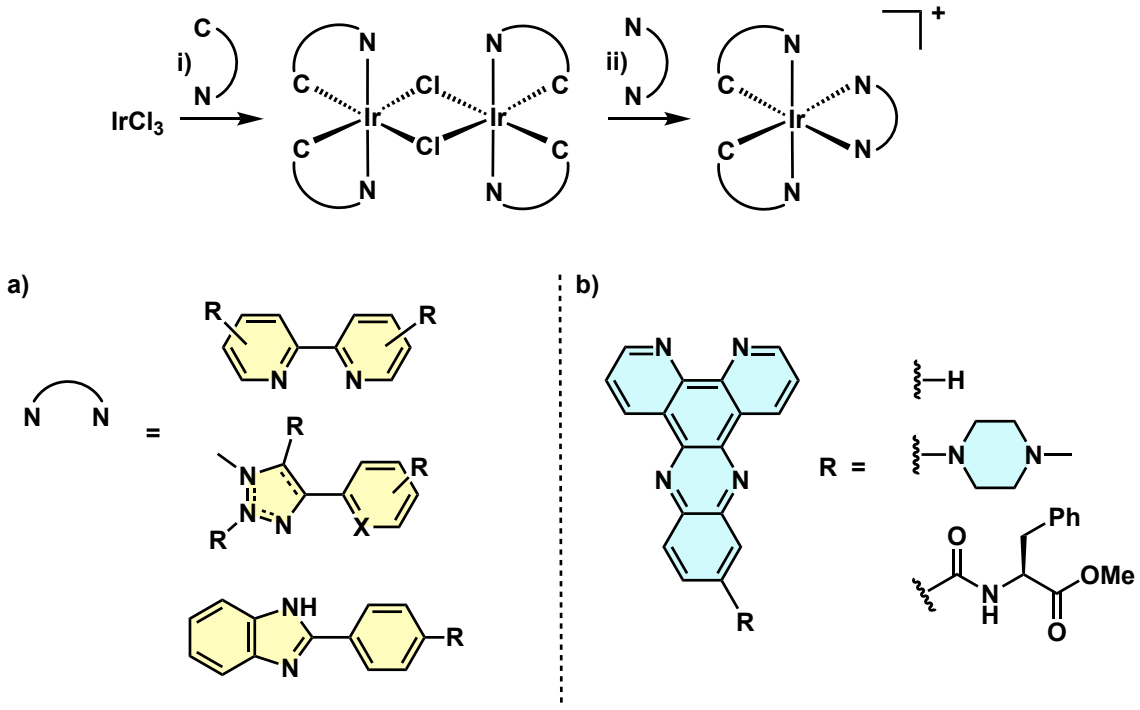


Figure 54. The Combinatorial iridium methodology. a) Heteroleptic iridium(III) complexes pioneered and investigated by Bernhard and co-workers. b) Vilar's group recently expanded this approach.

The same group expanded their approach and developed a library of 1152 iridium(III) compounds, which they screened as photocatalysts for the dehalogenation of aryl bromides.[324] More recently, the development of iridium(III) combinatorial libraries for biological applications has begun to attract attention. Vilar and co-workers have recently established a semi-automated synthesis platform for generating libraries of photo-cytotoxic heteroleptic iridium(III) complexes for potential use of photodynamic therapy (PDT).[325] By the same group, a combinatorial library of 78 phototoxic octahedral

iridium(III) complexes with cylometalating polyaromatic (*C^N*) and phenanthroline-imidazole or dipyridophenazine derivatives (*N^N*) ligands was established as a source of potential antibacterial agents.[326] Recently we established a combinatorial approach using CuAAc 'Click' chemistry to synthesize 288 iridium complexes for antibacterial and photophysical evaluation.[327]

3.1.2.3 Schiff-base Chemistry for Combinatorial Synthesis

Schiff bases take their name from Hugo Schiff, who first reported them in the journal 'Jestus Liebigs Annalen der Chemie' in 1864.[328] Since then, they have become widely used as ligands in metal complexes and have played an important role in the development of coordination chemistry. Schiff bases are obtained through the condensation of a primary amine with an aldehyde or ketone. During this reaction, the carbonyl group is converted into an azomethine, or imine, functional group Schiff bases offer broad structural flexibility and can be readily tailored for metal coordination. Among the strategies explored in the literature, Schiff-base chemistry has emerged as particularly suitable for combinatorial metal complex synthesis due to its simplicity, modularity, and adaptability under mild reaction conditions. In 2014, the Ang group utilized a one pot metal-based three-component assembly (3CA) to develop water-soluble Ru-arene Schiff-base complexes. A library of 450 complexes was screened against different cancer cell lines.[329] This Schiff-base chemistry was further utilized by the same group to generate different ruthenium complex libraries and investigate their biological and catalytic properties.[330–333]

Building on the three-component assembly (3CA) platform, our group subsequently integrated machine learning (ML) into this methodology to guide the discovery of antibacterial ruthenium complexes. In this study, an initial training set of 288 ruthenium arene Schiff-base complexes was generated by combining six picolinaldehydes, twelve aniline derivatives, and four ruthenium arene precursors. Following biological evaluation, the resulting antibacterial activity data were used to train ML models to predict active compounds across a larger virtual chemical space. This approach was particularly valuable because conventional molecular representations, such as SMILES-based descriptors, are often poorly suited to transition-metal complexes. To overcome this limitation, the complexes were encoded using a ligand-based fingerprinting strategy, thereby translating the modular structural information of each building block into a machine-readable format. The trained models were then utilised to predict a new set of compounds displaying antibacterial potency. A virtual library of approximately 77 million

complexes was initially generated and subsequently filtered to a chemical space of around 2 million candidates that are likely to be active against MRSA. From this narrowed library, 15 commercially available building blocks were selected, enabling the synthesis of the second-generation library of 54 novel ruthenium complexes. Experimental validation of this ML-predicted library demonstrated that nearly 54% of the new library inhibited the growth of methicillin-resistant *S. aureus* (MRSA) at 20 μM, representing a nearly sixfold increase. Notably, none of the building blocks exhibited antibacterial potency up to 20 μM. Seven complexes were subsequently re-synthesised, purified, and fully characterised. It was confirmed that the observed antibacterial activity originated from the ruthenium complexes rather than from unreacted building blocks or side products in the crude mixtures. Overall, this study demonstrated that the combination of modular 3CA chemistry, high-throughput biological screening, and machine-learning-guided compound prediction can significantly improve the efficiency of metalloantibiotic discovery and provide a data-driven route for navigating underexplored metal-complex chemical space.[125]

The Schiff-base chemistry approach has recently been expanded by our group to synthesise 420 manganese(I) tricarbonyl complexes by combining 7 picolinaldehydes, 10 aniline derivatives and 6 axial ligands. The generated crude compound library was screened against MRSA, leading to the identification of 10 hit compounds (**Figure 55**). These hits were subsequently resynthesised and evaluated against a panel of Gram-positive bacteria to confirm their biological activity and further characterise them. The lead compound, **Mn15** (**Figure 55**), exhibited low cytotoxicity against a human dermal fibroblast cell line, with a therapeutic index of 109.[161] Although this approach enables the facile synthesis and evaluation of relatively large chemical libraries, complex formation requires a prior activation of the manganese precursor with silver triflate under inert conditions to form a solvated manganese tricarbonyl intermediate. This additional activation step introduces operational complexity and limits the practicality of the methodology for rapid library generation. Therefore, the development of more streamlined combinatorial approaches, ideally using air-stable precursors and requiring minimal synthetic steps, remains important for expanding the accessible chemical space and accelerating the discovery of biologically active metal complexes.

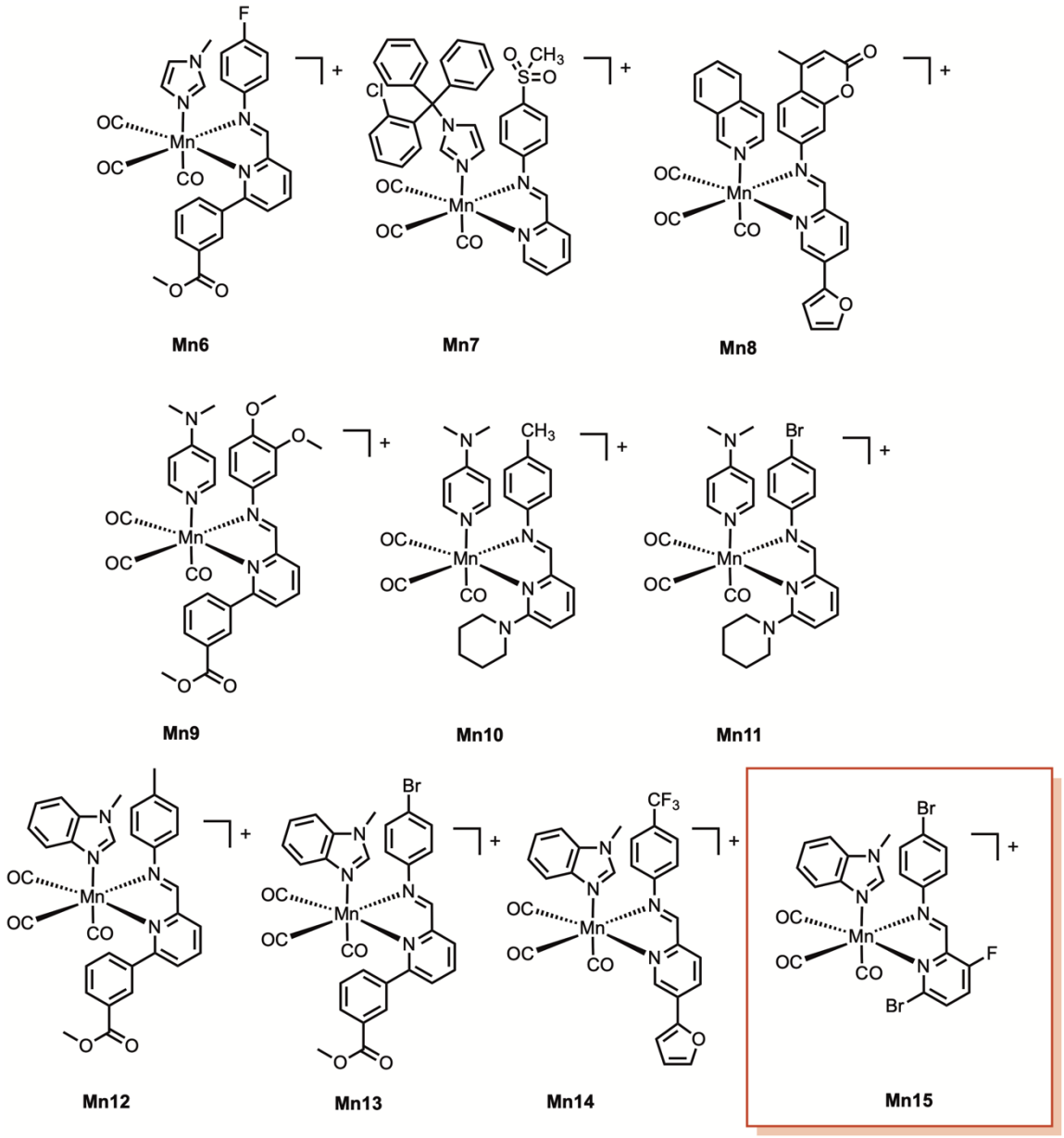


Figure 55. Hit manganese(I) tricarbonyl complexes selected from the combinatorial library of 420. The lead complex (Mn15) was highlighted with the red square. Counterion is TFA or triflate, omitted for the clarity in the paper.

Recently, the Karges group applied a similar strategy to the combinatorial synthesis of a library of 495 Fe(III) complexes from aminophenol, hydroxybenzaldehyde, and pyridine derivativesThey screened this library for cytotoxic activity against human breast adenocarcinoma cells and noncancerous human fibroblasts. Two complexes were re-synthesised, and their biological potency validated. Although this study identified a promising new compound with activity against challenging cancer models, the

combinatorial synthesis workflow had several practical limitations. In particular, the preparation of the compound library required a two-step synthetic sequence and the use of anhydrous solvent, which may reduce the operational simplicity and scalability of the approach. In addition, methanol was used as the reaction solvent, which is not directly compatible with biological assays at high concentrations. As a result, the reaction solvent had to be removed prior to biological screening, introducing an additional step before the stock solutions could be evaluated.

3.1.3 Direct-2-Biology (D2B) Approach

Combinatorial chemistry provides a powerful platform for exploring diverse chemical space. However, translating large compound libraries into biological screening workflows often requires additional processing steps, particularly solvent removal, because many reaction solvents are not directly compatible with biological assays. Consequently, high-yielding reactions in biocompatible solvents are essential to allow the direct application of crude reaction mixtures in biological assays.[334] To this end, it is important to further accentuate the requirements of combinatorial chemistry in direct-to-biology approaches, which enable rapid screening of compound libraries with minimal or no purification. In 2001, Torrance and co-workers reported a biological screening platform using isogenic human cancer cells to identify compounds with selective toxicity in defined oncogenic genotypes. In this approach, fluorescently labelled colon cancer cells carrying mutant K-Ras were co-cultured with an isogenic derivative in which the mutant K-Ras allele had been deleted. It enabled the identification of the compounds with genotype-selective activity directly from mixed-cell assays. Screening of this large library led to the discovery of a cytidine nucleoside analogue with selective activity against mutant Ras cells, which also exhibited a potency in tumour xenograft models. This study provided an early demonstration of how cell-based assays can be integrated with high-throughput screening to identify compounds with improved therapeutic selectivity.[335] The utility of this approach was further demonstrated by Thomas and co-workers at GlaxoSmithKline (GSK), by developing a high-throughput reactive fragment screening platform for the rapid discovery of covalent fragment hits. In this approach, library of 1073 photoreactive fragments (**PhABits**) were synthesised in 384-well plates and screened directly as crude reaction mixtures against a protein target, without a need for prior purification (**Figure 56**). The use of assay-compatible reaction conditions, together with an intact-protein LC-MS readout, enabled rapid identification of covalent fragment hits while providing

confirmation of hit identity through the observed protein mass shift. This workflow allowed more than 1073 photoreactive fragments to be prepared within 24 hours and screened directly against human carbonic anhydrase I, leading to the identification of several hits. Notably, the platform also enabled rapid follow-up synthesis and screening of hit compounds, highlighting the potential of direct-to-biology high-throughput chemistry to accelerate conventional 'design-make-test cycles' for early-stage hit discovery and biological optimisation of relevant compounds.

Together, these studies demonstrate that direct-to-biology approaches can substantially accelerate early-stage discovery by reducing the need for compound purification and enabling rapid screening of crude reaction mixtures. However, the application of this concept to metal-based antimicrobial discovery remains relatively underdeveloped. Many reported combinatorial metal complex platforms still require multiple synthetic steps, inert, anhydrous conditions, solvent removal, precursor activation, or additional purification before biological evaluation. These requirements reduce the workflow's operational simplicity and limit the speed at which large libraries can be generated, screened, and optimised. Therefore, there remains a clear need for robust, modular, and biologically compatible synthetic platforms that enable the efficient generation of structurally diverse metal complexes and their ready integration into antimicrobial screening workflows.

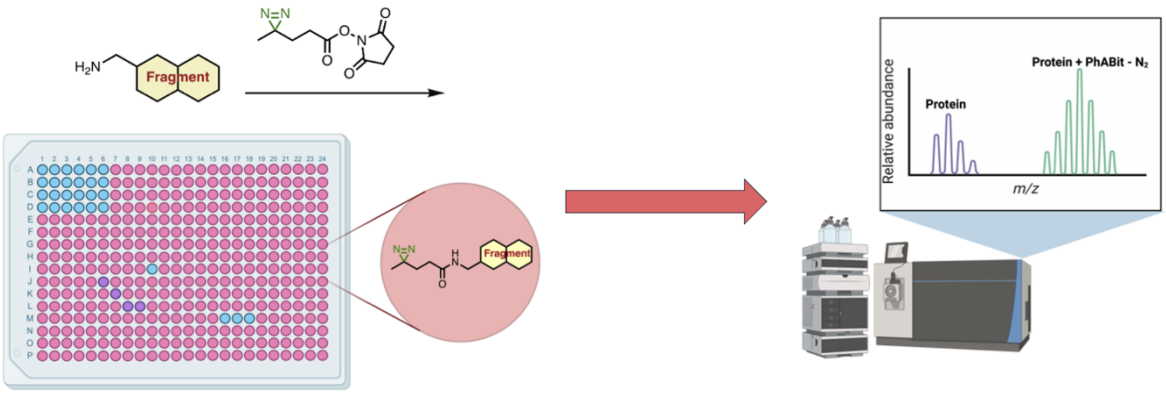


Figure 56. D2B-HTC PhABit screening platform developed by GSK. Direct-to-biology high-throughput chemistry (D2B-HTC) enables the synthesis and screening of photoreactive fragments, termed PhotoAffinity Bits (PhABits), without intermediate purification. Amine-containing fragments are coupled with a diazirine-bearing N-hydroxysuccinimide ester in 384-well plates over 24 h to generate amide-linked photoreactive fragments. Following quenching of the remaining activated ester, the crude reaction mixtures are incubated with the target protein, exemplified here by human carbonic anhydrase I (CAI), and irradiated with UV light at 302 nm for 10 min. Photoactivation of the diazirine group releases nitrogen and generates reactive intermediates that can covalently crosslink fragments to nearby protein residues. Intact-protein

liquid chromatography-mass spectrometry (LC-MS) is subsequently used to detect protein-fragment adducts through the corresponding increase in protein mass, accounting for nitrogen loss, and to quantify crosslinking yields for hit identification. Created in https://BioRender.com.

3.2 Aims and Objectives

Inspired by the success of iridium complexes as antibiotics and the compatibility of Schiff-base chemistry with combinatorial approaches, the aim of this chapter was to develop and evaluate a robust, scalable, and structurally diverse combinatorial platform for the discovery of antimicrobial iridium Cp Schiff-base complexes. This work sought to expand the accessible chemical space of iridium through high-throughput one-pot synthesis, to identify structure-activity relationships within the scaffold, and to select the most promising compounds for further hit-validation studies. Upon validation of the biological activity of the purified hit compounds, the initial mode of action of the hit compound was studied.

In addition, this chapter aimed to explore the antifungal potential of the IrCp Schiff base scaffold against *Aspergillus fumigatus*, identify antifungal hit compounds, and validate their activity through further assays for antifungal potency, mammalian cytotoxicity, and haemolysis. Overall, this chapter aimed to provide a foundation for the future optimisation of iridium(III) Cp Schiff base complexes as antimicrobial agents.

3.3 Results and Discussion

3.3.1 Combinatorial synthesis of Ir(III) Cp library

Schiff-base combinatorial chemistry has been pioneered by Ang and his co-workers as facile and robust methodology for one pot three component assembly (3CA) combinatorial chemistry.[329] The promising antibacterial activity of IrCp complexes reported by the Sadler group[278], together with the versatile combinatorial approach developed by Ang and co-workers[329], inspired us to expand the approach to the synthesis of iridium-based scaffolds. Initially, a test reaction was conducted using **IrCp1** an iridium complex, synthesized from a commercially available pentamethylcyclopentadienyl (Cp*) precursor.[336] After reacting the iridium dimer with a model aniline and picolinaldehydes derivative for 3 days under ambient conditions, LC-MS indicated a promising conversion to the target complex. Following the successful test reaction, the building block library was selected based on the availability and structural diversity (**Figure 57**). A protocol was developed using an Opentrons OT-2 liquid handling robot to dispense the stock

solutions into the corresponding wells of the 96 well plates. The reaction plates were allowed to stand for three days, yielding a combinatorial library of 360 **IrCp1** complexes.

After establishing the initial compound library, the structural diversity was further expanded by incorporating modified Cp ligands (**Figure 57**). Notably, iridium(III) cyclopentadienyl complexes bearing biphenyl moieties (**Cp2**) have been first reported by the Sadler group with potent anticancer activity[337], and previously been reported as effective antibacterial agents.[278] The substituents for **Cp2**, **Cp3** and **Cp4** were selected to increase lipophilicity, which is known to enhance membrane permeability and cellular uptake.[338] Ligand **Cp2** was initially attempted to be synthesized using an *n*-BuLi-mediated synthetic route. However, this approach was unsuccessful, likely due to the sensitivity of the reaction conditions or partially quenched *n*-BuLi reagent due to the exposure to trace amounts of water or other protic impurities. Subsequently, the synthetic route was changed to a Grignard reaction. To this end, biphenyl bromide was refluxed in anhydrous THF with excess amount (6 equiv.) of freshly ground metallic magnesium turnings for 4 hours. Then, the stirred solution of 2,3,4,5-tetramethyl-2-cyclopentenone was added dropwise, and the reaction was refluxed overnight under N_2 atmosphere. The reaction mixture was acidified with concentrated (37%) $HCl_{(aq)}$ and stirred for an hour. The desired product was obtained by column chromatography using a mobile phase of 99:1 *n*-hexane/toluene. Purification using only *n*-hexane was initially unsuccessful, as the brominated starting material and desired product co-eluted. The addition of a small proportion of toluene improved the chromatographic resolution, enabling isolation of the desired **Cp2** ligand. While column chromatography is governed primarily by polarity differences of analytes, the use of toluene may introduce additional solvent-analyte interactions that influence retention behaviour. In this case, the relatively planar and rigid biphenyl bromide starting material is likely to interact favourably with toluene via aromatic π–π interactions, facilitating a faster elution from the column. In contrast, incorporation of the bulky five-membered cyclopentadienyl ring into the product disrupts planarity and reduces the molecule's ability to engage in close aromatic packing with toluene. This difference in interaction likely contributed to the slower elution of the Cp-biphenyl product as a distinct band, enabling the isolation of pure fractions from the column. However, this improved chromatographic resolution came at the expense of toluene in the product-containing fractions. Although the interaction between toluene and the desired product appeared to be weaker than that observed for the brominated starting material, sufficient association remained to complicate complete solvent removal. The residual toluene was removed by repeated washing of the concentrated product with *n*-hexane. The identity

and purity of the desired product were verified by ^{1}H and ^{13}C NMR spectroscopy and HRMS. In the ^{1}H NMR spectrum, the expected number of aromatic protons was observed, together with a proton at 3.24 ppm assigned to the methine proton on the cyclopentadiene carbon bearing the biphenyl substituent, and signals corresponding to 12 methyl protons. **Cp3** and **Cp4** were subsequently synthesised following a similar synthetic approach. In contrast to **Cp2**, these ligands lack an extended aromatic system, which made their purification comparatively more straightforward. The identity and purity of the desired products were verified by ^{1}H and ^{13}C NMR spectroscopy and HRMS. **Cp4** was used for the next step without further purification.

Next, iridium half-sandwich dimers (**IrCp2** and **4**) were synthesised efficiently analogous to **IrCp1** with microwave irradiation according to a reported procedure.[336] The dimer bearing bis(fluorophenyl) substituents (**IrCp3**) could not be obtained under the established conditions, which may be attributed to the strongly electron-withdrawing nature of the fluorine substituents. Such substituents are known to reduce ligand donor ability, potentially weakening metal-ligand interactions and increasing the energy barrier for complexation.[339] To synthesise the **IrCp3** dimer, the reaction was carried out in the microwave for 16 hours at 132°C and successfully precipitated from the reaction mixture. The identity and purity of the desired product were verified by ^{1}H and ^{13}C NMR spectroscopy. Clear differences were observed between the ^{1}H NMR spectra of the free substituted Cp ligand and the corresponding iridium dimer. In particular, the disappearance of the methine proton on the cyclopentadiene ring carbon bearing the biphenyl substituent, together with the doubling of the aromatic proton integrals, provided clear evidence for dimer formation. Additionally, the ligand displayed four distinct methyl proton peaks, each integrating to 3H, whereas the iridium dimer exhibited two methyl resonances, each integrating to 12H. This change reflects the increased symmetry of the Cp moiety upon η^5-coordination to Ir(III) and is consistent with formation of the chlorido-bridged dimer. In the free substituted cyclopentadiene ligand, there is a lower symmetry arising from the sp^3 hybridized methin carbon bearing the biphenyl substitution. This sp^3 centre interrupts cyclic conjugation and prevents the five-membered ring from adopting a symmetrical, fully delocalised electronic structure. As a result, the two directions around the cyclopentadiene ring are no longer equivalent, and the chemical environment of the four methyl groups is different. This gives rise to four separate methyl peaks in the ^{1}H NMR spectrum, each integrating to 3H. With the new IrCp dimers in hand, we successfully expanded the combinatorial library to 1440 Ir(III) Cp Schiff-base complexes.

3.3.2 LC-MS characterisation of the combinatorial library

The identity and purity of the crude reaction mixtures were assessed by LC-MS. Samples were prepared at concentrations of 50–100 µM in a 60:40 (v/v) acetonitrile/water mixture and analysed using the described 5 min LC-MS method (**Table 33**). Briefly, LC-MS data were processed via a semi-automated workflow that converted .raw files to .mzML and subsequently to .csv format.[340] Target masses were extracted using custom Python scripts, and the corresponding UV peaks at 254 nm were integrated to determine relative peak areas. This wavelength was selected because both ligands and complexes contain aromatic and conjugated groups that absorb at 254 nm, enabling their detection and peak-area analysis. The average conversion of the library varied substantially with the Cp moiety (**Figure 58** and **Figure 59**). The variation in average conversion across the Cp series implies the strong dependence of scaffold formation efficiency on ligand structure. The Cp* derivative **Cp1** gave the highest average conversion (62 ± 25%), consistent with the well-established stabilising effect of the electron-rich and sterically balanced Cp* ligand.[341]

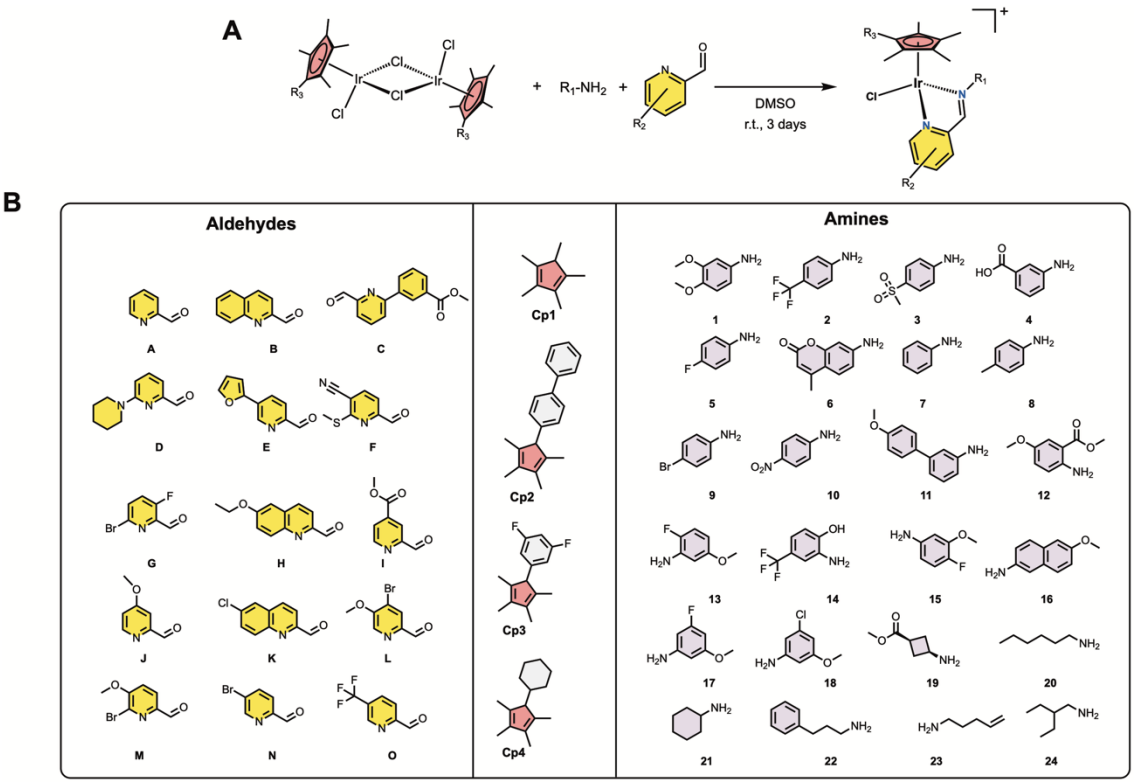


Figure 57. (**A**) General reaction scheme for the combinatorial synthesis of iridium scaffolds. (**B**) Selected building block library consisting of 15 picolinaldehydes, 24 amines, and 4 Cp*/Cp derivatives. Counterion is chloride.

Cp3 also exhibited similarly high average conversion (61 ± 22%), suggesting that its substitution pattern remains compatible with efficient complex formation despite increased structural modification of the Cp* ring. By contrast, **Cp2**, bearing a biphenyl substituent, showed the lowest average conversion (42 ± 18%). This relatively lower yield may arise from the greater steric hindrance and conformational rigidity[342] of the biphenyl group, which could hinder coordination or reduce the efficiency of complexation. **Cp4**, containing a cyclohexyl substituent, displayed intermediate conversion (55 ± 21%), indicating that the bulky but more flexible aliphatic substituent is better tolerated than the rigid aromatic biphenyl group, although still less effective than **Cp1** and **Cp3.** Overall, these data suggest that both steric profile and substituent electronics of the Cp ligand play an important role in determining the efficiency of iridium scaffold formation. With regards to the aldehyde building blocks, steric bulk in the 6-position resulted in generally lower average conversion rates (**Figure 59**). Conversely, aldehydes with no substitution at the 6-position have significantly higher average conversion rates. Within the amine building blocks two trends are visible. Firstly, aliphatic amines tend to give lower conversion rates. Strong electron-withdrawing groups seem to negatively affect conversion rates as well. On the other hand, simple or bicyclic anilines seem to lead to very high conversions (**Figure 59**).

3.3.3 Single-dose response biological activity of the combinatorial library

We initially screened the 1440 compound crude IrCp Schiff base library against *S. aureus* at 12.5 and 50 μM, and against *E. coli* at 50 μM. These were selected as representative Gram-positive and Gram-negative bacteria strains, respectively, to enable assessment of antibacterial activity across different cellular membrane structures. Notably, none of the compounds within the library exhibited activity against *E. coli* at 50 μM which is in line with previously found trends that most metal-based and organic compounds[343] are not able to penetrate Gram-negative bacteria.[92] For the **Cp1** library, we observe only a minority of compounds (26%) was active at 50 μM, while only 2.5% of compounds exhibiting measurable activity at 12.5 μM (**Figure 61A** and **Figure 62**). In contrast, all compounds completely inhibited *S. aureus* growth at 50 μM, and nearly 70% of the **Cp2** library exhibited antibacterial activity at 12.5 μM. The superior antibacterial activity of biphenyl substituted (**Cp2)** Cp iridium(III) complexes have been also observed by Sadler and co-workers.[278] The observed difference in activity may be attributed to the increased lipophilicity and rigidity of the biphenyl moiety, which could facilitate improved uptake through the bacterial membrane.[338] The majority of the **Cp3** library was active against *S. aureus* at 50 μM, however, only 42% exhibited complete growth inhibition at 12.5 μM

(**Figure 62**). When we consider **Cp4** complexes, 91% were active at 50 μM, whereas only 26% inhibited bacterial growth at 12.5 μM (**Figure 62**). At the level of individual building blocks, the aldehyde component exerts a dominant influence on antibacterial activity, with several aldehydes consistently associated with strong growth inhibition across multiple Cp* cores and amines.

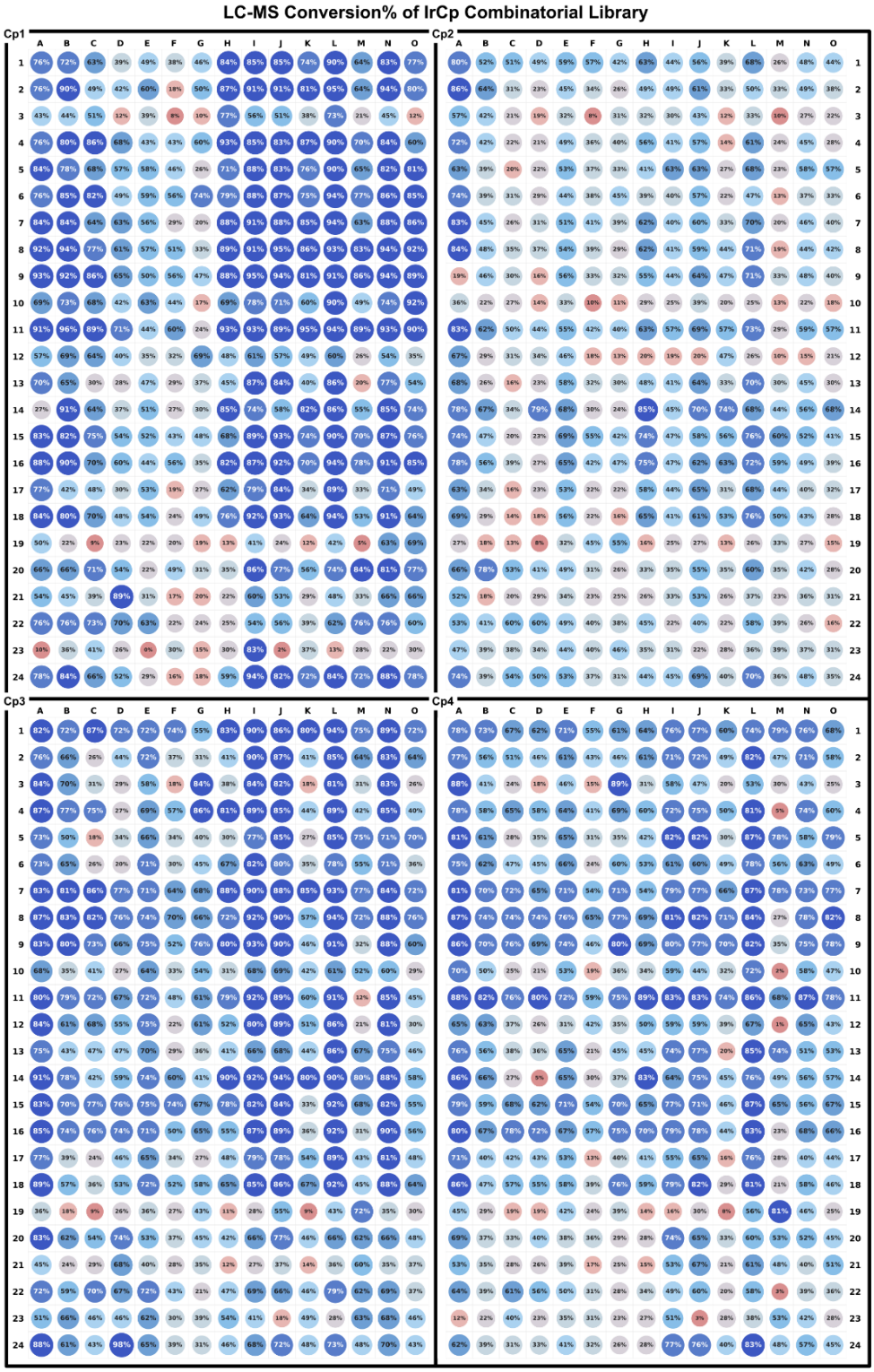


Figure 58. Purity of the metal complex libraries determined as LC-MS peak area percentages at 254 nm (top left: **Cp1**; top right: **Cp2**; bottom left: **Cp3**; bottom right: **Cp4**). Compound peaks were automatically identified based on the target ion mass, and the corresponding UV signals were integrated using custom Python scripts (see Experimental section for details). Reported conversions represent the combined signal of the parent ion (M^+) and the MeCN adduct $(M + MeCN)^{2+}$. The colour scale represents LC-MS-derived conversion percentages, ranging from red

for low conversion through pale shades for intermediate conversion to dark blue for high conversion. The value within each circle indicates the conversion percentage for the corresponding aldehyde-amine combination.

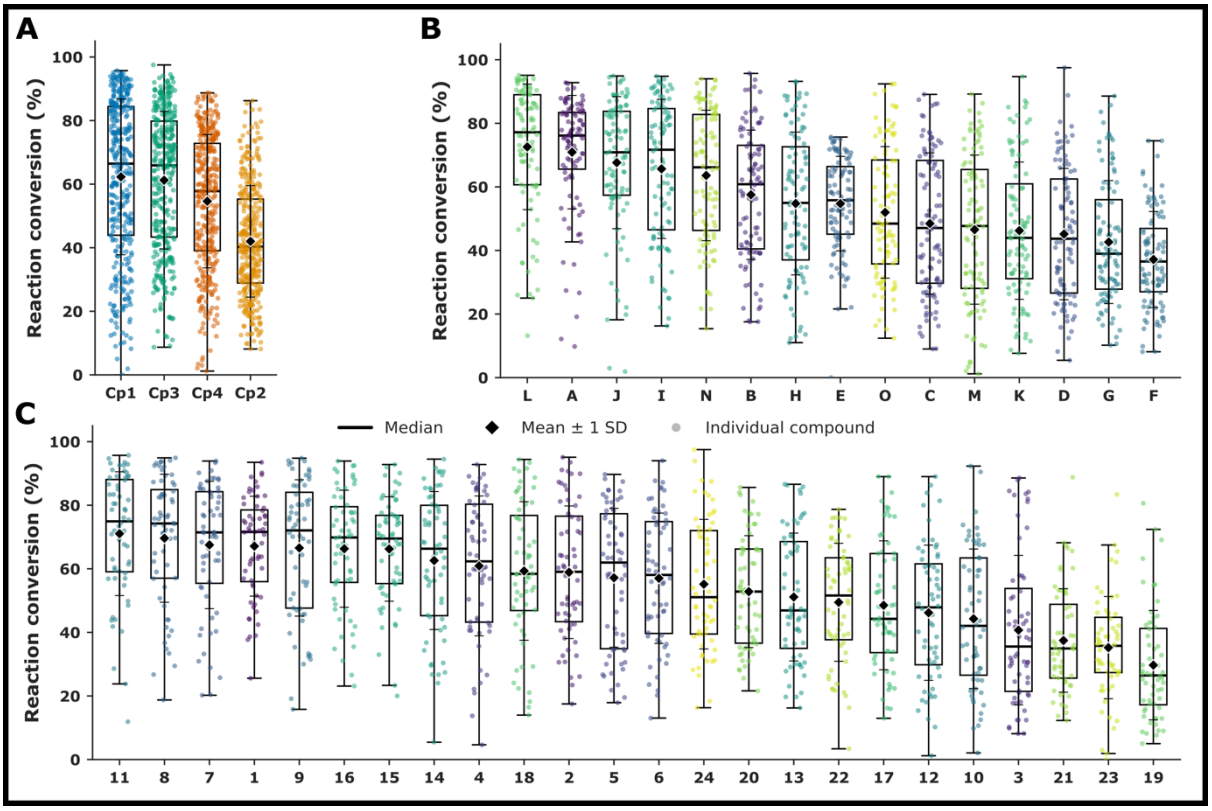


Figure 59. LC-MS Based conversion distribution of the building blocks. (**A**) Conversion distribution of compounds across cyclopentadiene moieties. (**B**) Conversion distribution of compounds across aldehyde moieties (**C**) Conversion distribution of compounds across amine moieties.

In particular, aldehydes **B** (quinoline)**, E** (furan-2-yl)**, H** (ethoxy-quin)**,** and **K** (chloro-quin) exhibit high rates of activity at 12.5 μM, with 50–70% of compounds containing these building blocks being active (**Figure 61B** and **Figure 63**). These most active aldehydes share extended aromatic and heteroaromatic motifs, suggesting that increased π-interactions and hydrophobic character contribute to enhanced antibacterial performance. This observation is consistent with the established role of quinoline as a 'privileged scaffold in medicinal chemistry'.[344] Quinoline derivatives exhibit a broad range of biological activities, including antimicrobial, anticancer, antidepressant, anti-inflammatory, antiviral, and antiparasitic effects, making this heterocyclic framework a widely utilised motif in drug discovery.[344,345] In contrast, fewer than 30% of compounds with aldehydes **A** (pyridine), **F** (*o*-thiomethoxy-*m*-nitrile), **I** (*p*-methoxycarbonyl)**, J** (*p*-methoxy)**,** and **M** (*o*-bromo-*m*-methoxy) display activity at 12.5 μM (**Figure 61B** and

Figure 63). These lower-activity aldehydes are monocyclic pyridines and incorporate more polar functionality. These observations are consistent with the hypothesis that increased hydrophobicity and structural rigidity facilitate more effective interaction with bacterial membranes or intracellular targets.[346,347] In comparison, the amine component exerts a more moderate effect on antibacterial activity. Amines **8** (*p*-methyl)**, 11** (*m*-methoxyphenyl)**, 16** (6-methoxynapthyl)**, 20** (hexyl)**, 22** (propan-phenyl)**, 23** (pentenyl) and **24** (2-ethylbutan) are consistently associated with higher activity, with 50–70% of compounds active at 12.5 μM (**Figure 61C** and **Figure 64**). On the other end, compounds with amines **3** (*p*-sulfonyl)**, 4** (*m*-carboxy)**, 6** (coumarin), **10** (*p*-nitro), **12** (*o*-methoxycarbonyl-*p*-methoxy), **14** (*o*-hydroxy-*m*-trifluoromethyl) and **19** (methyl 3-aminocyclobutane-1-carboxylate) only show activity in a minority of the cases (3-23%, **Figure 64**). Structurally, amines with increased aromatic character or flexible hydrophobic substituents have higher activity-rates, whereas lower-activity amines tend to be more polar or electron poor. Overall, antibacterial activity is strongly dependent on the Cp scaffold, with the **Cp2** (biphenyl) series showing the highest potency, followed by **Cp3** and **Cp4**, while **Cp1** is largely inactive. Activity is primarily driven by the aldehyde component, with more hydrophobic, aromatic motifs enhancing potency, whereas the amine plays a secondary role, with hydrophobic substituents generally improving activity.

Following the single-dose evaluation of antibacterial activity, the cytotoxicity of the crude compounds was assessed against HEK293T cells at 50 μM. This *in vitro* kidney cell line is widely regarded as a gold-standard tool for nephrotoxicity screening in drug discovery, as the kidneys are a primary target of chemically induced injury and play a crucial role in drug excretion.[348] For the iridium library with the **Cp1** moiety, viability ranged from 9–100% (mean 59%, median 65%), with 70% of compounds achieving ≥50% viability, indicating a shift toward higher viability (**Figure 60** and **Figure 61A**, **Figure 65**). In contrast, the **Cp2** library showed lower viability overall, ranging from 0.8–83% (mean 24%, median 19%), with only 2% of compounds achieving ≥50% viability. Both **Cp3** and **Cp4** libraries also shifted toward higher viability (**Figure 60** and **Figure 61A**, **Figure 65**). **Cp3** showed viability of 0.2–89% (mean 30%, median 28%), with ~20% of compounds achieving ≥50% viability, while **Cp4** ranged from 4–85% with slightly higher overall viability (mean 32%, median 27%) and 22% of compounds achieving ≥50% viability. These data reveal a clear dependence of cytotoxicity on the Cp core, with **Cp1** affording the highest overall viability and **Cp2** the lowest, while **Cp3** and **Cp4** display intermediate cytotoxicity profiles (**Figure 60** and **Figure 61A**, **Figure 65**). Aldehydes associated with strong antibacterial activity, (**B**, **E**, **K**, **H**) consistently correspond to lower average cell

viability in the range of 18–31%. In contrast, aldehydes associated with lower antibacterial activity (**A**, **F**, **I**, **J**, and **M**) result in significantly higher viability (42–56%), indicating reduced cytotoxicity (**Figure 61B** and **Figure 66**). The picture is slightly less clear with the amine building blocks where overall mean cell viability ranges from 24-52% **Figure 61C, Figure 67**). In general, amines with higher rates of antibacterial activity also have lower mean cell viability, suggesting that the aldehydes have a stronger influence on the cytotoxicity profile of the resulting compounds (**Figure 60** and **Figure 61**, **Figure 64** and **Figure 67**).

While many compounds that showed significant antibacterial activity also displayed high toxicity, there was a small subset of compounds that retain antibacterial activity at 12.5 μM while maintaining ≥50% HEK293T cell viability, indicating the presence of a selectivity window within the library. Although such combinations are relatively rare, their consistent occurrence demonstrates that antibacterial activity and cytotoxicity are not strictly coupled within this scaffold. These 'balanced' compounds are predominantly observed within **Cp2–4**.

At the aldehyde level, these combinations are most frequently associated with aldehydes with high average cell viability percentages (**A**, **F**, **I,** and **M**) and a few representing lower viability ones (**E**, **K**, **L**, and **N**) (**Figure 60, Figure 61**, **Figure 66**). Amongst the amines, **11** stands out as it appears most frequently (**Figure 67)**. In general, the occurring amines are on the lower end of the mean cell viability with **5**, **11**, **16**, **20**, and **22** all coming in below 35% (**Figure 60** and **Figure 61**, **Figure 67**). This may suggest that for compounds with balanced properties the antibacterial contribution stems from the amine while the aldehyde seems to drive the non-toxic component.

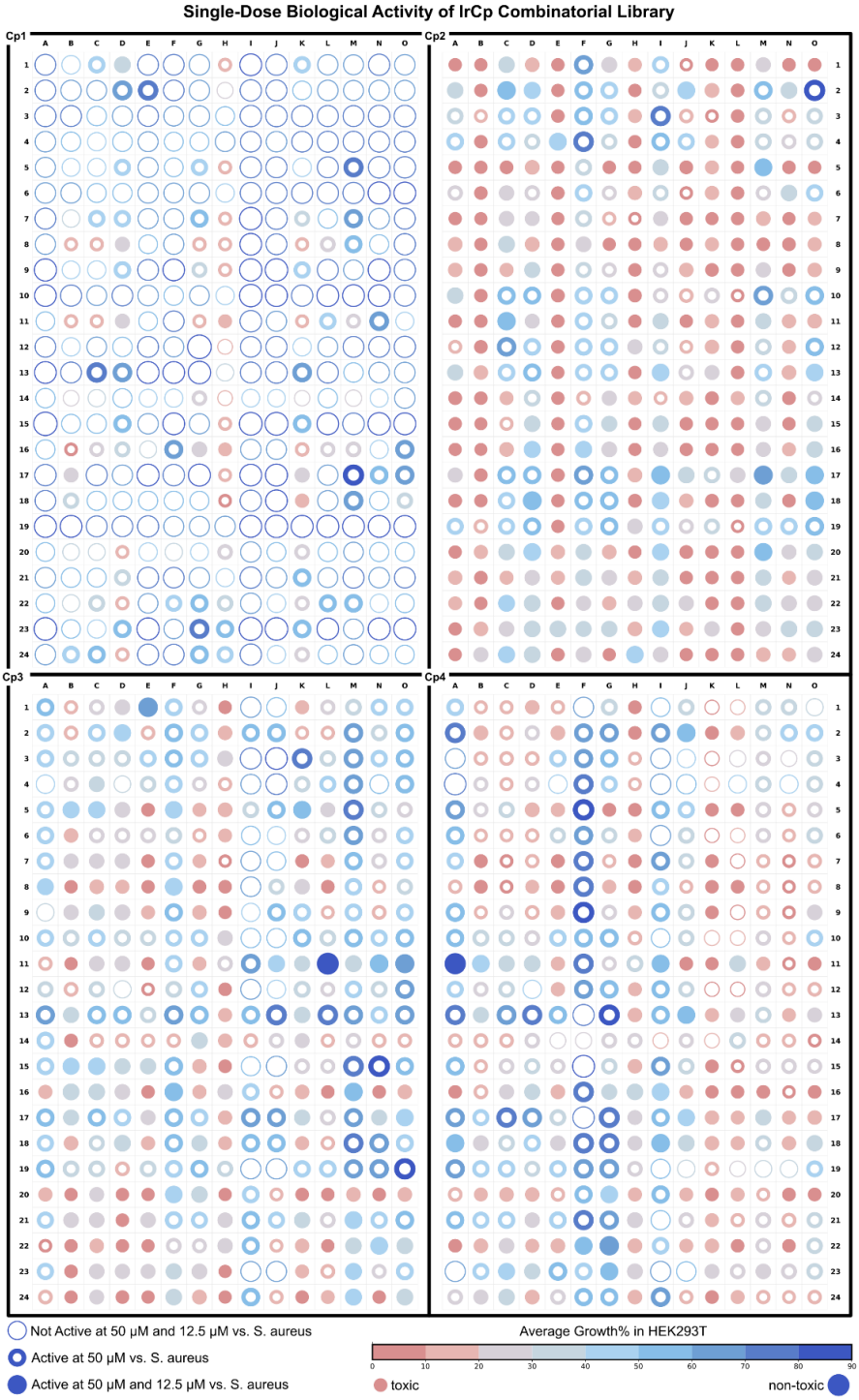


Figure 60. Single-dose biological characterisation of the combinatorial library against *S. aureus* CCUG 62707 (top left: **Cp1**; top right: **Cp2**; bottom left: **Cp3**; bottom right: **Cp4**). Filled circles indicate measurable antibacterial activity at both 50 µM and 12.5 µM. Small white circles denote compounds that are active only at 50 µM, while empty circles indicate no detectable activity against *S. aureus* under the tested conditions. The colour intensity corresponds to the single dose cytotoxic activity against HEK293T cells. The circle size is proportional to viability of HEK293T cells.

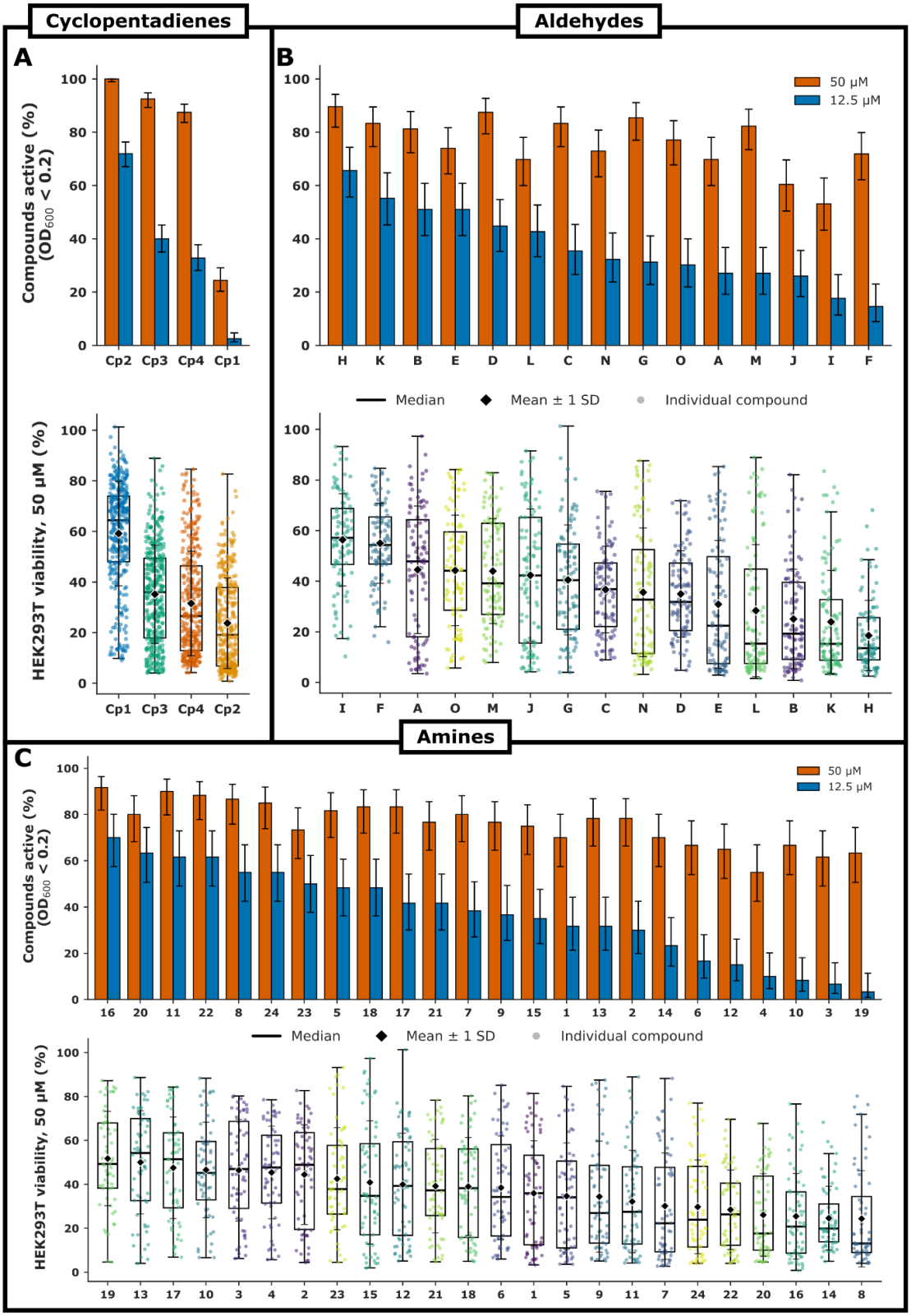


Figure 61. Activity distribution of the building blocks. (**A**) Antibacterial activity distribution of compounds across cyclopentadiene moieties against *S. aureus* at 50 µM (red) and 12.5 µM (blue), and HEK293T cell viability at 50 µM. (**B**) Antibacterial activity distribution of compounds across aldehyde moieties against *S. aureus* at 50 µM (red) and 12.5 µM (blue), and HEK293T

cell viability at 50 μM. (**C**) Antibacterial activity distribution of compounds across amine moieties against *S. aureus* at 50 μM (red) and 12.5 μM (blue), and HEK293T cell viability at 50 μM.

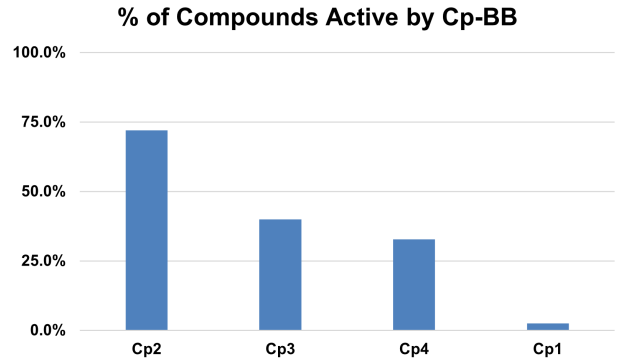


Figure 62. % of active compounds by Cp building block (OD_{600}<0.1).

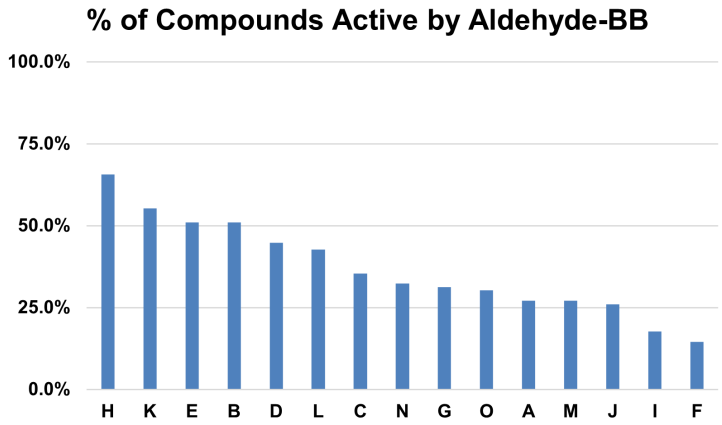


Figure 63. % of active compounds by aldehyde building blocks (OD_{600}<0.1).

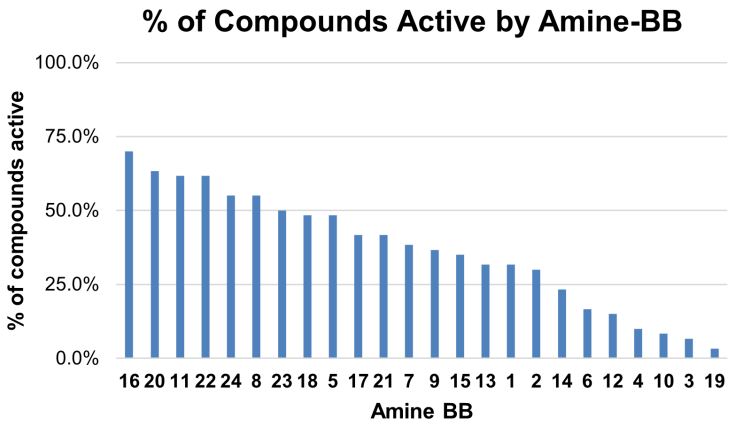


Figure 64. % of active compounds by amine building blocks (OD_{600}<0.1).

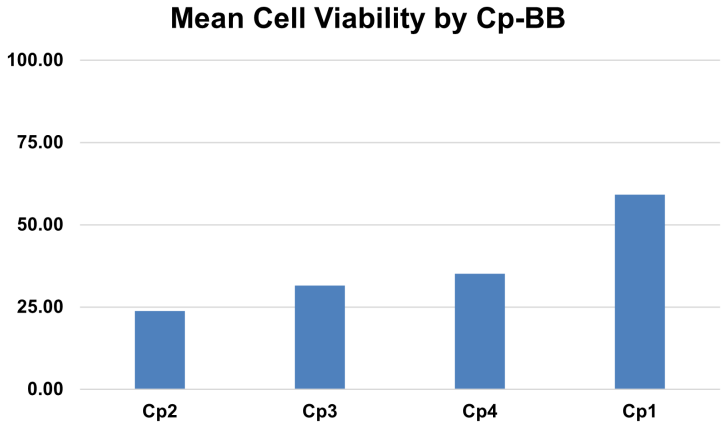


Figure 65. Mean HEK293T viabilities based on the Cp building blocks.

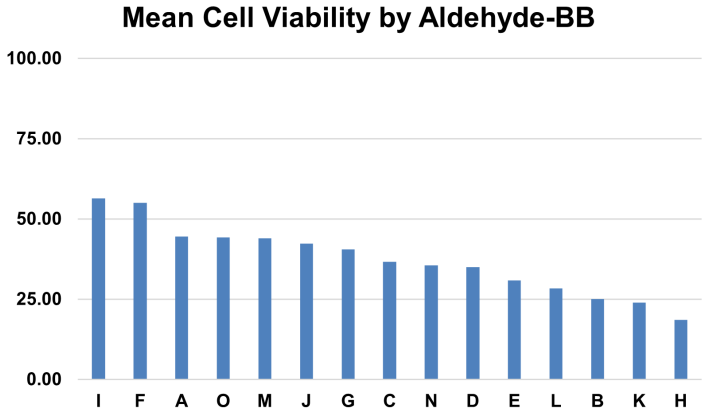


Figure 66. Mean HEK293T viabilities based on the aldehyde building blocks.

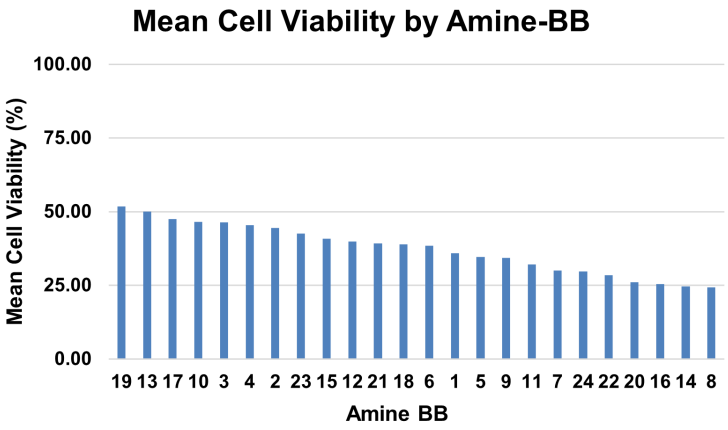


Figure 67. Mean HEK293T viabilities based on the amine building blocks.

3.3.4 Dose-response biological activity of selected complexes

A subset of 19 compounds (**Figure 68**) that achieved growth inhibition at 12.5 μM against *S. aureus* while maintaining ≥50% HEK293T viability was selected from the library for dose-response validation. At this point, to confirm that the antibacterial activity of our crude mixtures originates from the putative complexes themselves, we examined the antibacterial activity of all **15 picolinaldehydes**, **24 amines (Table 9)** and **4 IrCp dimers (Table 9).** Except the **IrCp2** dimer (MIC = 12.5 μM), none of the building blocks exhibited any antibacterial activity up to 100 μM indicating that any activity observed from the crude reaction mixtures likely originates from the targeted Schiff-base iridium(III) metal complex. We screened these 19 compounds against *S. aureus* and *E. coli* in dose-dependent assays. Several of the selected compounds exhibited antibacterial activity against *S. aureus* with MIC values ranging from 6.25 to 50 μM. This is in line with what was seen during the initial screening of the library. Among these, **Ir4**, **Ir9**, **Ir10**, **Ir13**, **Ir14**, **Ir15**, and **Ir16** emerged as the most active derivatives. Notably, **Ir10**, **Ir14**, and **Ir16** displayed the highest potency, each exhibiting MIC values of 6.25 μM, (**Table 10**).

Table 9. MIC values of building blocks against *S. aureus* CCUG 62707.

Aldehydes	MIC (μM)	Amines	MIC (μM)	Amines	MIC (μM)
A	>200	**1**	>200	**16**	>200
B	>200	**2**	>200	**17**	>200
C	>200	**3**	>200	**18**	>200
D	>200	**4**	>200	**19**	>200
E	>200	**5**	>200	**20**	>200
F	>200	**6**	>200	**21**	>200
G	>200	**7**	>200	**22**	>200
H	>200	**8**	>200	**23**	>200
I	>200	**9**	>200	**24**	>200
J	>200	**10**	>200	**IrCp1**	>100
K	>200	**11**	>200	**IrCp2**	12.5
L	>200	**12**	>200	**IrCp3**	100
M	>200	**13**	>200	**IrCp4**	100
N	>200	**14**	>200		
O	>200	**15**	>200		

No antibacterial activity against *E. coli* was observed for any of the compounds at concentrations up to 100 μM. However, enhanced activity was detected in the presence of the membrane permeabilizer Polymyxin B nonapeptide (PMBN).[244] Unlike polymyxin B, PMBN does not possess intrinsic antibacterial activity, making it a valuable adjuvant for use in combination therapies.[349] In particular, the MIC of **Ir16** against *E. coli* was reduced from >100 μM down to 12.5 μM in the presence of PMBN. This observation indicates that the lack of activity against Gram-negative bacteria is likely attributable to limited uptake or increased efflux across the outer membrane, rather than an absence of intrinsic antibacterial potency (**Table 1**).

The cytotoxicity of the compounds was evaluated in HEK293T cells in a dose-dependent manner, revealing a broad range of CC_{50} values and highlighting notable differences in selectivity across the series. Several compounds exhibited moderate to high cytotoxicity, with CC_{50} values below 30 μM, including **Ir4**, **Ir6**, **Ir7**, **Ir8**, and **Ir10**. Importantly, some of the most promising antibacterial compounds maintained a favourable balance between potency and cytotoxicity. **Ir9**, **Ir14**, **Ir15**, and especially **Ir16** exhibited relatively high CC_{50}

values (50 ± 2 μM, 33 ± 8 μM, 51 ± 12 μM, and 42 ± 8 μM, respectively) in combination with promising MIC values, resulting in the highest therapeutic indices (TI = 4.0, 5.2, 4.1, and 6.7, respectively) (**Table 10**). These compounds therefore represent the most selective candidates within the series and were selected for batch synthesis, purification, and subsequent hit validation.

3.3.5 Batch synthesis of selected complexes

Following single-dose and dose-response assays, four iridium(III) complexes, **Ir9**, **Ir14**, **Ir15**, and **Ir16**, were selected for scale-up synthesis and purification. This selection was based on their therapeutic index (TI), with a threshold value of 4.0 applied. The iridium dimer (0.5 equiv.) was combined with the corresponding amine (1 equiv.) and aldehyde (1 equiv.) in DCM/MeOH (1:1) and stirred at room temperature overnight. Reaction progress was monitored by LC-MS. Upon completion, excess *n*-hexane was added to precipitate the product, which was subsequently isolated and purified by flash column chromatography. Although **Ir16** was identified as the most promising compound in the dose-response assays, repeated attempts to purify this complex were unsuccessful. Multiple purification strategies were explored, including column chromatography under varying stationary phases and solvent systems, recrystallisation attempts, and repeated washing procedures. Each purification attempts consistently yielded NMR spectra exhibiting residual aromatic impurities. Whereas **Ir9**, **Ir14** and **Ir15** were synthesized successfully with 27%, 45%, and 47% yield, respectively. During the purification of the lead compounds, a similar co-elution problem to that previously observed for the **Cp2** ligand was observed. Specifically, the desired products co-eluted with the IrCp2 dimer when 90:10 DCM:MeOH was used as the mobile phase. The separation between the desired products and the **IrCp2** dimer was subsequently optimised by introducing 2% toluene. Compound purity and identity was confirmed by LC-MS and NMR characterisation, and high-resolution mass spectra (HRMS).

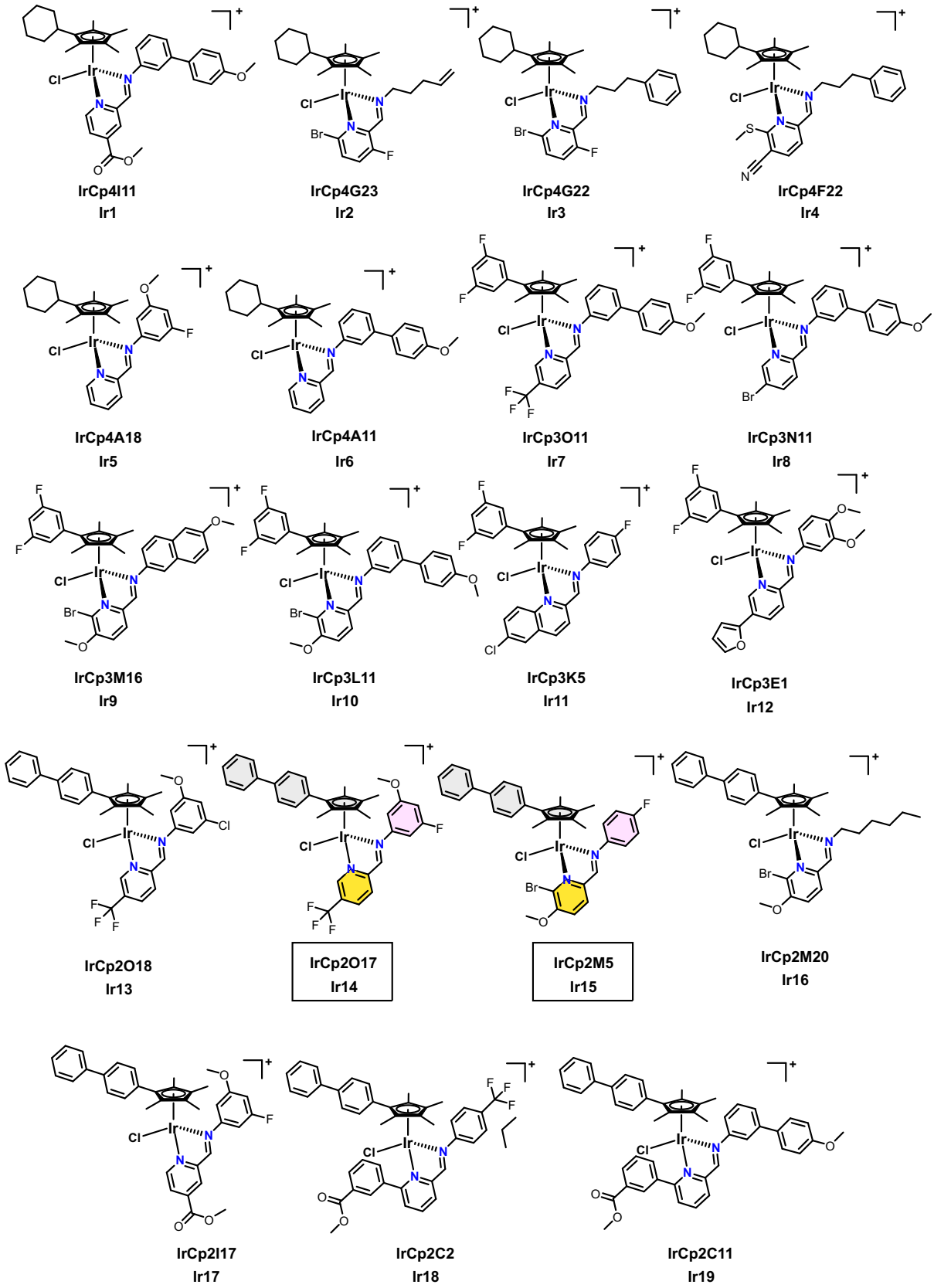


Figure 68. Selection of lead compounds from the initial screening library for dose-response biological characterisation. A total of 19 compounds were selected based on their antibacterial

activity against *S. aureus* at 12.5 µM. Compounds were further filtered to retain those maintaining >50% single-dose (50 µM) viability in HEK293T cells. Hit compounds are shown in boxes. Counterion, chloride, was omitted for clarity.

Table 10. Selected 19 compounds from the single-dose biological assays. %Conv. is the conversion percentage determined by LC-MS. MIC values are given in µM and determined against *S. aureus* CCUG 62707 and *E.coli* NCTC 13476. PMBN was used as an outer membrane permeabilizer at a sublethal concentration (10 µg/mL). Cytotoxicity was determined against Human Embryonic Kidney cells (HEK293T) and is given as CC_{50}. Therapeutic index (TI) is given as the ratio of CC_{50} and MIC against *S. aureus*. Experiments were repeated as three biological replicates in triplicate.

Compound		**% Conv.**	**MIC** (µM)			**CC_{50}** (µM)	**TI**
			S. aureus	***E. coli***	***E. coli* + PMBN**	**HEK293T**	
Ir1	**IrCp4I11**	83	50	>100	100	65 ± 4	1.3
Ir2	**IrCp4G23**	23	25	>100	100	50 ± 3	2
Ir3	**IrCp4G22**	28	25	>100	100	47 ± 2	1.9
Ir4	**IrCp4F22**	31	12.5	>100	25	25 ± 9	2
Ir5	**IrCp4A18**	86	100	>100	>100	58 ± 8	0.6
Ir6	**IrCp4A11**	88	25	>100	>100	19 ± 1	0.7
Ir7	**IrCp3O11**	45	25 – 50	>100	100	23 ± 8	0.9 – 2.1
Ir8	**IrCp3N11**	85	25	>100	100	23 ± 9	0.9
Ir9	**IrCp3M16**	31	12.5	>100	>100	49 ± 20	4.0
Ir10	**IrCp3L11**	91	6.25	>100	25	15 ± 3	2.4
Ir11	**IrCp3K5**	27	25	>100	100	31 ± 10	1.2
Ir12	**IrCp3E1**	72	50	>100	>100	32 ± 7	1.6
Ir13	**IrCp2O18**	28	12.5	>100	50	45 ± 14	3.5
Ir14	**IrCp2O17**	32	6.25	>100	25	33 ± 8	5.2
Ir15	**IrCp2M5**	23	12.5	>100	50	51 ± 12	4.1
Ir16	**IrCp2M20**	35	6.25	>100	12.5	42 ± 8	6.7
Ir17	**IrCp2I17**	45	25	>100	>100	64 ± 20	2.6
Ir18	**IrCp2C2**	31	50 – 100	>100	100	>120	-
Ir19	**IrCp2C11**	50	12.5 – 50	>100	25	33 ± 8	0.7

3.3.6 Antibacterial activity of lead complexes: Hit validation

To validate the antibacterial activity observed in the crude mixtures, the purified complexes **Ir9**, **Ir14** and **Ir15** were re-screened against *S. aureus*. We observed that pure **Ir9** was insoluble in various biological growth media at the test concentrations and therefore excluded it from further biological evaluation. Notably, the antibacterial activity of **Ir15** increased following purification, with the MIC decreasing from 12.5 µM to 3.13 µM (**Table 11**), whereas the activity of **Ir14** unexpectedly diminished with the MIC increasing from 6.25 µM to 25 µM (**Table 12**). Crude LC-MS analysis provides an explanation for the observed activity difference of **Ir14**, showing multiple species (**Figure 69** and **Figure 70**) in the crude mixture compared to the cleaner profile of **Ir15 (Figure 71** and **Figure 72)**. The reduced antibacterial activity upon purification suggests that the

biological activity of the crude sample is not solely attributable to the target complex, but rather that the active species may be present only in the crude mixture.

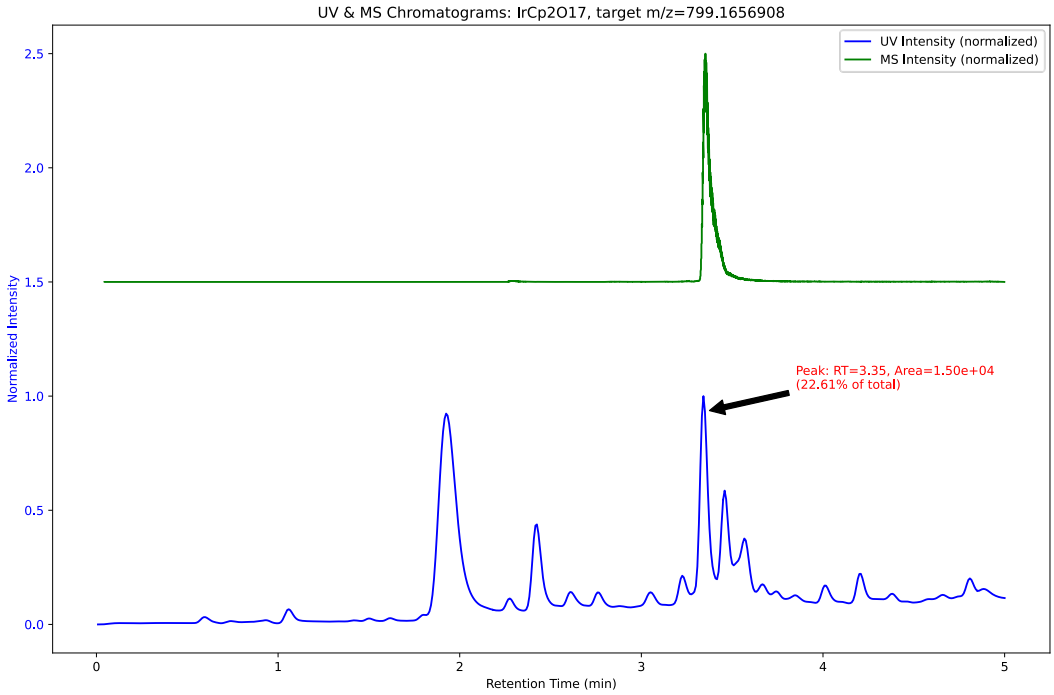


Figure 69. Processed LC-MS spectrum for **Ir14** (crude). The lower graph is UV trace at 254 nm, and the upper trace is extracted ion chromatography for the target mass of the complex.

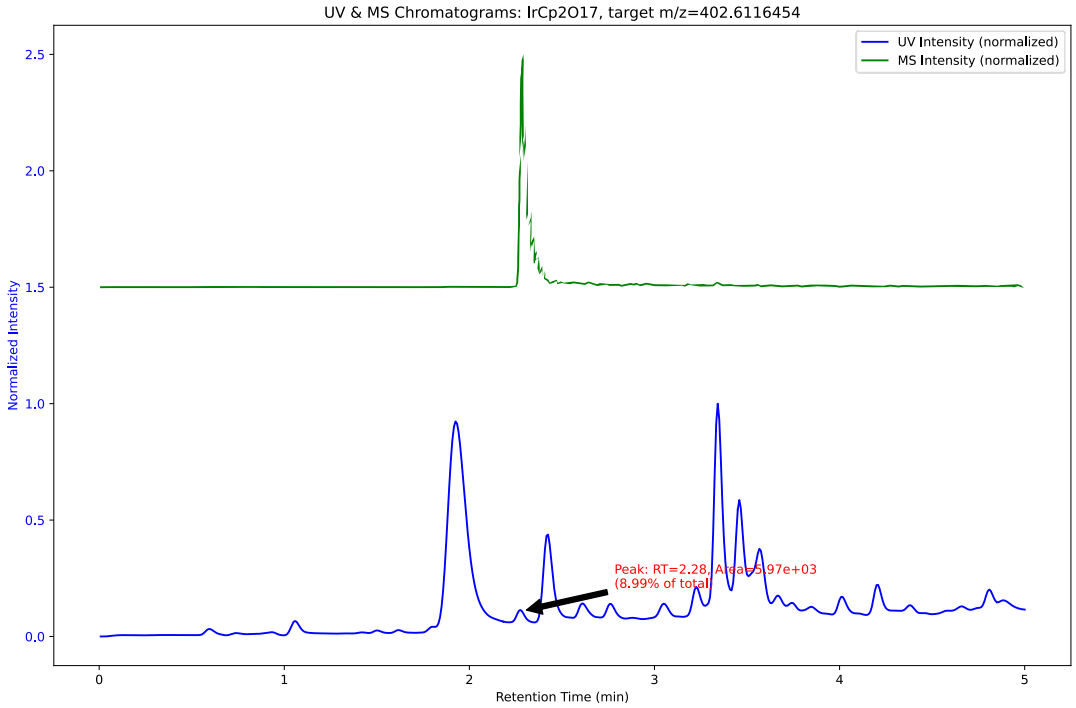


Figure 70. Processed LC-MS spectrum for **Ir14** (crude). The lower graph is UV trace at 254 nm, and the upper trace is extracted ion chromatography for the **[(M–Cl)+ MeCN]$^{2+}$** ion of the complex.

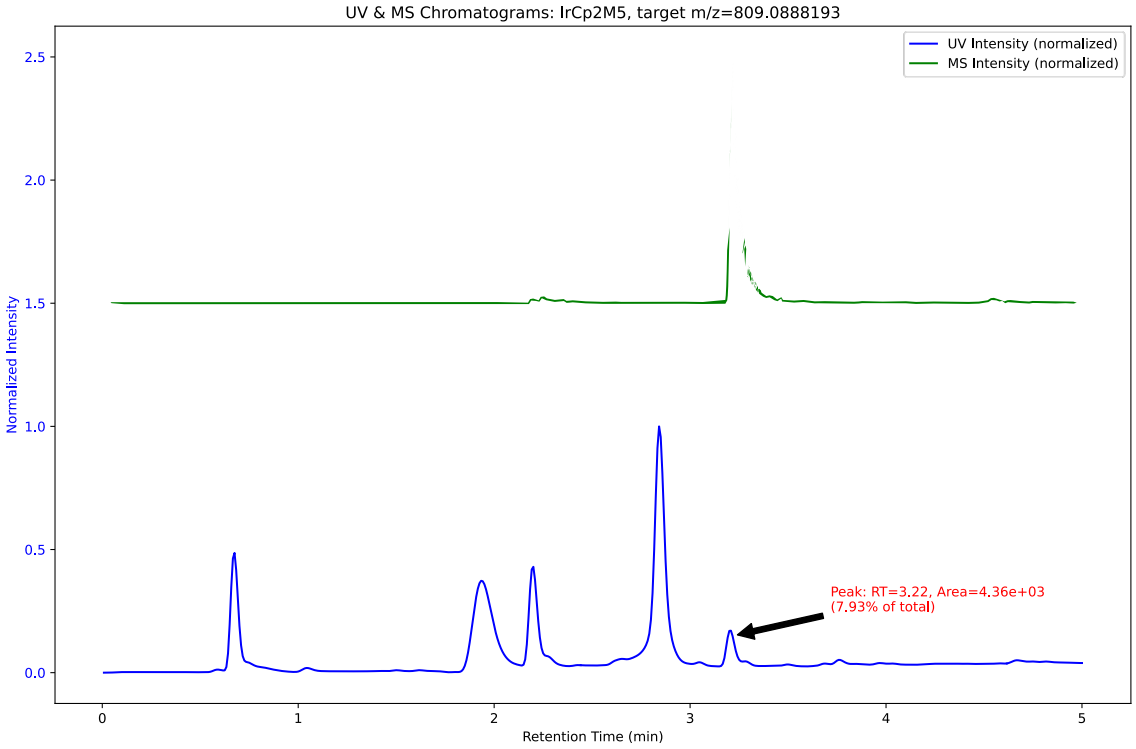


Figure 71. Processed LC-MS spectrum for **Ir15** (crude). The lower graph is UV trace at 254 nm, and the upper trace is extracted ion chromatography for the target mass of the complex.

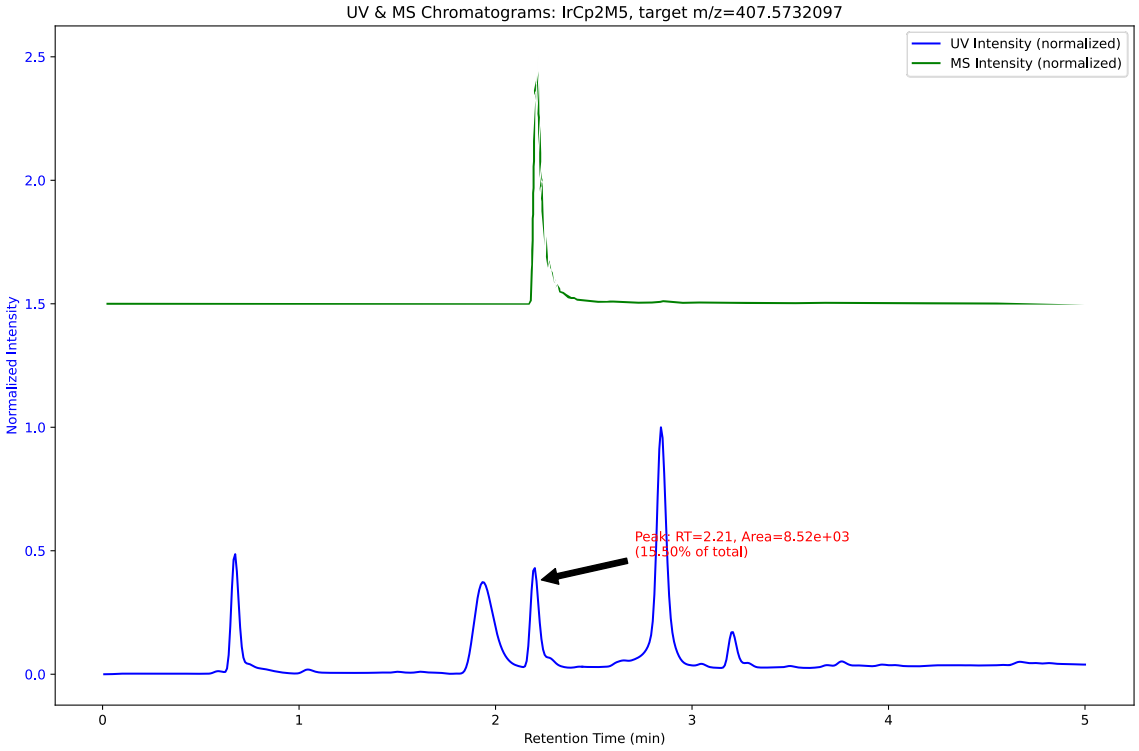


Figure 72. Processed LC-MS spectrum for **Ir15** (crude). The lower graph is UV trace at 254 nm, and the upper trace is extracted ion chromatography for the $[(M–Cl)+ MeCN]^{2+}$ ion of the complex.

Based on these findings, **Ir15** was selected for further biological characterisation and subsequently screened against an expanded panel of Gram-positive strains. **Ir15** demonstrated promising antibacterial activity against the Gram-positive panel, with MICs in the low-micromolar range. Against *S. aureus*, **Ir15** exhibited strain-dependent activity, with MIC values ranging from 1.56–6.25 μM. Comparable activity was observed against *S. epidermidis* and enterococci species (**Table 2**). In line with the results from the crude reaction screening, **Ir15** displayed limited antibacterial activity against Gram-negative strains, with no measurable activity against *E. coli* (MIC >100 μM) and only moderate activity against *A. baumannii* (MIC = 50 μM). However, upon treatment with sublethal concentrations of PMBN a notable enhancement in activity was observed (12.5 μM for both *E. coli* and *A. baumannii*, **Table 11**)**.** This indicates that **Ir15** possesses intrinsic activity against Gram-negative bacteria but is unable to efficiently penetrate the outer membrane.

Next, we investigated if the bacterial growth inhibition stems from a bacteriostatic or bactericidal effect. We determined the minimum bactericidal concentration (MBC) of the purified lead complexes (**Ir14** and **Ir15**) against *S. aureus*. For both complexes, MBC were values found in the same range as MIC values, and the MBC/MIC ratio is lower 4 (**Table 13**), which classifies the compounds as bactericidal.[350]

Table 11. Antibacterial activity of **Ir15** against Gram-positive panel, *S. aureus* CCUG 62707, MRSA (JE2), *S. aureus* (SH1000), *S. epidermidis* TU3298, and *Bacillus subtilis* MW168, *Enterococcus feacium* CUG 19434, and *Enterococcus faecalis* CCUG 19916T; Gram-negative panel, *Escherichia coli* NCTC 134376, *A. baumannii* AB5075. *indicates the presence of sublethal concentration (10 μg/mL) of PMBN, outer membrane permeabilizer. Control is positive control antibiotic Vancomycin (VCM) for Gram-positive, Polymyxin B (PMB) for Gram-negative. MIC values were given in μM. Experiments were repeated as three biological replicas as triplicates.

Antibacterial activity of Ir15

Strain		Ir15	Control
S. aureus	**CCUG 62707**	**3.13 — 6.25**	**0.86**
	JE2	**1.56 — 3.13**	
	SH1000	**3.13**	
S. epidermidis	**TU3298**	**3.13**	**0.86**
B. subtilis	**MW168**	**3.13 — 6.25**	**0.22**
E. faecium	**CUG 19434**	**6.25**	**0.86**
E. faecalis	**CCUG 19916T**	**6.25**	**0.43**
E. coli	**NCTC 13476**	**>100**	**<0.01**
		12.5*	
A. baumannii	**AB5075**	**50**	**0.03**
		12.5*	

Table 12. Antibacterial activity of **Ir14** against Gram-positive panel, *S. aureus* CCUG 62707, *E. feacium* CUG 19434, and *E. faecalis* CCUG 19916T. MIC values were given in μM.

Antibacterial activity of Ir14

	S. aureus CCUG 19434	***E. faecium*** CUG 19434	***E. faecalis*** CCUG 19916T
Ir14	25	25	25

Table 13. MIC and MBC values of **Ir14** and **Ir15** against *S. aureus.* MIC and MBC values were given in μM.

	MIC	**MBC**	**MBC/MIC**
Ir14	25	25	1
Ir15	3.13 — 6.25	6.25	0.5 — 1

3.3.7 Haemolytic and cytotoxic properties of lead complexes

The ability of antibacterial compounds to selectively target bacteria while minimizing cytotoxic effects on mammalian cells is essential. Therefore, cytotoxicity of the lead compounds was reevaluated against the HEK293T mammalian cell line. **Ir14** displays high cytotoxicity, with a CC_{50} value of 13 ± 4 μM. Notably, this result is not in an agreement with that observed in the crude mixture single-dose screening and dose-response assays, where **Ir14** did not display comparable cytotoxicity. The lower CC_{50} value in conjunction with the higher MIC for **Ir14** also results in a reduced selectivity (TI = 0.5). **Ir15** exhibits a CC_{50} value of 48 ± 4 μM (**Table 14, Figure 73)** which is consistent with the one measured in the crude reaction mixture (CC_{50} = 51 ± 12 μM). This indicates a moderate effect on mammalian cell viability. The TI was found between 8—31 (CC_{50} value over MIC values against *S. aureus* strains). Notably, the selectivity of **Ir15** improved, with a TI increase from 4.1 to 8—31 upon purification. It demonstrates the ability of **Ir15** retain antibacterial efficacy while maintaining an acceptable safety margin under the tested conditions.

Table 14. Cytotoxicity of **Ir14** and **Ir15** against HEK293T and human red blood cells. CC_{50} , HC_{10}, and HC_{50} values were given in μM.

Toxicity Assays

	CC_{50}	**HC_{10}**	**HC_{50}**
Ir14	13 ± 4	64 ± 13	125 ± 9
Ir15	48 ± 4	124 ± 7	141 ± 5

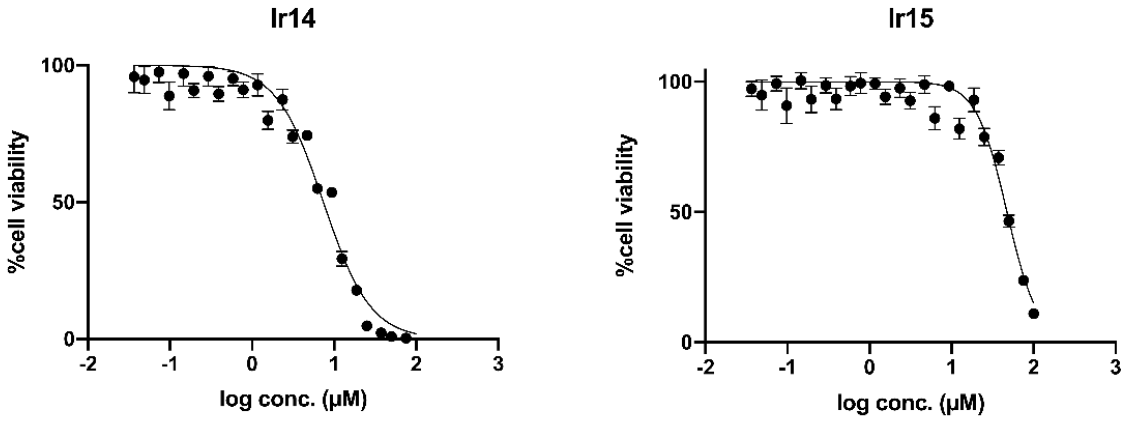


Figure 73. Dose-response plots of Ir14 and Ir15 against HEK293T cells.

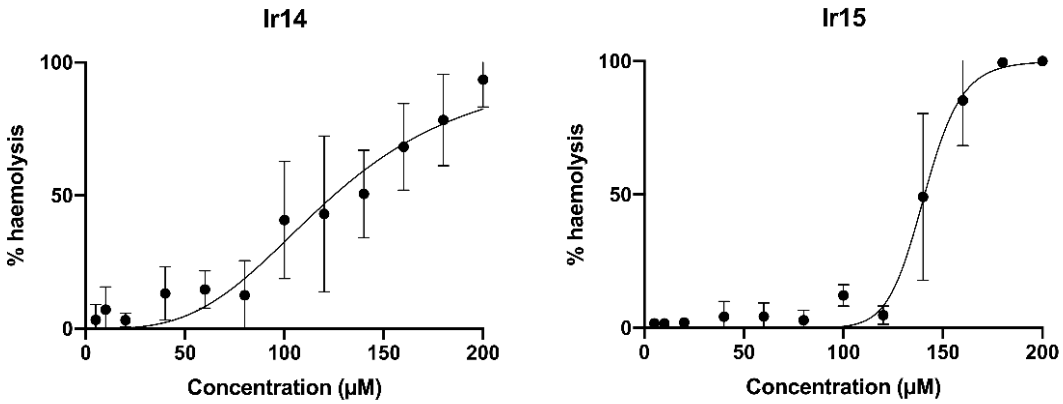


Figure 74. Dose-response heamolysis plots of Ir14 and Ir15 against hRBC.

Crude LC-MS analysis explains the observed difference in cytotoxicity for **Ir14**, revealing multiple species in the crude mixture (**Figure 69** and **Figure 70**) compared to the cleaner profile of **Ir15 (Figure 71** and **Figure 72)**. The enhanced cytotoxicity upon purification suggests that the biological activity of the crude sample is not solely attributable to the isolated parent complex. Rather, the less cytotoxic species may be present only in the crude mixture, and purification revealed the intrinsic toxicity of **Ir14**. To further assess the cytotoxic properties of the lead complexes, 10% and 50% haemolytic concentrations (HC_{10} and HC_{50}) were determined using human red blood cells (RBC). **Ir14** shows relatively higher haemolytic activity, with an HC_{10} value of 64 ± 13(**Table 14, Figure 74**). While **Ir15** exhibits very low haemolytic activity with HC_{10} values of 124 ± 7 μM, 20-40 times higher than the MIC value (**Table 14, Figure 74**).

Taken together, these findings emphasise the importance of follow-up validation of crude screening hits and demonstrate that **Ir15** represents a more favourable candidate, combining retained antibacterial activity with a more consistent and moderate cytotoxicity profile. While crude library screening provides an efficient starting point for exploring and narrowing down chemical space, these results highlight the need for subsequent validation with purified compounds to accurately assess biological activity and cytotoxicity. Overall, **Ir15** shows promising antibacterial activity against a broad panel of Gram-positive pathogens, does not cause significant haemolysis and exhibits only minor toxicity against mammalian cells, showcasing a favorable therapeutic window.

3.3.8 Stability of Ir15

We began investigating the stability of the lead compound by determining whether pre-incubation of the lead compound **Ir15** in the bacterial growth medium (MH) would affect its antibacterial activity. Standard serial dilution plates were prepared, and bacteria were added either immediately or after 24 hours of incubation under MIC assay conditions. For the replica inoculated immediately, the MIC remained 3.13–6.25 µM, consistent with previous results. However, when bacteria were added after 24 h, antibacterial activity was significantly reduced, with an MIC of 50 µM. These results indicate that, although **Ir15** is sufficiently stable to produce consistent antibacterial effects across replicates and bacterial strains, it undergoes speciation, potentially through replacement of the chlorido ligand by water, followed by reactions with nucleophilic components of the medium, such as amino and carboxylate groups present in casein hydrolysate and beef extract. Additionally, hydrolysis of the Schiff-base ligand system could generate the corresponding aldehyde and amine, allowing medium components to coordinate to the remaining iridium fragment. The resulting mixture may therefore contain aqua complexes, ligand-substitution products and Schiff-base hydrolysis products with reduced antibacterial activity (**Table 15**).

Table 15. MIC values of Ir15 against *S. aureus* CCUG 62707, bacteria inoculated immediately, and after 24 hours.

	MH (0 h)	**MH (24h)**
Ir15	3.13-6.25 µM	50 µM

Following this, we conducted stability studies in different biologically relevant solvent systems by measuring UV/Vis absorbance at 37°C over 20 hours (**Figure 75**). In DMSO

and DMSO:H_2O (1:1), **Ir15** exhibited good stability, with no significant decrease in absorbance over the measured period (**Figure 75A&B** and **Table 16**). In contrast, significant changes in the UV/Vis spectrum were observed in both H_2O (**Figure 75C** and **Table 16**) and PBS (1X) (**Figure 75D** and **Table 16**). A clear decline in absorbance was detected over time, suggesting degradation of the complex. As we observed degradation of **Ir15** under certain conditions, we further investigated the compound's stability using LC-MS. Briefly, **Ir15** was dissolved in DMSO to prepare solutions at a concentration of 5 mM. These were diluted down to 100 µM for stability test with DMSO:H_2O (1:1), H_2O, and PBS and measured with LC-MS every 24 minutes for 21 hours at 37°C. In H_2O, LC-MS spectra was measured immediately after **Ir15** exhibits degradation, primarily driven by chloride dissociation and subsequent ligand substution with acetonitrile (MeCN) in the mobile phase, and **$[(M - Cl) + MeCN]^{2+}$** complex formed (**Figure 76**). Notably, after 6 hours, two dimeric IrCp species emerged (**Figure 77**). Although degradation was also observed in the DMSO:H_2O mixture, a significant fraction of the parent complex remained detectable even after 21 hours (**Figure 78**). However, LC-MS analysis showed that **Ir15** exhibits good stability in PBS where most of the parent complex remains intact (**Figure 79**). To quantify the stability of **Ir15** over time, LC-MS data were processed using custom Python scripts. Relative acquisition times were calculated from file timestamps, and chromatographic peak areas corresponding to the parent complex were determined by numerical integration of the UV254 signal within a defined retention time window. The resulting time-resolved peak areas enabled quantitative monitoring of compound degradation under different solvent conditions over the 21 hours incubation period. Quantification of **Ir15** peak area over time supported the qualitative LC-MS observations and revealed a clear solvent-dependent stability pattern (**Figure 80**). Compound degredation was evaluated by calculating the decrease in LC-MS peak area between T=0 h and T=21 h. In H_2O, **Ir15** underwent rapid degradation, with the parent complex largely disappearing within 6–8 h, consistent with the formation of acetonitrile-substituted and dimeric species observed in the mass spectra. In DMSO:H_2O (1:1), degradation proceeded more gradually, and a substantial fraction of the parent complex remained detectable after 21 h. The highest stability was observed in PBS, where only a minor decrease in peak area occurred throughout the experiment and most of the parent complex remained intact after 21 h. This is likely due to the high chloride concentration in PBS (137 mM), preventing chloride dissociation from the parent complex.[351] Overall, while an aqueous environment generally promotes hydrolysis, the presence of excess chloride shifts the equilibrium toward the intact chlorido complex. Notably, the

antibacterial activity of **Ir15** was consistent across biological replicates, indicating that the complex retains sufficient stability under biological conditions to exert its activity. Despite the observed solvent-dependent degradation in aqueous media, these results suggest that **Ir15** remains intact over the timescale relevant for antibacterial activity.

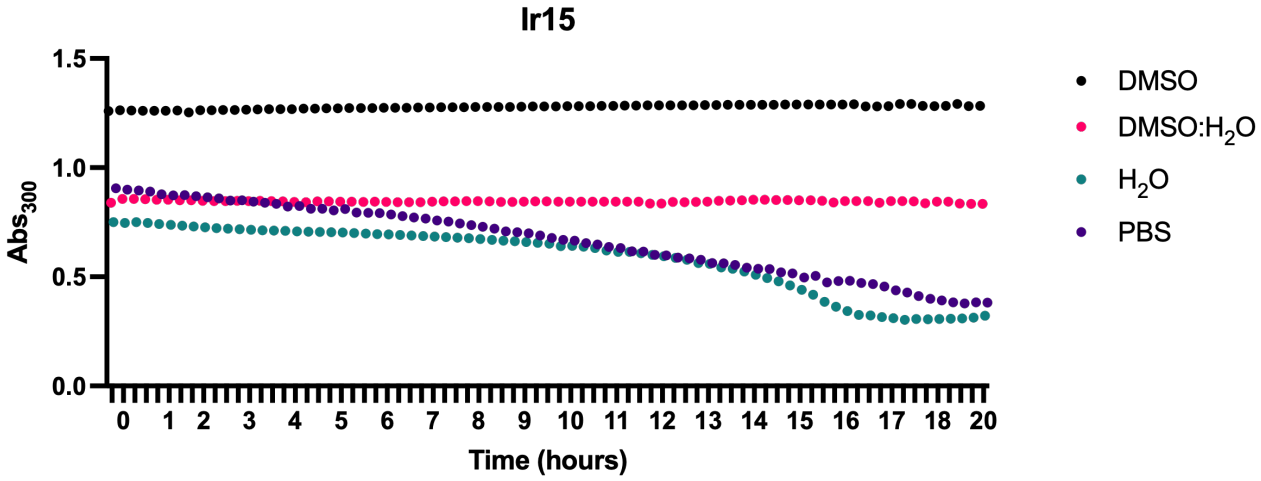


Figure 75. Stability of the hit compound, Ir15. The absorbance was measured at 300 and 37°C.

Table 16. Absorbance (a.u.) at 300 nm changes of Ir15 in different solvents.

	Solvent			
	DMSO	**DMSO:H_2O(1:1)**	**H_2O**	**PBS**
Ir15	0.0233	0.0046	0.429	0.523

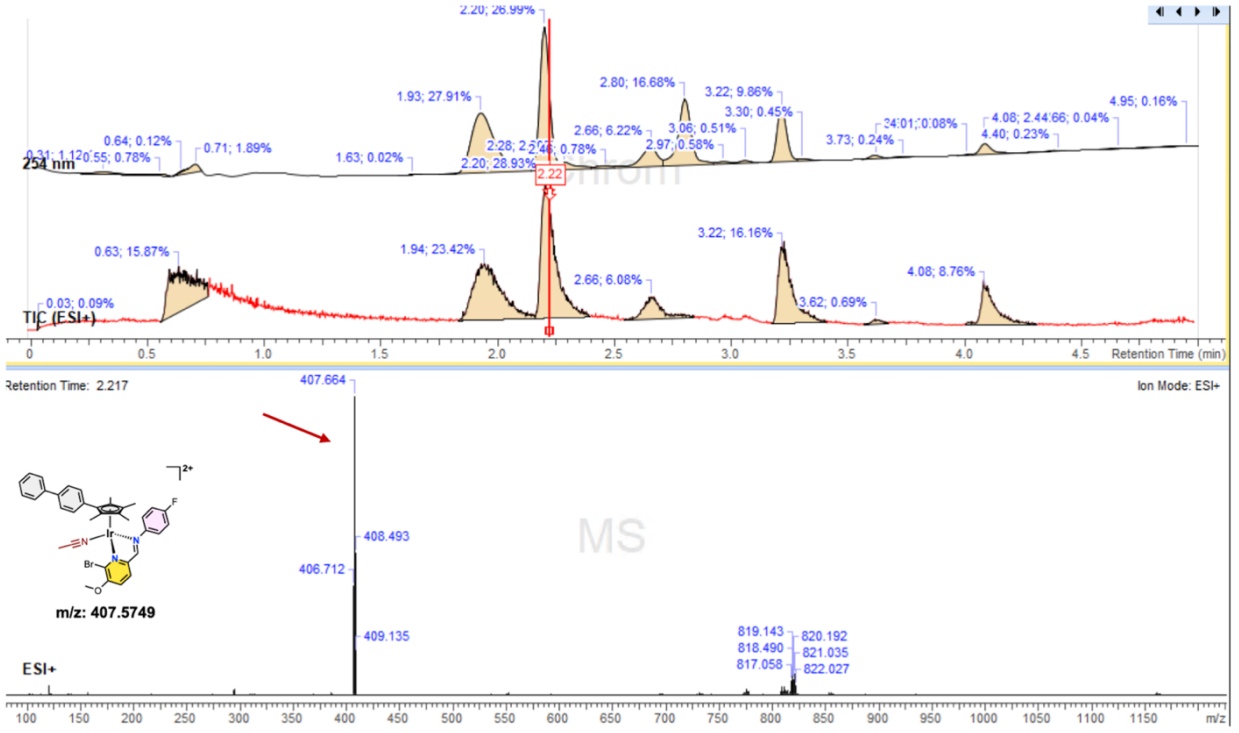


Figure 76. LC-MS spectra of Ir15 in H_2O at t_{15}. Rt :3.22 shows the mass of the parent complex.

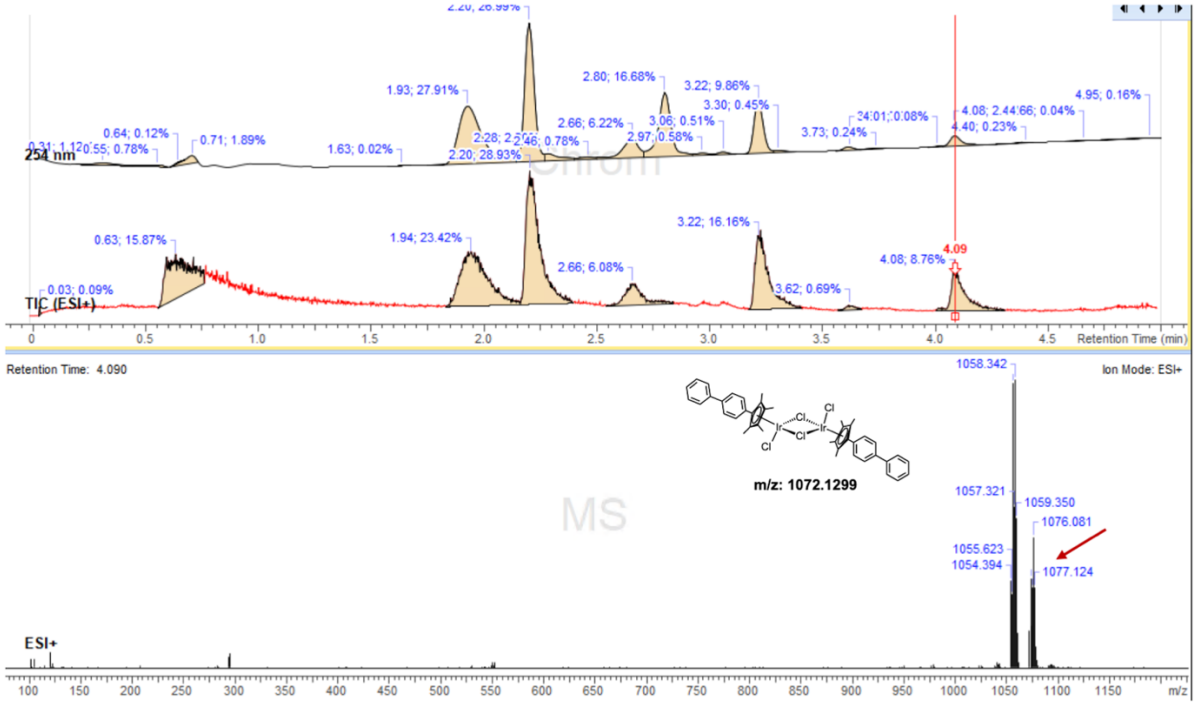


Figure 77. LC-MS spectra of Ir15 in H_2O at t_{15}, Rt :4.09 shoes the two dimeric IrCp species

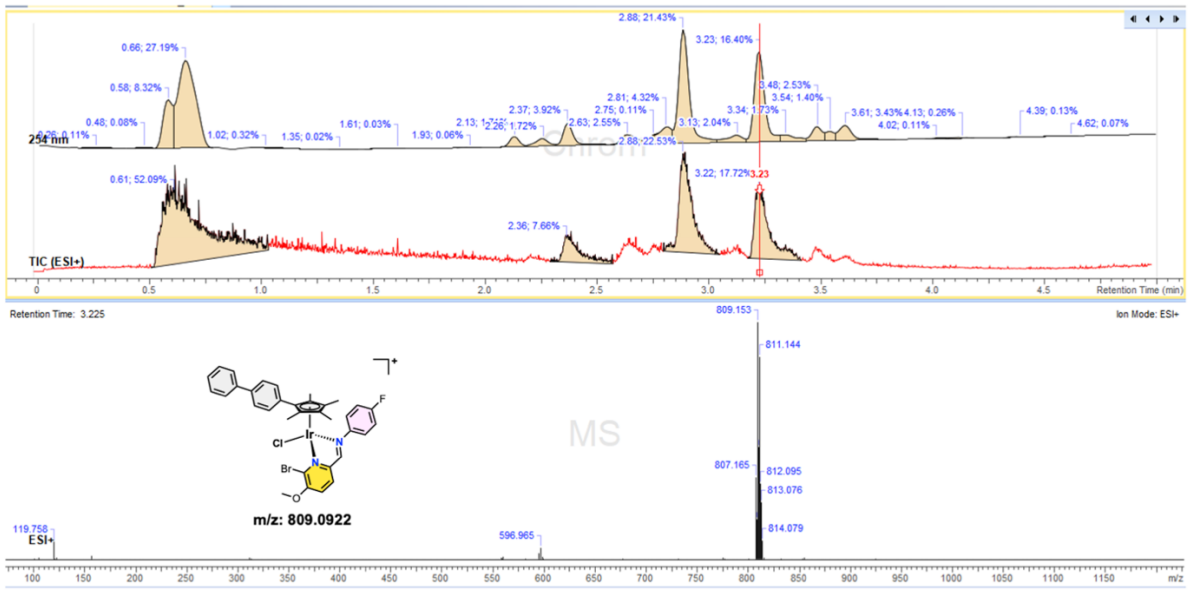


Figure 78. LC-MS spectra of Ir15 in H_2O:DMSO at t_{53}. R_t :3.22 shows the mass of the parent complex.

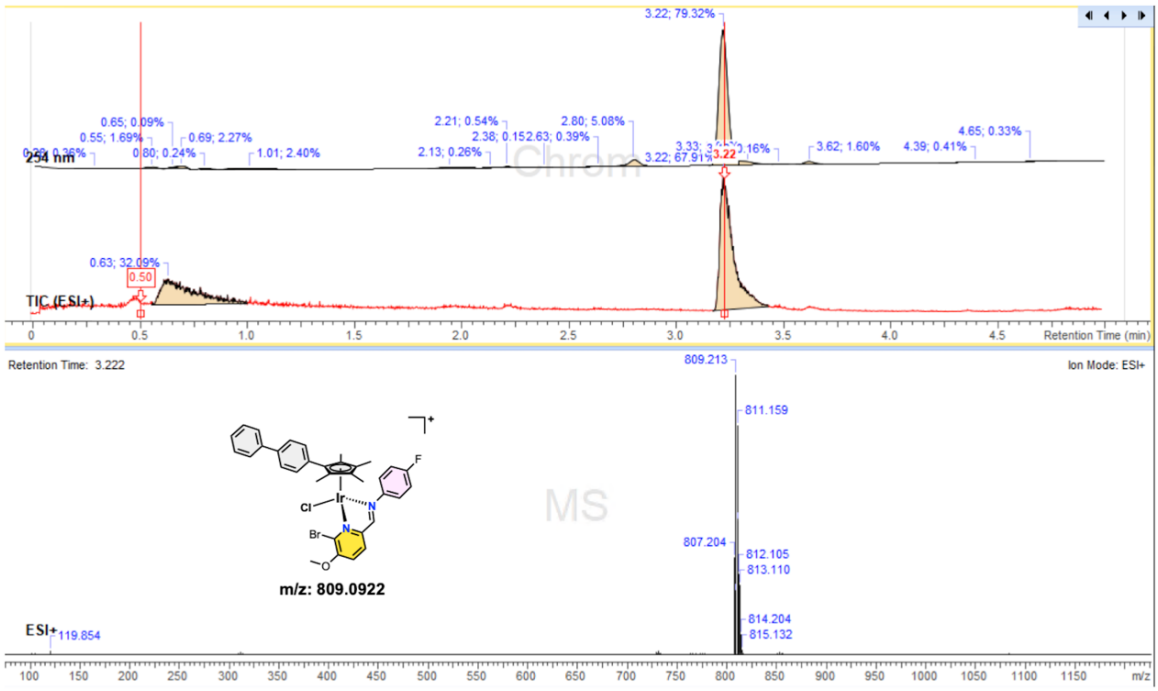


Figure 79. LC-MS spectra of Ir15 in PBS at t_{53}. R_t :3.22 shows the mass of the parent complex.

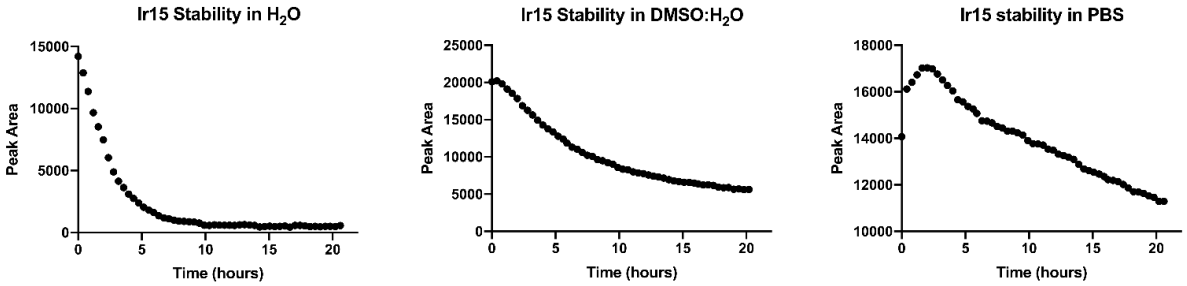


Figure 80. LC-MS stability of Ir15. The peak area for each time point was calculated with Python script and plotted against time in hours.

Table 17. UV_{254} peak area changes (a.u.) of Ir15 in different solvents.

	Solvent		
	H_2O	**DMSO:H_2O (1:1)**	**PBS**
Ir15	12313.3	14476.7	2779.0

3.3.9 Preliminary Mode of action studies

3.3.9.1 Bacterial Cytological Profiling

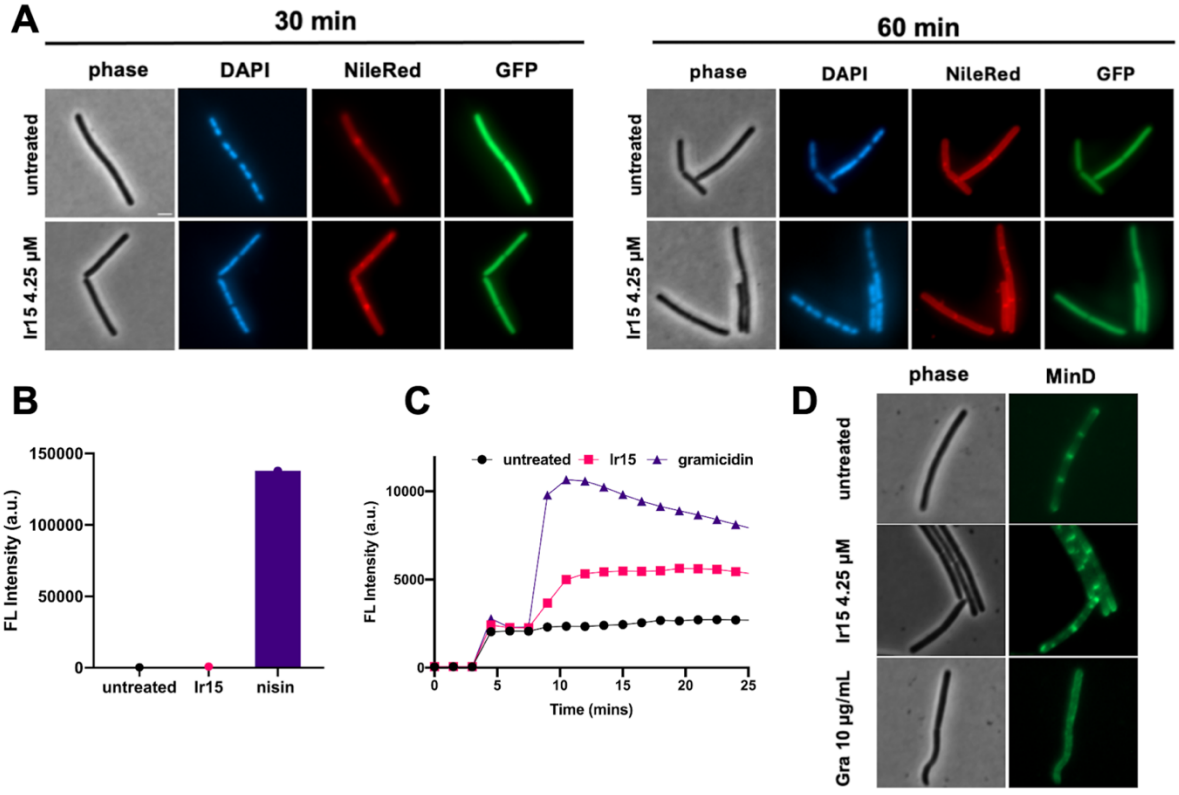


Figure 81. Initial mode of action of **Ir15**, hit compound. (**A**) Bacterial cytological profiling of *B. subtilis* bSS82, constitutively expressing GFP from the PrpsD promoter, stained with Nile red

(membrane) and DAPI (DNA) after 30 and 60 minutes of incubation. (**B**) Propidium Iodide staining of *B. subtilis* 168CA (pore formation assay). 1.6 µg/mL nisin was used as a positive control. (**C**) $DiSC_3(5)$) assay in *B. subtilis* 168CA (membrane depolarizstion assay). 1 µg/mL gramicidin was used as positive control. **(D**) Localization of MinD-GFP in *B. subtilis* TB35 (Pxyl-gfp-minD). Localization of MinD depends on the membrane potential. 10 µg/mL gramicidin was used as positive control. All assays were performed after treatment with 4.25 µM Ir15. Scale bar 2 µm.

Encouraged by the promising biological characteristics of **Ir15**, we conducted initial mode of action investigations of this compound class with phenotypic analysis in the Gram-positive model organism *B. subtilis*. To this end, we first confirmed the MIC against *B. subtilis* 168CA, the background strain of our reporter construct. Here, **Ir15** exhibited comparable antibacterial activity, with an MIC value of 3.13–6.25 µM (**Table 11).** Based on the MIC value, we determined the optimal stressor concentration (OSC) in acute shock experiments. The OSC is defined as the concentration that reduces bacterial growth by 50–70% during the mid-exponential phase, thereby applying sufficient stress to induce a clear phenotype without causing excessive cell death or lysis that could obscure primary effects of the compound.[255] The growth curve (described in **chapter 2**) analysis (**Figure 82**) identified an OSC of **4.25 µM**.

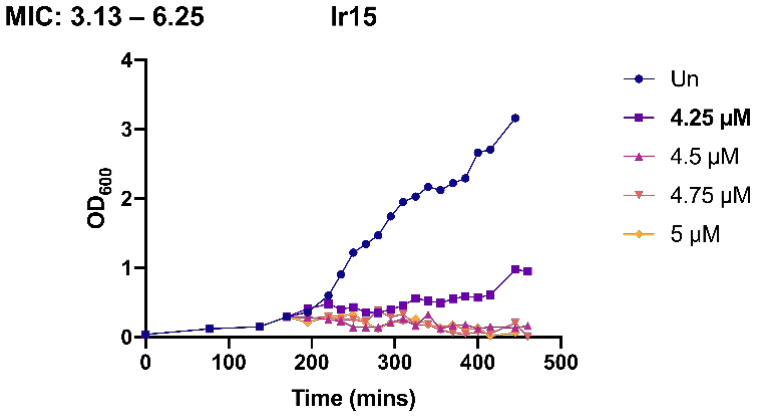


Figure 82. Determination of optimal stressor concentrations (OSC) (indicated in bold) of Ir15.

To get an overview of the cellular effects of the compounds, we employed bacterial cytological profiling (BCP) as described in **chapter 2**. To this end, we used a strain that intracellularly expresses green fluorescent protein (GFP) from the strong, constitutive *PrpsD* promoter (*B. subtilis* bSS82), stained with the membrane dye Nile red and the DNA dye 4′,6-diamidino-2-phenylindole (DAPI). When combined with phase-contrast microscopy, this setup enables simultaneous assessment of cell morphology, cell lysis, pore formation, membrane morphology, and nucleoid morphology in a single assay.[255]

Upon treatment with **Ir15**, no apparent differences in overall cell morphology (phase contrast) or membrane integrity (GFP) were observed (**Figure 81A**)**.** Notably, Nile Red foci formation was observed, suggesting aberrations in bacterial membrane organisation. Although no leakage of cytoplasmic GFP was detected, these findings suggest that perturbation of membrane organisation may contribute to the antibacterial activity

A substantial effect of **Ir15** was observed on the bacterial nucleoid, showing visible changes in its morphology (**Figure 81A**). Particularly, after 60 minutes of treatment, the phenotype points towards compromised DNA integrity which can indicate DNA fragmentation or other structural changes.[352]

3.3.9.2 Cell envelope stress

The Nile Red staining suggested that **Ir15** may exert partial membrane-associated activity. To further investigate this, we examined whether it facilitates the passage of molecules smaller than GFP across the cell membrane.[255] As a first step, we assessed the uptake of the membrane-impermeable, red-fluorescent dye propidium iodide (PI). In these experiments **Ir15** did not result in increased PI uptake, confirming that it does not form large pores (**Figure 81B**).

In contrast, membrane depolarization was observed using the potentiometric fluorescent dye 3,3′-dipropylthiadicarbocyanine iodide ($DiSC_3(5)$)[261] (**Figure 81C**), indicating that **Ir15** induces ion translocation and disrupts membrane polarization. This finding was independently confirmed by assessing the localisation of the cell division regulation protein MinD, which localises at the midcell and poles in healthy cells, but delocalizes into membrane-associated clusters upon loss of membrane potential (**Figure 81D**).[263] Here, **Ir15** induces a mild delocalization of MinD after 30 minutes of treatment. Taken together, these results demonstrate that **Ir15** induces membrane stress by disrupting membrane polarization, while not causing large pore formation or detectable structural damage to the cellular membrane.

3.3.9.3 DNA binding properties

DAPI staining revealed that **Ir15** induces alterations in bacterial nucleoid structure after 60 minutes of treatment (**Figure 81A**). To further investigate this effect, we sought to assess the DNA-binding properties of the compound by performing an MIC shift assay in the presence of difference concentrations of calf-thymus DNA. While the positive control Actinomycin D, an antibiotic known to interact with GC-rich DNA sequences[353],

exhibits decreasing antibacterial activity with increasing concentration of DNA, the MIC of **Ir15** remains unchanged (**Figure 83**).

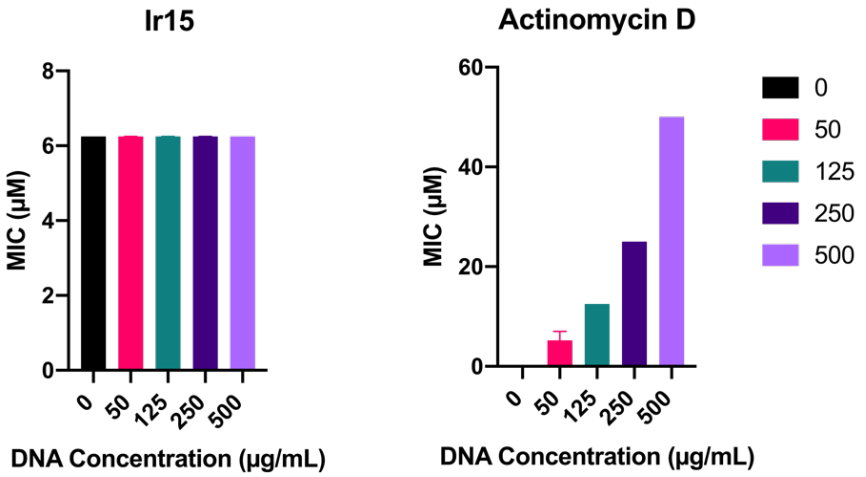


Figure 83. MIC values of Ir15 (left) and Actinomycin D (right) in the presence of 0, 50, 125, 250, and 500 µg/mL CT DNA. Compound concentrations ranged from 0.78 to 100 µM (0.63–80.91 µg/mL).

To specifically evaluate a possible DNA intercalation mechanism, an ethidium bromide (EtBr) fluorescence displacement assay was performed. In this assay, EtBr intercalates into DNA, resulting in a strong fluorescence signal.[354,355] Upon addition of a competing intercalating agent, EtBr is displaced from the DNA duplex, leading to a decrease in fluorescence intensity. Treatment of the calf thymus DNA-Ethidium complex with serial dilutions of **Ir15**, only minimal interaction (5% displacement) was observed at concentrations corresponding to the MIC. No significant DNA intercalation was detected under these conditions. Noticeable displacement of EtBr (45–50%) was only observed at the highest concentration tested (200 µM, **Figure 84**), indicating that DNA intercalation is unlikely to occur at biologically relevant concentrations.

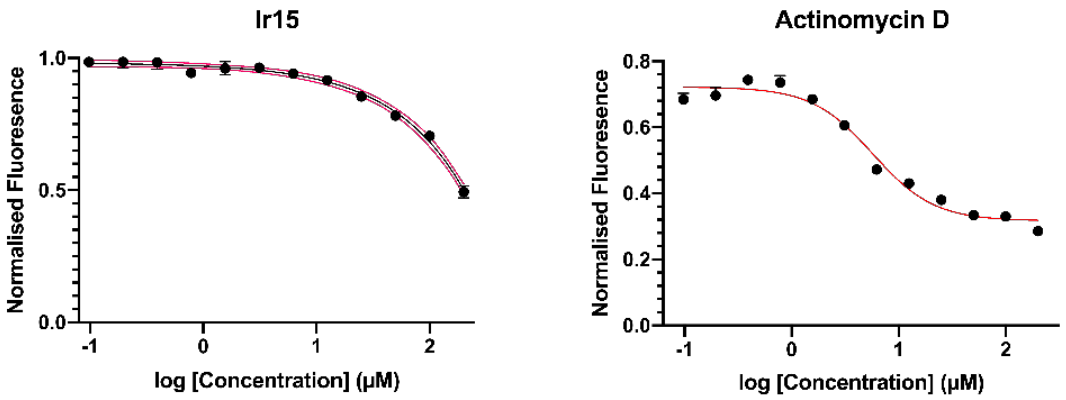


Figure 84. Fluorescence competitive EtBr displacement assay for Ir15 (left) and Actinomycin D (right) at 30th minute time point. EtBr:CT DNA ratio is 1:0.8

3.3.9.4 MIC in glucose-defined medium

To better mimic physiological conditions and assess whether the lead compound is taken up via active or passive transport, MIC assays were conducted in glucose-defined M9 medium. We observed that *S. aureus* failed to grow under these conditions as reported in the literature[356], hence the medium was supplemented with 10% (v/v) TSB to support bacterial growth. MIC values against *S. aureus* remain unchanged under standard experimental conditions and glucose-defined M9 growth media (**Table 18**). This suggests that the antibacterial activity of the lead compound is not strongly dependent on nutrient conditions, implying that uptake is not strictly energy driven. Antibacterial activity is often governed by permeability and efflux rather than active transport alone, and passive diffusion mechanisms can contribute to transport across the cellular membrane.[133]

Table 18. MIC values of Ir15 in MH and glucose-defined M9 media against *S. aureus*. MIC values were given in μM.

	MH	GDMM
Ir15	3.13 — 6.25	3.13

3.3.9.5 Determination of synergy with clinically relevant antibiotics

We next expanded our study to explore the mode of action of the lead compound and to determine whether **Ir15** can synergistically interact with clinically relevant antibiotics. We conducted a combination study using checkerboard assays with four antibiotics (vancomycin, ciprofloxacin, chloramphenicol, and kanamycin) against our Gram-positive

model organism, *S. aureus* (CCUG 62707). Neither synergistic nor antagonistic effects were observed with any of the tested antibiotics, indicating that the mode of growth inhibition of **Ir15** is unrelated to that of other antibiotics (**Figure 85**).

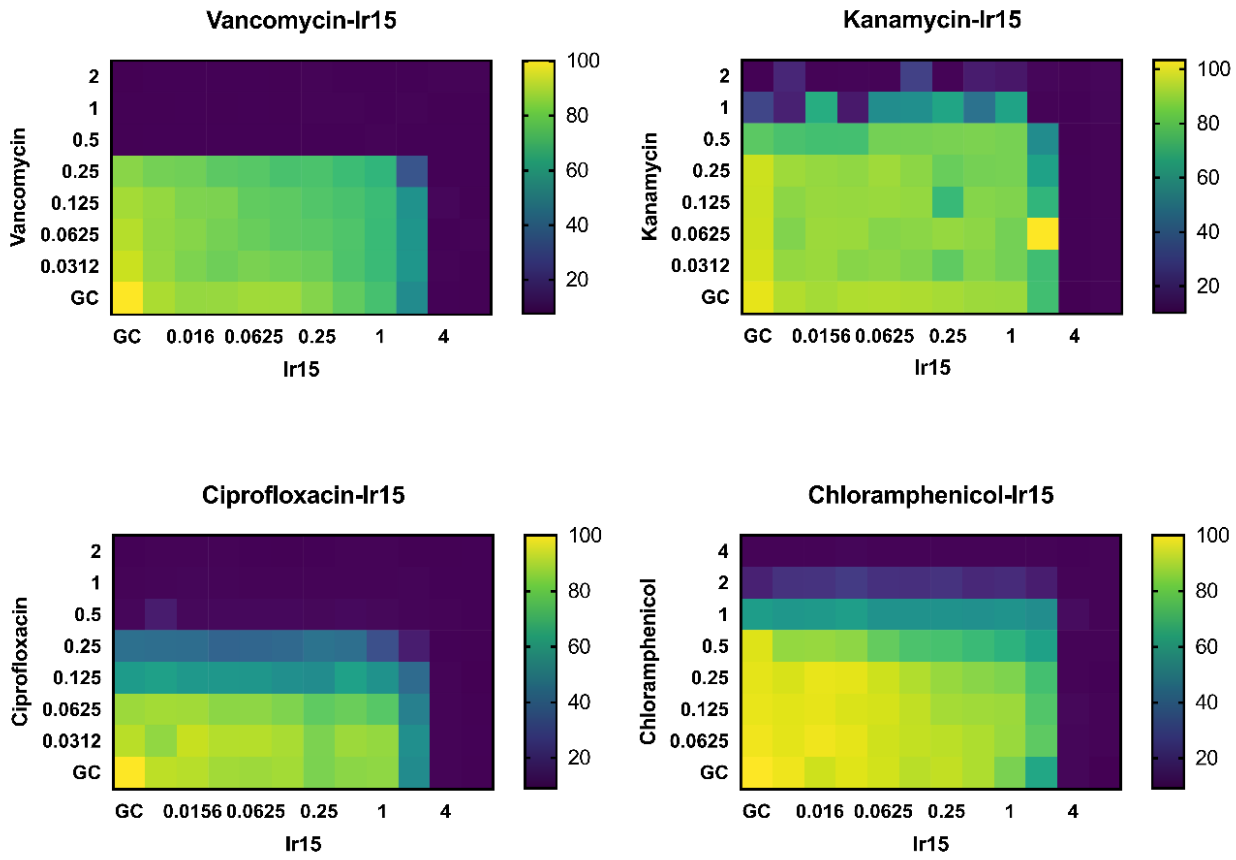


Figure 85. Checkerboard assay against *S. aureus* CCUG 62707 with clinically relevant antibiotics, vancomycin (**A**), kanamycin (**B**), ciprofloxacin(**C**), and chloramphenicol (**D**) (one out of three biological replica is shown). Concentration values were given in µg/mL.

3.3.9.6 Reactive oxygen species

Metal complexes often induce oxidative stress (ROS) in cells, which can significantly contribute to membrane and DNA damage, mostly through generation of hydroxyl radicals.[357] Although iridium cannot replace iron or copper in a Fenton reaction to create hydroxyl radicals from hydrogen peroxide, a cyclometallated iridium(III) complex has been shown to increase intracellular reactive oxygen species formation.[358] Notably, we previously demonstrated that iridium Cp complexes can catalyse transfer hydrogenation reactions[327]; this redox activity may further disrupt cellular redox balance, thereby promoting ROS accumulation.[359] Bacterial cells contain high amounts of iron and the Fenton reaction is a common source of hydroxyl radicals.[271] To asses if bacterial growth inhibition of **Ir15** involves reactive oxygen species, a scavenger assay was employed. In

this modified MIC assay, the activity of a test compound is determined in: scavenger-free medium, medium containing the superoxide scavenger tiron, the hydroxyl radical scavenger thiourea, and a mix of both. If the mode of action involves ROS formation, an increase in the MIC value is expected in the medium containing a scavenger specific to the generated ROS. In our case, MIC values against *B. subtilis* 168CA in the presence of Tiron remain unchanged, whereas we unexpectedly obtained a 2-fold lower MIC value (1.56–3.13 µM) in the presence of thiourea (**Table 19**). This led us to conduct further investigations to determine whether thiourea modulates the antibacterial activity of **Ir15**. A checkerboard synergy assay against *B. subtilis* 168CA was initially performed (**Figure 87).** The interaction between thiourea and **Ir15** was evaluated using the fractional inhibitory concentration index (FICI), calculated from MIC values with $OD_{600} \leq 0.1$. Across six independent replicates, the mean FICI was **0.47 ± 0.11**, indicating an overall trend toward synergistic interaction.[360] However, variability between replicates was observed, with FICI values spanning the synergy-additive boundary. This suggests that while the combination might exhibit a synergistic effect, there is variability across the replicas. A checkerboard synergy assay was also performed against *S. aureus* (**Figure 88**) with a mean FICI of **0.53 ± 0.16**, indicating an overall trend toward additive interaction.[360] Finally, because the proposed mechanism of action of our lead compound involves mild membrane depolarisation, we examined whether thiourea enhances disruption of membrane polarisation. A $DiSC_3(5)$ assay performed in the presence of thiourea against *B. subtilis* 168CA showed no change in the membrane depolarisation profile (**Figure 86**). Overall, while thiourea does not potentiate membrane depolarisation, it contributes moderately to enhanced antibacterial activity, resulting predominantly in additive effects. Further studies will be required to identify the role of thiourea in the activity of **Ir15**.

Table 19. MIC values of Ir15 in MH, 150 mM tiron, 40 mM thiourea, and 150 mM tiron and 40 mM Thiourea. H_2O_2 was used positive control for thiourea. MIC values were given in µM for Ir15, and % for H_2O_2.

	MH	**Tiron**	**Thiourea**	**Tiron + Thiourea**
Ir15	6.25	12.5	1.56 — 3.13	3.13
H_2O_2	0.0094 — 0.019	0.0094 — 0.019	0.3	0.3

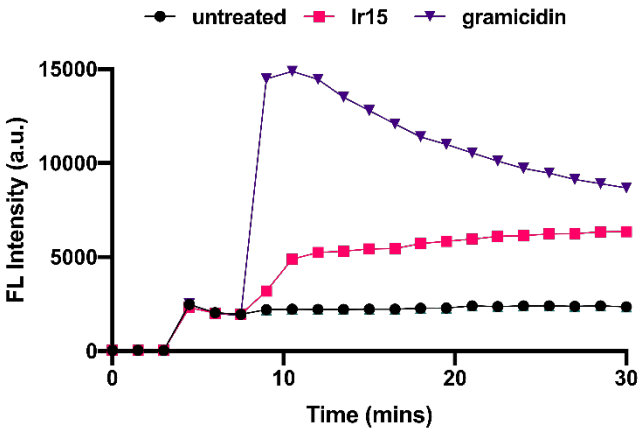


Figure 86. $DisC_3(5)$ membrane depolarisation assay in the presence of thiourea in *B. subtilis* 168CA.

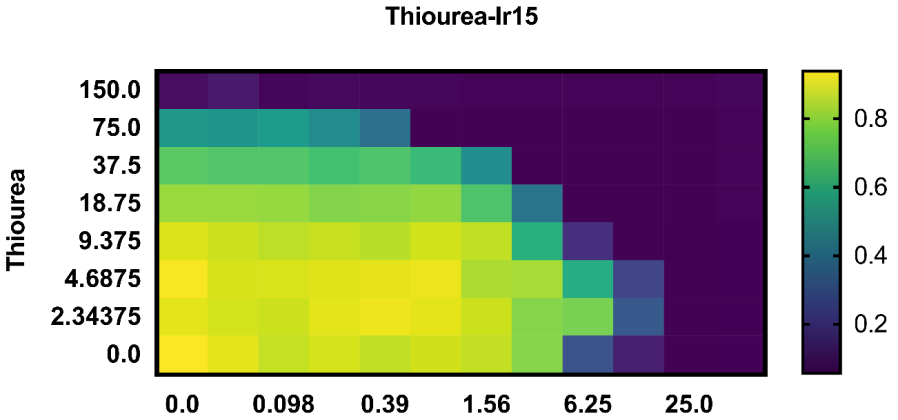


Figure 87. Synergy assay of Ir15 with thiourea against *B. subtilis* 168CA. Concentration values were given in µg/mL.

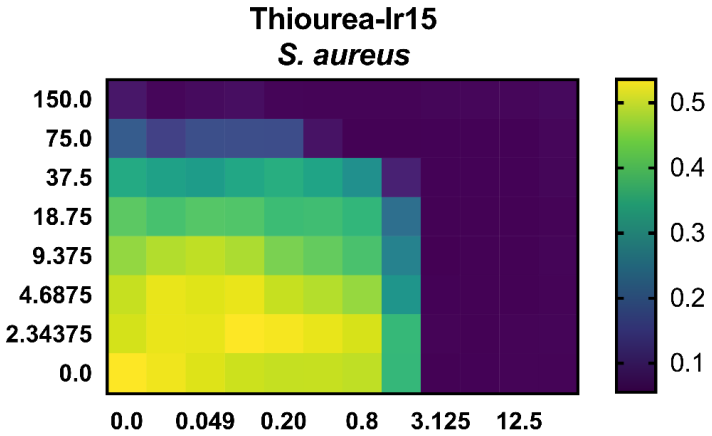


Figure 88. Synergy assay of Ir15 with thiourea against *S. aureus* CCUG 62707. Concentration values were given in µg/mL.

3.4 Antifungal Activity of IrCp Library

3.4.1 Introduction

Although antibacterial resistance has received greater scientific and public attention, antifungal resistance is increasingly recognised as a major threat to global health.[361] In 2022, WHO published the first list of fungal priority pathogens to guide research, surveillance, and public health resources. The critical pathogens include *Cryptococcus neoformans*, *Candida auris*, *Aspergillus fumigatus*, and *Candida albicans*, reflecting the substantial disease burden, limited treatment options, and growing concern over antifungal resistance associated with these pathogens.[362] Life-threatening fungal diseases are estimated to affect approximately 6.5 million people each year and to account directly for around 2.5 million deaths worldwide.[363] Despite this burden, treatment options for invasive fungal infections remain limited and depend largely on four major antifungal classes: azoles, polyenes, echinocandins and flucytosine.[364] Among these agents, azoles are of particular concern because structurally related compounds with the same mechanism of action are used both clinically and as agricultural fungicides. More than 70% of agricultural fungicides are reported to belong to the demethylation inhibitor class, which disrupts sterol biosynthesis through the same molecular target as clinically used azoles.[365] The dual use of azoles exerts sustained selective pressure and drives the emergence and spread of azole-resistant fungal pathogens.[366]

Under these circumstances, the exploration of novel chemical spaces is essential to identify antifungal scaffolds with distinct mechanisms. Over the last decade, various metal complexes have been evaluated as potential antifungal scaffolds. In the following section, a few representative studies will be discussed. In 2016, Rubbiani and Gasser reported a ferrocenyl sedaxane derivative, **Fe1** (**Figure 89**), termed a sedaxicene, as a novel metal-based antifungal scaffold. It was demonstrated that **Fe1** exhibited moderate antifungal activity against *Saccharomyces cerevisiae* with IC_{50} value of 43.3 ± 6.2 μM, while no off-target toxicity was observed against human fibroblasts and retinal pigment epithelial cell lines up to 100 μM. Notably, the ruthecene analogue of the compound did not exhibit any antifungal activity up to 100 μM, which was attributed to the lack of reactive oxygen species formation.[367] Later, the same group expanded the ferrocenyl-based antifungal agents with fluconazole modification. Among the four synthesised derivatives, **Fe2** (**Figure 89**) exhibited the highest potency with an IC_{50} value of 3.02 ± 2.18 μM against *S. cerevisiae*. Notably, fluconazole alone exhibited an IC_{50} value of 51.0 ± 3.7 μM. Further *in vitro* activity characterisation was performed against clinical isolates,

and a 400-fold improvement in activity was observed for **Fe2** compared to fluconazole against azole-resistant strains. The enhanced antifungal activity was partly attributed to the ferrocene moiety, which reduced *ERG11* expression. This gene encodes lanosterol 14α-demethylase, a key enzyme in the ergosterol biosynthetic pathway and the primary molecular target of azole antifungals; its overexpression is a well-established mechanism of azole resistance. The compound also showed *in vivo* efficacy in a murine model of *Candida albicans* infection.[368] Together, these studies proved that incorporation of organometallic scaffolds into the clinically approved moieties might pave the way to combat antifungal resistance.

In 2018, in the previously mentioned study by the Sadler group, synthesised iridium (III) Cp-biguanide complexes were also screened against *C. neoformans* and *C. albicans*, pathogenic fungal species. Compounds **33**−**37** (**Figure 52**) exhibited promising antifungal activity with MIC values between 0.34−1.45 μM, which is nearly a 76-fold increase in activity against *C. neoformans* relative to fluconazole. While incorporation of the halido ligand had little effect on the antifungal activity, the sulfonyl group slightly decreased the activity (MIC values of 1.1−2.4 μM).[278]

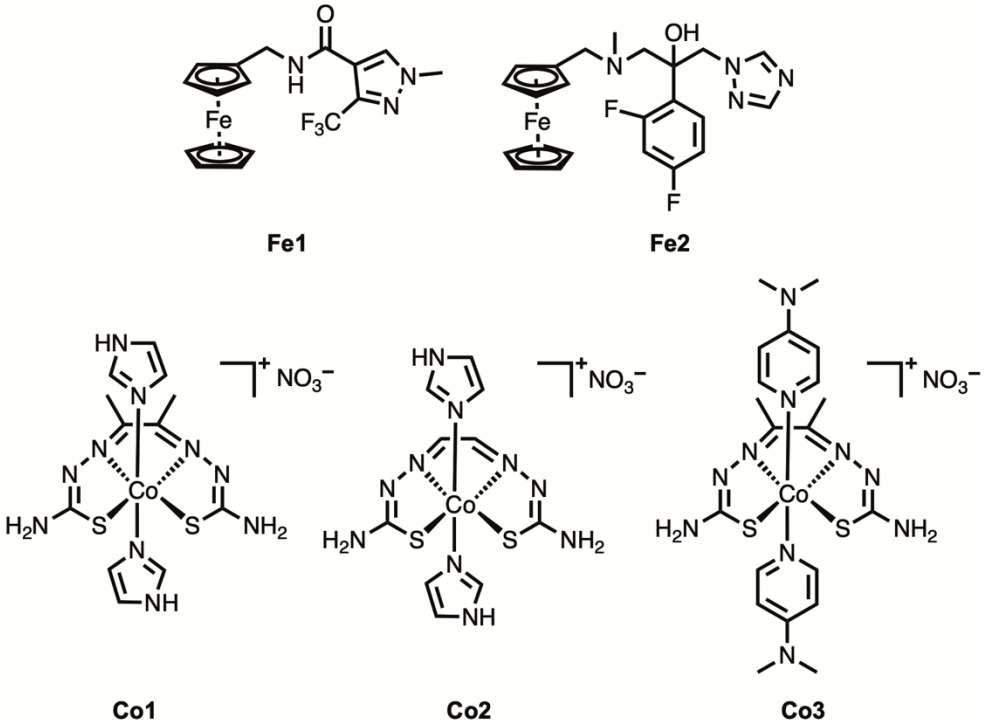


Figure 89. Selected complexes with antifungal activity.

In 2021, Frei and coworkers studied the broad-spectrum antifungal activity of cobalt(III) Schiff-base complexes (only the ones with antifungal activity were shown, **Figure 89**). Among the seven synthesised complexes, four exhibited promising antifungal activity.

Co1 was demonstrated as the most promising lead, which exhibited MIC values between 0.39−1.56 μM against a broad panel of antifungal strains including clinical isolates and multidrug-resistant ones. The other two complexes exhibited slightly lower but comparable activity: **Co2** MIC values between 0.78−25 μM and **Co3**, with MIC values between 0.39−50 μM. Notably, the complexes exhibited mostly improved antifungal activity relative to clinically approved drugs fluconazole, ketoconazole and micafungin. Additionally, complexes with antifungal activity did not exhibit significant cytotoxicity against HEK293T cells and hRBC (hemolytic), except for a slight hemolytic activity of **Co3,** with an HC_{10} value of 73.1±20.4 μM.[369]

Subsequently, in the previously mentioned CO-ADD study[92], 20.9% of the evaluated metal complexes exhibited antifungal activity against *Candida* and *Cryptococcus* strains. From this compound library, 90 metal complexes (with different metal centres) (8.7%) were found to be non-cytotoxic and non-haemolytic at therapeutic concentrations. The authors obtained 21 of them fresh for further testing, of which 15 had not previously been evaluated against fungi. They comprise 11 metal centres: cobalt(III), nickel(II), rhodium(III), palladium(II), silver(I), europium(III), iridium(III), platinum(II), molybdenum(VI), gold(I), and gold(III). Overall, it was demonstrated that these complexes exhibited low micromolar/microgram activity against fungal species (including multidrug-resistant strains), and low cytotoxicity (HEK) and hemolytic activity (hRBC).[274]

Taken together, these studies highlight metal complexes as promising scaffolds for antifungal drug development, in addition to their well-established anticancer and antibacterial activities. By expanding the accessible chemical space and enabling distinct mechanisms of action, metal complexes offer a novel platform for antifungal drug discovery. Building on these findings, we screened our crude IrCp1 library against *A. fumigatus* and followed by hit validation with the selected compounds in *A. fumigatus* and *C. albicans*.

3.4.2 Single-dose response biological activity of the combinatorial library

Initially, the **IrCp1** library was screened against *Aspergillus fumigatus* to assess antifungal activity and identify promising candidates for further investigation. The fungal strain was treated with crude mixtures at 100 μM and incubated for 48 hours at 37°C. The mean growth inhibition across the library was 14.8%, while the median inhibition was 7.1%, indicating that most compounds exhibited low antifungal potency. Growth inhibition values ranged from -33.9% to 100%, highlighting the substantial variability in activity across the library. When only compounds that completely inhibited fungal growth

were considered, the number of active hits was substantially decreased to 7, with only a small subset of the library retaining complete inhibitory activity (**K11**, **B11**, **K8**, **B8**, and **K7)**.

Structure-activity relationships emerged at the building block level. Aldehydes **H** (ethoxyquinoline), **K** (chloroquinoline), and **B** (quinoline) exhibited the highest mean antifungal activities across the library, with average growth inhibition values of 40.3%, 39.9%, and 39.4%, respectively. The similar activities observed for these aldehydes suggest that the quinoline scaffold is a key contributor to antifungal activity, while substitution on the quinoline ring has a comparatively modest effect. Moderate activity was also observed for compounds derived from **L** (bromo-methoxy) and **N** (bromo), whereas simpler pyridine aldehydes, **A**, **I** (methoxycarbonyl) and **J** (methoxy) appeared as less potent. On the amine side, aromatic amines such as **7** (aniline), **8** (*p*-toluidine), **9** (*p*-bromo), and **11** (4-methoxybiphenyl) were frequently found among the most active compounds, whereas aliphatic amines such as **20** (hexylamine), **21** (cyclohexyl), **22** (phenethyl), **23** (allyl), and **24** (2-ethylbutyl) generally resulted in lower activity. These observations indicate that antifungal activity is associated with specific combinations of aromatic aldehyde and aromatic amine building blocks. The most active compounds were predominantly derived from quinoline-based aldehydes and aromatic amines. It highlights the importance of both building block classes in determining biological activity. However, the compounds displaying the highest antifungal activity also tended to exhibit increased cytotoxicity against HEK293T cells, suggesting a relationship between the two properties. Compounds **K7**, **B7**, **L7** were selected and **B8 (Figure 91)** were selected for further hit validation.

Table 20. Selected 4 compounds from the single-dose biological assays. %Conv. is the conversion percentage determined by LC-MS. % Growth inhibition is given as the ratio of OD_{600} of the drug-free control and the treated replicas with corresponding compounds at 100 µM. % Cell viability was measured in the presence of 50 µM of corresponding compounds against HEK293T cells.

Compound	%Conv.	% Growth inhibition	%Cell viability
		A. fumigatus	HEK293T
IrCp1K7	80	100	30 ±11
IrCp1L7	83	98	57± 5
IrCp1B7	77	99	40 ± 16
IrCp1B8	80	100	10 ± 6

The selection was based on their antifungal activity against *A. fumigatus*, cytotoxicity profiles against HEK293T cells, and the availability of the corresponding building blocks.

Compounds **K7**, **B7**, and **L7** were selected because they exhibited fungal growth inhibition and lower cytotoxicity than the most potent compounds in the library. **B8** was additionally included despite its higher cytotoxicity, as it exhibited nearly complete inhibition and served as a benchmark for evaluating the relationship between antifungal potency and mammalian cell toxicity. The inclusion of a more cytotoxic compound also provided a control to assess whether compounds excluded based on cytotoxicity might represent false negatives during hit selection.

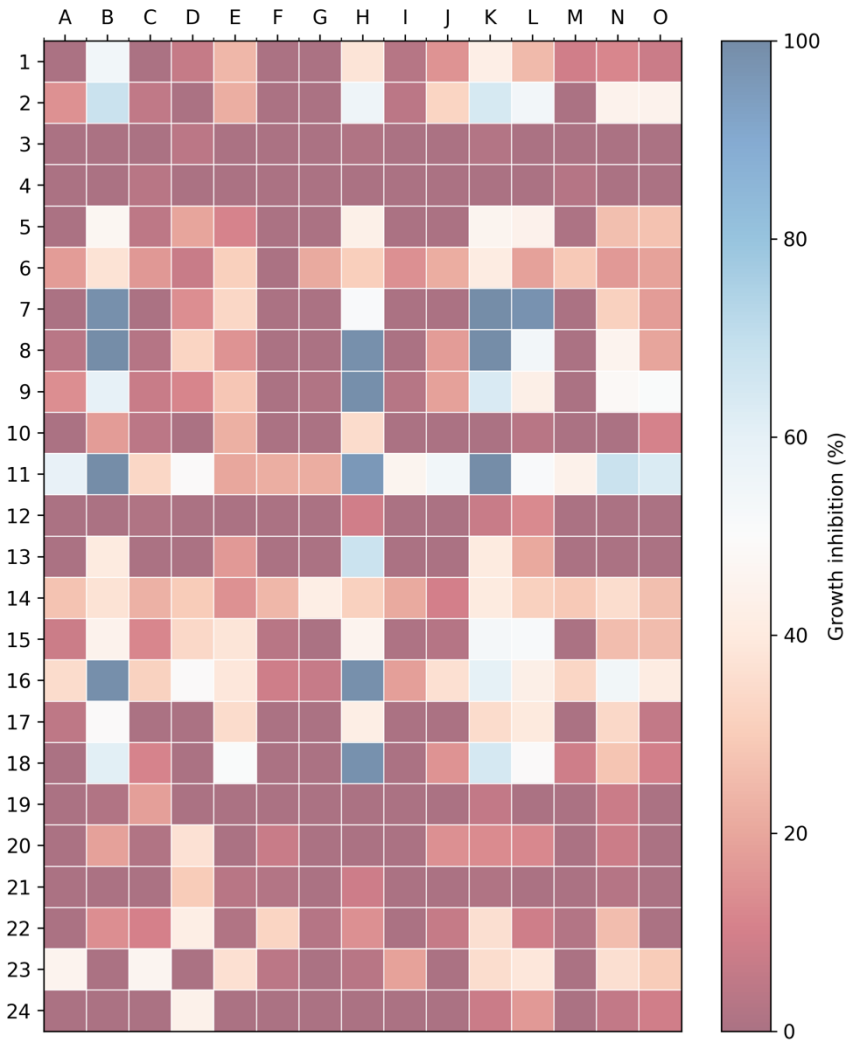


Figure 90. Single-dose biological characterisation of the IrCp1 combinatorial library against *A.fumigatus*. Compounds are arranged according to their aldehyde building block (A–O, x-axis) and amine building block (1–24, y-axis). Each cell represents the percentage growth inhibition relative to the untreated control. Growth inhibition values were normalised to a scale of 0–100%. The colour intensity corresponds to the antifungal activity.

3.4.3 Batch syntheses of selected complexes

Following single-dose antifungal screening, four iridium(III) complexes, **IrCp1K7**, **IrCp1B7**, **IrCp1L7**, and **IrCp1B8**, were selected for scale-up synthesis and purification. The iridium dimer (0.5 equiv.) was combined with the corresponding amine (1 equiv.) and aldehyde (1 equiv.) in DCM/MeOH (1:1) and stirred at room temperature overnight. Reaction progress was monitored by LC-MS. Upon completion, excess *n*-hexane was added to precipitate the product. The compounds were synthesised successfully with nearly quantitative yields. Compound purity and identity were confirmed by LC-MS and NMR characterisation, high-resolution mass spectra (HRMS), and X-ray diffraction (XRD) (**Figure 91**).

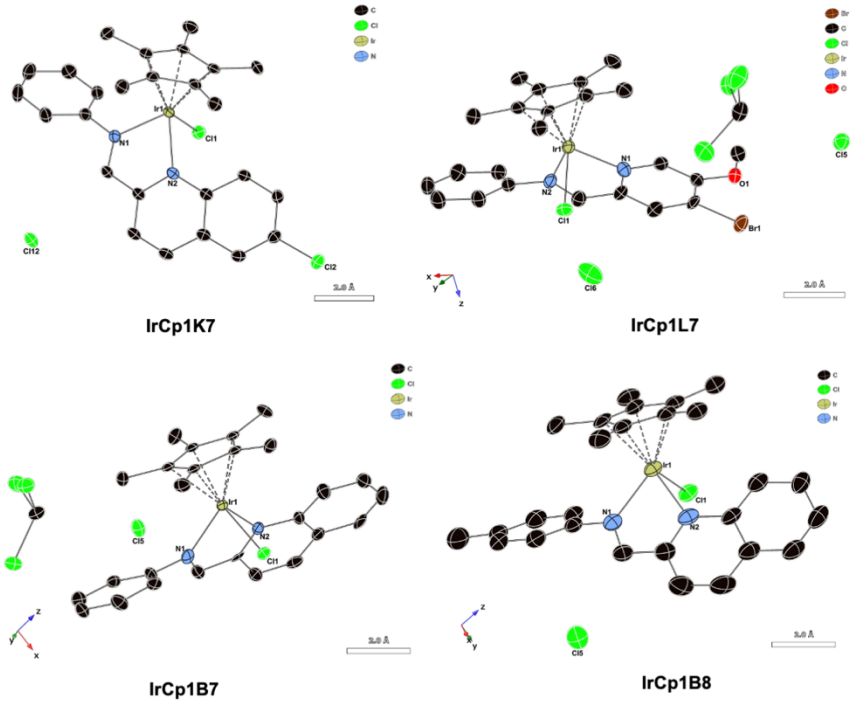


Figure 91. Purified lead compounds for dose-response antifungal testing and single X-ray diffraction structures of IrCp1K7, IrCp1B7, IrCp1L7, and IrCp1B8 thermal ellipsoids are shown at a probability level of 50% (hydrogen atoms have been omitted for clarity).

Single crystals suitable for X-ray diffraction were obtained by solvent diffusion using chloroform and pentane. X-ray diffraction confirmed coordination of the iridium centre to the Cp ring, the two nitrogen donors of the Schiff-base ligand, and a chlorido ligand. For **IrCp1K7**, The **Ir-C** distances ranged from 2.138(2) to 2.203(2) Å, while the Ir-N bond lengths were 2.0863(18) and 2.119(2) Å. The **C_{20}-N_1** distance of 1.282(3) Å was

consistent with the imine bond.[370] The Ir-Cl bond length of 2.3949(5) Å was comparable to reported Cp*Ir(III) complexes.[371] Additionally, the **Ir–N** bond lengths of 2.0863(18) and 2.119(2) Å were comparable to those reported for a related half-sandwich iridium(III) complex bearing an N^N acylhydrazone Schiff-base ligand (2.09 and 2.11 Å).[372]

3.4.4 Antifungal activity of lead complexes: Hit validation

To validate the antifungal activity observed in the crude mixtures, the purified complexes were re-screened against *C. albicans* and *A. fumigatus* **(Table 21)**. Dose-response biological characterisation showed a limited antifungal potency for the selected compounds. **IrCp1K7**, **IrCp1L7**, and **IrCp1B7** didn't inhibit the growth completely up to 100 µM against *C. albicans*, while **IrCp1B8** displayed an MIC of 100 µM. The reduced activity observed against *C. albicans* compared with the single-dose screening results highlights the importance of dose-response validation following hit identification from crude reaction mixtures. Notably, except **K7**, with MIC value of 100 µM compounds exhibited higher potency against *A. fumigatus*, with MIC values between 12.5 and 25 (**Table 21**).

Table 21. Antifungal activity of IrCp1 K7, L7, B7, B8 against *C. albicans* ATCC 90028 and *A. fumigatus* A1160. MIC values were given in µM. Experiments were repeated as three biological replicates and triplicates.

Compound	MIC (µM)	
	C. albicans	*A. fumigatus*
IrCp1K7	>100	100
IrCp1L7	>100	25
IrCp1B7	>100	12.5
IrCp1B8	100	12.5

Although this activity difference wasn't investigated further, the observed antifungal activity difference between *A. fumigatus* and *C. albicans* can be rationalised by fundamental differences in the cell wall architecture of these two morphologically distinct pathogens. *C. albicans*, as a yeast-form organism, possesses a densely decorated outer cell wall enriched with heavily mannosylated glycoproteins, which collectively function as a physicochemical barrier restricting the uptake of compounds. In contrast, *A. fumigatus*, as a filamentous mould, presents a comparatively less glycosylated outer surface, potentially conferring greater permeability to the iridium complexes and facilitating their access to intracellular targets.[373,374]

3.4.5 Haemolytic and cytotoxic properties of lead complexes

The development of effective antifungal agents necessitates not only potent activity against pathogenic fungi, but also a favourable selectivity profile with respect to mammalian host cells. Therefore, cytotoxicity of the lead compounds was reevaluated against the HEK293T mammalian cell line (**Table 22)**.

Table 22. Cytotoxicity of IrCp1K7, IrCp1L7, IrCp1B7, and IrCp1B8 against HEK293T and human red blood cells(hRBC). CC_{50} and HC_{50} values were given in μM. Therapeutic index (TI) is given as the ratio of CC_{50} and MIC against A. fumigatus. Experiments were repeated as three biological replicas as triplicates.

Compound	Toxicity		TI
	HEK293T	hRBC	
IrCp1K7	14 ± 1	>200	0.1
IrCp1L7	55± 7	>200	2.2
IrCp1B7	26 ± 3	>200	2.1
IrCp1B8	12 ± 1	>200	1.0

IrCp1K7 exhibited high cytotoxicity against HEK293T cells, with a CC_{50} of 14.1 ± 1.2 μM. Consistent with this observation, **IrCp1K7** also exhibited the lowest therapeutic index (TI = 0.1), indicating poor selectivity between antifungal activity and mammalian cell toxicity. **IrCp1L7** exhibited a CC50 value of 54.5 ± 6.8 μM, the lowest cytotoxicity among the compounds tested. This translated into the highest therapeutic index (TI = 2.2), indicating the most favourable balance between antifungal activity and mammalian cell viability within the series. **IrCp1B7** displayed moderate cytotoxicity, with a CC_{50} value of 25.7 ± 2.8 μM. Combined with its antifungal activity, this resulted in a therapeutic index of 2.1, comparable to that of **IrCp1L7**. Although **IrCp1B7** and **IrCp1B8** exhibited the most favourable selectivity profiles among the compounds investigated, their therapeutic indices remained low, providing insufficient safety margins to justify further optimisation or biological evaluation.

IrCp1B8 was among the most cytotoxic compounds evaluated, exhibiting a CC_{50} value of 12 ± 1μM. However, its greater antifungal potency resulted in a therapeutic index of 1.0, representing an improvement over **IrCp1K7** despite the similar level of cytotoxicity. No haemolytic activity was detected for any of the compounds at concentrations up to 200 μM.

Taken together, while **IrCp1L7** and **IrCp1B7** displayed the most favourable balance between antifungal activity and mammalian cell toxicity, none of the compounds demonstrated sufficient selectivity to do further biological characterisation.

3.4.6 Summary, conclusion and outlook

Antibacterial resistance continues to drive the need for exploring novel chemical space beyond conventional organic scaffolds. Metal-based compounds have emerged as a promising class of antibiotic candidates, demonstrating high hit rates against priority bacterial pathogens without exhibiting increased toxicity compared to purely organic molecules. Iridium(iii) complexes have been identified as promising antibacterial compounds in the literature. In parallel, combinatorial chemistry provides a powerful and efficient strategy for generating large, structurally diverse libraries, enabling rapid screening and systematic investigation of structure-activity relationships. This strategy facilitates the identification of molecular features that drive antibacterial activity and enables the optimisation of lead compounds. In this work, we have applied a robust and operationally simple one-pot, three-component combinatorial strategy for the rapid generation of structurally diverse piano-stool Ir(III) Cp Schiff-base complexes. By combining 15 picolinaldehydes, 24 amines, and four cyclopentadienyl iridium scaffolds, we generated a library of 1440 complexes and demonstrated that this approach is compatible for direct-to-biology screening without the need for purification. This platform enables efficient exploration of metal-based chemical space and provides a scalable route to identifying novel antibacterial scaffolds.

Crude libraries were analysed by LC-MS, and conversion rates were calculated with in-house Python code. This confirmed that the efficiency of complex formation is strongly influenced by the nature of the Cp ligand, with electron-rich and sterically balanced systems affording higher conversions. Despite these variations, the combinatorial workflow proved sufficiently robust to generate a large and chemically diverse library amenable to biological evaluation. Importantly, this highlights the compatibility of Schiff-base chemistry with high-throughput synthesis of organometallic compounds, further establishing it as a versatile tool in metal-based drug discovery.

Biological screening of the crude library revealed a clear dependence of antibacterial activity on the Cp scaffold and on the structures of other building blocks. Complexes with the biphenyl-substituted Cp ligand (**Cp2**) exhibited the highest antibacterial activity against *S. aureus*, consistent with previous reports and attributable to increased lipophilicity and improved membrane permeability. In contrast, the Cp* (**Cp1**) library exhibited limited activity, whereas **Cp3** and **Cp4** showed intermediate profiles. At the building block level, aldehydes emerged as the dominant contributors to antibacterial activity, with extended aromatic and heteroaromatic systems enhancing potency. Amines

played a more secondary role, although hydrophobic and flexible substituents generally contributed positively to activity.

Cytotoxicity screening against HEK293T cells revealed a broad distribution of viability across the library, with a clear dependence on the Cp core and ligand environment. While many compounds exhibiting strong antibacterial activity also displayed cytotoxicity, a subset retained antibacterial activity while maintaining mammalian cell viability, indicating a selectivity window within the library. These findings emphasise the importance of balancing hydrophobicity and structural features to optimise both potency and selectivity.

From this dataset, 19 compounds were selected for dose-response validation, leading to the identification of four candidates with low-micromolar antibacterial activity against *S. aureus*. Among these, **Ir9**, **Ir14**, **Ir15**, and **Ir16** emerged as the most promising compounds, following resynthesis and purification. However, **Ir9** exhibited poor solubility in MH and DMEM, whereas **Ir16** could not be successfully purified. Consequently, subsequent hit-validation studies were conducted using **Ir14** and **Ir15**. Notably, the comparison between crude and purified samples highlighted the importance of downstream validation, as exemplified by **Ir14**, where apparent activity in crude mixtures could not be fully attributed to the isolated complex. This observation emphasises that direct-to-biology screening, while powerful, must be complemented by hit validation with the purified compounds to accurately determine biological activity.

Ir15 demonstrated consistent antibacterial activity across a panel of Gram-positive pathogens, including MRSA, *S. epidermidis*, and enterococcal species, with MIC values in the low-micromolar range. Importantly, **Ir15** displayed only moderate cytotoxicity and low haemolytic activity, resulting in a favourable therapeutic index of (8—31). The compound exhibited only limited activity against Gram-negative bacteria. However, this activity was significantly enhanced in the presence of a sublethal concentration of polymyxin B nonapeptide, indicating that outer membrane permeability is a key barrier to activity rather than an absence of intrinsic antibacterial potency.

Mechanistic investigations provide initial insight into the mode of action of **Ir15**. Bacterial cytological profiling of *B. subtilis* with PrpsD-*gfp* promoter reveals that the compound induces mild membrane stress, as evidenced by subtle membrane aberrations observed with Nile red staining and membrane depolarisation assays without causing large pore formation or complete membrane disruption. This is further supported by the delocalisation of MinD, consistent with loss of membrane potential. Therefore, **Ir15** appears to interfere with membrane function in a subtler manner, potentially affecting ion

homeostasis, proton-motive force, and membrane-associated cellular processes. Such disruption could have broad downstream effects on bacterial physiology, including defects in the respiratory chain, cell division and protein translation machinery.

In parallel, alterations in nucleoid morphology were observed after 60 minutes of incubation, suggesting an additional intracellular effect. However, DNA-binding studies, including MIC shift and ethidium bromide displacement assays, did not support direct DNA intercalation as the primary mechanism. Furthermore, reactive oxygen species scavenger assays indicated that oxidative stress is unlikely to be involved in antibacterial activity. Taken together, these initial results suggest a mode of action involving membrane depolarisation and downstream intracellular effects, rather than a single specific molecular target.

Stability studies revealed that **Ir15** remains stable in DMSO and DMSO:H_2O but undergoes gradual degradation in aqueous media. LC-MS stability analysis revealed that this occurs through chloride dissociation and aquation. Nevertheless, sufficient stability is retained over the timescale of biological assays to enable reproducible antibacterial activity. The observed stabilising effect of chloride-rich environments, such as PBS, further highlights the importance of solution conditions in modulating the behaviour of these complexes. Although aqueous lability represents a potential limitation for further development, it may also contribute to biological activity by enabling conversion of the parent complex into a more reactive aquated species under physiological conditions. While aquation was not directly observed under the LC-MS conditions used in this study, the lower chloride concentration in intracellular environments may favour chloride dissociation, generating a biologically active species within bacterial cells. Therefore, the antibacterial activity of **Ir15** may not arise solely from the intact parent complex but may instead reflect a dynamic equilibrium between chlorido and aquated forms. Further studies will be required to determine whether aquation is necessary for activity or contributes to off-target reactivity and reduced stability.

Screening of the **IrCp1** combinatorial library identified several compounds capable of inhibiting the growth of *A. fumigatus* and revealed clear structure-activity relationships at the building-block level. Relatively higher antifungal potency was observed among the compounds containing quinoline-derived aldehydes and aromatic amines, highlighting the importance of these motifs for biological activity. However, dose-response studies of purified compounds demonstrated only modest potency against *C.albicans* and revealed low selectivity due to cytotoxicity against the mammalian cell line (HEK293T). In contrast,

three of the four compounds (**IrCp1L7**, **IrCp1B7**, and **IrCp1B8**) displayed improved activity against *A. fumigatus*, suggesting species-dependent susceptibility and indicating that filamentous fungi may be a more relevant target for this scaffold. Despite the promising activity observed in the primary screen, none of the compounds exhibited sufficient potency and selectivity to justify further progression. Nevertheless, the identification of quinoline-containing building blocks as key contributors to antifungal activity provides a foundation for the rational design of next-generation iridium complexes with improved selectivity towards fungi over mammalian cells.

Overall, this study demonstrates that combinatorial organometallic chemistry, combined with D2B screening, represents a powerful strategy for antibiotic discovery. By enabling rapid access to large, diverse libraries, this approach facilitates the identification of active, selective compounds within large chemical space that would be difficult to explore with conventional synthetic methods. Future work should focus on further optimisation of the lead scaffold to improve antibacterial potency, selectivity, and aqueous stability. To further investigate the role of chlorido ligand lability in antibacterial activity, future analogues could be prepared in which the chlorido ligand is replaced with a less labile ligand, such as pyridine. Comparing the antibacterial activity, stability, and speciation of these analogues with those of the parent chlorido complex would help determine whether chloride dissociation and subsequent aquation are beneficial for activity or mainly contribute to instability and off-target reactivity. Additionally, as antibacterial activity against Gram-negative bacteria was enhanced in the presence of the outer membrane permeabiliser PMBN, the lack of activity against Gram-negative bacteria is likely due to limited cellular uptake rather than an absence of intrinsic antibacterial activity. This limitation could potentially be addressed by incorporating cationic substituents to promote interactions with the negatively charged outer membrane and facilitate bacterial uptake. Alternatively, a Trojan horse strategy could be employed by conjugating the scaffold to a siderophore, thereby exploiting bacterial iron acquisition pathways to enhance intracellular delivery. In addition, more detailed mechanistic studies will be required to fully elucidate the molecular targets and pathways involved in the antibacterial mode of action. Although no evidence of large membrane pores was observed, membrane depolarisation measurements and MinD localisation assays indicated that the compound strongly perturbs membrane polarity and membrane-associated cellular processes. Future studies should therefore investigate whether these effects are directly linked to disruption of membrane organisation, dissipation of the

proton-motive force, or interference with proteins that depend on the membrane potential and spatial regulation for their correct localisation and function.

Expanding this combinatorial platform to other metal centres and ligand classes may further broaden the accessible chemical space and accelerate the discovery of next-generation antimicrobial agents.

Chapter 4: Additional Research Contributions and Supervised Research Projects

In this chapter, a summary of collaborative projects and supervised bachelor's and master's thesis projects will be provided.

4.1 Expanding Iridium Chemical Space for Antibiotic Discovery through High-Throughput Click Chemistry in a Direct-to-Biology Approach

4.1.1 Introduction

Since its discovery in 2001 by Sharpless and coworkers, copper(I)-catalysed azide-alkyne cycloaddition (CuAAC) has emerged as one of the most widely utilised reactions in modern synthetic chemistry.[375–377] The resulting 1,2,3-triazole scaffold is not found in nature and possesses appealing physicochemical properties, including high stability, a strong dipole moment, and hydrogen-bond accepting ability.[377] In addition to its broad utility in medicinal chemistry[378], the presence of nitrogen enables the triazole ring to coordinate to metal centres.[379,380] The versatility of click chemistry enables systematic tuning of the ligand's electronic and steric properties, facilitating the generation of structurally diverse compound libraries with a broad range of biological activities and potencies. The incorporation of an additional coordination site, such as a pyridine group, enables the formation of a triazole in a bidentate ligand and binding to metal centres through five- or six-membered rings.[380] The coordination behaviour can be altered by changing the position of substitution on the triazole ring, which gives ligands with different steric and electronic properties. Coordination most commonly occurs via the more electron-rich N3 atom, whereas binding via N2 is less common and may lead to less stable complexes.[381] Triazole derivatives can also coordinate to metals as N-heterocyclic carbenes rather than through the ring nitrogen atoms.[382]

Metal complexes with bidentate pyridyl-triazole ligands were widely investigated for their biological potency. The Metzler-Nolte and Bandow groups have modified sulfonamide-based ligands through click chemistry and subsequently synthesised $[Ru^{II}(CO)_2Cl_2]$ and $[Re^{I}(CO)_5X]$ complexes. The synthesised complexes exhibited moderate activity against a panel of *S. aureus* strains, with MIC values ranging from 16 to 256 µg/mL. Notably, the metallated analogues exhibited higher antibacterial activity than sulfamethoxazole and showed no growth inhibition up to 512 µg/mL.[383] Subsequently, as mentioned before, the Thomas and Elliot groups established tri-homoleptic osmium complexes with photo-active antibacterial activity.[208] Friaes and coworkers demonstrated antibacterial activity

of manganese(I) tricarbonyl complexes with 1,2,3-triazole ligands with Clotrimazole as an axial ligand against Gram-negative bacteria.[152]

Although CuAAc was widely employed to generate ligand libraries, and their metal complexes were subsequently evaluated as potential antibacterials, the approach relies on the formation of organic azides via a batch reaction between sodium azide and alkyl bromides. These reactions involve toxic sodium azide, may pose an explosion risk, often employ undesirable solvents, and can generate substantial quantities of impurities.[384,385]

To overcome these limitations, Meng and coworkers established sulfur(VI) fluoride exchange (SuFEx) chemistry to generate azides from any primary amine under ambient conditions.[386]

Recently, our group employed this approach to generate a combinatorial library of 192 bidentate pyridyl-1,2,3- triazole ligands, which were subsequently used to prepare 672 metal complexes. The crude complexes were initially screened against *S. aureus* (12.5 μM and 50 μM) and *E. coli* (50 μM), and cytotoxicity was assessed in HEK293T cells at 50 μM. Together with subsequent dose-response antibacterial assays, this demonstrated that these complexes exhibited metal scaffold-dependent biological potency. For the IrCN complex library, although 71 out of 96 complexes showed MIC values of 12.5 μM or lower, 97.7% of the library reduced the viability of HEK293T cells to below 50%. This indicated that, while this compound library has high potency against bacteria, its toxicity is largely unselective. In contrast, for the $Re(CO)_3$ complexes, more balanced selectivity was observed: while only 37 out of 96 compounds exhibited MIC values equal to or lower than 12.5 μM, only 26% of the complexes reduced HEK293T cell viability to below 50%. For the $Mn(CO)_3$ and RuCy libraries, most compounds did not inhibit bacterial growth. From the initial screening, six compounds were selected for hit validation studies. While these complexes exhibited MIC values between 1.56 μM and 12.5 μM in crude screening against *S. aureus*, the MIC values substantially decreased (at the lowest, 2-fold; at the highest, 16-fold), down to 0.20 μM for **IrCN(M12Y1)**. Notably, the lead compounds exhibited high antibacterial potency against Enterococcus (*E. faecium* and *E. faecalis*) strains. The cytotoxicity of the pure compounds was evaluated against hRBC and HEK293T cells. It was demonstrated that although 4 out of 6 complexes exhibited slight hemolytic activity (HC_{10} values between 36 and 87 μM), the HC_{10} values were at least 46-fold higher than the antibacterial concentration window. Additionally, the increased potency upon purification was also observed in HEK293T cell toxicity. The compounds exhibited lower CC_{50} values than anticipated during the initial cytotoxicity assessment,

with the exception of **IrCN(M8Y4)**, which showed 27 ± 6 % viability at 50 μM and a later CC_{50} of 38.5 ± 5.5 μM. However, despite the increased cytotoxicity, most of the purified complexes exhibited favourable therapeutic indices. **IrCN(M8Y4)** showed the highest TI value, ranging from 49 to 99.

Overall, these findings demonstrated that SuFEx chemistry, combined with a Direct-to-Biology (D2B) approach, enables rapid exploration of large, previously underexplored chemical spaces to identify potential metal-based antibacterial scaffolds.

Together with the success of the combinatorial IrCp Schiff-base library that we expanded to 1440 complexes with modification of the Cp moiety (described in **Chapter 3**), we further investigated the high-throughput SuFEx chemistry with different Cp moieties (**Cp2**–**Cp4)**, and studied their preliminary biological characterisation.

4.1.2 Results and Discussion

4.1.2.1 Preparation of pyridine-triazole ligand libraries

The combinatorial library was generated by Dr. David R. Husbands.The pyridine-triazole ligands were generated via *in situ* azidation of primary amines, followed by CuAAC click reactions with 2-alkynylpyridines.[386] Initially, the FSO_2N_3 reagent was prepared from 1-(fluorosulfonyl)-2,3-dimethyl-1H-imidazol-3-ium trifluoromethanesulfonate and sodium azide as the source of azide through nucleophilic substitution at the electrophilic sulfur(VI) centre of a fluorosulfuryl imidazolium precursor. Upon the attack of the azide anion, a transient hypervalent sulfur intermediate is formed, and subsequently the imidazolium group leaves to afford the product. After the product concentration was determined by ^{19}F NMR spectra, it was reacted with the corresponding amine in a basic biphasic mixture. Previously, it was reported that the diazotransfer reaction step is an equilibrium between two azide species, and that a basic aqueous environment shifts the equilibrium towards the hydrolysis of FSO_2N_3.[386] Mechanistic studies using isotopically labelled substrates and azidating reagents demonstrated that the amine nitrogen is retained in the final azide, while the two additional nitrogen atoms are derived from the diazotransfer reagent. The reaction proceeds through nucleophilic attack of the amine on the terminal nitrogen of the sulfonyl azide, followed by formation of a triazene-type intermediate and subsequent fragmentation to afford the azide.[387] Upon the *in situ* formation of the azide, it was reacted with an alkyne derivative in the presence of sodium ascorbate, as a reducing reagent, and tris(2-benzimidazolylmethyl)amine $(BimH)_3$, as a stabiliser of the Cu catalyst. In our hands, $(BimH)_3$ gave a better yield than the previously reported ligand. Additionally, the phosphate buffer used under the reported conditions

was unnecessary, and catalyst/ligand loadings as low as 2.5 mol% were sufficient for the reaction. An Opentrons liquid-handling robot was utilised to generate a library of 96 triazole-4-pyridine (**Tz-4-P**) (**Figure 92**) with 4 pyridine alkynes and 24 primary amines (**Figure 92**), and 96 triazole-4-methylpyridine (**Tz-4-MP**) (**Figure 92**) with 12 alkyne and 8 picolylamines (**Figure 92**).

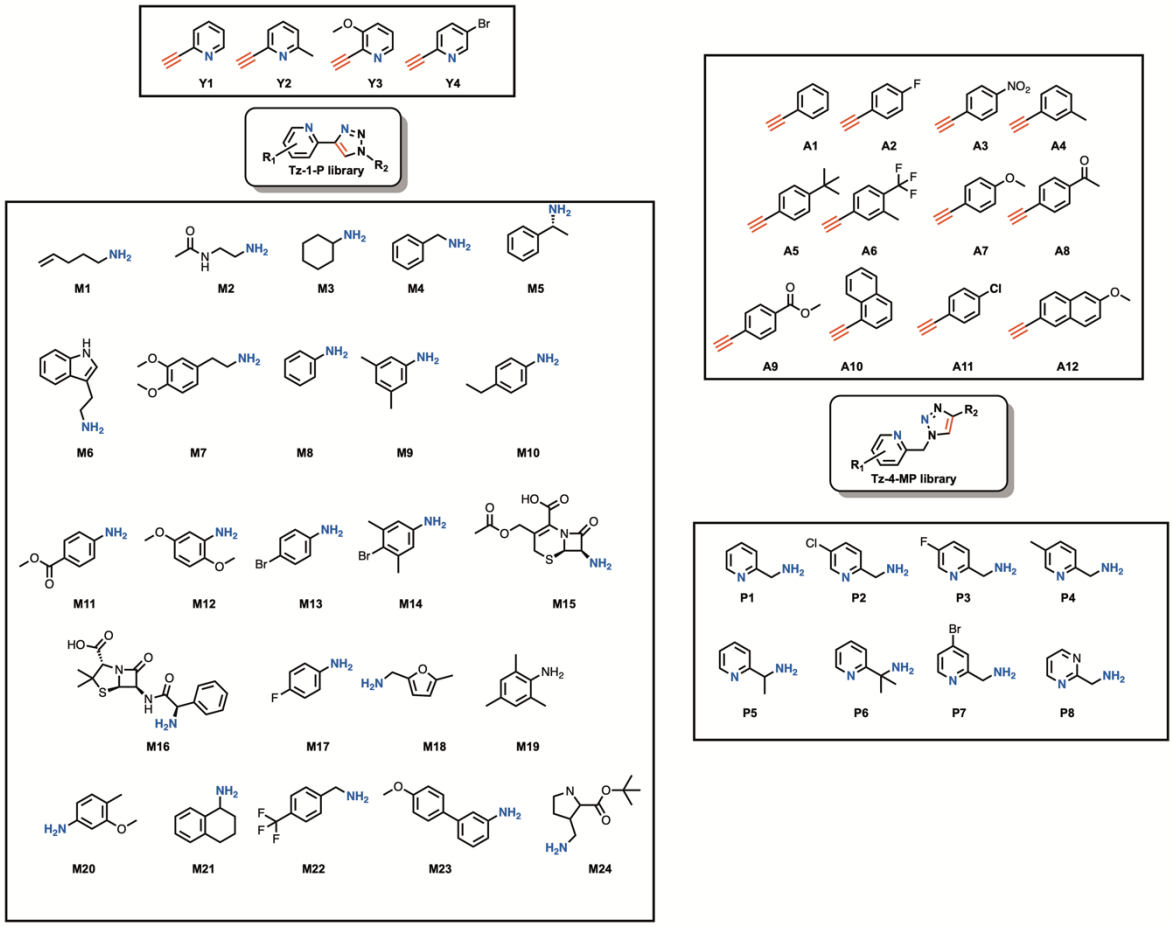


Figure 92. Building blocks used to generate a library of 96 **Tz-1-P** ligands and a library of 96 **Tz-4-MP** ligands.

4.1.2.2 LC-MS characterisation of ligand library

The identity and purity of the crude reaction mixtures were assessed by LC-MS. Samples were prepared at concentrations of 50–100 µM in a 60:40 (v/v) acetonitrile/water mixture and analysed using the described 7 min LC-MS method (**Table 34**). Briefly, LC-MS data were processed via a semi-automated workflow that converted .raw files to .mzML and subsequently to .csv format.[340] Target masses were extracted using custom Python scripts, and the corresponding UV signals at 254 nm were integrated to determine relative peak areas.

The conversion rates of **Tz-1-P** ligands varied (**Figure 93**), with an average of 75 ± 16% and a median of 80%. It was influenced more strongly by the amine component than by the pyridine alkyne component. The four pyridine alkyne ligands exhibited comparable average conversions; **Y3** (methoxy) showed the highest average, at 77 ± 16%.

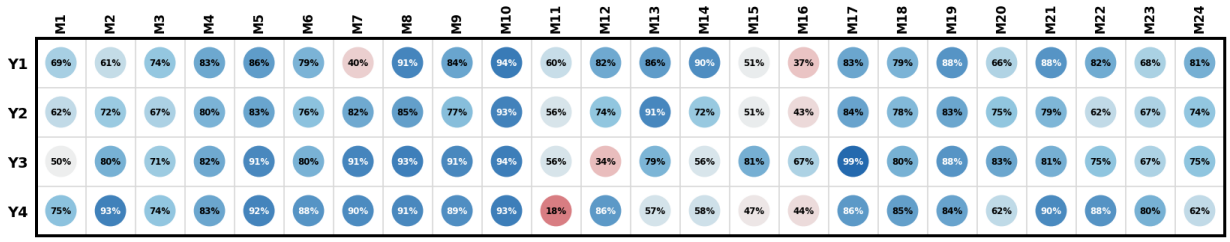


Figure 93. The conversion rates for the library of 96 **Tz-1-P** ligands. Compound peaks were automatically identified based on the target ion mass, and the corresponding UV signals were integrated using custom Python scripts. The colour scale represents the percentage values shown in each well, with darker blue indicating higher values, pale colours indicating intermediate values, and darker red indicating lower values.

Among the amine building blocks, **M10** (propyl) showed the highest average conversion, 94 ± 1 %, and a median conversion of 94%. Additionally, **M8** (aniline), **M17** (fluoro), **M5** (α-methyl), and **M19** (trimethyl) showed average conversions of 90 ± 4%, 88 ± 7%, 88 ± 4%, and 86 ± 3%, respectively. It demonstrates that relatively simple aromatic amines and amines with hydrophobic alkyl groups or halogen substituents, such as **M10** (propyl), **M17** (fluoro), and **M19** (trimethyl), are favourable in the **Tz-1-P** ligand synthesis. On the other hand, lower conversion rates were generally observed for more hydrophilic and sterically hindered amine ligands. For example, **M11** (methyl ester) and **M16** (ampicillin) showed average conversions of 48 ± 20% and 48 ± 13%, respectively. The lower conversion of **M11** (methyl ester) may be attributed to the electron-withdrawing ester substituent, which can reduce the nucleophilicity of the amine and therefore reduce the efficiency of azide formation.

The **Tz-4-MP** (**Figure 94**) exhibited a slightly higher average conversion, 78 ± 12% and a median of 79%. Among the picolylamines building blocks, **P6** (*gem*-dimethyl) showed the highest average conversion, 89 ± 6%. Lower conversions were observed for **P4** (methyl, 65 ± 10%) and **P8** (67 ± 13%). For the alkyne building blocks, the highest conversions were observed for **A6** (trifluoromethyl), 86 ± 7%, **A1** (phenylacetylene), 86 ± 8%, **A2** (fluoro), 85 ± 7%, and **A4** (methyl), 85 ± 6%. These results revealed that simple aryl alkynes and alkynes with small hydrophobic or halogenated substituents exhibit higher conversion rates. Since both electron-withdrawing substituents, such as **A6** (trifluoromethyl) and **A2** (fluoro), and electron-donating substituents, such as **A4**

(methyl), exhibited high conversions, the electronic nature of the alkyne substituent does not appear to be the prominent factor controlling the ligand formation. At 12.5 μM, the SAR became more apparent.

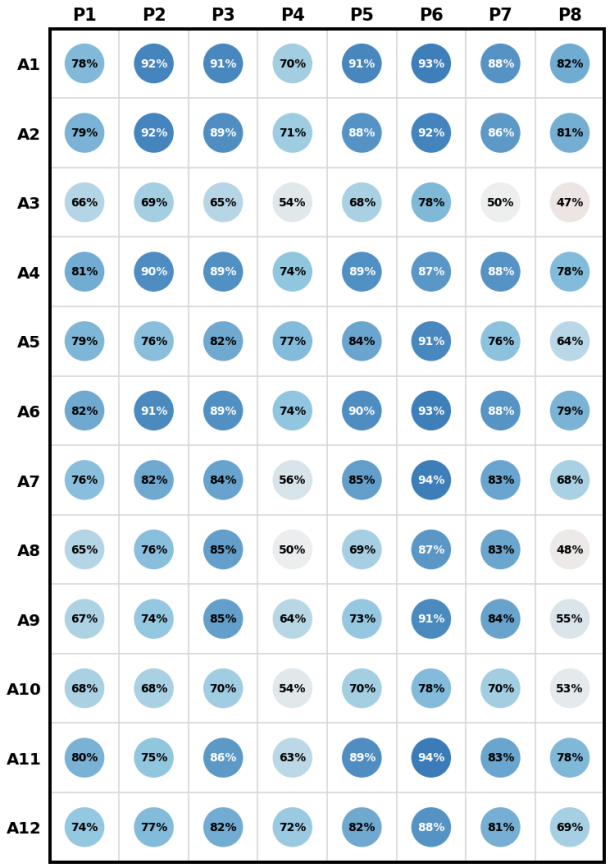


Figure 94. The conversion rates for the library of 96 **Tz-4-MP** ligands. Compound peaks were automatically identified based on the target ion mass, and the corresponding UV signals were integrated using custom Python scripts. The colour scale represents the percentage values shown in each well, with darker blue indicating higher values, pale colours indicating intermediate values, and darker red indicating lower values.

Taken together, both libraries were generated with promising conversion rates, which appear to be governed not by a simple electronic trend but by a combination of steric effects, hydrophobicity and substituent position.

4.1.2.3 Combinatorial synthesis of iridium(III) Cp library

Upon confirmation of the formation of the ligand libraries, iridium (III) cyclopentadienyl (Cp*) complexes were synthesised. Given that the antibacterial potency of iridium Cp* complexes has been demonstrated in the literature[278,292,297,299] and, more recently, in our group, we explored this chemical space with the same ligand system[327] and a Schiff-base ligand system[388] (described in **Chapter 3**); this platform was selected as a promising avenue for further exploration. Following the successful synthesis of the **Cp1**

library, we expanded the chemical space in the recent study to include **Cp2**, **Cp3**, and **Cp4**. A protocol was developed using an Opentrons OT-2 liquid-handling robot to dispense the stock solutions into the corresponding wells of 96-well plates. The reaction plates were allowed to stand overnight at ambient conditions, yielding a combinatorial library of 576 **Tz-1-P** and **Tz-4-MP Cp2, Cp3** and **Cp4** complexes. Notably, iridium(III) cyclopentadienyl complexes bearing biphenyl moieties (**Cp2**) were first reported by the Sadler group with potent anticancer activity[337], and have previously been reported as effective antibacterial agents.[278] The substituents for **Cp2**, **Cp3** and **Cp4** were selected to increase lipophilicity, which is known to enhance membrane permeability and cellular uptake.[338] The syntheses of Cp ligands were broadly discussed in **Chapter 3**.

4.1.2.4 LC-MS characterisation of iridium(III) combinatorial library

The average conversion of the library varied moderately with the Cp moiety, with an apparent Cp-dependent pattern (**Figure 95** and **Figure 98** For the **Tz-1-P** complex library, **Cp3** exhibited the highest average conversion (61 ± 12%), with a median of 65%, suggesting that this scaffold efficiently formed **Tz-1-P** complexes. A comparable pattern was also demonstrated in the Schiff-base ligand system. **Cp2** also showed promising conversion (57 ± 11%), with a median conversion of 60%, indicating that the biphenyl-substituted Cp scaffold remains favourable for complex formation in this ligand system. By contrast, **Cp4** gave the lowest average conversion, 50 ± 9%, with a median conversion of 51%. Interestingly, this trend differs from that observed in the Schiff-base library, where **Cp2** showed the lowest, and **Cp4** showed a moderate conversion. Therefore, **Cp2** does not appear to be intrinsically unfavourable for iridium complex formation; rather, it depends strongly on the ligand framework and reaction pathway.

For the **Tz-4-MP** complex library (**Figure 98**), a similar Cp-dependent pattern was revealed (**Figure 98**). **Cp3** exhibited the highest average conversion 55 ± 19%, with a median of 59%, followed closely by **Cp2** (54 ± 14%), with a median of 56%. In contrast, **Cp4** gave the lowest average conversion (47 ± 19%), with a median of 47%. This suggests that **Cp2** and **Cp3** are similarly favourable for the formation of **Tz-4-MP** complexes, whereas the cyclohexyl-substituted **Cp4** scaffold is less favourable under these reaction conditions.

Overall, these findings demonstrate that the influence of the Cp scaffold on complex formation is strongly dependent on the ligand framework and reaction pathway, rather than being dictated solely by the intrinsic steric or electronic properties of the Cp substituent.

For the **Tz-1-P** library (**Figure 95**,**Figure 96Figure 97**), within the pyridine alkyne ligands, the average conversions were relatively similar across the series. **Y1** and **Y2** exhibited the highest average conversions, both at 57 ± 12%, followed closely by **Y4**, 55 ± 12%, and **Y3**, 55 ± 9%. It was found that the pyridine alkyne components did not significantly influence the complexation rate.

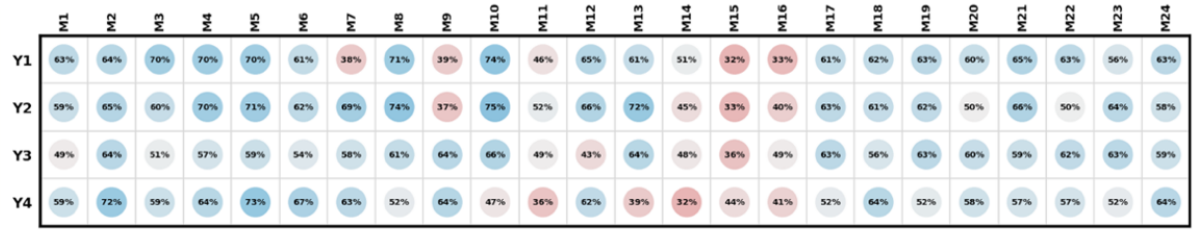


Figure 95. The conversion rate of the library of 288 **Tz-1-P**-based iridium **Cp2** complexes. It was determined from LC-MS peak area percentages at 254 nm. Compound peaks were automatically identified based on the target ion mass, and the corresponding UV signals were integrated using custom Python scripts. Reported conversions represent the combined signal of the parent ion (M^+) and the MeCN adduct $(M + MeCN)^{2+}$. The colour scale represents the percentage values shown in each well, with darker blue indicating higher values, pale colours indicating intermediate values, and darker red indicating lower values.

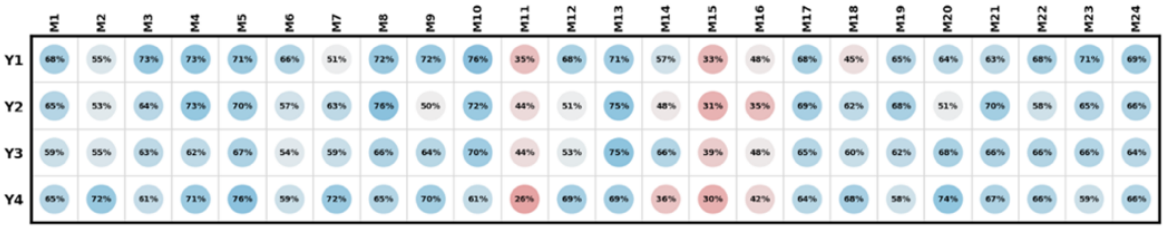


Figure 96. The conversion rate of the library of 288 **Tz-1-P**-based iridium **Cp3** complexes. It was determined from LC-MS peak area percentages at 254 nm. Compound peaks were automatically identified based on the target ion mass, and the corresponding UV signals were integrated using custom Python scripts. Reported conversions represent the combined signal of the parent ion (M^+) and the MeCN adduct $(M + MeCN)^{2+}$. The colour scale represents the percentage values shown in each well, with darker blue indicating higher values, pale colours indicating intermediate values, and darker red indicating lower values.

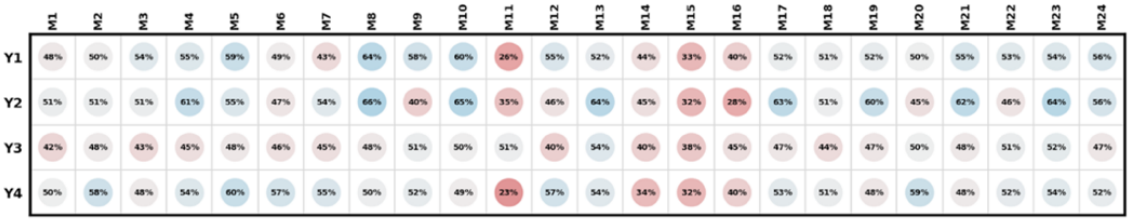


Figure 97. The conversion rate of the library of 288 **Tz-1-P**-based iridium **Cp4** complexes. It was determined from LC-MS peak area percentages at 254 nm. Compound peaks were automatically identified based on the target ion mass, and the corresponding UV signals were integrated using custom Python scripts. Reported conversions represent the combined signal of the parent ion

(M^+) and the MeCN adduct $(M + MeCN)^{2+}$. The colour scale represents the percentage values shown in each well, with darker blue indicating higher values, pale colours indicating intermediate values, and darker red indicating lower values.

Within the level of the amine building blocks, an apparent pattern in complex formation was observed. The highest average conversions were observed with **M5** (α-methyl), 65 ± 9%, **M10** (propyl), 64 ± 11%, **M8** (aniline), 64 ± 9%, M4 (benzyl), 63 ± 9%, and **M13** (*p*-bromo, 63 ± 11%. These results suggest that relatively simple aromatic or benzylic amines are more favourable for the formation of **Tz-1-P** iridium complexes. In contrast, lower average conversions were observed for more structurally complex or hydrophilic amines, such as **M15** (7-aminocephalosporanic acid), 34 ± 4%; **M11** (methyl ester), 39 ± 10%; and **M16** (ampicillin), 41 ± 6%. Additionally, the reasonable conversions observed for aliphatic amines such as **M1**, **M2**, and **M3** suggest that electronic factors are not a prominent determinant of complex formation, but rather steric effects. For the **Tz-4-MP** complex library (**Figure 98**), both the picolylamines and alkyne building blocks influenced the conversion rate of iridium complexes.

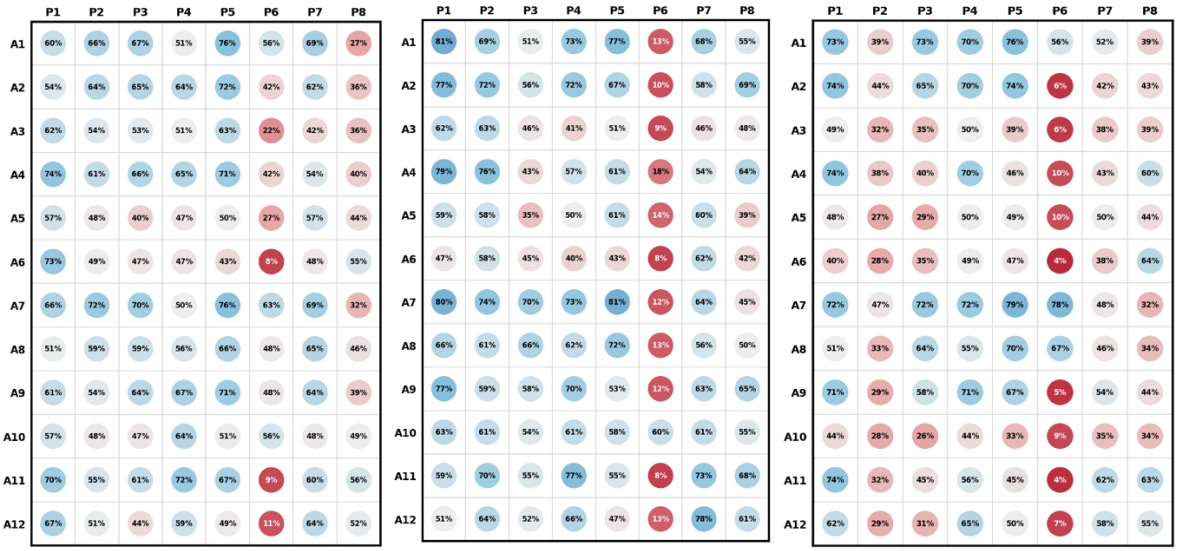


Figure 98. The conversion rate of the library of 288 **Tz-4-MP**-based iridium complexes. It was determined from LC-MS peak area percentages at 254 nm (right: **Cp2**; middle: **Cp3**; left: **Cp4**). Compound peaks were automatically identified based on the target ion mass, and the corresponding UV signals were integrated using custom Python scripts. Reported conversions represent the combined signal of the parent ion (M^+) and the MeCN adduct $(M + MeCN)^{2+}$. The colour scale represents the percentage values shown in each well, with darker blue indicating higher values, pale colours indicating intermediate values, and darker red indicating lower values.

At the level of the picolylamines building blocks, **P1** (benzyl) exhibited the highest average conversion, 64 ± 11%, followed by **P4** (methyl), 60 ± 11%, **P5** (α-methyl), 60 ± 13%), and **P7** (bromo), 56 ± 10%. In contrast, **P6** (*gem*-dimethyl) showed a markedly

lower average conversion (25 ± 22%), despite giving high conversion in the ligand formation. It was attributed to the steric hindrance of *gem*-dimethyl groups, which appears to outweigh any potential benefits of the Thorpe-Ingold effect[389] and instead hinders the effective coordination to the iridium centre. Within the alkyne building blocks, complex formation rate varied. The highest average conversions were observed for **A7** (methoxy), 62 ± 18%; **A1** (phenylacetylene), 60 ± 17%; and **A2** (fluoro), 57 ± 19%. In contrast, lower average conversions were observed for **A6** (trifluoromethyl), 43 ± 17%, **A3** (nitro) 43 ± 15%, and **A5** (tert-butyl, 44 ± 14%).

Taken together, **Tz-1-P** and **Tz-4-MP** iridium complex libraries were generated at variable conversions, demonstrating that complex formation is influenced by the combined effects of the Cp scaffold, ligand framework, and the structure of the building block.

4.1.2.5 Single-dose response biological activity of the combinatorial complex library

We initially screened the crude library of 768 **IrCp Tz-1-P** and **Tz-4-MP** complexes against *S. aureus* at 12.5 and 50 μM, and against *E. coli* at 50 μM. To provide a clearer profile of the structure-activity relationship, **IrCp1** complexes were also included. These were selected as representative Gram-positive and Gram-negative bacterial strains, respectively, to assess antibacterial activity across different cellular membrane structures. Notably, none of the compounds in the library exhibited activity against *E. coli* at 50 μM, consistent with previously reported trends indicating that most metal-based and organic compounds[343] are unable to penetrate Gram-negative bacteria.[92] For the **Tz-1-P** library, within the **Cp1** scaffold, we observe that only a minority of compounds (18.8%) were active at 50 μM, while only 2.1% were active at 12.5 μM (**Figure 99**). In contrast, all compounds completely inhibited *S. aureus* growth at 50 μM, and the majority (84.4%) of the **Cp2** library exhibited antibacterial potency at 12.5 μM. The superior antibacterial activity of biphenyl-substituted (**Cp2)** Cp iridium(III) complexes has also been observed in our Schiff-base system as discussed in **Chapter 3**. The observed difference in activity may be attributed to the increased lipophilicity and rigidity of the biphenyl moiety, which could facilitate improved uptake through the bacterial membrane.[338] Nearly all compounds of the **Cp3** library completely inhibited the growth of *S. aureus* at 50 μM; however, only 47% exhibited complete growth inhibition at 12.5 μM (**Figure 99**). Among **Cp4** complexes, nearly all compounds were active at 50 μM,

and 75% inhibited bacterial growth at 12.5 μM (**Figure 99**). At the level of individual building blocks, the amine component exhibited a substantial effect, and several amines were consistently associated with strong growth inhibition across multiple Cp cores. At 50 μM, all the complexes with **M16** (ampicillin) and **M23** (methoxy biphenyl) inhibited bacterial growth. Additionally, **M14** (bromo-dimethylaniline) and **M19** (trimethylaniline) also exhibited high potency, with 87.5% of complexes inhibiting bacterial growth. **M9** (dimethylaniline), **M11** (methyl aminobenzoate), **M17** (fluoroaniline), **M21** (aminotetralin), **M22** (trifluoromethylbenzyl), and **M24** (Boc-protected aminomethylpiperidine) each exhibited promising potency, with 81.3% of complexes inhibiting bacterial growth. **M2** (acetamidoethyl) was the least active at 50 μM, with 62.5% activity. At 12.5 μM, the SAR pattern became more apparent. **M23** (methoxy-biphenyl aniline) remained the most favourable amine component, with 81.3% activity. This suggests that the extended biphenyl system, combined with a methoxy substituent, increased π interactions and hydrophobic character, thereby providing an optimal balance of lipophilicity for bacterial uptake. **M13** (bromoaniline) was the second-most-active building block, with 75% activity. Several substituted aromatic amine building blocks showed similarly strong activity, including **M9** (dimethylaniline), **M10** (ethylaniline), **M14** (bromo-dimethylaniline), **M19** (trimethylaniline), **M21** (aminotetralin), and **M22** (trifluoromethylbenzylamine), each exhibiting 68.8% activity. These results indicate that the combination of an aromatic ring with alkyl and/or halogen substituents is a favourable scaffold for promising antibacterial activity. However, alkyne-pyridine building blocks moderately tuned the antibacterial activity. The effect of the alkyne-pyridine building block was more apparent at 12.5 μM; **Y3** (*o*-methoxy) and **Y4** (*p*-bromo) were identified as the most potent building blocks, with activities of 64.6% and 59.4%, respectively. However, **Y1** exhibited relatively lower potency, 47.2%. It was revealed that substituted pyridine ring-bearing alkyne scaffolds were favoured over unsubstituted ones.

For the **Tz-4-MP** library, 94.3% of complexes inhibited bacterial growth at 50 μM. At 12.5 μM, this ratio decreased to 39.3%. The picolylamines showed a modest influence on antibacterial activity, with **P1** exhibiting the highest activity (66.7%). The general trend showed that modification of the pyridine ring decreased antibacterial potency. At the alkyne-building-block level, there was a more pronounced SAR pattern than with picolylamines. All of the complexes bearing the **A10** (naphthyl) moiety inhibited bacterial growth, and the majority (81.3%) of the complexes with **A5** (*p*-tert-butyl) exhibited high potency. Additionally, the unsubstituted alkyne **A1** exhibited a 37.5% activity rate, whereas methyl incorporation at the meta position increased it to 50%. It is likely that the

increased antibacterial activity is correlated with increased lipophilicity. On the other hand, upon modification of the pyridine ring with an electron-withdrawing group, despite the high conversion rates, the activity substantially decreased; e.g. **A3** (*p*-nitro) exhibited 6.3% activity, **A9** (*p*-methyl ester) exhibited 9.4% activity, and **A2** (*p*-fluoro) exhibited 21.9% activity. This substantial drop in antibacterial activity can be attributed to two main factors. First, the electron-withdrawing or electronegative (F) groups reduce the electron density of the aromatic ring, which may weaken favourable π interactions with biological targets.[390] In contrast, the **A10** (naphthyl)-bearing complexes showed complete growth inhibition, suggesting that an extended, electron-rich aromatic surface is highly favourable for antibacterial activity. Second, strongly electron-withdrawing substituents also increase the polarity and hydrogen-bond-accepting character of the aryl fragment, which may disrupt the lipophilicity balance required for efficient bacterial interaction or accumulation.[391]

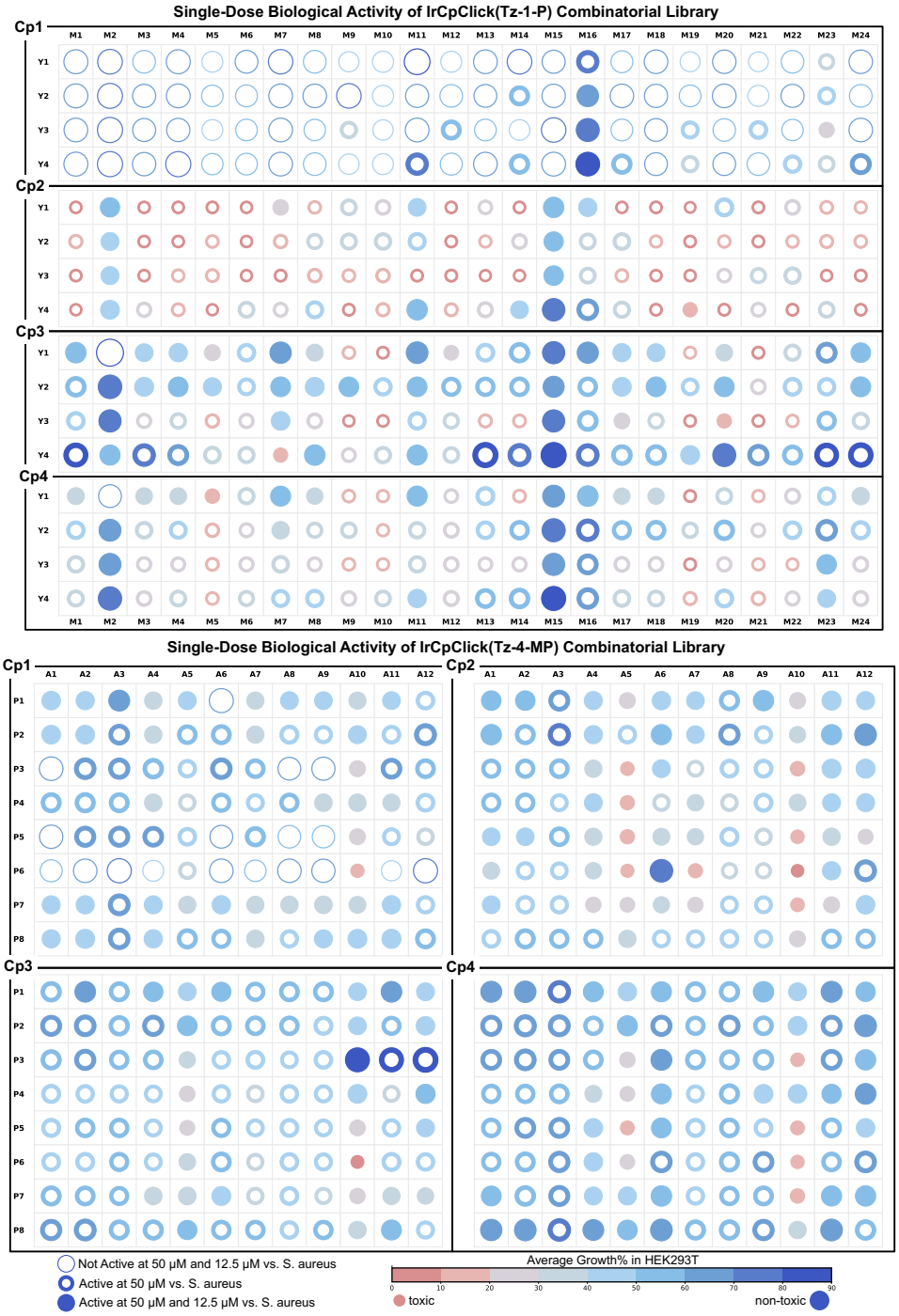


Figure 99. Single-dose biological characterisation of the combinatorial library against *S. aureus* CCUG 62707. The top part shows **Tz-1-P** complexes classified by their Cp scaffold. The bottom part shows **Tz-4-MP** complexes classified by their Cp scaffold. Filled circles indicate measurable antibacterial activity at both 50 µM and 12.5 µM. Small white circles denote compounds that are active only at 50 µM, while empty circles indicate no detectable activity against *S. aureus* under the tested conditions. The colour intensity corresponds to the single-dose cytotoxic activity against HEK293T cells. The circle size is proportional to the viability of HEK293T cells.

Overall, antibacterial activity in the iridium complex libraries was strongly influenced by both the Cp scaffold and the other building blocks. **Cp2** and **Cp4** were the most

favourable Cp scaffolds, while **Cp1** exhibited reduced potency. Across both ligand systems, activity was enhanced by hydrophobic or extended aromatic substituents, **M23**, **A10**, and **A5**, whereas polar or strongly electron-withdrawing groups reduced activity. These observations are consistent with the hypothesis that increased hydrophobicity and structural rigidity facilitate more effective interaction with bacterial membranes or intracellular targets.[346,347]

Following the single-dose evaluation of antibacterial activity, the cytotoxicity of the crude compounds was assessed against HEK293T cells at a concentration of 50 μM. For the **Cp1** moiety, viability ranged from 11.8–80.8% (mean 54.4%, median 55.5%), with 60% of compounds achieving ≥50% viability, indicating a shift toward higher viability (**Figure 99**). In contrast, the **Cp2** library exhibited lower viability overall, ranging from 2.4–73.7% (mean 31.5%, median 33.6%), with only 16.7% of compounds achieving ≥50% viability (**Figure 99**). Notably, both **Cp3** an**d Cp4** libraries exhibited relatively intermediate toxicity, with mean viabilities of 47.3% and 45.0%, respectively, and a median of 48.2% for both. The viability ranges were wide for both Cp scaffolds: 6.1–90.1% and 9.3–83.3%, respectively. These data revealed a clear dependence of cytotoxicity on the Cp scaffold, with **Cp1** affording the highest overall viability and **Cp2** the lowest, while **Cp3** and **Cp4** display intermediate cytotoxicity profiles. Although **Cp1** was demonstrated as the least toxicity-associated Cp scaffold, it also demonstrated the weakest antibacterial potency within the series. On the other hand, the high antibacterial potency of Cp2 was shown to be unselective, as it also exhibited high cytotoxicity. **Cp3** showed an intermediate cytotoxic profile and moderate antibacterial activity.

For the **Tz-1-P** library, a similar trend was also observed. Amine building blocks associated with high antibacterial activity, such as **M23** (methoxy-biphenyl aniline), **M13** (bromoaniline), **M14** (bromo-dimethylaniline), and **M19** (trimethylaniline), generally corresponded to lower average HEK293T viabilities in the range of 24–43% (**Figure 99**). In contrast, amine building blocks with low antibacterial potency, such as **M2** (acetamidoethylamine) and **M15** (7-aminocephalosporanic acid), showed substantially higher average viabilities of 65.9% and 68.2%, respectively, indicating lower cytotoxicity (**Figure 99**). It was revealed that the same hydrophobic or aromatic features that promote antibacterial activity also tend to increase mammalian cell toxicity. Additionally, it was revealed that the alkyne scaffold had a weaker influence on selectivity than the amine scaffold, likely attributable to differences in variety.

In the **Tz-4-MP** library, piconylamine building blocks had a modest influence on cytotoxicity. **P1** showed the highest antibacterial activity at 12.5 µM and maintained a moderate average HEK293T viability of 50.4%, whereas **P7** (*m*-bromo) also exhibited strong antibacterial activity but a higher toxicity profile, with a viability of 42.5%. In contrast, **P2** (*p*-chloro) and **P8** (diazinylmethyl) showed only moderate antibacterial activity (35.4 %) but higher average viabilities of 54.1% and 52.4%, respectively. On the other hand, the alkyne building block exerted a stronger effect on cytotoxicity. **A10** (naphthyl) and **A5** (*p*-tert-butyl), which were associated with the highest antibacterial activity, exhibited moderate cytotoxicity, with viabilities of 31.1% and 35.4%, respectively. In contrast, alkyne building blocks associated with lower antibacterial activity, such as **A3** (*p*-nitro), **A8** (*p*-acetyl), **A9** (*p*-methyl ester), and **A2** (*p*-fluoro), showed higher average viabilities ranging from 48.8–58.1%, indicating reduced cytotoxicity. It was revealed that sterically hindered, hydrophobic, and electron-dense aromatic rings enhanced biological potency, with low-to-medium selectivity. Together, it was revealed that the Cp core had the most prominent effect on the biological activity of iridium complexes, while specific ligand systems fine-tuned the antibacterial potency and cytotoxicity. It enabled us to identify a small but promising set of ligand systems.

Subsequently, the biological activity of the free ligands was assessed to determine if the potency of the complexes originated from the ligand or the complex itself. Overall, the 192 **Tz-1-P** and **Tz-1-MP** ligands showed minimal toxicity toward HEK293T cells. Only one ligand, **M12Y3**, reduced cell viability below 50%, giving an average viability of 45 %, indicating that the ligand library did not exhibit cytotoxic properties in mammalian cells. Additionally, the antibacterial potency of the ligands was also evaluated. Growth inhibition observed only for **M7Y1** at 50 µM, **M16Y2** and **M16Y3** at 12.5 µM, and **M23Y3** at 50 µM. The activity of the **M16**-containing ligands was expected, as this building block incorporates the broad-spectrum antibiotic ampicillin. In addition, the relatively low conversions observed for these ligand-forming reactions suggest that the activity may be associated with the ampicillin-containing triazole products or residual ampicillin scaffold. Follow-up dose-response experiments against *S. aureus* showed MIC values of 50 µM for **M7Y1** and **M23Y3**, whereas the ampicillin-derived triazoles were more active, with MIC values of 12.5 µM and 3.13 µM.

Overall, these findings indicate that the observed antibacterial potency is primarily attributable to complex formation rather than to the intrinsic activity of the free ligands.

4.1.2.6 Batch synthesis of preliminary hit complexes

Upon the completion of the single-dose biological characterisation, preliminary hit complexes were selected for hit validation studies. Due to limitations in chemical availability and the time available for follow-up experiments, three favourable complexes (**Figure 100**) were selected for further investigation.

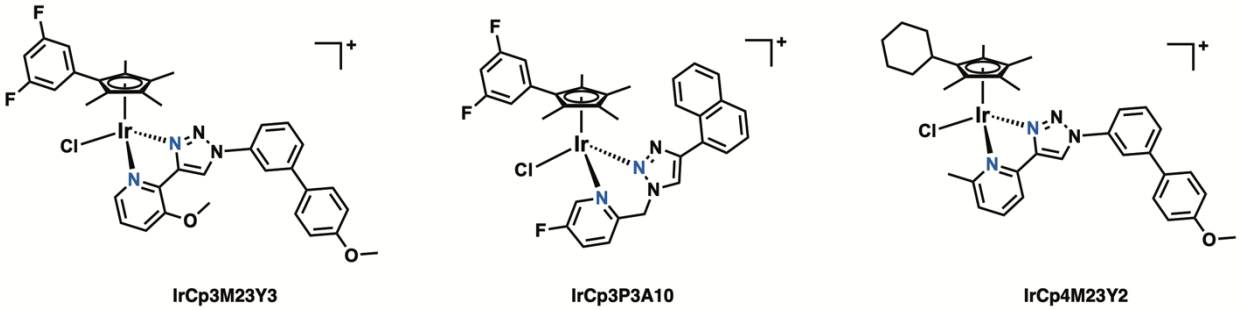


Figure 100. Selected lead complexes for batch synthesis and hit validation. Counterion is chloride.

Initially, the ligands for the selected complexes were synthesised. **FSO_2N_3** was synthesised from the trifluoromethanesulfonate reagent and sodium azide. Upon stirring of the reaction mixture at 0°C in a biphasic mixture of MTBE, MeCN, and water for 15 mins, it was left to settle at room temperature for 15 minutes. Subsequently, the organic phase was decanted and diluted with 3 mL DMF. During the synthesis of this reagent for a combinatorial ligand library, this step was carried out in DMSO to improve biocompatibility. Then, the concentration of the freshly generated azide reagent was determined by quantitative ^{19}F NMR using *p*-toluenesulfonyl fluoride as an internal standard. During the quantification analyses, a 10 s relaxation time was used to minimise saturation effects, allow longitudinal relaxation of the nucleus between scans, and ensure accurate signal integration.[392] Then, the prepared reagent was mixed with the corresponding amine in DMF, in the presence of $KHCO_3$, and stirred overnight at room temperature. The generated *in situ* azide was reacted with the corresponding alkyne in the presence of sodium ascorbate, $(BimH)_3$, and $CuSO_4$ to obtain the final triazole ligand. Reaction progress was monitored with LC-MS, and the corresponding masses were the primary peak in the chromatogram. The target compounds were obtained by column chromatography and isolated in yields of 57%, 52%, and 70% for **M23Y3**, **M23Y2**, and **P3A10**, respectively. Compound purity and identity were confirmed by LC-MS, NMR characterisation, and high-resolution mass spectrometry (HRMS). Subsequently, the iridium dimer (0.5 equiv.) was combined with the corresponding synthesised ligand (1 equiv.) in DCM/MeOH (1:1) and stirred at room temperature overnight. Reaction

progress was monitored by LC-MS. The target compounds were obtained by column chromatography. However, **IrCp3M23Y3** could not be purified; a small aromatic impurity was observed in the ^{1}H NMR spectrum. Compound purity and identity for **IrCp4M23Y2** and **IrCp3P3A10** were confirmed by LC-MS, NMR characterisation, and high-resolution mass spectrometry (HRMS).

4.1.2.7 Antibacterial activity of lead complexes: Hit validation

To confirm the antibacterial activity observed in the crude mixtures, the purified complexes **IrCp3P3A10** and **IrCp4M23Y2** and were re-screened against *S. aureus* (**Table 23**). Although **IrCp3P3A10** showed growth inhibition at 12.5 µM in the initial single-dose experiments, it exhibited an MIC value of 100 µM (**Table 23**) in the dose-response hit validation assays. This discrepancy raised questions about its stability in DMSO and MH media. To investigate this, LC-MS analysis was performed on both the solid sample and a freshly prepared DMSO stock solution. While analysis of the solid sample showed a single major peak corresponding to the intact complex, the DMSO solution revealed that the complex was completely degraded to the ligand.

Table 23. Antibacterial activity and cytotoxicity of IrCp4M23Y2 against Gram-positive panel, *S. aureus* CCUG 62707, MRSA (JE2), and *B. subtilis* MW168, and HEK293T. The positive control was the antibiotic Vancomycin (VCM); MIC values were reported in µM. Experiments were repeated as three biological replicates and three technical replicates. n.d : no data.

	MIC (µM)			**CC_{50} (µM)**
	S.aureus	MRSA	*B. subtilis*	HEK293T
IrCp4M23Y2	12.5	12.5	12.5	54.4 ± 4.1
Control	0.84	0.84	0.21	*n.d.*

IrCp4M23Y2 exhibited consistent antibacterial potency, with a MIC of 12.5 µM against the Gram-positive panel, comparable to the single-dose antibacterial evaluation against *S. aureus*. On the other hand, while it exhibited 83% viability in HEK293T cells at a treatment concentration of 50 µM, the CC_{50} value of the purified compound was 54.4 ± 4.1. This discrepancy may be attributed to poor conversion in the crude reaction mixture, where the presence of unreacted ligand and/or less cytotoxic side products effectively diluted the active cytotoxic complex. However, the conversion rate was 55%, and single-dose cytotoxicity testing of the ligand showed 108% cell viability. This difference likely arises from a combination of less cytotoxic products and human pipetting error, as single-dose assays are more prone to such errors than dose-response assays. It highlights the cruciality of follow-up dose-response assays after the initial single-dose screening.

4.1.2.8 Summary, conclusion and outlook

In this chapter, the combinatorial approach to explore novel chemical space as potential metalantibiotics was expanded to include iridium(III) Cp complexes with a pyridine-triazole ligand system. The overall aim was to expand the range of accessible IrCp-based antibacterial scaffolds by combining automated synthesis, LC-MS-based reaction monitoring, and single-dose biological screening. Through this approach, structurally diverse ligand and complex libraries were prepared and evaluated, enabling the establishment of preliminary structure-activity relationships and the advancement of selected hit compounds for validation.

Initially, pyridine-triazole ligand libraries were prepared via *in situ* diazotransfer followed by CuAAC click chemistry. The use of FSO_2N_3 as the diazotransfer reagent, followed by reaction with substituted pyridine alkynes, provided an efficient and adaptable route to the desired ligand scaffolds. Importantly, the reaction conditions were successfully modified relative to previously reported protocols, with tris(2-benzimidazolylmethyl)amine ($BimH_3$) giving improved performance as a copper-stabilising ligand, while phosphate buffer was found to be unnecessary. These adjustments simplified the reaction conditions and made the methodology more suitable for small-scale library synthesis. LC-MS analysis confirmed that both the **Tz-1-P** and **Tz-4-MP** ligand libraries were generated with generally high conversions. Individual building blocks influenced reaction efficiency. Following confirmation of ligand formation, the corresponding iridium(III) Cp complexes were generated using an Opentrans liquid-handling robot. This enabled the rapid preparation of an expanded library of 576 complexes with **Cp2**, **Cp3**, and **Cp4** moieties. LC-MS characterisation revealed that complex formation was strongly dependent on both the Cp scaffold and the ligand framework.

Single-dose biological screening of the crude iridium complex library revealed a SAR pattern. None of the compounds showed measurable activity against *E. coli* at 50 µM. In contrast, many of the complexes inhibited *S. aureus* growth, particularly those bearing the **Cp2**, **Cp3**, and **Cp4** scaffolds, which primarily influenced antibacterial potency. **Cp1** was the least active scaffold, whereas **Cp2** and **Cp4** were the most favourable, with Cp2 showing particularly strong activity at both 50 µM and 12.5 µM. Cp3 displayed an intermediate activity profile. These results are consistent with the hypothesis that increased hydrophobicity and structural rigidity can enhance bacterial uptake. At the ligand-building-block level, antibacterial activity was enhanced by hydrophobic and

extended aromatic substituents. In the **Tz-1-P** series, **M23**, bearing a methoxy-biphenyl motif, was the most favourable amine component, while several substituted aromatic amines containing alkyl, halogen, or extended aromatic groups also promoted activity. In the **Tz-4-MP** series, the alkyne building block exerted a stronger influence on antibacterial potency than the picolylamine component. Complexes bearing **A10**, containing a naphthyl group, showed complete growth inhibition, while **A5**, containing a *tert*-butyl substituent, was also strongly associated with activity. In contrast, electron-withdrawing or more polar substituents, including nitro, ester, acetyl, and fluoro groups, generally reduced antibacterial activity. Overall, these observations indicate that antibacterial potency in this library is favoured by lipophilic, electron-rich, and extended aromatic groups, which may enhance interactions with bacterial membranes or intracellular targets.

However, it was revealed that these structural features generally improved unselective biological potency. Cytotoxicity screening against HEK293T cells showed a clear Cp-dependent toxicity. **Cp1** complexes were generally the least cytotoxic and the least antibacterial, whereas **Cp2** complexes were the most potent against *S. aureus* but also showed the highest cytotoxicity. **Cp3** and **Cp4** displayed intermediate cytotoxicity profiles. Similar trends were observed at the building-block level, where hydrophobic and aromatic motifs associated with strong antibacterial activity often corresponded to lower HEK293T viability. It highlights a key challenge in the development of this compound class: increasing lipophilicity and aromatic surface area can improve antibacterial potency but may also reduce selectivity by enhancing non-specific interactions with mammalian cells. Therefore, future optimisation should focus not only on improving potency but also on identifying structural features that promote bacterial selectivity over general cytotoxicity.

Screening of the corresponding free ligands provided an important control experiment. The ligand libraries showed minimal cytotoxicity toward HEK293T cells and only limited antibacterial activity, with activity observed for a small number of compounds. The strongest ligand activity was associated with ampicillin-containing derivatives, which was expected due to the intrinsic antibacterial properties of the ampicillin scaffold. Overall, these results confirmed that the antibacterial activity observed in the complex library was primarily attributable to iridium complex formation rather than to the free ligands themselves. Following single-dose screening, selected complexes were synthesised and purified on a larger scale to validate hits. This step was essential, as crude-library

screening provides valuable SAR information but can be influenced by incomplete conversion, side products, residual ligand, and human errors. The validation studies revealed that **IrCp3P3A10**, despite showing promising activity in the crude single-dose screen, had a substantially weaker MIC value of 100 µM when tested as a purified compound. This was attributed to the complex's poor stability in DMSO, which degraded within a few minutes.

In contrast, **IrCp4M23Y2** retained antibacterial activity after purification, showing an MIC value of 12.5 µM against *S. aureus*, MRSA, and *B. subtilis*. This confirmed that the initial screening workflow could identify active compounds, although hit validation was still crucial to confirm the antibacterial activity.

Due to time constraints, only a preliminary study was presented. Future work will focus on dose-response screening of promising compounds from the crude library against a Gram-positive panel and HEK293T cells, followed by hit determination. Upon successful validation of the hit, the mechanism of action of the lead compound will be studied. As revealed in our previous studies[388,393], iridium compounds tend to affect membrane-associated mechanisms in bacteria.

4.2 Combinatorial Synthesis and Direct-to-Biology Antibacterial Evaluation of Ruthenium(II) and Iridium(III) N^O-Schiff-Base Complexes and Their Initial Mode of Action Studies

Stefano Zineddu, Athi Welsh, **Çağrı Özsan**, Anson Kwok-Hei Chau, David R. Husbands, Kiera Robinson, Luigi Messori, Angelo Frei. Combinatorial Synthesis and Direct-to-Biology Antibacterial Evaluation of Ruthenium(II) and Iridium(III) N^O-Schiff-Base Complexes. ChemRxiv.

Recently, we have expanded the chemical space with 176 iridium and ruthenium Schiff-base ligand systems (N^O) complexes and investigated their biological potency. Selected complexes (**Figure 101**), **RuCy-J2**, **RuCy-J3**, and **IrCp-B5** were re-synthesised for subsequent hit validation studies.

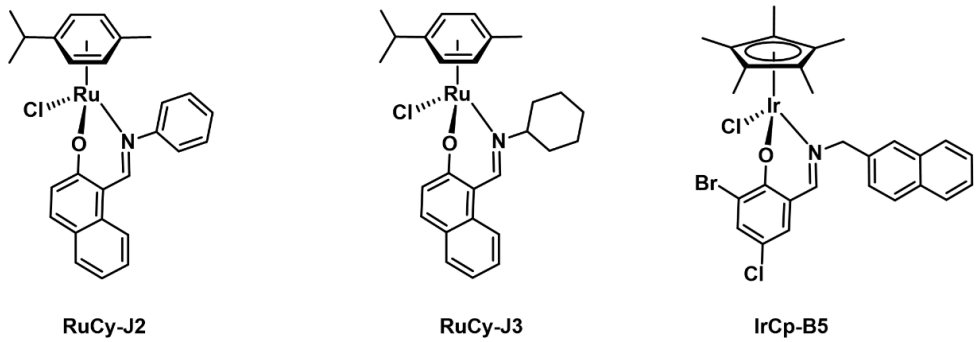


Figure 101. The selected complexes from the library of 176 complexes for hit validation studies.

4.2.1 Biological characterisation of the lead compounds

Initially, we determined the MIC values against a panel of seven Gram-positive bacterial strains. The complexes exhibited potent activity against a variety of tested Gram-positive strains, with MIC values ranging from 1.56 μM to 12.5 μM. The highest potency was demonstrated against *S. aureus*, with **RuCy-J2** and **RuCy-J3** exhibiting a MIC of 1.56 μM, while **IrCp-B5** had a MIC of 3.13 μM. Notably, the activity of complex **RuCy-J2** against both MSSA and MRSA is comparable to that of vancomycin.

Table 24. Minimum Inhibitory Concentration (MIC) and toxicity data for the lead compounds against a selection of bacterial strains. Antibacterial activity is displayed as μM. The positive controls are the antibiotics Vancomycin (VCM) for Gram-positive and polymyxin B (PMB) for Gram-negative. MIC values were given in μM. PMBN: polymyxin B nonapeptide (10 μg / mL); CC_{50} and crude toxicity in HEK293T cells at 50 μM, the error recorded is the standard deviation; HC_{10} – 10% hemolytic concentration in human red blood cells; TI – therapeutic index, determined by dividing the lowest value between CC_{50} and the lowest MIC value for each compound against *S. aureus.* MIC determined with n = 3 across two biological replicates.

	MIC (μM)							Cytotoxicity	
Compound	***Sa***	***Efs***	***Efm***	**MSSA**	**MRSA**	***Bs***	***Ec*+PMBN**	**CC_{50}**	**HC_{10}**
RuCy-J2	1.56	3.13 – 6.25	6.25	1.56	1.56	6.25	>100	25.5 ± 4.0	>200
RuCy-J3	1.56	6.25 – 12.5	12.5	3.13	3.13	6.25	>100	26.0 ± 3.7	>200
IrCp-B5	3.13	6.25 – 12.5	6.25 – 12.5	3.13	3.13	3.13	12.5 – 25	45.4 ± 8.8	>200
Control	0.43	0.43	0.43	0.86	0.86	1.73	0.24		

Against *E. coli*, no activity was detected with purified compounds. However, upon treatment with the membrane-permeabilizing agent polymyxin B nonapeptide (PMBN[245], a moderate antibacterial activity was observed for compound **IrCp-B5** (12.5 – 25 μM). This suggests that the lack of activity against Gram-negative pathogens is likely attributed to poor uptake, rather than intrinsic inactivity.

We determined the 50% cytotoxic concentration (CC_{50}) in HEK293T cells and the hemolytic activity in human red blood cells (hRBC), given as the 10% hemolytic concentration (HC_{10}) for the lead complexes. It was revealed that the potency of the compounds was not selective; it also exhibited cytotoxicity against mammalian cells. Notably, they exhibited therapeutic indices of 15. Moreover, the HC_{10} determination confirmed that the compounds classify as non-hemolytic, as all exhibited HC_{10} values above 200 μM (**Table 24**).

4.2.2 Evaluation of the initial mode of action

Given the favourable biological characteristics of the lead complexes, we decided to conduct preliminary mechanistic studies to elucidate their potential modes of action.

Based on their favourable therapeutic indices, **IrCp-B5** and **RuCy-J3** were selected for further investigation. To gain initial insights into their mode of action, these compounds were subjected to phenotypic profiling using the Gram-positive model organism *B. subtilis*. To this end, we first confirmed the MIC against *B. subtilis* 168CA, the background strain of our reporter construct. Both **IrCp-B5** and **RuCy-J3** exhibited comparable

antibacterial activity against *B. subtilis*, with a MIC of 6.25 µM (**Table 24**). Based on the MIC values, we determined the optimal stressor concentration (OSC) for acute shock experiments. The OSC is defined as the concentration that reduces bacterial growth by 50–70% during the mid-exponential phase, thereby applying sufficient stress to induce a clear phenotype without causing excessive cell death or lysis that could obscure the compounds' primary effects.[255] The growth curve analysis (**Figure 102**) identified an OSC of 1.56 µM for both hit compounds.

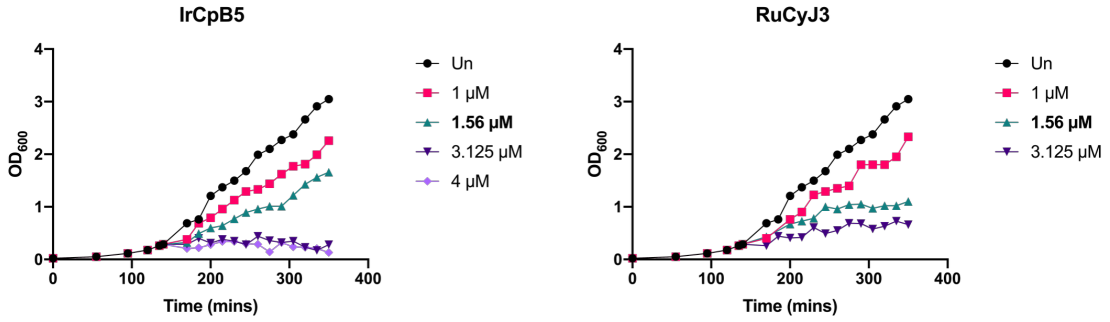


Figure 102. Determination of optimal stressor concentrations (OSC) (indicated in bold) of IrCpB5 and RuCyJ3.

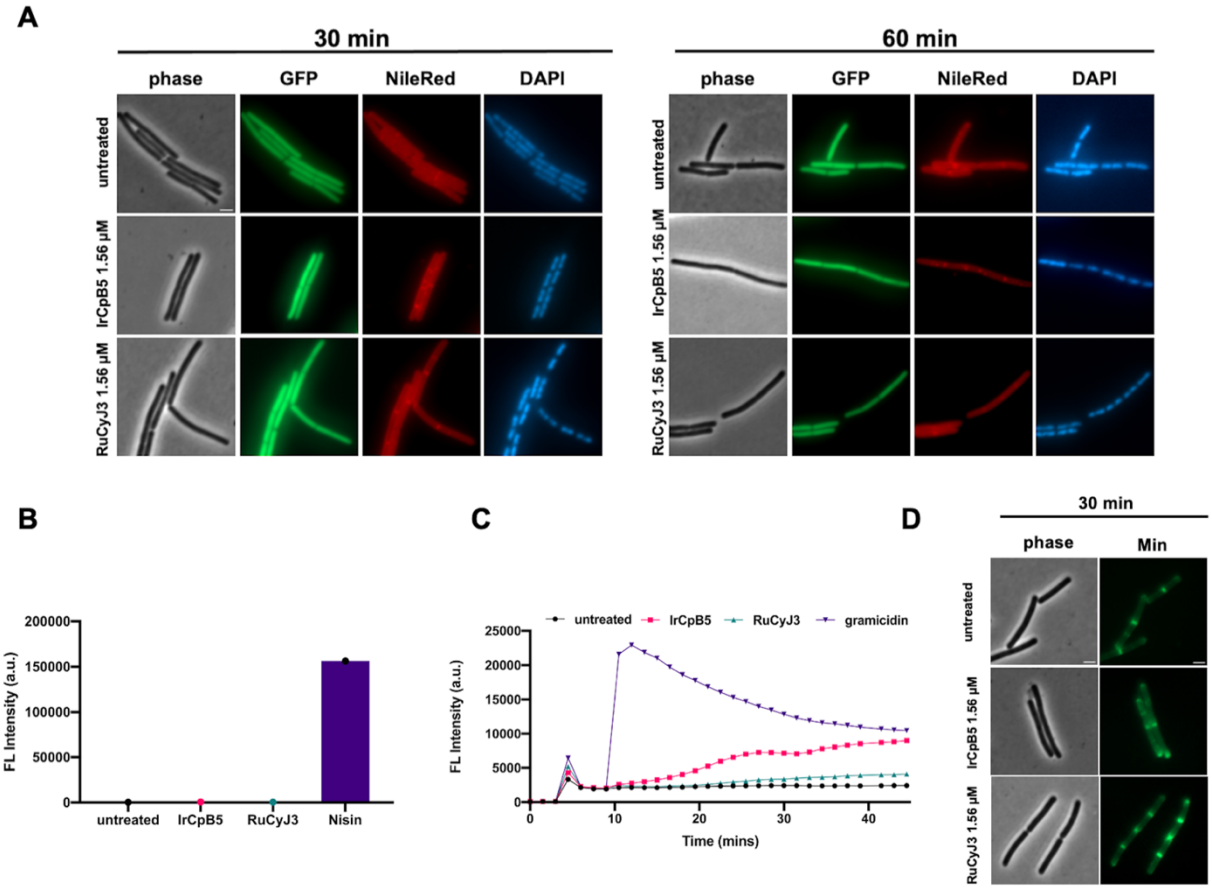


Figure 103. Initial mode of action of IrCp-B5 and RuCy-J3, hit compounds. (**A**) Bacterial cytological profiling of *B. subtilis* bSS82, constitutively expressing GFP from the PrpsD promoter, stained with Nile red (membrane) and DAPI (DNA) after 30 and 60 minutes of incubation. (**B**) Propidium Iodide staining of *B. subtilis* 168CA (pore formation assay). 1.6 µg/mL nisin was used as positive control. (**C**) $DiSC_3(5)$ assay in B. subtilis 168CA (membrane depolarization assay). 1 µg/mL gramicidin was used as a positive control. (**D**) Localisation of MinD-GFP in *B. subtilis* TB35 (Pxyl-gfp-minD). Localisation of MinD depends on the membrane potential. 10 µg/mL gramicidin was used as a positive control. All assays were performed after treatment with 1.56 µM of hit compounds. Scale bar 2 µm.

To get an overview of the cellular effects of the compounds, we employed bacterial cytological profiling (BCP).[394] To this end, we used a strain that expresses green fluorescent protein (GFP) intracellularly from the strong, constitutive *PrpsD* promoter (*B. subtilis* bSS82), and stained it with the membrane dye Nile red and the DNA dye DAPI. When combined with phase-contrast microscopy, this setup enables simultaneous assessment of cell morphology, cell lysis, pore formation, membrane morphology, and nucleoid morphology in a single assay.[255]

Upon treatment with **IrCp-B5**, no apparent differences in overall cell morphology (phase contrast) or membrane integrity (GFP) were observed (**Figure 103A**). Notably, Nile red foci formation was observed, indicating mild membrane stress. These results suggest that although membrane integrity remained largely unaffected, the antibacterial activity of **IrCp-B5** likely involves membrane-related mechanisms. In contrast, **RuCy-J3** did not induce membrane stress.

A substantial effect of **RuCy-J3** on the bacterial nucleoid (DAPI) was observed, with visible changes in nucleoid morphology after 30 min (**Figure 103A**). In particular, after 60 minutes of treatment, the phenotype revealed compromised DNA integrity, potentially indicating DNA fragmentation or other structural changes. In contrast, **IrCp-B5** caused only a mild effect on nucleoid morphology after 60 min.

The distinct phenotypes observed for **RuCy-J3** and **IrCp-B5** suggest different antibacterial modes of action. **RuCy-J3** induced rapid and pronounced alterations in nucleoid morphology, which became more apparent after 60 min of treatment, indicating that its primary target is likely associated with DNA integrity or DNA-associated cellular processes.[352] Additionally, inductively coupled plasma optical emission spectroscopy (ICP-OES) was used to assess the cellular uptake and distribution of the complexes **IrCp-B5** and **RuCy-J3**. Overall, 3.1x more **RuCy-J3** was found in the combined bacterial lysate and cell debris. **IrCp-B5** was found to preferentially associate with the bacterial cell membrane (72%) rather than the cytosol (28%). In contrast, **RuCy-J3** showed

substantial accumulation within the cytosolic fraction (70%) relative to the membrane (30%) fractions (**Figure 104**). Together, these results support the conclusion that the two complexes exhibit distinct cellular localisation patterns, consistent with their different phenotypes.

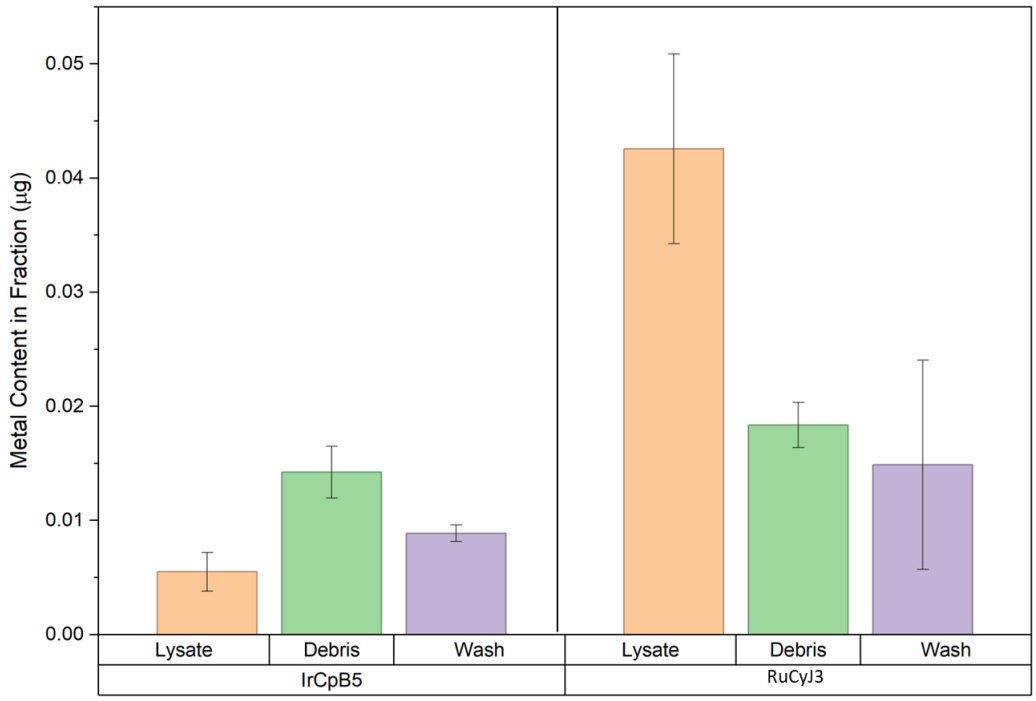


Figure 104. ICP-OES analysis of cellular uptake and distribution of complexes IrCp-B5 and RuCy-J3. Results are represented as the mass of specific metal present within cellular fractions after 60 mins of treatment with complexes of interest. Lysate, Debris and Wash represent the cell cytosol, cell membrane and the first wash with Tris/EDTA buffer, respectively. Error bars represent the standard deviation of 3 replicates.

4.2.2.1 Cell envelope stress

Nile red staining suggested that **IrCp-B5** may exert partial membrane-associated activity. To further investigate this, we examined whether it facilitates the passage of molecules smaller than GFP across the cell membrane.[255] As a first step, we investigated the uptake of the membrane-impermeable, red-fluorescent dye propidium iodide (PI). Neither **RuCy-J3** nor **IrCp-B5** resulted in increased PI uptake, confirming that they do not form large pores (**Figure 103B**).

In contrast, mild membrane depolarization was observed for **IrCp-B5** using the potentiometric fluorescent dye 3,3′-dipropylthiadicarbocyanine iodide ($DiSC_3(5)$) (**Figure 103C**), indicating that **IrCp-B5** induces ion translocation and disrupts membrane

polarisation. This finding was independently supported by the localisation pattern of the cell division regulatory protein MinD, which normally localises at mid-cell and cell poles in healthy cells, but redistributes into membrane-associated clusters upon loss of membrane potential **Figure 103D**).[263] Consistently, **IrCp-B5** induced mild delocalisation of MinD after 30 min of treatment. Together, these results demonstrate that **IrCp-B5** induces membrane stress by disrupting membrane polarisation without causing large-pore formation or detectable structural damage. In contrast, **RuCy-J3** did not produce a positive $DiSC_3(5)$ response, suggesting that membrane depolarization is not a primary mechanism of its antibacterial activity. Combined with the pronounced nucleoid alterations observed upon **RuCy-J3** treatment, these findings support distinct modes of action for the two compounds, with **IrCp-B5** primarily affecting membrane-associated processes and **RuCy-J3** likely targeting intracellular DNA-related pathways.

4.2.2.2 DNA binding properties

DAPI staining revealed that **RuCy-J3** induces alterations in bacterial nucleoid structure after 30 minutes and **IrCp-B5** after 60 minutes of treatment (**Figure 103A**). To further investigate this phenotype, we sought to assess the DNA-binding properties of the compounds. To this end, we performed a MIC shift assay in the presence of different concentrations of calf thymus DNA. While the positive control, Actinomycin D, an antibiotic known to interact with GC-rich DNA sequences[353], exhibits decreasing antibacterial activity with increasing DNA concentration, the MIC of both **RuCy-J3** and **IrCp-B5** remain unchanged (**Table 25**).

Table 25. MIC values of IrCp-B5, RuCy-J3, Actinomycin D and Vancomycin (VCM) in *S. aureus* in the presence of 0, 50, 125, 250, and 500 µg/mL Calf-Thymus (CT) DNA. MIC values were given in µM.

Compound	0	50	125	250	500
IrCp-B5	3.13—6.25	3.13	3.13	3.13	3.13
RuCy-J3	3.13	3.13	3.13	3.13	3.13
Actinomycin D	< 0.05	1.56	6.25	12.5	50
VCM	0.42	0.42	0.42	0.42	0.42

To specifically evaluate a possible DNA intercalation mechanism, an ethidium bromide (EtBr) fluorescence displacement assay was performed. In this assay, EtBr intercalates into DNA, resulting in a strong fluorescence signal. Upon addition of a competing intercalating agent, EtBr is displaced from the DNA duplex, leading to a decrease in

fluorescence intensity.[354,355] Upon treatment of the calf thymus DNA-EtBr complex with serial dilutions of the complexes **RuCy-J3** and **IrCp-B5** (up to 200 μM), no significant interaction was observed at concentrations corresponding to the MIC. Noticeable displacement of EtBr (*ca.* 30%) was only observed at the highest concentration tested (200 μM) (**Figure 105**), indicating that DNA intercalation is unlikely to occur at biologically relevant concentrations. These findings suggest that the DNA effects observed in the BCP are likely secondary and not due to direct metal-complex interactions with DNA.

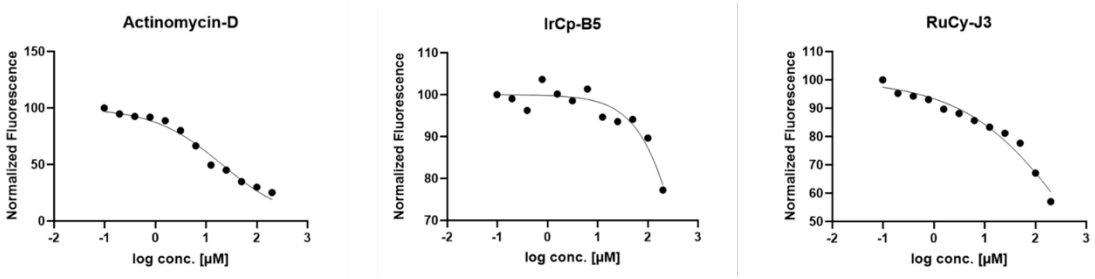


Figure 105. Fluorescence competitive EtBr displacement assay for Actinomycin-D, IrCp-B5, **RuCy-J3**.

4.2.2.3 Reactive oxygen species

The ability of the compounds to produce reactive oxygen species (ROS) was also investigated. It was demonstrated that tiron had no effect on complex activity, suggesting that the compound does not induce superoxide formation (**Table 26**). In contrast, the presence of thiourea significantly enhanced compound activity, reducing the median MIC of **RuCy-J3** by a factor of eight from 3.12 μM to 0.39 μM and even more so, the MIC of **IrCp-B5** was reduced 32-fold from 3.12 μM to 0.098 μM (**Table 26**). These results suggest that not only are ROS species not involved in the antibacterial activity of these compounds, but there may also be a synergistic interaction between the compounds and thiourea.

Table 26. Median MIC values of hit compounds in *B. subtilis* in MH, 10 mM tiron, 40 mM thiourea, and 10 mM tiron and 40 mM Thiourea. H_2O_2 was used as a positive control for thiourea. MIC values are given in μM for IrCp-B5 and RuCy-J3, % for H_2O_2, and ug/mL for control antibiotics.

Compound	**Condition**			
	MH	**Thiourea**	**Tiron**	**T+T**
IrCp-B5	3.12	0.098	3.12	0.78
RuCy-J3	3.12	0.39	3.12	0.39
H_2O_2 (%)	0.0188-0.0092	>0.6	0.0188-0.0092	>0.6-0.3
Chloramphenicol (ug/mL)	0.625	0.625	0.625-0.312	0.625

Next, we investigated whether thiourea synergistically modulates the activity of the lead complexes against Gram-positive *S. aureus* and *B. subtilis* using checkerboard assays (**Figure 106A**).[395] The interaction between thiourea and the complexes was evaluated using fractional inhibitory concentration indices (FICI), which were calculated based on MIC values defined as OD_{600} ≤ 0.1 across six replicates. The average FICI across all three complexes in *B. subtilis* is 0.313, consistent with synergistic interactions (FICI < 0.5).[396,397] Additionally, both **RuCy-J3** and **IrCp-B5** showed an FICI of 0.313 against *S. aureus*, demonstrating a synergistic interaction.

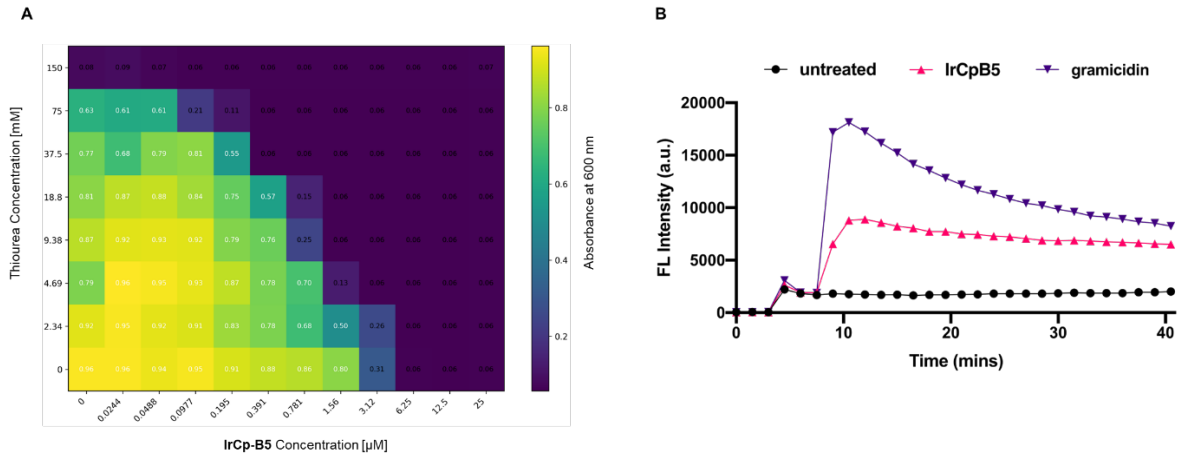


Figure 106. (**A**) An exemplary checkerboard assay evaluating the synergistic behaviour of IrCp-B5 against B. subtilis in the presence of different concentrations of the ROS scavenger thiourea. Biological activity is displayed as OD_{600}, with values <0.1 indicating no significant bacterial growth. (**B**) $DiSC_3(5)$ assay in *B. subtilis* 168CA (membrane depolarisation assay) in the presence of 40 mM thiourea. 1 µg/mL gramicidin was used as a positive control.

Motivated by these findings, we repeated the membrane depolarization $DiSC_3(5)$ assays in the presence of 40 mM thiourea using the compound that showed the strongest effect, i.e., **IrCp-B5** (**Figure 106B**). An altered membrane depolarization effect, in which depolarization occurred abruptly, was observed with **IrCp-B5** in the presence of thiourea.

4.2.3 Summary, conclusion and outlook

In this study, the combinatorial chemistry approach was expanded to N^O Schiff-Base ligand systems of iridium(III) and ruthenium(III) complexes. The library of 176 complexes was generated by Dr. Stefano Zineddu (visiting PhD student in our group). Biological characterisation of the lead complexes demonstrated low micromolar activity against a panel of Gram-positive bacteria, with therapeutic indices of 15. Notably, these compounds did not exhibit significant haemolytic activity against hRBC up to 200 µM

Mechanistic investigations revealed that **RuCy-J3** and **IrCp-B5** possess distinct modes of action. While **IrCp-B5** exerts its activity primarily by disrupting membrane-associated processes, **RuCy-J3** appeared to act through intracellular DNA-related pathways. Additionally, it was demonstrated that the lead compounds act synergistically with thiourea in *S. aureus* and *B. subtilis*. Further studies will be required to identify the role of thiourea in the activity of these compounds. Potentially, **IrCp-B5** acts through bacterial membrane-associated pathways and subsequent downstream effects. On the other hand, preliminary data exhibited that **RuCy-J3** accumulated in the cytosol and potentially has a more specific DNA-related bacterial target.

Further studies will focus on elucidating the exact mode of action of this compound class and determining its specific targets.

4.3 Copper(I) Photosensitisers for Antimicrobial Photodynamic Therapy: from Solution Studies to Silica-Immobilised Composite Materials

This subchapter summarises the author's contribution to the following paper, which is currently under peer review:

Alexander Dukalski,[†,] **Çağrı Özsan**,[†,] Florian Doettinger,[a] Anastasiia Riabchunova, Lukas Geciauskas, Sofia Fulgencio, Stefanie Tschierlei, Michael Karnahl, and Angelo Frei. Copper(I) photosensitisers for antimicrobial photodynamic therapy: from solution studies to silica-immobilised composite materials.

4.3.1 Introduction

Photodynamic therapy (PDT) was discovered serendipitously in 1900 by a medical student, who investigated the toxicity of acridine red on *Paramecium spp*. The results of the experiments were inconsistent; later it was noticed that the results depended on the time of day and sunlight exposure.[398] Subsequently, Tappeiner utilised this approach to treat skin carcinomas and used the term 'photodynamic phenomenon'. Tappeiner and Huber were first to report the photodynamic inactivation of bacteria separately in 1904[399] and 1905.[400]

Anti-cancer PDT was widely investigated in the 20th century, and the first PDT agent, Photofrin, was approved for oesophageal cancer[401] and other medical conditions; Levulan, aminolevulinic acid and its derivatives for actinic keratoses[402]; Visudyne for subfoveal choroidal neovascularisation.[403]

Building on these, antimicrobial photodynamic therapy (aPDT) has emerged as a promising strategy for treating drug-resistant bacterial infections.[400] In this approach, light irradiation activates a photosensitiser (PS), leading to the formation of reactive oxygen species (ROS) with high spatial and temporal control. Although the requirement for light generally limits its application to infections that can be readily irradiated, aPDT offers several advantages over conventional antibacterial therapy. The short-lived and highly reactive species generated during treatment can damage cellular compartments, such as membrane lipids, and biomolecules such as proteins and nucleic acids, which reduces the likelihood of developing resistance by altering a single biological target.[400,404] Consistent with this multifaceted mechanism of action, clinically significant resistance to aPDT has not yet been documented.[405] Additionally, both the PS and the light source can be confined to the affected area when treating localised infections, thereby limiting systemic exposure and reducing the risk of off-target toxicity. As in anticancer photodynamic therapy, metal complexes have been receiving increasing attention as photosensitisers for antimicrobial applications.[406] This arises from their favourable

photophysical properties, including long-lived excited states and, in many cases, high singlet oxygen quantum yields. Additionally, the ligand environments can be readily modified, allowing systematic tuning of their photophysical characteristics and biological activity.[407] Recently, ruthenium[408–418], iridium[282,326,419,420], osmium[208], rhenium[107], platinum[231], iron[421], nickel[422], and metal-based porphyrins[423], were investigated as metal-based PSs.

Copper complexes have also shown promising light-dependent activity against various cancer cell lines[424–427]; however, investigations on their antibacterial activity remain relatively limited. Appleby and coworkers investigated the heteroleptic diimine-diphosphine copper(I) complex with 2,9-dimethyl-1,10-phenanthroline and xant, which represents xantphos, as well as a silica-immobilised form of the complex. Upon irradiation with 405 nm light, the silica-immobilised complex exhibited antibacterial activity against both MRSA and *E. coli*. The immobilised complex exhibited minimal potency in the absence of light, and complete killing was observed after 2 hours of treatment against MRSA and 3 hours against *E. coli*. [428]

Building on this, the antibacterial evaluation of six heteroleptic copper(I) complexes (**Figure 107**) and their silica-immobilised analogues for potential applications in antimicrobial photodynamic therapy has been investigated.

4.3.2 Results and disccussion

In this study, the antibacterial evaluation of six heteroleptic Copper(I) complexes (**Figure 107**) and their silica-immobilised analogues for potential applications in antimicrobial photodynamic therapy has been investigated.

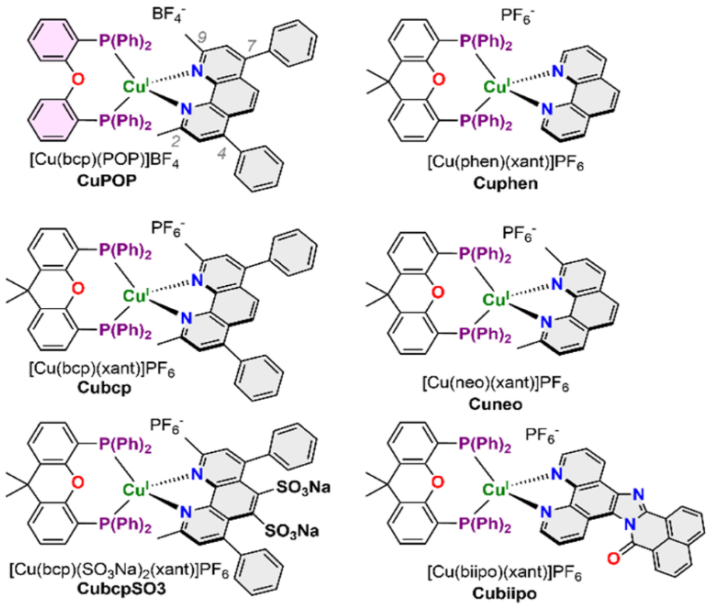


Figure 107. Overview of the investigated Copper(I) complexes and their abbreviations. With phen = 1,10-phenanthroline, neo = neocuproine, bcp = bathocuproine, bcpSO_3 = bathocuproine-5,6-disulfonate disodium salt, biipo = 16H-benzo-[4′,5′]-isoquinolino-[2′,1′,:1,2]-imidazo-[4,5-f]-[1,10]-phenanthrolin-16-one, POP = bis[(2-diphenylphosphino)phenyl] ether, xant = xantphos.

The selected complexes share a common $[Cu(N^N)(P^P)]^+$ design, enabling a targeted variation of the diimine and/or diphosphine environment while maintaining a comparable coordination framework.

4.3.2.1 Biological evaluation of the copper complexes

Upon photophysical characterisation, the antibacterial properties of Copper(I) photosensitisers against *S. aureus* (MRSA) *and E. coli* were evaluated. To assess light-dependent activity, the 96-well plates containing freshly added compound were irradiated using an Atlas Photonics LUMOS BIO irradiator, followed by overnight incubation. Initially, three excitation wavelengths (600, 505 and 405 nm) were screened. No measurable light-enhanced antibacterial effect was observed at 600 and 505 nm,

consistent with the absorption behaviour of these complexes. Therefore, 405 nm irradiation was used for all subsequent experiments. An irradiation time of 10 min was found to be a practical compromise between light dose and assay throughput. No significant antibacterial activity was observed against Gram-negative *E. coli* up to the highest tested concentration (100 µM) under either dark or light conditions (**Table 27**).

Table 27. Minimum inhibitory concentrations (MICs, µM) of the Copper(I) photosensitisers against MRSA and *E. coli* under dark conditions and after 405 nm irradiation (10 min, 250 mW/LED). The phototoxicity index (PTI = MIC_{dark}/MIC_{light}) quantifies the light-driven enhancement of activity. CC_{50}: concentration at which 50% of HEK293T cells are not viable (mean ± standard deviation). HC_{10}: concentration at which 10% haemolysis is observed in human red blood cells.

Complex	MIC (MRSA) (µM)			MIC (*E. coli*) (µM)		CC_{50} (µM)	HC_{10} (µM)
	Dark	Light	PTI	Dark	Light		
CuPOP	>100	25	>4	>100	>100	4 ± 1	>200
Cubcp	>100	>100	1	>100	>100	11 ± 4	>200
$CubcpSO_3$	25—50	6.25	4—8	>100	>100	18 ± 1	78.8 ± 12.0
Cuphen	6.25	3.125	2	>100	>100	1 ± 0.4	>200
Cuneo	6.25	3.125	2	>100	>100	1 ± 0.2	>200
Cubiipo	>100	6.25	>16	>100	>100	11 ± 5	>200

On the other hand, complexes exhibited promising antibacterial activity against MRSA. Under dark conditions, **Cuphen** and **Cuneo** showed significant growth inhibition with a MIC value of 6.25 µM, whereas **$CubcpSO_3$** displayed only moderate activity and **Cubcp**, **Cubiipo** and **CuPOP** were inactive up to 100 µM (**Table 27**). Upon 405 nm irradiation, all complexes except **Cubcp** exhibited enhanced activity, yielding low-micromolar MIC values for **$CubcpSO_3$**, **Cubiipo**, **Cuphen** and **Cuneo**. **Cubiipo** showed the most pronounced light response with a phototoxicity index (PTI = MIC_{dark}/MIC_{light}) >16.

To exclude contributions from potentially uncoordinated ligands, key ligands used in complex synthesis were tested against the same bacteria. No significant antibacterial activity was observed for these ligands up to 100 µM (**Table 28**), demonstrating that the antibacterial effects observed for the copper(I) complexes arise from the coordination compounds rather than from the ligands.

Table 28. MIC values of the ligands of the most promising copper(I) complexes.

Ligand Name	*MRSA*	*E. coli*
POP	>100	>100
Xant	>100	>100
$BcpSO_3$	>100	>100
Biipo	>100	>100

Subsequently, cytotoxicity of the complexes against human embryonic kidney cells (HEK293T) and haemolysis in human red blood cells was assessed. Only **CubcpSO$_3$** showed detectable haemolysis within the tested range, causing 10% haemolysis (HC_{10}) at 79 ± 12μM, whereas all other compounds displayed HC_{10} values >200 μM (**Table 27**). In contrast, all complexes exhibited measurable cytotoxicity towards HEK293T cells, with **Cuphen**, **Cuneo** and **CuPOP** showing CC_{50} values in the low micromolar range (≈ 1-4 μM), whereas **Cubcp, CubcpSO$_3$** and **Cubiipo** displayed higher CC_{50} values (≥11 μM, **Table 27***).*

As the molecular complexes did not exhibit sufficient selectivity for bacteria over human cells, further development of these as soluble antibacterial agents was considered limited. We therefore shifted the application to a heterogeneous, light-activated disinfection platform. Immobilisation of the photosensitisers on silica confines the active compound to a solid surface, reducing direct exposure of mammalian cells to free complexes while enabling local generation of reactive oxygen species upon irradiation. This allows short-lived reactive oxygen species to be generated locally at the material-bacterium interface, where they can oxidatively damage bacterial envelope components, including membrane lipids and cell wall-associated biomolecules. Inspired by the work of Appleby and co-workers, who demonstrated that Copper(I) diimine complexes immobilised on silica can efficiently kill both Gram-positive and Gram-negative bacteria in water under visible light, we explored this heterogeneous format as an alternative application for the Copper(I) photosensitisers.[428,429]

The biological activity of the silica-immobilised Copper(I) complexes (Copper(I)@SiO_2) was evaluated in a dose-dependent manner analogous to the assays conducted for the molecular complexes (**Table 30**). Consistent with the behaviour of the free compounds, no antibacterial activity was detected against *E. coli* up to the highest tested particle concentration, neither in the dark nor upon irradiation.

Table 29. Copper(I) complexes immobilised on SiO_2 and their activity against methicillin-resistant *Staphylococcus aureus* (MRSA). Minimum inhibitory concentration (MIC) values (mg / mL) of Copper(I)@SiO_2 composite materials against MRSA under dark conditions and after 405 nm irradiation (10 min, 250 mW/LED).

Immobilised complex	MRSA (mg / mL)		
	Dark	**Light**	**PTI**
CuPOP@SiO_2	>4.92	2.46	>2
Cubcp@SiO_2	2.46—4.92	1.23—2.46	1—4
CubcpSO3@SiO_2	4.92	0.62—1.23	4—8
Cuphen@SiO_2	0.31—0.62	0.62—1.23	0.25—1
Cuneo@SiO_2	0.62—1.23	0.62—1.23	1—2
Cubiipo@SiO_2	2.46—4.92	0.62—1.23	2—8

Encouragingly, measurable antibacterial activity was observed against MRSA, and most composite materials showed enhanced growth inhibition upon 405 nm irradiation (**Table 29**), indicating a retained light response in the heterogeneous format. **Cubiipo@SiO_2** exhibited the most pronounced light-driven enhancement, in line with the trends observed for the corresponding molecular complex. Overall, the data demonstrate that immobilisation on silica preserves antibacterial photoactivity across the series, although the magnitude of the dark/light separation (phototoxicity index) is generally reduced in the particle format.

ICP-OES analysis revealed comparable copper loadings across the immobilised materials, ranging from 0.26–0.58 mg Cu/g SiO_2 (0.026–0.058 wt% Cu; **Table 30**), indicating that differences in antibacterial performance are not driven by major variations in Cu loading. Accordingly, MIC values for the composite materials are reported on a particle-mass basis (mg/mL). The increased activity seen upon light irradiation mirrors the effect observed for the molecular complexes, suggesting that the Copper(I) photosensitisers largely retain their photoresponse upon immobilisation. Nevertheless, the phototoxicity index (MIC_{dark} / MIC_{light}) was reduced to ≈2–8. Taken together, the observation of light-enhanced antibacterial activity in Copper(I)@SiO_2 materials supports their potential as heterogeneous photosensitisers for local disinfection and surface sanitation applications, in which recovery and re-use of the photoactive material are desirable.

Table 30. Copper loading in silica-immobilised samples quantified by ICP-OES (Cu mg/g, measured at 324.754 nm).

Immobilised Complex	Cu loading (mg/g) @ 324.754 nm
CuPOP@SiO_2	0.34
Cubcp@SiO_2	0.26
CubcpSO_3@SiO_2	0.58
Cuphen@SiO_2	0.32
Cuneo@SiO_2	0.29
Cubiipo@SiO_2	0.31

In this work, we evaluated 6 copper (I) complexes as potential antibacterial scaffolds. We revealed that although they exhibited moderate-to-low potency in the dark, upon irradiation with 405 nm for 10 minutes, 5 out of 6 complexes demonstrated up to 16-fold antibacterial activity improvement. Unfortunately, it was revealed that their biological potency was not selective and complexes exhibited unfavourable toxicity in HEK293T cells. Notably, except for **CubcpSO_3,** none of the complexes caused significant haemolysis up to 200 μM. Subsequently, the application area was shifted from solution to silica-immobilised composite materials to assess their suitability for antimicrobial photodynamic therapy. A key practical outcome is that immobilisation on silica preserves light-enhanced antibacterial activity in the heterogeneous format. Although the dark/light differences generally decrease relative to molecular complexes, the retention of photoactivity demonstrates that Cu(I) photosensitisers can be used as recoverable composite materials. This provides a realistic direction for Cu(I)-based aPDT where re-use and handling in aqueous media are desirable, for example in local disinfection or surface sanitation scenarios.

4.4 Supervised Research Projects

4.4.1 Synthesis and evaluation of antibacterial activity of bis(diphosphine) rhenium (v) dioxo complexes

This subchapter summarises the work done under the author's direct supervision for the Bachelor project of **Mr. Robin Knüsel** at the University of Bern in Spring 2023.

Rhenium complexes as antibacterial scaffolds were discussed in detail in **Chapter 1**.

Given the promising antibacterial potency of rhenium(v) dioxo complexes[109], we further investigated rhenium(I) complexes (**Figure 108**) as potential antibacterial compounds and conducted their cytotoxic evaluation against hRBC and HEK293T cells.

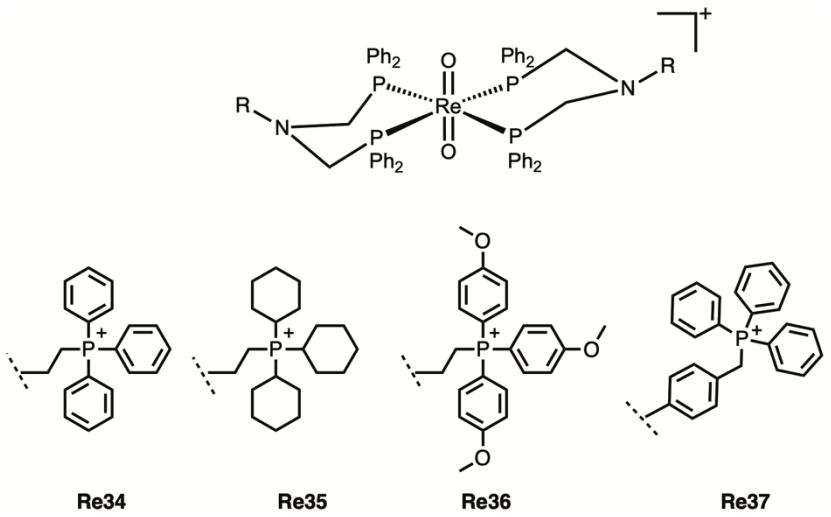


Figure 108. Rhenium(v) complexes synthesised by the supervised bachelor student.

4.4.1.1 Synthesis of bis(diphosphine) rhenium(v) dioxo complexes

Initially, the iridium precursor, **$ReIO_2(PPh_3)_2$**, was prepared in the presence of sodium perrhenate, triphenylphosphine, and hydroiodic acid, and then hydrolysed in aqueous acetone. Subsequently, Bis(hydroxymethyl)diphenylphosphonium chloride (**45**) was synthesised by acid-promoted condensation of diphenylphosphine with formaldehyde in concentrated hydrochloric acid, affording 78% yield. In parallel, the corresponding aminopropyl phosphonium salts were prepared by alkylation of triphenylphosphine for **Re34**, tricyclohexylphosphine for **Re35**, and trimethoxyphenylphosphine for **Re36** with 3-bromopropylamine hydrobromide in refluxing *n*-butanol. For **Re37**, 1,4-bis(bromomethyl)benzene was converted to the corresponding mono-phosphonium salt,

and the remaining bromide was subsequently converted to an amine in ethanol in the presence of aqueous ammonia, with quantitative yield. The prepared phosphonium salts were converted to bis(diphosphine) ligands through a phospha-Mannich reaction. Rhenium complexes were obtained via complexation in DCM at room temperature. All ligands and final complexes were characterised by NMR and HRMS.

4.4.1.2 Biological characterisation of rhenium(v) complexes

Initially, we determined the MIC values against a panel of two Gram-positive, MRSA and *B. subtilis*, and four Gram-negative bacterial strains. The complexes exhibited potent activity against the tested Gram-positive strains, with MIC values ranging from>0.78 to 6.25 μM. Slightly higher activity was observed against MRSA than *B. subtilis*. Interestingly, three out of four complexes also exhibited activity against the Gram-negative panel. Among them, **Re37** was the most potent complex, with MIC values of 6.25 and 25 μM against *K. pneumoniae* and *A. baumannii*. Except for **Re37**, with a MIC value of 100 μM, none of the complexes exhibited antibacterial potency against *Pseudomonas aeruginosa*, which was attributed to its well-known high levels of intrinsic and acquired resistance.[430] Overall, the investigated rhenium complexes were revealed as potent antibacterial scaffolds against Gram-positive bacteria, including methicillin-resistant *S. aureus*, and even though it varied, potent activity against the Gram-negative panel.

Table 31. Minimum Inhibitory Concentration (MIC) of rhenium complexes against selected bacterial strains. The positive controls are the antibiotics Vancomycin (VCM) for Gram-positive and polymyxin B (PMB) for Gram-negative. MIC values were given in μM. n.d.: no data.

	MIC (μM)					
	MRSA	***B. subtilis***	***E. coli***	***P.aeruginosa***	***K. pneumoniae***	***A. baumannii***
Re34	1.5625	3.13—6.25	1.56—3.13	> 100	25	12.5
Re35	<0.78	1.56—3.13	1.562	> 100	25	25
Re36	1.562	3.125	3.125	> 100	>100	>100
Re37	*n.d.*	*n.d.*	3.125	100	6.25	25
Antibiotic (μg/mL)	1	*n.d.*	0.5	0.5	0.5	0.5

Following demonstration of the favourable antibacterial properties of the complexes, their cytotoxicity was investigated. Initially, haemolytic properties were evaluated. It was revealed that the complexes did not exhibit significant cytotoxicity up to 200 μM (**Table 32**). Notably, they showed high toxicity against HEK293T cells, with CC_{50} values between 5.0 and 9.4 μM. However, when it comes to selectivity, therapeutic indices were

considered, and they exhibited moderate toxicity, with the most favourable one, **Re35**, having a TI value of 8.6. Although **Re35** did not exhibit very promising antibacterial potency against *K. pneumoniae* and *A. baumannii*, the favourable selectivity index paves the way for further improvement of its antibacterial activity.

Table 32. Cytotoxicity evaluation of the rhenium complexes. HC_{10} was determined in hRBC; CC_{50} was determined in HEK293T cells; they were given in μM. TI is the ratio of the CC_{50} value against HEK293T cells and MIC values against MRSA.

	Cytotoxicity(μM)		
	HC_{10}	**CC_{50}**	**TI**
Re34	>200	9 ± 1	6
Re35	>200	7 ± 3	>8.6
Re36	>200	5 ± 0.2	2.9
Re37	>200	5 ± 0.3	-

4.4.1.3 Summary and outlook

In this project, we expanded the rhenium(v) compound library, which has been shown to be a potent antibacterial scaffold. Following successful synthesis of the ligands and corresponding complexes (**Re34—37**), antibacterial potency was evaluated. It was revealed that the compounds exhibited low-micromolar activity against the Gram-positive panel and moderate-to-low activity against Gram-negative bacteria. As combating Gram-negative bacteria is well known to be challenging, these compounds appear promising as scaffolds. On the other hand, cytotoxicity evaluation revealed that these complexes exhibited low-micromolar IC_{50} values against HEK293T cells. However, **Re35** exhibited a favourable therapeutic index, higher than 8.6. Future studies should focus on the structural modifications that increase selective potency against bacteria and enlightining the mode of action of this compound class.

Chapter 5: Summary, conclusions and Future Work

Antimicrobial resistance (AMR) has emerged as one of the most significant health problems of the 21st century. Additionally, conventional drug discovery campaigns in the pharmaceutical industry have not exhibited sufficient progress in the last decade. Under these circumstances, exploring novel chemical spaces has become increasingly important for identifying antibacterial scaffolds with distinct mechanisms of action and potential to overcome existing resistance mechanisms. Metal complexes are promising candidates for antibacterial activity owing to their highly three-dimensional structures, geometric diversity, and distinct modes of action that small organic molecules lack.

In this thesis, novel metal complexes have been investigated as potential antibacterial scaffolds. In Chapter 2, building on the previous report on platinum cyclooctadiene complexes[239], SAR evaluation was initially performed. The halogen ligands on the platinum centre are crucial, as alteration to methyl- or hydroxy-containing ligands led to reduced activity and/or increased toxicity. Switching the metal centre to palladium resulted in a complete loss of antibacterial activity and significant haemolysis, leading to the conclusion that the platinum centre is crucial for favourable antibacterial activity. As in the last study, the sole effect of modification on the COD ligand wasn't investigated; in this chapter, more synthetically challenging modifications to the COD were explored. It was found that modifying the double bond in the COD ligand was detrimental to antibacterial activity, and the allylic position modification, resulting in a compound that was significantly less active than the original hit compound (**Pt1**). Both **Pt1** and **Pt8** showed broad activity against a range of clinical isolates of drug-resistant *S. aureus,* low cytotoxicity, and low haemolysis values. It was revealed that the halido ligand on the platinum centre and the unsubstituted double bond position of the COD ligand were essential for favourable antibacterial activity. The significance of the halido ligands might be attributable to these platinum complexes behaving as a prodrug, which, upon cellular internalisation, the complexes might undergo a ligand exchange, perhaps an aquation reaction to exchange the halido ligand to generate active species. Subsequently, the origin of potency of this compound class was also investigated and was shown that the activity of the complexes originates solely from the intact platinum complexes (**Pt1**) rather than from the ligands, platinum metal, or general platinum complexes.

Despite the promising Gram-positive activity, these complexes did not exhibit antibacterial activity against Gram-negative bacteria. In this study, *E. coli* was treated with **Pt1** in the presence of a sublethal concentration of outer membrane permeabiliser,

PMBN and no activity improvement was observed. Together with the previous study, the absence of Gram-negative activity wasn't able to be attributed to the general uptake challenge into Gram-negative bacteria.

Upon successful SAR and biological characterisation, the mechanism of action of this compound class was investigated in *B. subtilis*. Bacterial cytological profiling and RecA recruitment experiments demonstrated that **Pt1** and **Pt8** induce substantial DNA damage and activate the SOS response, whereas cisplatin produced a distinct cellular phenotype despite its structural similarity. Direct single-molecule imaging further confirmed DNA fragmentation by the lead compounds.

The greater antibacterial potency of **Pt1** was attributed in part to its approximately three-fold higher bacterial uptake compared with **Pt8**, while the inactivity of cisplatin was associated with poor uptake. **Pt1** also induced oxidative stress through hydroxyl radical formation, supporting a multifaceted mode of action that may contribute to the absence of high-level resistance development over 36 passages.

Finally, **Pt1** reduced the bacterial load by approximately 1.9 $\log_{10}$ CFU/g in a topical *S. aureus* skin infection mouse model. Overall, **Pt1** emerged as a promising lead compound with potent activity against antibiotic-resistant pathogens, low cytotoxicity, a multifaceted mechanism of action, low resistance development, and *in vivo* efficacy.

Although this work provided substantial insight into the mode of action of this compound class, several important questions remain unanswered. In particular, the identity of the active platinum species and the basis for the lack of activity against Gram-negative bacteria remain unclear. More broadly, it is also important to understand how bacteria can survive despite substantial activation of the DNA-damage SOS response following cisplatin treatment. Future work should also focus on improving the serum stability of this compound class to support its potential development for systemic applications. Additionally, the origin of the lack of activity against Gram-negative bacteria should also be further investigated to develop broad-spectrum compounds. As increased outer-membrane permeability and disruption of TolC-mediated efflux did not fully restore antibacterial activity, other factors such as intracellular inactivation, differences in compound speciation, or limited accessibility to the target may contribute to the observed lack of potency. A better understanding of these could enable rational modification of the scaffold or the development of targeted delivery strategies to improve accumulation and activity in Gram-negative pathogens.

In chapter 3, we investigated a one-pot, three-component combinatorial strategy for the generation of 1440 piano-stool iridium(III) cyclopentadienyl Schiff-base complexes as potential antibacterial agents. The library was screened initially directly from the crude mixtures, as the reaction solvent was DMSO; no prior purification or solvent evaporation step was necessary. This enabled us to develop a semi-automated workflow through which, under optimal instrument availability, library generation, analytical characterisation, and screening of the entire library could be completed in under 5 days. The crude reaction mixtures were characterised by LC-MS, and the conversion rates were calculated using custom Python scripts. It was demonstrated that the efficiency of iridium(III) Schiff-base complex formation is governed by a combination of steric and electronic effects.

The antibacterial activity of the library was evaluated against *S. aureus* at 12.5 and 50 μM and against *E. coli* at 50 μM. None of the complexes exhibited antibacterial activity against *E. coli* under the initially tested conditions. On the other hand, promising antibacterial activity was observed across the libraries with a clear SAR. The Cp scaffold exerted the strongest influence on antibacterial activity. The biphenyl-substituted **Cp2** library exhibited the highest potency as reported by the Sadler group[278], followed by **Cp3** and **Cp4**, whereas the **Cp1** library was substantially less active. The increased activity of **Cp2** was attributed to the increased lipophilicity and rigidity of the biphenyl substituent, which may promote interactions with the bacterial membrane and improve cellular uptake.The SAR analysis showed that antibacterial activity was generally enhanced by incorporating more hydrophobic and aromatic building blocks, particularly in the Cp and aldehyde components.

Subsequently, the cytotoxicity of the crude compound library was investigated against HEK293T cells. Cytotoxicity was strongly influenced by the Cp scaffold, with **Cp1** complexes exhibiting the lowest overall cytotoxicity and **Cp2** complexes displaying the highest. Similar trends were observed at the building-block level, where building blocks associated with enhanced antibacterial activity often also reduced mammalian cell viability. This highlighted one of the major challenges in antibacterial scaffold development, as increasing lipophilicity can enhance antibacterial activity while simultaneously increasing cytotoxicity.

The 19 most promising crude compounds were selected for dose-response biological characterisation, which identified **Ir9**, **Ir14**, **Ir15**, and **Ir16** as the most promising compounds in the library (therapeutic indices >4).

These complexes were selected for batch synthesis, purification, and hit-validation studies. Consequently, **Ir14** and **Ir15** were advanced for further biological characterisation. Upon purification, **Ir14** exhibited substantially greater cytotoxicity than anticipated from the crude-mixture screening and showed poor selectivity. In contrast, **Ir15** retained high antibacterial activity and exhibited a favourable toxicity profile consistent with the initial screenings. These findings further demonstrated the importance of validating crude screening hits with purified compounds, as biological activity in crude mixtures may be affected by incomplete conversion, side products, or differences in the concentrations of active species.

Despite the use of independent biological replicates, several false-positive results were observed. This indicated that biological replication alone was insufficient to eliminate artefacts arising from screening crude reaction mixtures, which may contain side products or variable amounts of the desired complex. It nevertheless enabled the rapid evaluation of large compound libraries within a relatively short period. The use of crude reaction mixtures enabled assessment of biological activity without the need to isolate and purify each individual complex, substantially reducing the time and resources required during the initial screening stage. This made it possible to identify SAR and prioritise the most promising compounds for further investigation. However, variations in reaction conversion, compound concentration, solubility, stability and the presence of unreacted starting materials or side products limited the reliability of individual screening results. Therefore, this approach is most valuable as an efficient first-stage screening strategy for narrowing large libraries to a smaller number of promising candidates, rather than as a definitive measure of biological potency. Subsequent hit validation with purified compounds remains essential to confirm the identified activity.

Ir15 exhibited broad low-micromolar-range antibacterial activity against a panel of Gram-positive bacteria and **Ir15** exerts a bactericidal effect. **Ir15** exhibited moderate cytotoxicity against HEK293T cells and low haemolytic activity, resulting in therapeutic indices between 8 and 31, depending on the bacterial strain. Taken together, these findings identified **Ir15** as the most promising antibacterial compound within the investigated library.

Although **Ir15** exhibited limited activity against Gram-negative bacteria, its antibacterial potency against both *E. coli* and *A. baumannii* was substantially enhanced in the presence of a sublethal concentration of the outer-membrane permeabiliser PMBN. This revealed that **Ir15** possesses intrinsic antibacterial activity against Gram-negative

bacteria but is unable to efficiently internalise through the outer membrane. In contrast to the platinum compounds investigated in Chapter 2, the lack of Gram-negative potency of **Ir15** can therefore be at least partly attributed to cellular uptake.

Subsequently, the stability of **Ir15** was investigated under biologically relevant conditions. Its antibacterial activity was substantially reduced following 24 hours of pre-incubation in MH medium, indicating degradation or speciation over extended incubation periods. Rapid degradation was observed in H_2O, where chloride dissociation and the formation of substituted and dimeric iridium species were detected. Although the aqueous lability of **Ir15** represents a potential limitation, the complex remained sufficiently stable under the assay conditions to exert its antibacterial effect. Therefore, the identity of the biologically active iridium species remains unclear and requires further investigation.

Upon successful hit validation, the initial mode of action of **Ir15** was investigated and bacterial cytological profiling revealed mild membrane-associated alterations and changes in nucleoid morphology. Membrane depolarisation was confirmed using $DiSC_3(5)$ and by the delocalisation of MinD. Taken together, these findings demonstrated that **Ir15** perturbs membrane polarisation and ion homeostasis without causing extensive structural damage to the bacterial membrane.

Although alterations in bacterial DNA morphology were observed, no evidence for substantial direct DNA binding or intercalation was obtained, suggesting that the nucleoid changes are likely downstream effects of broader cellular stress rather than the result of direct DNA targeting. Reactive oxygen species scavenger experiments also did not indicate involvement of superoxide or hydroxyl radical formation. Overall, the initial mode-of-action studies suggest that **Ir15** primarily affects membrane polarisation and membrane-associated processes, leading to downstream alterations in DNA morphology. Although we established a modular workflow to generate and screen a library of 1440 iridium complexes and identified extensive structure-activity relationships, a promising hit, and a preliminary antibacterial mode of action, several unanswered questions remained.

Firstly, the speciation of the iridium(III) Cp complexes should be investigated. Although the complexes appeared sufficiently stable to exert their antibacterial effects, ligand dissociation and the possible formation of dimeric species may influence biological activity. Identifying the iridium species present under biologically relevant conditions would therefore be essential for clarifying the relationship between complex stability, speciation and antibacterial activity. Additionally, a more detailed investigation of the

antibacterial mechanism of **Ir15** is warranted. Based on the preliminary findings, its primary effect may involve disruption of the bacterial membrane potential, thereby inhibiting the respiratory chain. This could initially be investigated by measuring intracellular ATP levels. Additionally, the delocalisation of MinD suggested that disruption of the membrane potential may subsequently interfere with bacterial cell division. This could be investigated with FtsZ recruitment experiment. Furthermore, transcriptomic and proteomic profiling of treated bacteria could provide broader insights into the cellular pathways affected by **Ir15** and help identify its direct or downstream molecular targets. Finally, upon co-administration with PMBN, **Ir15** exhibited promising antibacterial activity against *E. coli* and *A. baumannii*. Further studies should also focus on improving the intrinsic uptake of these compounds, potentially by modifying ligands with a free primary amine or with groups that carry localised positive charge, such as PPh_3.[338] Additionally, a Trojan horse approach could be utilised by incorporating siderophore moieties to enhance uptake by targeting the bacterial iron acquisition system.[171,237,238,431–433]

In addition to antibacterial activity, the antifungal potential of the IrCp1 library was investigated. It was revealed that quinoline-derived aldehydes and aromatic amines were most frequently associated with antifungal activity. Four compounds, **IrCp1K7**, **IrCp1L7**, **IrCp1B7**, and **IrCp1B8**, were selected for resynthesis and hit validation. The purified compounds exhibited limited activity against *C. albicans*, whereas **IrCp1L7**, **IrCp1B7**, and **IrCp1B8** showed improved activity against *A. fumigatus*. However, the antifungal compounds exhibited only modest selectivity over HEK293T cells, and none displayed a sufficiently favourable potency and selectivity profile to justify further progression. Nevertheless, the identification of quinoline-derived aldehydes and aromatic amines as favourable building blocks provides a basis for the future optimisation of this scaffold as a potential antifungal agent.

Although further optimisation and mechanistic investigation are necessary, this workflow provides a versatile platform to identify novel metal-based antimicrobial scaffolds.

In Chapter 4, the antibacterial chemical space was expanded through collaborative and supervised research projects. In the first part, the previously published iridium(III) Cp* chemical space[327] was expanded through incorporation of three additional Cp scaffolds (**Cp2**–**Cp4**).

Single-dose antibacterial screening demonstrated that the **Cp2** and **Cp4** libraries exhibited the strongest activity against *S. aureus*, whereas the **Cp1** library was the least active within the series. At the building-block level, extended aromatic and lipophilic

building blocks were generally associated with greater activity. However, these features also reduced HEK293T cell viability, particularly within the **Cp2** library. The building blocks generally did not exhibit antibacterial activity, confirming that coordination to iridium was required for the observed biological effects.

Based on the single-dose screening and chemical availability, three preliminary hit compounds, **IrCpM23Y3**, **IrCp3P3A10**, and **IrCp4M23Y2**, were selected for hit validation studies.

IrCp4M23Y2 retained activity against the tested Gram-positive bacteria after purification, whereas **IrCp3PA10** showed substantially weaker activity and rapidly degraded in DMSO. Future work will focus on dose-response screening of the combinatorial library to identify hits more accurately and on elucidating the mechanism of action.

In the second part, the evaluation of 67 macrocyclic and medium-sized lactams unfortunately did not identify antibacterial activity against either *S. aureus* or *E. coli* at 100 μM.

In the third part, the biological characterisation and mode of action of ruthenium(II) and iridium(III) N^O Schiff-base complexes were investigated. The lead compounds did not cause significant haemolysis and exhibited therapeutic indices of approximately 15. In the mode of action assays, comparative studies of ruthenium(II) and iridium(III) Schiff-base complexes further demonstrated that structurally related metal complexes can exhibit substantially different intracellular distributions and antibacterial phenotypes, with **IrCp-B5** primarily associated with membrane effects and **RuCy-J3** displaying higher cytosolic accumulation and alterations on nucleoid morphology. Further studies should focus on identifying the direct bacterial target of **RuCy-J3** and mapping the affected cellular pathways.

In the fourth part, the biological activity of six photoactive heteroleptic copper(I) complexes was investigated. Upon irradiation with 405 nm light, five of the complexes exhibited enhanced antibacterial activity against MRSA, with improvements of up to more than 16-fold. On the other hand, the complexes did not exhibit sufficient selectivity towards bacteria over mammalian cells. Therefore, the application area was shifted from solution to silica-immobilised composite materials to assess their suitability for antimicrobial photodynamic therapy. Although the phototoxicity index slightly decreased, we observed promising antibacterial activity with silica-immobilised complexes. Future work should focus on assessment of photosensitiser leaching, repeated use, long-term

stability and activity against bacterial biofilms. Evaluation on coated surfaces or in contaminated-water models would provide a more relevant assessment of their potential application.

Finally, the supervised project identified bis(diphosphine) rhenium(v) oxo complexes with low-micromolar activity against Gram-positive bacteria and measurable activity against Gram-negative strains. Building on the previous report[109], we synthesised four complexes with different phosphine scaffolds. The rhenium(V) oxo complexes represented only compound classes investigated in this thesis with intrinsic broad-spectrum activity. However, limited selectivity towards mammalian cells remains a major barrier, and future optimisation should therefore aim to improve bacterial selectivity while retaining Gram-negative activity, a Trojan horse approach, siderophore incorporation, might be useful to increase bacterial uptake and decrease mammalian cell uptake.[237,432,434]

Overall, this thesis explored several metal-based chemical spaces to identify structurally distinct antimicrobial scaffolds and to advance the most promising compounds beyond initial activity screening. At the beginning of this project, the number of metal-based antibacterial scaffolds with experimentally supported mechanisms of action remained relatively limited, and many studies in the field of metallantibiotics were still largely centred on compound synthesis followed by preliminary biological evaluation. Over the course of this work, however, the field has increasingly moved beyond identifying active metal complexes towards a more detailed understanding of their stability, cellular uptake, intracellular distribution, and target engagement. Understanding the effect of structural changes on those parameters is key to enabling the rational design of metal complexes with favourable activity.

In this context, phenotypic drug discovery appeals as a promising approach to identify novel metalloantibiotic scaffolds. This approach has historically contributed substantially to the discovery of first-in-class drugs and is particularly valuable for antibiotic discovery, where potent activity against an isolated bacterial target does not necessarily translate into whole-cell antibacterial activity, as this also depends on efficient cellular uptake, sufficient intracellular accumulation, and maintenance of a biologically active species within the relevant bacterial compartment.[435,436] Target-based approaches, however, offer the advantage of enabling compound design and optimisation around a defined and validated bacterial target. On the other hand, many successful antibiotics exert their activity through multifaceted mechanisms.[437] Relying only on target-based drug

discovery approaches may therefore overlook compounds whose antibacterial effects arise from simultaneous interactions with multiple cellular targets or pathways. Rather than considering these strategies as competing approaches, their respective strengths could be combined. Phenotypic screening could first be used to identify metal-based scaffolds that can access the relevant bacterial compartment and produce a measurable antibacterial effect. After hit selection and validation, elucidating the mechanism of action of the corresponding compounds would provide further information about their potential molecular targets and affected cellular pathways. Once these targets have been identified and validated, target-based approaches could subsequently be used to guide the rational optimisation of the scaffold and design focused compound libraries with improved potency and selectivity. Knowledge of validated bacterial targets and previously established SAR could therefore guide the design of focused metal-complex libraries[118], which could then be evaluated phenotypically to ensure that target activity is retained *in vitro*.

This combined strategy could be further strengthened by high-throughput synthesis, direct-to-biology screening, and automated workflows, which have enabled substantially larger and more diverse areas of metal-based chemical space to be explored systematically, while considerably reducing the time and resources required to investigate the same chemical space using conventional synthesis, purification, and screening approaches. This experimental workflow can be incorporated into a ‘data-driven approach’, where the generated datasets can be used to develop machine-learning models. Existing antibacterial activity and physicochemical data reported across the literature could initially be incorporated, where sufficiently comparable. These models could subsequently be improved through iterative experimental approaches in which predicted compounds are synthesised and screened, and the resulting data are incorporated back into the model to identify regions of metal-based chemical space with a higher probability of producing potent and selective antibacterial scaffolds. Importantly, large-scale experimental campaigns would remain necessary not only for identifying active compounds but also for generating high-quality negative data, which are essential for training models capable of distinguishing favourable from unfavourable chemical space. In this way, phenotypic screening, target-driven optimisation, high-throughput experimentation, and machine-learning-guided prioritisation could operate as complementary components of a more rational and iterative strategy for future metalloantibiotic discovery. Additionally, systematic investigation of structurally diverse metal-complex libraries could enable the establishment of general structure-

accumulation relationships for bacteria, providing a framework to identify the structural and physicochemical features that promote bacterial accumulation and guide the rational design of future metalloantibiotics. To the best of our knowledge, although there are studies on entry rules for organic compounds[338,438–440], no systematic study has yet established general structure-accumulation rules specifically for antibacterial metal complexes.

While these approaches may facilitate the identification and rational optimisation of promising metalloantibiotic scaffolds, their progression towards preclinical development will ultimately depend on whether favourable antibacterial properties are retained under physiological conditions. In particular, future work in the field should focus on understanding the biological speciation and degradation products, as the species responsible for antibacterial activity may differ substantially from the initially administered complex.[441] Similarly, cytotoxicity assessment should extend beyond single mammalian cell lines to determine whether antibacterial selectivity is maintained across more physiologically relevant models and to identify potential organ-specific toxicity. For compounds intended for systemic administration, pharmacokinetic and biodistribution studies will also be essential to determine plasma stability, protein binding, circulation time, clearance, and accumulation at the site of infection. Ultimately, these data should be integrated with pharmacodynamic studies to establish whether therapeutically relevant concentrations of the active species can be achieved at the site of infection while maintaining an acceptable safety profile.[442]

In conclusion, this thesis further demonstrates the potential of metal complexes as antibacterial scaffolds. Combination of batch and high-throughput synthesis and screening, SAR studies, and mechanistic elucidation, this work identified several promising antibacterial scaffolds and provided further insight into the chemical and biological properties that govern their activities. Although considerable challenges remain in translating these scaffolds towards clinical development, number of metal-based compounds progressing through clinical trials provides further encouragement for their potential as future antibiotics.

Chapter 6: Experimental

6.1 Compounds preparative techniques

6.1.1 Chapter 2

All reagents were available and used without further purification unless otherwise noted. Column chromatography was performed by using thick-walled glass columns and silica Gel 60 (Sigma Aldrich 230 – 400 mesh). Thin layer chromatography on pre-cut plates (Marcherey-Nagel, ALUGRAM Xtra Sil G/UV_{254}), and visualization was provided by UV lamp at 254 nm and potassium permanganate stain. Argon was used as an inert gas.

6.1.2 Chapter 3, and 4

All reagents were commercially available and used without further purification unless otherwise noted. Flash column chromatography was performed by using CombiFlash automated column machine. Thin layer chromatography on pre-cut plates (Marcherey-Nagel, ALUGRAM Xtra Sil G/UV_{254}), and visualization was provided by UV lamp at 254 nm. Nitrogen was used as an inert gas.

6.2 Instrument details and methods for compound characterization

6.2.1 Chapter 2

^{1}H NMR ,^{13}C NMR and ^{195}Pt spectra were recorded at room temperature on Bruker (operating at 300 MHz and 400 MHz for ^{1}H NMR, 75 MHz for ^{13}C NMR, and 86 MHz for^{195}Pt NMR) in $CDCl_3$, CD_2Cl_2-d_2, DMSO and Acetone-d_6 with tetramethylsilane (TMS) as internal standard. Coupling constants *(J values*) are given in Hz and chemical shifts are reported as parts per million (ppm). Splitting patterns are designated as s (singlet), d (doublet), t (triplet), q (quartet), m (multiplet), and p (pentet). NMR spectra were processed with MestReNova. High resolution mass analyses were performed in positive ion mode with a ThermoScientific LTQ Orbitrap XL, fitted with an NSI ion source.

6.2.2 Chapter 3 and 4

^{1}H NMR ,^{13}C NMR and ^{19}F spectra were recorded at room temperature on JEOL ECS400 spectrometer (operating at 400 MHz for ^{1}H NMR, 101 MHz for ^{13}C NMR, and 377 MHz for ^{19}F NMR) in $CDCl_3$, CD_2Cl_2-d_2, and DMSO-d_6 with tetramethylsilane (TMS) as internal standard. Coupling constants *(J values*) are given in Hz and chemical shifts are reported as parts per million (ppm). Splitting patterns are designated as s (singlet), d (doublet), t (triplet), q (quartet), m (multiplet), and p (pentet). NMR spectra were processed with MestReNova. High resolution mass analyses were performed in positive ion mode with a Bruker Daltronics micrOTOF MS, Agilent series 1200LC with

electrospray ionization (ESI). Liquid Chromotography Mass Spectrometry (LC-MS) data was collected using a Dr. Maisch Repro Sil-Pur 120 ODS-3, 2.4 µm, 50 mm x 3 mm column, on a ThermoScientific Vanquish instrument, coupled to a ThermoScientific HCT ultra ETD II ion trap. Mass spectrometry (ESI) was run in the positive mode. The solvent system consisted of H_2O / MeCN, both containing 0.1% formic acid. The gradient used for the method is described in **Table 33**. The UV channels correspond to UV1: 200 nm, UV2: 220 nm, UV3:254 nm. Characterization data and assessments of purity on the generated libraries were done using 254 nm absorbances.

Table 33. Flow gradient for LC-MS method.

Time / min	Flow / mL min^{-1}	% MeCN
0.0	0.500	10.0
4.0	0.500	90.0
4.5	0.500	90.0
4.6	0.500	10.0
5.0	0.500	10.0

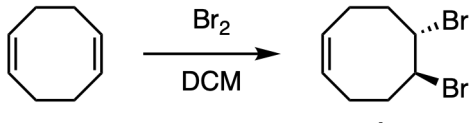
Table 34. Flow gradient for LC-MS method (7 minutes method).

Time / min	Flow / mL min^{-1}	% MeCN
0.0	0.500	10.0
4.0	0.500	90.0
6.3	0.500	90.0
6.4	0.500	10.0
7.0	0.500	10.0

6.3 Synthesis Procedures

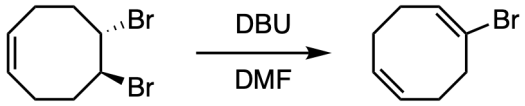
6.3.1 Chapter 2: A Platinum Butterfly Effect: Small Changes Turn an Anticancer Drug into a Non-toxic Metalloantibiotic with In Vivo Efficacy

Synthesis of **COD-Br$_2$**[443]



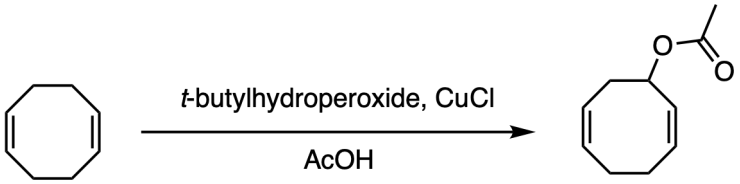
1,5-cyclooctadiene (1.00 g, 9.24 mmol) was dissolved in DCM (30 mL) and a bromine (0.200 mL, 3.85 mmol) solution in DCM (6 mL) was added dropwise over 30 minutes. The reaction progress was monitored by TLC. After it was stirred for another 30 minutes at room temperature, reaction mixture was concentrated *in vacuo*. **COD-Br$_2$** was obtained through column chromatography (Heptane) as colourless oil (0.616 g, 77% yield). ^{1}H NMR ($CDCl_3$, 300 MHz) δ 5.64 (t, *J* = 4.1 Hz, 2H, olefinic CH), 4.67 – 4.63 (m, 2H, Br-CH), 2.75 – 2.52 (m, 4H, aliphatic CH_2), 2.30 – 2.17 (m, 4H, aliphatic CH_2); ^{13}C NMR ($CDCl_3$, 75 MHz) δ 128.8, 59.6 (Br-CH), 35.4, 25.0 (aliphatic CH_2)

Synthesis of **COD-Br**[444]



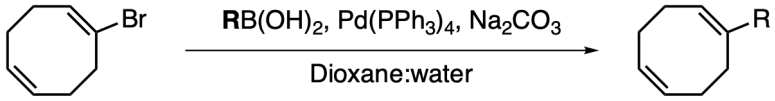
COD-Br$_2$ (1.13 g, 4.22 mmol) was dissolved in anhydrous DMF (12 mL) under inert conditions, and 1,8-diazabicyclo(5.4.0)undec-7-ene(DBU) (0.674 g, 4.43 mmol) was added dropwise. The reaction mixture was stirred overnight at 80°C. Reaction progress was monitored by TLC. Upon completion, 1M HCl (20 mL) was added and extracted three times with EtOAc. The organic phase was dried over Na_2SO_4 and concentrated *in vacuo*. **COD-Br** was obtained through column chromatography (Heptane) as a yellow oil (1.23 g, 21% yield). ^{1}H NMR (300 MHz, $CDCl_3$) δ 6.03 (p, *J* = 3.4 Hz, 1H, olefinic CH), 5.64 – 5.47 (m, 2H, olefinic CH), 2.82 (dd, *J* = 8.0, 5.3 Hz, 2H, aliphatic CH_2), 2.47 – 2.37 (m, 2H, aliphatic CH_2), 2.37 – 2.27 (m, 4H, aliphatic CH_2). ^{13}C NMR (75 MHz, $CDCl_3$) δ 130.3, 128.3, 127.9, 125.1 (olefinic C), 39.0, 28.4, 27.5, 27.3 (aliphatic CH_2).

Synthesis of **27**[445]



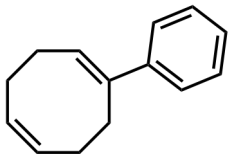
1,5-cyclooctadiene (5.29 g, 48.9 mmol) was dissolved in acetic acid (1.6 mL) and *t*-butyl hydroperoxide (1.87 g, 20.8 mmol), and a catalytic amount of CuCl was added. The reaction mixture was refluxed at 120 °C for 52 hours. Reaction progress was monitored by TLC. Upon completion, the reaction mixture was diluted with Et_2O and washed twice with distilled water and one time with brine. The organic phase was dried over Na_2SO_4 and concentrated *in vacuo*. Compound **27** was obtained through column chromatography (3:1 Heptane: EtOAc) as a yellow oil (2.95 g, 11 % yield). ^{1}H NMR (300 MHz, $CDCl_3$) δ 5.51 – 5.36 (m, 1H, aliphatic O-CH), 5.29 – 4.92 (m, 4H, olefinic CH), 2.49 – 1.59 (m, 6H, aliphatic CH_2), 1.56 (dd, *J* = 5.6, 0.7 Hz, 3H, aliphatic CH_3); ^{13}C NMR (75 MHz, $CDCl_3$) δ 170.3 (C=O), 129.6, 129.1, 129.0, 125.1 (olefinic CH), 72.3 (aliphatic O-CH), 33.8, 27.9, 27.8 (aliphatic CH_2), 21.2 (aliphatic CH_3).

6.3.1.1 General synthetic procedure for double bond-modified 1,5-cyclooctadiene ligands



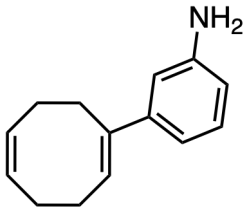
COD-Br (0.200 g, 1.06 mmol) was suspended in 1,4-dioxane (3 mL) and water (1.5 mL). Boronic acid derivative (2.5 eq), tetrakis-(triphenylphosphine)-palladium (0.03 eq.), and Na_2CO_3(3 eq.) were added to the reaction mixture. The reaction mixture was refluxed for 5 hours at 110 °C. Reaction progress was monitored by TLC, and upon completion, the reaction mixture was diluted with EtOAc. The organic phase was separated, and the aqueous phase was washed three times with EtOAc. The combined organic phase was washed with brine. The combined organic phases were dried over Na_2SO_4 and concentrated *in vacuo*. The desired products were obtained through column chromatography (Heptane:EtoAc).

Compound **23**



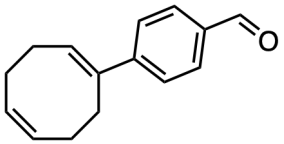
Colorless oil, 0.0404 g, 0.22 mmol, 36% yield. ^{1}H NMR (300 MHz, $CDCl_3$) δ 7.22 – 7.08 (m, 5H, aromatic CH), 5.78 (t, *J* = 6.5 Hz, 1H, olefinic CH), 5.51 (t, *J* = 6.0 Hz, 2H, olefinic CH), 2.76 – 2.70 (m, 2H, aliphatic CH_2), 2.47 – 2.32 (m, 6H, aliphatic CH_2); ^{13}C NMR (75 MHz, CD_2Cl_2) δ 145.4 (olefinic quaternary C), 140.1 (aromatic quaternary C), 128.8, 128.5, 128.1, 127.4, 127.3, 127.1, 126.4, 126.2 (aromatic/olefinic CH), 31.2, 28.2, 28.2, 28.1 (aliphatic CH_2).

Compound **24**



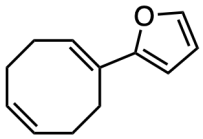
Pale yellow oil, 0.077 g, 0.39 mmol, 41% yield. ^{1}H NMR (300 MHz, $CDCl_3$) δ 7.09 (t, *J* = 7.8 Hz, 1H, aromatic CH), 6.79 – 6.73 (m, 1H, aromatic CH), 6.67 (t, *J* = 1.9 Hz, 1H, aromatic CH), 6.56 (ddd, *J* = 7.8, 2.4, 1.0 Hz, 1H, aromatic CH), 5.86 (t, *J* = 6.4 Hz, 1H, olefinic CH), 5.68 – 5.56 (m, 2H, olefinic CH), 3.60 (*br*. s, 2H, NH_2), 2.83 – 2.76 (m, 2H, aliphatic CH_2), 2.57 – 2.40 (m, 6H, aliphatic CH_2); ^{13}C NMR (75 MHz, $CDCl_3$) δ 146.6 (aromatic C-NH_2), 146.2 (olefinic quaternary C), 140.2 (aromatic quaternary C), 129.0, 128.7, 128.6, 126.9, 116.9, 113.4 (aromatic/olefinic CH), 31.2, 28.3, 28.1, 28.1 (aliphatic CH_2; HRMS (ES+): m/z calculated for $C_{14}H_{18}N^+$ 200.1434: found 200.1434 $[M+H]^+$.

Compound **25**



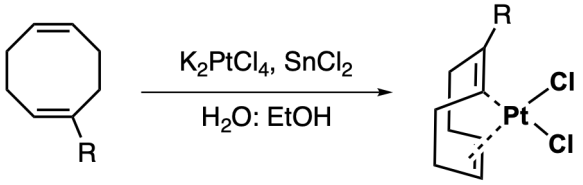
Yellow oil, 0.225 g, 1.06 mmol, 41% yield. ^{1}H NMR (300 MHz, $CDCl_3$) δ 9.94 (s, 1H, CHO), 7.76 (d, *J* = 8.6 Hz, 2H, aromatic CH), 7.44 (d, *J* = 8.3 Hz, 2H, aromatic CH), 5.98 (t, *J* = 6.6 Hz, 1H, olefinic CH), 5.57 (p, *J* = 2.9 Hz, 2H, olefinic CH), 2.80 (t, *J* = 6.8 Hz, 2H, aliphatic CH_2), 2.57 – 2.38 (m, 6H, aliphatic CH_2); ^{13}C NMR (75 MHz, $CDCl_3$) δ 192.0 (C=O), 151.5, 139.3, 134.6 (aromatic/olefinic quaternary), 130.3, 129.8, 128.8, 128.4, 126.7, 117.5 (aromatic/olefinic CH), 30.8, 28.3, 28.2, 27.8 (aliphatic CH_2). HRMS (ES+): m/z calculated for $C_{15}H_{17}O^+$ 213.1279: found 213.1272 $[M+H]^+$.

Compound **26**



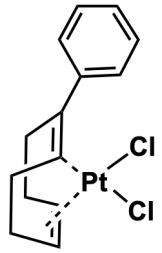
Pale yellow oil, 0.110 g, 0.63 mmol, 24% yield. ^{1}H NMR (300 MHz, $CDCl_3$) δ 7.33 (d, *J* = 2.6 Hz, 1H, aromatic CH), 6.39 – 6.30 (m, 2H, aromatic & olefinic CH), 6.20 (d, *J* = 3.5 Hz, 1H, aromatic CH), 5.65 – 5.58 (m, 2H, olefinic CH), 2.80 – 2.74 (m, 2H, aliphatic CH_2), 2.62 – 2.47 (m, 6H, aliphatic CH_2). ^{13}C NMR (75 MHz, $CDCl_3$) δ 156.3, 141.1 (aromatic C), 129.4, 128.7, 128.5, 124.2 (olefinic C), 111.0, 103.7 (aromatic CH, 28.20, 27.9 (aliphatic CH_2). HRGCMS: t_R: 10.7 min: m/z calculated for $C_{12}H_{14}O$ 174.1045; found 174.1042 [M].

6.3.1.2 General synthetic procedure for Pt(II) complexes with double bond-modified 1,5-cyclooctadiene ligands[239]



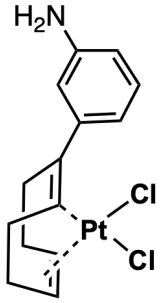
K_2PtCl_4 (0.100 g, 0.240 mmol) was suspended in water (3 mL) and ethanol (3 mL) and COD ligand (0.960 mmol, 4 eq.) was added. Then, catalytic amount of $SnCl_2$ was added to the reaction mixture and stirred for 2 days at room temperature. Upon precipitation, the reaction mixture was concentrated *in vacuo* and desired products were obtained through column chromatography (Heptane: EtOAc).

Compound **Pt2**



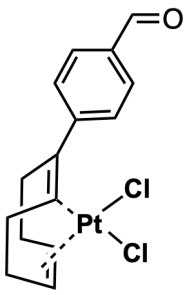
Pale yellow solid, 0.052 g, 0.12 mmol, 52% yield. ^{1}H NMR (400 MHz, $CDCl_3$) δ 7.53 (d, *J* = 7.2 Hz, 2H, aromatic CH), 7.37 (dd, *J* = 22.8, 11.3 Hz, 3H, aromatic CH), 6.25 – 6.04 (m, 1H, olefinic CH), 5.73 (d, *J* = 45.0 Hz, 2H, olefinic CH), 3.23 – 3.11 (m, 1H, aliphatic CH), 3.03 (m, 1H, aliphatic CH), 2.92 – 2.84 (m, 1H, aliphatic CH), 2.73 – 2.61 (m, 2H, aliphatic CH), 2.56 – 2.35 (m, 2H, aliphatic CH), 2.15 – 2.02 (m, 1H, aliphatic CH); ^{13}C NMR (101 MHz, $CDCl_3$) δ 141.3 (aromatic quaternary C), 130.1, 128.4, 127.7, 120.9, 100.4, 98.3, 91.9 (aromatic/olefinic C), 38.1, 33.5, 32.8, 29.4 (aliphatic CH_2); ^{195}Pt NMR (86 MHz, DMSO) δ -3187.27; HRMS (ES+): m/z calculated for $C_{14}H_{20}Cl_2NPt^+$ 467.0615: found 467.0610 $[M+NH_4]^+$.

Compound **Pt3**



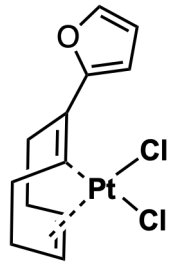
Brown solid, 0.0099 g, 0.021 mmol, 22% yield. ^{1}H NMR (300 MHz, acetone-d_6) δ 7.42 (s, 1H, aromatic CH), 7.21 – 7.09 (m, 3H, aromatic CH), 6.40 (s, 1H), 5.89 (t, *J* = 6.5 Hz, 1H, olefinic CH), 5.55 (t, *J* = 3.7 Hz, 2H, olefinic CH), 2.78 (dd, *J* = 7.6, 6.1 Hz, 2H, aliphatic CH), 2.47 (tt, *J* = 12.7, 5.2 Hz, 6H, aliphatic CH). HRMS (ES+): m/z calculated for $C_{14}H_{17}ClNPt^+$ 429.0697: found 429.0690 $[M-Cl]^+$.

Compound **Pt4**



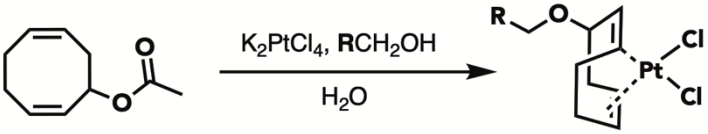
Yellow solid, 0.042 g, 0.088 mmol, 33% yield. ^{1}H NMR (400 MHz, $CDCl_3$) δ 9.99 (s, 1H, CHO), 7.82 (d, *J* = 8.5 Hz, 2H, aromatic CH), 7.68 (d, *J* = 8.2 Hz, 2H, aromatic CH), 6.17 (d, *J* = 9.7 Hz, 1H, olefinic CH), 5.87 – 5.71 (m, 2H, olefinic CH), 3.26 – 3.13 (m, 1H, aliphatic CH), 3.05 (m, 1H, aliphatic CH), 2.84 – 2.75 (m, 1H, aliphatic CH), 2.70 – 2.60 (m, 2H, aliphatic CH), 2.58 – 2.49 (m, 2H, aliphatic CH), 2.45 – 2.36 (m, 2H, aliphatic CH).^{13}C NMR (101 MHz, $CDCl_3$) δ 191.6 (C=O), 147.4, 136.7 (aromatic quaternary), 129.7, 128.5 (aromatic CH), 116.9, 101.6, 99.6, 93.7 (olefinic C), 37.8, 33.5, 33.0, 29.2 (aliphatic CH_2);^{195}Pt NMR (86 MHz, $CDCl_3$) δ -3190.91. HRMS (ES+): m/z calculated for $C_{15}H_{20}Cl_2NOPt^+$ 495.0564: found 495.0579 $[M+NH_4]^+$.

Compound **Pt5**



Yellow solid, 0.034 g, 0.077 mmol, 29% yield. ^{1}H NMR (300 MHz, CD_2Cl_2) δ 7.61 (dd, *J* = 1.8, 0.8 Hz, 1H, aromatic CH), 6.79 (dd, *J* = 3.6, 0.8 Hz, 1H, aromatic CH), 6.46 (dd, *J* = 3.5, 1.8 Hz, 1H, aromatic CH), 5.91 (dd, *J* = 7.4, 3.4 Hz, 1H, olefinic CH), 5.68 (td, *J* = 7.7, 4.3 Hz, 1H, olefinic CH), 5.57 (td, *J* = 7.3, 3.1 Hz, 1H, olefinic CH), 3.12 (ddd, *J* = 14.5, 9.2, 4.8 Hz, 1H, aliphatic CH), 3.03 – 2.78 (m, 3H, aliphatic CH), 2.78 – 2.63 (m, 2H, aliphatic CH), 2.53 – 2.39 (m, 2H, aliphatic CH); ^{13}C NMR (101 MHz, CD_2Cl_2) δ 151.6, 145.7 (aromatic C), 114.1, 113.9, 112.9, 101.4, 98.1, 87.5 (aromatic/olefinic C), 35.5, 31.7, 31.5, 30.6 (aliphatic C); ^{195}Pt NMR (86 MHz, acetone-d_6)) δ -3151.48. HRMS (ES+): m/z calculated for $C_{12}H_{14}ClOPt^+$ 404.0381: found 404.0373 [M-

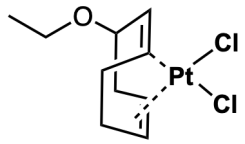
6.3.1.3 General synthetic procedure for Pt(II) complexes with allylic modified 1,5-cyclooctadiene ligands



27 **Pt6-Pt10**

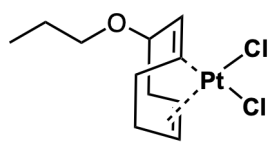
K_2PtCl_4 (1 eq.) was suspended in water (1.5 mL), and a primary alcohol (20 eq.) and compound **27** (5 eq.) were added. The reaction mixture was heated by microwave to 90°C for 75 minutes (low absorbance setting). Upon completion, the reaction mixture was concentrated *in vacuo* and the desired product was obtained through column chromatography (Heptane: EtOAc).

Compound **Pt6**



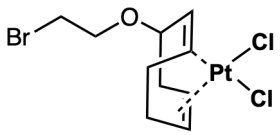
Light brown solid, 0.009 g, 0.022 mmol, 9% yield.^{1}H NMR (400 MHz, $CDCl_3$) δ 5.77 – 5.64 (m, 2H, olefinic CH), 5.55 – 5.46 (m, 1H, olefinic CH), 5.25 – 5.10 (m, 1H, olefinic CH), 4.65 (td, *J* = 8.7, 6.0 Hz, 1H, aliphatic O-CH), 3.60 (qd, *J* = 7.0, 3.4 Hz, 2H, aliphatic O-CH_2), 3.01 – 2.82 (m, 2H, aliphatic CH_2), 2.57 (ddt, *J* = 20.5, 11.4, 5.2 Hz, 2H, aliphatic CH), 2.29 (ddd, *J* = 21.4, 14.1, 6.5 Hz, 2H, aliphatic CH_2), 1.19 (s, 3H, aliphatic CH_3); ^{13}C NMR (101 MHz, $CDCl_3$) δ 103.5, 99.5, 94.2, 88.8 (olefinic C), 78.9 (aliphatic O-CH), 65.5 (O-CH_2), 32.8, 31.5, 27.7 aliphatic CH_2, 14.5 (aliphatic CH_3); ^{195}Pt NMR (86 MHz, $CDCl_3$) δ -3346.0; HRMS (ES+): m/z calculated for $C_{10}H_{20}Cl_2NOPt^+$ 435.0570: found 435.0573 $[M+NH_4]^+$.

Compound **Pt7**



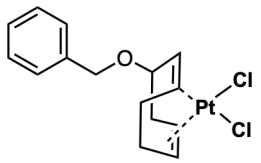
White solid, 0.014 g, 0.032 mmol, 13% yield. ^{1}H NMR (300 MHz, $CDCl_3$) δ 5.77 – 5.63 (m, 2H, olefinic CH), 5.51 (td, *J* = 8.2, 5.9 Hz, 1H, olefinic CH), 5.21 (tdd, *J* = 8.0, 6.5, 1.2 Hz, 1H, olefinic CH), 4.64 (td, *J* = 8.5, 5.9 Hz, 1H, aliphatic O-CH), 3.49 (td, *J* = 6.6, 1.9 Hz, 2H, aliphatic O-CH_2), 3.05 – 2.79 (m, 2H, aliphatic CH_2), 2.68 – 2.49 (m, 2H, aliphatic CH_2), 2.30 (tt, *J* = 14.1, 6.6 Hz, 2H, aliphatic CH_2), 1.61 (m, 2H, aliphatic CH_2), 0.92 (t, *J* = 7.4 Hz, 3H, aliphatic CH_3). ^{13}C NMR (101 MHz, $CDCl_3$) δ 104.4, 100.5, 95.2, 89.9 (olefinic C), 80.1 (aliphatic O-CH), 72.7 (aliphatic O-CH_2), 33.9, 32.4, 28.8, 23.2 (aliphatic CH_2), 10.5 (aliphatic CH_3); ^{195}Pt NMR (86 MHz, $CDCl_3$) δ -3343.2; HRMS (ES+): m/z calculated for $C_{11}H_{18}Cl_2KOPt^+$ 470.0014: found 470.0011 $[M+K]^+$.

Compound **Pt8**



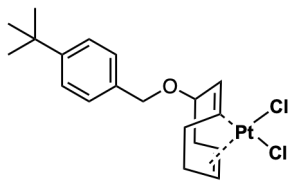
Dark brown solid, 0.036 g, 0.072 mmol, 10% yield. ^{1}H NMR (400 MHz, $CDCl_3$) δ 5.76 (ddd, *J* = 16.6, 8.2, 3.3 Hz, 4H, olefinic CH), 4.16 – 4.02 (m, 1H, aliphatic O-CH), 3.96 – 3.81 (m, 2H, aliphatic O-CH_2), 3.50 (t, *J* = 5.9 Hz, 2H, CH_2-Br), 2.79 – 2.66 (m, 2H, (aliphatic CH_2), 2.61 – 2.46 (m, 2H, (aliphatic CH_2), 2.18 – 2.08 (m, 1H, aliphatic CH_2), 1.90 – 1.79 (m, 1H, (aliphatic CH_2); ^{13}C NMR (101 MHz, $CDCl_3$) δ 101.4, 101.0, 97.6, 97.5 (olefinic C), 81.0 (aliphatic O-CH), 69.8 (aliphatic O-CH_2), 39.8, 32.5, 30.6, 30.1 (aliphatic CH_2); ^{195}Pt NMR (86 MHz, $CDCl_3$) δ -3638.5.

Compound **Pt9**



Yellow solid, 0.014 g, 0.030 mmol, 8% yield. ^{1}H NMR (400 MHz, $CDCl_3$) δ 7.41 – 7.29 (m, 5H, aromatic CH), 5.77 – 5.60 (m, 2H, olefinic C), 5.49 (td, *J* = 8.2, 5.9 Hz, 1H, olefinic C), 5.17 (q, *J* = 7.3 Hz, 1H, olefinic C), 4.72 (td, *J* = 8.8, 6.0 Hz, 1H, O-CH), 4.61 (s, 2H, aliphatic CH), 2.97 – 2.81 (m, 2H, aliphatic CH), 2.66 – 2.51 (m, 2H, aliphatic CH), 2.40 – 2.25 (m, 2H, aliphatic CH). ^{13}C NMR (101 MHz, $CDCl_3$) δ 137.03, 128.76, 128.5, 127.8, 104.7 (aromatic C), 100.5, 94.8, 89.5 (olefinic C), 79.3 (O-CH), 72.9 (O-CH_2), 33.7, 32.6, 28.7 (aliphatic CH_2); ^{195}Pt NMR (86 MHz, $CDCl_3$) δ -3342.0. HRMS (ES+): m/z calculated for $C_{15}H_{22}Cl_2NOPt^+$ 497.0721: found 497.0717 $[M+NH_4]^+$.

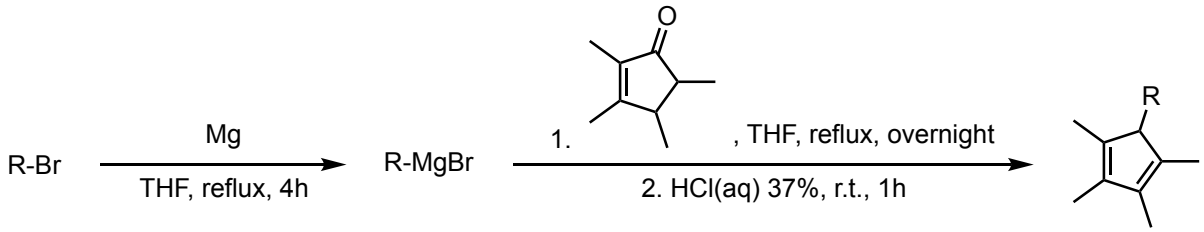
Compound **Pt10**



Yellow solid, (0.022 g, 0.042 mmol, 12% yield). ^{1}H NMR (400 MHz, $CDCl_3$) δ 7.31 (d, *J* = 8.2 Hz, 2H, aromatic CH), 7.18 – 7.13 (m, 2H, aromatic CH), 5.66 – 5.58 (m, 1H, olefinic C), 5.57 – 5.48 (m, 1H, olefinic C), 5.47 – 5.35 (m, 1H, olefinic C), 5.12 – 4.95 (m, 1H, olefinic C), 4.66 – 4.56 (m, 1H, aliphatic O-CH), 4.48 (s, 1H, aliphatic CH), 2.88 – 2.73 (m, 2H, aliphatic CH), 2.55 – 2.41 (m, 2H, aliphatic CH), 2.22 (ddd, *J* = 21.0, 11.8, 7.3 Hz, 3H, aliphatic CH), 1.23 (s, 9H, *tert*-butyl CH_3); ^{13}C NMR (101 MHz, $CDCl_3$) δ 151.6, 133.9, 127.8, 126.9, 125.7 (aromatic C), 104.7, 100.6, 95.0, 89.6 (olefinic C), 79.0 (O-CH), 72.6 (O-CH_2), 34.7 (*tert*-butyl quaternary C), 33.6, 32.6, 31.3, 28.7 (aliphatic C); ^{195}Pt NMR (86 MHz, $CDCl_3$) δ -3343.4.

6.3.2 Unlocking Iridium Chemical Space for Antibiotic Discovery through One-Pot Combinatorial Synthesis in a Direct-to-Biology Approach

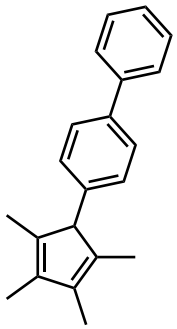
6.3.2.1 General synthesis procedure for cyclopentadenyl (Cp) ligands



Previously dried double-neck round-bottom flask was loaded with Mg turnings (6 eq.), 1 grain I_2, anhydrous THF (50 mL), and corresponding bromide (1 eq.) and the reaction mixture was refluxed at 72 °C for 4 hours under N_2 atmosphere. After it was cooled down to room temperature, it was added dropwise to the stirred solution of 2,3,4,5-tetramethyl-

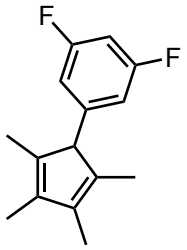
2-cyclopentenone (1.2 eq.) in anhydrous THF (40 mL). The reaction mixture was stirred at 65°C overnight under N_2 atmosphere. Afterward, the reaction mixture was cooled to room temperature and acidified with 30 mL of 37% HCl(aq). It was stirred at room temperature for 1 hour. The reaction progress was monitored by TLC, and upon completion, the reaction mixture was diluted with EtOAc. The organic phase was separated, and the aqueous phase was washed three times with EtOAc. The combined organic phase was washed with distilled water, dried over $MgSO_4$, and concentrated in vacuo. The desired products were obtained through flash column chromatography (for Cp**2** and **3**, Hexane: Toluene (99:1); for Cp**4**, Hexane).

Compound **Cp2**



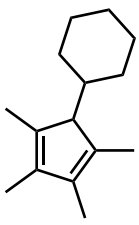
Yellow solid, 1.80 g, 6.55 mmol, 41% yield. ^{1}H NMR (400 MHz, $CDCl_3$) δ 7.66 – 7.59 (m, 4H, aromatic C), 7.47 – 7.42 (m, 2H, aromatic C), 7.36 – 7.31 (m, 3H, aromatic C), 3.25 (d, *J* = 9.4 Hz, 1H, aliphatic CH), 2.09 (d, *J* = 1.8 Hz, 3H, aliphatic CH_3), 1.96 (d, *J* = 1.1 Hz, 3H, aliphatic CH_3), 1.90 – 1.87 (m, 3H, aliphatic CH_3), 1.01 (d, *J* = 7.7 Hz, 3H, aliphatic CH_3); ^{13}C NMR (101 MHz, $CDCl_3$) δ 142.3, 141.1, 138.1, 137.7, 136.2, 135.3, 128.8, 128.8, 127.1, 127.0, 126.9 (aromatic and olefinic C), 50.1 (aliphatic CH), 15.0, 13.0, 12.1, 11.2 (CH_3). HRMS (ES+): m/z calculated for $C_{21}H_{23}^+$ 275.1794: found 275.1788 $[M+H]^+$.

Compound **Cp3**



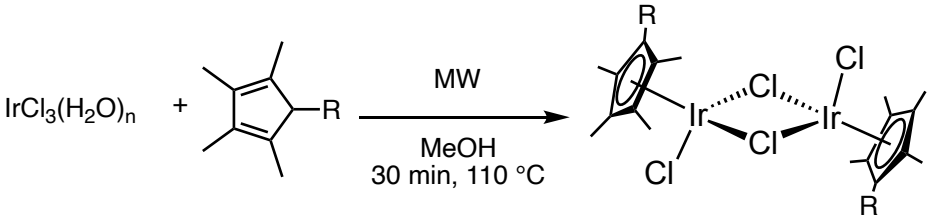
Bright yellow oil, 2.66 g, 11.35 mmol, 37% yield. ^{1}H NMR (400 MHz, $CDCl_3$) δ 6.76 (ddt, *J* = 8.0, 4.2, 2.1 Hz, 2H, aromatic CH), 6.68 – 6.61 (m, 1H, aromatic CH), 3.14 (s, 1H, aliphatic CH), 2.09 – 2.03 (m, 3H, CH_3), 1.95 (dd, *J* = 4.4, 1.1 Hz, 3H, CH_3), 1.88 (dd, *J* = 3.5, 2.1 Hz, 3H, CH_3), 1.03 – 0.96 (m, 3H, CH_3); ^{13}C NMR (101 MHz, $CDCl_3$) δ 164.35 (aromatic C-F), 161.75 (aromatic C-F), 142.13, 139.81, 135.20, 110.77, 110.71, 100.88, 100.62, 100.37 (aromatic and olefinic C), 50.12, 14.66, 12.86, 11.97, 11.08 (CH_3); ^{19}F NMR (376 MHz, $CDCl_3$) δ -110.96. HRMS (ES+): m/z calculated for $C_{15}H_{17}F_2^+$ 235.1293: found 235.1303 $[M+H]^+$.

Compound **Cp4**



Yellow oil, 0.700 g, 19% yield. m/z calculated for $C_{15}H_{25}^+$ 205.1951: found 205.1952 $[M+H]^+$. GC-MS was analysis performed, R_t: 5.79 min. m/z calculated for $C_{15}H_{24}$ 204.1878: found 204.1868. This product was used without further purification.

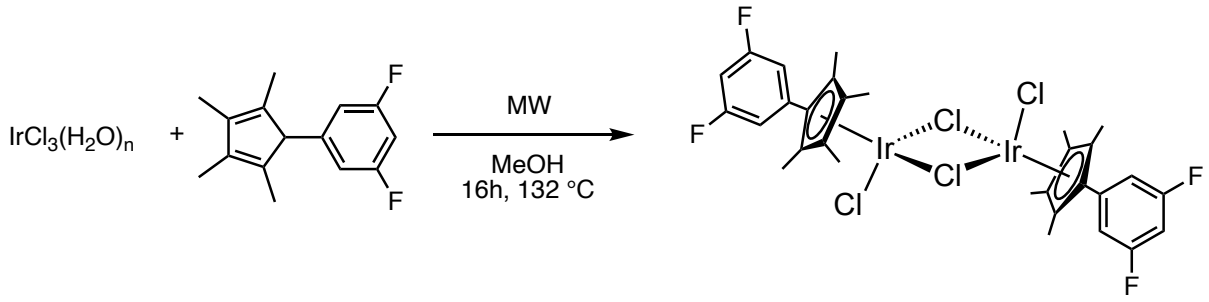
6.3.2.2 General Synthesis Procedure for Ir(Cp-R) Dimers (IrCp1 (Cp*), Cp2, and Cp4)[336]



$IrCl_3(H_2O)_n$ (0.500 g, 1 eq.), and the corresponding Cp derivative were suspended in 4 mL MeOH in a microwave vial. The reaction mixture was irradiated with microwave at 110°C for 30 minutes. Upon the reaction completion, 4 mL *n*-pentane was added into reaction mixture and stirred vigorusly. The formed precipitate was collected and washed with *n*-pentane (3 x 4 mL). The final precipiate was dried *in vacuo* and the desired product was obtained. *As we do not know the molecular weight of iridium starting material, the yields of the reactions cannot be calculated.*

Note on compound nomenclature: Compounds labelled **Ir[number]** represent selected isolated iridium complexes based on the dose-response biological screening of crude mixtures, whereas **IrCp1**–**4** refer to the corresponding iridium cyclopentadienyl dimer. Compounds labelled as **IrCp1**(K, L, B)(7, 8) are antifungal hit compounds where the letter represents the corresponding aldehyde and the number the corresponding amine building blocks. Unprefixed numbers refer to the compounds as numbered in the synthetic and characterisation section.

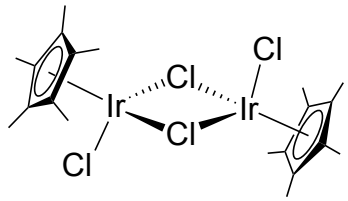
6.3.2.3 Synthesis of IrCp3 dimer



$IrCl_3(H_2O)_n$ (0.500 g, 1 eq.), and **Cp3** (2.00 g, 8.53 mmol, 4 eq.) were suspended in 4 mL MeOH in a microwave vial. The reaction mixture was irradiated with microwave at 132°C for 30 16 hours. Upon the reaction completion, 4 mL *n*-pentane was added into reaction mixture and stirred vigorusly. The formed precipitate was collected and washed with *n*-pentane (3 x 4 mL). The final precipiate was dried *in vacuo* and the desired product was obtained as orange solid. Orange solid, 0.350 g. ^{1}H NMR (400 MHz, $CDCl_3$) δ 7.16 (s,

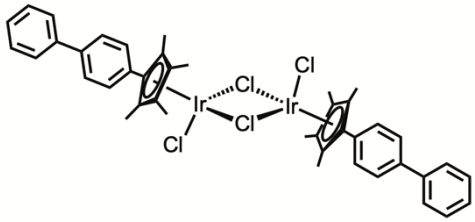
4H, aromatic CH), 6.87 – 6.80 (m, 2H, aromatic CH), 1.74 (s, 12H, CH_3), 1.64 (s, 12H, CH_3); ^{13}C NMR (101 MHz, $CDCl_3$) δ 163.3 (aromatic C-F), 163.2 (aromatic C-F), 160.8 (aromatic C-F), 160.7 (aromatic C-F), 132.7, 112.6, 112.3, 103.31, 92.8, 85.3 (aromatic C), 9.3, 8.5 (CH_3); ^{19}F NMR (376 MHz, $CDCl_3$) δ -108.25. HRMS (ESI+): m/z calculated for $C_{30}H_{31}Cl_2F_4Ir_2^+$ 923.0992: found 923.0979 $[M-2Cl+H]^+$. *As we do not know the molecular weight of iridium starting material, the yield of the reaction cannot be calculated.*

Compound **IrCp1**



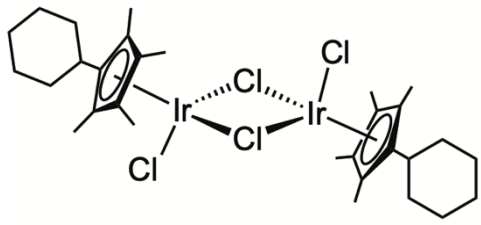
Orange solid, 0.350 g, ^1H NMR (400 MHz, $CDCl_3$) δ 1.55 (s, 30H).

Compound **IrCp2**



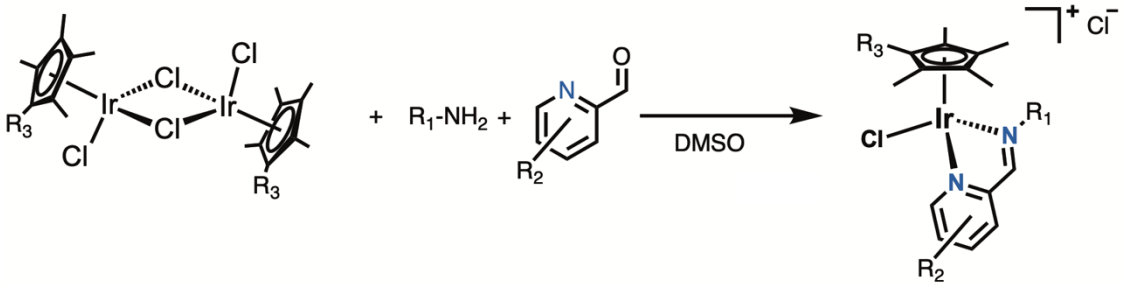
Dark yellow solid, 0.240 g. ^1H NMR (400 MHz, $CDCl_3$) δ 7.65 (d, *J* = 8.4 Hz, 4H, aromatic CH), 7.60 – 7.56 (m, 8H, aromatic CH), 7.44 (t, *J* = 7.9 Hz, 4H, aromatic CH), 7.38 – 7.33 (m, 2H, aromatic CH), 1.75 (s, 12H, CH_3), 1.69 (s, 12H, CH_3); ^{13}C NMR (101 MHz, $CDCl_3$) δ 141.4, 140.7, 130.8, 129.0, 127.6, 127.6, 127.2, 93.6, 85.8 (aromatic

Compound **IrCp4**



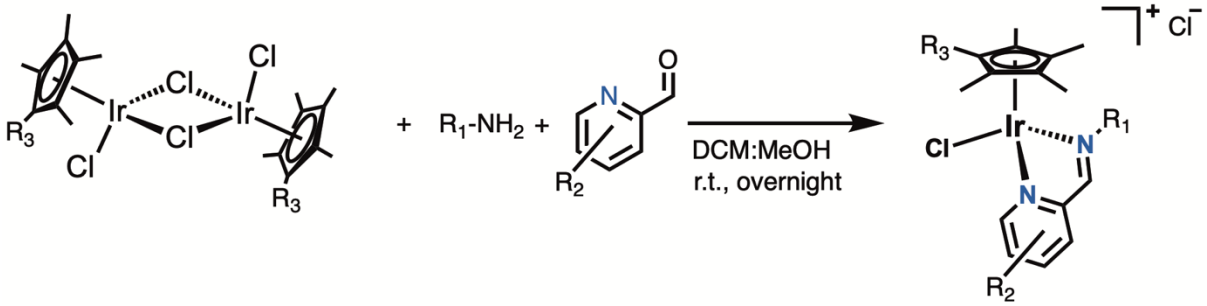
Orange solid, 0.225 g. ^1H NMR (400 MHz, $CDCl_3$) δ 2.07 – 1.98 (m, 2H, aliphatic CH), 1.89 (d, *J* = 12.1 Hz, 3H, aliphatic CH), 1.72 (d, *J* = 3.9 Hz, 3H, aliphatic CH), 1.65 (s, 12H, CH_3), 1.57 (s, 11H, aliphatic CH), 1.37 – 1.20 (m, 7H, aliphatic CH), 1.18 – 1.05 (m, 2H, aliphatic CH), 0.04 (s, 5H, aliphatic CH); ^{13}C NMR (101 MHz, $CDCl_3$) δ 90.7, 86.0 35.7, 30.8, 27.0, 26.2 (cyclohexyl aliphatic C), 10.7, 9.7 (CH_3).

6.3.2.4 Combinatorial synthesis of compound libraries



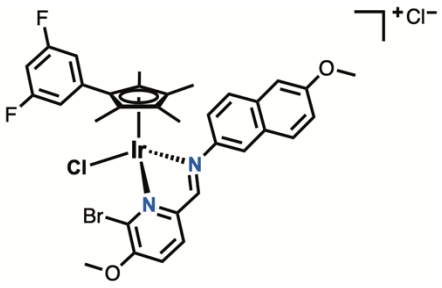
Stock solutions of IrCp dimers (15 mM), amines (30 mM), and aldehydes (30 mM) were prepared in DMSO. 60 µL of each component was dispensed into 96-well plates using an Opentrons OT-2 liquid handling robot. The reaction mixtures were incubated at room temperature for three days. After incubation, the plates were analysed by LC-MS.

6.3.2.5 Syntheses of hit compounds



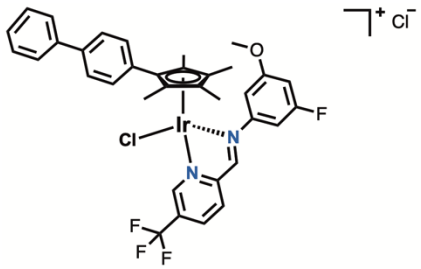
Ir dimer (0.5 eq.), corresponding aldehyde (1 eq.) and amine (1 eq.) were dissolved in DCM:MeOH (1:1) and stirred overnight. Reaction progress was monitored by LC-MS. Upon completion, excess amount of *n*-hexane was added and the precipitate collected. The desired product was obtained by flash column chromotography (DCM:MeOH for **IrCp3 complex**, for **IrCp2 complexes** DCM:MeOH:Toluene 90:8:2).

Compound **Ir9**



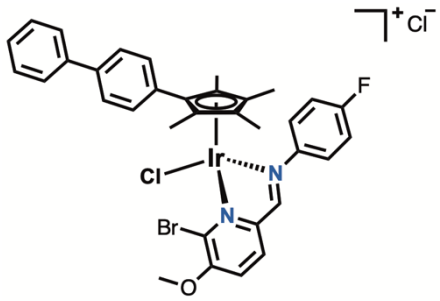
Orange solid, 0.026 g, 0.031 mmol, 27% yield. R_T: 3.09 min. ^{1}H NMR (400 MHz, DMSO-d_6) δ 9.60 (s, 1H, CH=N), 8.43 (d, *J* = 8.6 Hz, 1H, aromatic CH), 8.15 (d, *J* = 2.2 Hz, 1H, aromatic CH), 8.04 (d, *J* = 8.7 Hz, 1H, aromatic CH), 7.96 (d, *J* = 8.9 Hz, 1H, aromatic CH), 7.87 (dd, *J* = 8.8, 2.2 Hz, 1H, aromatic CH), 7.82 (d, *J* = 9.0 Hz, 1H, aromatic CH), 7.43 (tt, *J* = 4.7, 2.3 Hz, 2H, aromatic CH), 7.28 (dd, *J* = 9.0, 2.5 Hz, 1H, aromatic CH), 7.20 – 7.14 (m, 2H, aromatic CH), 4.12 (s, 3H, O-CH_3), 3.91 (s, 3H, O-CH_3), 1.53 (d, *J* = 1.9 Hz, 6H, CH_3), 1.30 (d, *J* = 5.3 Hz, 6H, CH_3); ^{13}C NMR (176 MHz, DMSO- d_6) δ 169.5 (CH=N), 159.0 (aromatic C-F), 158.4 (Ar-F), 148.4, 144.6 (Ar-F), 140.5, 134.9, 131.8, 130.3, 128.6, 127.9, 122.0, 121.9, 121.2, 120.9, 113.6, 113.5, 106.8 (aromatic C), 99.7, 97.9, 90.2, 88.9, 81.2 (Cp ring C), 58.9, 55.9 (O-CH_3), 11.0, 9.9, 9.7, 8.8 (CH_3); ^{19}F NMR (376 MHz, DMSO-d_6) δ -108.36. HRMS (ES+): m/z calculated for $C_{33}H_{30}ClF_2IrN_2O_2^+$ 831.0776: found 831.0771 $[M]^+$.

Compound **Ir14**



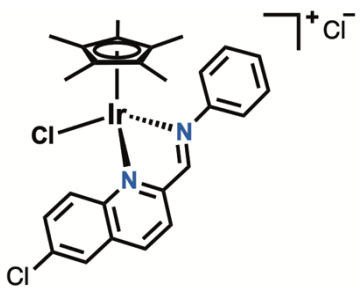
Dark orange solid, 0.025 g, 45% yield. R_T: 3.31 min. ^{1}H NMR (500 MHz, DMSO-d_6) δ 9.67 (s, 1H, CH=N), 8.82 (d, *J* = 8.1 Hz, 1H, aromatic CH), 8.72 (d, *J* = 8.2 Hz, 1H, aromatic CH), 8.58 (s, 1H), 7.82 (d, *J* = 8.0 Hz, 2H, aromatic CH), 7.73 (d, *J* = 7.6 Hz, 2H, aromatic CH), 7.65 (d, *J* = 7.9 Hz, 2H, aromatic CH), 7.53 (t, *J* = 7.6 Hz, 2H, aromatic CH), 7.44 (t, *J* = 7.3 Hz, 1H, aromatic CH), 7.21 (s, 1H, aromatic CH), 7.16 (d, *J* = 8.9 Hz, 1H, aromatic CH), 7.13 – 7.08 (m, 1H, aromatic CH), 3.84 (s, 3H, O-CH_3), 1.79 (s, 3H, CH_3), 1.57 (s, 3H, CH_3), 1.50 (s, 3H, CH_3), 1.38 (s, 3H, CH_3); ^{13}C NMR (176 MHz, DMSO) δ 170.4 (CH=N), 163.8, 162.4 (Ar-F), 161.4, 159.2, 141.5, 139.7, 131.4, 130.9, 129.6 (aromatic C), 128.5, 128.5 (C-F_3), 128.0, 127.6, 127.2, 106.1, 103.4 (aromatic C), 95.3, 93.2, 85.2, 83.5 (Cp* ring C), 56.7 (O-CH_3), 10.1, 9.6, 8.5, 8.5 (CH_3); ^{19}F NMR (471 MHz, DMSO) δ -61.68.HRMS (ES+): m/z calculated for $C_{35}H_{31}ClF_2IrN_2O^+$ 799.1690: found 799.1692 $[M]^+$.

Compound **Ir15**



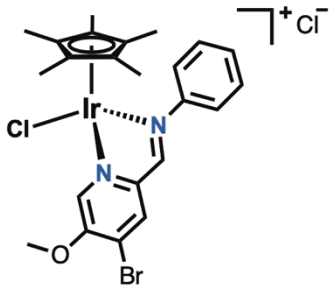
Dark orange solid, 0.053 g, 47% yield. R_T: 3.23 min. ^{1}H NMR (400 MHz, CD_2Cl_2-d_2) δ 10.19 (s, 1H, CH=N), 9.07 (d, *J* = 8.0 Hz, 1H, aromatic CH), 8.05 (dd, *J* = 9.0, 4.5 Hz, 2H, aromatic CH), 7.66 – 7.60 (m, 5H, aromatic CH), 7.44 (td, *J* = 8.2, 1.8 Hz, 4H, aromatic CH), 7.39 – 7.34 (m, 1H, aromatic CH), 7.15 (t, *J* = 8.6 Hz, 2H, aromatic CH), 4.02 (s, 3H, O-CH_3), 1.70 (s, 3H), 1.52 (s, 3H), 1.36 (s, 3H), 1.26 (s, 3H); ^{13}C NMR (101 MHz, CD_2Cl_2-d_2) δ 169.9 (CH=N), 161.6, 157.9 (Ar-F), 149.3, 145.4, 141.5, 139.9, 139.8, 132.9, 130.3, 129.2, 129.0, 127.9, 127.6, 127.0, 125.3, 125.2, 120.2, 116.6, 116.3 (aromatic C), 98.1, 87.3, 84.9 (Cp* ring C), 58.1 (O-CH_3), 10.8, 10.2, 9.0, 8.8 (CH_3); ^{19}F NMR (471 MHz, DMSO) δ -111.43.HRMS (ES+): m/z calculated for $C_{34}H_{31}BrClFIrN_2O^+$ 809.0922: found 809.0916 $[M]^+$.

Compound **IrCp1K7**



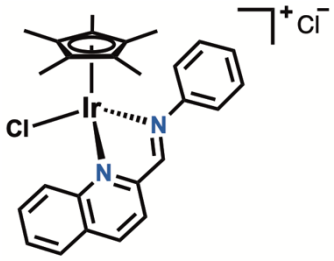
Dark brown solid, 0.063 g, 0.100 mmol, 94% yield. LC-MS R_T: 2.65 min. ^{1}H NMR (400 MHz, $CDCl_3$) δ 9.97 (s, 1H, CH=N), 8.83 (d, *J* = 8.4 Hz, 1H, aromatic CH), 8.47 (d, *J* = 9.3 Hz, 1H, aromatic CH), 8.37 (d, *J* = 7.9 Hz, 1H, aromatic CH), 8.32 (d, *J* = 8.4 Hz, 2H, aromatic CH), 8.01 (d, *J* = 2.3 Hz, 1H, aromatic CH), 7.80 (dd, *J* = 9.2, 2.3 Hz, 1H, aromatic CH), 7.54 (t, *J* = 7.7 Hz, 2H, aromatic CH), 7.46 (t, *J* = 7.5 Hz, 1H, aromatic CH), 1.44 (s, 15H, CH_3); ^{13}C NMR (101 MHz, $CDCl_3$) δ 169.3 (CH=N), 143.9, 139.6, 136.2, 133.1, 130.9, 130.6, 130.0, 129.7, 127.8, 127.1, 123.9 (aromatic C), 90.3 (Cp* ring C), 9.1 (CH_3). HRMS (ES+): m/z calculated for $C_{26}H_{26}Cl_2IrN_2^+$ 629.1102: found 629.1075 $[M]^+$.

Compound **IrCp1L7**



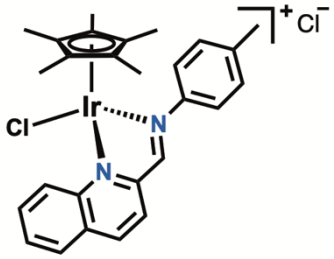
Orange solid, 0.094 g, 0.143 mmol,, 100% yield. LC-MS R_T: 2.46 min. ^{1}H NMR (400 MHz, $CDCl_3$) δ 9.58 (s, 1H, CH=N), 8.86 (s, 1H, aromatic CH), 8.20 (s, 1H, aromatic CH), 7.94 (d, *J* = 11.6 Hz, 2H, aromatic CH), 7.48 (t, *J* = 7.7 Hz, 2H, aromatic CH), 7.42 – 7.37 (m, 1H, aromatic CH), 4.19 (s, 3H, O-CH_3), 1.51 (s, 15H, CH_3); ^{13}C NMR (101 MHz, $CDCl_3$) δ 167.2 (CH=N), 156.7, 151.0, 149.2, 134.8, 133.6, 129.6, 126.0, 123.4 (aromatic C), 90.0 (Cp* ring C), 57.9, 8.9. HRMS (ES+): m/z calculated for $C_{23}H_{26}BrClIrN_2O^+$ 653.0546: found 653.0511 $[M]^+$.

Compound **IrCp1B7**



Dark red solid, 0.046 g, 0.077 mmol, 72% yield. LC-MS R_T: 2.74 min. ^{1}H NMR (400 MHz, $CDCl_3$) δ 10.02 (s, 1H, CH=N), 8.85 (d, *J* = 8.4 Hz, 1H, aromatic CH), 8.53 – 8.45 (m, 2H, aromatic CH), 8.32 (d, *J* = 7.6 Hz, 2H, aromatic CH), 8.02 (d, *J* = 9.7 Hz, 1H, aromatic CH), 7.91 – 7.86 (m, 1H, aromatic CH), 7.81 (t, *J* = 6.9 Hz, 1H, aromatic CH), 7.54 (t, *J* = 7.6 Hz, 2H, aromatic CH), 7.45 (t, *J* = 7.3 Hz, 1H, aromatic CH), 1.43 (s, 15H, CH_3); ^{13}C NMR (101 MHz, $CDCl_3$) δ 169.9 (CH=N), 158.4, 149.44, 145.6, 141.0, 130.3, 130.0, 130.0, 129.7, 129.5, 129.3, 126.3, 124.0 (aromatic C), 90.3 (Cp* ring C), 9.1. HRMS (ES+): m/z calculated for $C_{26}H_{27}ClIrN_2^+$ 595.1492: found 595.1474 $[M]^+$.

Compound **IrCpB8**



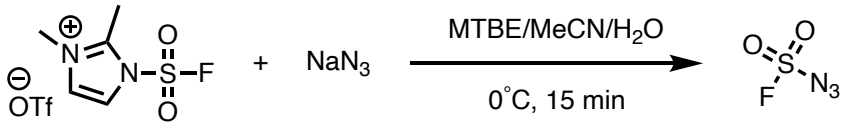
Brown solid, 0.060 g, 0.01 mmol, 100% yield. LC-MS R_T: 2.60 min. ^{1}H NMR (400 MHz, $CDCl_3$) δ 10.01 (s, 1H, CH=N), 8.86 (d, *J* = 8.4 Hz, 1H, aromatic CH), 8.47 (dd, *J* = 17.7, 8.5 Hz, 2H, aromatic CH), 8.19 (d, *J* = 6.6 Hz, 2H, aromatic CH), 8.00 (dd, *J* = 8.1, 1.6 Hz, 1H, aromatic CH), 7.79 (ddd, *J* = 8.1, 6.9, 1.3 Hz, 1H, aromatic CH), 7.31 (t, *J* = 8.0 Hz, 2H, aromatic CH), 2.42 (s, 3H, Ar-CH_3), 1.42 (s, 15H, CH_3); ^{13}C NMR (101 MHz, $CDCl_3$) δ 169.2 (CH=N), 158.4, 147.1, 145.6, 140.9, 140.4, 132.2, 130.2, 129.9, 129.4, 129.2, 126.2, 123.8 (aromatic C), 90.1 (Cp* ring C), 21.5 (Ar-CH_3), 9.0 (CH_3). HRMS (ES+): m/z calculated for $C_{27}H_{29}ClIrN_2^+$ 609.1649: found 609.1635 $[M]^+$.

6.3.3 Additional Research Contributions and Supervised Research Projects

6.3.3.1 Preparation of ligand library

The following procedure was carried out using an Opentrons liquid handling robot OT2, utilizing both 300 µL and 20 µL pipettes (Gen2). This procedure generates ligands at nominal concentration of 20 mM in 400 µL of solvent. It should be noted that the solubility of some ligands is an issue, with a number precipitating or crystallizing out of solution over time. This can be mitigated to a certain extent by further dilution, or by sonicating the individual reaction vials to pulverize the crystals. For accurate additions, these ligand solutions were aspirated 3 times to ensure efficient mixing before dispensing.

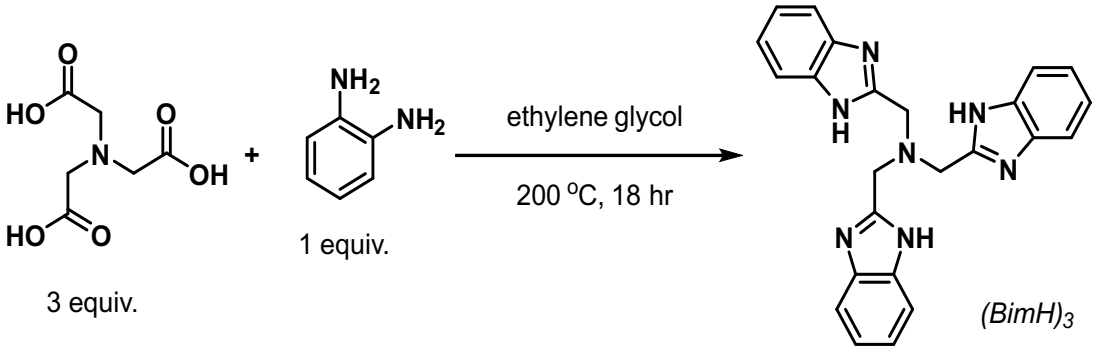
FSO_2N_3 reagent[386]



NaN_3 (99 mg, 1.524 mmol, 1 equiv.) was dissolved in deionized water (3.0 mL) in a 15 mL falcon tube. Sodium azide (NaN_3) is highly toxic and may form volatile, highly toxic hydrazoic acid upon contact with acids. It can also react with heavy metals to produce shock-sensitive explosive metal azides. Therefore, it was handled in a fume hood using appropriate personal protective equipment, and all waste was collected separately for disposal as hazardous waste. To this, 3.0 mL of MTBE was added and the mixture stirred vigorously at 0°C. Separately, 1-(fluorosulfonyl)-2,3-dimethyl-1H-imidazol-3-ium trifluoromethanesulfonate (600 mg, 1.83 mmol, 1.2 equiv.) was dissolved in 150 µL of MeCN in a falcon tube and was added to the reaction mixture. A further 150 µL of MeCN was used to wash the falcon tube and ensure efficient transfer of material, with this also being added to the reaction mixture. The mixture was stirred vigorously at 0 °C with the lid loosely screwed on top for 15 min, then allowed to settle at r.t. for 30 min The upper organic layer was decanted and diluted with 3 mL DMSO, giving a solution of FSO_2N_3 of approximately 173 mM (calculated according to the method described by Meng *et al.*).[386]

The following procedure assumes a concentration of 173 mM for FSO_2N_3 and describes the addition to 1 well of a Paradox® 96 well plate (700 µL glass vial) using a Opentrons OT2 liquid handling robot (P300 Gen2 300 µL pipette and P20 Gen2 20 µL pipette). It is also adapted from Meng *et al.*[386]

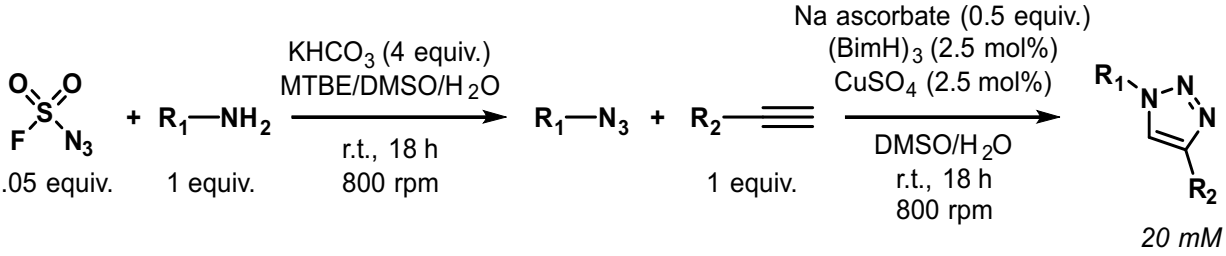
Compound **$(BimH)_3$**



Nitrilotriacetic acid (2.49 g, 13 mmol, 1 equiv.), *o*-phenylenediamine (4.22 g, 39 mmol, 3 equiv.) and ethylene glycol (30 mL) were charged into a round bottom flask fitted with an

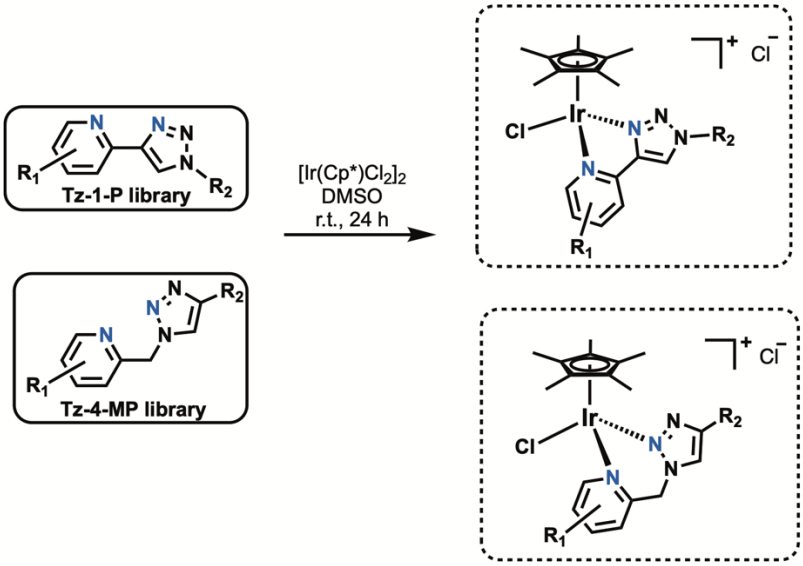
air condenser. The reaction was heated to 200 °C using a metal heating block and stirred for 18 h. The mixture was poured into a beaker containing ice-water, and stirred for 5 min, giving a thick beige precipitate. This precipitate was collected by filtration, transferred to a round bottom flask with 50 mL of MeOH and charcoal (2 heaped tsp) and refluxed for 30 min. The mixture was filtered hot, and the MeOH evaporated to approx. 15 mL in a conical flask. The flask was cooled on ice, and upon scratching, crystals formed. These were isolated by filtration, washed with a small quantity of cold MeOH to remove the red impurity, and dried *in vacuo*. The desired product was filtrated, washed with small quantity of cold MeOH, dried *in vacuo* and obtained as beige crystals (1.26 g, 24%). ^{1}H NMR (600 MHz, DMSO-d_6) δ 12.60 – 12.34 (m, 3H, benzimidazole NH), 7.57 (d, J = 45.7 Hz, 6H, aromatic CH), 7.29 – 7.09 (m, 6H, aromatic CH), 4.15 (s, 6H, N-CH_2); ^{13}C NMR (151 MHz, DMSO-d_6) δ 152.2, 143.2, 134.2, 122.0, 121.1, 118.6, 111.2 (aromatic C), 51.4 (N-CH_2); HRMS (ES+): m/z calculated for $C_{24}H_{22}N_7^+$) 408.1931: found 408.1937 $[M]^+$.

6.3.3.2 Preparation of the ligand library



To the reaction well, sat. $KHCO_3$ solution (11 µL, 4 equiv., nominally 3 M), followed by DMSO (65 µL, Note: this is the volume required to make up the total volume to 200 µL, while additionally accounting for evaporation of MTBE, which is half the volume of the FSO_2N_3 stock solution) was added, then amine stock solution (100 µL, 80 mM, 1 equiv.). FSO_2N_3 stock solution was then added (48 µL, 173 mM 1.05 equiv., Note: the pipette was aspirated 3 times to equilibrate solvent vapor pressure. It is recommended to prepare a significant excess (25%) of the Sharpless reagent to account for evaporation during addition). The reaction vials were then sealed, and shaken at 800 rpm for 18 h at r.t. Next, to each reaction well, sodium ascorbate solution (80 µL, 50 mM, 0.5 equiv.) was added and the reaction shaken for a further 15 min at r.t. To each reaction well, alkyne stock solution (100 µL, 80 mM, 1 equiv.) was added, followed by $(BimH)_3$ solution in DMSO (10 µL, 20 mM, 2.5 mol%), then $CuSO_4$ solution in water (10 µL, 20 mM, 2.5 mol%). The reaction was sealed, and shaken at 800 rpm for 18 h at r.t. The reaction mixture was analysed by LC-MS.

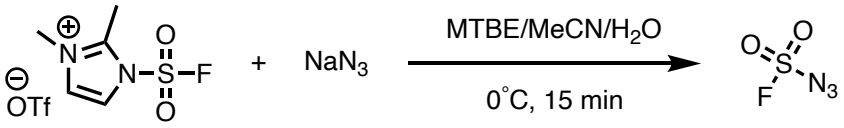
6.3.3.3 Synthesis of IrCp(Tz-1-P) and IrCp(Tz-4-MP) libraries



Stock solutions of IrCp dimers (10 mM) were prepared in DMSO. Ligand stock solutions (30 µL, 20 mM) and IrCp stock solutions (30 µL, 10 mM) were dispensed into 96-well plates using the Opentrons OT-2 liquid handling robot. The reaction plates were allowed to stand for 24 hours at room temperature and analysed by LC-MS.

6.3.3.4 Batch syntheses of hit compounds

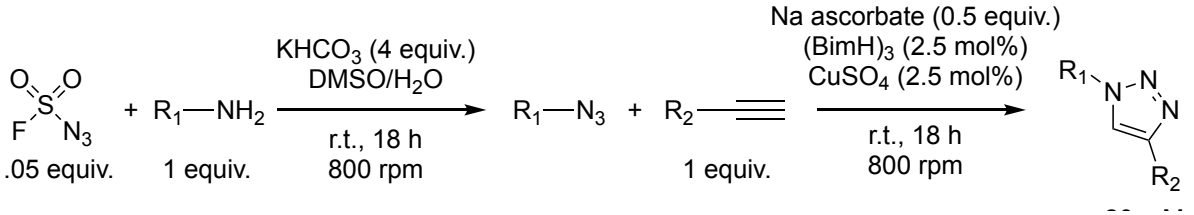
FSO_2N_3 reagent



NaN_3 (99 mg, 1.524 mmol, 1 equiv.) was dissolved in deionized water (3.0 mL) in a 15 mL falcon tube. Sodium azide (NaN_3) is highly toxic and may form volatile, highly toxic hydrazoic acid upon contact with acids. It can also react with heavy metals to produce shock-sensitive explosive metal azides. Therefore, it was handled in a fume hood using appropriate personal protective equipment, and all waste was collected separately for disposal as hazardous waste.To this, 3.0 mL of MTBE was added and the mixture stirred vigorously at 0°C. Separately, 1-(fluorosulfonyl)-2,3-dimethyl-1H-imidazol-3-ium trifluoromethanesulfonate (600 mg, 1.83 mmol, 1.2 equiv.) was dissolved in 150 µL of MeCN in a falcon tube and was added to the reaction mixture. A further 150 µL of MeCN

was used to wash the falcon tube and ensure efficient transfer of material, with this also being added to the reaction mixture. The mixture was stirred vigorously at 0 °C with the lid loosely screwed on top for 15 min, then allowed to settle at r.t. for 30 min The upper organic layer was decanted and diluted with 3 mL DMSO, giving a solution of FSO_2N_3 of approximately 175.67 mM (calculated according to the method described by Meng *et al.*).[386]

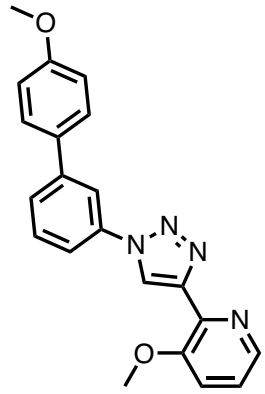
6.3.3.5 Batch syntheses of ligands



FSO_2N_3 was synthesized as before and diluted with DMF to approx. 176 mM in 1:1 MTBE:DMF. The desired amine (0.56 mmol, 1.0 equiv.) was charged into a 50 mL polypropylene Falcon tube, followed by DMF (7 mL). Sat. $KHCO_3$ solution (0.8 mL, approx. 2.4 mmol, 4 equiv. in water) was added, followed by FSO_2N_3 solution (1.05 equiv.). The resulting mixture was stirred at r.t. for 18 h. Sodium ascorbate solution (5.6 mL, 50 mM, 0.5 equiv. in water) was added, and the mixture was stirred for a further 10 mins. 7 mL of DMF was added, followed by alkyne (0.56 mmol, 1.0 equiv.), then $(BimH)_3$ solution (0.7 mL, 20 mM, 2.5 mol% in DMF) and $CuSO_4$ solution (0.7 mL, 20 mM, 2.5 mol% in water). The resulting mixture was stirred for a further 18 h at r.t.

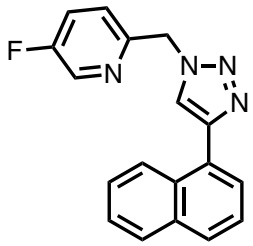
The crude reaction mixture was analyzed by LC-MS, then 100 mL of deionized water was added. The mixture was extracted with three times $CHCl_3$: water, followed by two times EtOAc. The combined organic layers were washed with heptane, dried ($MgSO_4$), filtered, and the solvent evaporated. Purification was achieved by flash column chromatography (Combiflash, 12g SiO_2 cartridges, 0% to 100% gradient of EtOAc in hexane.

Compound **M23Y3**



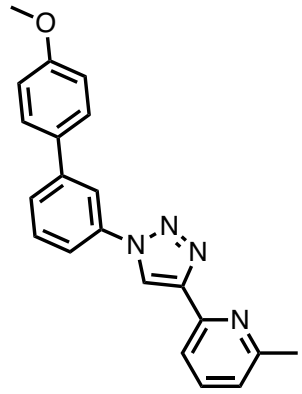
White solid, 0.100 g, 0.28 mmol, 57% yield. ^{1}H NMR (400 MHz, $CDCl_3$) δ 8.64 (s, 1H, triazole CH), 8.44 (dd, *J* = 4.8, 1.6 Hz, 1H, aromatic CH), 8.00 (t, *J* = 2.1 Hz, 1H, aromatic CH), 7.71 (dt, *J* = 7.8, 1.6 Hz, 1H, aromatic CH), 7.65 – 7.54 (m, 4H, aromatic CH), 7.39 (dd, *J* = 8.5, 1.6 Hz, 1H, aromatic CH), 7.32 (dd, *J* = 8.2, 4.6 Hz, 1H, aromatic CH), 7.04 – 6.99 (m, 2H, aromatic CH), 4.03 (s, 3H, O-CH_3), 3.87 (s, 3H, O-CH_3). ^{13}C NMR (101 MHz, $CDCl_3$) δ 159.9, 152.9, 142.8, 137.6, 132.2, 130.1, 128.4, 127.1, 123.6, 122.8, 119.2, 119.0, 114.5 (aromatic C including triazole C), 55.8, 55.5 (O-CH_3). HRMS (ES+): m/z calculated for $C_{21}H_{19}N_4O_2^+$ 359.1508: found 359.1516 $[M+H]^+$; m/z calculated for $C_{21}H_{18}N_4NaO_2$+ 381.1322 : found 381.1334 $[M+Na]^+$.

Compound **P3A10**



Yellow oil, 0.103 g, 0.33 mmol, 52% yield. ^{1}H NMR (400 MHz, $CDCl_3$) δ 8.43 (d, *J* = 2.9 Hz, 1H, triazole CH), 8.41 – 8.35 (m, 1H, aromatic CH), 7.98 (s, 1H, aromatic CH), 7.89 – 7.83 (m, 2H, aromatic CH), 7.69 (dd, *J* = 7.2, 1.4 Hz, 1H, aromatic CH), 7.52 – 7.46 (m, 3H, aromatic CH), 7.41 – 7.34 (m, 1H, aromatic CH), 7.32 – 7.27 (m, 1H, aromatic CH), 5.71 (s, 2H, N-CH_2-Pyr); ^{13}C NMR (101 MHz, $CDCl_3$) δ 160.5, 158.0, 150.5, 150.4, 147.4, 138.4, 138.1, 134.0, 131.1, 129.1, 128.6, 128.0, 127.3, 126.8, 126.1, 125.5, 125.4, 124.2, 124.1, 123.9, 123.9, 123.3 (aromatic C including triazole C), 55.0 (N-CH_2-Pyr); ^{19}F NMR (376 MHz, $CDCl_3$) δ -126.47 (dd, *J* = 8.7, 4.3 Hz). HRMS (ES+): m/z calculated for $C_{18}H_{14}FN_4^+$ 305.1202: found 305.1204 $[M+H]^+$; m/z calculated for $C_{18}H_{13}FN_4Na^+$ 327.1016 : found 327.1025 $[M+Na]^+$.

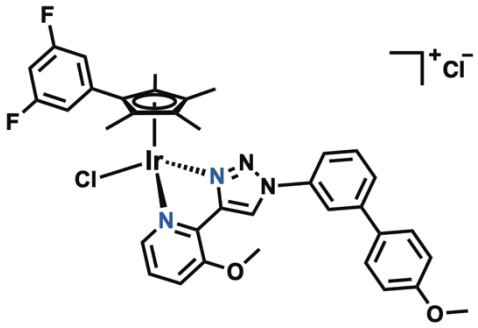
Compound **M23Y2**



White solid, 0.267 g, 0.78 mmol, 70% yield. R_T: 3.95 min. ^{1}H NMR (700 MHz, $CDCl_3$) δ 8.65 (s, 1H, triazole CH), 8.06 (d, *J* = 7.7 Hz, 1H, aromatic CH), 8.02 (t, *J* = 2.0 Hz, 1H, aromatic CH), 7.75 (td, *J* = 7.8, 1.1 Hz, 1H, aromatic CH), 7.70 (t, *J* = 7.7 Hz, 1H, aromatic CH), 7.63 (td, *J* = 7.7, 1.1 Hz, 1H, aromatic CH), 7.61 – 7.56 (m, 3H, aromatic CH), 7.14 – 7.12 (m, 1H, aromatic CH), 7.03 – 7.01 (m, 2H, aromatic CH), 3.87 (s, 3H, O-CH_3), 2.61 (s, 3H, Pyr-CH_3). ^{13}C NMR (176 MHz, $CDCl_3$) δ 159.8, 158.4, 149.4, 149.3, 142.7, 137.5, 137.1, 132.1, 130.1, 128.3, 127.0, 122.7, 120.0, 118.7, 118.5, 117.5, 114.5 (aromatic C including triazole C), 55.3 (O-CH_3), 24.6 (Pyr-CH_3). HRMS (ES+): m/z calculated for $C_{21}H_{19}N_4O^+$ 343.1553: found 343.1553 $[M+H]^+$; m/z calculated for $C_{21}H_{18}N_4NaO^+$ 365.1373 : found 365.1374 $[M+Na]^+$; m/z calculated for $C_{21}H_{18}N_4KO^+$ 381.1112 : found 381.1117 $[M+K]^+$.

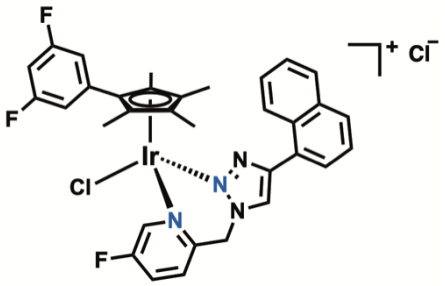
6.3.3.6 Batch Synthesis of the lead complexes

Compound **IrCp3M23Y3**



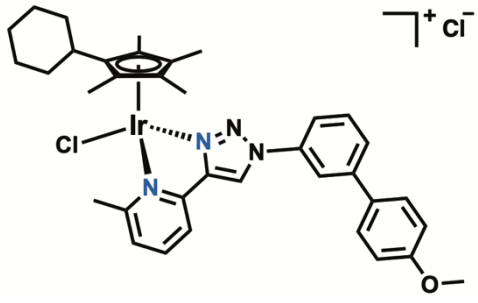
Dark yellow solid. *The product could not be purified*. LC-MS R_T: 3.05 min. ^{1}H NMR (400 MHz, CD_2Cl_2-d_2) δ 8.91 (s, 1H, triazole CH), 8.15 (dd, *J* = 5.5, 1.0 Hz, 1H, aromatic CH), 8.04 (t, *J* = 2.0 Hz, 1H, aromatic CH), 7.81 (dt, *J* = 7.5, 1.7 Hz, 2H, aromatic CH), 7.73 – 7.68 (m, 3H, aromatic CH), 7.67 – 7.63 (m, 2H, aromatic CH), 7.58 (dd, *J* = 8.7, 5.5 Hz, 1H, aromatic CH), 7.31 – 7.26 (m, 2H, aromatic CH), 7.07 (d, *J* = 2.2 Hz, 1H, aromatic CH), 7.05 (d, *J* = 2.1 Hz, 1H, aromatic CH), 7.02 – 6.98 (m, 1H, aromatic CH), 6.54 (dd, *J* = 7.7, 2.4 Hz, 1H, aromatic CH), 4.19 (s, 3H, O-CH_3), 3.88 (s, 3H, O-CH_3), 1.97 (s, 6H, CH_3), 1.81 (s, 6H, CH_3); ^{19}F NMR (376 MHz, CD_2Cl_2-d_2) δ -107.80, -108.10. HRMS (ES+): m/z calculated for $C_{36}H_{33}ClF_2IrN_4O_2^+$ 819.1889: found 819.1895 $[M]^+$.

Compound **IrCp3P3A10**



Yellow solid, 0.038 g, 0.05 mmol, 16% yield. LC-MS R_T: 3.05 min. ^{1}H NMR (400 MHz, DMSO-d_6) δ 8.68 (d, *J* = 0.9 Hz, 1H, triazole CH), 8.59 (d, *J* = 2.9 Hz, 1H, aromatic CH), 8.53 – 8.47 (m, 1H, aromatic CH), 8.03 – 7.95 (m, 2H, aromatic CH), 7.85 – 7.75 (m, 2H, aromatic CH), 7.62 – 7.51 (m, 4H, aromatic CH), 7.41 – 7.29 (m, 3H, aromatic CH), 5.85 (s, 2H, N-CH_2-Pyr), 1.72 (d, *J* = 0.9 Hz, 6H, CH_3), 1.69 (d, *J* = 0.9 Hz, 6H, CH_3); ^{13}C NMR (101 MHz, DMSO-d_6) δ 151.9, 146.2, 138.3, 138.0, 134.1, 130.7, 129.1, 129.0, 127.4, 127.2, 126.6, 126.1, 125.9, 125.4, 124.9, 124.6, 124.5, 101.9 (aromatic C including triazole C), 90.9 (Cp ring C), 54.3 (N-CH_2-Pyr) 9.7, 8.8 (CH_3); ^{19}F NMR (376 MHz, DMSO-d_6) δ -109.41 (t, *J* = 8.7 Hz), -128.15 (dd, *J* = 9.0, 4.7 Hz). HRMS (ES+): m/z calculated for $C_{33}H_{28}ClF_3IrN_4^+$ 765.1584: found 765.1594 $[M]^+$.

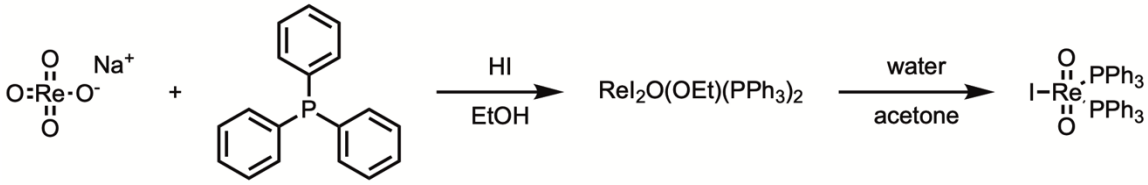
Compound **IrCp4M23Y2**



Yellow solid, 0.014 g, 0.018 mmol, 31% yield. LC-MS R_T: 3.36 min. ^{1}H NMR (400 MHz, CD_2Cl_2-d_2) δ 11.92 (s, 1H, triazole CH), 8.94 (s, 1H, aromatic CH), 8.47 (s, 1H, aromatic CH), 8.15 (s, 1H, aromatic CH), 7.97 (s, 1H, aromatic CH), 7.78 (dd, *J* = 16.9, 7.8 Hz, 3H), 7.66 (s, 1H, aromatic CH), 7.49 (d, *J* = 6.6 Hz, 1H, aromatic CH), 7.04 (d, *J* = 7.7 Hz, 2H, aromatic CH), 3.85 (s, 3H, O-CH_3), 3.01 (s, 3H, Pyr-CH_3), 2.15 (t, *J* = 12.0 Hz, 1H, cycloheyxyl CH), 1.81 (d, *J* = 9.8 Hz, 6H, aliphatic CH_2), 1.70 (s, 3H), 1.65 (s, 3H, aliphatic CH), 1.59 – 1.47 (m, 3H, aliphatic CH), 1.38 (t, *J* = 11.9 Hz, 2H, aliphatic CH), 1.28 – 1.20 (m, 2H, aliphatic CH), 1.15 (d, *J* = 6.1 Hz, 3H, aliphatic CH). ^{13}C NMR (101 MHz, CD_2Cl_2-d_2) δ 161.3, 160.1, 150.3, 148.8, 142.8, 140.5, 136.8, 131.4, 130.5, 128.5, 128.0, 126.4, 121.7, 118.2, 114.4 (aromatic C including triazole C), 93.6, 92.7, 90.0, 89.5, 88.1 (Cp ring C), 55.4, 36.0, 30.8, 30.7, 28.9, 27.0, 26.9, 25.8, 25.2 (cyclohexyl C), 10.5, 10.1, 9.8, 9.4 (CH_3). HRMS (ES+): m/z calculated for $C_{36}H_{41}ClIrN_4O^+$ 773.2598: found 773.2627 $[M]^+$.

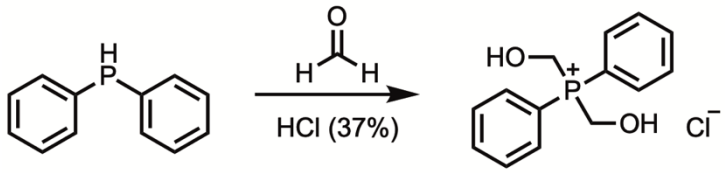
6.3.4 Sythesis of rhenium complexes

6.3.4.1 Synthesis of $ReIO_2(PPh_3)_2$[446]



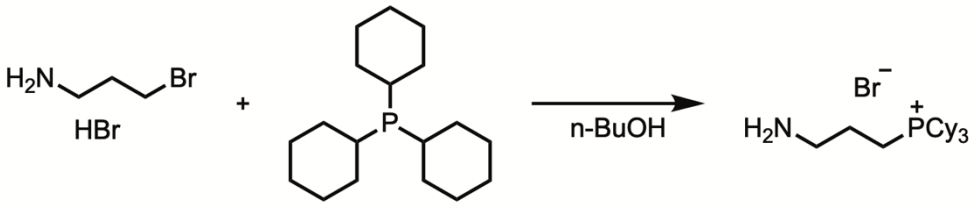
Hydroiodic acid (1.70 mL, 57%) and ethanol (10 mL) were mixed and sodium perrhenate (0.307 g, 1.13 mmol) and triphenylphosphine (1.49 g, 5.68 mmol) were added. The mixture was then refluxed at 85 °C for 40 minutes, and the yellow solution first turned to brown, then to grey-green. The mixture was cooled to room temperature. The solution was filtered off and dried *in vacuo*. $[ReI_2O(OEt)(PPh_3)_2]$ (1.13g, 1.10 mmol) was dissolved in the mixture of acetone (50 mL) and water (2 mL) and stirred for 1 hour and 10 minutes turning to a deep violet mixture. The violet solids were filtered off and dried in vacuo. **$ReIO_2(PPh_3)_2$** was obtained through recrystallisation from heptane and toluene (1:1) as a violet solid (0.635 g, 65% yield). ^{1}H NMR (300 MHz, $CDCl_3$) δ 7.97 – 7.16 (m, 30H, aromatic CH). ^{31}P NMR (121 MHz, $CDCl_3$) δ 4.6.

Synthesis of **45**[447]



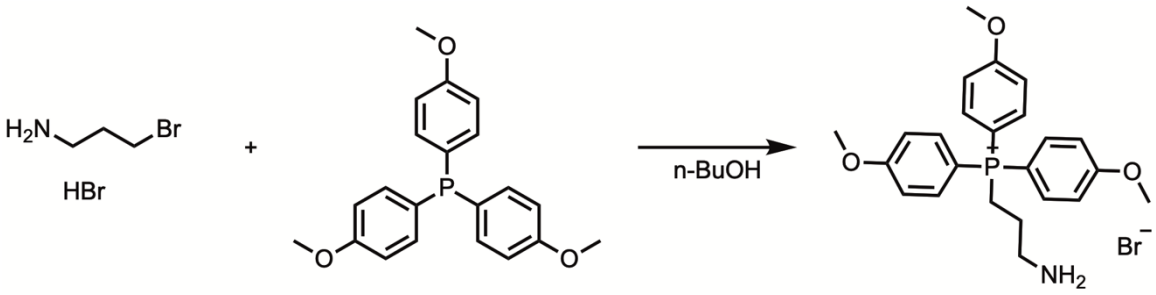
Diphenyl phosphine (3.00 mL, 17.2 mmol) and formaldehyde (3.30 mL, 37% in H_2O stabilized with 10-15% MeOH) were mixed. The solution turned immediately white in colour and an exothermic reaction took place. HCl (1.50 mL, 36%) was added at 0 °C and the solution was stirred for 5 hours at room temperature. The reaction was monitored by TLC. Upon completion, the reaction mixture was concentrated under reduced pressure and re-dissolved in acetone to obtain a clear viscous liquid. Compound (**45**) was obtained through precipitation in acetone at 4°C and concentrated *in vacuo* as a white solid (3.79 g, 78% yield). ^{1}H NMR (300 MHz, D_2O) δ 7.87 – 7.70 (m, 6H, aromatic CH), 7.68 – 7.62 (m, 4H, aromatic CH), 5.10 (s, 4H, CH_2-OH). ^{13}C NMR (75 MHz, D_2O) δ 135.4, 133.4, 133.2, 131.2, 130.2, 130.0, 129.0, 128.6, 114.8, 113.8, 81.7 (aromatic CH), 58.5, 53.9, 53.1. ^{31}P NMR (121 MHz, D_2O) δ 16.5.

Synthesis of **46**



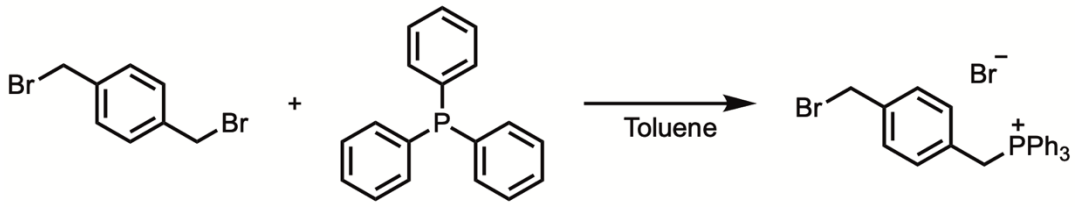
3-Bromopropylamine hydrobromide (0.500 g, 2.29 mmol) was dissolved in 1-butanol (10 mL), and tricyclohexylphosphine (0.649 g, 2.31 mmol) was added. The reaction mixture was stirred at 120 °C for 18 hours in a sealed microwave tube. The reaction was monitored by TLC. Upon completion, heptane (6 mL) was added, and the mixture was stirred for 20 minutes. The reaction mixture was concentrated under reduced pressure to give a clear viscous liquid. Compound (**46**) was obtained through precipitation in cold heptane as a white solid (1.11 g, quantitative yield). ^{1}H NMR (300 MHz, $CDCl_3$) δ 8.52 (s, 3H), 3.61 (t, *J* = 6.6 Hz, 2H, aliphatic CH_2), 3.44 – 3.35 (m, 2H, aliphatic CH_2), 2.93 – 2.74 (m, 2H, aliphatic CH_2), 2.61 – 2.34 (m, 6H, aliphatic CH/CH_2), 1.78 (s, 3H), 1.68 – 1.47 (m, 12H, aliphatic CH_2), 1.45 – 1.33 (m, 12H, aliphatic CH_2). ^{31}P NMR (121 MHz, $CDCl_3$) δ 32.8.

Synthesis of **47**



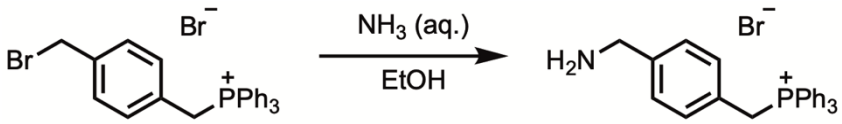
3-Bromopropylamine hydrobromide (0.514 g, 2.35 mmol) was dissolved in 1-butanol (20 mL). Tris(p-methoxyphenyl) phosphine (0.831 g, 2.36 mmol) was added, and the mixture was stirred at 120 °C for 18 hours. The reaction was monitored by TLC. Upon completion, compound (**47**) was obtained through precipitation with heptane as a white solid (0.605 g, 53% yield). ^{1}H NMR (300 MHz, $CDCl_3$) δ 8.61 (s, 2H, NH_2), 7.67 (dd, *J* = 12.1, 8.9 Hz, 5H, aromatic CH), 7.13 (dd, *J* = 9.0, 2.6 Hz, 5H, aromatic CH), 3.87 (s, 6H, O-CH_3), 3.81 (s, 1H), 3.60 (t, *J* = 6.5 Hz, 1H), 3.38 (s, 2H, aliphatic CH_2), 2.28 (s, 2H, aliphatic CH_2), 1.58 – 1.45 (m, 2H), 1.41 – 1.21 (m, 2H).

Synthesis of **48**



Triphenylphosphine (1.00 g, 3.8 mmol, 1 eq) and α, α'-dibromo-*p*-xylene (1.06 g, 4.05 mmol, 1.06 eq) were dissolved in anhydrous toluene (15 mL) under an inert atmosphere. The reaction mixture was refluxed at 125 °C for 4.5 hours. The reaction was monitored by TLC. Upon completion, the mixture was cooled to room temperature and filtered off. Compound (**48**) was obtained without further purification as a white solid (1.92 g, 96% yield). ^{1}H NMR (300 MHz, $CDCl_3$) δ 7.79 – 7.68 (m, 9H, aromatic CH), 7.64 – 7.55 (m, 6H, aromatic CH), 7.11 (s, 4H, aromatic CH), 5.50 (d, *J* = 14.6 Hz, 2H, CH_2-PPh_3), 4.37 (d, *J* = 1.3 Hz, 2H, CH_2-Br). ^{31}P NMR (121 MHz, $CDCl_3$) δ 23.5.

Synthesis of **49**



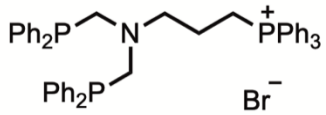
Compound **48** (1.52 g, 2.89 mmol) was dissolved in absolute ethanol (150 mL). Then, NH_3 (aq) (50 mL, 25%) was added, and the reaction mixture was stirred at room temperature for 3 days. The reaction was monitored by TLC. Upon completion, the reaction mixture was concentrated under reduced pressure. Compound (**49**) was obtained without further purification as a white solid (1.39 g, quantitative yield). ^{1}H NMR (300 MHz, MeOD-d_4) δ 7.96 – 7.51 (m, 15H, aromatic CH), 7.47 – 7.32 (m, 1H, aromatic CH), 7.24 – 7.08 (m, 2H, aromatic CH), 7.03 – 6.94 (m, 1H, aromatic CH), 5.01 (d, *J* = 16.4 Hz, 2H, CH_2-PPh_3), 4.15 – 4.08 (m, 1H, aliphatic), 3.41 (d, *J* = 13.2 Hz, 1H, aliphatic). ^{31}P NMR (121 MHz, I) δ 22.9.

6.3.4.2 General procedure a, for the synthesis of the $NP_2^{Ph}X^R$ Ligands[109]

The primary amine (1 eq.) and [$Ph_2P(CH_2OH)_2$] Cl (**45**) (2.19 eq.) were added into a microwave tube under argon atmosphere. Then, absolute methanol (2.5 mL/ 100 mg of the primary amine) and DIPEA (2.76 eq.) were added via syringe. The reaction mixture was irradiated at 120 °C for 1.5 hours in the microwave. Then, the mixture was concentrated *in vacuo* and then dissolved in a minimum of EtOH and precipitated with

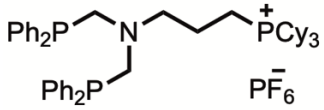
saturated $KPF_{6\ (aq)}$ solution. The dark brown solids were filtered off and dried under reduced pressure to obtain the product as white solid.

Synthesis of **50**



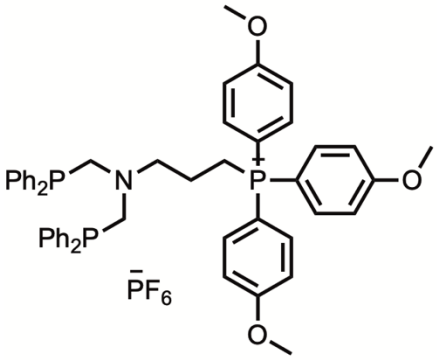
White solid (0.723 g, 0.91 mmol, quantitative yield). ^{1}H NMR (300 MHz, DMSO-d_6) δ 7.90 (td, *J* = 7.5, 1.9 Hz, 3H, aromatic CH), 7.75 (td, *J* = 7.8, 3.4 Hz, 7H, aromatic CH), 7.67 – 7.47 (m, 7H, aromatic CH), 7.43 – 7.32 (m, 3H, aromatic CH), 7.29 (d, *J* = 4.9 Hz, 15H), 3.21 (s, 2H, aliphatic CH_2), 3.12 (dd, *J* = 7.3, 4.1 Hz, 4H, aliphatic CH_2), 2.98 (q, *J* = 5.6 Hz, 2H, aliphatic CH_2), 1.61 – 1.46 (m, 2H, aliphatic CH_2). ^{31}P NMR (121 MHz, DMSO-d_6) δ 24.4, -

Synthesis of **51**



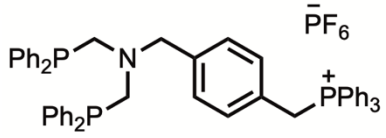
White solid (0.217 g, 0.26 mmol, 59% yield). ^{1}H NMR (300 MHz, MeOD-d_4) δ 7.48 – 7.26 (m, 20H, aromatic CH), 3.61 – 3.55 (m, 4H, aliphatic CH_2), 3.09 (t, *J* = 5.3 Hz, 1H, aliphatic), 1.98 – 1.73 (m, 19H, aliphatic), 1.46 – 1.28 (m, 17H, aliphatic CH_2), 1.18 (t, *J* = 7.0 Hz, 2H, aliphatic CH_2). ^{31}P NMR (121 MHz, MeOD-d_4) δ 32.6, -27.6.

Synthesis of **52**



White solid (0.268 g, 0.28 mmol, 66% yield). ^{1}H NMR (300 MHz, $CDCl_3$) δ 7.39 – 7.31 (m, 8H), 7.31 – 7.20 (m, 18H, aromatic CH), 7.09 (dt, *J* = 9.0, 2.7 Hz, 6H, aromatic CH), 3.91 (s, 9H, O-CH_3), 3.77 – 3.65 (m, 4H, aliphatic CH_2), 3.54 – 3.45 (m, 3H), 3.01 (s, 1H, aliphatic), 2.54 (q, *J* = 12.3 Hz, 2H). ^{31}P NMR (121 MHz, $CDCl_3$) δ 21.8, -28.0.

Synthesis of **53**



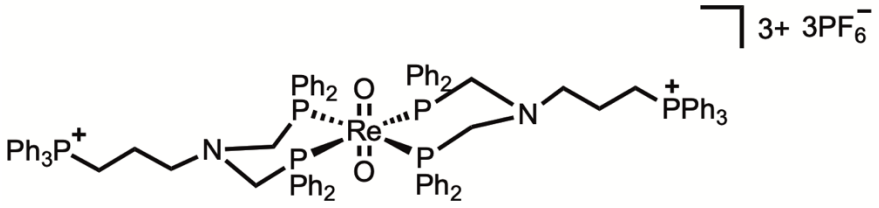
White solid (0.281 g, 0.30 mmol, 67% yield). ^{1}H NMR (300 MHz, $CDCl_3$) δ 7.79 – 7.70 (m, 3H, aromatic CH), 7.64 – 7.54 (m, 6H, aromatic CH), 7.52 – 7.43 (m, 6H, aromatic CH), 7.39 – 7.20 (m, 20H, aromatic CH), 7.06 – 6.82 (m, 2H), 6.77 – 6.63 (m, 2H), 4.53 (dd, *J* = 14.0, 7.4 Hz, 2H, CH_2-PPh_3), 3.93 (s, 1H, aliphatic), 3.79 (d, *J* = 3.8 Hz, 1H, aliphatic), 3.74 – 3.64 (m, 1H, aliphatic), 3.50 (d, *J* = 2.7

6.3.4.3 General procedure b, for the synthesis of the complexes[109]

[$RelO_2(PPh_3)_2$] (0.050 g, 0.05749 mmol, 1 eq.) was dissolved in DCM (11 mL). The $NP_2^{Ph}X^R$ Ligand (2.2 eq.) was added and stirred at room temperature for 24 hours. The solvent was then evaporated under reduced pressure. The brown oily residual was then redissolved in a minimum of acetonitrile and precipitated with saturated $KPF_{6\ (aq)}$. The

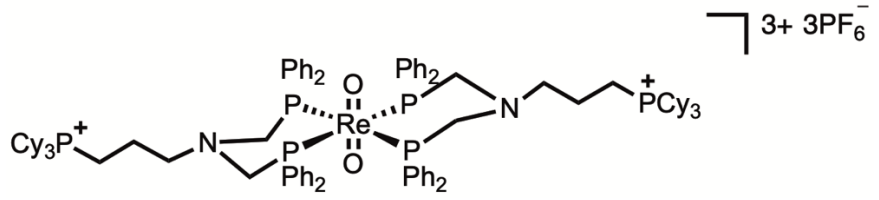
brown solids were filtered off and redissolved in a minimum of DCM and precipitated out with heptane. The brown solids were then isolated by filtration and dried *in vacuo* to give the product.

Compound Re34



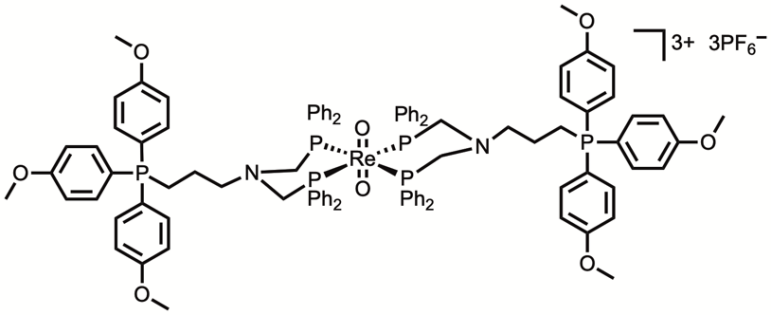
Brown solid (0.0652 g, 0.07 mmol, 49% yield). ^{1}H NMR (400 MHz, DMSO-d_6) δ 7.99 – 6.95 (m, 70H, aromatic CH), 3.89 (s, 4H, aliphatic), 3.51 (s, 6H, aliphatic), 2.73 (s, 3H, aliphatic), 1.34 – 1.22 (m, 5H, aliphatic), 0.88 – 0.80 (m, 2H, aliphatic). ^{31}P NMR (162 MHz, DMSO-d_6) δ 24.3, -37.0. HRMS (ES+) calculated for $[M]^{3+}$ $C_{94}H_{90}N_2O_2P_6Re^{3+}$ 550.499, found 550.4985. HRMS (ES+) calculated for $[M+PF_6]^{2+}$ $C_{94}H_{90}F_6N_2O_2P_7Re^{2+}$ 898.2310; found 898.2307. EA calculated for $C_{94}H_{90}F_{18}N_2O_2P_9Re$ (%): C, 54.11; H, 4.35; N, 1.34; found: C, 49.02; H, 4.11; N, 1.1. *The carbon content determined by elemental analysis was lower than the calculated value. This discrepancy may arise from residual inorganic impurities, retained solvent or incomplete combustion; however, its origin could not be established. Consequently, elemental analysis did not satisfactorily confirm the bulk purity of the isolated material.*

Compound Re35



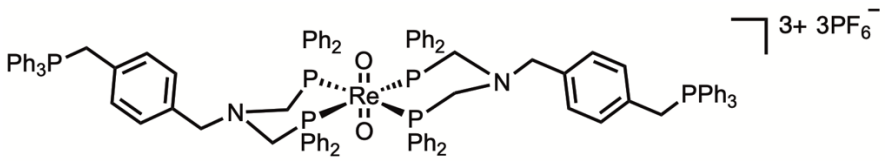
Light brown solid (0.0826 g, 0.009 mmol, 64% yield). ^{1}H NMR (400 MHz, DMSO-d_6) δ 8.02 – 6.85 (m, 40H, aromatic CH), 3.95 (s, 6H, aliphatic), 3.43 (s, 7H, aliphatic), 2.30 (d, *J* = 10.2 Hz, 5H, aliphatic), 1.96 – 1.07 (m, 66H, aliphatic), 0.91 – 0.75 (m, 2H, aliphatic). ^{13}C NMR (101 MHz, DMSO-d_6) δ 130.6, 128.0 (aromatic), 39.5, 28.5, 28.1, 25.9, 24.8 (aliphatic). ^{31}P NMR (162 MHz, DMSO) δ 33.2, 36.7. HRMS (ES+) calculated for $[M]^{3+}$ $C_{94}H_{126}N_2O_2P_6Re^{3+}$ 562.593; found 562.5923. HRMS (ES+) calculated for $[M+PF_6]^{2+}$ $C_{94}H_{126}F_6N_2O_2P_7Re^{2+}$ 916.372; found 916.3715. EA calculated for $C_{94}H_{126}F_{18}N_2O_2P_9Re$ (%): C, 53.64; H, 6.03; N, 1.33. Found: C, 49.67; H, 5.63; N, 1.24.

Compound Re36



Brown solid (0.101 g, 0.102 mmol, 67% yield). ^{1}H NMR (400 MHz, DMSO-d_6) δ 8.01 – 6.83 (m, 64H, aromatic CH), 4.12 (s, 1H, aliphatic), 3.89 (s, 20H,O-CH_3), 3.73 (s, 13H, aliphatic), 2.82 (s, 1H, aliphatic), 1.57 (d, *J* = 34.2 Hz, 3H, , aliphatic). ^{13}C NMR (101 MHz, DMSO) δ 164.0, 135.3, 130.6, 128.6, 128.0, 109.6, 108.6, 55.9, 39.5. ^{31}P NMR (162 MHz, DMSO) δ 21.9, -37.0. HRMS (ES+) calculated for $[M]^{3+}$ $C_{100}H_{102}N_2O_8P_6Re^{3+}$ 610.5203, found 610.5203. HRMS (ES+) calculated for $[M+PF_6]^{2+}$ $C_{100}H_{102}F_6N_2O_8P_7Re^{2+}$ 988.263, found 988.2635.

Compound Re37



Brown solid (0.056.1 g, 0.06 mmol, 41% yield). ^{1}H NMR (400 MHz, DMSO-d_6) δ 7.89 (d, *J* = 18.9 Hz, 8H, aromatic CH), 7.71 – 6.87 (m, 70H, aromatic CH), 5.22 – 4.98 (m, 4H, aliphatic), 3.79 – 3.58 (m, 4H, aliphatic), 3.52 – 3.26 (m, 8H, aliphatic). ^{13}C NMR (101 MHz, DMSO-d_6) δ 135.0, 134.0, 133.9, 130.1, 129.9, 128.0, 39.5, 34.8, 31.2, 25.8 (aliphatic). ^{31}P NMR (162 MHz, DMSO-d_6) δ 23.0, -36.6. HRMS (ES+) calculated for $[M]^{3+}$ $C_{104}H_{94}N_2O_2P_6Re^{3+}$ 591.8427, found 591.8427. HRMS (ES+) calculated for $[M+PF_6]^{2+}$ $C_{104}H_{94}F_6N_2O_2P_7Re^{2+}$ 960.2465, found 960.2471.

6.4 X-ray crystallography

Diffraction data were collected at 110 K on an Oxford Diffraction SuperNova diffractometer with Cu-K_α radiation (λ = 1.54184 Å) or Mo-K_α radiation (λ = 0.71073), using an EOS CCD camera. The crystal was cooled with an Oxford Instruments Cryojet. Diffractometer control, data collection, initial unit cell determination, frame integration and unit-cell refinement was carried out with “Crysalis”. Face-indexed absorption corrections were applied using spherical harmonics, implemented in SCALE3 ABSPACK scaling algorithm. OLEX2[448] was used for overall structure solution and refinement . Within OLEX2, the algorithm used for structure solution was “ShelXT dual-space”. Refinement

was carried out by full-matrix least-squares used the SHELXL-97[449] algorithm within OLEX2. All non-hydrogen atoms were refined anisotropically. Crystalmaker® software was used to visualize the structures as well as generating the figures presented herein.

Table 35. Crystal data and structure refinement for **IrCp1K7**.

Identification code	af24002
Empirical formula	$C_{29}H_{29}Cl_{12}IrN_2$
Formula weight	1023.14
Temperature/K	110.00(10)
Crystal system	triclinic
Space group	P-1
a/Å	10.8649(3)
b/Å	11.2184(3)
c/Å	16.8615(4)
α/°	75.817(2)
β/°	85.299(2)
γ/°	68.569(3)
Volume/Å^3	1854.71(10)
Z	2
ρ_{calc}g/cm^3	1.832
μ/mm^{-1}	15.124
F(000)	996.0
Crystal size/mm^3	0.181 × 0.114 × 0.018
Radiation	Cu Kα (λ = 1.54184)
2Θ range for data collection/°	5.406 to 136.492
Index ranges	-12 ≤ h ≤ 13, -12 ≤ k ≤ 13, -18 ≤ l ≤ 20
Reflections collected	33938
Independent reflections	6788 [R_{int} = 0.0364, R_{sigma} = 0.0285]
Data/restraints/parameters	6788/0/402
Goodness-of-fit on F^2	1.043
Final R indexes [I>=2σ (I)]	R_1 = 0.0198, wR_2 = 0.0458
Final R indexes [all data]	R_1 = 0.0209, wR_2 = 0.0462
Largest diff. peak/hole / e Å^{-3}	1.01/-0.55

Table 36. Bond lengths for **IrCp1K7.**

Atom	Atom	Length/Å	Atom	Atom	Length/Å
C1	C2	1.446(3)	C17	C18	1.362(4)
C1	C5	1.425(4)	C18	C19	1.401(4)
C1	C6	1.506(4)	C19	C20	1.447(4)
C1	Ir1	2.138(2)	C19	N2	1.349(3)
C2	C3	1.426(4)	C20	N1	1.282(3)
C2	C7	1.490(4)	C21	C22	1.392(3)
C2	Ir1	2.203(2)	C21	C26	1.387(4)
C3	C4	1.462(4)	C21	N1	1.436(3)
C3	C8	1.498(3)	C22	C23	1.391(4)
C3	Ir1	2.189(2)	C23	C24	1.378(4)
C4	C5	1.431(3)	C24	C25	1.394(4)
C4	C9	1.487(4)	C25	C26	1.389(4)
C4	Ir1	2.171(2)	Cl1	Ir1	2.3949(5)
C5	C10	1.503(3)	Ir1	N1	2.0863(18)
C5	Ir1	2.182(2)	Ir1	N2	2.119(2)
C11	C12	1.417(3)	C27	Cl3	1.758(3)
C11	C16	1.424(4)	C27	Cl4	1.769(3)
C11	N2	1.374(3)	C27	Cl5	1.764(3)
C12	C13	1.373(4)	C28	Cl6	1.767(3)
C13	C14	1.405(4)	C28	Cl7	1.762(3)
C14	C15	1.369(3)	C28	Cl8	1.765(4)
C14	Cl2	1.738(2)	C29	Cl9	1.754(3)
C15	C16	1.416(4)	C29	Cl10	1.758(3)
C16	C17	1.412(3)	C29	Cl11	1.766(3)

Table 37. Crystal data and structure refinement for **IrCp1L7**.

Identification code	af24003
Empirical formula	$C_{24}H_{28}BrCl_5IrN_2O_{1.5}$
Formula weight	817.84
Temperature/K	110.00(10)
Crystal system	orthorhombic
Space group	Pbcn
a/Å	24.6479(3)
b/Å	21.2906(3)
c/Å	10.86580(10)
α/°	90
β/°	90
γ/°	90
Volume/Å^3	5702.03(12)
Z	8
ρ_{calc}g/cm^3	1.905
μ/mm^{-1}	15.206
F(000)	3160.0
Crystal size/mm^3	0.136 × 0.024 × 0.015

Radiation	Cu Kα (λ = 1.54184)
2Θ range for data collection/°	5.486 to 136.43
Index ranges	-29 ≤ h ≤ 29, -24 ≤ k ≤ 25, -12 ≤ l ≤ 4
Reflections collected	22428
Independent reflections	5208 [R_{int} = 0.0363, R_{sigma} = 0.0311]
Data/restraints/parameters	5208/0/318
Goodness-of-fit on F^2	1.046
Final R indexes [I>=2σ (I)]	R_1 = 0.0277, wR_2 = 0.0622
Final R indexes [all data]	R_1 = 0.0331, wR_2 = 0.0643
Largest diff. peak/hole / e $Å^{-3}$	1.16/-0.70

Table 38. Bond lengths for **IrCp1L7**.

Atom	Atom	Length/Å	Atom	Atom	Length/Å
Br1	C20	1.876(4)	C13	C14	1.379(6)
C1	C2	1.428(5)	C14	C15	1.382(6)
C1	C5	1.457(6)	C15	C16	1.389(6)
C1	C10	1.496(6)	C17	C18	1.452(6)
C1	Ir1	2.169(4)	C17	N2	1.293(5)
C2	C3	1.444(6)	C18	C19	1.396(6)
C2	C9	1.494(5)	C18	N1	1.349(5)
C2	Ir01	2.190(4)	C19	C20	1.377(6)
C3	C4	1.449(6)	C20	C21	1.398(6)
C3	C8	1.495(6)	C21	C22	1.399(6)
C3	Ir1	2.172(4)	C21	O1	1.345(5)
C4	C5	1.431(6)	C22	N1	1.336(5)
C4	C7	1.498(6)	C23	O1	1.443(5)
C4	Ir01	2.166(4)	Cl1	Ir1	2.3938(9)
C5	C6	1.501(5)	Ir01	N1	2.101(3)
C5	Ir01	2.154(4)	Ir01	N2	2.080(3)
C11	C12	1.388(6)	C24	Cl2	1.759(5)
C11	C16	1.386(6)	C24	Cl3	1.761(5)
C11	N2	1.441(5)	C24	Cl4	1.768(5)
C12	C13	1.386(6)			

Table 39. Crystal data and structure refinement for **IrCp1B7**.

Identification code	af24004
Empirical formula	$C_{27}H_{28}Cl_5IrN_2$
Formula weight	749.96
Temperature/K	110.00(10)
Crystal system	monoclinic
Space group	$P2_1$
a/Å	7.67530(10)
b/Å	14.3897(3)
c/Å	12.5533(2)
α/°	90
β/°	97.869(2)
γ/°	90
Volume/Å^3	1373.40(4)
Z	2
ρ_{calc}g/cm^3	1.814
μ/mm^{-1}	14.037
F(000)	732.0
Crystal size/mm^3	0.07 × 0.04 × 0.03
Radiation	Cu Kα (λ = 1.54184)
2Θ range for data collection/°	7.108 to 136.498
Index ranges	-8 ≤ h ≤ 9, -17 ≤ k ≤ 7, -14 ≤ l ≤ 15
Reflections collected	8616
Independent reflections	3688 [R_{int} = 0.0525, R_{sigma} = 0.0614]
Data/restraints/parameters	3688/1/297
Goodness-of-fit on F^2	1.054
Final R indexes [I>=2σ (I)]	R_1 = 0.0362, wR_2 = 0.0796
Final R indexes [all data]	R_1 = 0.0394, wR_2 = 0.0807
Largest diff. peak/hole / e Å^{-3}	1.99/-2.01
Flack parameter	-0.026(17)

Table 40. Bond lengths for **IrCp1B7**.

Atom	Atom	Length/Å	Atom	Atom	Length/Å
C1	C2	1.388(14)	C17	C21	1.463(14)
C1	C6	1.39(2)	C17	C26	1.500(15)
C1	N1	1.443(13)	C17	Ir1	2.168(10)
C2	C3	1.405(15)	C18	C19	1.435(14)
C3	C4	1.355(18)	C18	C25	1.496(13)
C4	C5	1.405(16)	C18	Ir1	2.146(10)
C5	C6	1.405(14)	C19	C20	1.448(14)
C7	C8	1.452(14)	C19	C24	1.509(14)
C7	N1	1.282(14)	C19	Ir1	2.153(10)
C8	C9	1.404(14)	C20	C21	1.434(15)
C8	N2	1.330(13)	C20	C23	1.484(14)
C9	C10	1.360(15)	C20	Ir1	2.226(10)
C10	C11	1.395(16)	C21	C22	1.484(14)
C11	C12	1.422(14)	C21	Ir1	2.182(10)
C11	C16	1.427(15)	Cl1	Ir1	2.407(2)
C12	C13	1.365(18)	Ir1	N1	2.068(9)
C13	C14	1.406(16)	Ir1	N2	2.132(8)
C14	C15	1.365(14)	C27	Cl2	1.760(13)
C15	C16	1.435(14)	C27	Cl3	1.777(13)
C16	N2	1.375(12)	C27	Cl4	1.763(12)
C17	C18	1.413(14)			

Table 41. Crystal data and structure refinement for **IrCp1B8**.

Identification code	af24005
Empirical formula	$C_{28}H_{31.58}Cl_{5.25}IrN_2O_{0.79}$
Formula weight	787.05
Temperature/K	110.00(10)
Crystal system	monoclinic
Space group	$P2_1/c$
a/Å	19.3327(2)
b/Å	7.44460(10)
c/Å	22.0064(2)
α/°	90
β/°	105.3920(10)
γ/°	90
Volume/Å^3	3053.65(6)
Z	4
ρ_{calc}g/cm^3	1.712
μ/mm^{-1}	12.873
F(000)	1545.0
Crystal size/mm^3	0.19 × 0.05 × 0.05
Radiation	Cu Kα (λ = 1.54184)
2Θ range for data collection/°	8.334 to 136.5
Index ranges	-22 ≤ h ≤ 23, -7 ≤ k ≤ 8, -25 ≤ l ≤ 26
Reflections collected	20695
Independent reflections	5570 [R_{int} = 0.0228, R_{sigma} = 0.0182]
Data/restraints/parameters	5570/0/364
Goodness-of-fit on F^2	1.052
Final R indexes [I>=2σ (I)]	R_1 = 0.0291, wR_2 = 0.0749
Final R indexes [all data]	R_1 = 0.0321, wR_2 = 0.0783
Largest diff. peak/hole / e Å^{-3}	1.45/-1.08

Table 42. Bond lengths for **IrCp1B8**.

Atom	Atom	Length/Å	Atom	Atom	Length/Å
C1	C2	1.400(6)	C13	C15	1.487(6)
C1	C20	1.449(6)	C13	Ir1	2.188(4)
C1	N2	1.341(5)	C14	C16	1.507(6)
C2	C3	1.365(7)	C14	Ir1	2.148(4)
C3	C4	1.397(7)	C20	N1	1.279(5)
C4	C5	1.422(7)	C21	C22	1.383(6)
C4	C9	1.437(6)	C21	C26	1.393(6)
C5	C6	1.354(7)	C21	N1	1.432(5)
C6	C7	1.417(7)	C22	C23	1.396(6)
C7	C8	1.375(6)	C23	C24	1.391(7)
C8	C9	1.407(6)	C24	C25	1.374(7)
C9	N2	1.382(5)	C24	C27	1.517(7)

C10	C11	1.428(6)	C25	C26	1.390(7)
C10	C14	1.435(6)	Cl1	Ir1	2.4021(9)
C10	C17	1.500(5)	Ir1	N1	2.087(3)
C10	Ir1	2.196(4)	Ir1	N2	2.122(3)
C11	C12	1.464(5)	C28	Cl2	1.762(6)
C11	C18	1.485(6)	C28	Cl3	1.748(5)
C11	Ir1	2.185(4)	C28	Cl4	1.740(6)
C12	C13	1.433(6)	Cl7	Cl7^{1}	2.08(7)
C12	C19	1.491(5)	Cl7	O1	1.44(2)
C12	Ir1	2.170(4)	Cl6	Cl6^{1}	1.88(4)
C13	C14	1.442(6)			

6.5 LC-MS processing (Chapter 3 and 4)

LC-MS spectra were automatically processed using previously mentioned Python and R code. This processing was used to obtain purity data (as peak area% of the total spectrum), to characterise the compounds (using mass spec associated with the UV peak), to obtain retention times of the compounds as a pseudo logP measurement, and to generate the spectra in the supplementary data associated with this thesis. As a workflow, the LC-MS data was obtained from the ThermoScientific LC-MS as .raw files. These files were converted to .mzml files using the ThermoRawFileParser (version 1.4.4) integrated with Python.[340] .mzml files were then converted into .csv files using R code (using the RaMS library). A list of target masses for the complexes in the files being processed was prepared. Then, using custom Python code, the mass list was searched and filtered for the target mass, and the associated UV peak (using UV3, 254 nm) was found. The UV peak was integrated to determine the %peak area as a total area, and the UV trace and extracted ion chromatogram were plotted in a single graph (using normalized data). The peak was labelled, and its retention time was extracted. To allow for accurate integration and account for baseline drift, a baseline correction was used, by subtracting the UV3 trace of a blank sample (60% MeCN in H_2O) from the UV trace. An example of the spectra generated is shown below. For some of the IrCp libraries, both the **parent ion** and **the doubly charged [(M – Cl)+ MeCN]$^{2+}$** species were observed at different retention times. In this case, the sum of the two species was used for conversion, and only the parent ion retention time is used.

6.6 Stability testing of lead compounds

6.6.1 Determination of Pt1 and Pt8 stability (Chapter 1)

The stability of **Pt1** complex was measured by ^{1}H and ^{195}Pt NMRs. Approximately 7 mM of **Pt1** in DMSO-d_6 was prepared and NMR spectra were immediately measured.

Measurements were repeated after the 24 h and 48 h of incubations at 37°C. The stability of **Pt1** in aqueous environment was examined by ^{1}H NMR. NMR of approximately 15 mM **Pt1 and** 6 mM **Pt8** in DMSO-d_6 was recorded immediately after preparation. Then, 10% D_2O was added and 1H NMR was recorded immediately and after 24 h of incubation at 37 °C.

6.6.2 Determination of Ir15 stability (Chapter 2)

6.6.2.1 Ir15 stability with plate-reader

Purified compounds were dissolved in DMSO to make solutions at 5 mM concentration. These were diluted to 50 µM for stability tests with the following media: DMSO, DMSO:H_2O (1:1), DMSO:PBS 1X (1:1), H_2O, PBS (1X). UV-Vis spectra (300 – 600 nm, 10 flashes) were collected over 20 h to monitor the stability of these complexes at 37 °C.

1.1.1. Stability Testing of Hit Compound (Ir16) with LCMS

Purified compounds were dissolved in DMSO to make solutions at 5 mM concentration. These were diluted down to 100 µM for stability test with DMSO:H_2O (1:1), H_2O, and PBS and measured with LCMS every 24 minutes for 21 hours at 37°C.

6.7 Biological Testing

6.7.1 Antibacterial Testing

6.7.1.1 Determination of Antibacterial activity: Minimum Inhibitory Concentration Assay (Chapter 2) [352]

The compounds were tested for their antimicrobial activity against *Escherichia coli* W3110, *Staphylococcus aureus* COL (MRSA) clinical isolate methicillin susceptible *Staphylococcus aureus* (MSSA), and *Bacillus subtilis* MW168. The lead compounds were tested also against of *Escherichia coli* ATCC 25922, MSSA ATCC 29213; MRSA NRS 100, S119, 129, 186, 191, 192, 193, 194, 198, and vancomycin-resistant *Staphylococcus aureus (*VRSA*)* VRS 1, 4 and 12.

The MIC protocol was adapted from Cai *et al*.[450] A single colony of bacteria was grown in Luria-Bertani (LB) medium overnight at 37 °C. Stock solutions of 5 mM of the samples were prepared in DMSO and diluted to a starting concentration of 100 µM in Mueller Hinton (MH) medium. The overnight culture was diluted and incubated until the OD_{600} reached 0.6–1.0. The bacteria concentration was measured by measuring the optical density at 600 nm and diluted to an OD_{600} of 0.022 in MH medium. 5 µL of the diluted bacterial solution was used to inoculate 150 µL of the sample solutions, resulting in a final inoculation of about 5×10^5 cells/mL. The plates were then incubated at 37 °C for

18 hours. For each assay, a control of broth only and a growth control of broth with bacterial inoculum without antibiotics were included in two columns of the plate. Polymyxin B and vancomycin were used as control antibiotic for *E. coli,* MRSA, *B. subtilis,* and MSSA, respectively. The growth was measured by analysing the absorbance of the bacterial suspension at 600 nm. Each experiment was performed in triplicate.

6.7.1.2 Determination of antibacterial activity: Minimum inhibitory concentration assay against selection of Gram-positive and Gram-negative strains (Chapter 2)[451]

Before starting the experiment, a single colony was picked from MHA plate, inoculated in MHBII and incubated overnight at 37 °C with shaking for 18–24 hours to get the starter culture. Antibiotic susceptibility testing was conducted according to the CLSI guidelines using the broth microdilution assay. 10 mg/mL stock solutions of test compounds were prepared in DMSO. Bacterial cultures were inoculated in MHBII and optical density (OD) was measured at 600 nm, followed by dilution to achieve ~10^6 CFU/mL. The compounds were tested from 64–0.5 mg/L in two-fold serial diluted fashion with 2.5 µL of each concentration added to well of a 96-well round bottom microtiter plate. Later, 97.5 µL of bacterial suspension was added to each well containing either test compound or appropriate controls. The plates were incubated at 37 °C for 18-24 h following which the MIC was determined. The MIC is defined as the lowest concentration of the compound at which there is absence of visible growth. For each test compound, MIC determinations were carried out independently three times using duplicate samples.

6.7.1.3 Single-dose antibacterial activity of crude iridium library (Chapter 3 and 4)

The combinatorial libraries were tested for their antibacterial activity against *Escherichia coli* NCTC 13476 and *Staphylococcus aureus* CCUG 19434.

A single colony of bacteria was grown in 5 mL of TSB (for *S.aureus*) or LB (*E. coli* and *A. baumanii*) and incubated overnight at 37 °C (140 rpm). 100 µL of this overnight culture was added to 5 mL of the same growth medium, and the day culture was incubated at 37 °C (200 rpm) until the mid-exponential phase (OD_{600} was 0.6 – 1.0). A sample of this culture was diluted with Mueller Hinton (MH) broth to OD_{600} = 0.022, about 5 × 10^5 cells/mL and added to all wells except sterile control. Samples were diluted to 750 µM and 1.5 mM using DMSO. From these stock solutions, 20 µL from 1.5 mM for 100 µM, 20 µL (for 50 µM) or 5 µL (for 12.5 µM) per sample was added to 96 well plates. MH growth media was added to each well (making up the volume to 290 µL), followed by the

relevant bacteria in MH growth media (10 µL). The plates were incubated for 16 – 20 h at 37 °C. Bacterial growth was assessed by measuring optical density at 600 nm (OD_{600}) using a microplate reader.

6.7.1.4 Determination of Antibacterial Activity: Minimum Inhibitory Concentration (MIC) Assay (Chapter 3 and 4)

The purified compounds were tested for their antibacterial activity against *Acinetobacter baumanii* AB5075, *Bacillus subtilis* MW168, *Enterococcus feacalis* CCUG 19916T*, Enterococcus faecium* CUG 19434, *Escherichia coli* NCTC 13476, *Staphylococcus aureus* CCUG 19434, *Staphylococcus aureus* JE2 (MRSA) methicillin susceptible *Staphylococcus aureus* (MSSA) SH1000*, Staphylococcus epidermidis* TU3298*.*

A single colony of bacteria was grown in 5 mL of TSB (for Gram-positive panel) or LB (Gram-negative panel) and incubated overnight at 37°C (140 rpm). Stock solutions of 5 mM of the samples (10 mM for building blocks) were prepared in DMSO and diluted to a starting concentration of 100 µM (200 µM for building blocks) in Mueller Hinton (MH) medium. The overnight culture was diluted and incubated until the OD_{600} reached 0.6 – 1.0. The bacteria concentration was measured by measuring the optical density at 600 nm and diluted to an OD_{600} of 0.022 in MH medium. 5 µL of the diluted bacterial solution was used to inoculate 150 µL of the sample solutions, resulting in a final inoculation of about 5×10^5 cells/mL. The plates were then incubated at 37 °C for 18 hours. For each assay, a control of broth only and a growth control of broth with bacterial inoculum without antibiotics were included in two columns of the plate. Polymyxin B and vancomycin were used as control antibiotic for Gram-negative panel *and* Gram-positive panel, respectively. Bacterial growth was assessed by measuring optical density at 600 nm (OD_{600}) using a microplate reader. Each experiment was performed in triplicate.

6.7.1.5 MIC Assay against *Bacillus subtilis* 168CA[306]

A single colony of bacteria was grown in 2 mL of LB media and incubated overnight at 37 °C (140 rpm). Stock solutions of 5 mM of the samples were prepared in DMSO and diluted to a starting concentration of 100 µM in Mueller Hinton (MH) medium. The overnight culture was diluted and incubated until the OD_{600} reached 0.6 – 1.0. The bacteria concentration was measured by measuring the optical density at 600 nm and diluted to an OD_{600} of 0.022 in MH medium. 5 µL of the diluted bacterial solution was used to inoculate 150 µL of the sample solutions, resulting in a final inoculation of about 5×10^5 cells/mL. The plates were then incubated at 37 °C for 18 hours. For each assay, a control of broth only and a growth control of broth with bacterial inoculum without

antibiotics were included in two columns of the plate. Vancomycin were used as control antibiotic for Gram-negative panel *and* Gram-positive panel, respectively. Bacterial growth was assessed by OD_{600} using a microplate reader. Each experiment was performed in triplicate.

6.7.1.6 Minimum Bacteriacidal Concentration (MBC) Assay (Chapter 3)

For MBC determination, MICs for the hit compound were evaluated as described previously. Then 5 µL of bacteria, coming from those wells where growth was inhibited by the pure compounds, were streaked onto TSB agar plates and further incubated at 37 °C for 24h. The lowest concentration of compound in which no CFU were observed after plating was determined to be the MBC. An antibiotic is regarded as bactericidal if MBC/MIC <4.

6.7.2 Checkerboard Assay: Determination of Synergy with Clinically-relevant Antibiotics (Chapter 2)

Interaction of **Pt1** with FDA-approved antibiotics was determined using chequerboard assays following CLSI guidelines. All compounds were freshly prepared for the experiment. Eight serial two-fold dilutions of **Pt1** were prepared from 1 to 0.0078 µg/mL. Test antibiotics were prepared in 12 serial two-fold dilutions as follows: ceftazidime 64–0.03125 µg/mL, daptomycin and vancomycin 8–0.0039 µg/mL, gentamicin, levofloxacin, meropenem, and minocycline 2-0.00095 µg/mL, linezolid 16–0.0078 µg/mL, rifampicin 0.06–0.000014 µg/mL. Dilution series were inoculated with 5×10^5 *S. aureus* ATCC 29213 CFU/mL and incubated for 16-20 h at 37 °C. Following incubation, the fractional inhibitory concentration index (FICI) was calculated with the formula FICI=FICA+FICB, whereby FICA= MIC of drug A in combination/MIC of drug A alone and FICB= MIC of drug B in combination/MIC of drug B alone. A drug combination is considered synergistic when ∑FICI is ≤0.5, indifferent when ∑FICI is >0.5 to 4, and antagonistic when ∑FICI is >4.

6.7.3 Checkerboard Assay: Determination of Synergy with Clinically-relevant Antibiotics (Chapter 3)

Interaction of the hit compound with FDA-approved antibiotics was determined using chequerboard assays following CLSI guidelines[395]. Pure compounds were two-fold serially diluted 11 times in a concentration range that spanned from 4 to 0.0039 µg/mL. Test antibiotics were prepared in 8 serial two-fold dilutions as follows: kanamycin, vancomycin and ciprofloxacin 2–0.03125 µg/mL, chloramphenicol 4–0.0625 µg/mL. Dilution series were inoculated with *S. aureus* at OD_{600}=0.022 and incubated for 16 – 20 h at 37 °C. Following incubation, the fractional inhibitory concentration index (FICI) was

calculated with the formula FICI=FIC_A+FIC_B, whereby FIC_A= MIC of drug A in combination/MIC of drug A alone and FICB= MIC of drug B in combination/MIC of drug B alone.

6.7.4 Postantibiotic effect (Chapter 2)

Postantibiotic effect (PAE) was determined as follows. Overnight culture of *S. aureus* ATCC 29213 were diluted in MHBII to ~10^5 CFU/mL, exposed to 1x and 10x MIC of **Pt1**, levofloxacin, and vancomycin, and incubated at 37°C for 1 h. Following incubation, cultures were centrifuged and washed twice with pre-warmed MHBII to remove any traces of antibiotics. Finally, cells were resuspended in drug-free MHBII and incubated further at 37 °C. Samples were taken every 1 h, serially diluted, and plated on tryptic soy agar (TSA) for enumeration of CFU. PAE was calculated as PAE = T – C; where T is the difference in time required for 1 log10 increase in CFU vs. CFU observed immediately after the removal of the drug, and C in a similarly treated drug-free control.

6.7.5 Resistance Induction[453] (Chapter 2)

S. aureus ATCC 29213 was serially passaged in the presence of 0.5×MIC of either **Pt1** or levofloxacin (positive control). The MICs of the passaged cultures were determined every 3 days and compared to that of wild type *S. aureus* ATCC 29213. MIC changes were recorded for 36 passages.

6.7.6 Cytotoxicity Testing of Compounds

6.7.6.1 Determination of Cytotoxicity of Lead Compounds against HEK293T (Human Embryonic Kidney) Cells (Chapter 2 and 5)[450]

Stock solutions of 5 mM of the compounds were prepared in DMSO and the stock solution of cisplatin and oxaliplatin were prepared in 1% NaCl as 4.3 mM and 2.5 mM respectively. The control for the experiments was DMSO. HEK293T cells were cultivated in DMEM high glucose supplemented with 10% heat-inactivated fetal bovine serum, 100 U/mL of penicillin and streptomycin and maintained at a temperature of 37 °C with 5% CO_2. Initially, 4000/well of cells were seeded into 96-well plates and incubated for 24 hours before being exposed to compounds at concentrations ranging from 0.78, 50, and 100 µM. After 24 hours of incubation, the compounds were added and serially diluted and incubated for 24 and 48 hours at 37 °C 5% CO_2, the cells were stained with alamar Blue, and the fluorescence excitation/ emission 540 nm/ 590 nm was measured using 96 well-plate reader. CC_{50} is defined as the lowest concentration of compound which leads to a 50% reduction in cell viability compared to untreated and DMSO control. Each experiment was repeated in triplicate.

6.7.6.2 Determination of cytotoxicity of lead compounds against Vero cells (Chapter 2)

Cell toxicity was performed against Vero cells using the MTT assay[454]. ~10^3 cells/well were seeded in 96 well plate and incubated at 37 °C with 5% CO_2 atmosphere. After 24 hours, compound was added ranging from 100-12.5 µg/mL concentration and incubated for 72 h. After the incubation was over, MTT was added in each well, incubated at 37°C for further 4 h, residual medium was discarded, 0.1 mL of DMSO was added to solubilise the formazan crystals and OD_{540} was taken for the calculation of IC_{50}. Doxorubicin was used as positive control and each experiment was repeated in triplicate.

6.7.6.3 Single Dose cytotoxicity of crude library against HEK293T cells (Chapter 3 and 4)

HEK293T cells were seeded at 10000 cells per well and incubated overnight to enable adhesion. Thereafter, the cells were treated with either the negative control (0.1%-0.28% DMSO depending on the concentration of the crude complexes) or the crude complexes at 50 µM for 24 hours. To quantify cell viability, the cells were treated with the 3-(4,5-dimethylthiazol-2-yl)-2,5 diphenyltetrazolium bromide (MTT) salt (Apollo Scientific, UK) according to the procedure described by Mosmann[455]. The absorbance at 590 nm was measured using a TECAN well plate reader instrument M1000. Each experiment was performed in duplicate, and the recorded absorbances were adjusted for the respective crudes and growth media

6.7.6.4 Dose-response cytotoxicity of selected combinatorial library against HEK293T (Chapter 3)

HEK293T cells were seeded at a density of 10000 cells per well and allowed to adhere overnight. Selected crude reaction mixtures (10 mM stock solutions) were diluted 1:2 and subsequently added to the cells to achieve final concentrations ranging from 20 to 120 µM in 20 µM increments and incubated for 24 hours. Thereafter, the MTT assay was used to quantify viable cells and at least three biological repeats in triplicate were conducted from which the CC_{50} was determined using GraphPad Prism v8.0.2 (GraphPad Software, California, USA). The absorbance at 590 nm was measured using a TECAN well plate reader instrument M1000. The experiment was performed as 3 biological repeats in triplicates.

6.7.6.5 Determination of cytotoxicity of purified iridium compounds against HEK293T (Chapter 3 and 4)

HEK293T cells were seeded at 10000 cells per well and incubated overnight. 5 mM stock solutions of hit compounds were prepared in DMSO. In a 1.5 mL 96 well dilution plate,

starting concentrations of 150 μM and 200 μM of each compound and serially diluted to 0.037 and 0.049 μM. 500 uL of media was then added to each well added to make 1 mL of each concentration (starting at 75 μM and 100 μM). 100 uL of these solutions were added into wells containing the cells and incubated for 24 h. Thereafter, the MTT assay was used to quantify viable cells and at least three biological repeats in triplicate were conducted from which the CC_{50} was determined using GraphPad Prism v8.0.2 (GraphPad Software, California, USA). The absorbance at 590 nm was measured using a TECAN well plate reader instrument M1000. 4 biological repeats in triplicate were done for this study (12 data points).

6.7.6.6 Determination of haemolytic activity in hRBCs: Haemolysis assay (Chapter 2, 3, and 4)

The compounds were tested on human red blood cells (hRBCs) using a haemolysis assay, adapted from previously published procedure[456]. 1.5 mL of whole blood was centrifuged at 3000 rpm for 15 minutes at 4 °C, and the plasma was discarded. The hRBC pellet was washed three times with PBS (pH 7.4) and then resuspended to a final volume of 10 mL in PBS. For the determination of HC_{50} of the lead compounds, the samples serially diluted starting from 200 μM. Samples stock solution was 5 mM in DMSO. Each plate included a blank medium control (PBS) and a haemolytic activity control (0.1% Triton TM X-100). The hRBC suspension was incubated with the samples in PBS in a V-shaped 96-well plate for 4 hours at 20 °C. After the incubation, 100 μL of supernatant was carefully pipetted to a flat bottom, clear 96-wells plate. Haemolysis was measured by analysing the absorbance at 540 nm using a plate reader. The percentage of haemolysis at each concentration was determined and the HC_{50} was calculated by inhibitor vs. normalized response fit. The haemolytic activity was measured by analysing the absorbance of free hemoglobin in the supernatants at 540 nm. Minimum inhibitory concentration (MHC) was determined by eye. Each experiment was repeated in triplicate.

6.7.6.7 Determination of Haemolytic Activity in hRBCs: Haemolysis Assay (Chapter 3 and 4)

The haemolysis assay was adapted from a previously reported procedure.[352] Whole blood (5 mL) was centrifuged (Thermo Scientific SL 8R) at 4500 rpm for 1 h at 4 °C, and the plasma was discarded. The remaining human red blood cell (hRBC) pellet was washed three times with PBS 1X (pH 7.4): for each wash, PBS was added up to 15 mL, followed by centrifugation at 4500 rpm for 1 h at 4 °C. After the final wash, the cells were resuspended in PBS to a final volume of 35 mL. The stock solutions for the samples to

be tested were 2.5 mM in PBS:DMSO (60:40). For the determination of HC_{50} and HC_{10} values, test compounds were diluted in PBS to give a concentration range from 200 µM down to 5 µM, giving a total volume of 125 µL. Dilutions were prepared in 20 µM decrements with the final points at 10 and 5 µM. Each plate included a blank medium control (PBS) and a haemolytic activity control (1% SDS in PBS). The hRBC suspension (125 µL) was incubated with the samples in PBS in a V-shaped 96-well plate for 4 hours at 25 °C. After incubation, 75 µL of supernatant was carefully pipetted to a flat bottom, clear 96-wells plate. Haemolysis was measured by absorbance at 540 nm using a plate reader (TECAN M1000). The percentage of haemolysis at each concentration was determined and the HC10 and HC50 were calculated by inhibitor vs. normalized response fit (Prism). The minimum haemolytic concentration (MHC) was determined by visual assessment of the wells after incubation. The MHC was defined as the lowest compound concentration at which visible haemolysis (red coloration of the supernatant and/or loss of intact red pellet) could be observed compared to the PBS control. Each experiment was repeated in triplicate.

6.7.7 Mode of Action Studies (Chapter 2, 3, and 4)

6.7.7.1 Determination of Optimal Stressor Concentration (OSC)

To establish a starting concentration for the OSC assay, MICs against parent strain *B.subtilis* 168CA were determined under conditions equivalent to those used for mode of action assays. MICs were determined according to the Clinical Laboratory Standardization Institute (CLSI) in a serial microdilution assay.[268] The compounds were serially 2-fold diluted in a 96-well plate and *B. subtilis* (168CA) was added to a final cell count of 5 x 10^5 CFU/mL. Cultures were incubated for 16 h at 37 °C under constant agitation. MICs were used as basis for OSC determination. To this end, growth curves were recorded using optical density measurements. Culture volumes of 20 mL were grown until reaching an OD_{600} of 0.3. Subsequently, the parent culture was split into 2 ml aliquots, followed by addition of different MIC multiples of compounds.[457] An untreated culture served as control. Growth was followed until cultures reached the stationary phase. A concentration achieving 50-70% growth inhibition in exponential phase was selected as optimal stressor concentration.

6.7.7.2 Fluorescence light microscopy

For chapter 2 experiments, microscopy images of bacteria were acquired on a Nikon Eclipse Ti2 equipped with a CFI Plan Apochromat DM Lambda 100X Oil objective (N.A. 1.45, W.D. 0.13 mm), a Photometrics PRIME BSI camera, a Lumencor Sola SE II FISH

365 light source, and an Okolab temperature incubation chamber.For chapter 3 experiments, microscopy images of bacteria were acquired on a Carl Zeiss Observer 7 equipped with a CFI Plan Apochromat DM Lambda 100X / 1.4 Oil objective, a monochrome Zeiss Axio 807 camera, Colbri 7 as an illumination light source. Images were obtained using zeiss Zen Blue software version 3.9. Images were obtained using the NIS elements AR software version 5.21.03/ 5.42.02. DNA stretching images were obtained on a Zeiss Observer.Z1 fluorescence microscope equipped with a Colibri 7 LED illumination system and an Andor iXON Ultra EMCCD camera. Image analysis was perfomred using ImageJ[458], MicrobeJ[459], and ObjectJ[460].

Table 43. *B. subtilis* strains used in mode of action assays for. mgfp= monomeric green-fluorescent protein.

Strain	Induction	Genotype	Reference
168CA	-	*trpC2*	461, 258
bSS82	-	*amyE::spc PrpsD-gfp*	457
UG10	0.5 % xylose	*amyE::spc Pxyl-recA-mgfp*	258,268
1048	1 % xylose	*cat rpoC-gfp Pxyl-'rpoC*	258,462
1049	1 % xylose	*amyE::spc Pxyl-rpsB-gfp*	258,462
LH131	0.1 % xylose*	*amyE::spc Pxyl-gfp-minD*	258,463
MW10	0.1 % xylose	*amyE::spc Pxyl-gfp-mreB*	457,464
2020	0.3 % xylose	*amyE::spc Pxyl-gfp-ftsZ*	465
BKE08820	-	*trpC2ΔkatA::erm*	466
BKE25020	-	*trpC2ΔsodA::erm*	467

6.7.7.3 Bacterial cytological profiling

BCP was performed according to Wenzel *et al*.[457] In short, *B. subtilis* strain MW54 (*PrpsD-gfp*) was grown to an OD_{600} of 0.3 prior to splitting of parent cultures and addition of antibiotics. Samples were taken for microscopy after 30, 60, and 120 min of antibiotic

treatment. Five minutes prior to sampling, cultures were stained with 0.5 µg/mL Nile red and 1 µg/mL DAPI for 5 min. Samples of 1 µL were then spotted onto 1% agarose slides[261] and images were taken immediately.

6.7.7.4 GFP localization studies

B. subtilis strains were grown in LB containing appropriate inducer concentrations as specified in Table S15. After reaching an OD_{600} of 0.3, cultures were split and treated with antibiotics. Samples were withdrawn after 30 and 60 min of treatment, spotted on glass slides covered with 1% agarose films[261], and immediately imaged.

6.7.7.5 Translation inhibition assay

B. subtilis strain TB35 (*Pxyl-minD-gfp*) was grown in LB without inducer. After reaching an OD_{600} of 0.3, antibiotics and inducer (0.1% xylose) were added consecutively. Samples were withdrawn for microscopy after 60 min of treatment, spotted on glass slides covered with 1% agarose films[261], and imaged without delay.

6.7.7.6 Propidium iodide pore assay[457]

Propidium iodide staining was performed as described previously *B. subtilis* 168CA was grown to an OD_{600} of 0.3 prior to splitting of the parent culture and treatment with the different antibiotics. After 15 and 45 min, samples were stained with 13.3 µg/mL propidium iodide for 15 min (total treatment times 30 and 60 min), and washed 3 times with phosphate-buffered saline (PBS). Fluorescence signals were recorded at an excitation wavelength of 535-15 nm and an emission wavelength of 617-20 nm in a BMG Clariostar Plus plate reader.

6.7.7.7 $DiSC_3(5)$-based membrane potential measurements[457]

The membrane potential was measured according to Winkel *et al.* with minor modifications.[261] *B. subtilis* 168CA was grown in LB containing 50 µg/mL bovine serum albumin (BSA). Cells were transferred to black 96-well polystyrene microtiter plates after reaching an OD_{600} of 0.3. $DiSC_3(5)$ was added to a final concentration of 1 µM, maintaining a constant concentration of 1% DMSO to avoid precipitation of the dye. After the fluorescence baseline had stabilized, antibiotic compounds were added, and measurements were continued for 30 min. Fluorescence was recorded at an excitation wavelength of 610-30 nm and an emission wavelength of 675-50 nm in a BMG Clariostar Plus plate reader.

6.7.7.8 Single-molecule imaging of DNA

DNA stretching was performed on silanized glass coverslips (18 × 18 mm^2) using a silanization protocol adapted from Wei *et al*..[468] Briefly, glass coverslips were arranged in a coverslip rack and submerged overnight in acetone solution containing 1 % APTES and 1% ATMS (v/v). The activated coverslips were then rinsed with a (2:1 v/v) acetone:water solution and dried with air purging. Prior to imaging, 138.6 ng of λ-DNA were treated with the respective compounds for 10 min, followed by staining with 320 nM YOYO-1 in 0.5× Tris-borate-EDTA (TBE) buffer. To minimize photobleaching, 2% β-mercaptoethanol (BME) was added. 3.2 µL of the stained DNA sample were placed at the interface between a silanized coverslip and a clean microscope slide to stretch the DNA molecules. A band-pass excitation filter (475/40 nm) and a band-pass emission filter (530/50 nm) were used for detecting YOYO-1 fluorescence.

6.7.7.9 DNA length analysis

To analyse the length of individual DNA molecules, the ImageJ[458] plugin MicrobeJ[459] was used. DNA molecules were detceted using medial axis detection with 1 µm minimum length, 0.3 to 1.5 µm width range with 0-0.04 variation, and a maximum circularity value of 0.7. DNA molecules that were not correctly detected were selected manually. DNA length measurements were analyzed and visualized with Origin 2023.

6.7.7.10 ROS scavenger assay

LB media were prepared to contain either 10 mM tiron, 150 mM thiourea, 10 mM tiron and 150 mM thiourea, or no scavanger. Serial two-fold dilutions of the different antibiotics were prepared in the respective media and transferred to 96-well plates. *B. subtilis* 168CA was added to a final cell count of 5 x 10^5 CFU/mL and cultures were incubated at 37 °C for 16 h under constant agitation. The OD_{600} was meassured in a BMG Clariostar Plus plate reader.

6.7.7.11 Antibiotic uptake assay[269] (Chapter 2)

A single colony of bacteria was grown in Luria-Bertani (LB) medium overnight at 37 °C. Stock solutions of 5 mM of the samples were prepared in DMSO for **Pt1** and **Pt8**, and 5.3 mM in 0.9% $NaCl_{(aq)}$ for **CisPt**. The overnight culture was diluted in 80 mL LB medium and grown until it reached an OD_{600} of 0.3-04. 10 mL of the culture were distributed to falcon tubes and cells were stressed with 1.56 µM **Pt1**, 6.25 µM **Pt8** and 100 µM **CisPt** for 30 and 60 min. Then, the cells were harvested at 4500 rpm for 10 min and the supernatant was collected. The cell pellets were washed with 1 mL washing buffer (100 mM Tris, 1 mM EDTA, pH 7.3) and centrifuged at 4500 rpm for 10 min each.

Subsequently, cell pellets were resuspended in 1 mL PBS (pH 7.5), treated with 500 µL lysing buffer (0.1 M glycine-HCl, pH 2.5), and incubated overnight at room temperature. Following incubation, samples were centrifuged at 14000 rpm for 5 min and supernatant (cell lysis) and pellet (cell debris) were collected. After pellets were resuspended in 750 µL PBS (pH 7.5), all samples were frozen in liquid N_2 and lyophilized overnight. Then, samples were treated with 300 µL nitric acid (69.7% (w/mL) in double-distilled water) and incubated for a week at room temperature, followed by incubation at 65°C for 4 hours. Then, the samples were diluted to 2% nitric acid content with double-distilled water and filtered through 0.22 µm syringe filters.

The ICP-MS system was operated in kinetic energy discrimination (KED) mode and the collision gas was He50 (AlphaGaz), pre-treated with a helium cell gas filtration system (Perkin Elmer, N8146004). The gas flow for KED was 5.3 mL/min. 2% HNO_3 (*w*/*w*) was used as matrix for all sample, calibration, and internal standard (IS) solutions. 2% HNO_3 (*w*/*w*) itself was prepared from 69.3% (*w*/*w*) HNO_3 (BASF, < 1 ppb ECME), diluted with ultrapure water (ρ = 18.2 MΩ·cm). Calibration solutions of 0.1, 1, 10 and 50 mg/L Mg, Mn, and Pt were prepared. For Mg and Mn, the 'ICP multi-element standard solution VIII' (Merck, 1.09492) was used as a stock solution. 'Platinum Standard for ICP' (Sigma-Aldrich, 19078) was used as a stock solution for Pt. All elements were combined in the same calibration solutions. 20 mg/L Ir and 20 mg/L Y in 2% HNO_3 were used as internal standards (IS) during the ICP-MS analysis. Y was used as IS for Mg and Mn. Ir was used as IS for Pt. Stock solutions were 'Iridium ICP standard' (Supelco, 1.70325) and 'Yttrium ICP standard' (Merck, 1.70368). Both elements were combined in the same IS solutions. The respective isotopes measured were: ^{24}Mg, ^{26}Mg, ^{55}Mn, ^{89}Y, ^{195}Pt, and ^{193}Ir. Each sample measurement consisted of 7 replicates and no automatic corrections for potential interferences were applied.

6.7.7.12 Antibiotic uptake assay with ICP-OES (Chapter 4)

A single colony of *S. aureus* CCUG 19434 was grown in TSB medium overnight at 37 °C. Stock solutions of 5 mM of the samples were prepared in DMSO. The overnight culture was diluted in 130 mL TSB medium and grown until it reached an OD_{600} of 0.3-04. 10 mL of the culture were distributed to falcon tubes and cells were stressed with different concentrations of antibiotics for 60 min. Then, the cells were harvested at 4500 rpm for 10 min and the supernatant was collected. The cell pellets were washed with 1 mL washing buffer (100 mM Tris, 1 mM EDTA, pH 7.3) and centrifuged at 4500 rpm for 10 min each. Subsequently, cell pellets were resuspended in 1 mL PBS (pH 7.5), treated

with 500 µL lysing buffer (0.1 M glycine-HCl, pH 2.5), and incubated overnight at room temperature. Following incubation, samples were centrifuged at 14000 rpm for 5 min and supernatant (cell lysis) and pellet (cell debris) were collected. After pellets were resuspended in 750 µL PBS (pH 7.5), all samples were frozen in liquid N_2 and lyophilized overnight. Then, samples were treated with 300 µL nitric acid (69.7% (w/mL) in double-distilled water) and incubated for 24 hours at 40°C. Samples were then made up to a total analytical volume of 10mL with ultrapure H_2O, giving a final HNO_3 volume of 2.1%.

6.7.7.13 Determination of MIC in Glucose Defined Minimal Medium (GDMM) (Chapter 3 and 5)

GDMM preparation was preapared based on the literature.[133] Briefly, M9 salts 5x were dissolved in distilled H_2O as per manufacturer's instruction (composition: KH_2PO_4 15 g/L, NaCl 2.5 g/L, Na_2HPO_4 33.9 g/L, NH_4Cl 5 g/L), pH was adjusted to 7.4 with concentrated NaOH and the solution was autoclaved. Prior to growth studies M9 5x solution was diluted to 1x with autoclaved distilled H_2O and further supplemented with 1 mM $MgCl_2$, 20 mM glucose (both of which previously filtered with a 0.2 µm filter) and Trace Elements solution 1x (composition: 5 g/L ethylenediaminetetraacetic acid (EDTA), 0.5 g/L $FeCl_3 \cdot 6H_2O$, 50 mg/L ZnO, 10 mg/L $CuCl_2 \cdot 2H_2O$, 10 mg/L $CoNO_3 \cdot 6H_2O$, 10 mg/L H_3BO_3, 0.12 mg/L $(NH_4)_2MoO_4$, 17 mg/L Na_2O_4Se).

Bacterial overnight cultures were grown overnight in the appropriate growth medium (TSB for *S. aureus*), then cells were centrifuged, washed once with GDMM and grown in GDMM supplemented with 10% v/v TSB to facilitate growth. MIC assay was then carried out as previously described. Each experiment was repeated in triplicate.

6.7.7.14 MIC Shift Assay (Chapter 3 and 5)

This protocol was adapted from the literature[469]. Commercially available UltraPure Calf Thymus (CT) DNA (10 mg/mL) was diluted in sterile TE buffer (10 mM Tris-HCl, 0.1 mM EDTA, pH adjusted to 8.2) to 7.50, 3.75, 1.88, and 0.75 mg/mL. MIC assay was then carried out as previously described for *B. subtilis* 168CA in MH medium with or without addition of 15 µL of DNA as final concentration 500, 250, 125, 50 µg/mL (from respective dilutions in TE). The plate was pre-incubated at 37°C for 15 minutes, followed by the addition of 5 µL of bacterial suspension (OD_{600}: 0.022). Then, the plates were incubated at and 37 °C for 20 h and bacterial growth was assessed by measuring optical density at 600 nm (OD_{600}) using a microplate reader. As a positive control, the DNA intercalator actinomycin D was included. Vancomycin was used as a negative control. The experiment consisted of three independent biological replicates with technical triplicates.

6.7.7.15 Fluorescence Quenching: Competitive Ethidium Bromide Displacement.[354,355] (Chapter 3 and 5)

Serial dilutions of **Ir15** were prepared from a 200 μM stock solution in a black 96-well plate to a final volume of 50 μL per well. A 10 mM (3.94 mg/mL) ethidium bromide (EtBr) stock solution and commercially available UltraPure calf thymus (CT) DNA (10 mg/mL) were diluted in HEPES buffer (80 mM HEPES, 25 mM NaCl, pH 7.16) to final concentrations of 1 μg/mL and 0.8 μg/mL, respectively. The DNA-EtBr mixture was then incubated with shaking at 37 °C for 30 min. After incubation, 50 μL of the DNA-EtBr solution was added to each well containing Ir16. Fluorescence kinetic measurements were subsequently recorded at at an excitation wavelength of 530 nm and an emission wavelength of 590 nm in a TECAN well plate reader instrument M100037 °C at 37 °C for 1 h .

6.7.8 Murine *In Vivo* Infection Model (Chapter 2)[470]

In vivo efficiacy was evaluated by Dr. Sidharth Chopra and co-workers. *In vivo* efficacy of **Pt1** was determined in a superficial skin infection model. Briefly, male Swiss mice, 4–6 weeks old, weighing ∼22–25 g, were used throughout the study. Mice were caged alone in an individually vented cage (IVC) to check cross-contamination and to maintain aseptic conditions throughout the experiment. Ketamine and xylazine were prepared in distilled water, 40 mg/kg and 8 mg/kg of body weight, respectively, and injected intraperitoneally (IP) as a mixture of 100 μL in each mouse for anaesthesia. Then, we proceeded with the removal of fur by applying depilatory cream. The area was cleaned with sterile distilled water. Approximately 2 cm^2 of skin area was scratched until it became visibly reddened and glistening without any bleeding. For bacterial infection, a 10 μL droplet containing 10^7 CFU/mL of *S. aureus* ATCC 29213 was applied to the reddened area of skin. To confirm the infection, post 4 h, untreated mice were sacrificed, skin homogenized, and various dilutions of the treatment groups (6 mice per group) were plated on TSA plates. Following this, treatment with 2% fusidic acid (positive control), 2% **Pt1**, and base (vehicle) was started, followed by a second dose post 16 h from the first dose. Henceforth, the drug regimen was comprised of twice daily application (in the morning and the evening, with an 8 h interval) for 4 days. Control mice were regularly treated with 25–30 mg each of 2% fusidic acid (LEO Pharma, Ballerup, Denmark), 2% infuzide, and base (vehicle). All groups were sacrificed post-18 h of the last dose to avoid carryover effects of the treatment group. Around ∼2 cm^2 of wounded skin were excised post sacrifice and homogenized in 500 μL PBS in 2 mL MP tissue grinding Lysing Matrix F tubes using MP FastPrep-24 set at 4.0 M/S for 30 s (3 cycles). Dilutions were plated

post homogenization on TSA plates, followed by overnight incubation at 37 °C, to determine the bacterial CFU count in each treatment group. Each experiment was repeated three times in duplicate and the mean and SEM of Log_{10} CFU/g were plotted.

List of Abbreviations

S. aureus	Staphylococcus aureus
MRSA	Methicillin-resistant *Staphylococcus aureus*
MSSA	Methicillin-susceptible *Staphylococcus aureus*
B.subtilis	Bacillus subtilis
E. feacium	Enterococcus faecium
E. faecalis	Enterococcus faecalis
E.coli	Escherichia coli
A. baumannii	*Acinetobacter baumannii*
K. pneumania	*Klebsiella pneumoniae*
E. cloacae	*Enterobacter cloacae*
P. aeruginosa	*Pseudomonas aeruginosa*
MIC	Minimum inhibitory concentration
HEK293T	Human Embryonic Kidney cells
hRBC	Human Red Blood Cells
TLC	Thin layer chromatography
LC-MS	Liquid chromatography mass spectrometry
GC-MS	Gas chromatography mass spectrometry
NMR	Nuclear magnetic resonance
ESI-MS	Electrospray ionization mass spectroscopy
ICP-MS	Inductively coupled plasma mass spectroscopy
ICP-OES	Inductively coupled plasma optical emission
Cp	Cyclopentadienyl
COD	1,5 Cyclooctadiene
DBU	1,8-Diazabicycloundec-7-ene
CuAAc	Copper(I)-catalyzed azide-alkyne cycloaddition
SuFEx	Sulphur(VI) fluoride exchange
DMF	Dimethylformamide
PMBN	Polymyxin B nonapeptide
BCP	Bacteria cytological profiling
DAPI	4’.6-diamidino-2-phenylindole
GFP	Green fluorescent protein
PI	Propidium Iodide
$DisC_3(5)$	3,3'-Dipropylthiadicarbocyanine iodide

DMSO	Dimethyl sulfoxide
PAE	Post antibiotic effect
MH	Mueller-Hinton
LB	Luria-Bertani
DMEM	Dulbecco’s modified eagle medium
ML	Machine Learning
D2B	Direct-2-Biology
HTE	High-throughput experimentation
FDA	Food and Drug Administiration

Chapter 7: Appendix

7.1 NMR Spectra



Figure 109. ^{1}H NMR spectrum of **COD-Br$_2$** in $CDCl_3$.

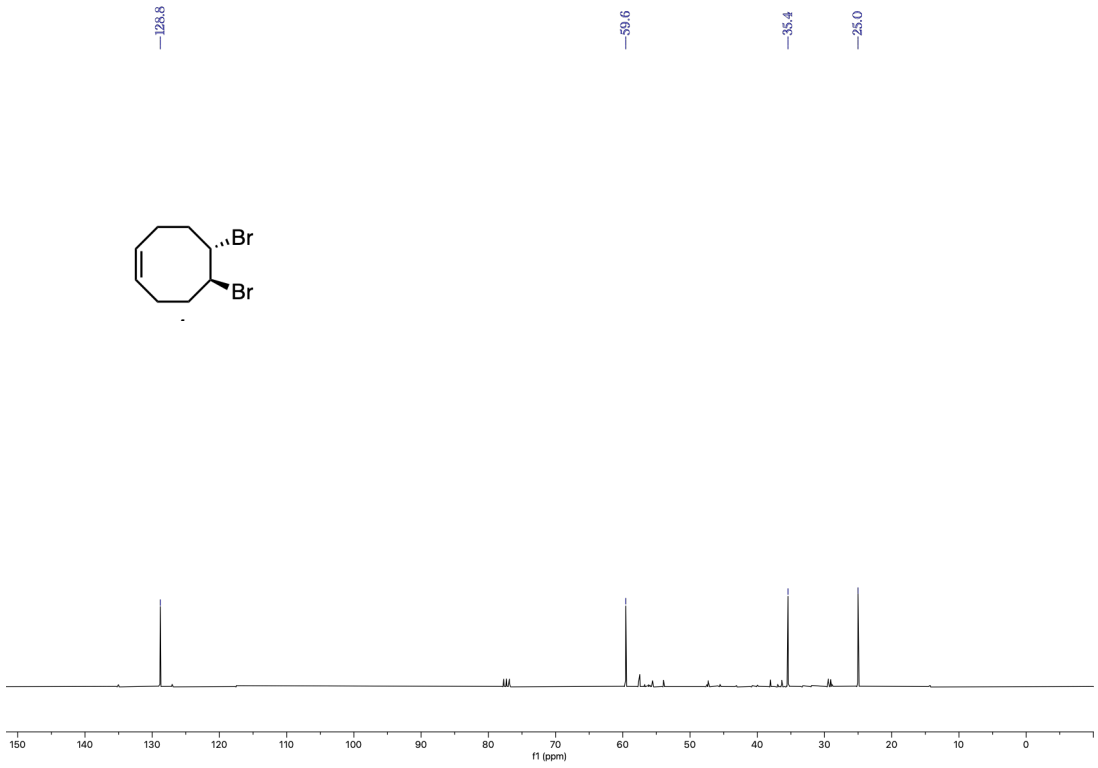


Figure 110. ^{1}H NMR spectrum of **COD-Br$_2$** in $CDCl_3$.

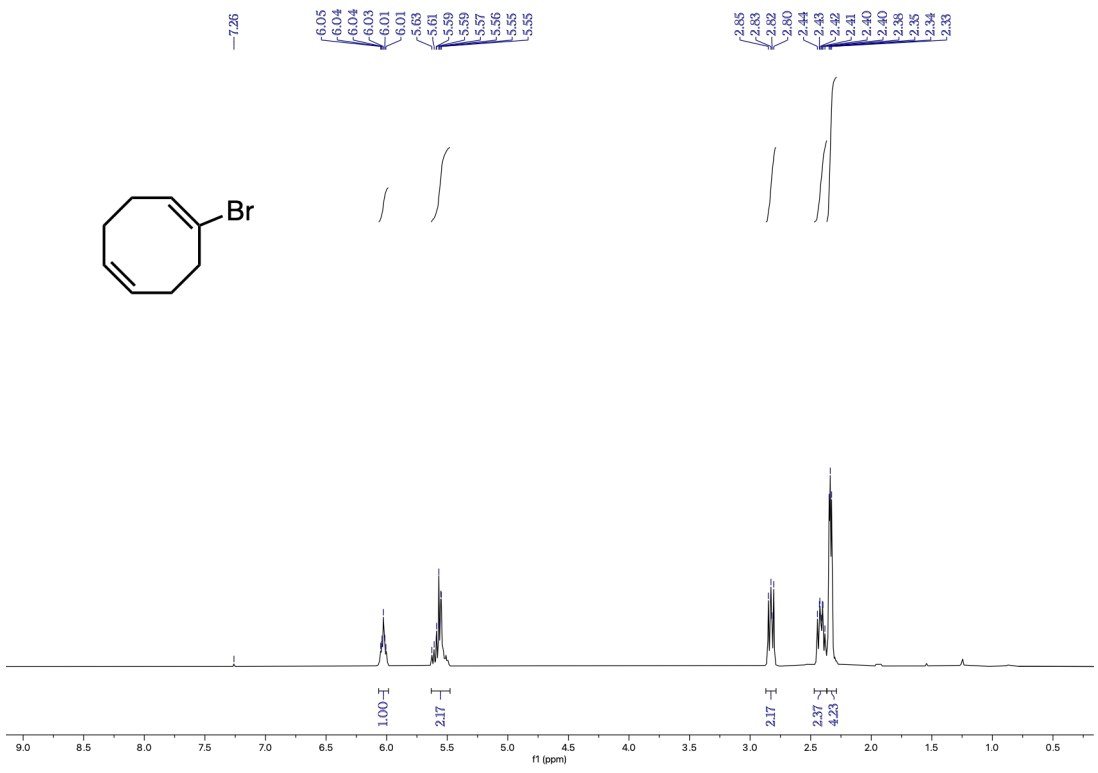


Figure 111. ^{1}H NMR spectrum of **COD-Br** in $CDCl_3$.

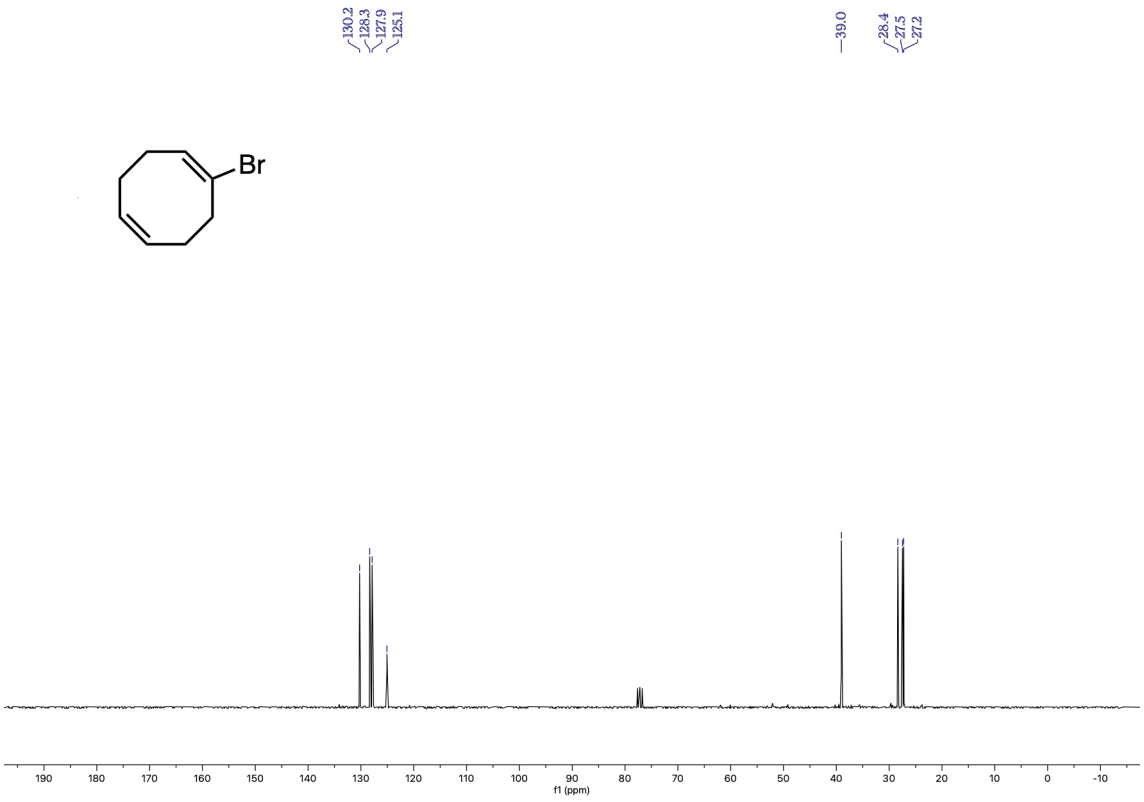


Figure 112.[13]C NMR spectrum of **COD-Br** in $CDCl_3$.

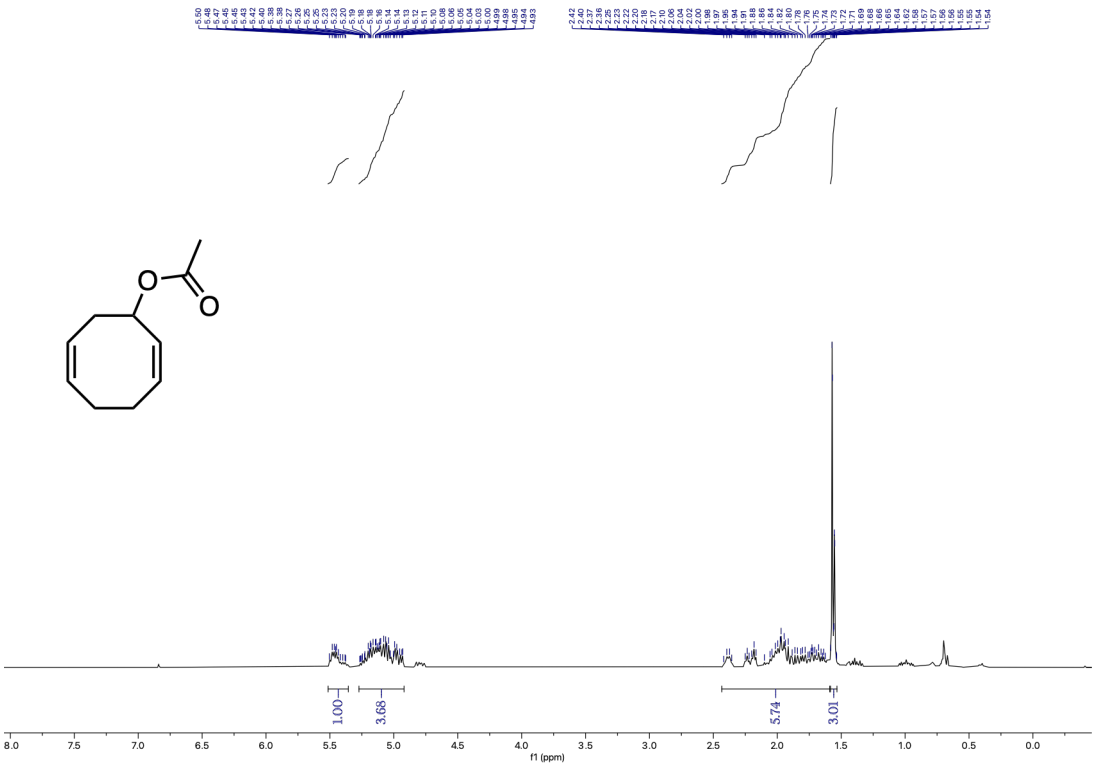


Figure 113. [1]H NMR spectrum of **27** in $CDCl_3$.

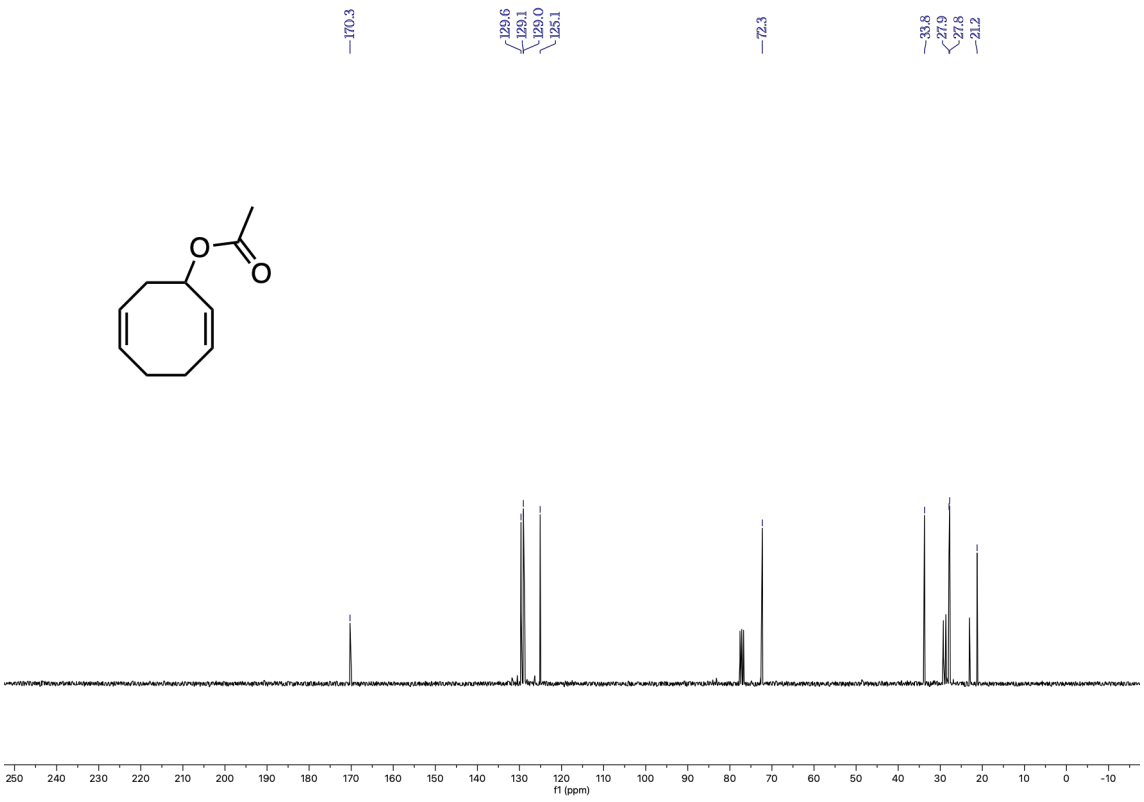


Figure 114. ^{13}C NMR spectrum of **27** in $CDCl_3$.

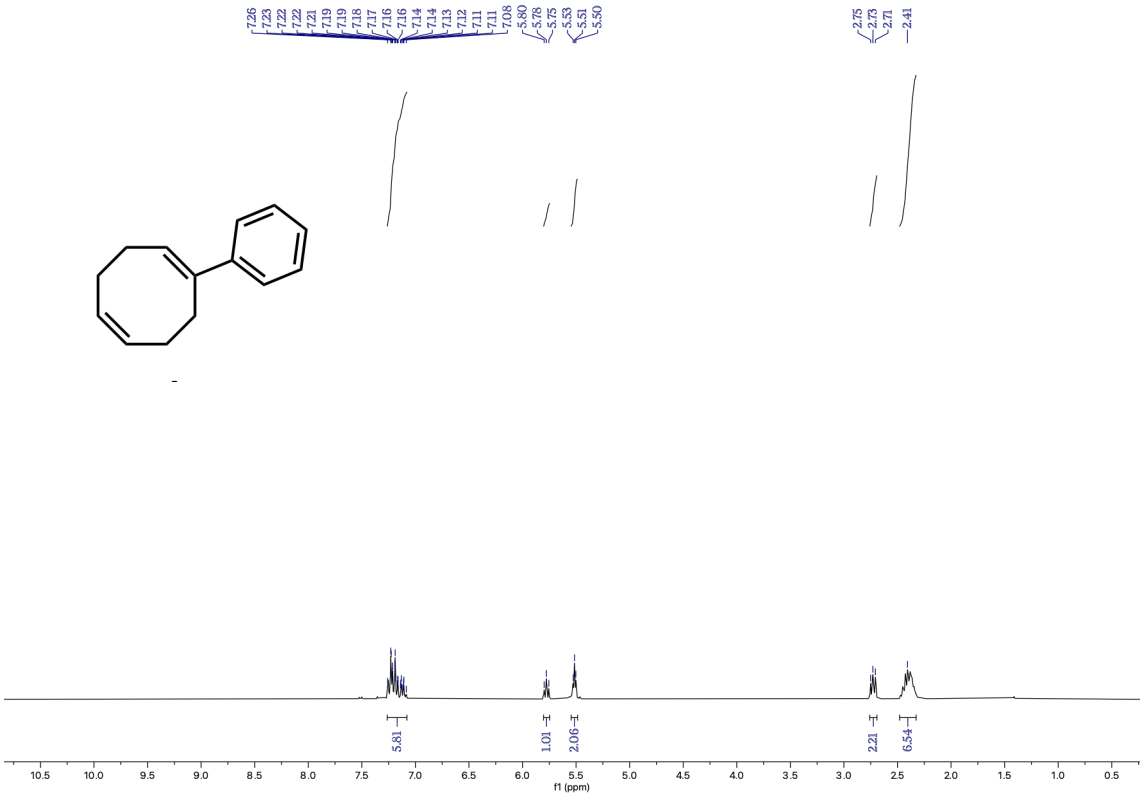


Figure 115. ^{1}H NMR spectrum of 23 in $CDCl_3$.

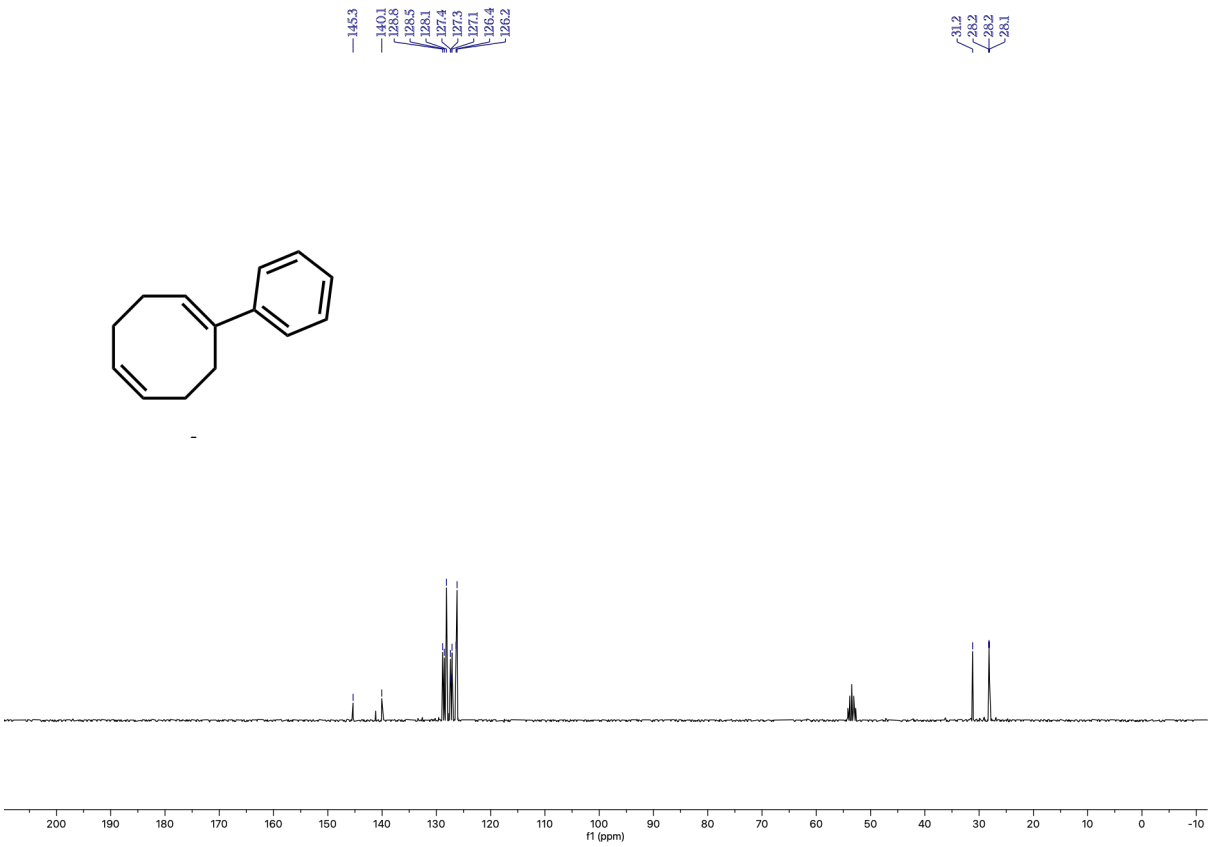


Figure 116. ^{13}C NMR spectrum of **23** in $CDCl_3$.

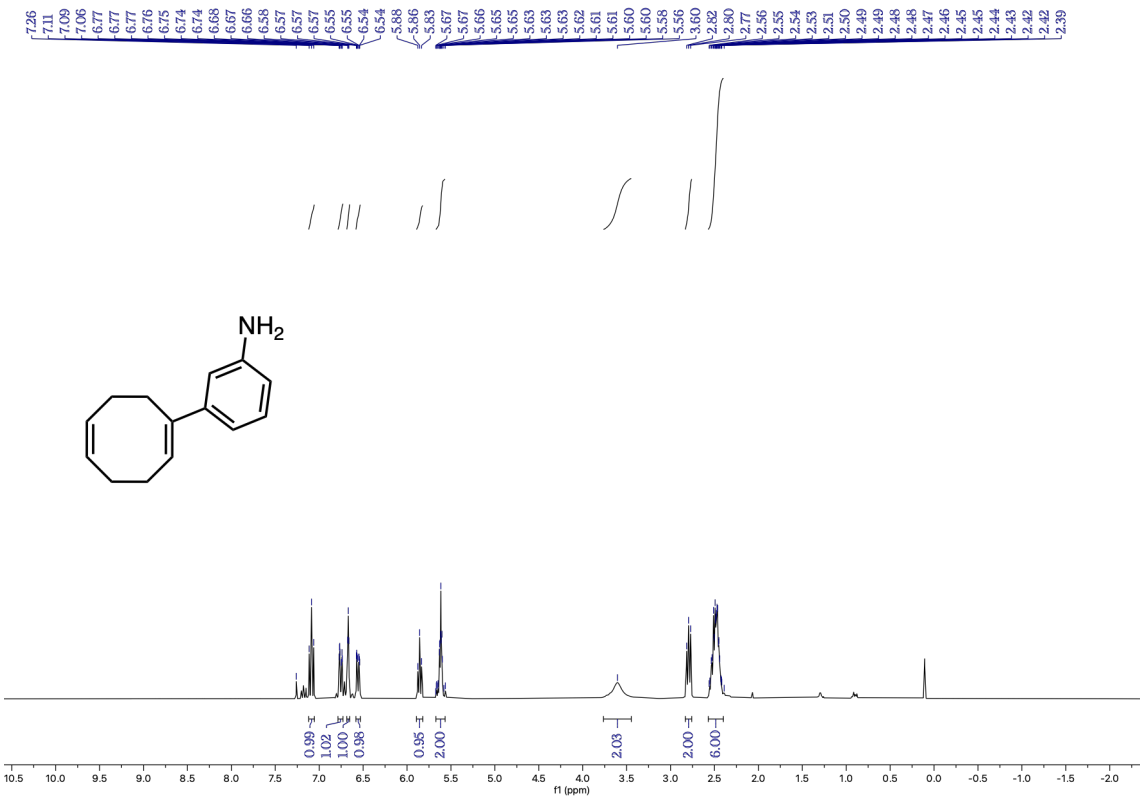


Figure 117. ^{1}H NMR spectrum of **24** in $CDCl_3$.

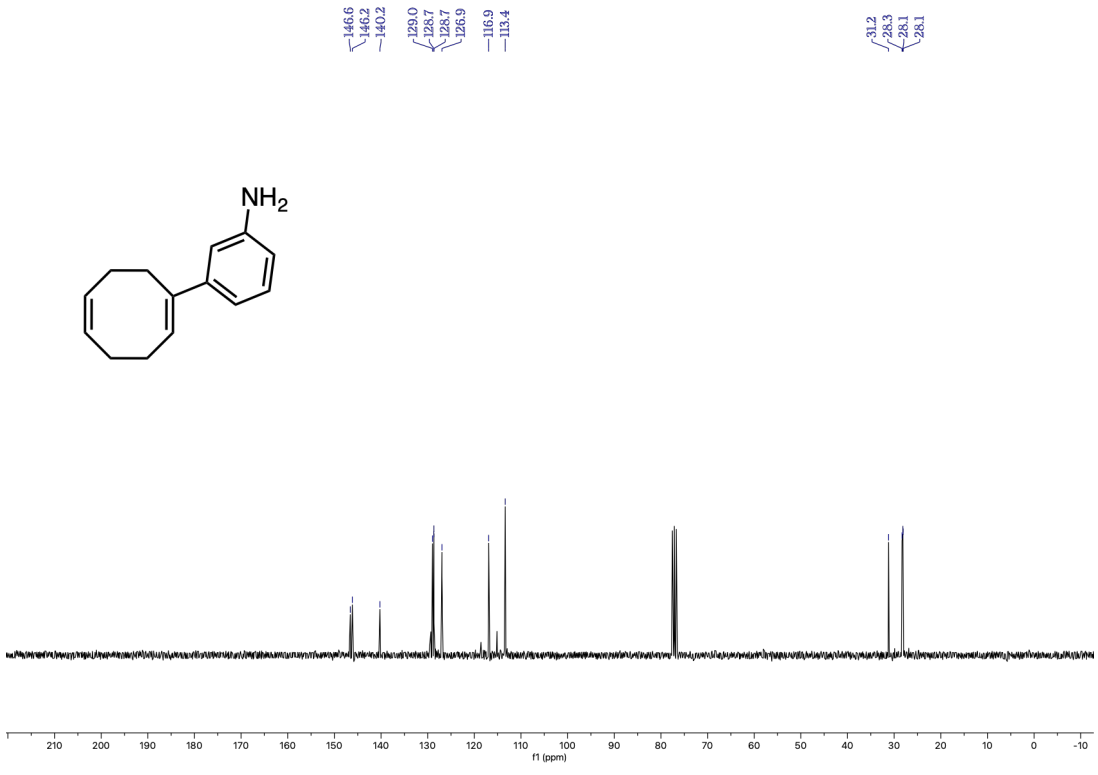


Figure 118. ^{13}C NMR spectrum of **24** in $CDCl_3$.

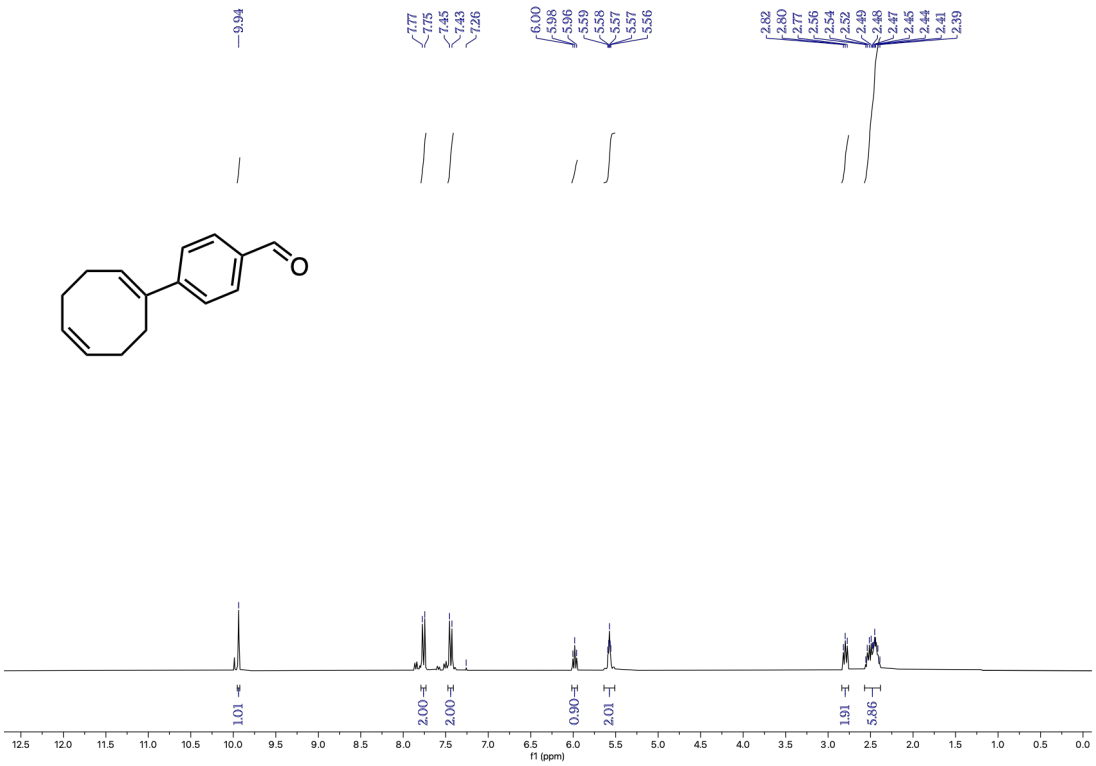


Figure 119. ^{1}H NMR spectrum of **25** in $CDCl_3$.

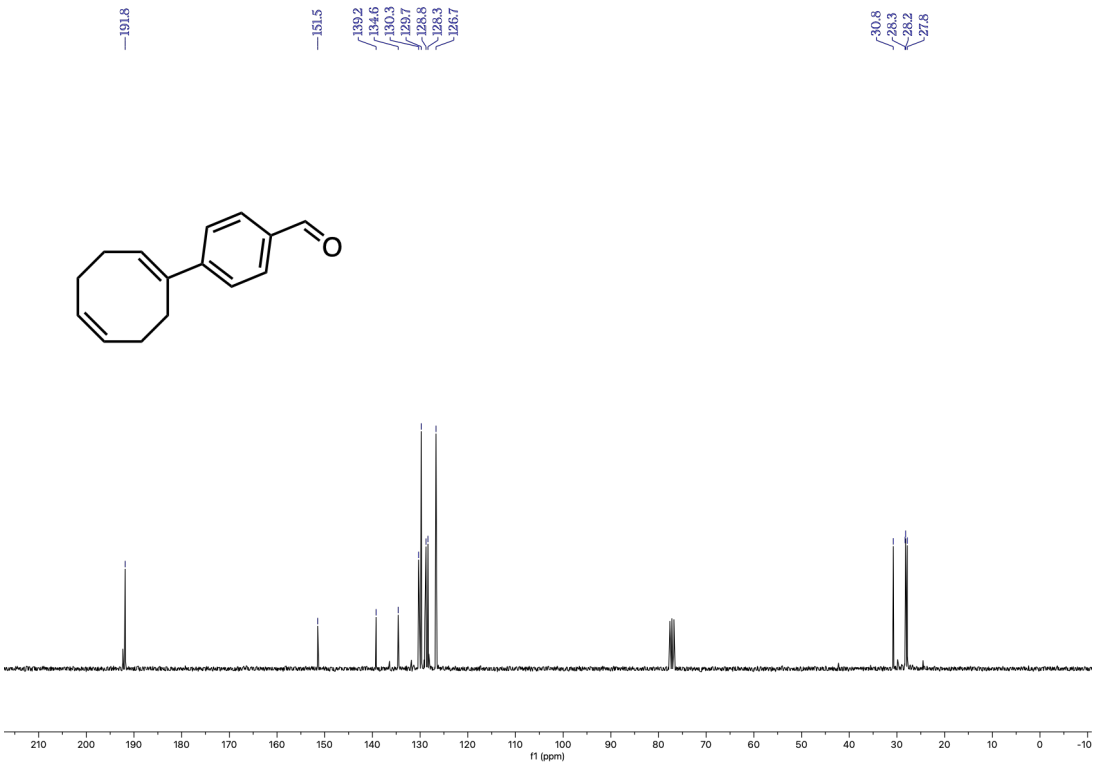


Figure 120. ^{13}C NMR spectrum of **25** in $CDCl_3$.

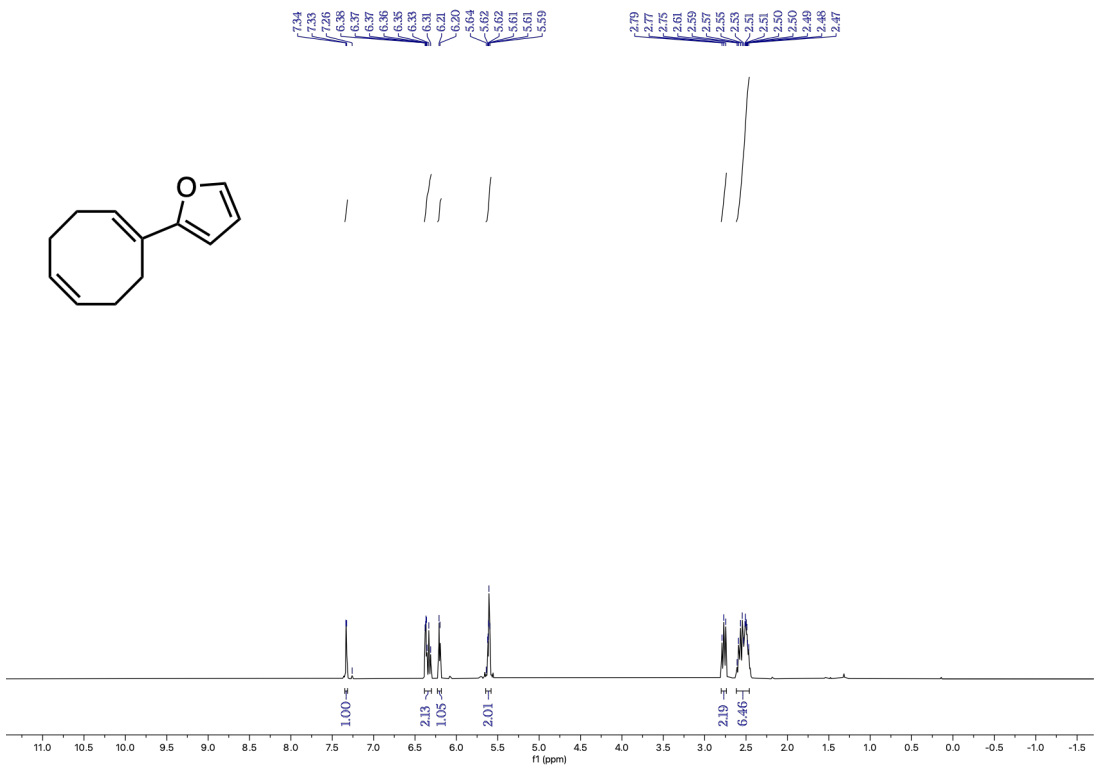


Figure 121. ^{1}H NMR spectrum of **26** in $CDCl_3$.

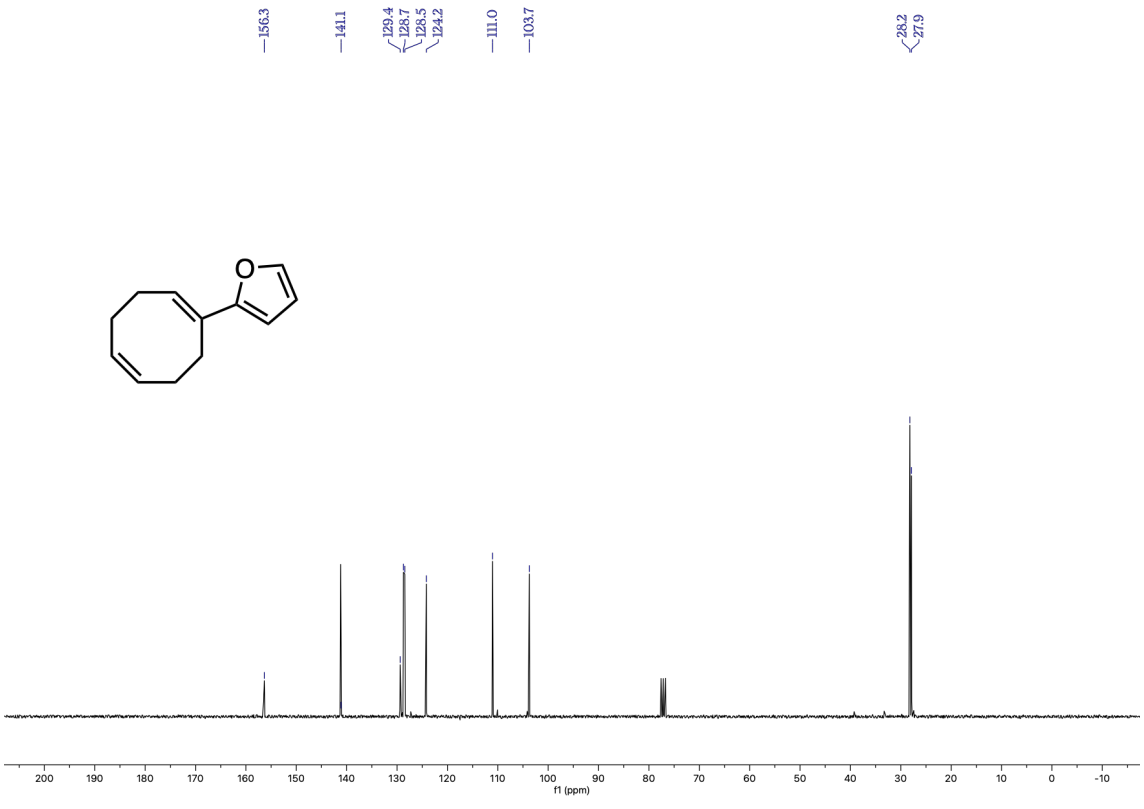


Figure 122. ^{13}C NMR spectrum of **26** in $CDCl_3$.

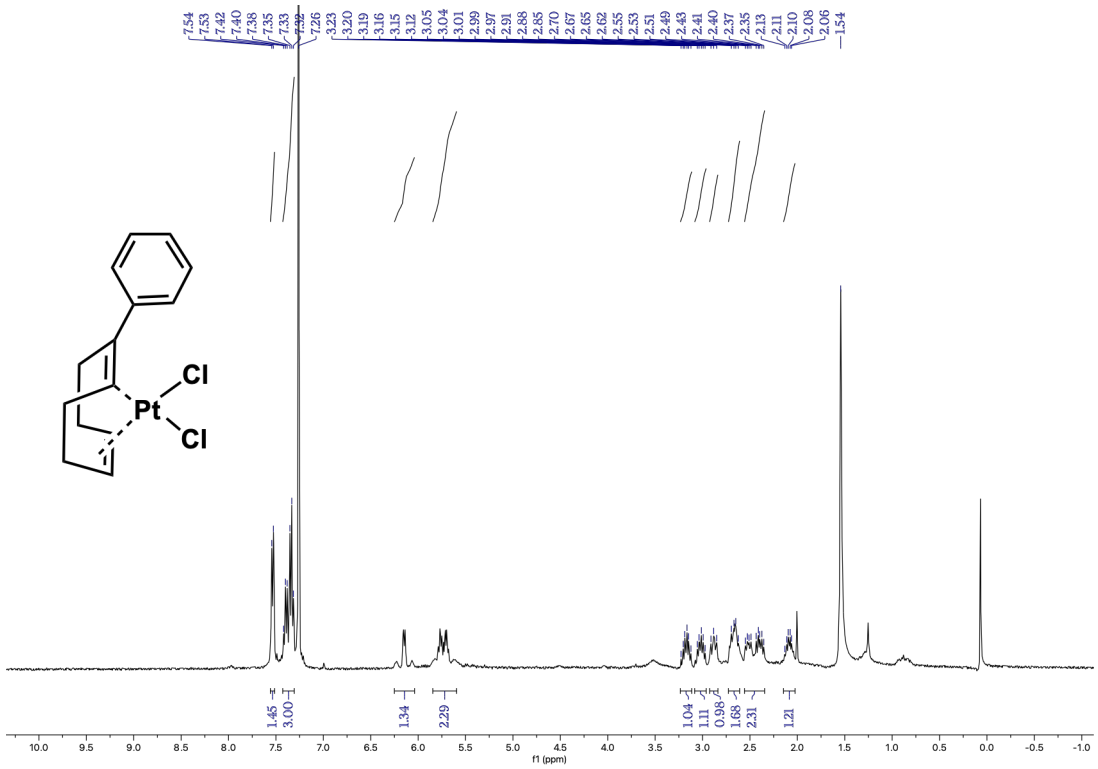


Figure 123. ^{1}H NMR spectrum of **Pt2** in $CDCl_3$.

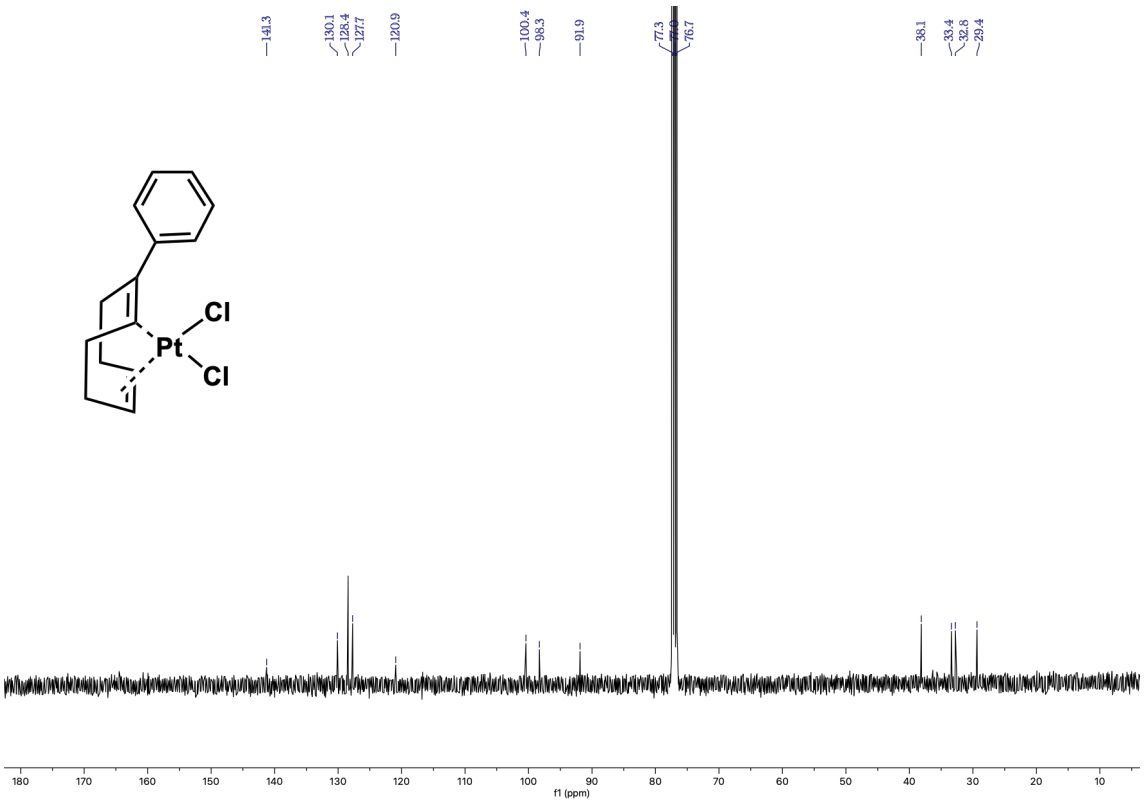


Figure 124. ^{13}C NMR spectrum of **Pt2** in $CDCl_3$.

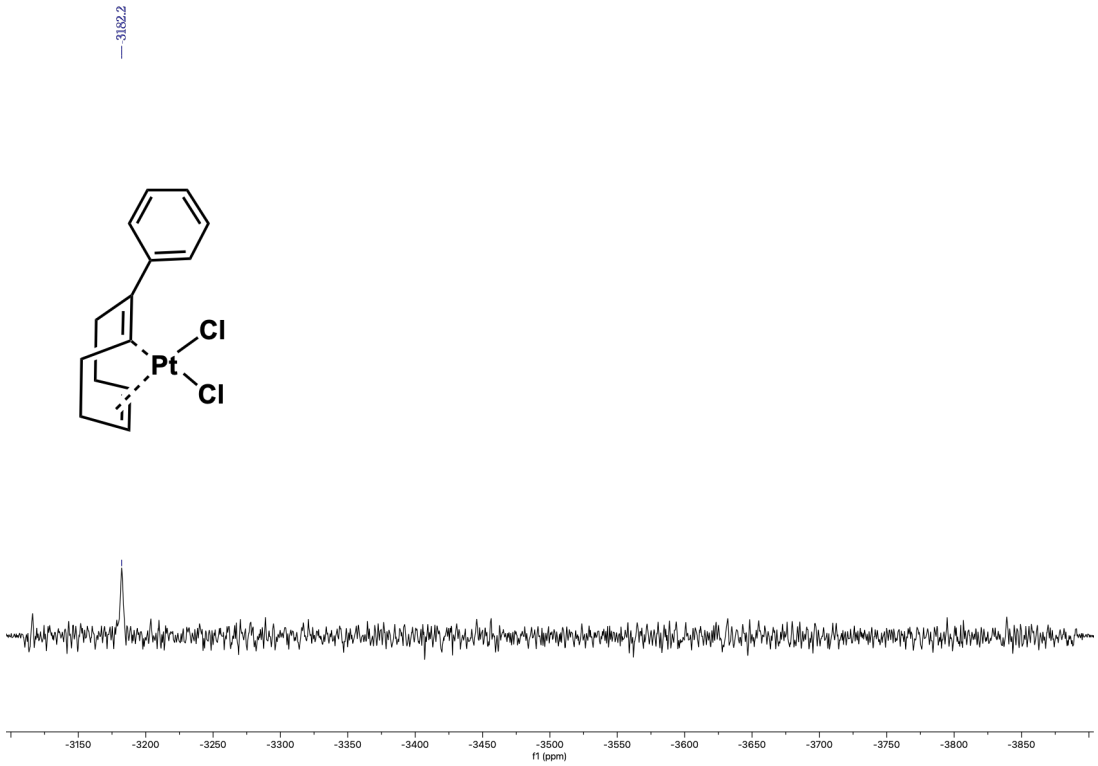


Figure 125. ^{195}Pt NMR spectrum of **Pt2** in DMSO-d*6*.

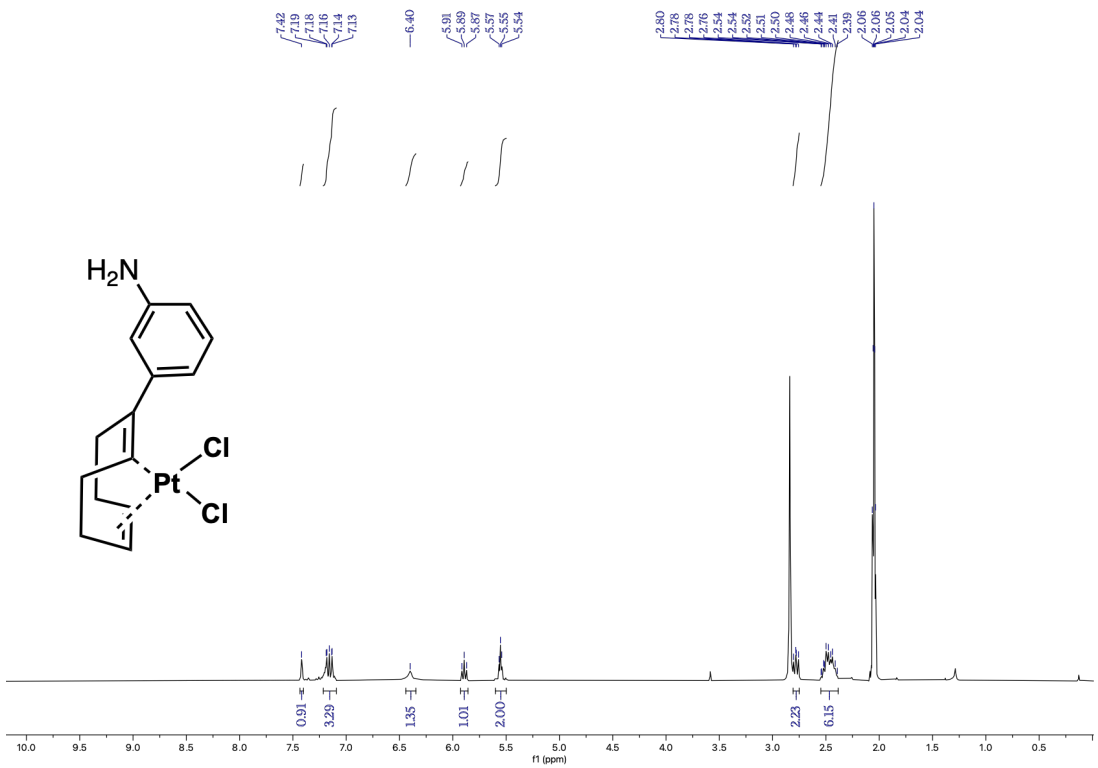


Figure 126. ^{1}H NMR spectrum of **Pt3** in acetone-d*6*.

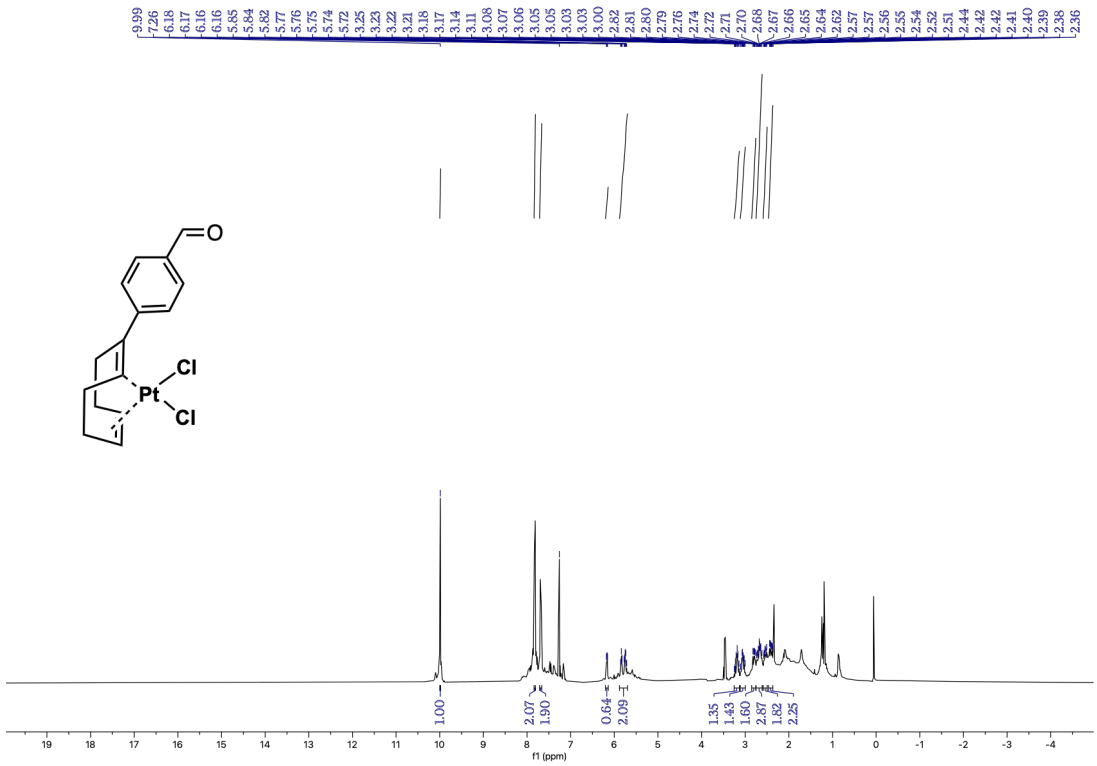


Figure 127. ^{1}H NMR spectrum of **Pt4** in $CDCl_3$.

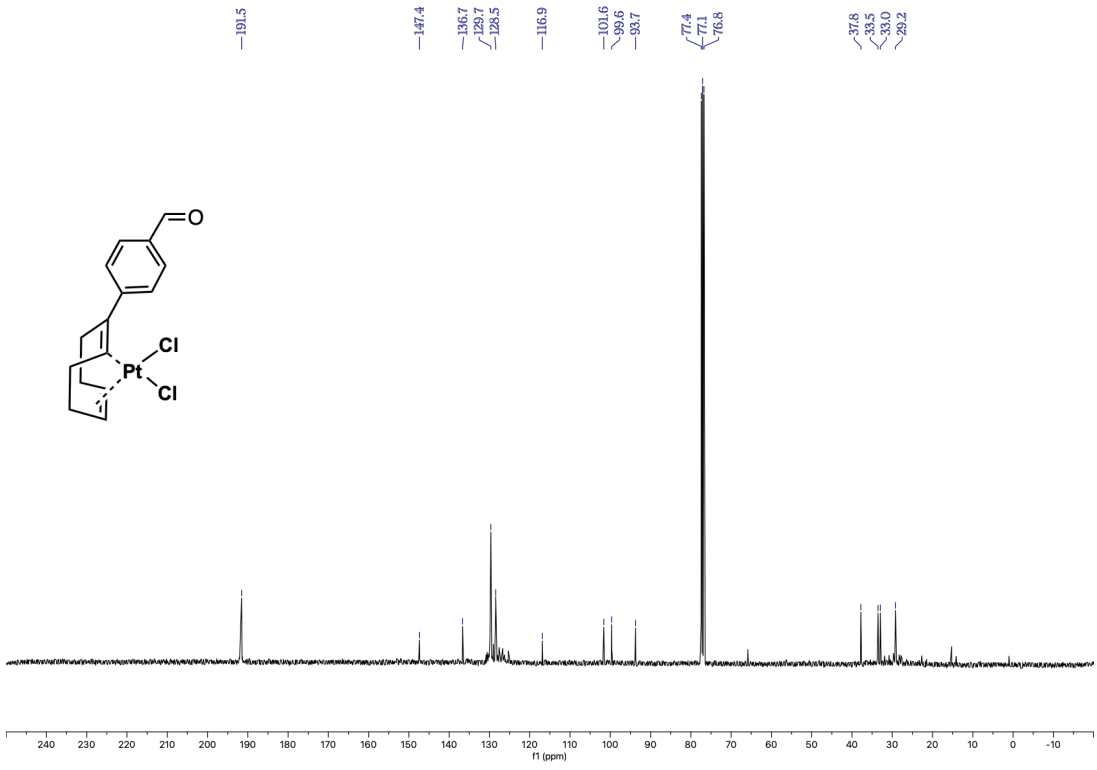


Figure 128. ^{13}C NMR spectrum of **Pt4** in $CDCl_3$.

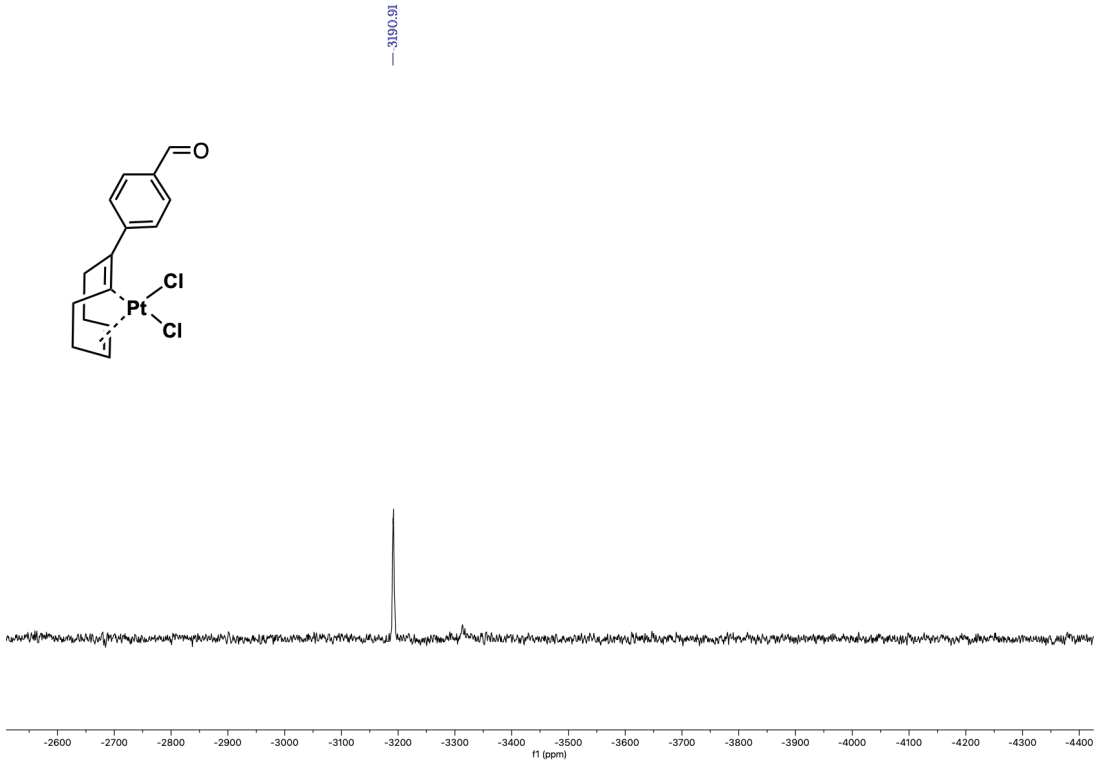


Figure 129. ^{195}Pt NMR spectrum of **Pt4** in $CDCl_3$.

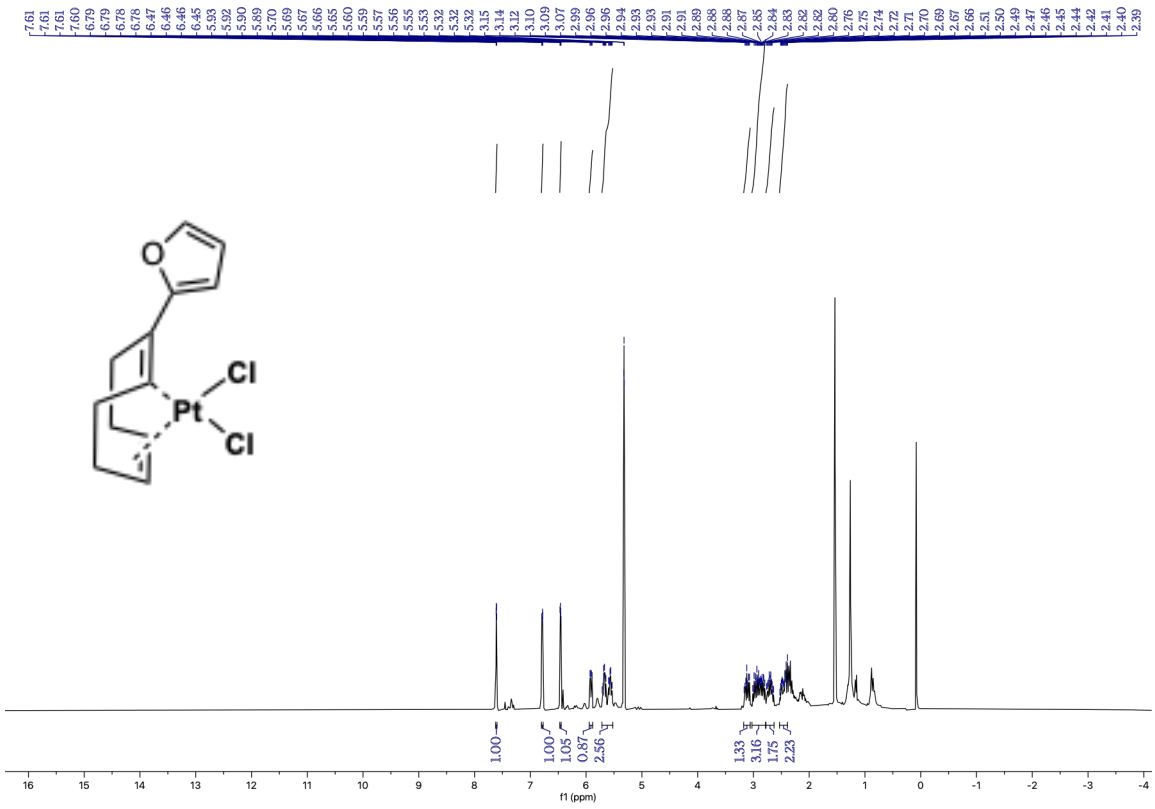


Figure 130. ^{1}H NMR spectrum of **Pt5** in CD_2Cl_2.

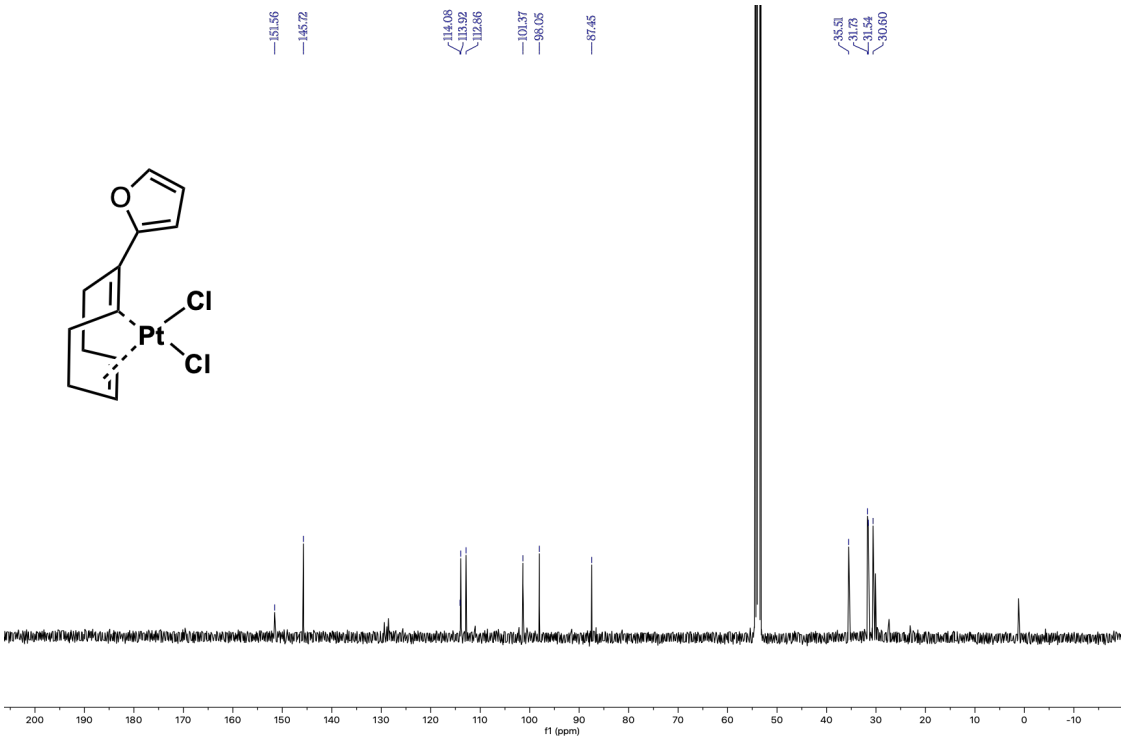


Figure 131. ^{13}C NMR spectrum of **Pt5** in $CDCl_3$.

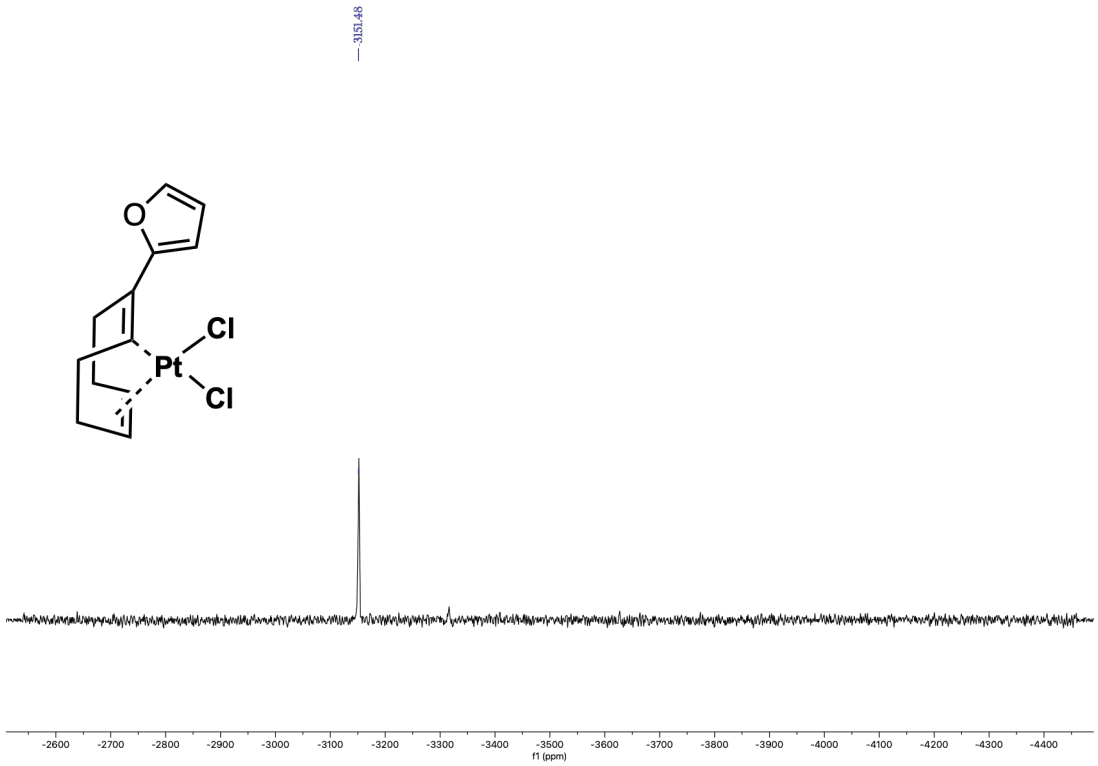


Figure 132. ^{195}Pt NMR spectrum of **Pt5** in acetone-d*6*.

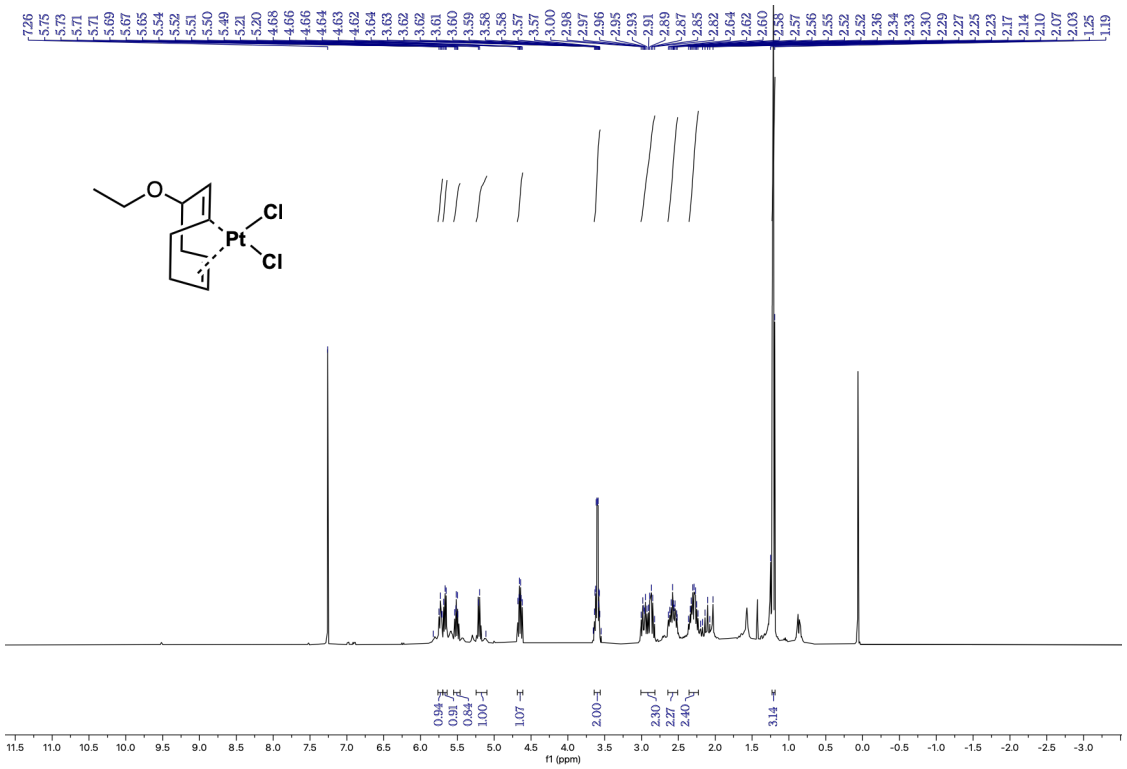


Figure 133. ^{1}H NMR spectrum of **Pt6** in $CDCl_3$.

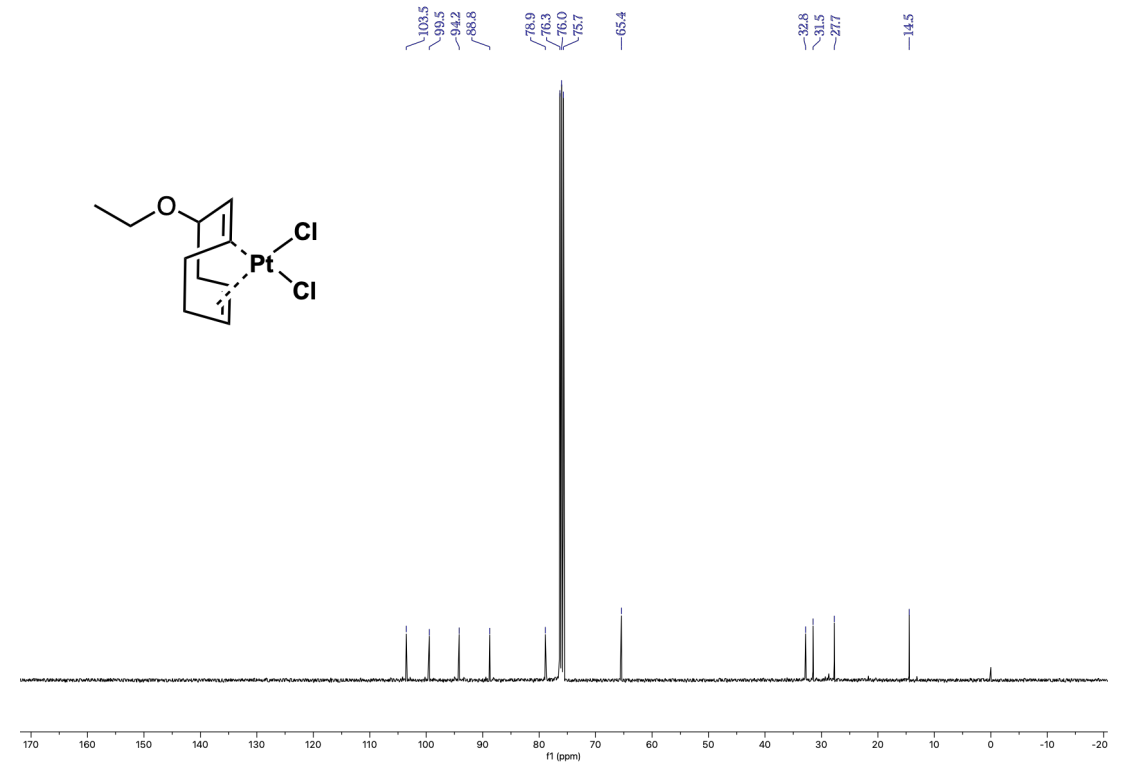


Figure 134. ^{13}C NMR spectrum of **Pt6** in $CDCl_3$.

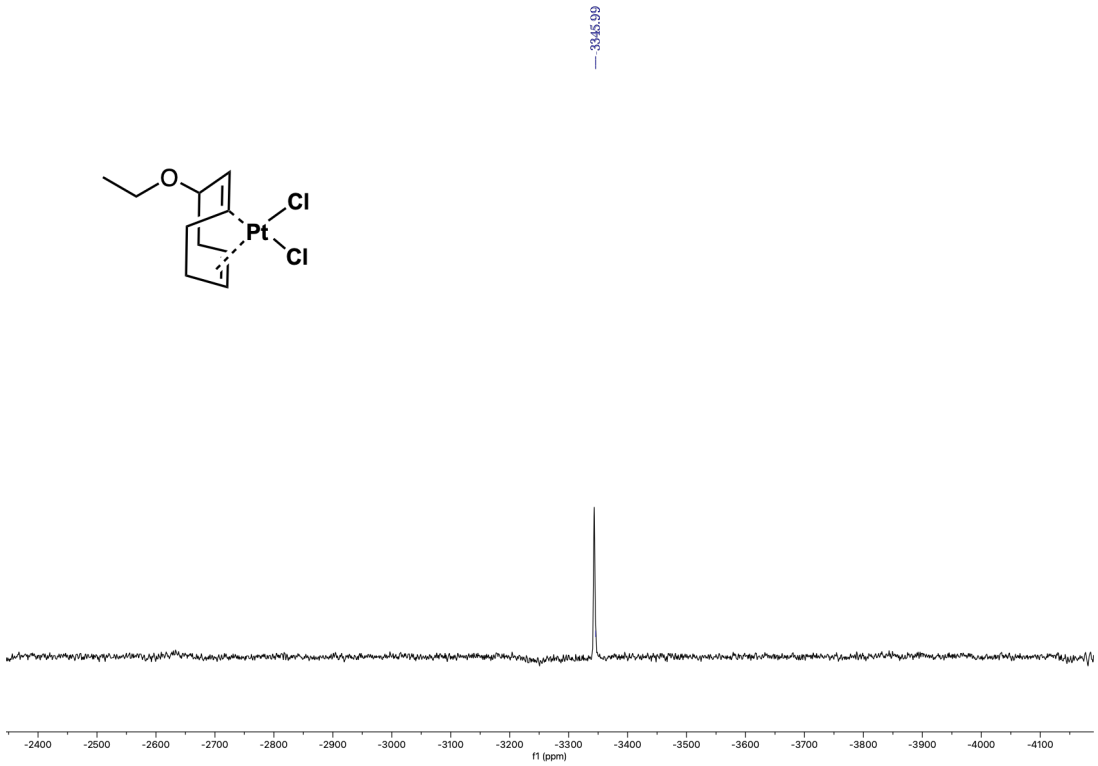


Figure 135. ^{195}Pt NMR spectrum of **Pt6** in $CDCl_3$.

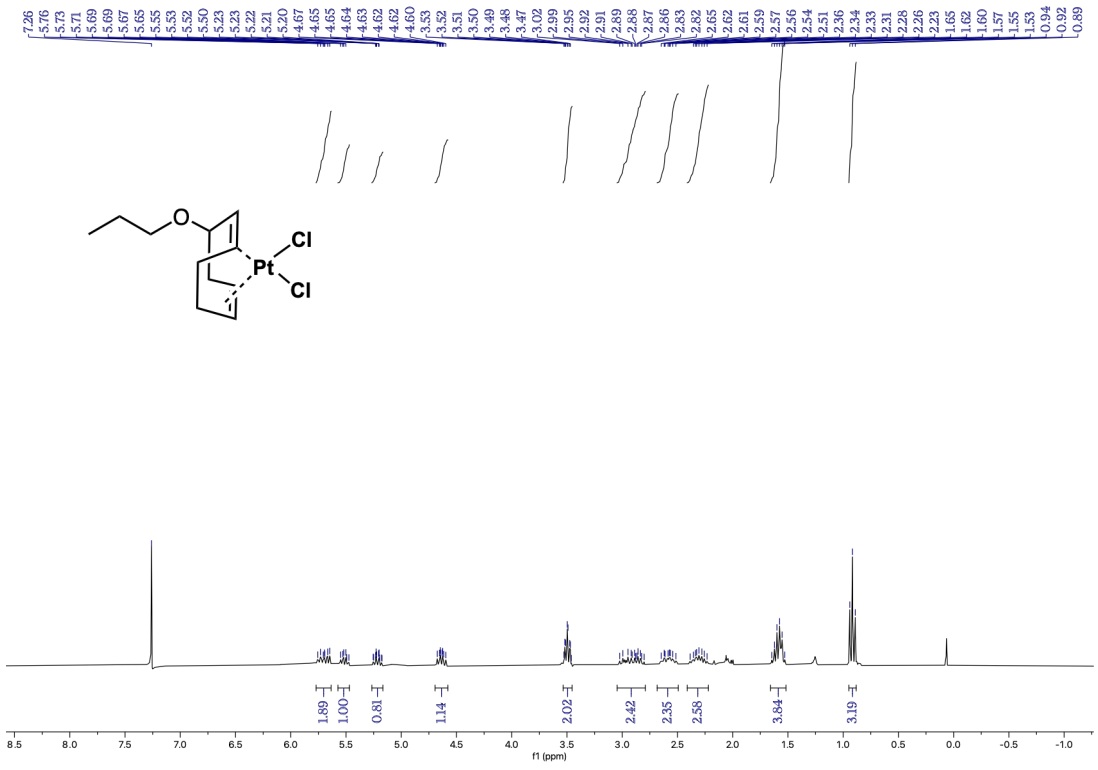


Figure 136. ^{1}H NMR spectrum of **Pt7** in $CDCl_3$.

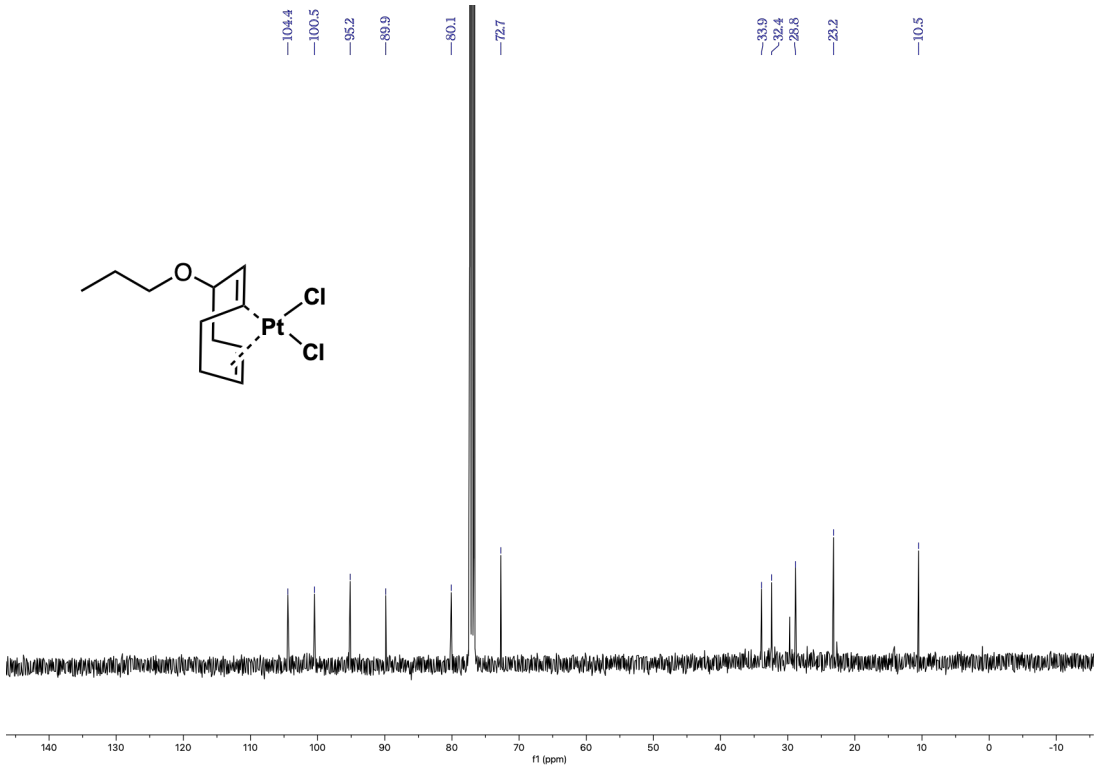


Figure 137. ^{13}C NMR spectrum of **Pt7** in $CDCl_3$.

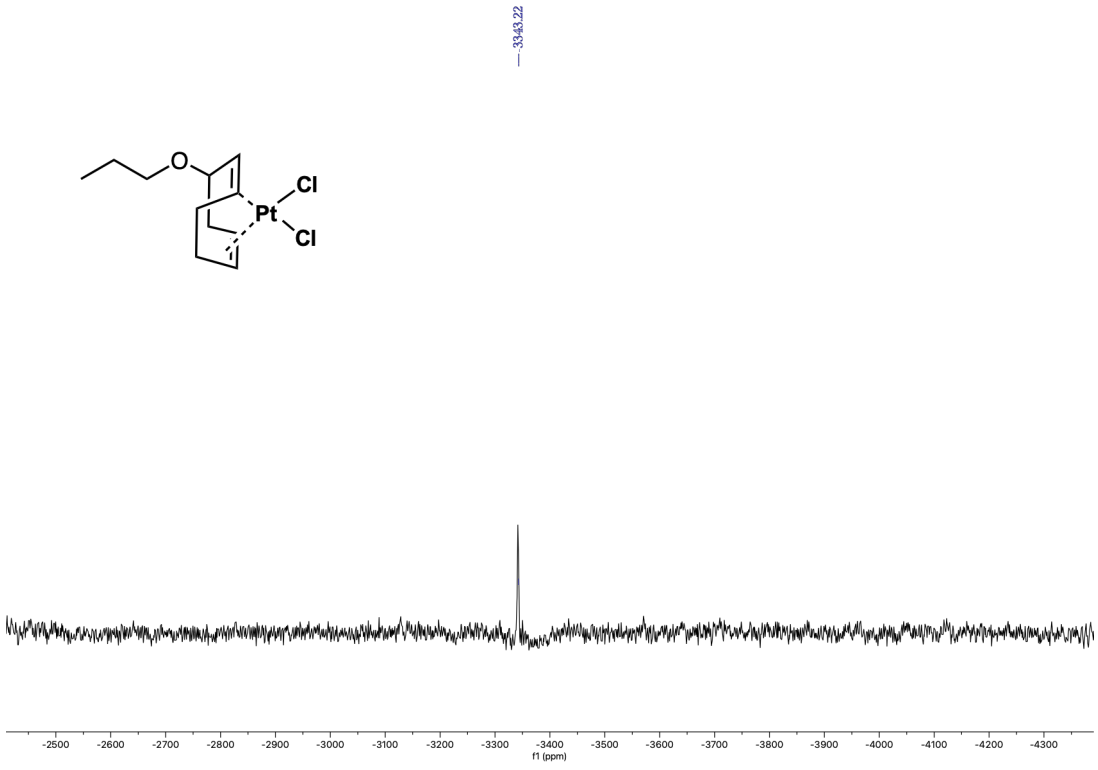


Figure 138. ^{195}Pt NMR spectrum of **Pt7** in $CDCl_3$.

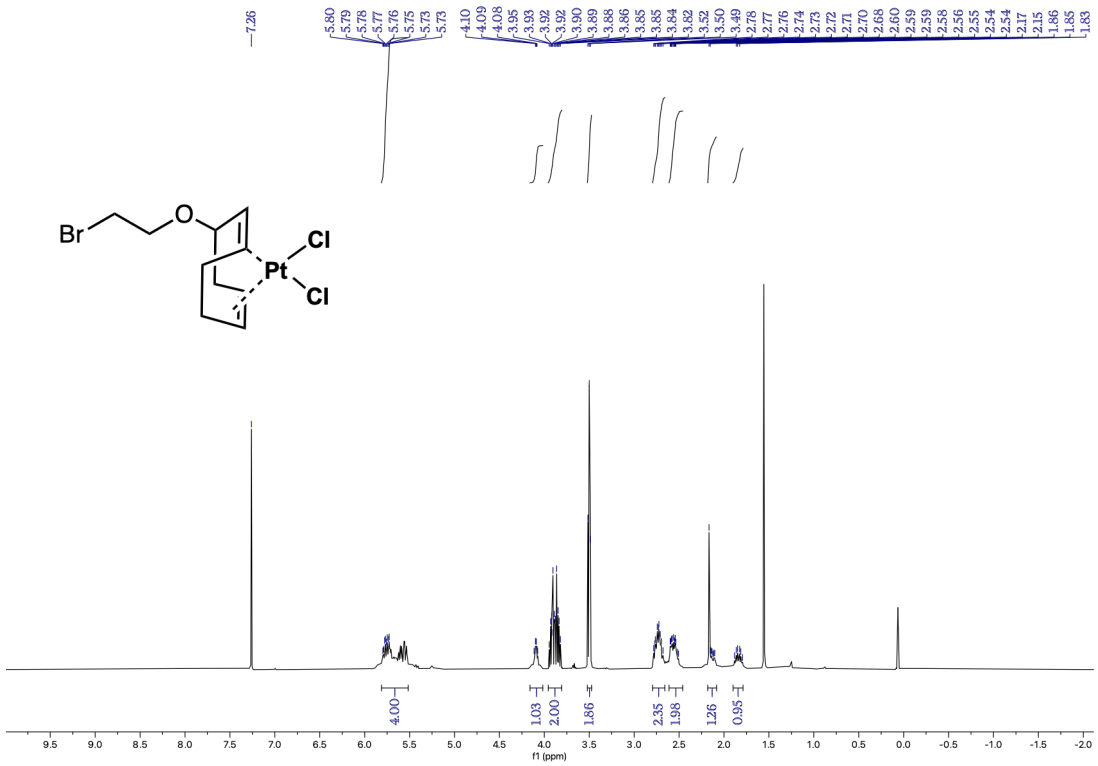


Figure 139. ^{1}H NMR spectrum of **Pt8** in $CDCl_3$.

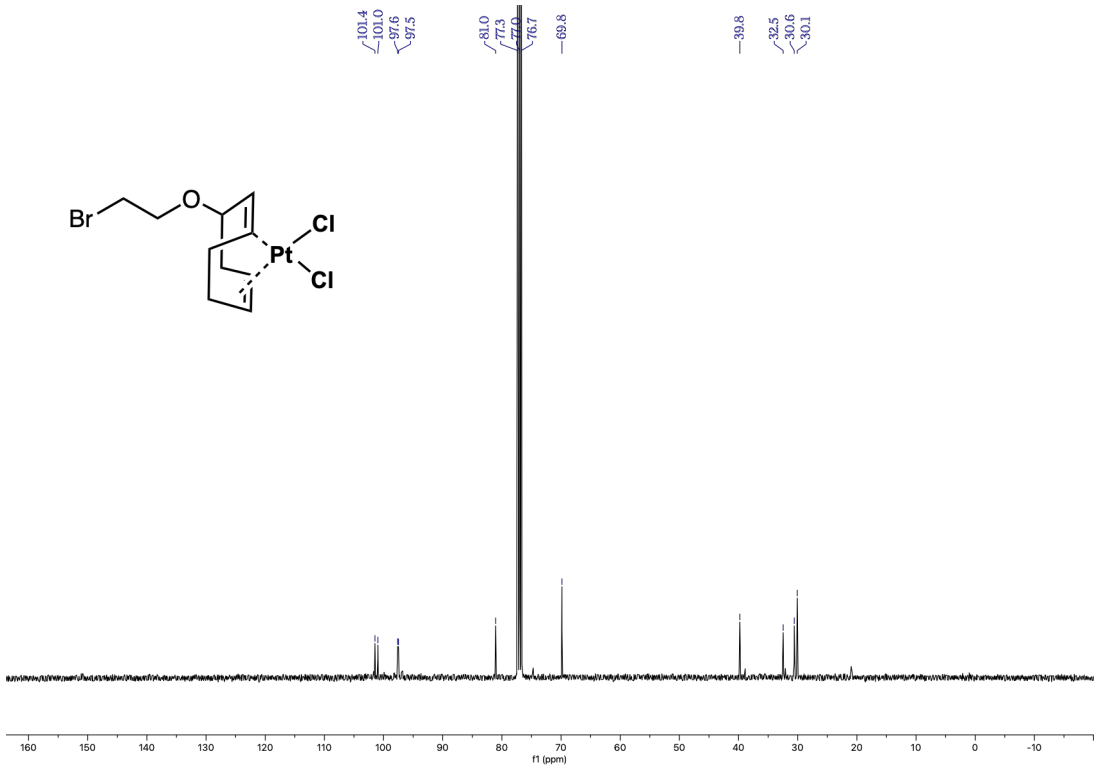


Figure 140. ^{13}C NMR spectrum of **Pt8** in $CDCl_3$.

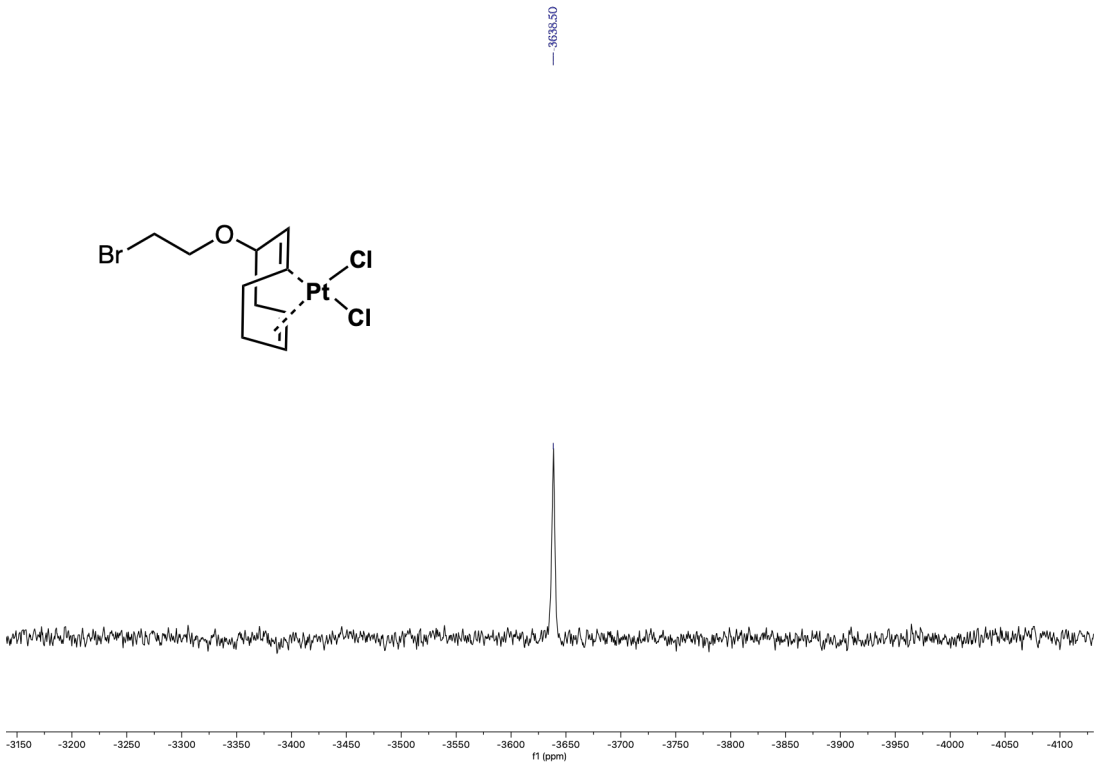


Figure 141. ^{195}Pt NMR spectrum of **Pt8** in $CDCl_3$.

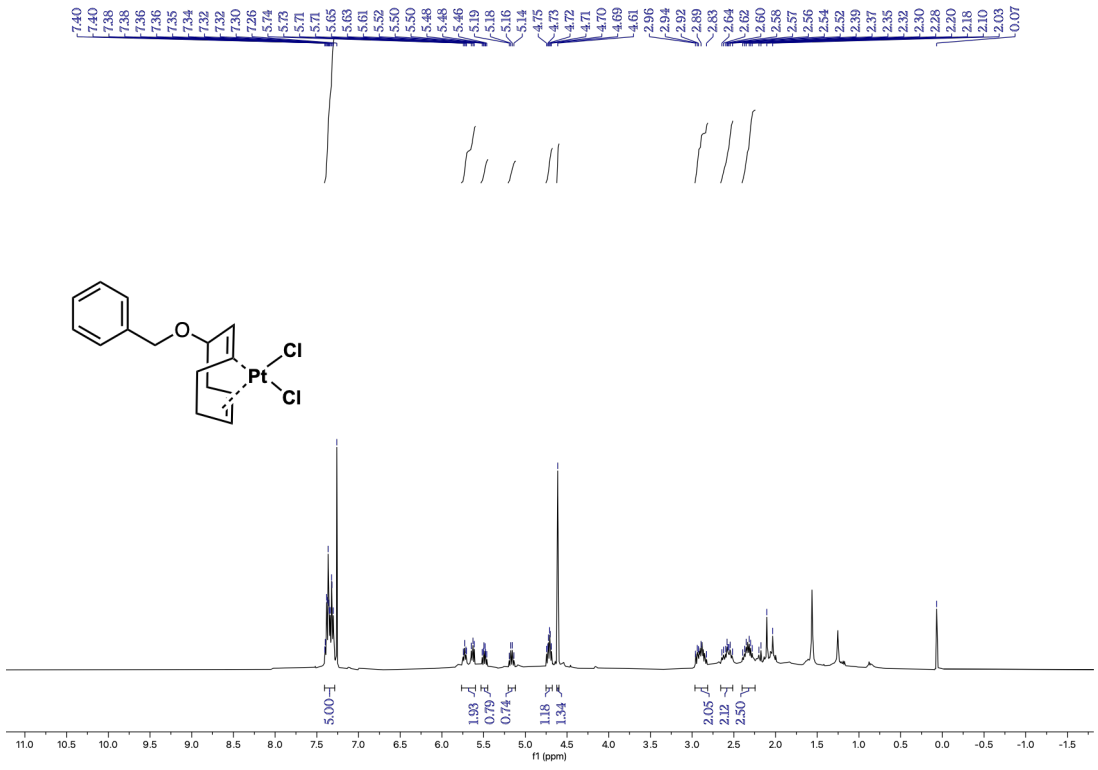


Figure 142. ^{1}H NMR spectrum of **Pt9** in $CDCl_3$.

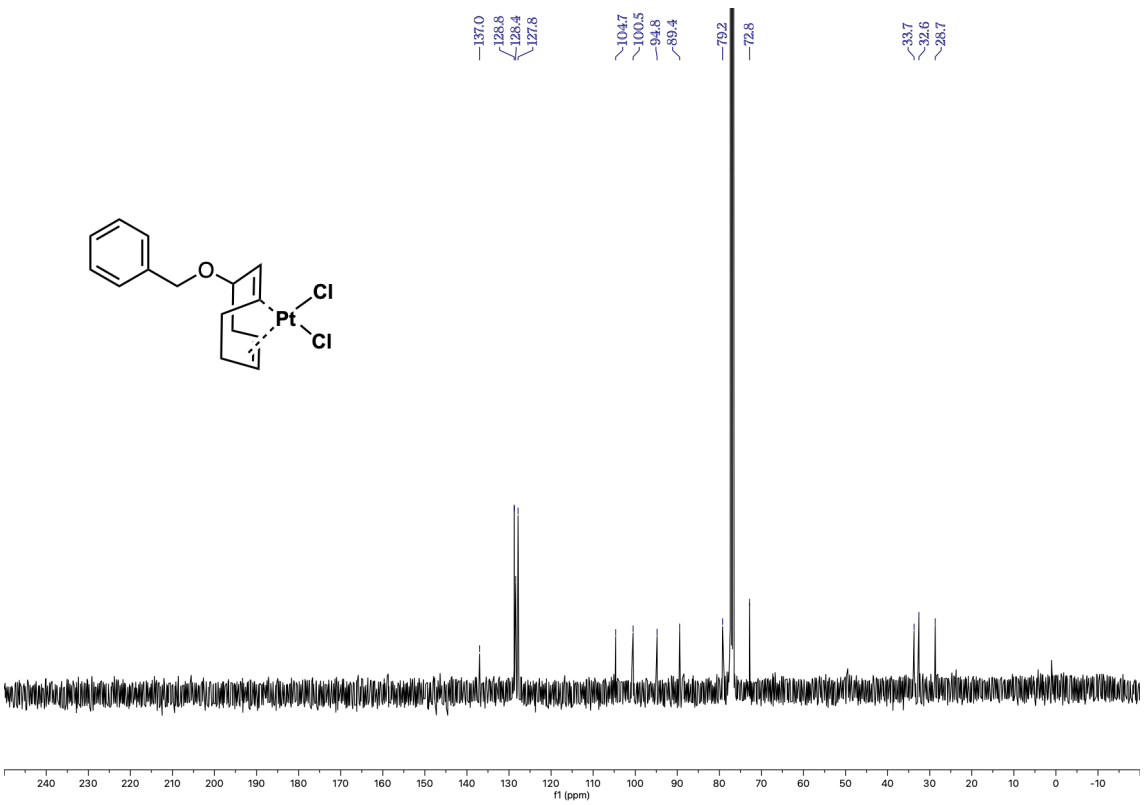


Figure 143. ^{13}C NMR spectrum of **Pt9** in $CDCl_3$.

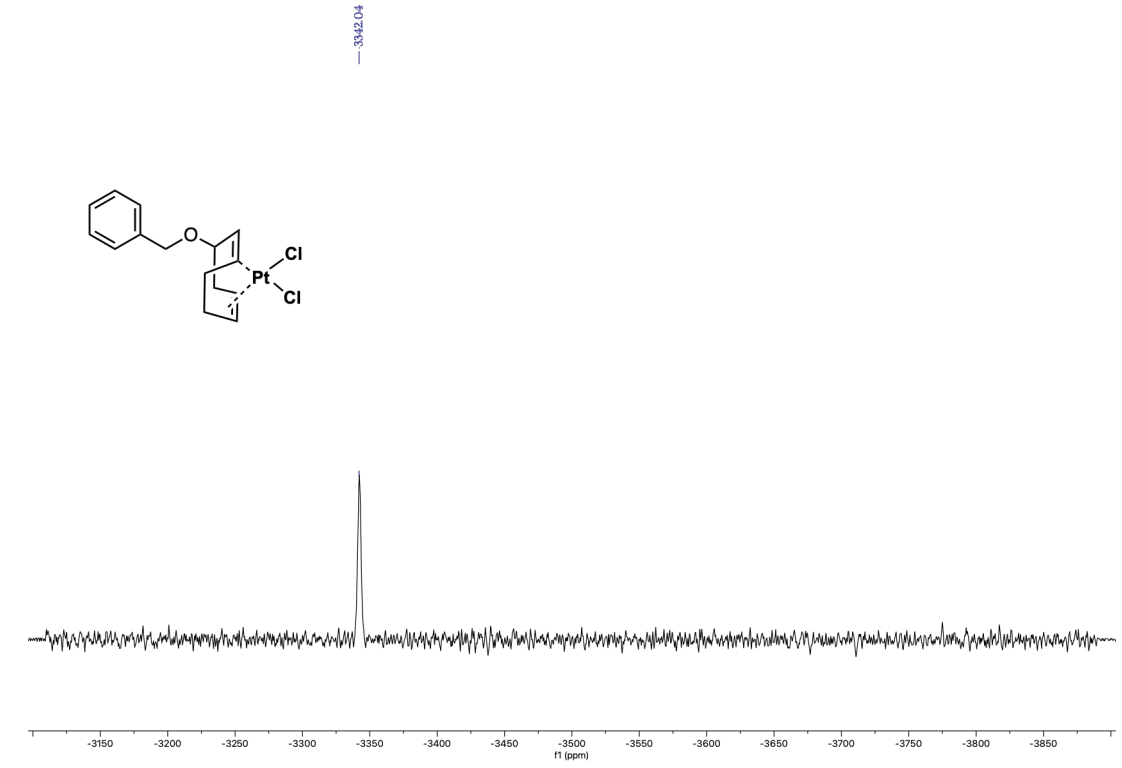


Figure 144. ^{195}Pt NMR spectrum of **Pt9** in $CDCl_3$.

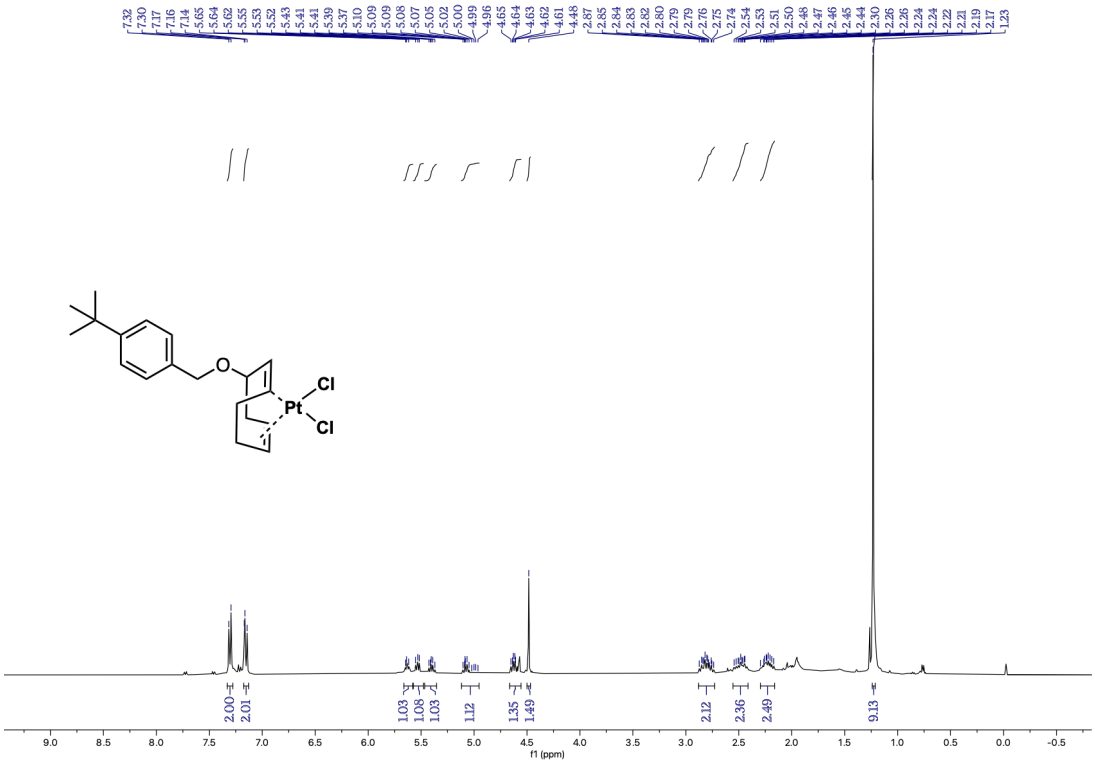


Figure 145. ^{1}H NMR spectrum of **Pt10** in $CDCl_3$.

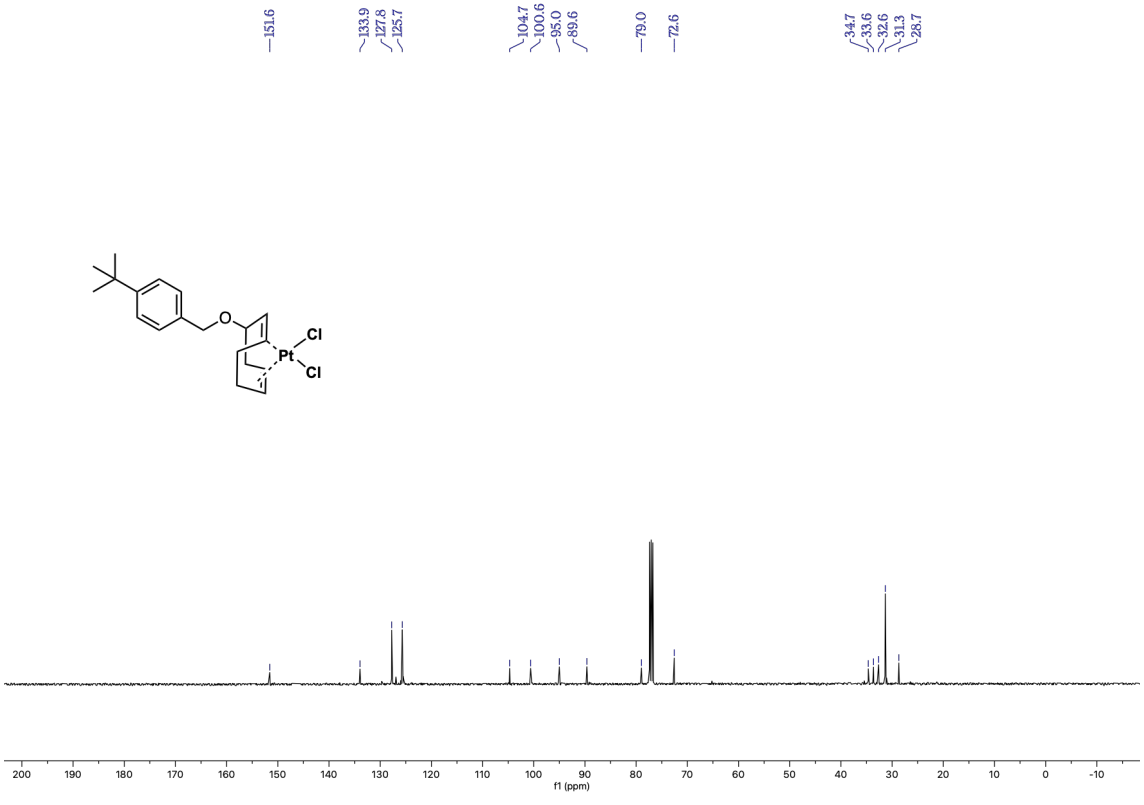


Figure 146. ^{13}C NMR spectrum of **Pt10** in $CDCl_3$.

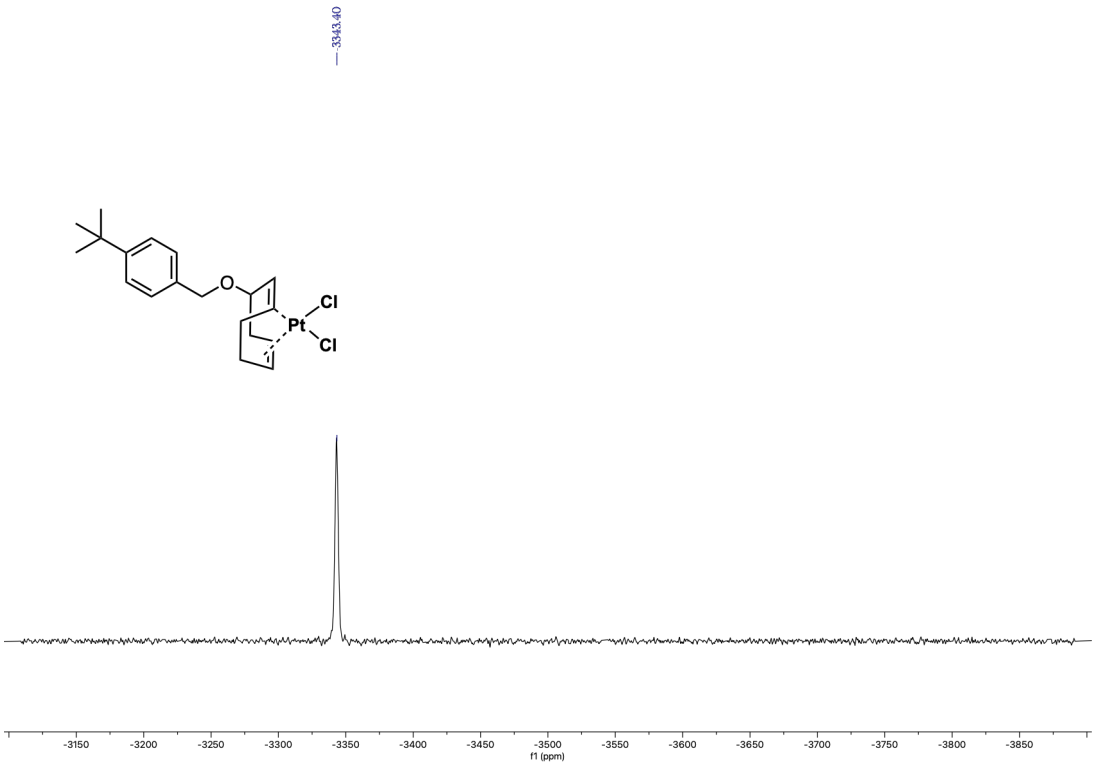


Figure 147. ^{195}Pt NMR spectrum of **Pt10** in $CDCl_3$.

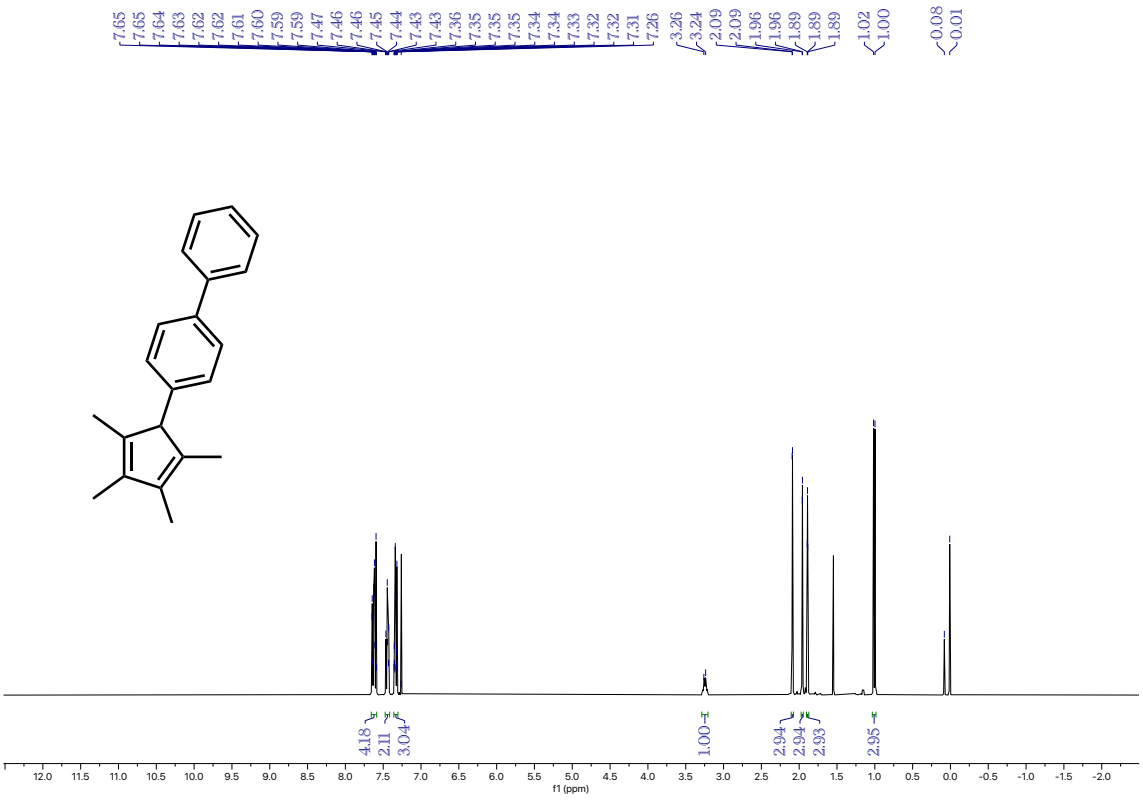


Figure 148. ^{1}H NMR spectrum of **Cp2** in $CDCl_3$.

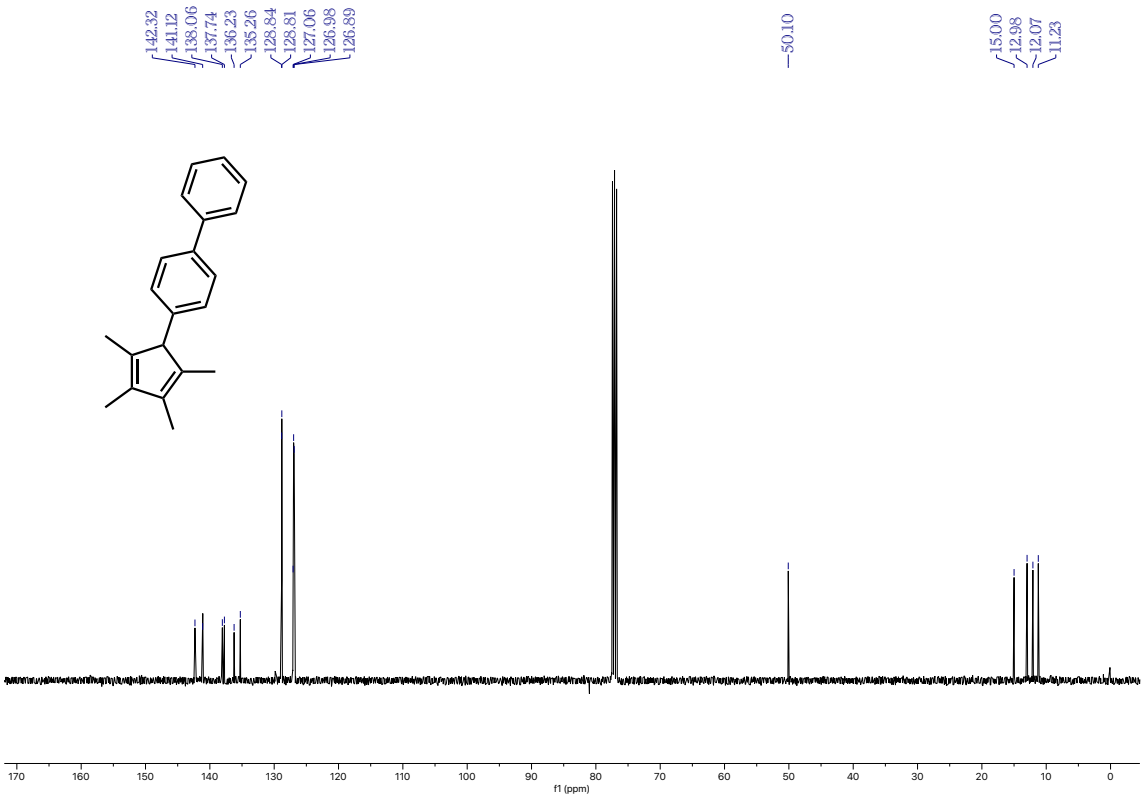


Figure 149. ^{13}C NMR spectrum of **Cp2** in $CDCl_3$.

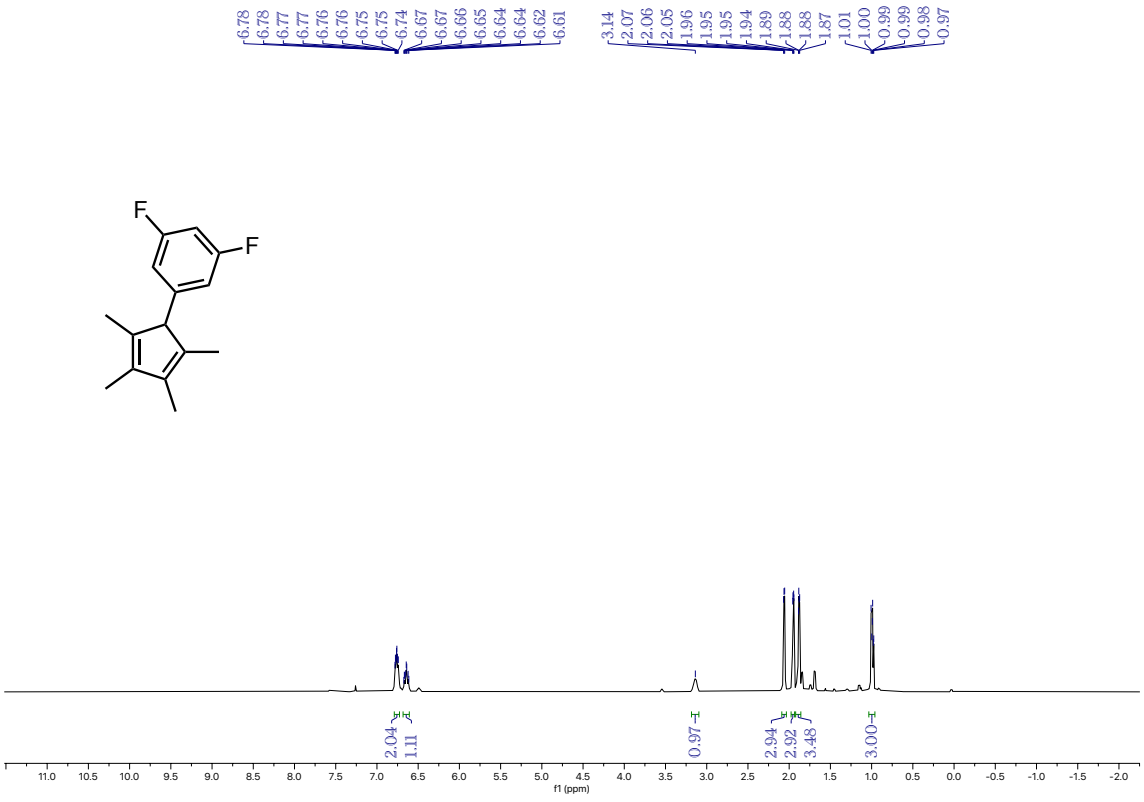


Figure 150. ^{1}H NMR spectrum of **Cp3** in $CDCl_3$.

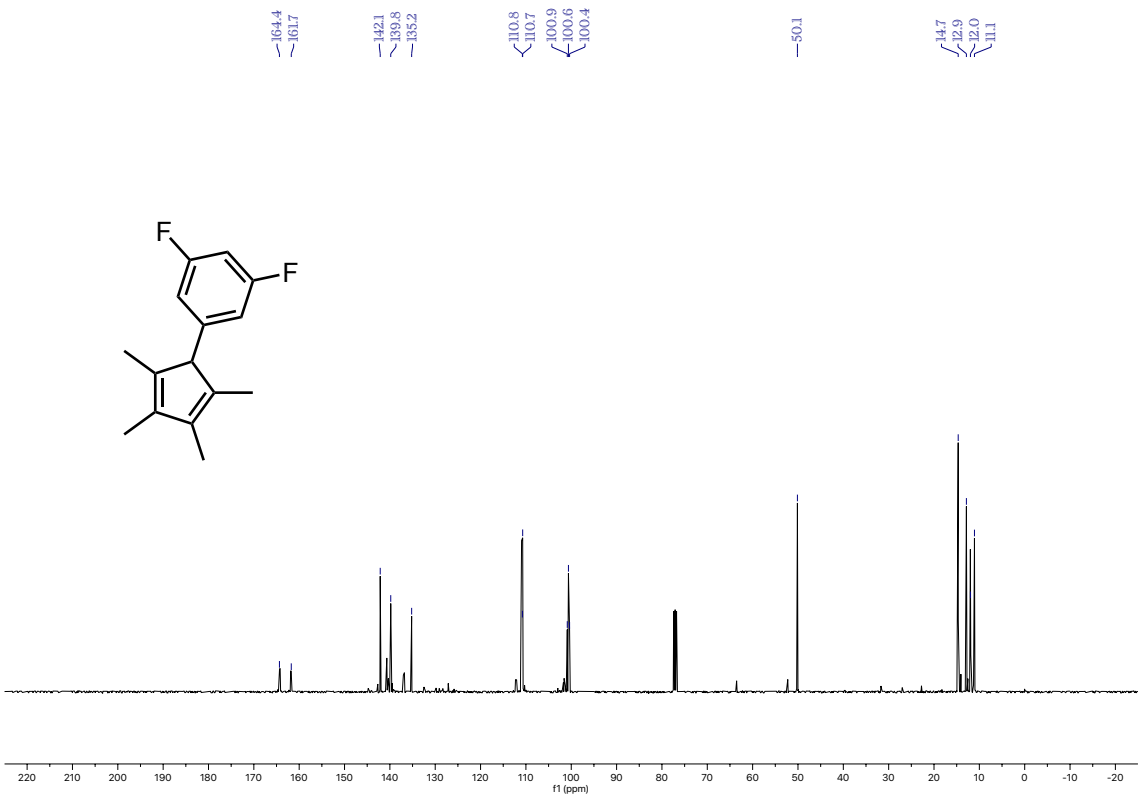


Figure 151. ^{13}C NMR spectrum of **Cp3** in $CDCl_3$.

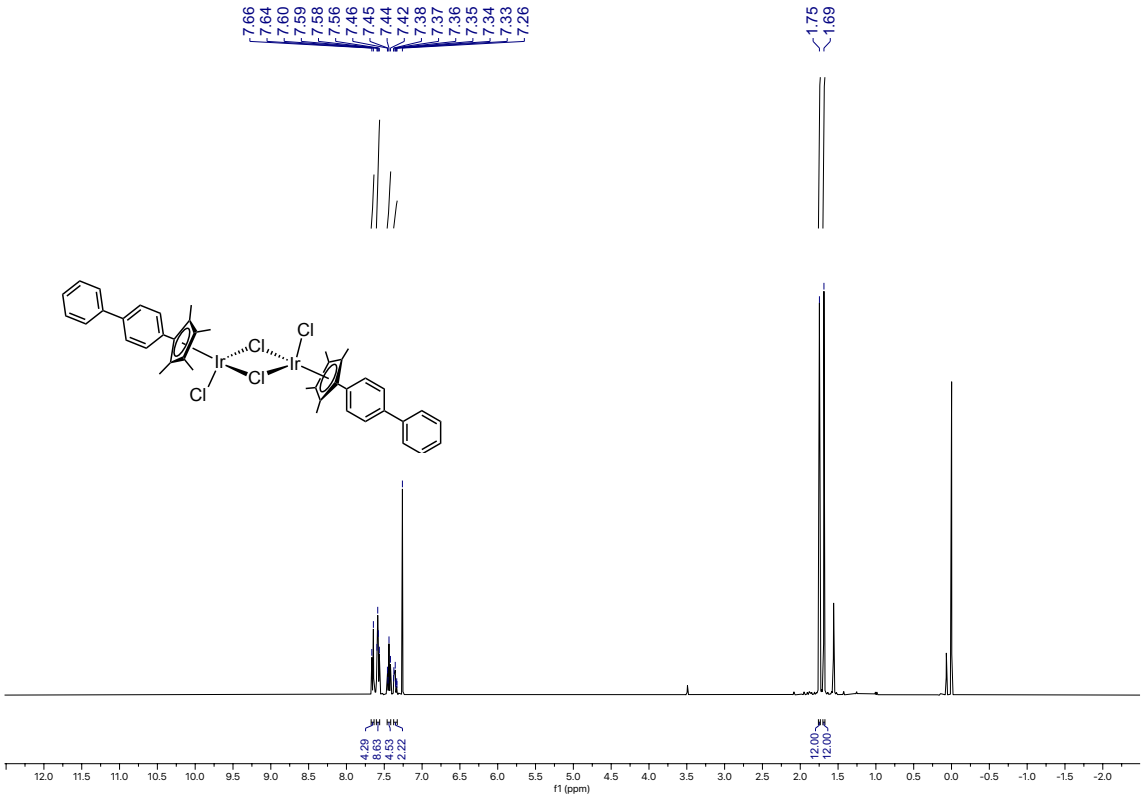


Figure 152. ^{1}H NMR of **IrCp2** in $CDCl_3$.

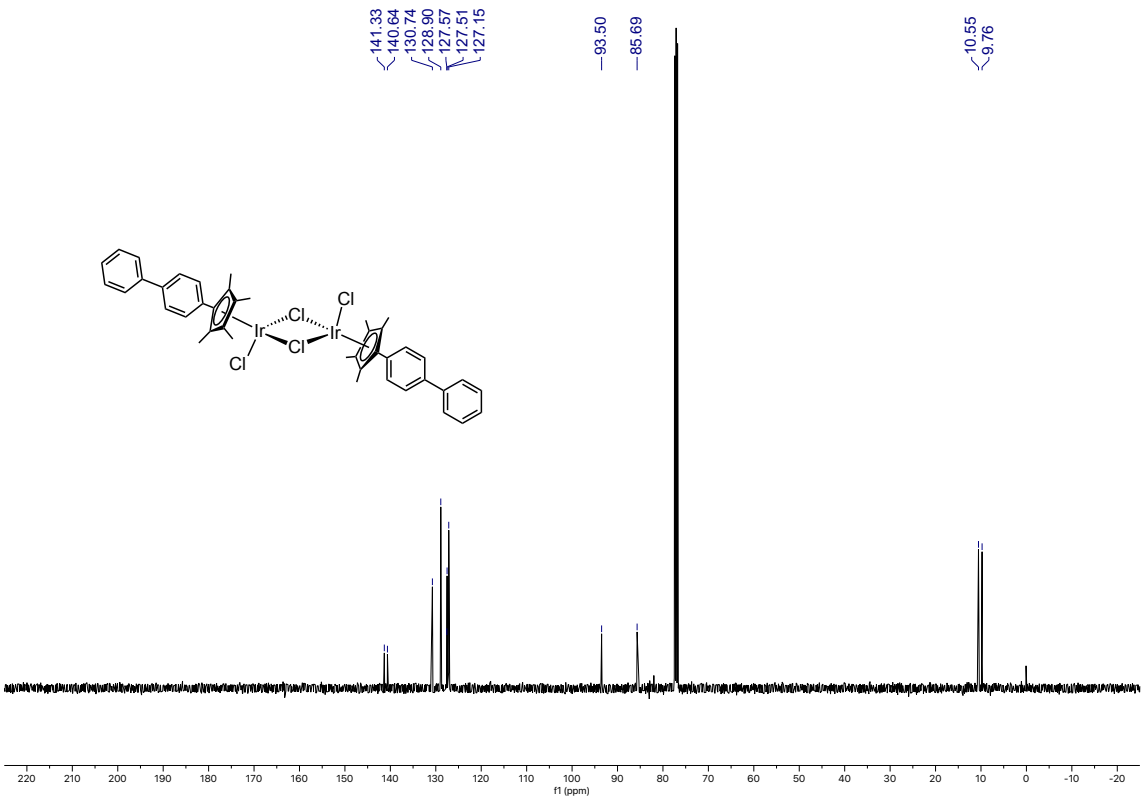


Figure 153. ^{13}C NMR of **IrCp2** in $CDCl_3$.

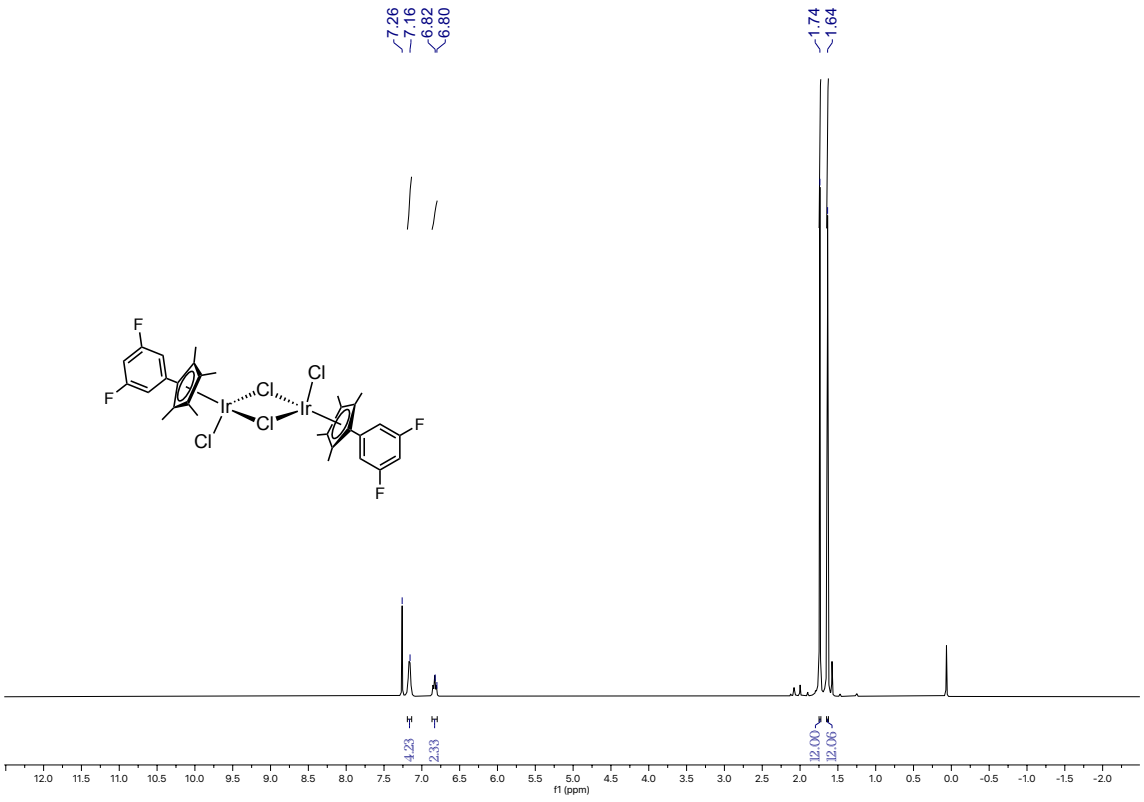


Figure 154. ^{1}H NMR of **IrCp3** in $CDCl_3$.

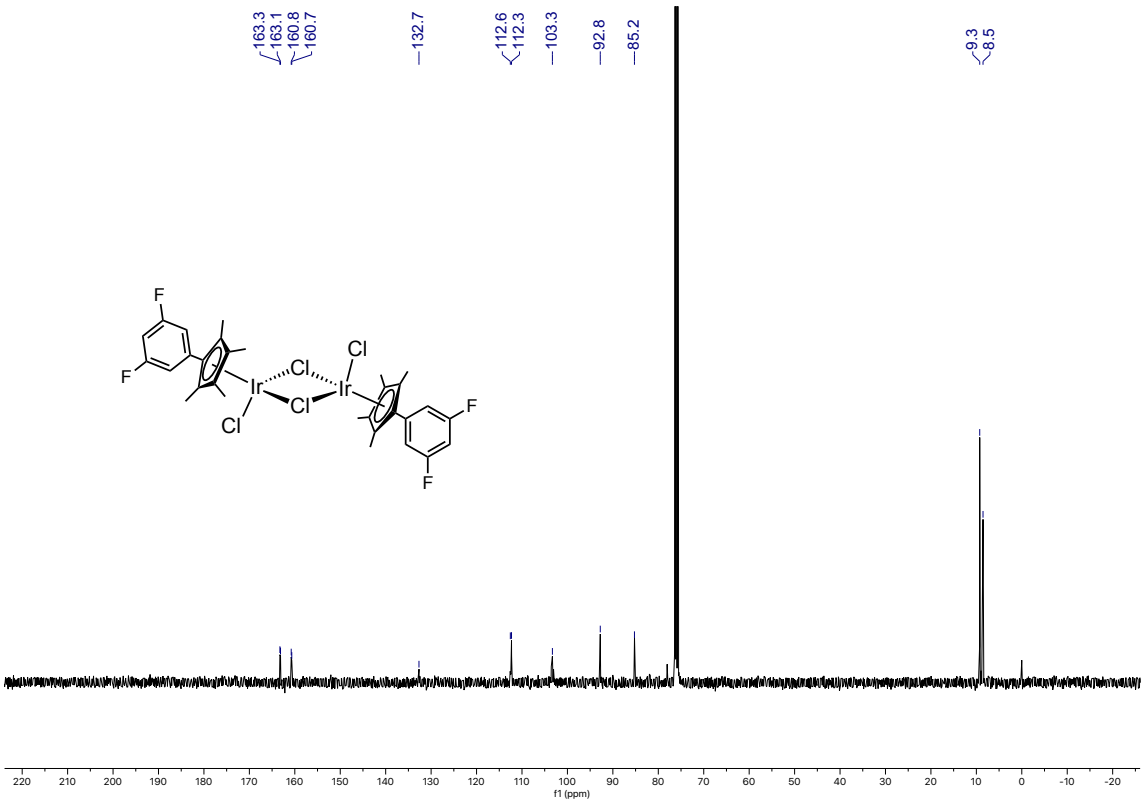


Figure 155. ^{13}C NMR of **IrCp3** in $CDCl_3$.

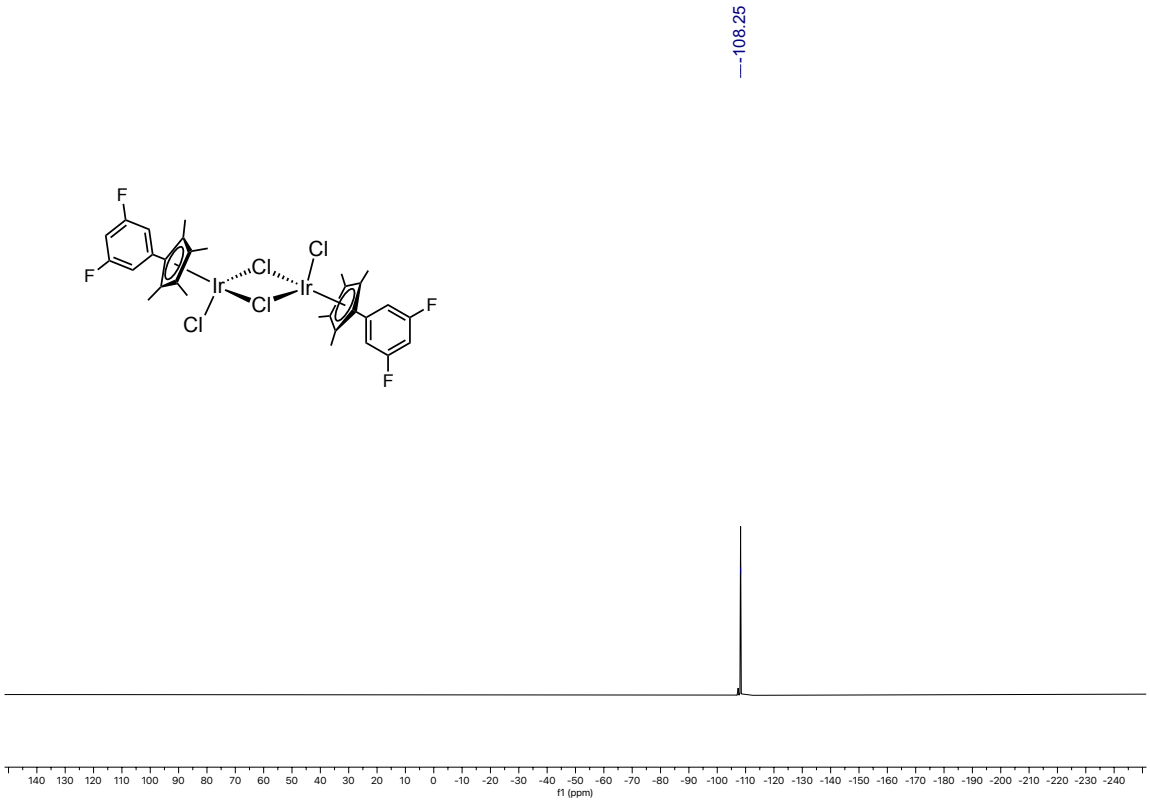


Figure 156. ^{19}F NMR of **IrCp3** in $CDCl_3$.

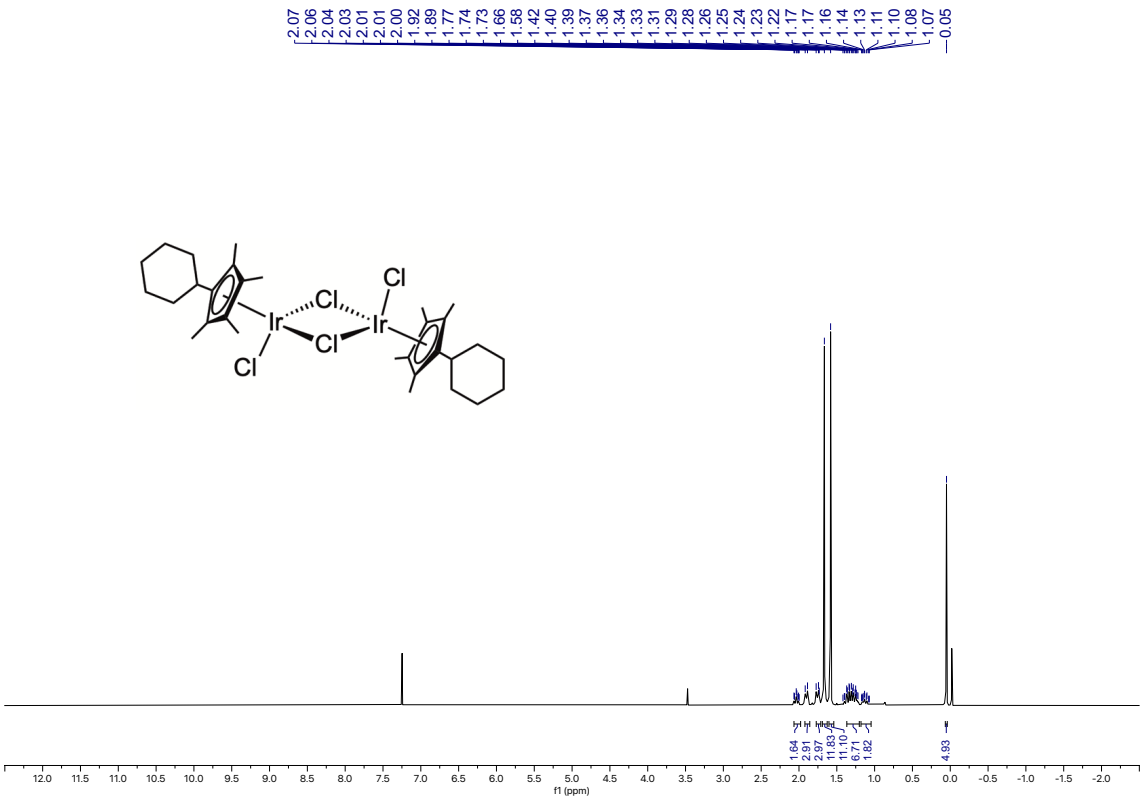


Figure 157. ^{1}H NMR of **IrCp4** in $CDCl_3$.

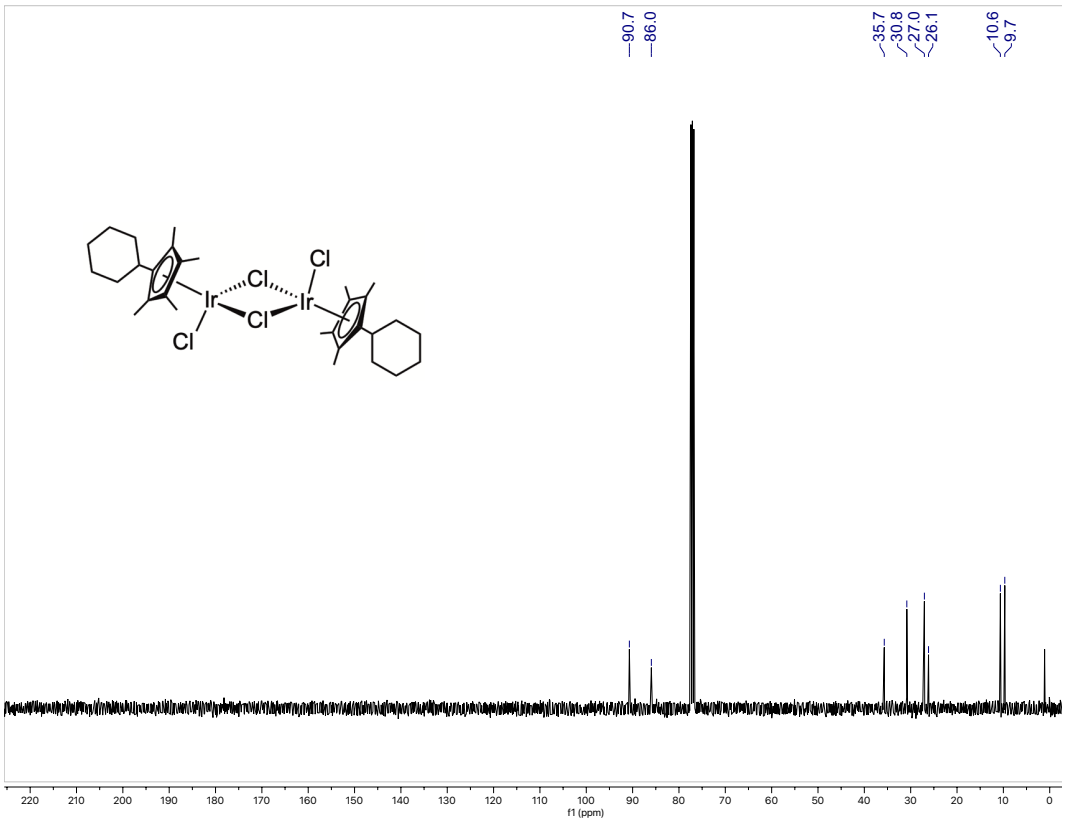


Figure 158. ^{13}C NMR of **IrCp4** in $CDCl_3$.

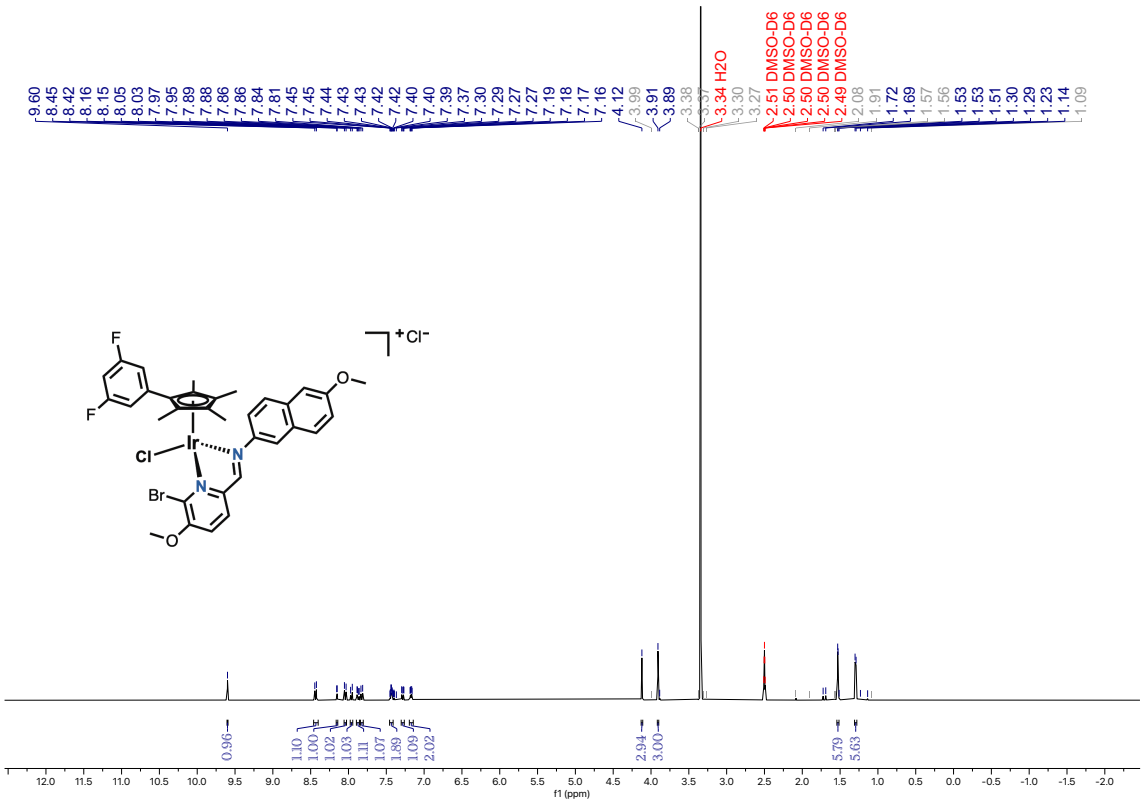


Figure 159. ^{1}H NMR of **Ir9** in DMSO-d$_6$.

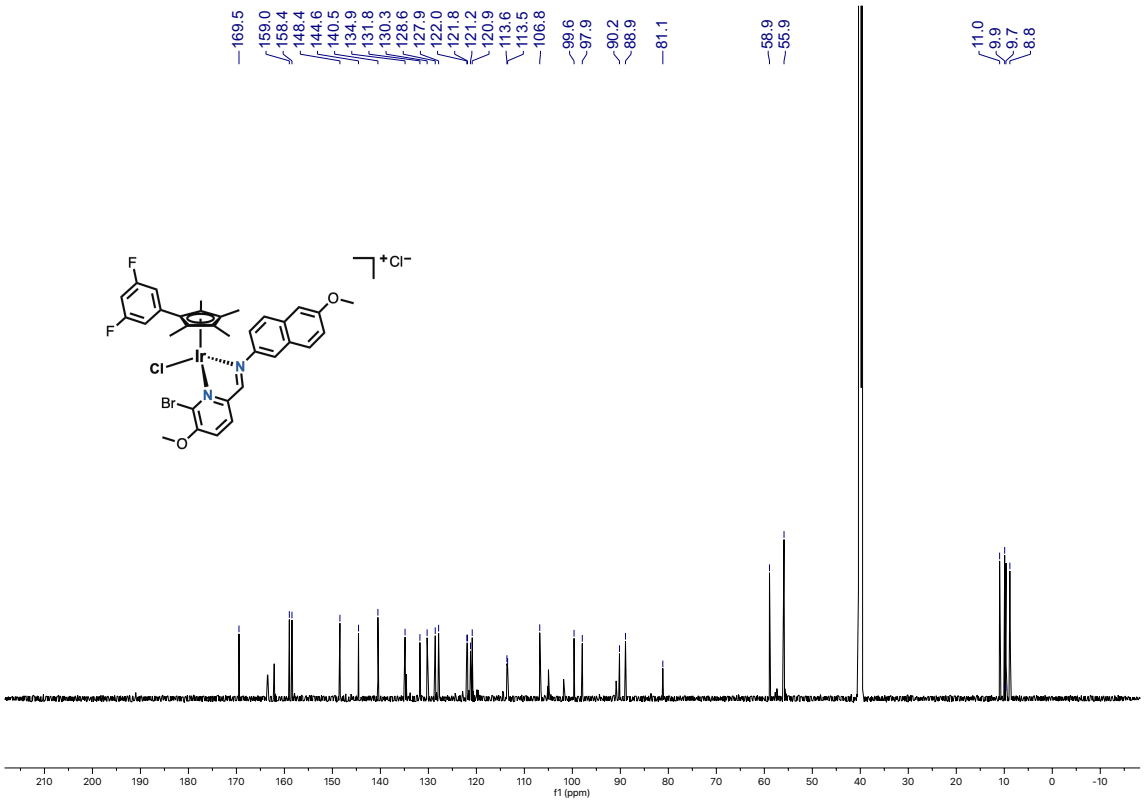


Figure 160. ^{13}C NMR of **Ir9** in DMSO-d$_6$.

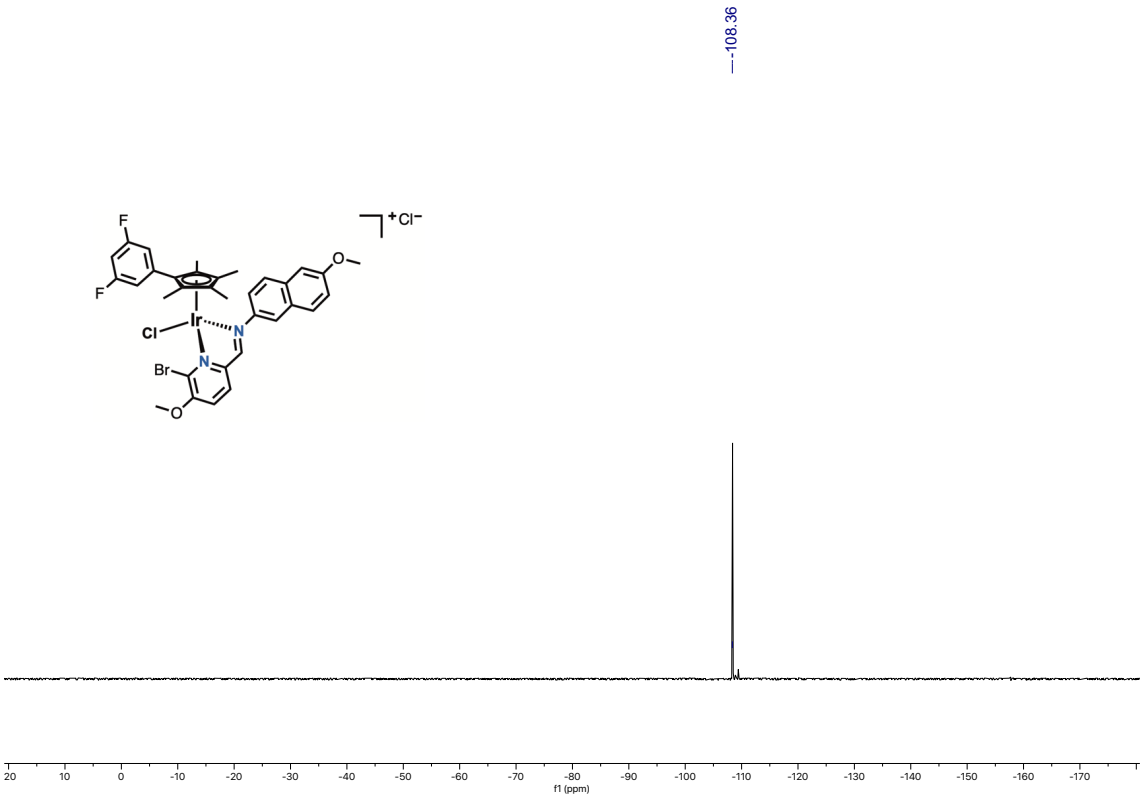


Figure 161. ^{19}F NMR of **Ir9** in DMSO-d$_6$.

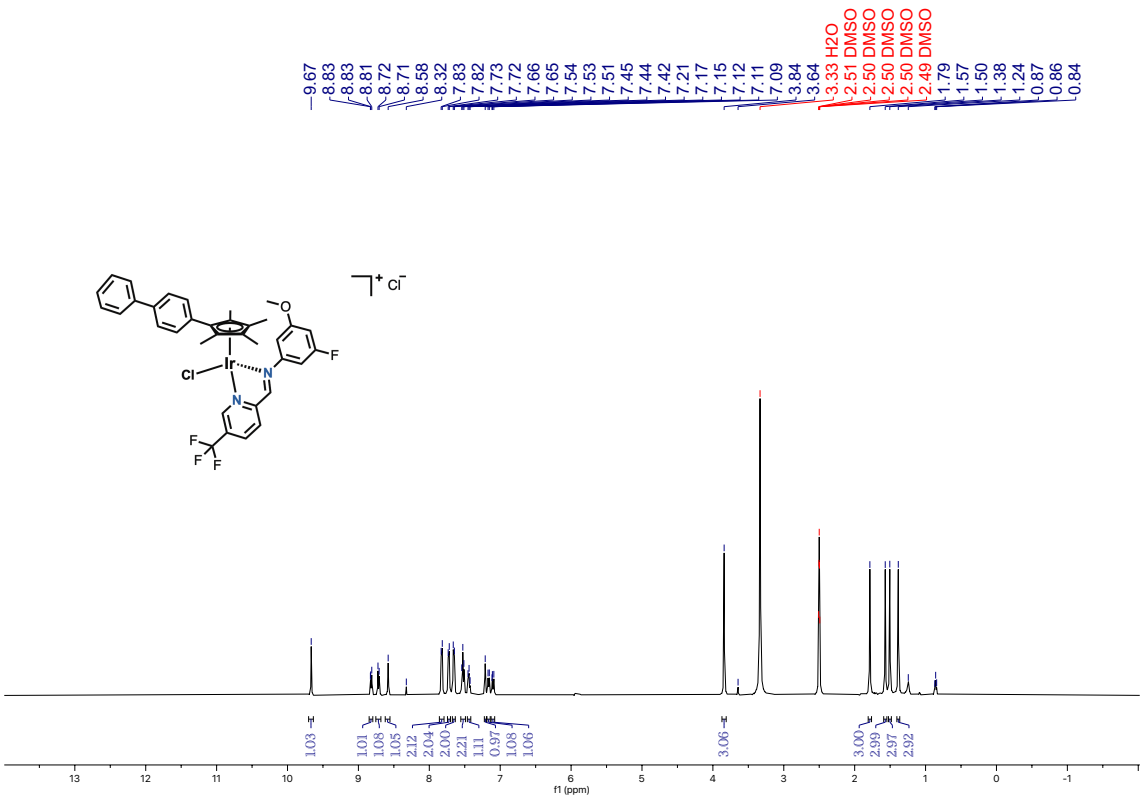


Figure 162. ^{1}H NMR of **Ir14** in DMSO-d$_6$.

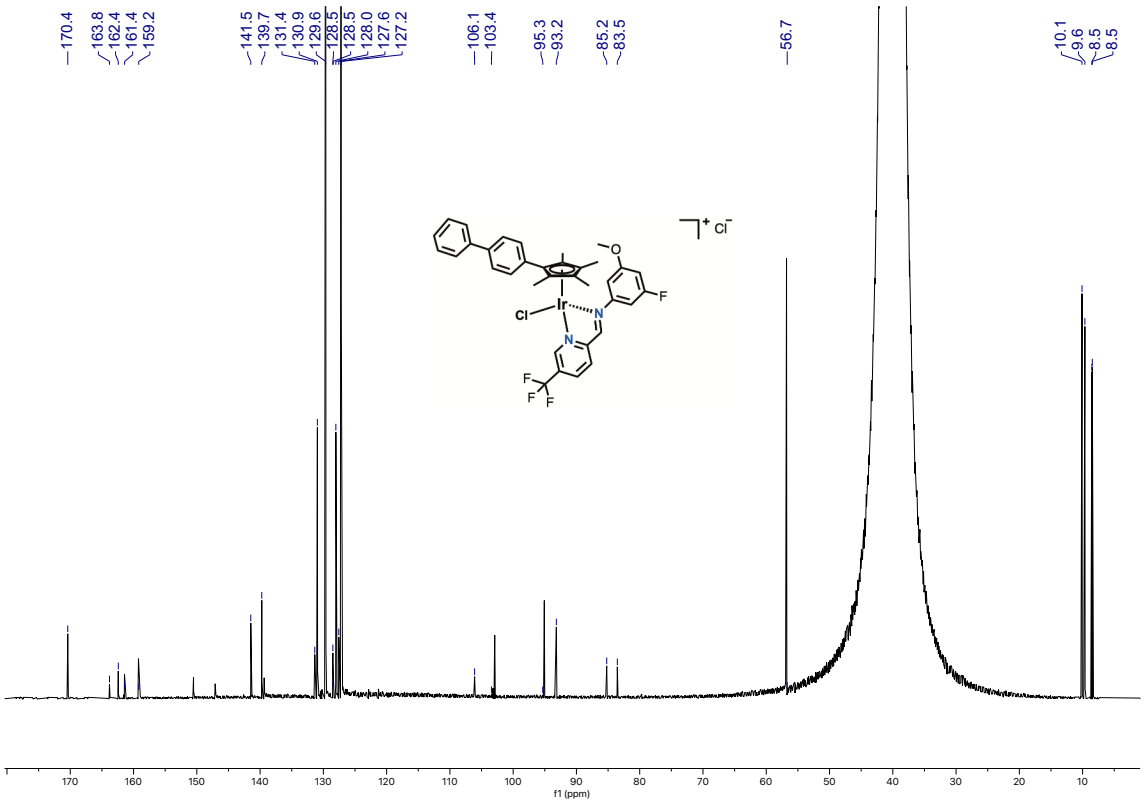


Figure 163. ^{13}C NMR of **Ir14** in DMSO-d_6.

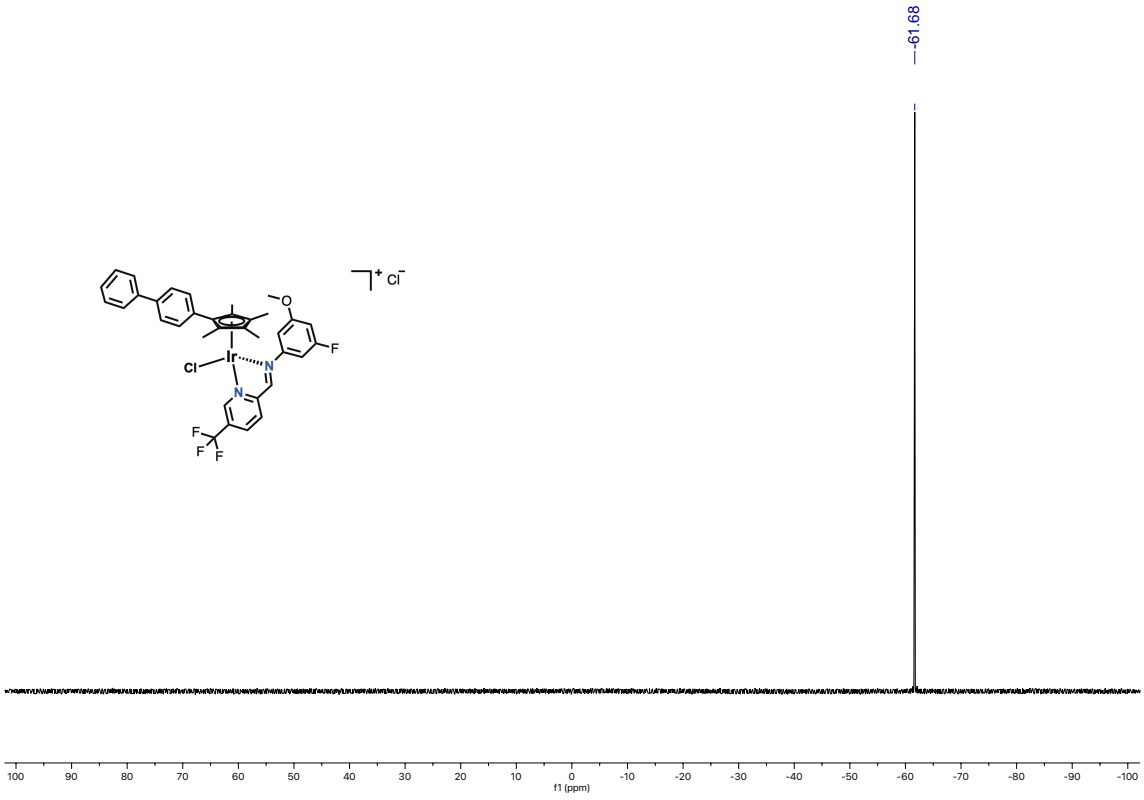


Figure 164. ^{19}F NMR of **Ir14** in DMSO-d_6.

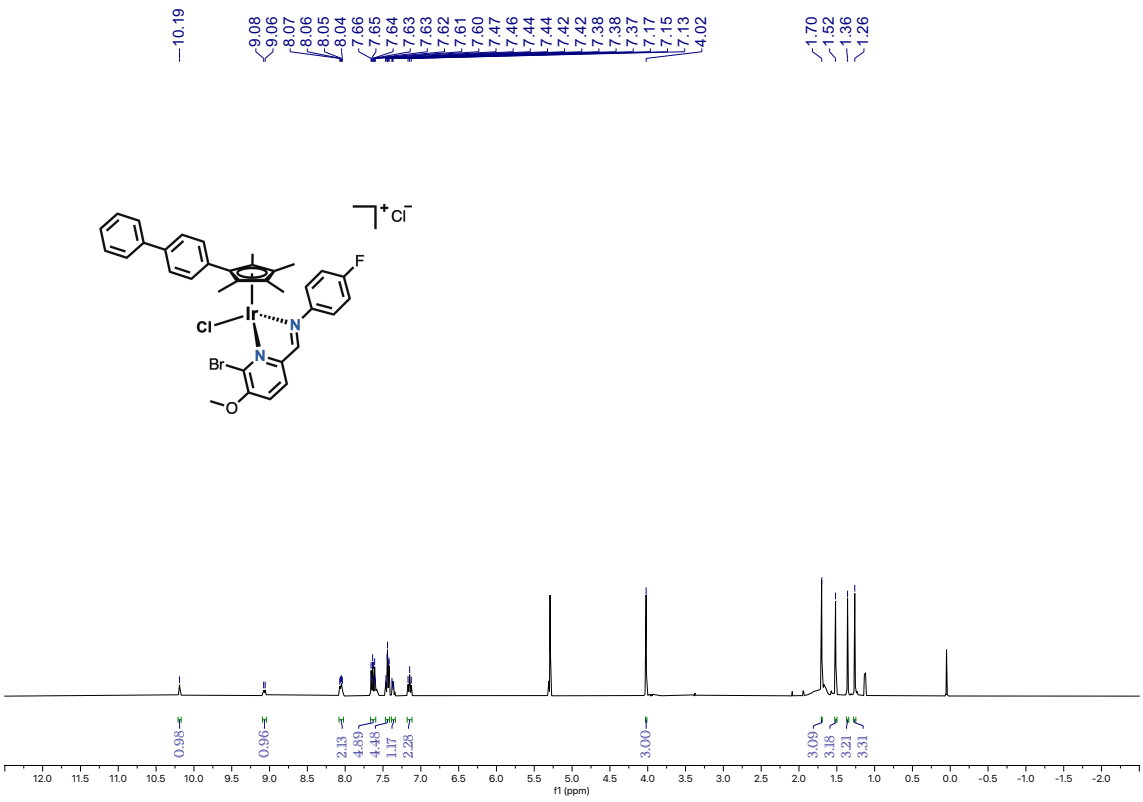


Figure 165. ^{1}H NMR of **Ir15** in DMSO-d$_6$.

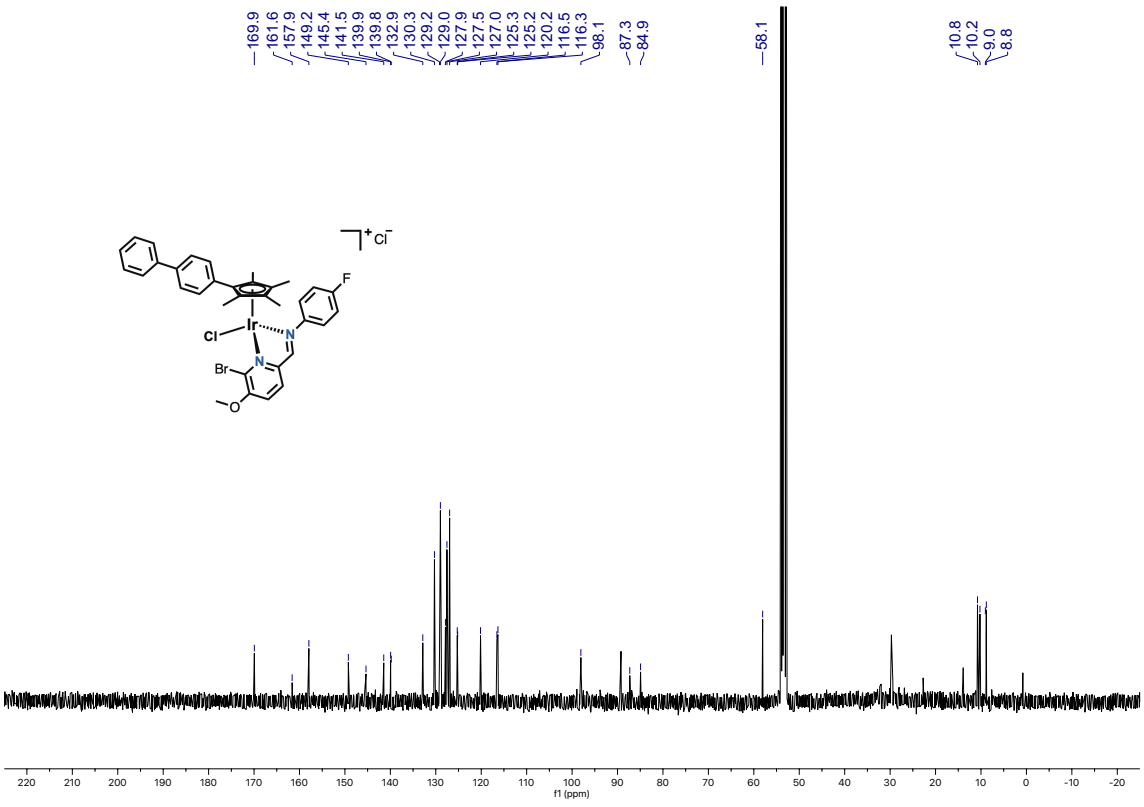


Figure 166. ^{13}C NMR of **Ir15** in DMSO-d$_6$.

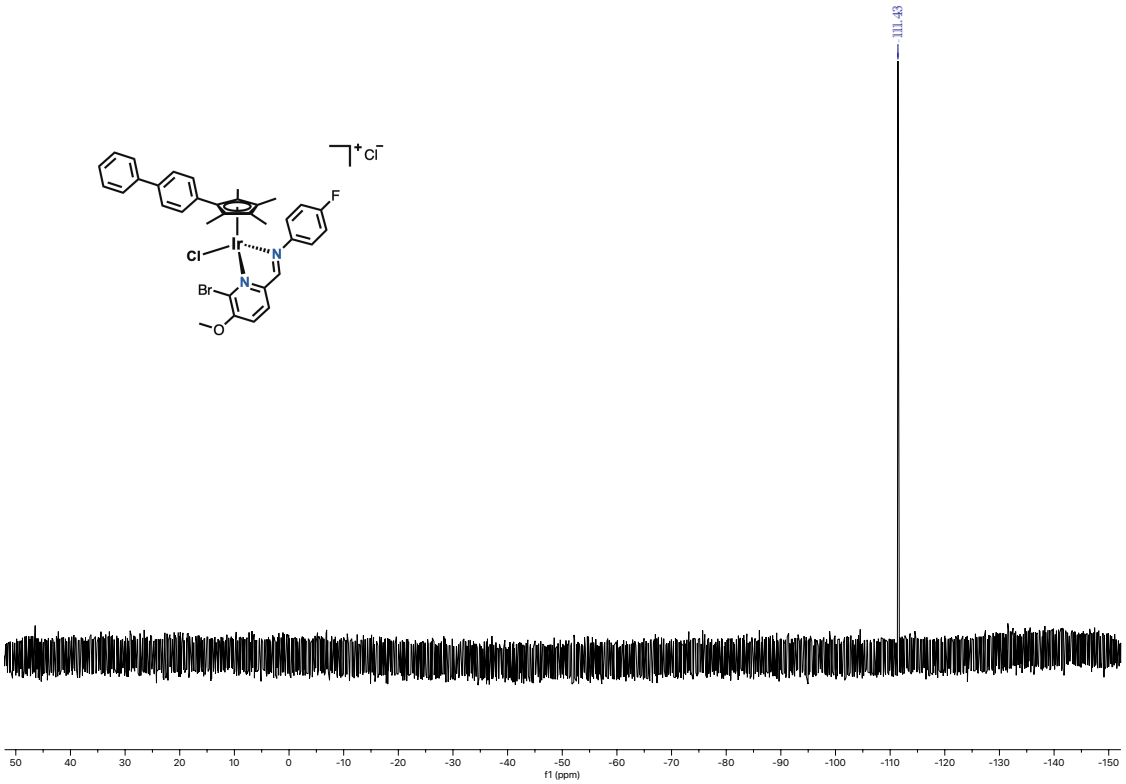


Figure 167. ^{19}F NMR of **Ir15** in DMSO-d_6.

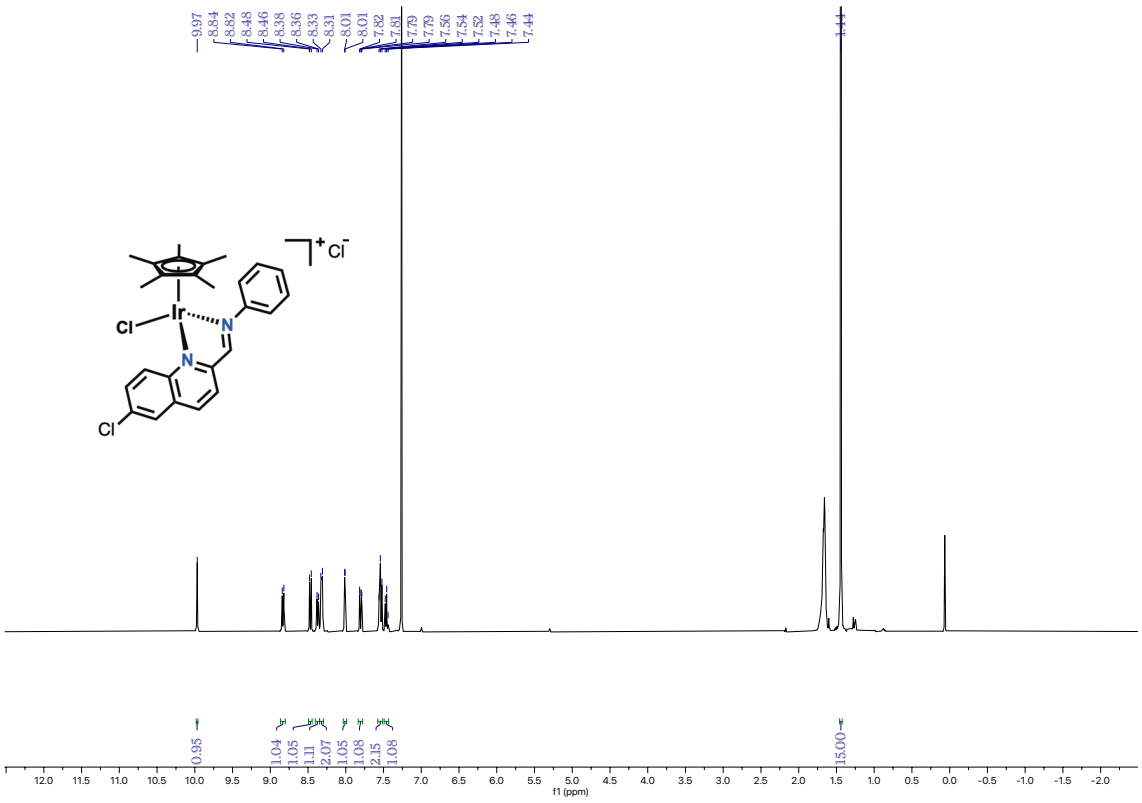


Figure 168. ^{1}H NMR of **IrCp1K7** in $CDCl_3$.

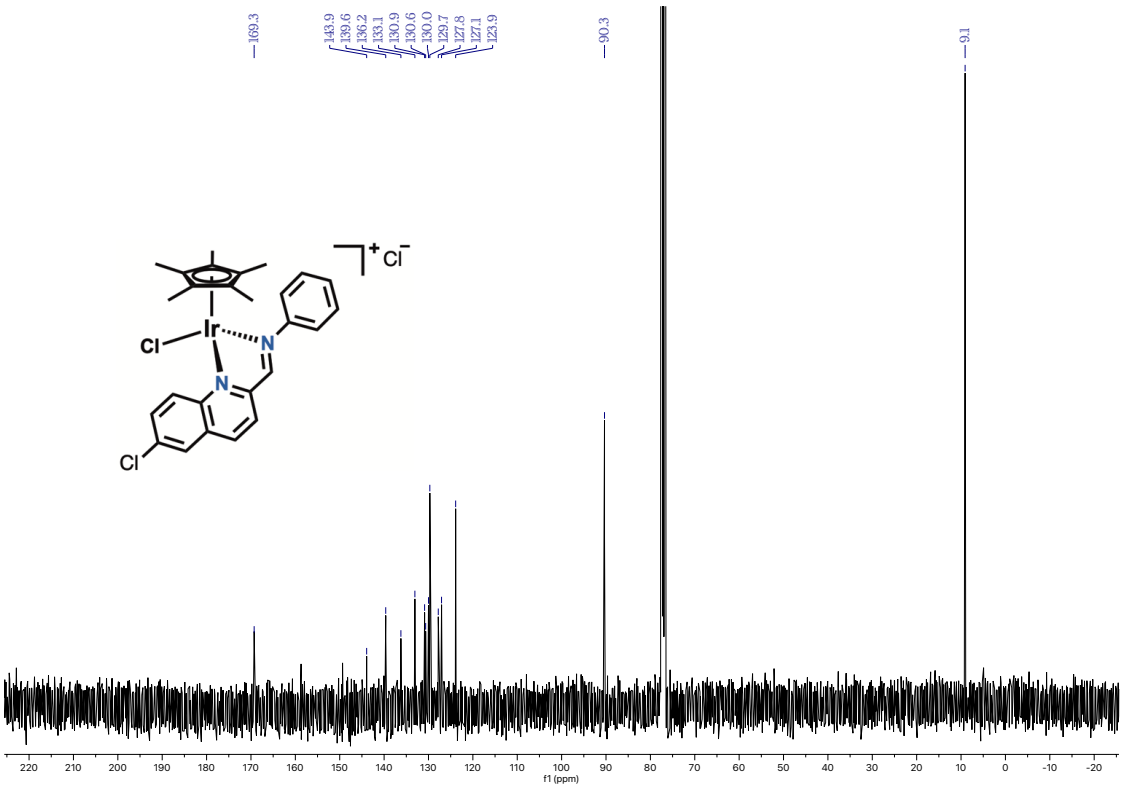


Figure 169. ^{13}C NMR of **IrCp1K7** in $CDCl_3$.

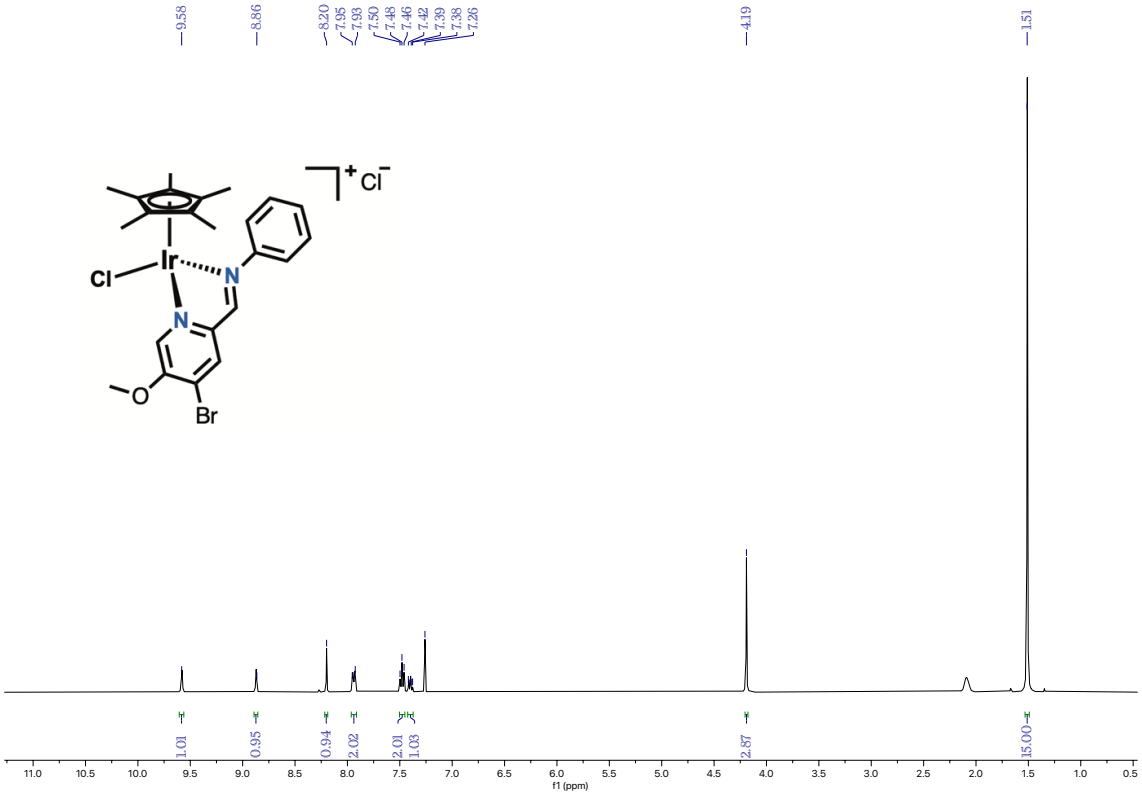


Figure 170. ^{1}H NMR of **IrCp1L7** in $CDCl_3$.

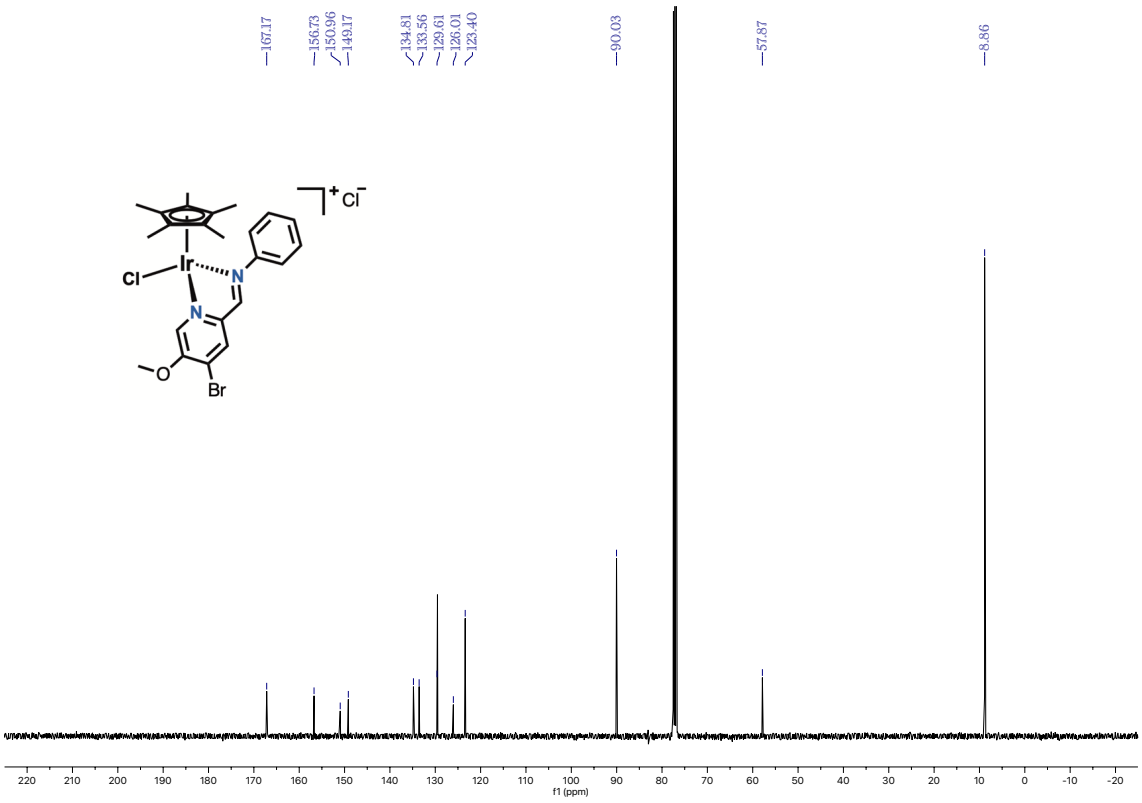


Figure 171. ^{13}C NMR of **IrCp1L7** in $CDCl_3$.

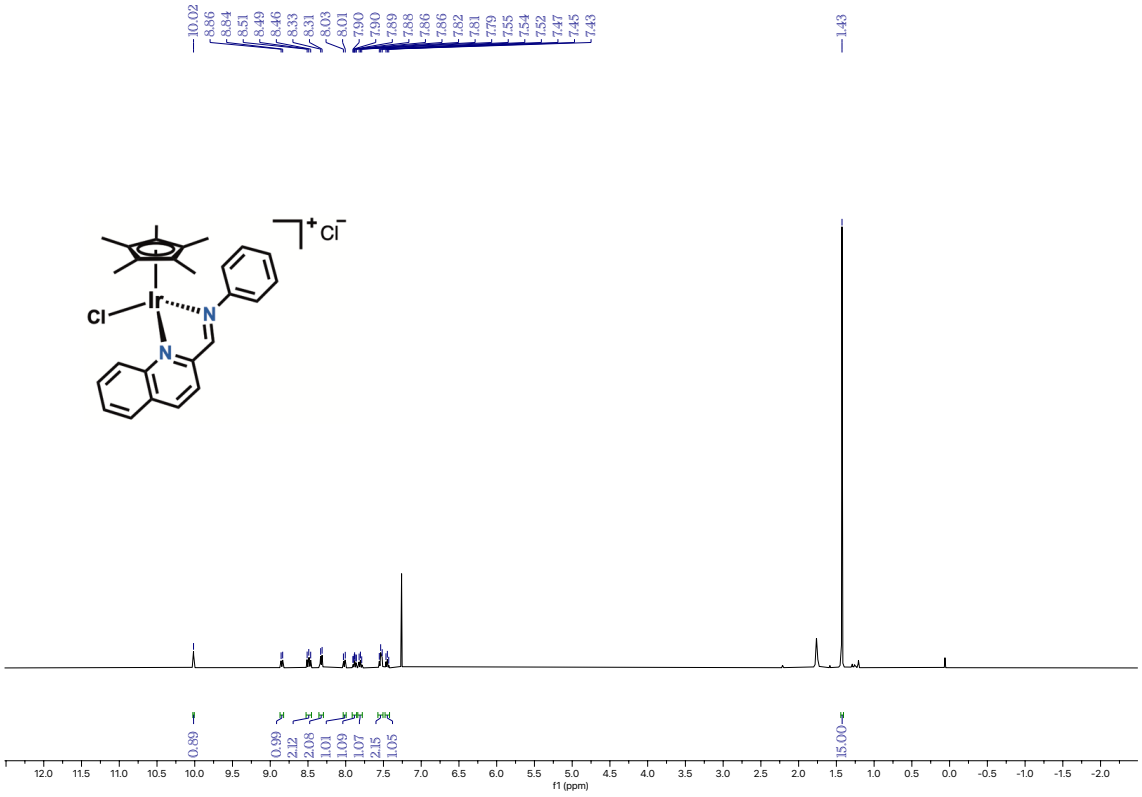


Figure 172. ^{1}H NMR of **IrCp1B7** in $CDCl_3$.

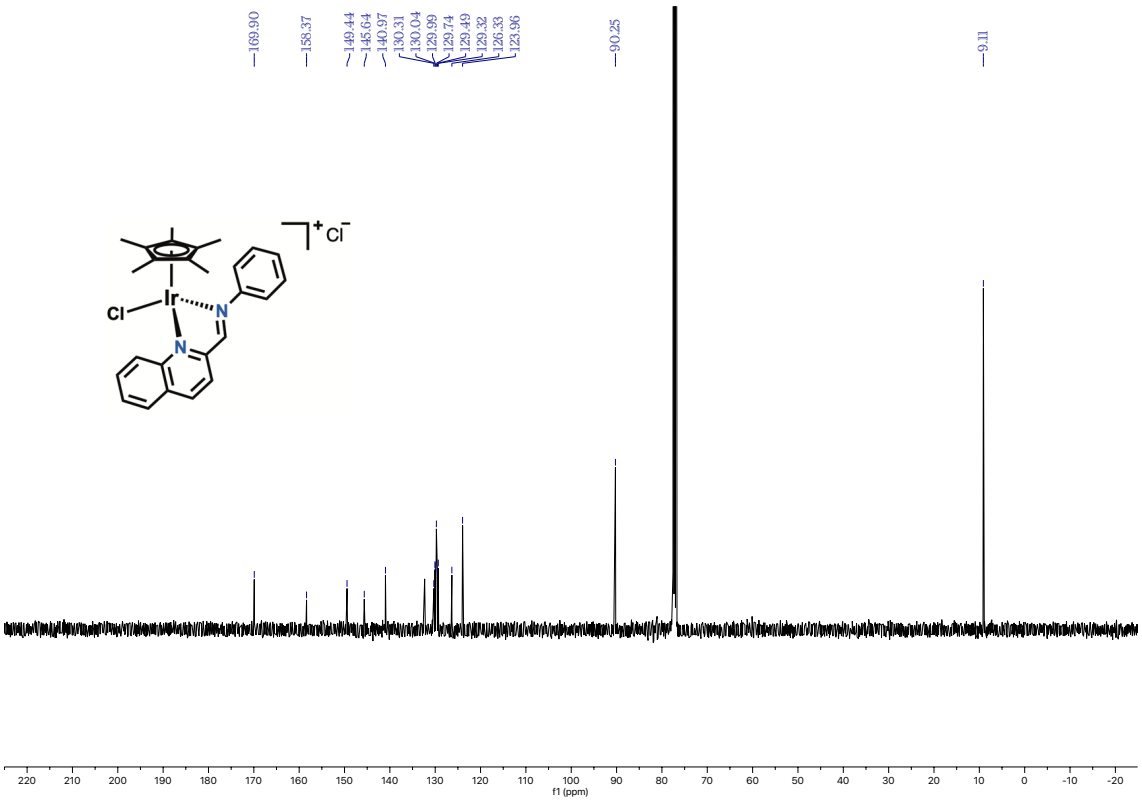


Figure 173. ^{13}C NMR of **IrCp1B7** in $CDCl_3$.

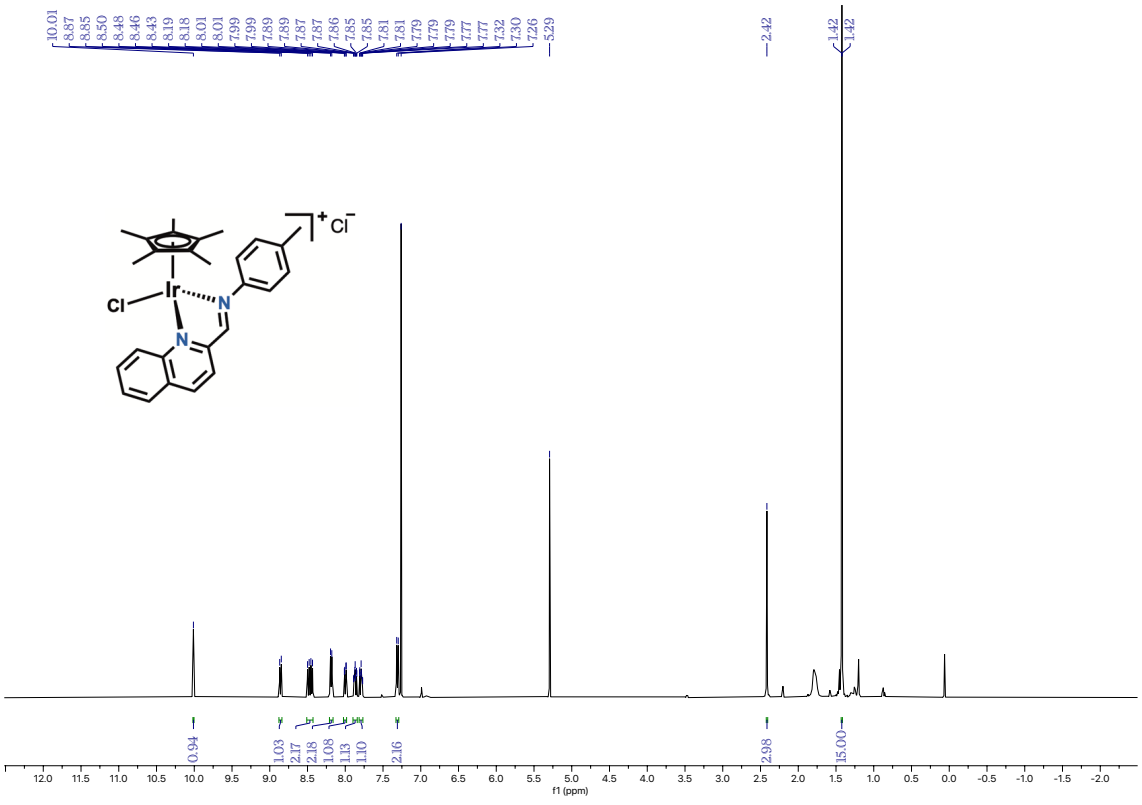


Figure 174. ^{1}H NMR of **IrCp1B8** in $CDCl_3$.

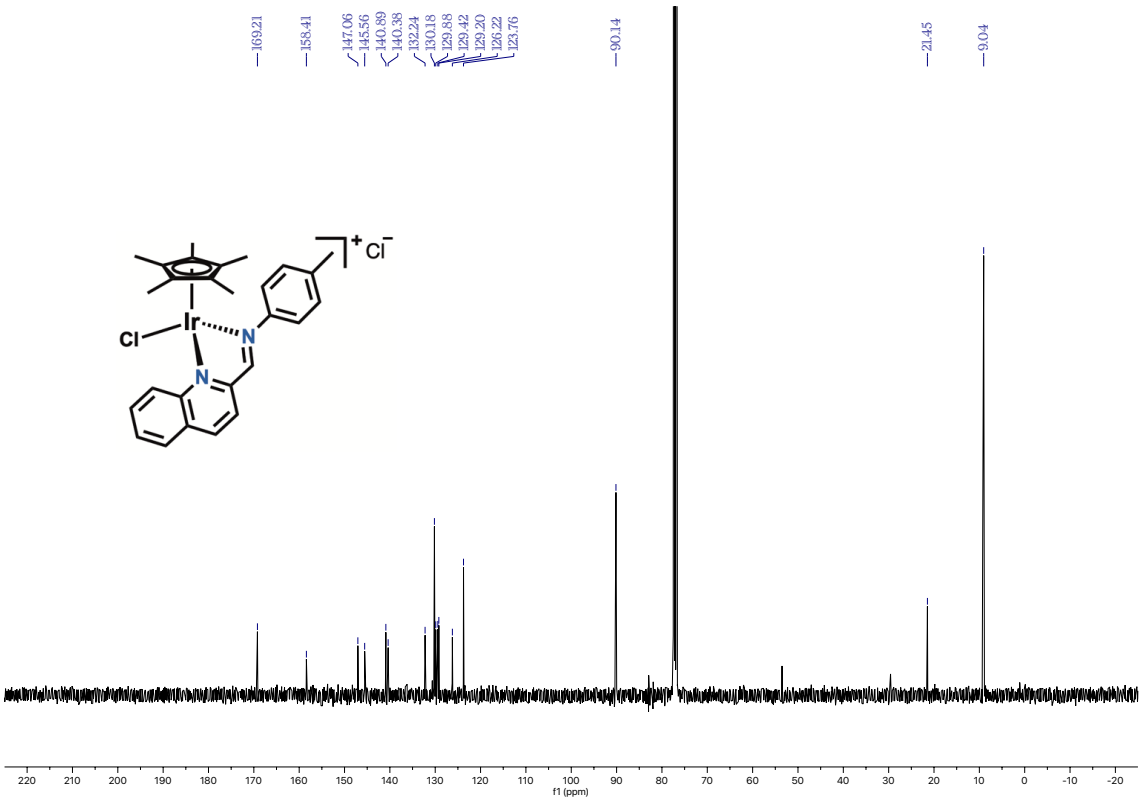


Figure 175. ^{13}C NMR of **IrCp1B8** in $CDCl_3$.

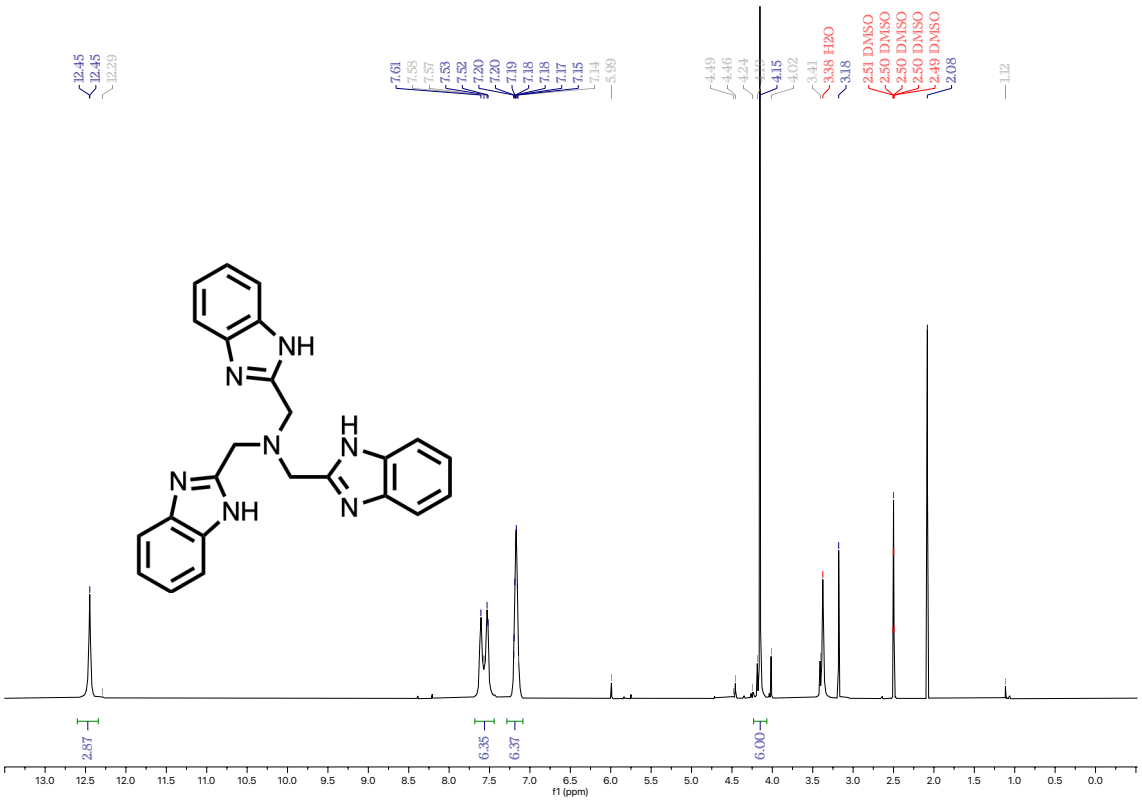


Figure 176. ^{1}H NMR of **(BimH)$_3$** in DMSO-d$_6$.

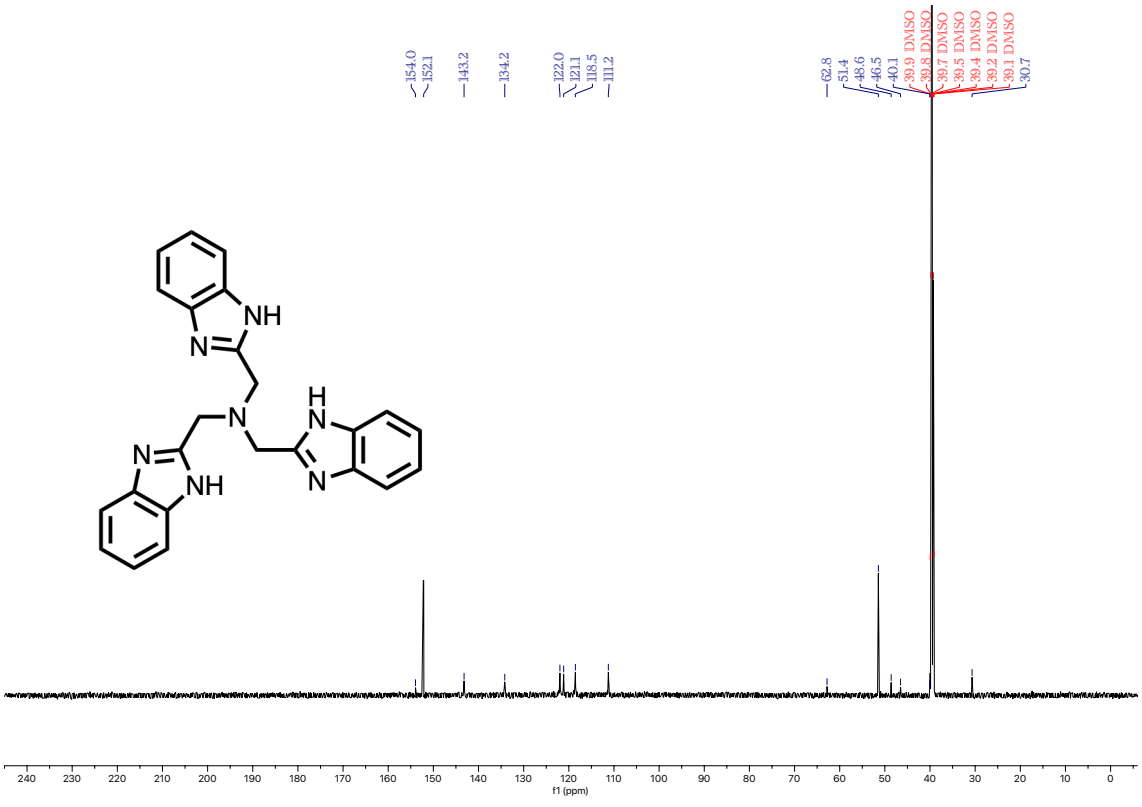


Figure 177. ^{13}C NMR of **(BimH)$_3$** in DMSO-d$_6$.

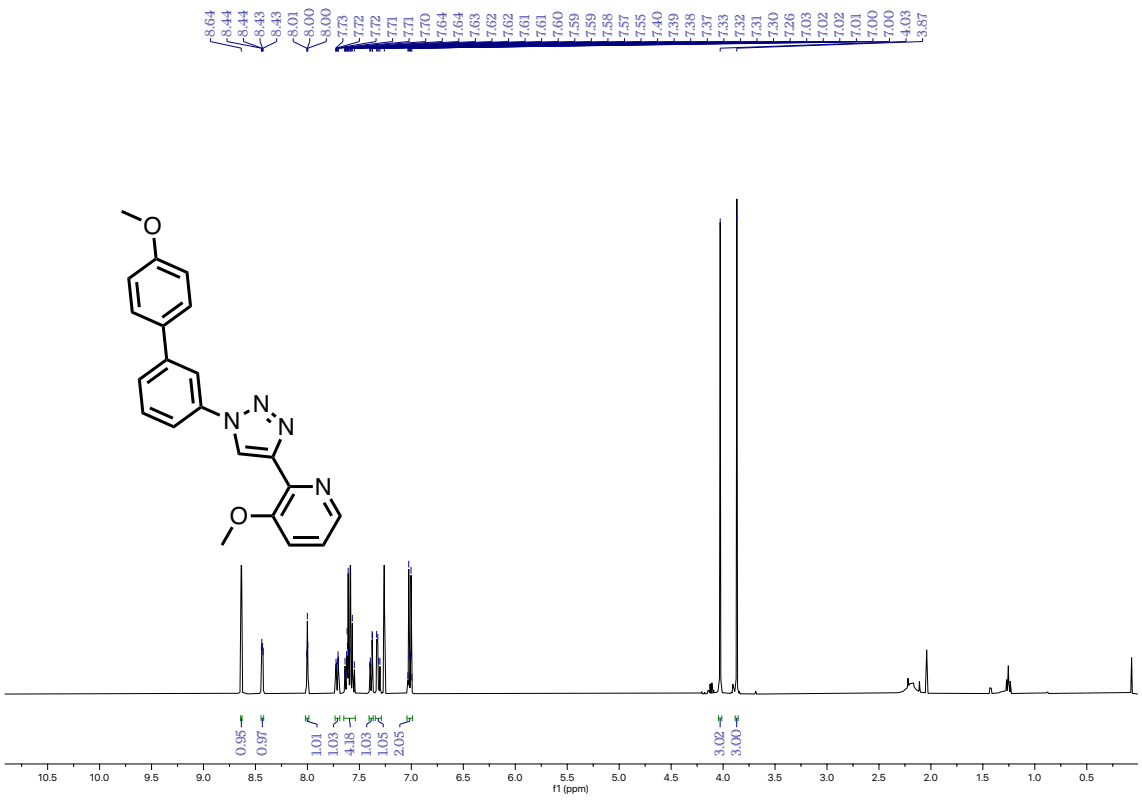


Figure 178. ^{1}H NMR of **M23Y3** in $CDCl_3$.

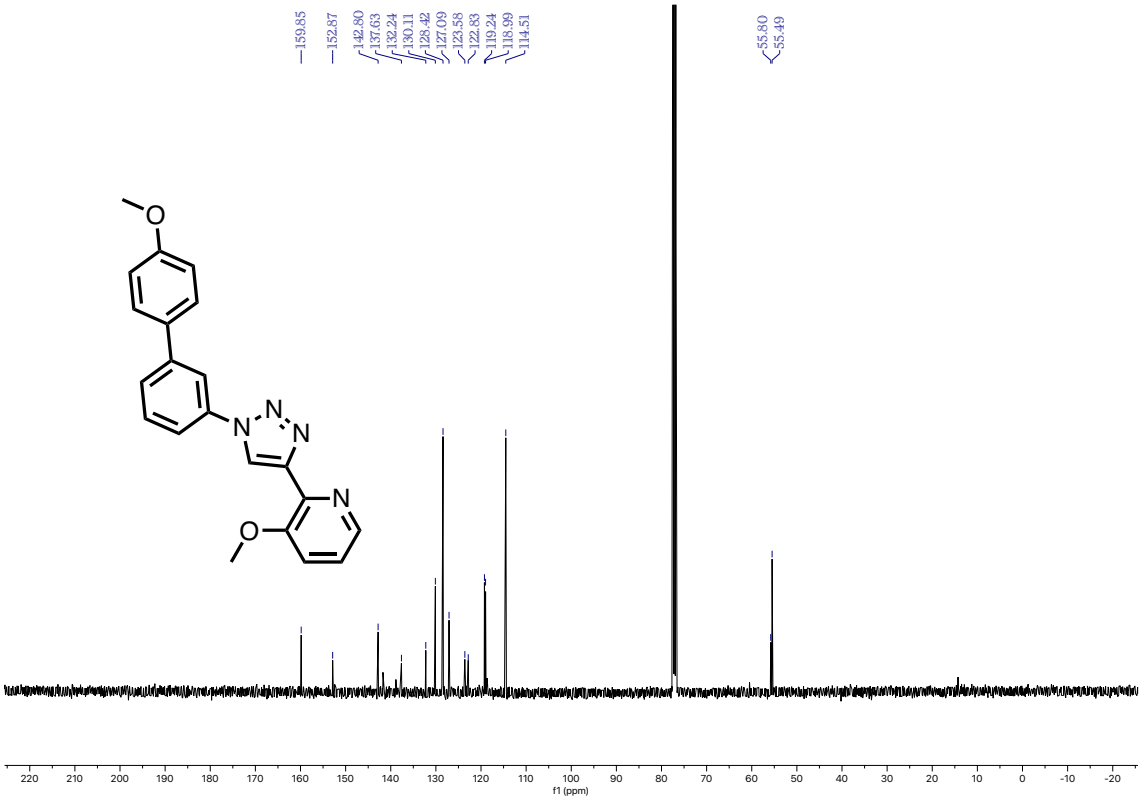


Figure 179. ^{13}C NMR of **M23Y3** in $CDCl_3$.

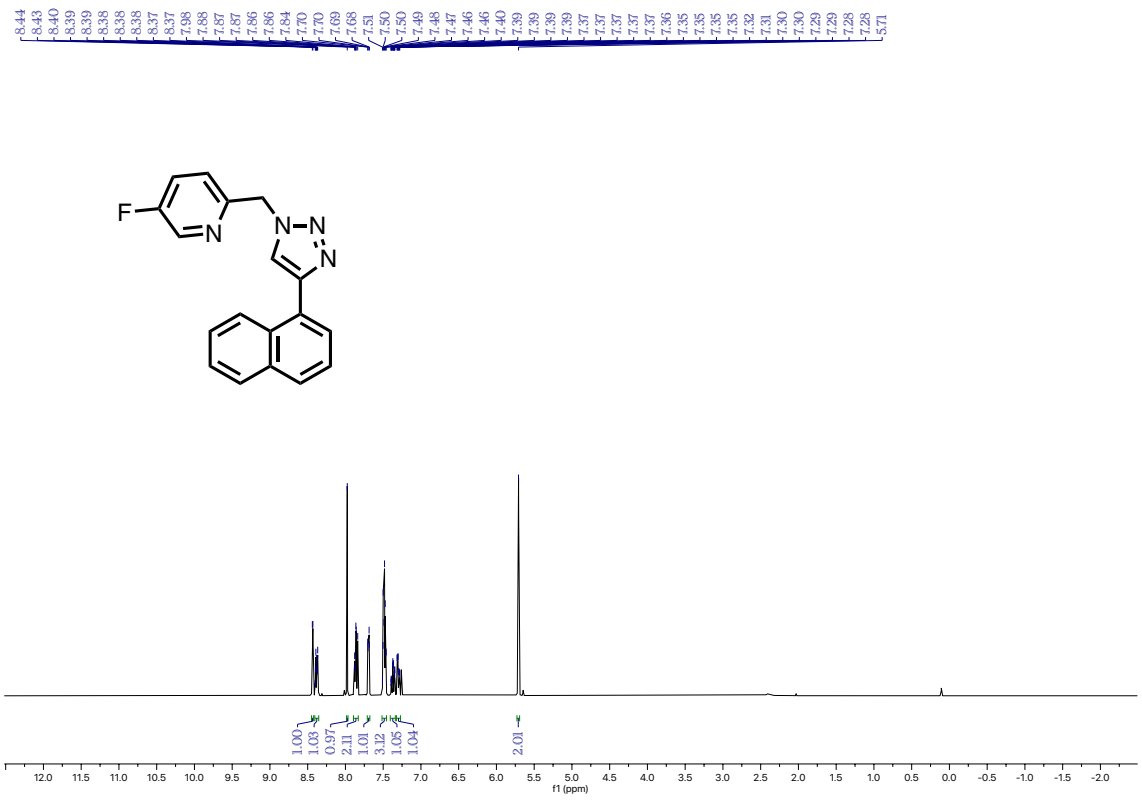


Figure 180. ^{1}H NMR of **P3A10** in $CDCl_3$.

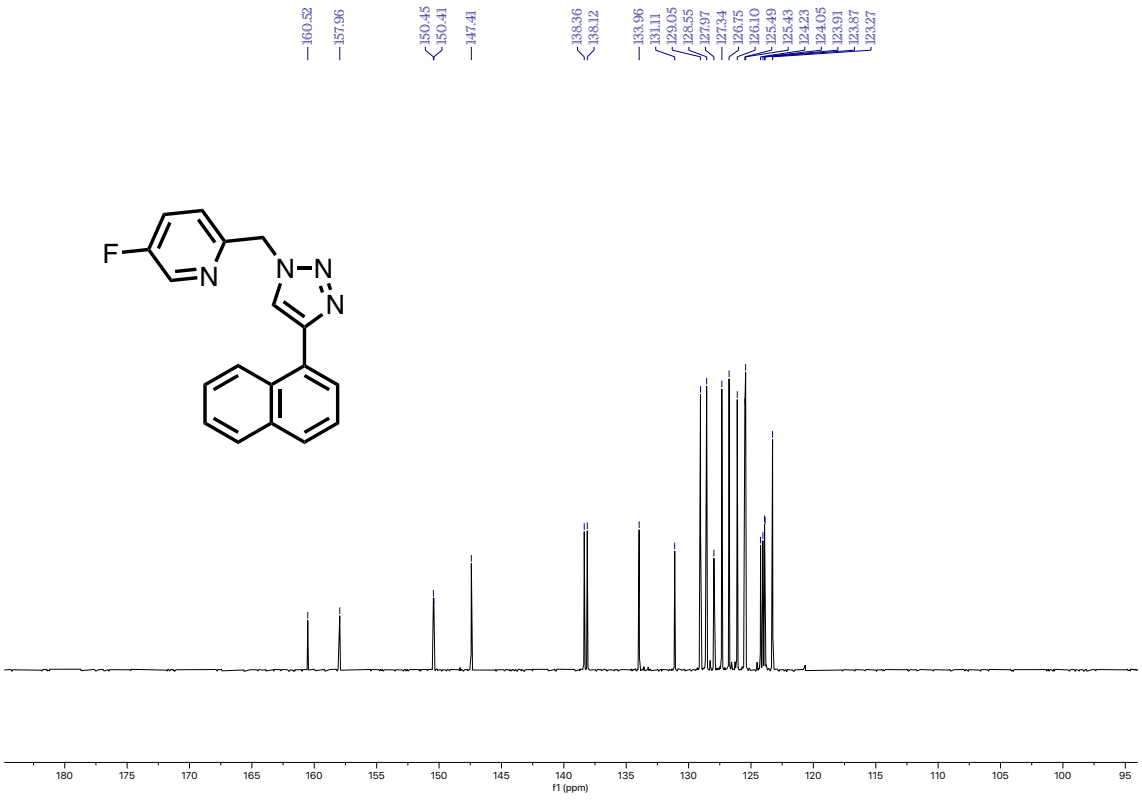


Figure 181. ^{13}C NMR of **P3A10** in $CDCl_3$.

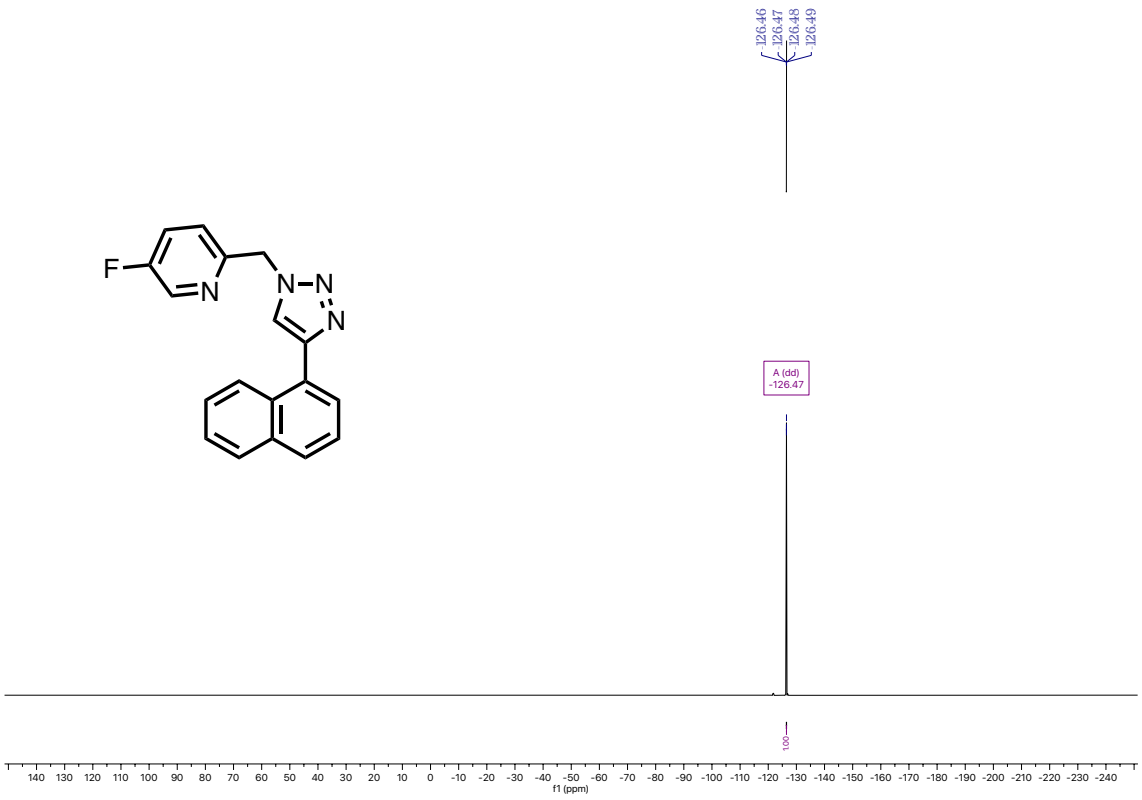


Figure 182. ^{19}F NMR of **P3A10** in $CDCl_3$.

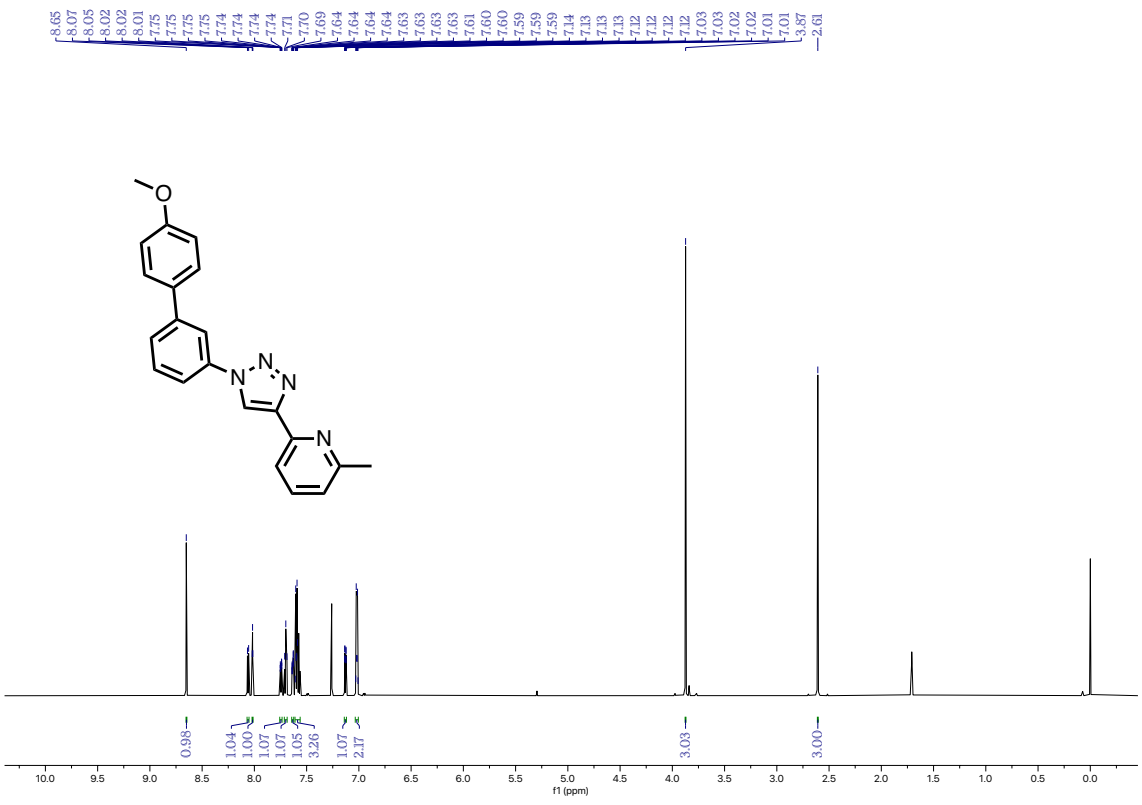


Figure 183. ^{1}H NMR of **M23Y2** in $CDCl_3$.

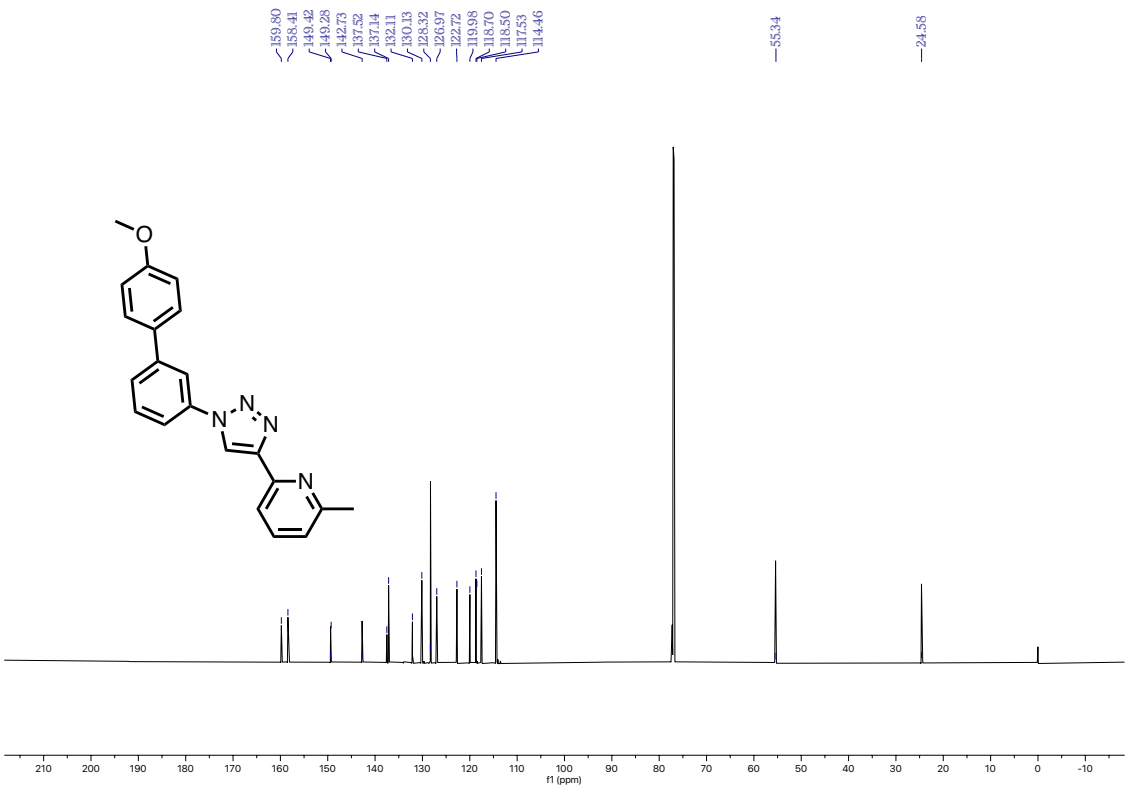


Figure 184. ^{13}C NMR of **M23Y2** in $CDCl_3$.

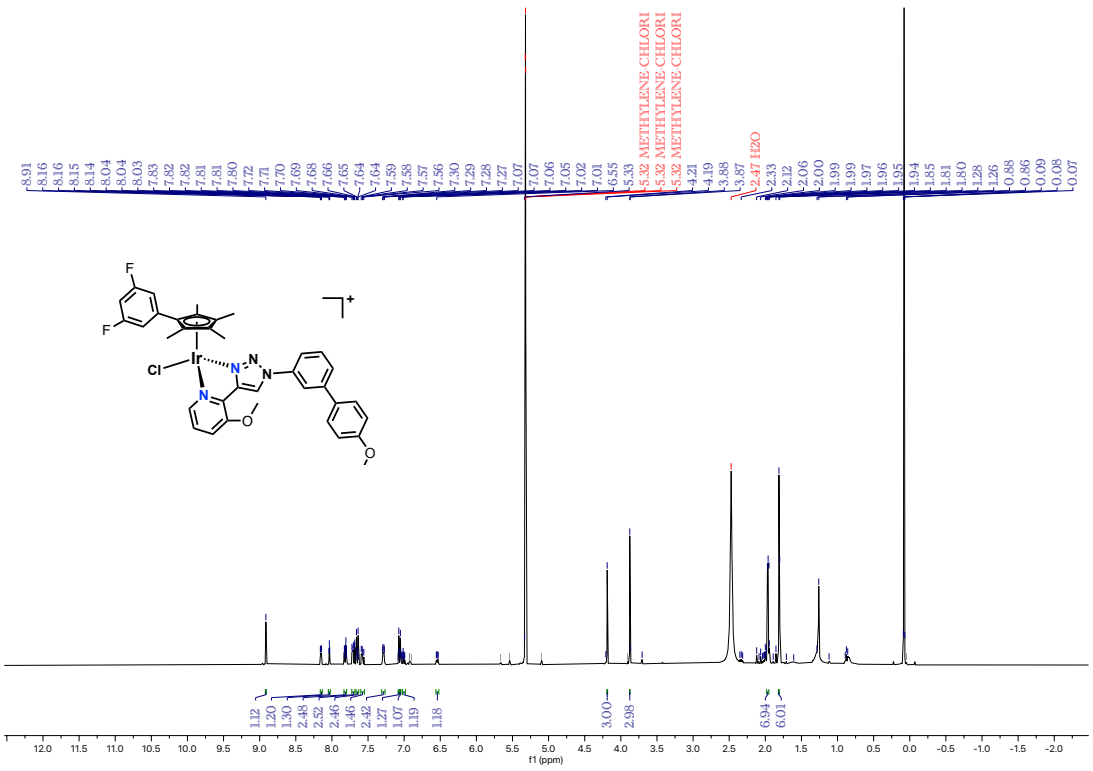


Figure 185. ^{1}H NMR of **IrCp3M23Y3** in CD_2Cl_2.

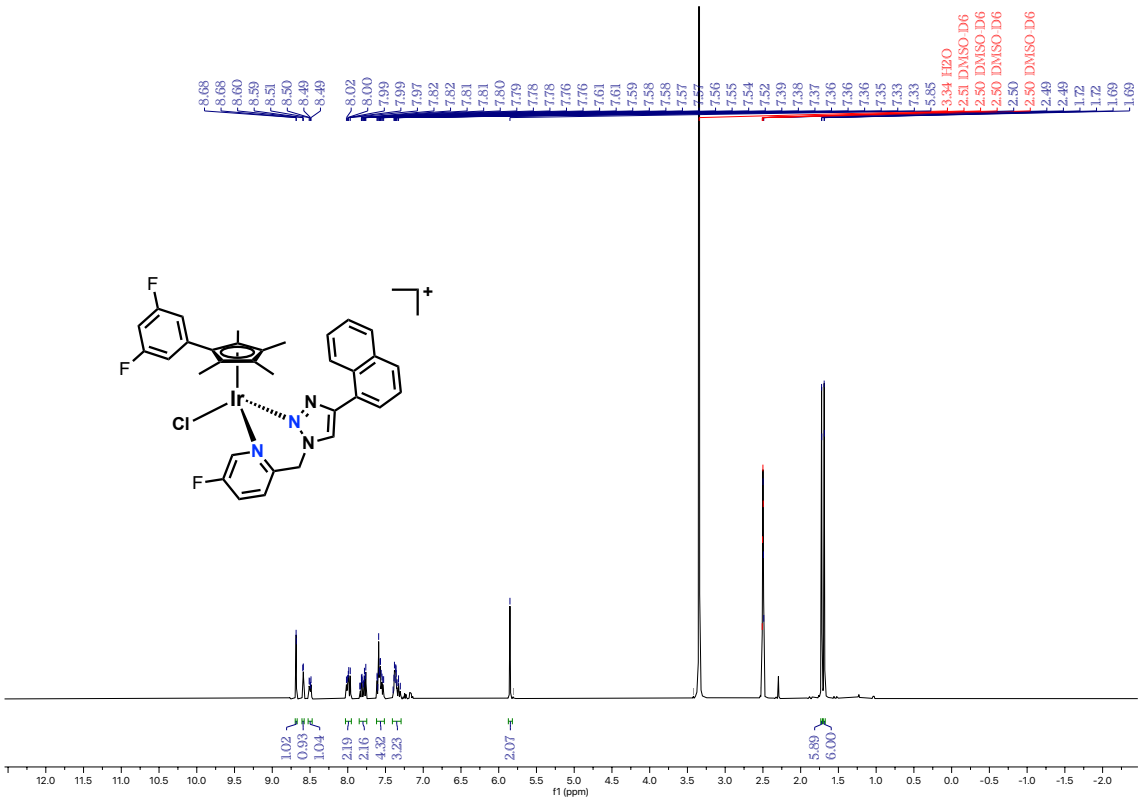


Figure 186. ^{1}H NMR of **IrCp3P3A10** in DMSO-d$_6$.

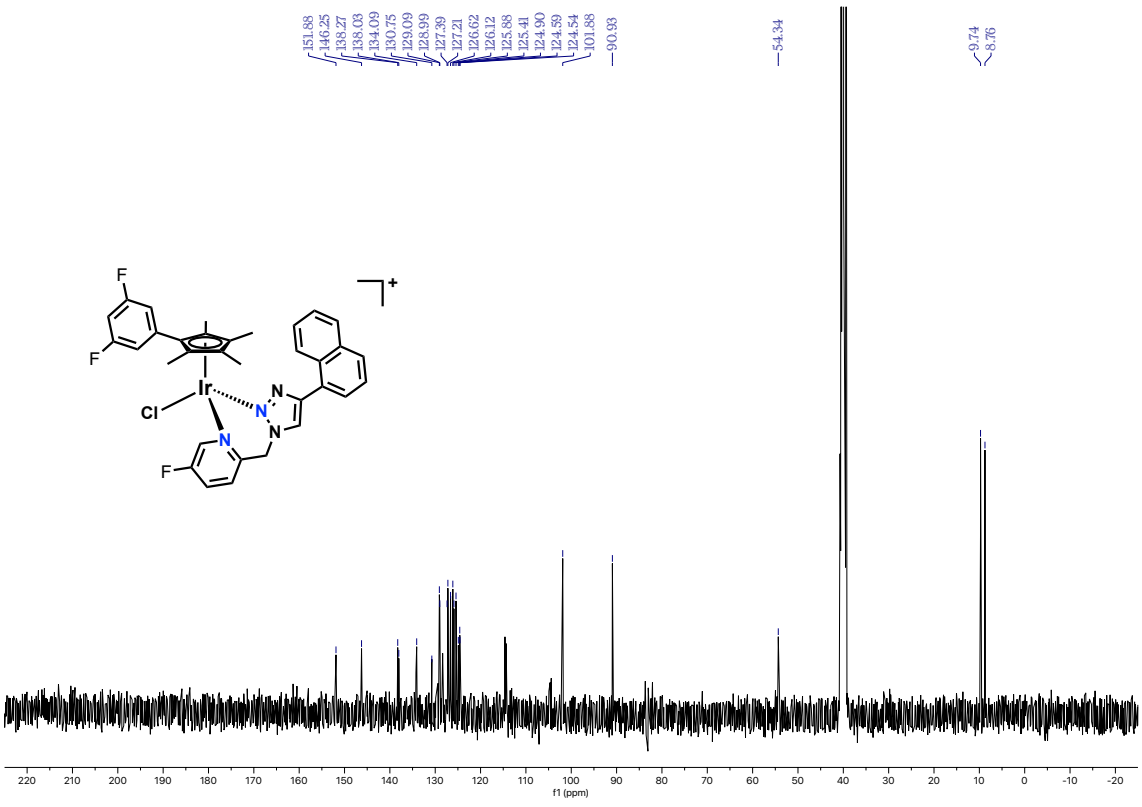


Figure 187. ^{13}C NMR of **IrCp3P3A10** in DMSO-d$_6$.

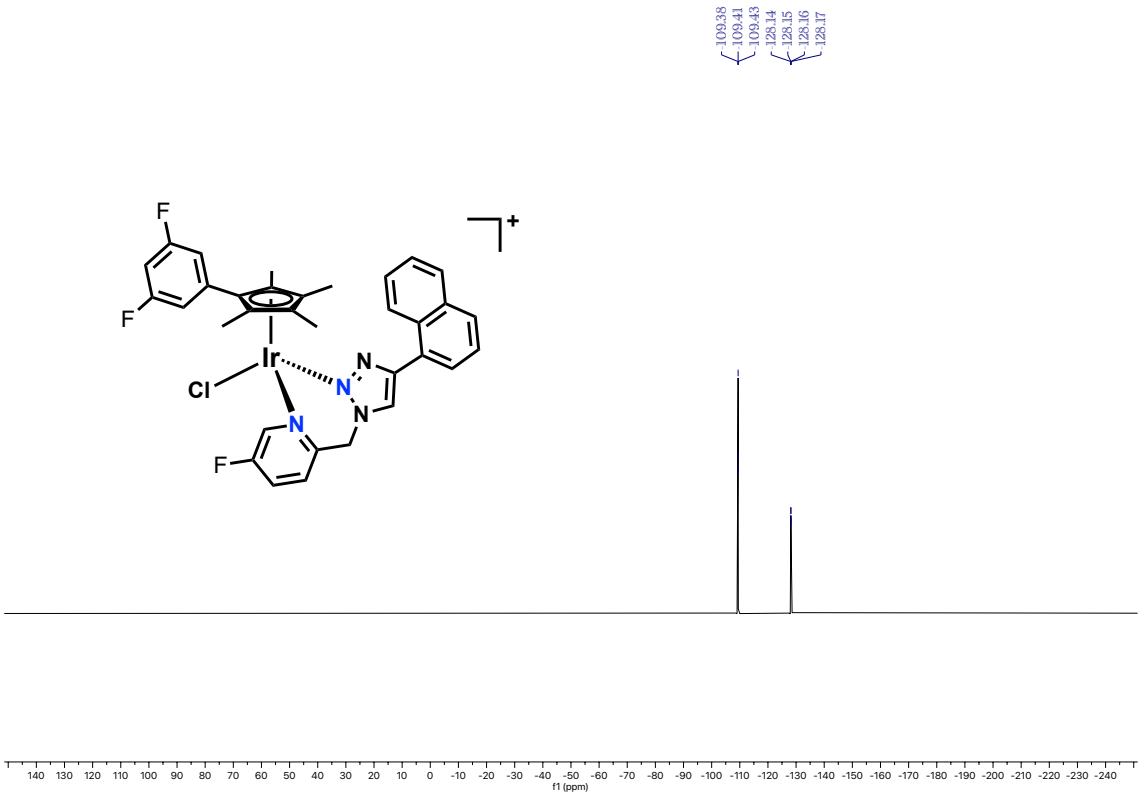


Figure 188. ^{19}F NMR of **IrCp3P3A10** in $CDCl_3$.

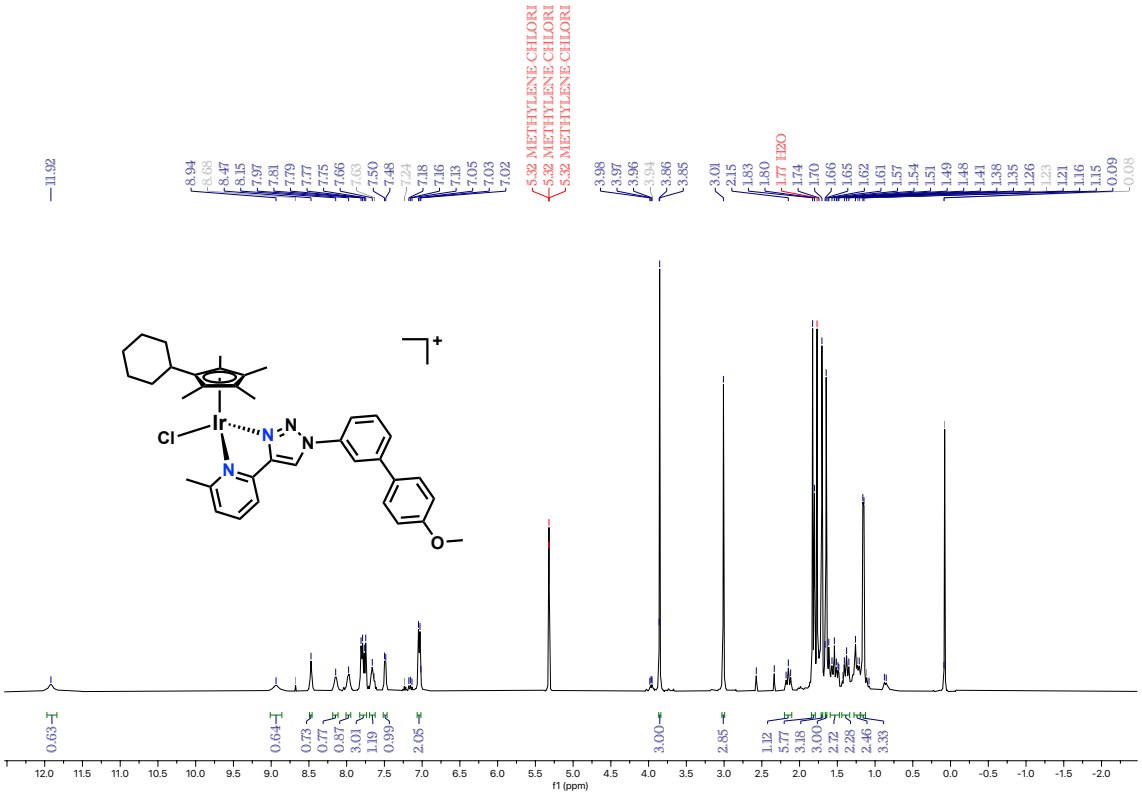


Figure 189. ^{1}H NMR of **IrCp4M23Y2** in DMSO-d_6.

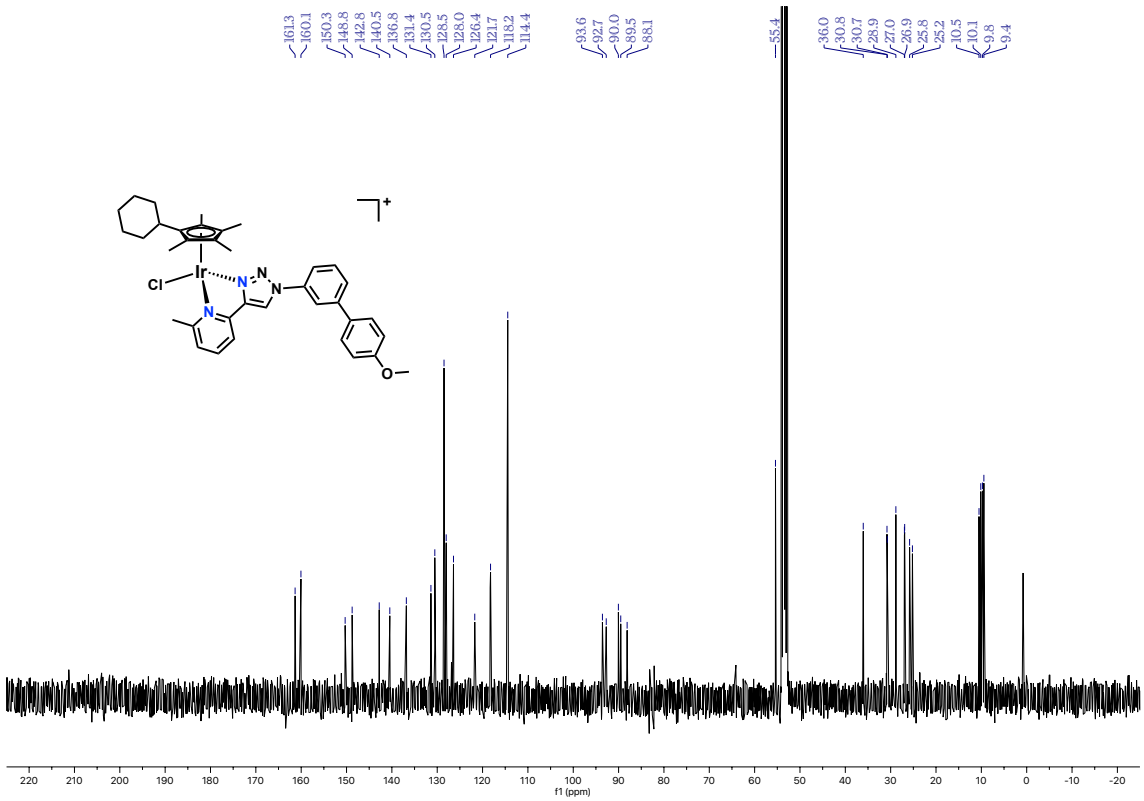


Figure 190. ^{13}C NMR of **IrCp4M23Y2** in DMSO-d_6.

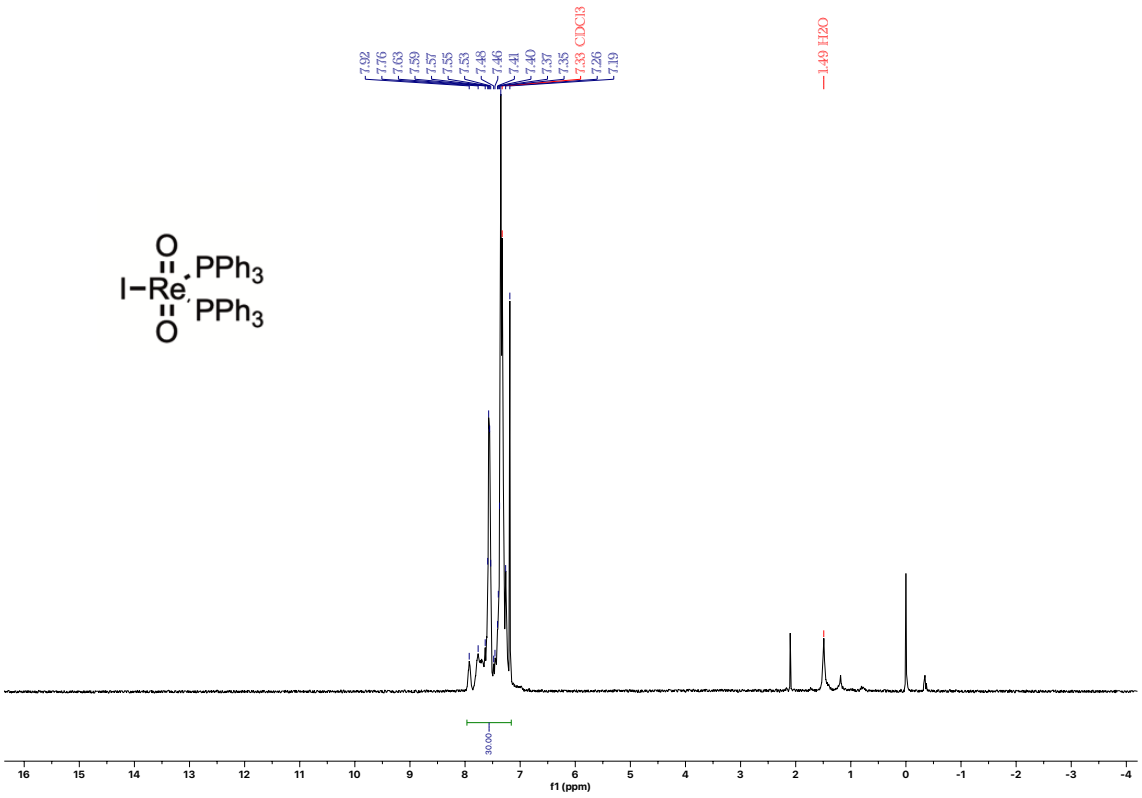


Figure 191. ^{1}H NMR of **$ReIO_2(PPh_3)_2$** in $CDCl_3$.

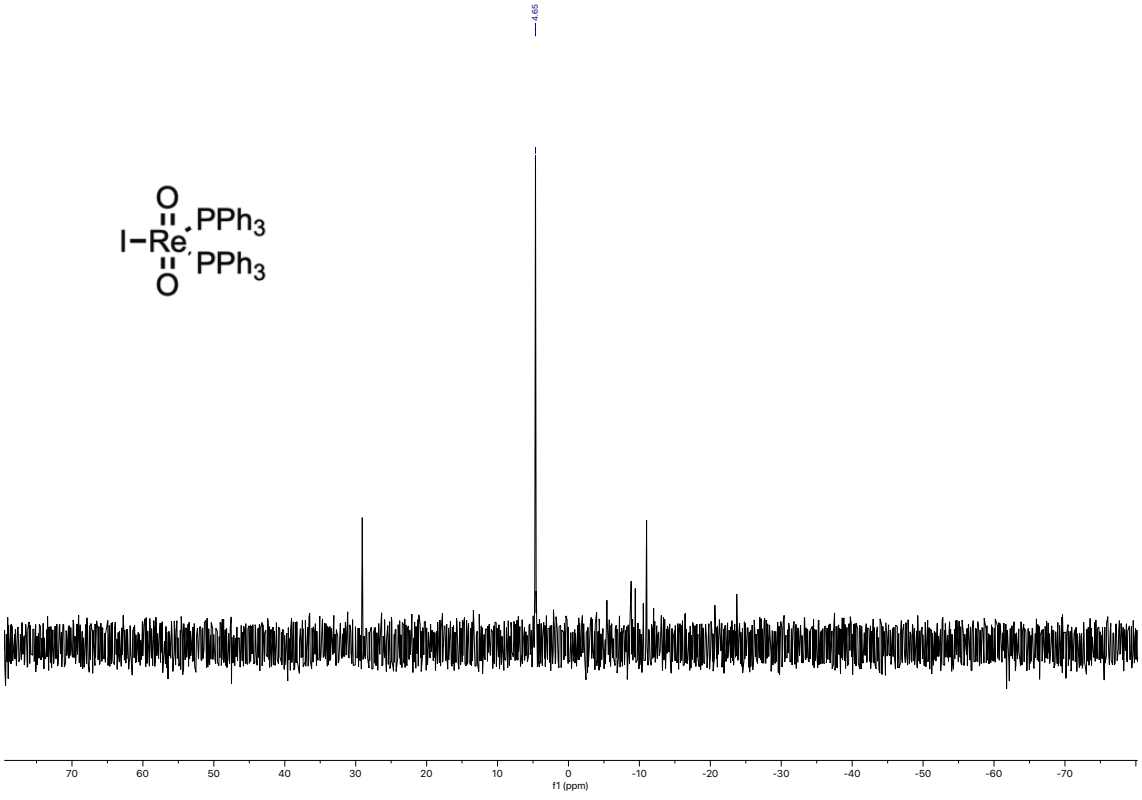


Figure 192. ^{31}P NMR of $ReIO_2(PPh_3)_2$ in $CDCl_3$.

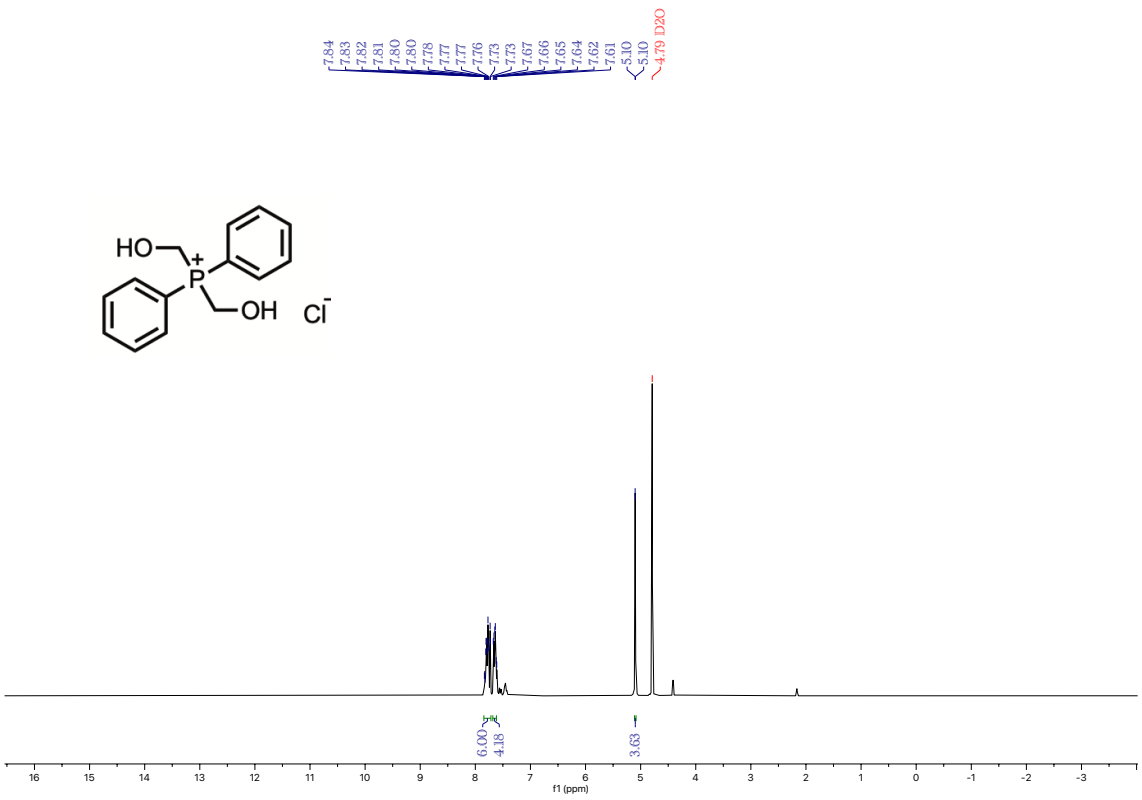


Figure 193. ^{1}H NMR of **45** in D_2O.

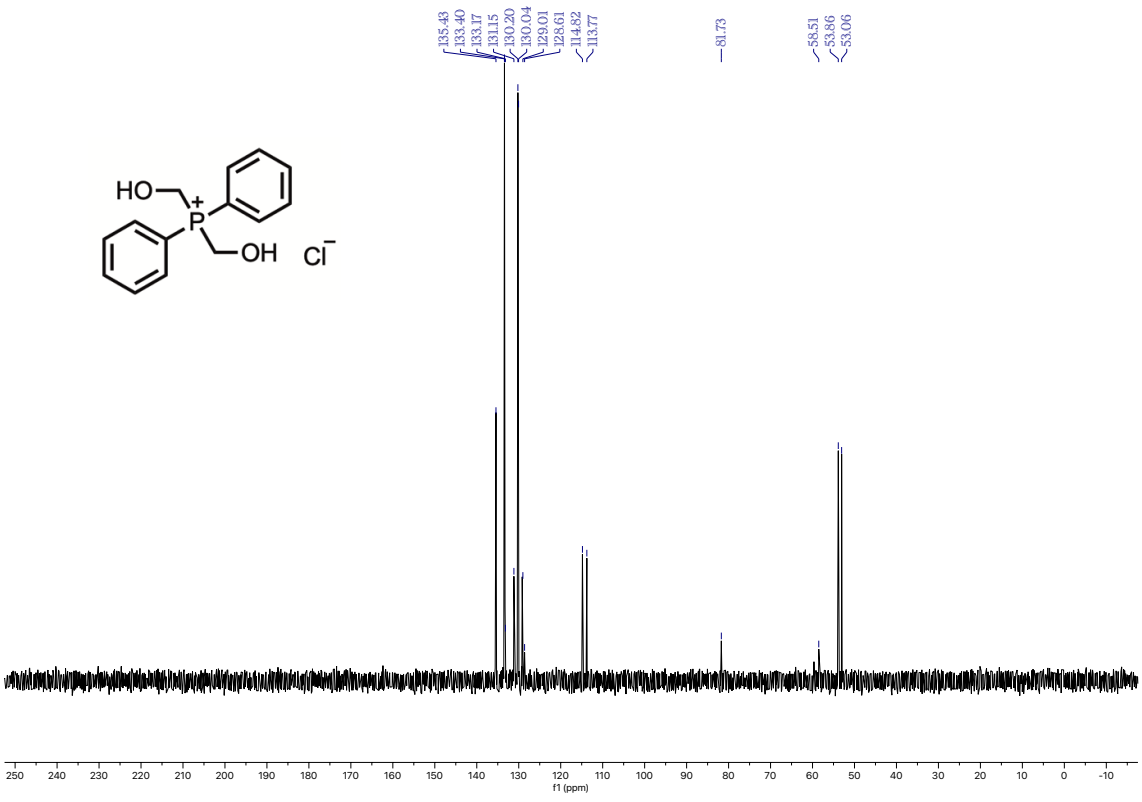


Figure 194. ^{13}C NMR of **45** in D_2O.

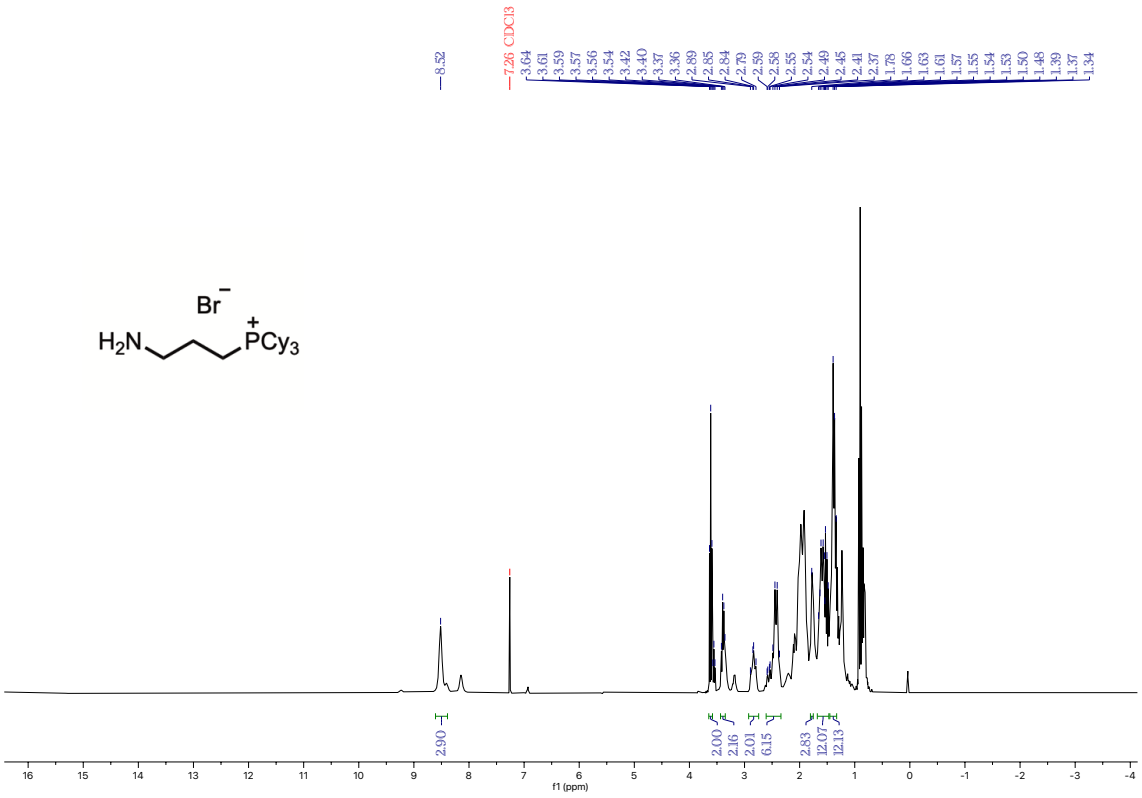


Figure 195. ^{1}H NMR of **46** in $CDCl_3$.

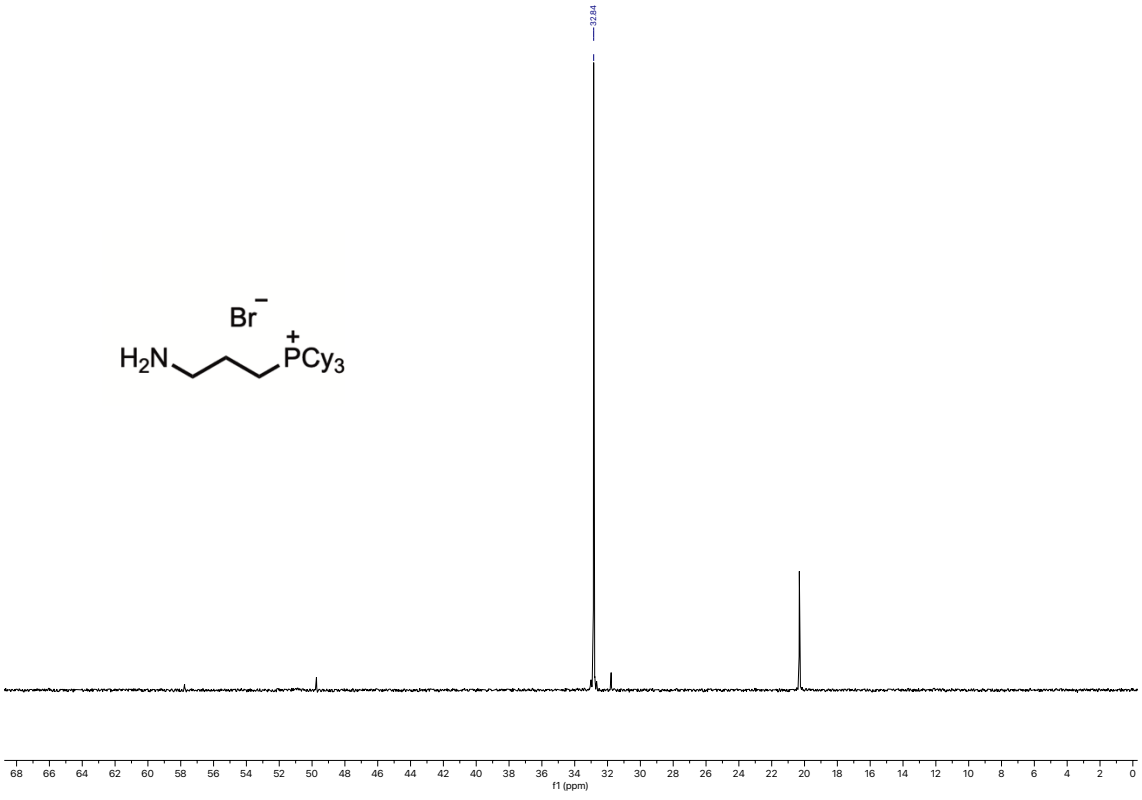


Figure 196. ^{31}P NMR of **46** in $CDCl_3$.

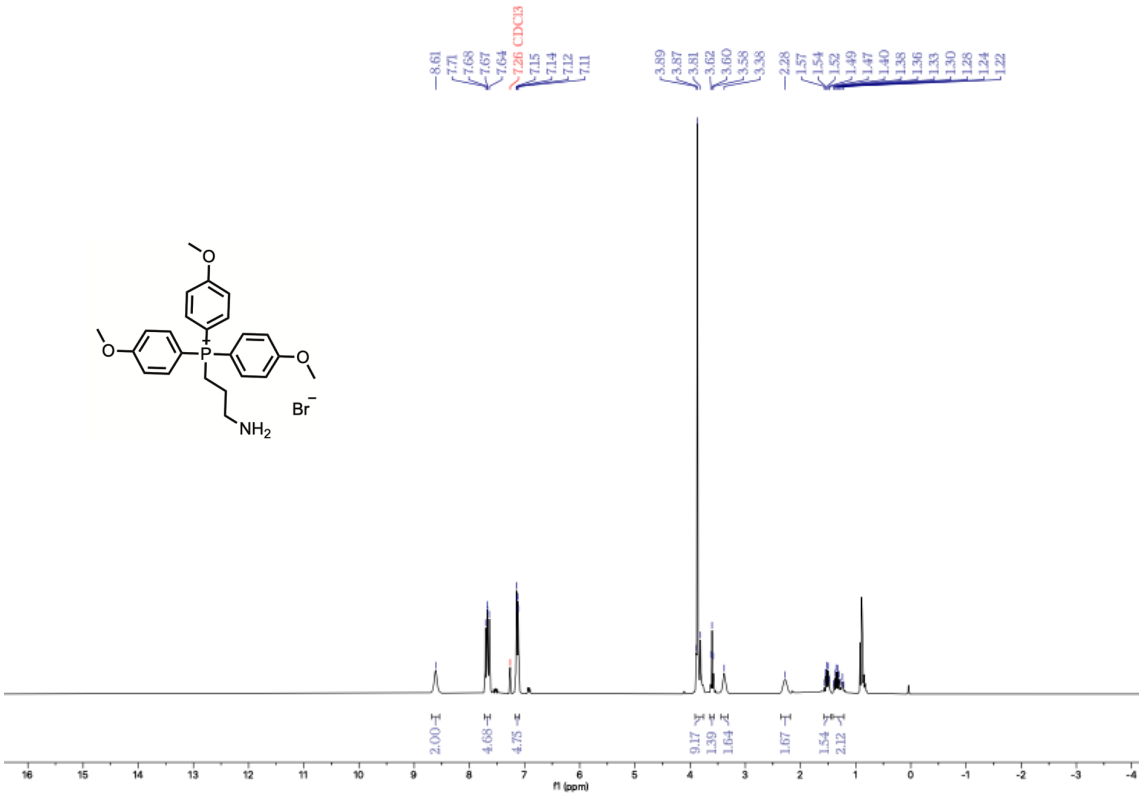


Figure 197. ^{1}H NMR of **47** in $CDCl_3$.

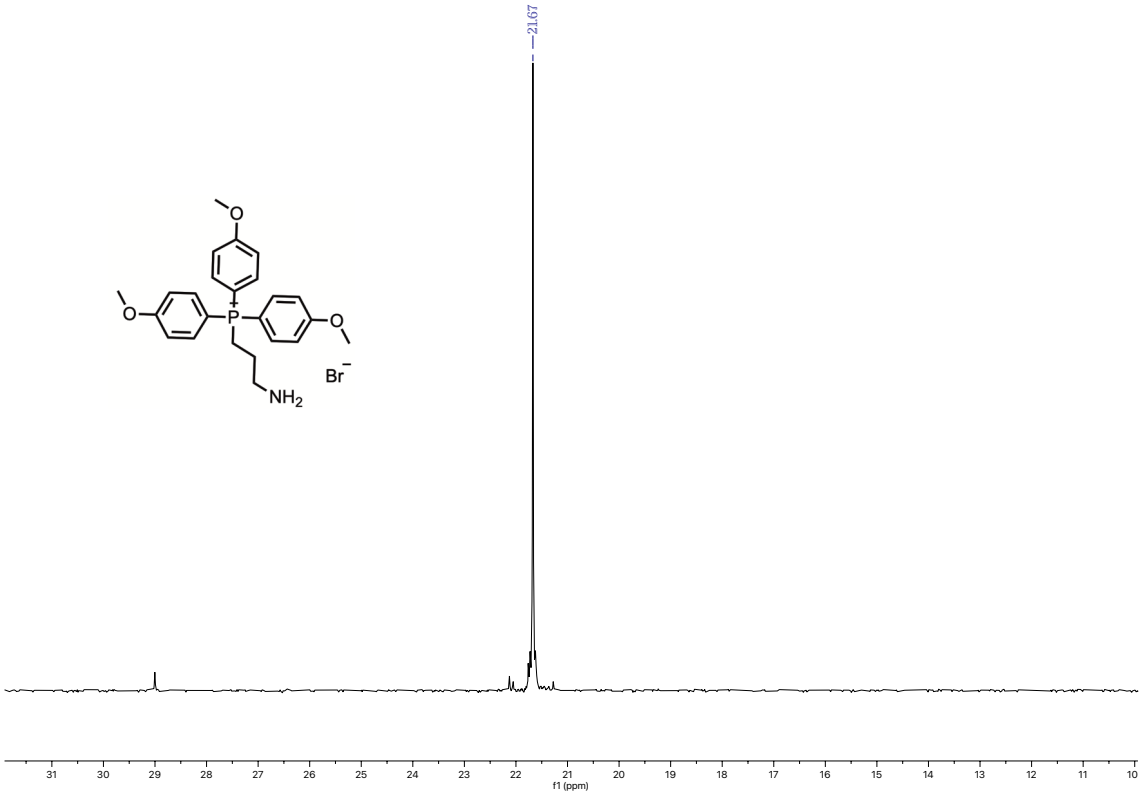


Figure 198. ^{31}P NMR of **47** in $CDCl_3$.

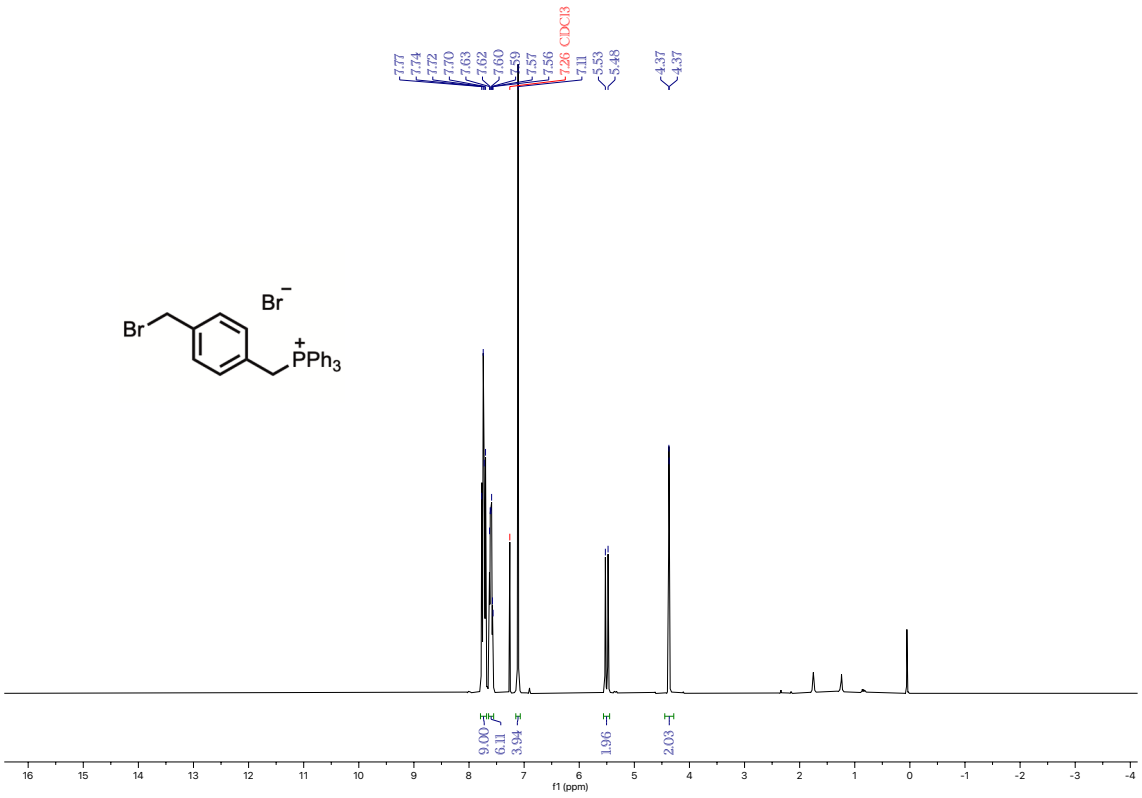


Figure 199. ^{1}H NMR of **48** in $CDCl_3$.

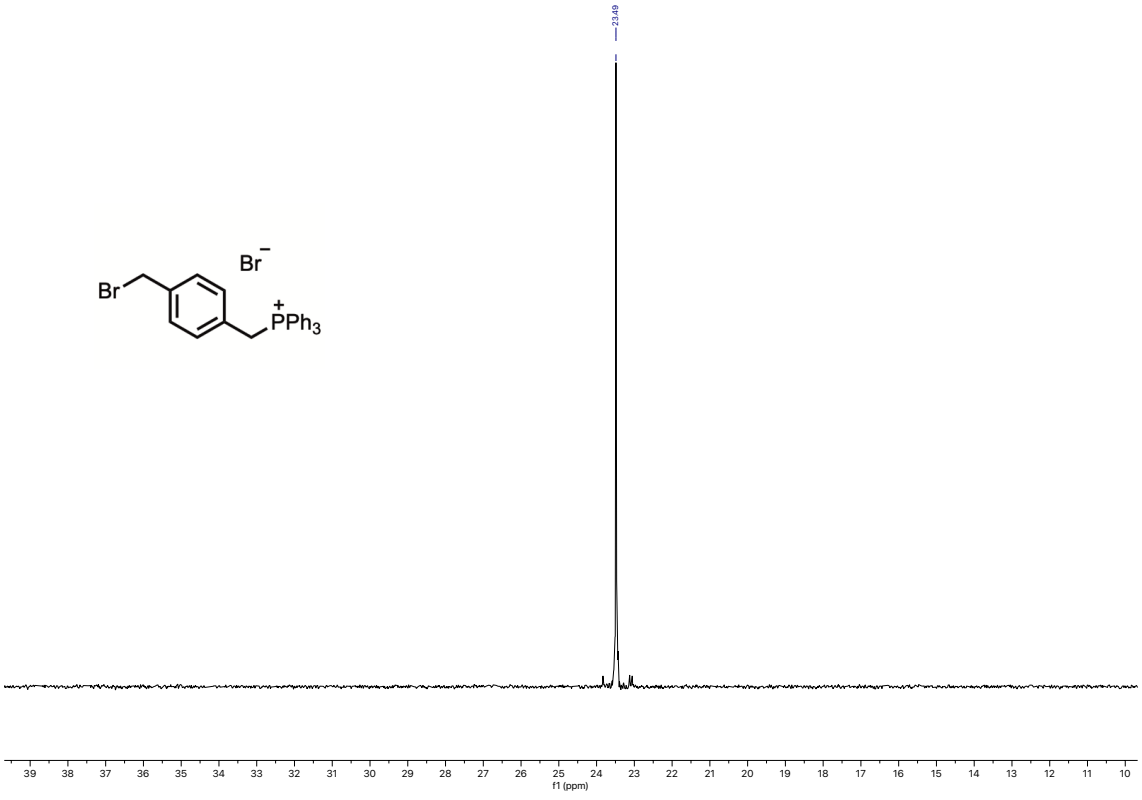


Figure 200. ^{31}P NMR of **48** in $CDCl_3$.

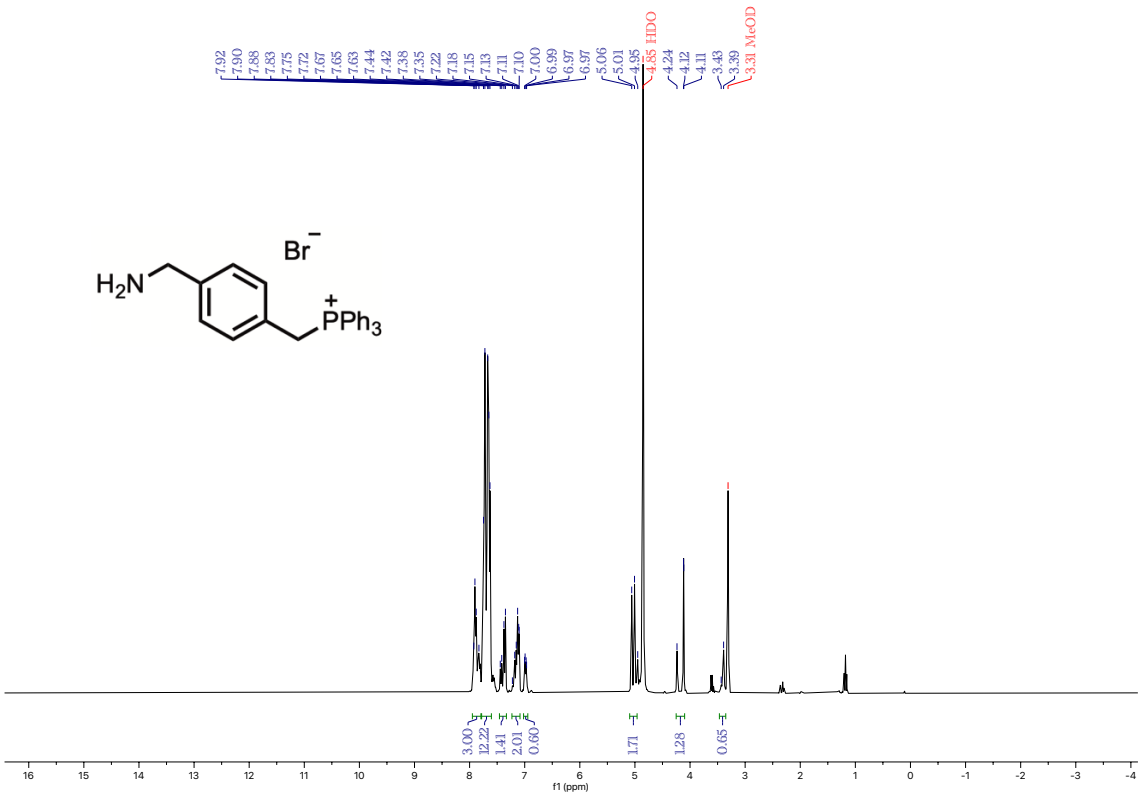


Figure 201. ^{1}H NMR of **49** in MeOD-d$_4$.

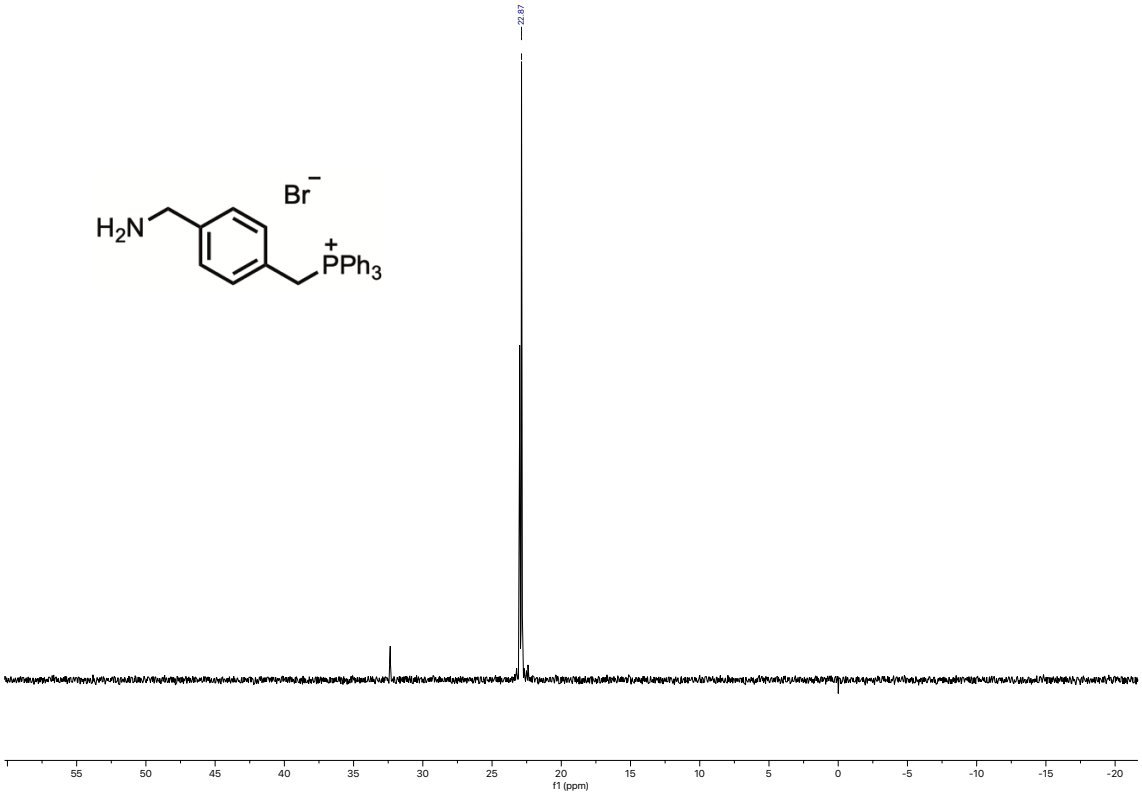


Figure 202. ^{31}P NMR of **4**9 in MeOD-d$_4$

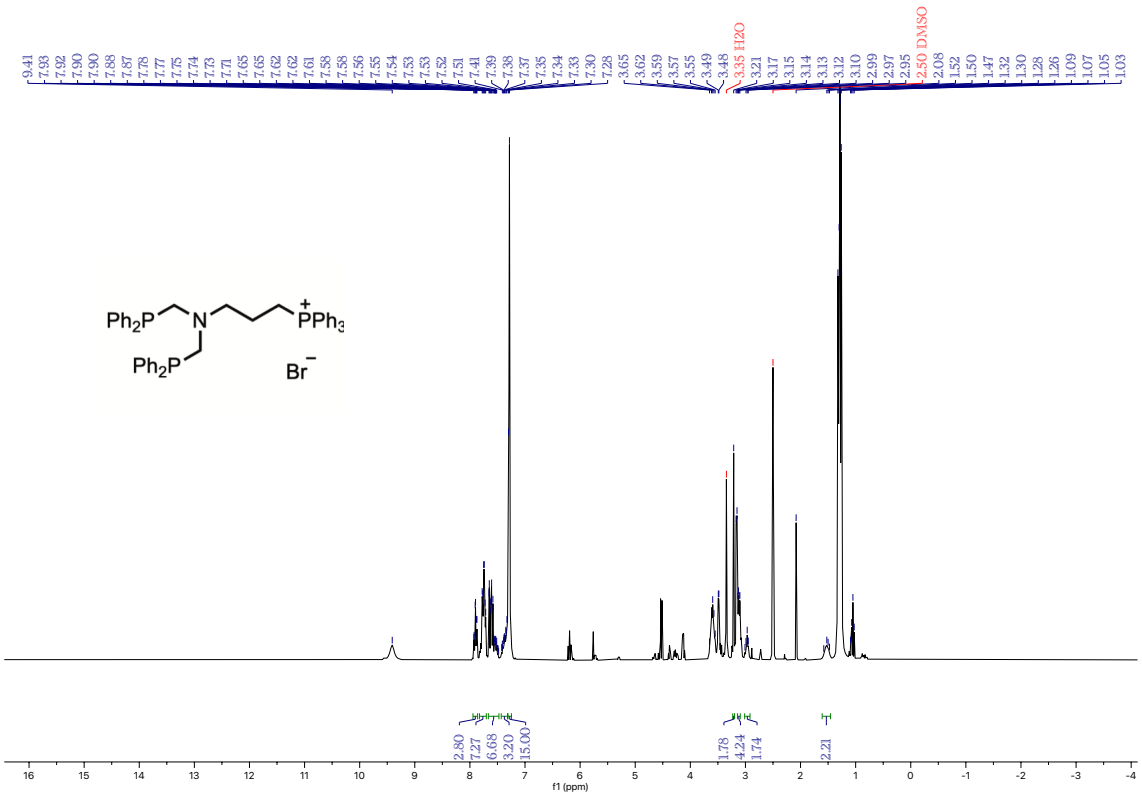


Figure 203. ^{1}H NMR of **50** in DMSO-d_6.

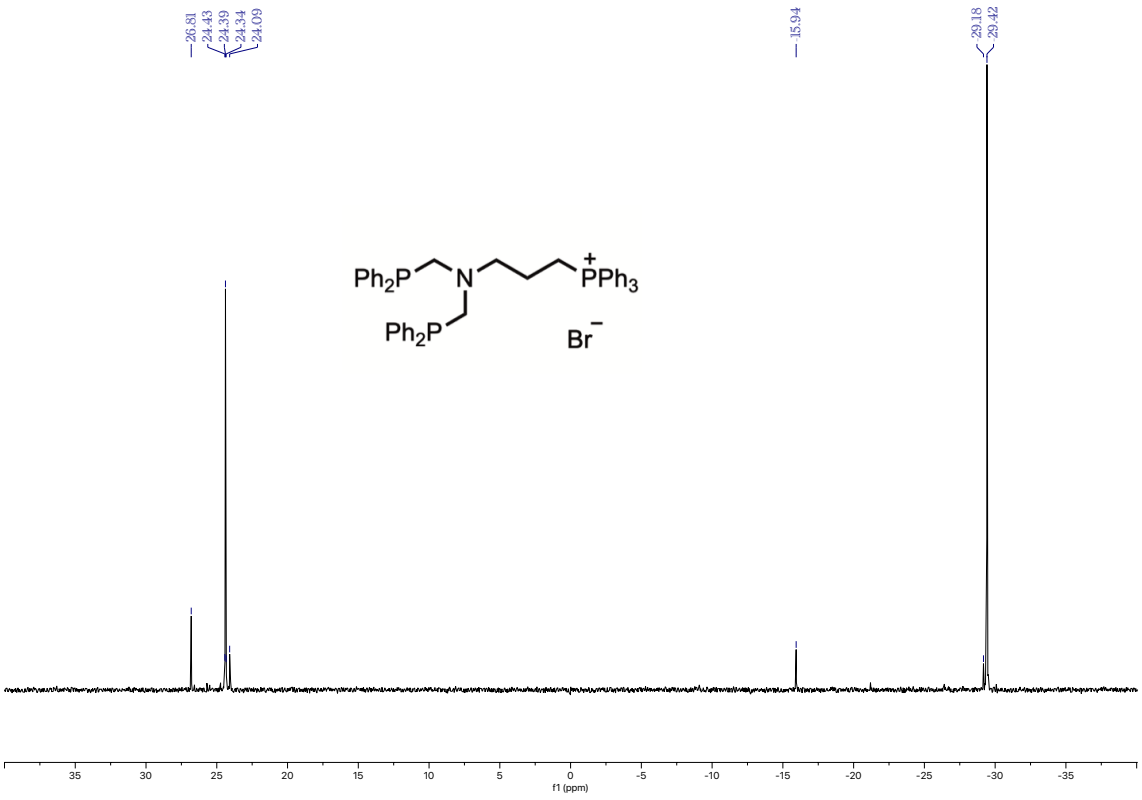


Figure 204. ^{31}P NMR of **50** in DMSO-d_6.

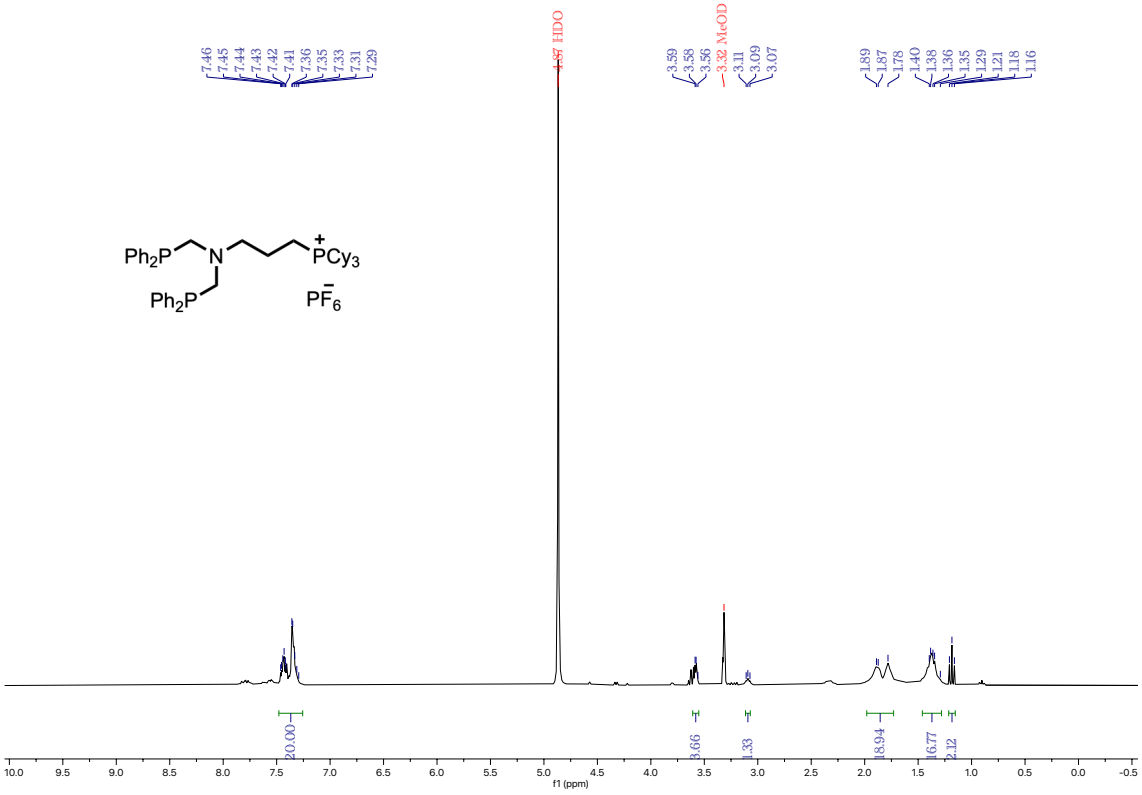


Figure 205. ^{1}H NMR of **51** in MeOD-d$_4$.

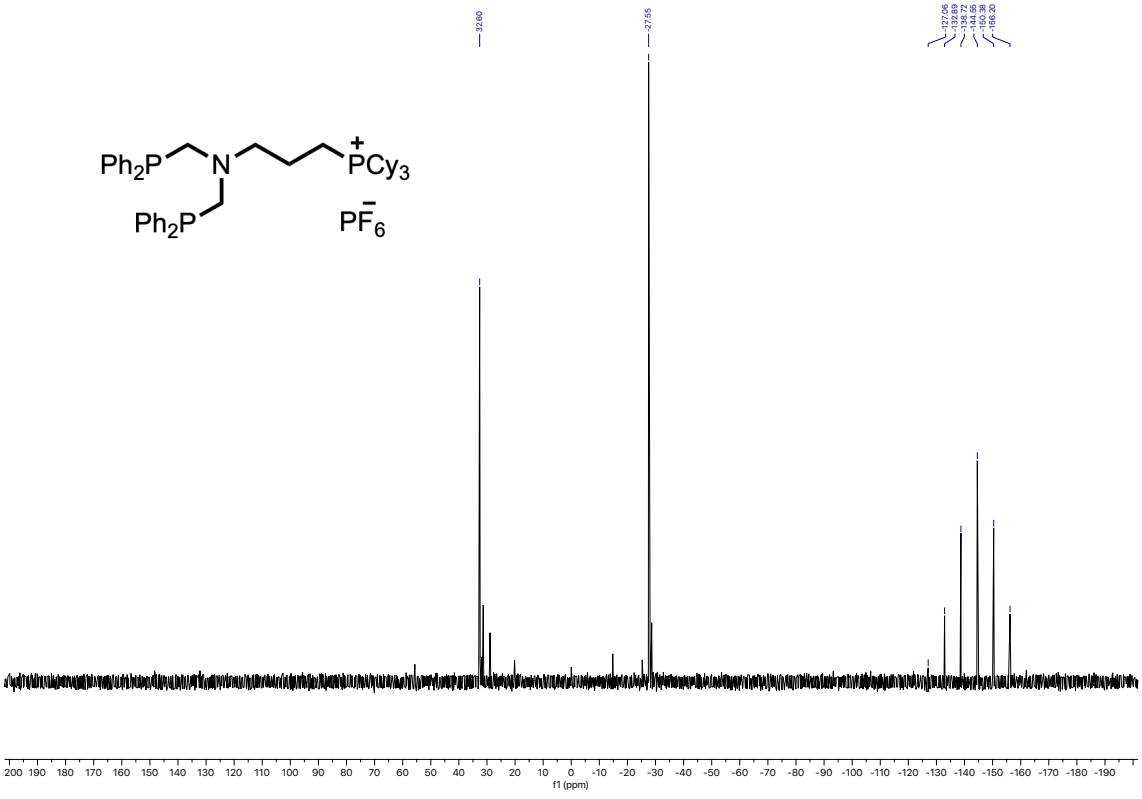


Figure 206. ^{31}P NMR of 51 in MeOD-d$_4$.

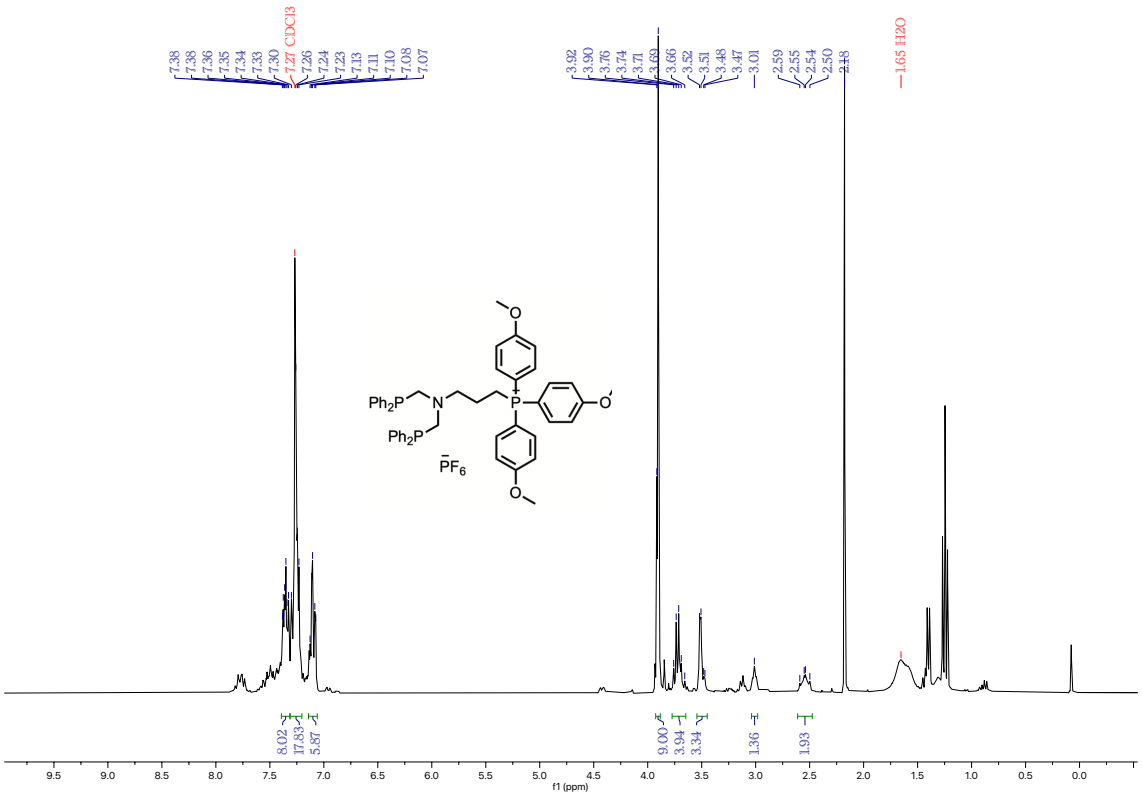


Figure 207. ^{1}H NMR of **52** in $CDCl_3$.

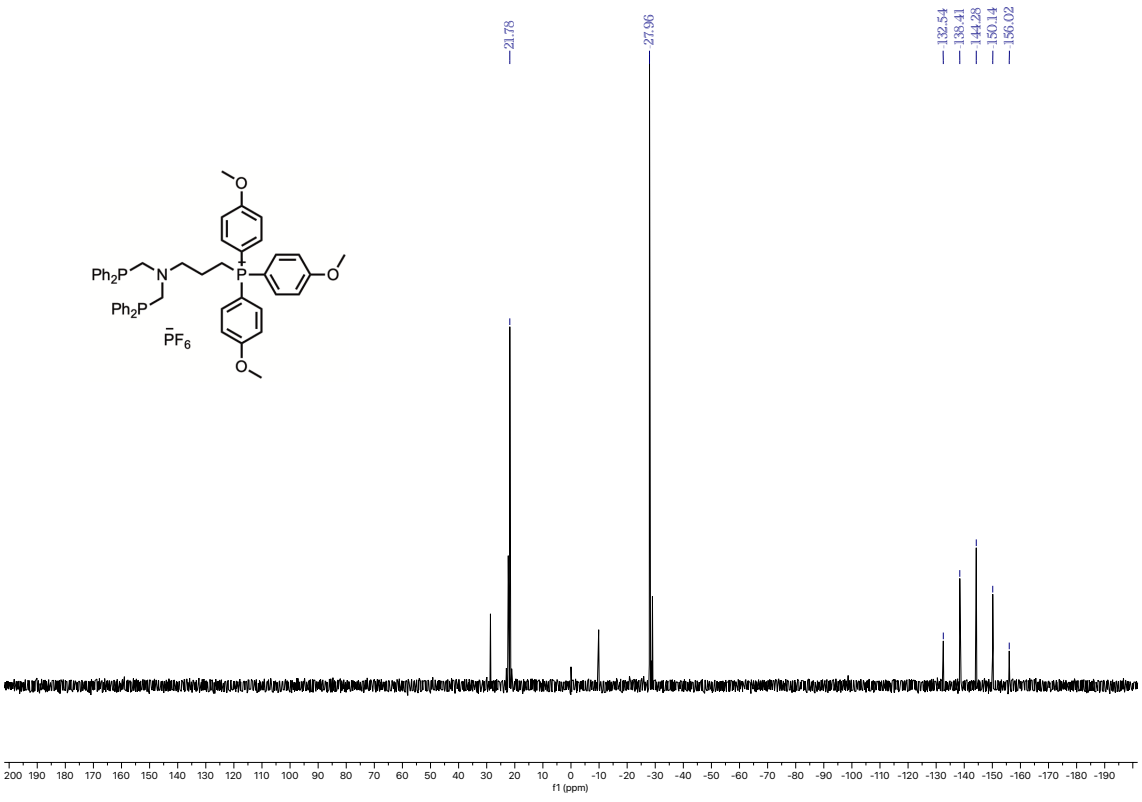


Figure 208. ^{31}P NMR of **52** in $CDCl_3$.

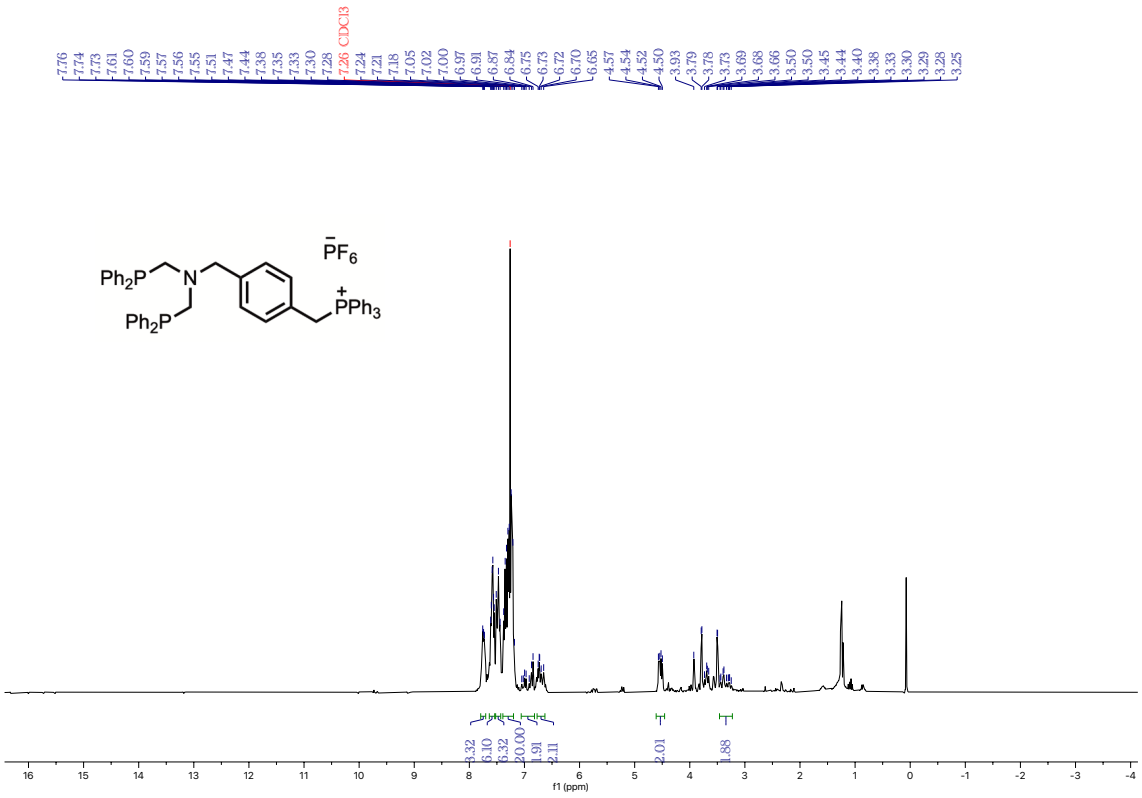


Figure 209. ^{1}H NMR of **53** in $CDCl_3$.

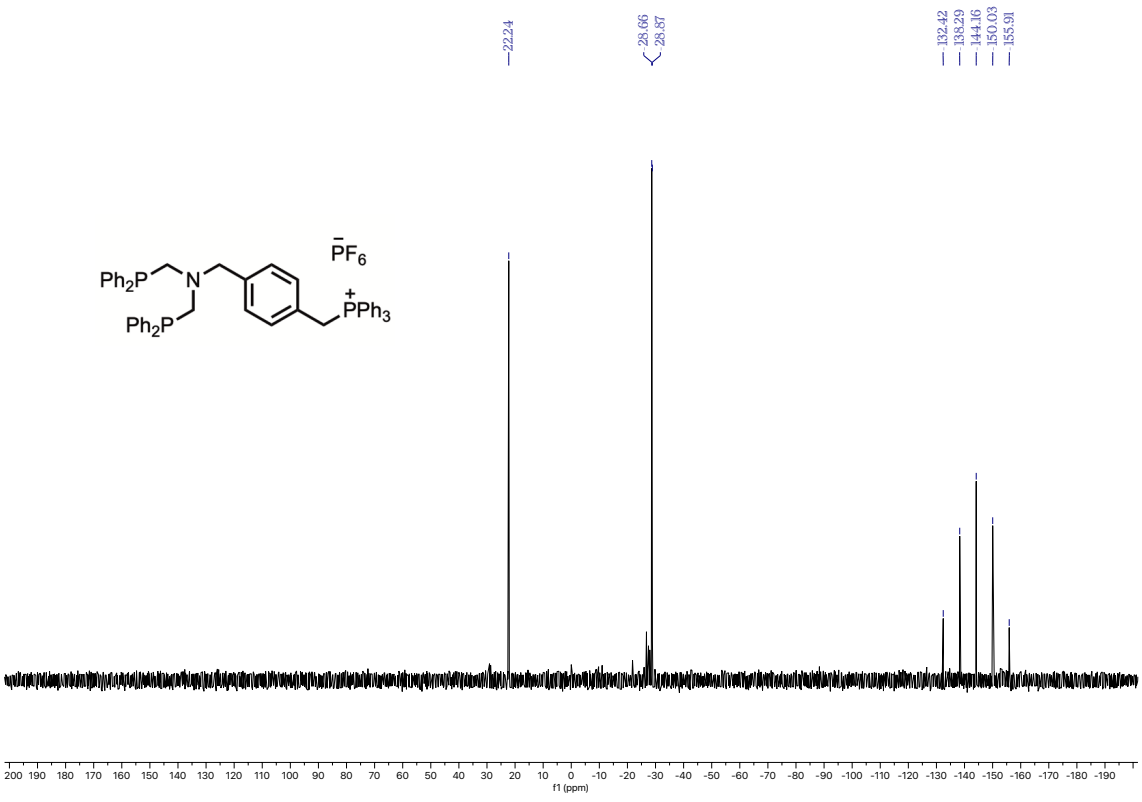


Figure 210. ^{31}P NMR of **53** in $CDCl_3$.

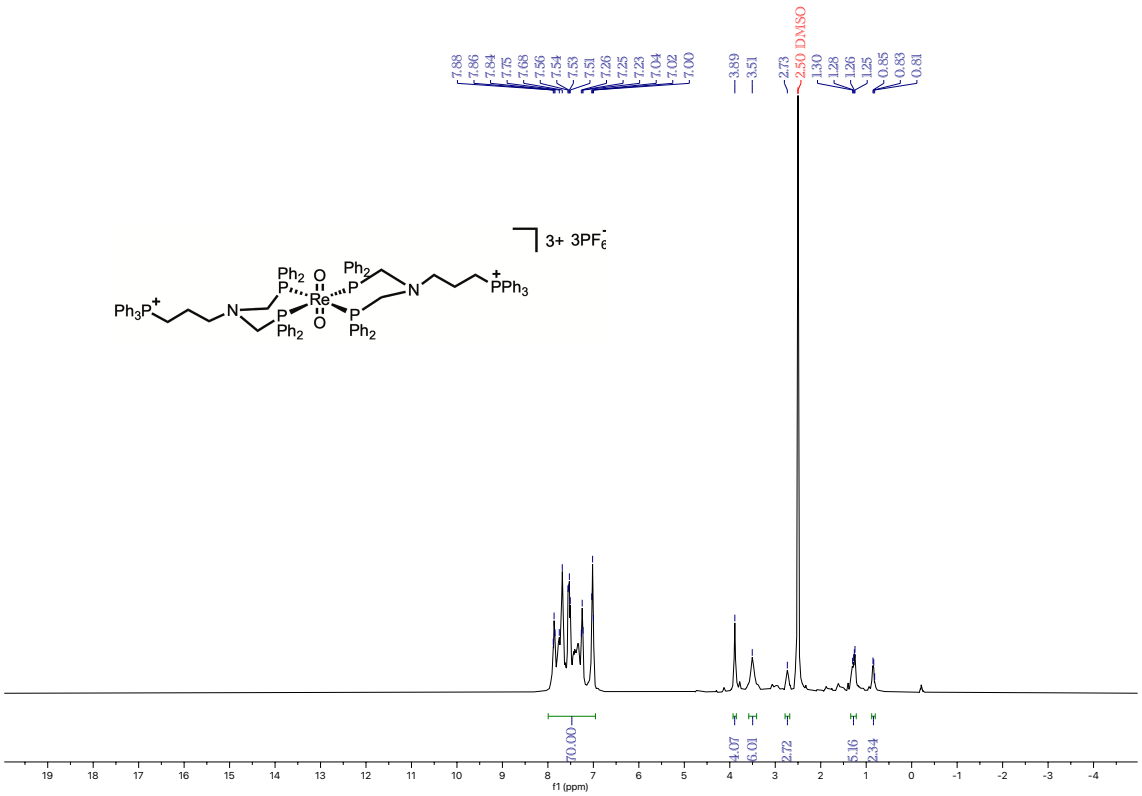


Figure 211. ^{1}H NMR of **Re34** in DMSO-d_6.

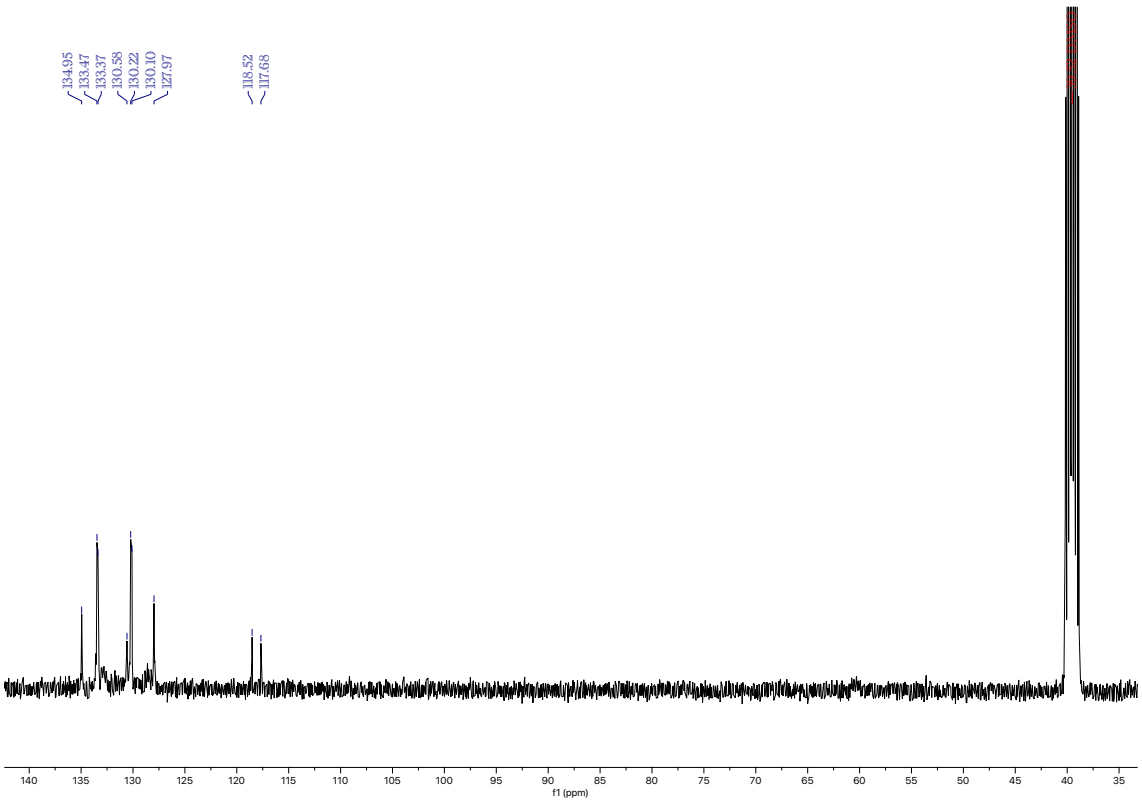


Figure 212. ^{13}C NMR of Re34 in DMSO-d_6.

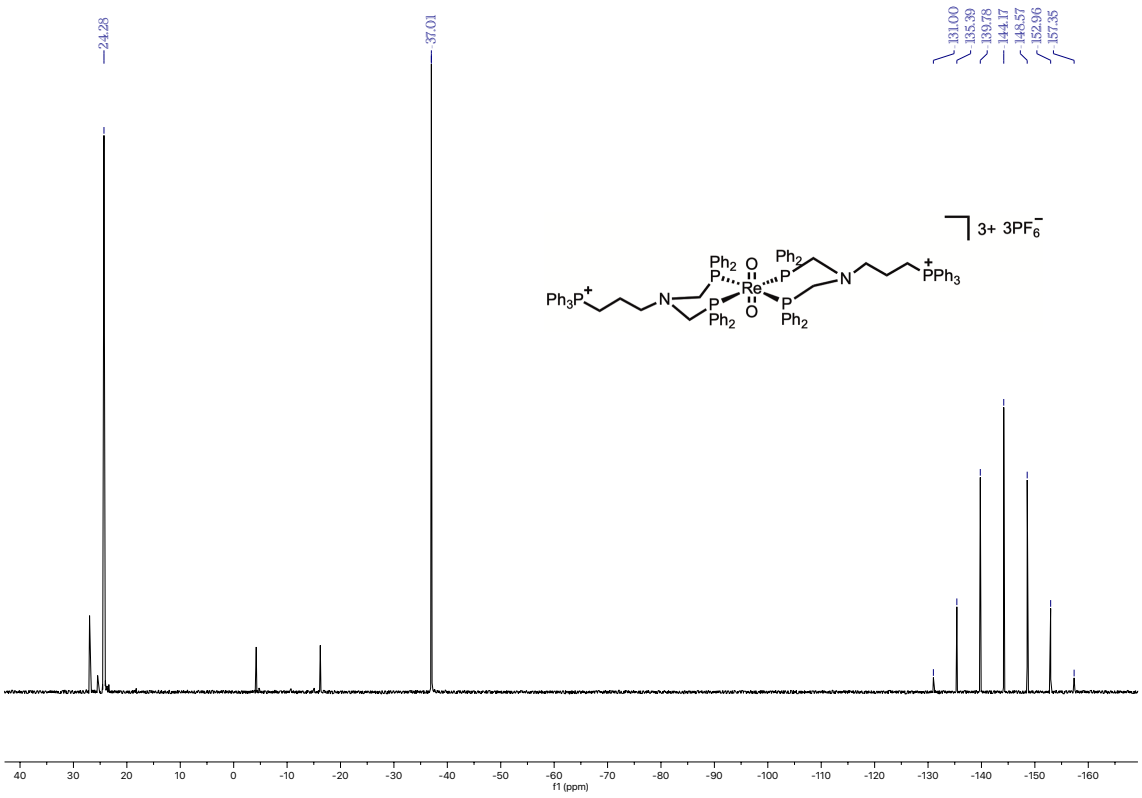


Figure 213. ^{31}P NMR of **Re34** in DMSO-d_6.

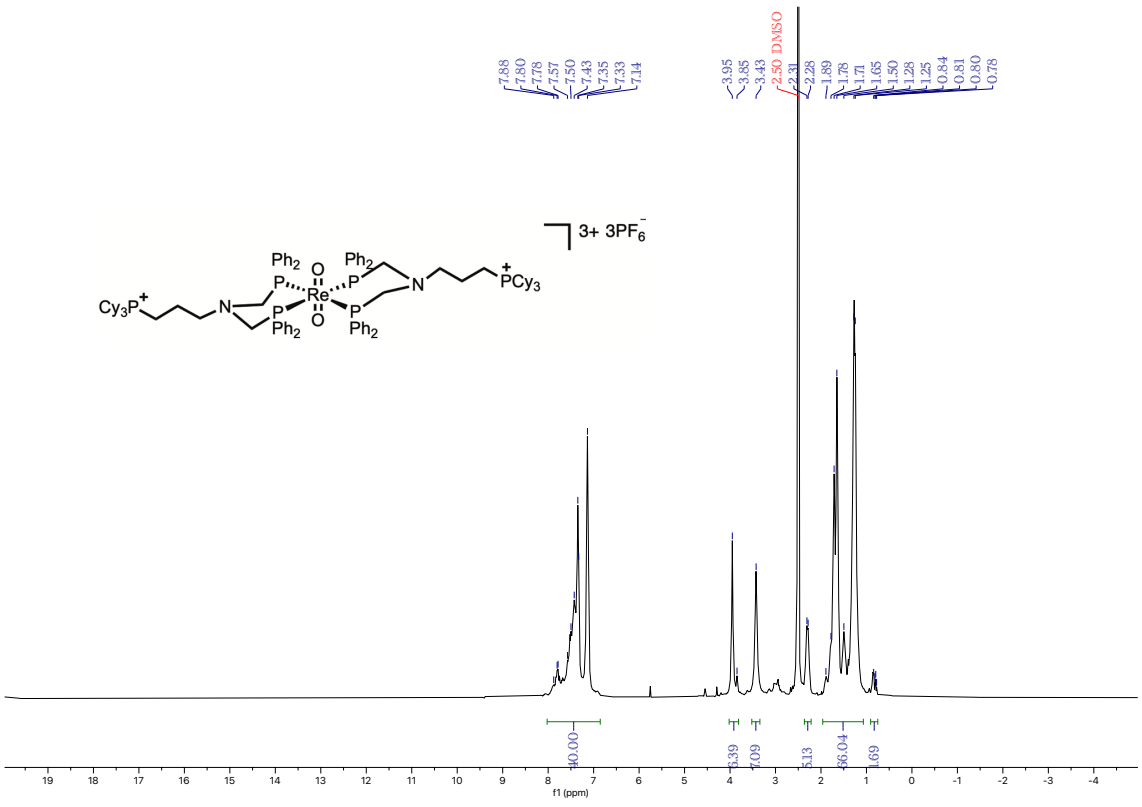


Figure 214. ^{1}H NMR of **Re35** in DMSO-d_6.

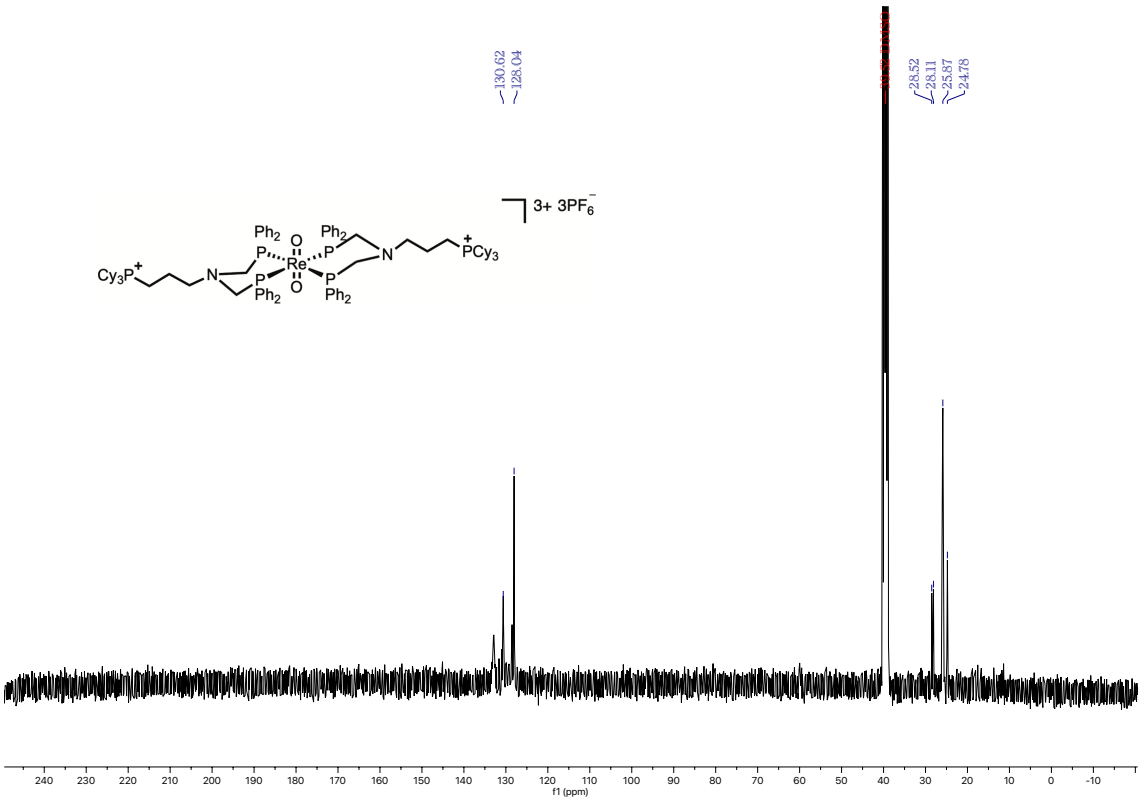


Figure 215. ^{13}C NMR of **Re35** in DMSO-d$_6$.

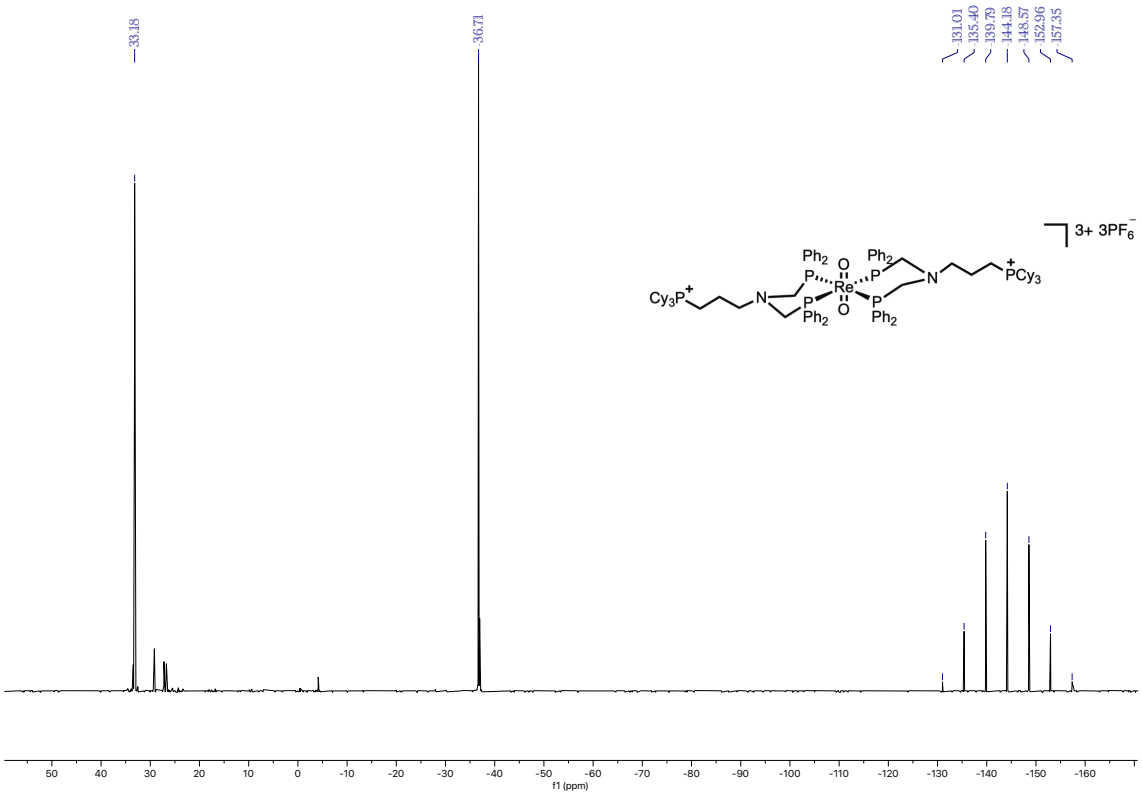


Figure 216. ^{31}P NMR of **Re35** in DMSO-d$_6$.

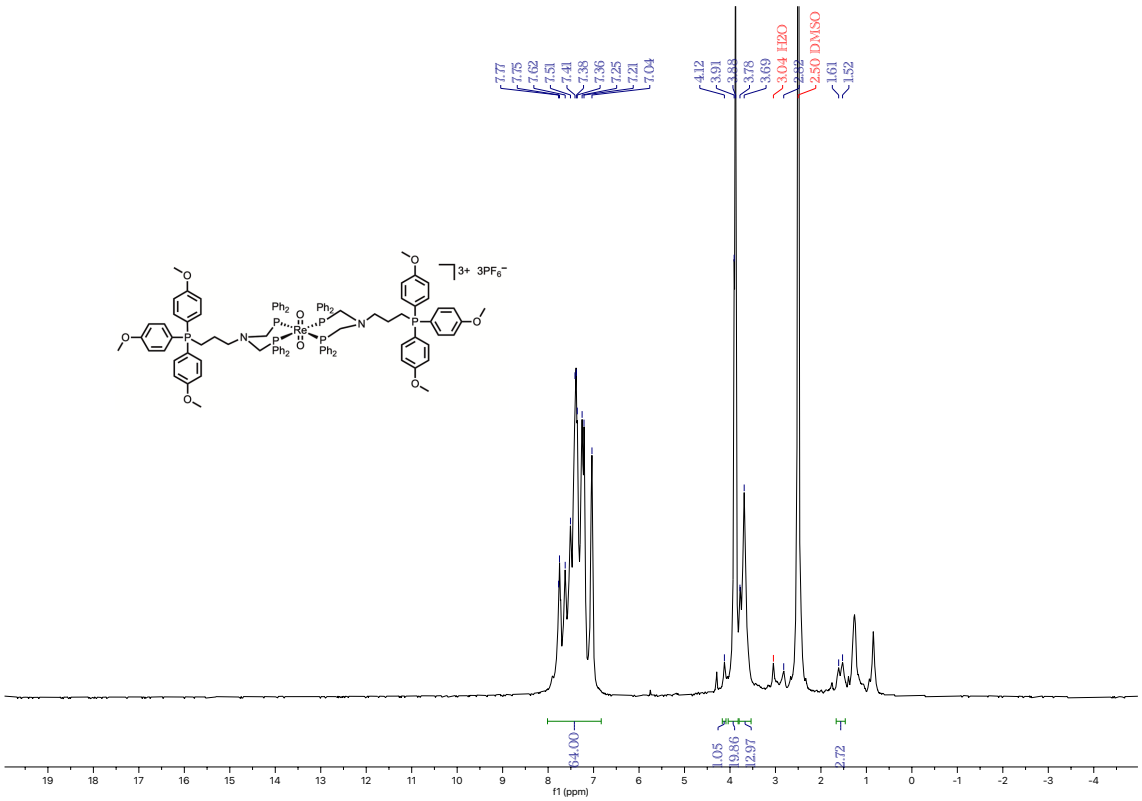


Figure 217. ^{1}H NMR of **Re36** in DMSO-d$_6$.

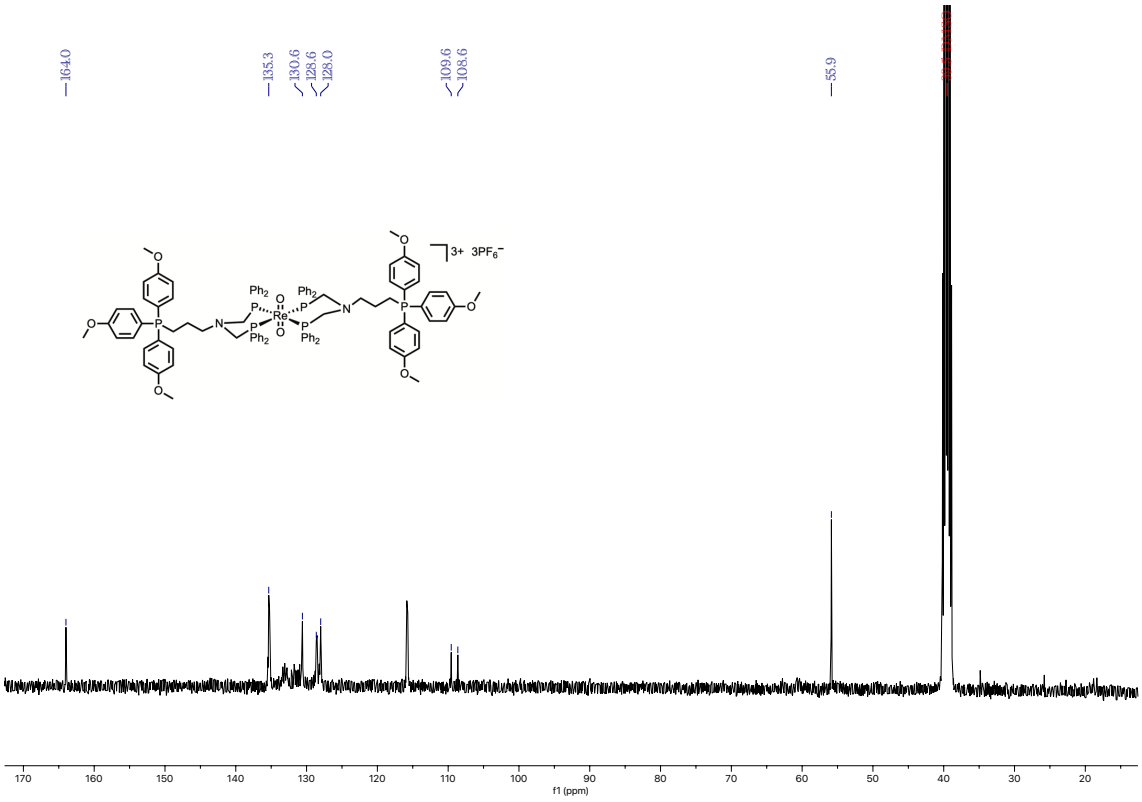


Figure 218. ^{13}C NMR of **Re36** in DMSO-d$_6$.

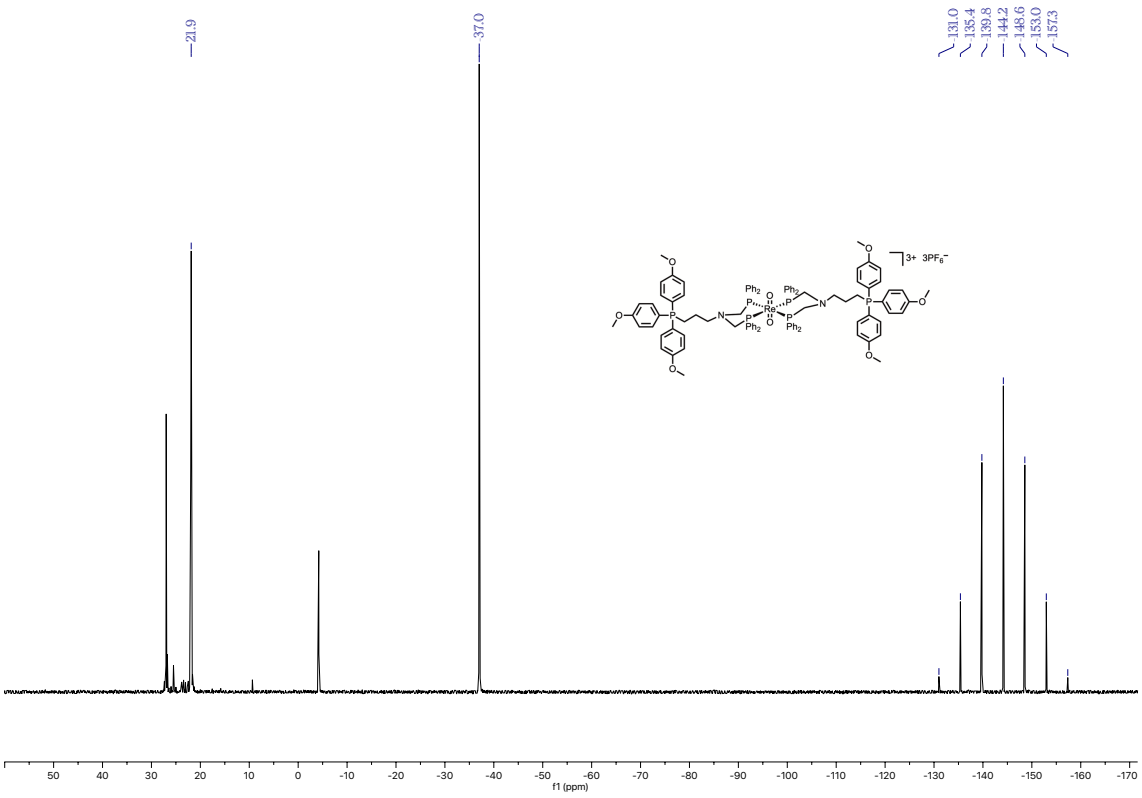


Figure 219. ^{31}P NMR of **Re36** in DMSO-d$_6$.

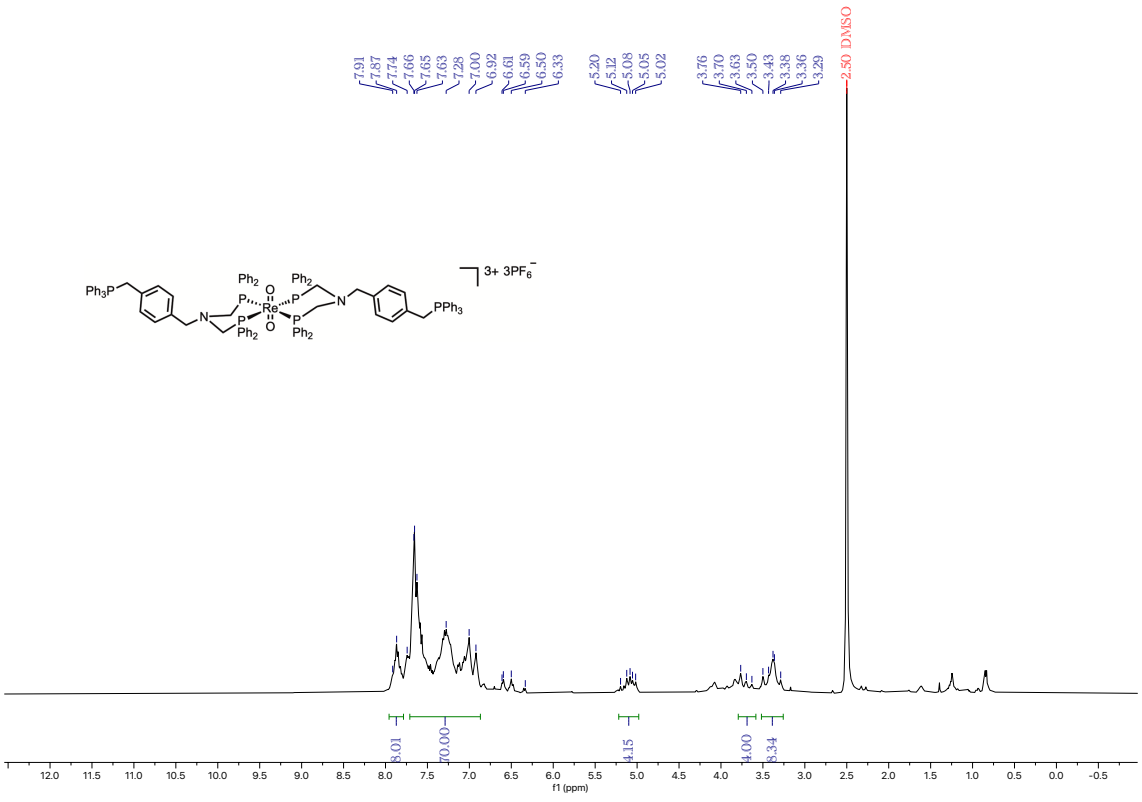


Figure 220. ^{1}H NMR of **Re37** in DMSO-d$_6$.

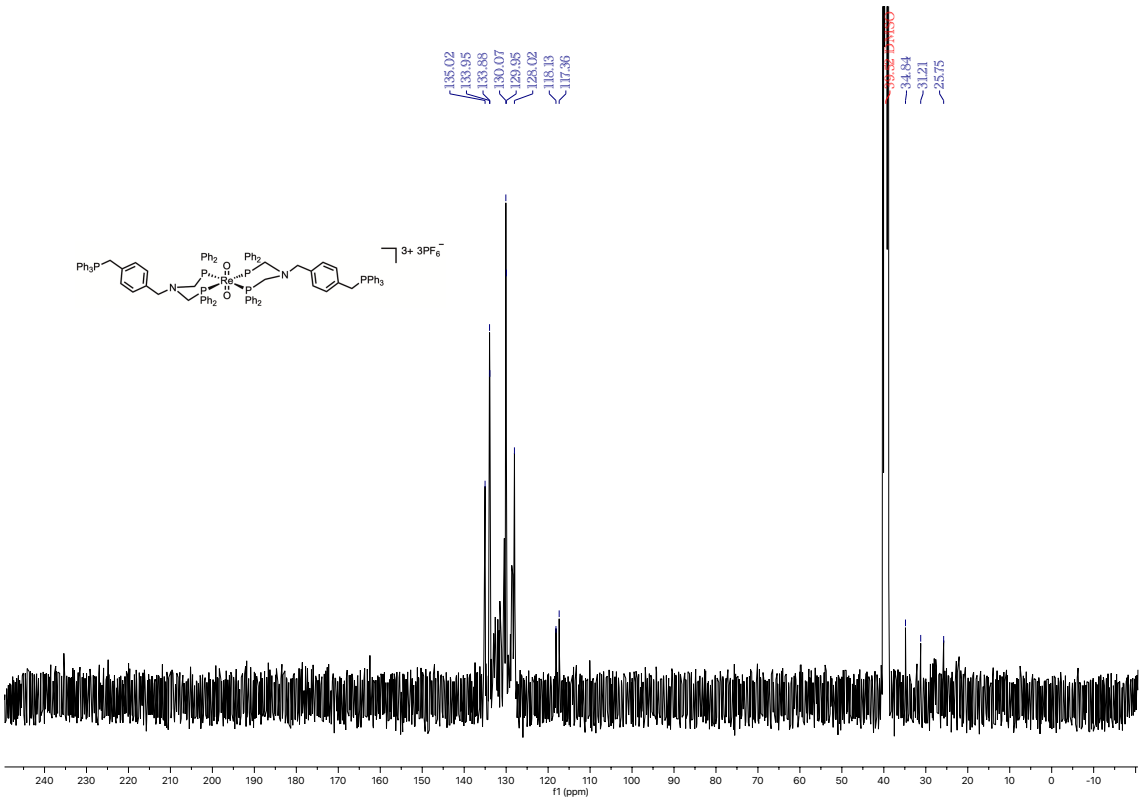


Figure 221. ^{13}C NMR of **Re37** in DMSO-d_6.

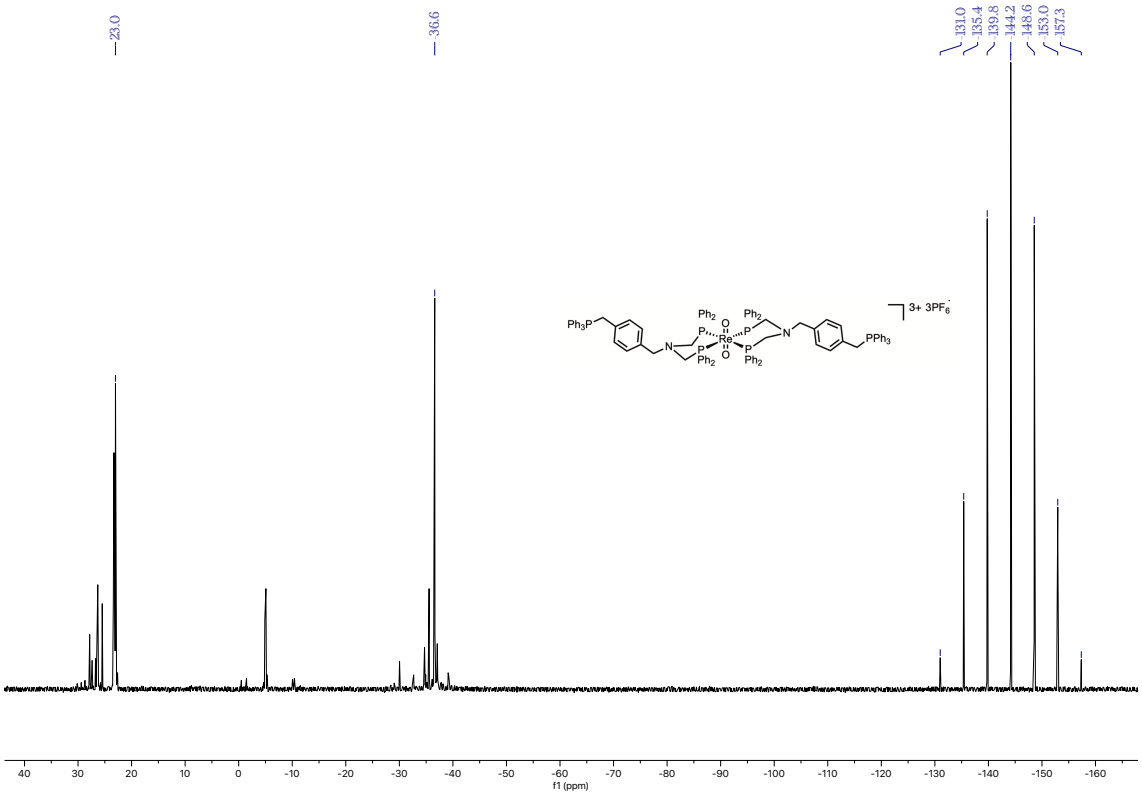


Figure 222. ^{31}P NMR of **Re37** in DMSO-d_6.

7.2 Mass spectra

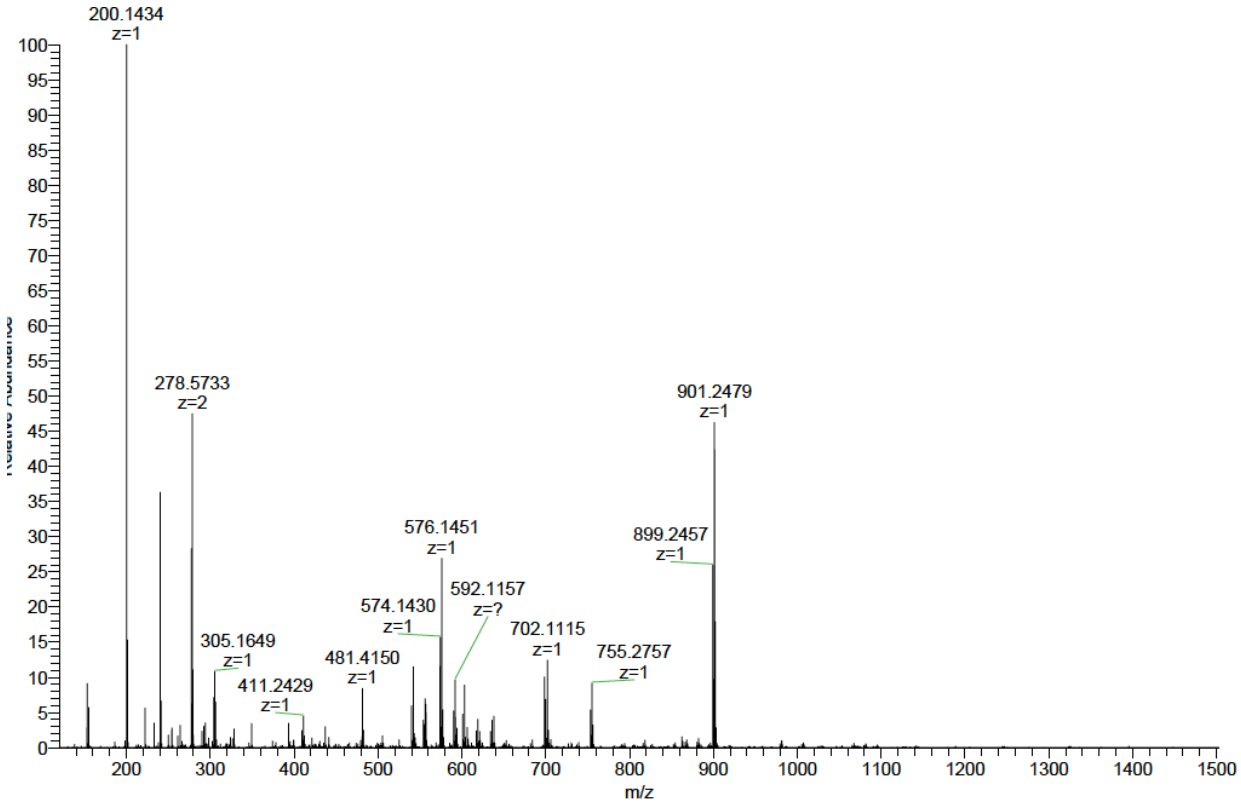


Figure 223. HRMS spectrum of **24** m/z calculated for $C_{14}H_{18}O^+$ 200.1434: found 200.1434 $[M+H]^+$. $[M+H]^+$.

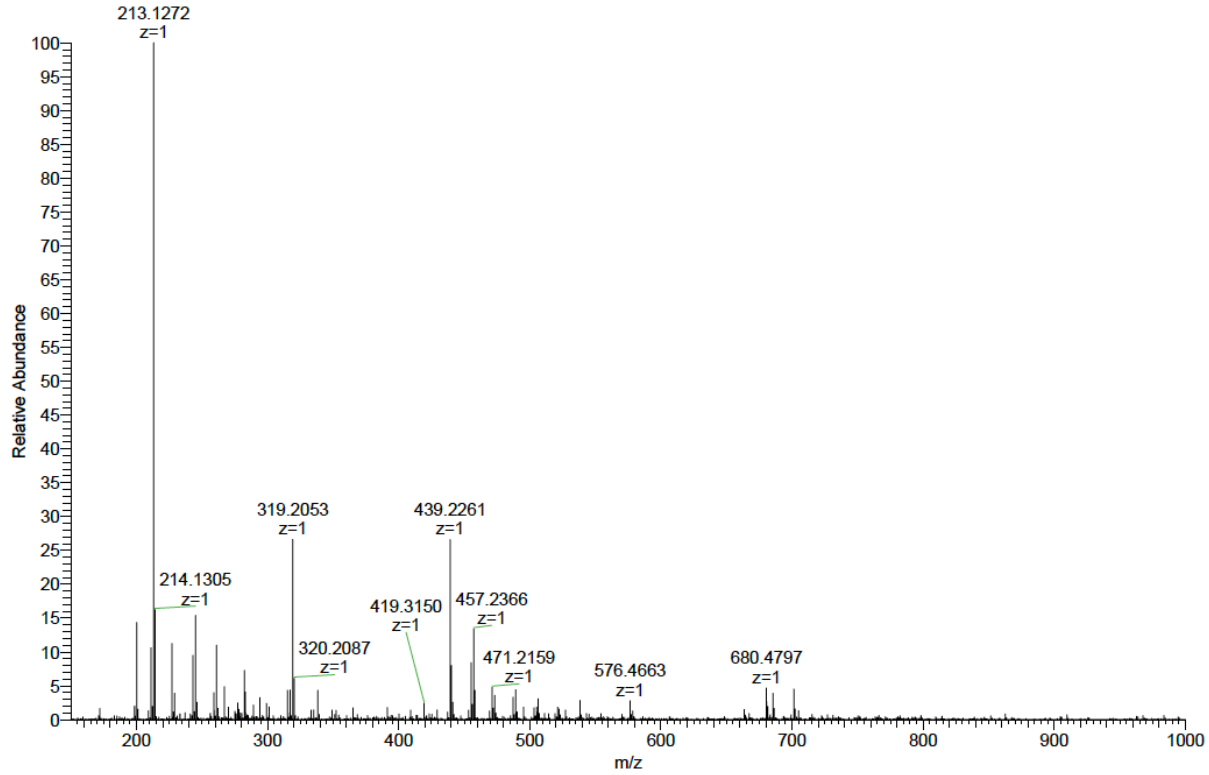


Figure 224. HRMS spectrum of **25**. m/z calculated for $C_{15}H_{17}O^+$ 213.1279: found 213.1272 $[M+H]^+$.

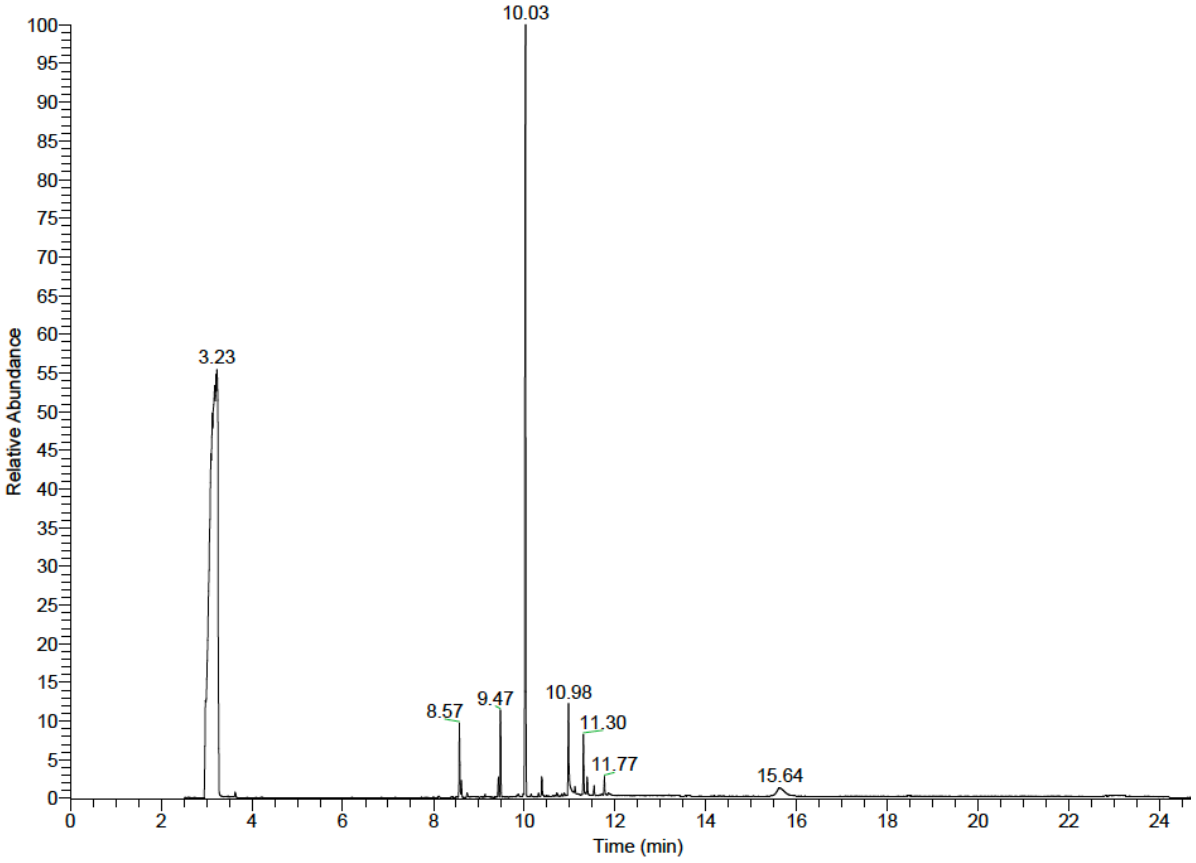


Figure 225. HRGCMS chromatogram of **26**. HRGCMS: t_R: 10.03 min.

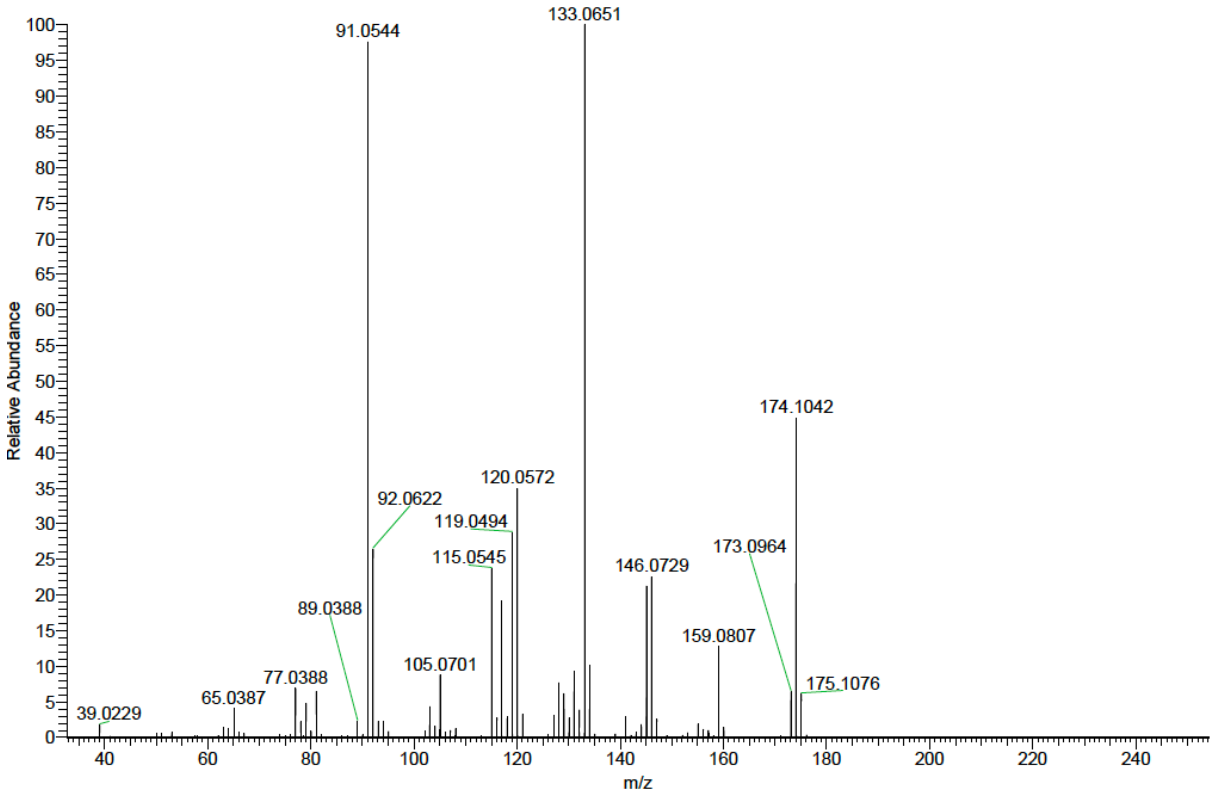


Figure 226. HRGCMS spectrum of **26**. m/z calculated for $C_{12}H_{14}O$ 174.1045; found 174.1042 [M].

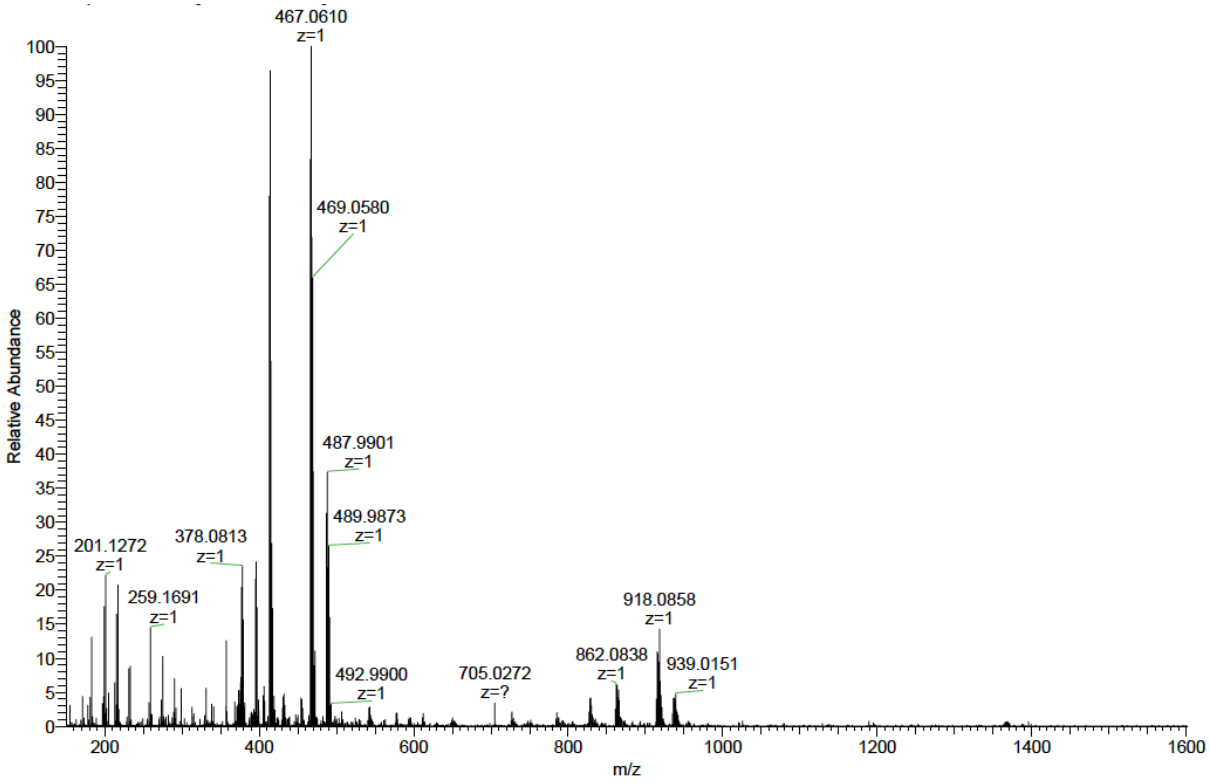


Figure 227. HRMS spectrum of **Pt2**. m/z calculated for $C_{14}H_{20}Cl_2NPt^+$ 467.0615: found 467.0610 $[M+NH_4]^+$.

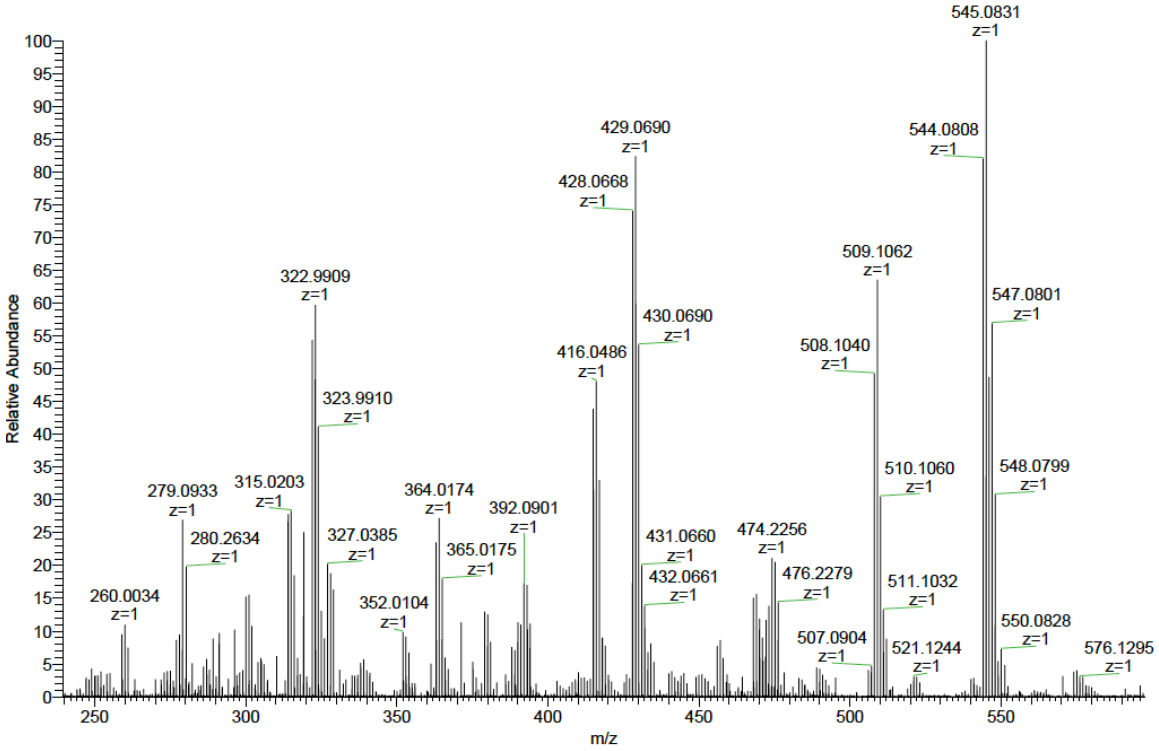


Figure 228. HRMS spectrum of **Pt3**. m/z calculated for $C_{14}H_{17}ClNPt^{+}$ 429.0697: found 429.0690 $[M\text{-}Cl]^{+}$.

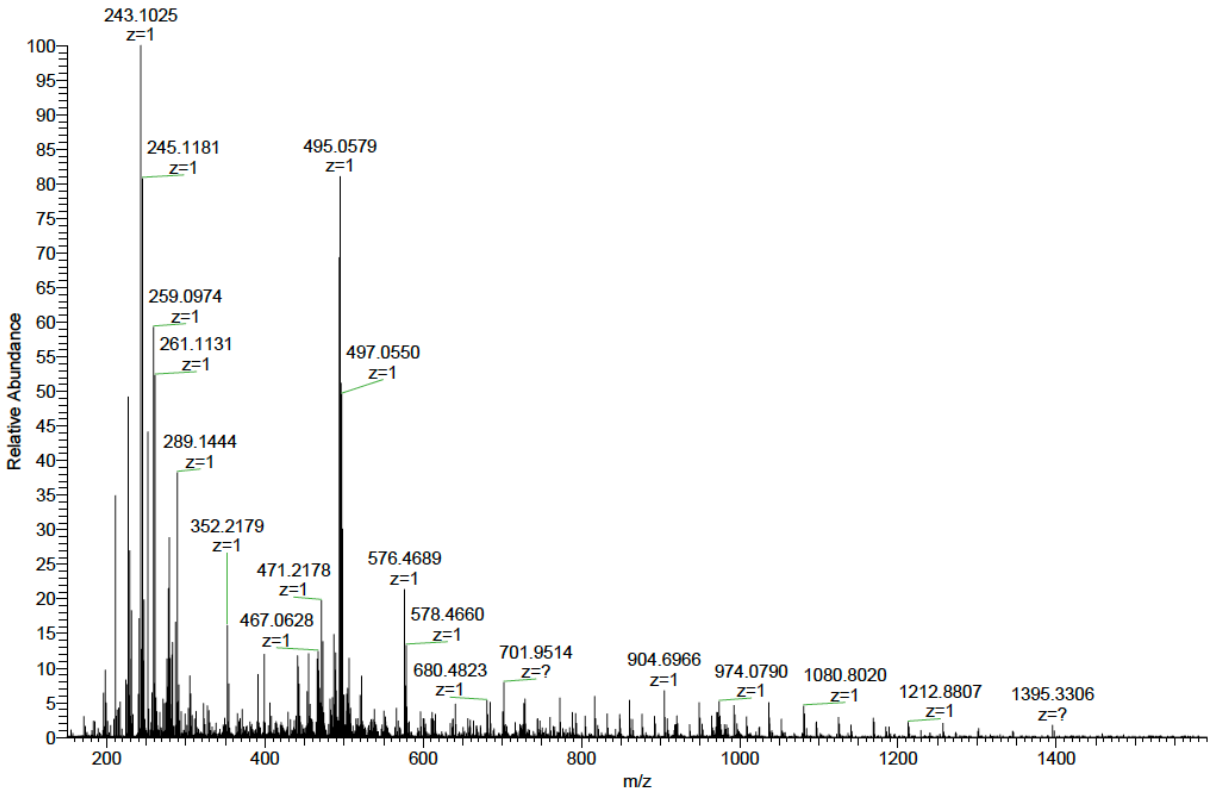


Figure 229. HRMS spectrum of **Pt4**. m/z calculated for $C_{15}H_{20}Cl_2NOPt^+$ 495.0564: found 495.0579 $[M+NH_4]^+$.

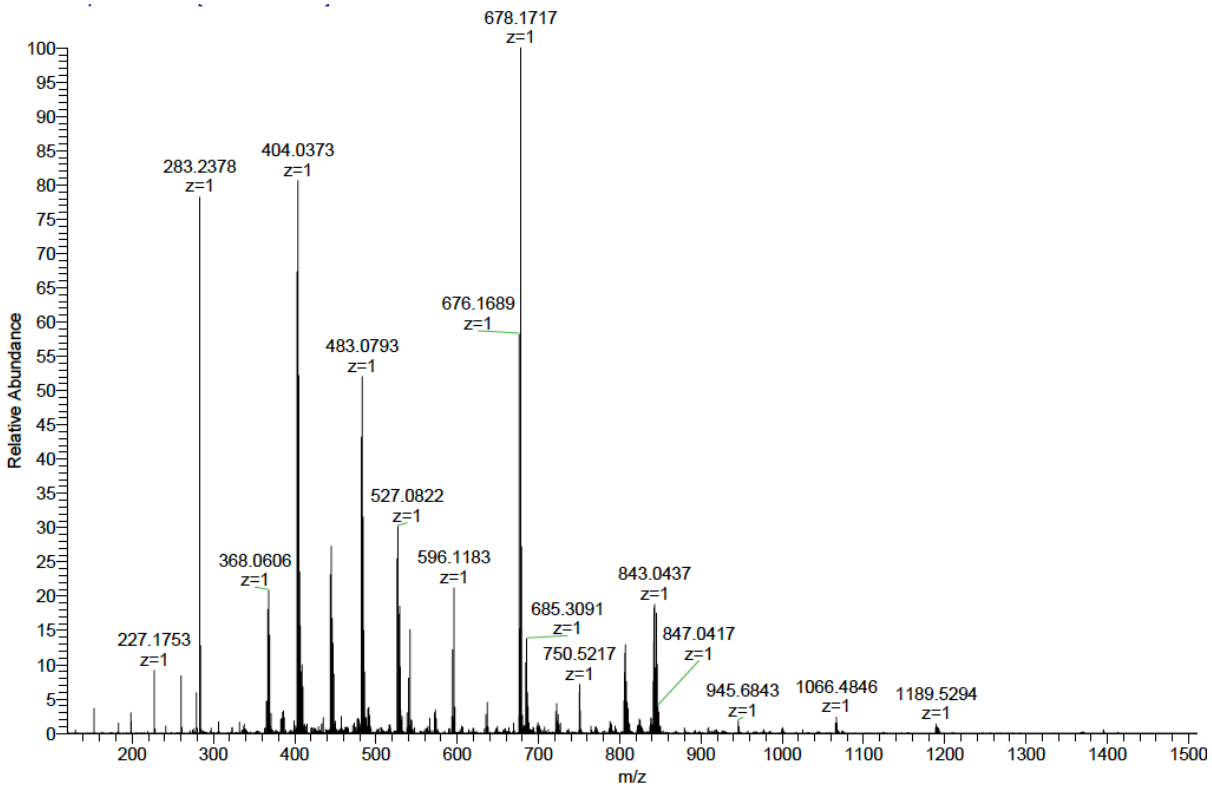


Figure 230. HRMS spectrum of **Pt5.** HRMS (ES+): m/z calculated for $C_{12}H_{14}ClOPt^+$ 404.0381: found 404.0373 $[M\text{-}Cl]^+$.

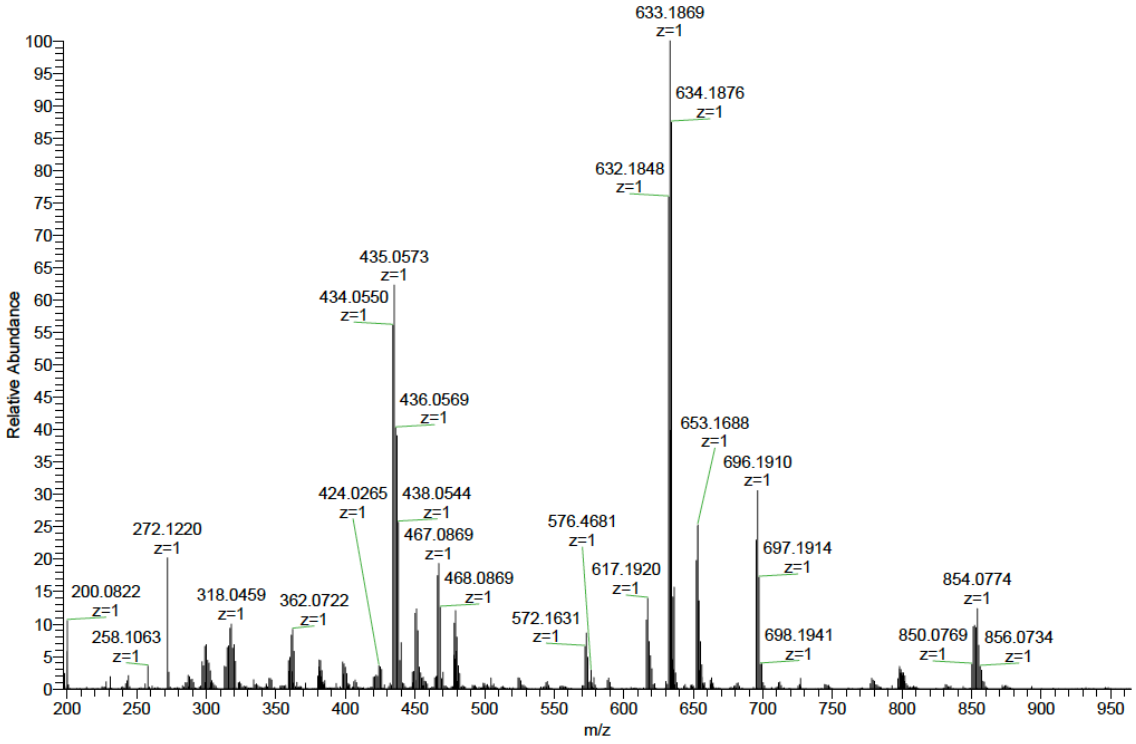


Figure 231. HRMS spectrum of **Pt6**. m/z calculated for $C_{10}H_{20}Cl_2NOPt^+$ 435.0570: found 435.0573 $[M+NH_4]^+$.

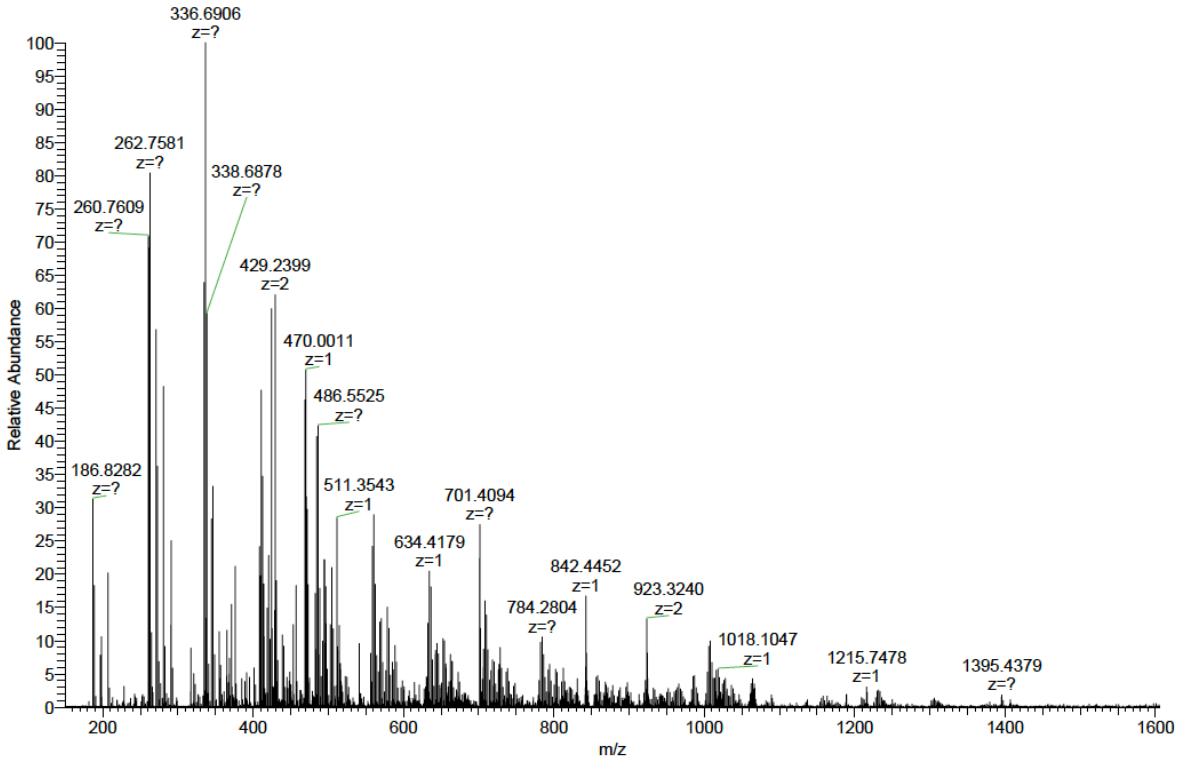


Figure 232. HRMS spectrum of **Pt7**. m/z calculated for $C_{11}H_{18}Cl_2KOPt^+$ 470.0014: found 470.0011 $[M+K]^+$.

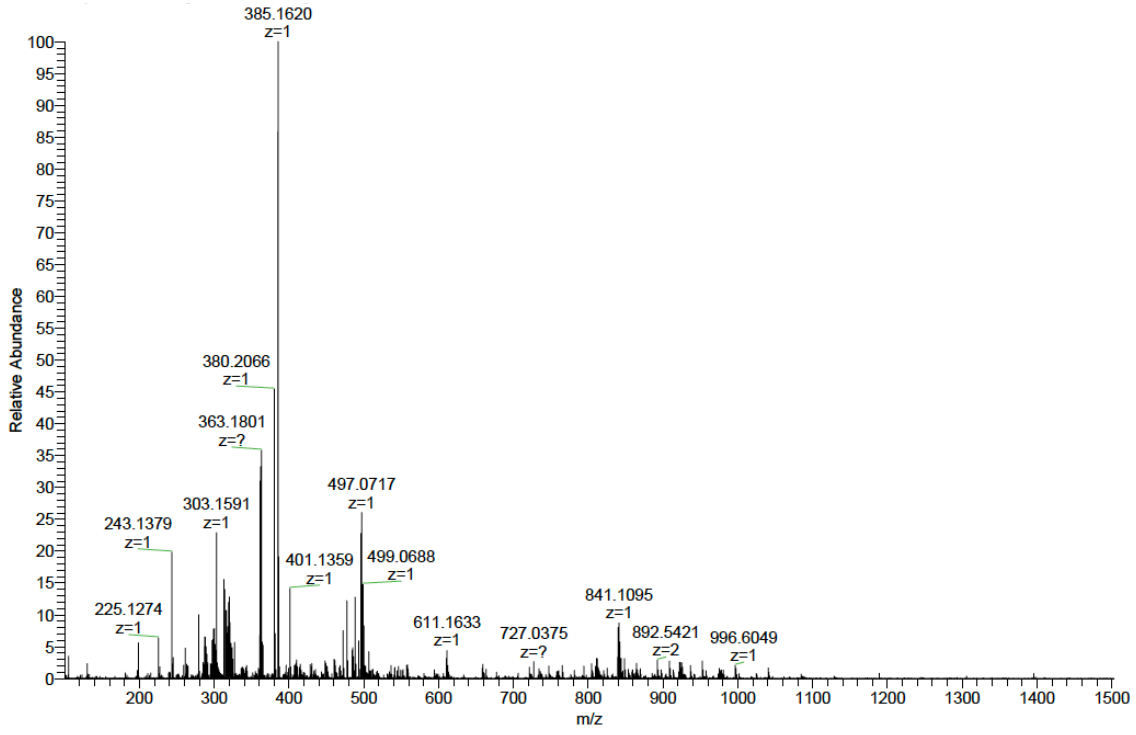


Figure 233. HRMS spectrum of **Pt9**. m/z calculated for $C_{15}H_{22}Cl_2NOPt^+$ 497.0721: found 497.0717 $[M+NH_4]^+$.

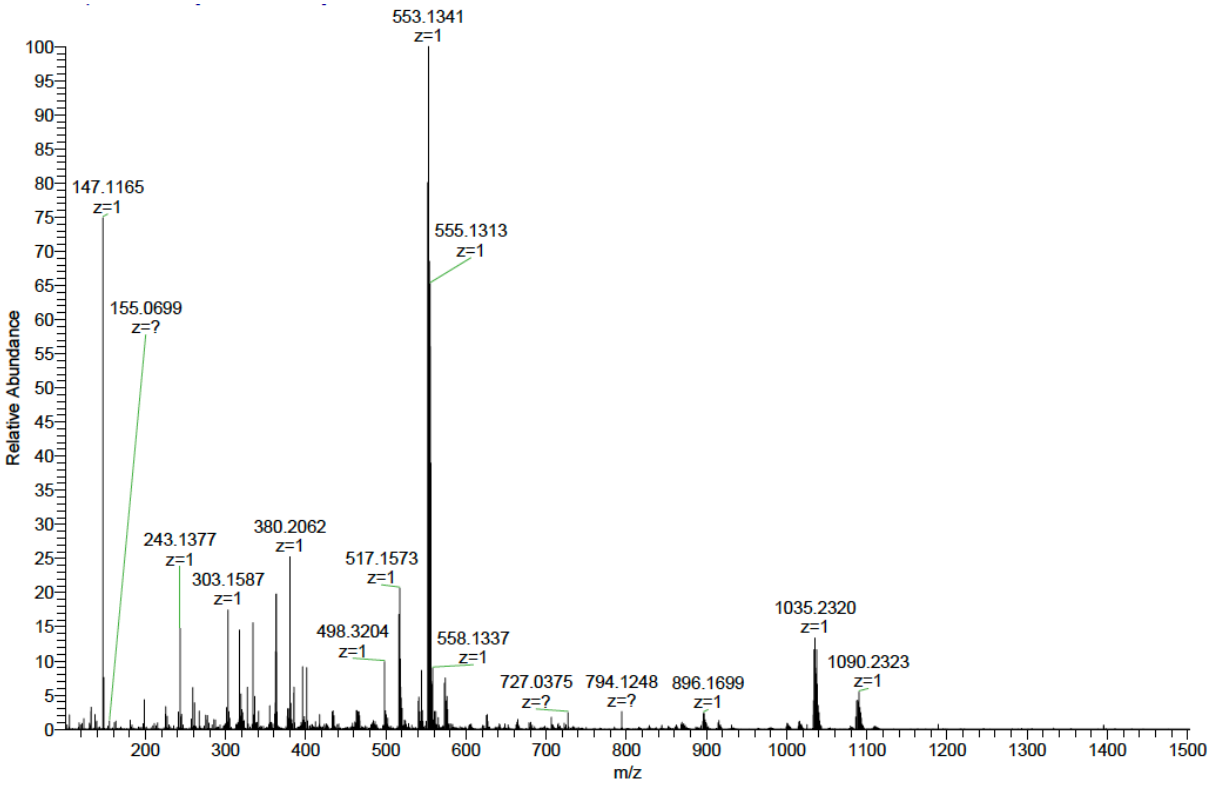


Figure 234. HRMS spectrum of **Pt10**. m/z calculated for $C_{19}H_{30}Cl_2NOPt^+$ 553.1347: found 553.1341 $[M+NH_4]^+$.

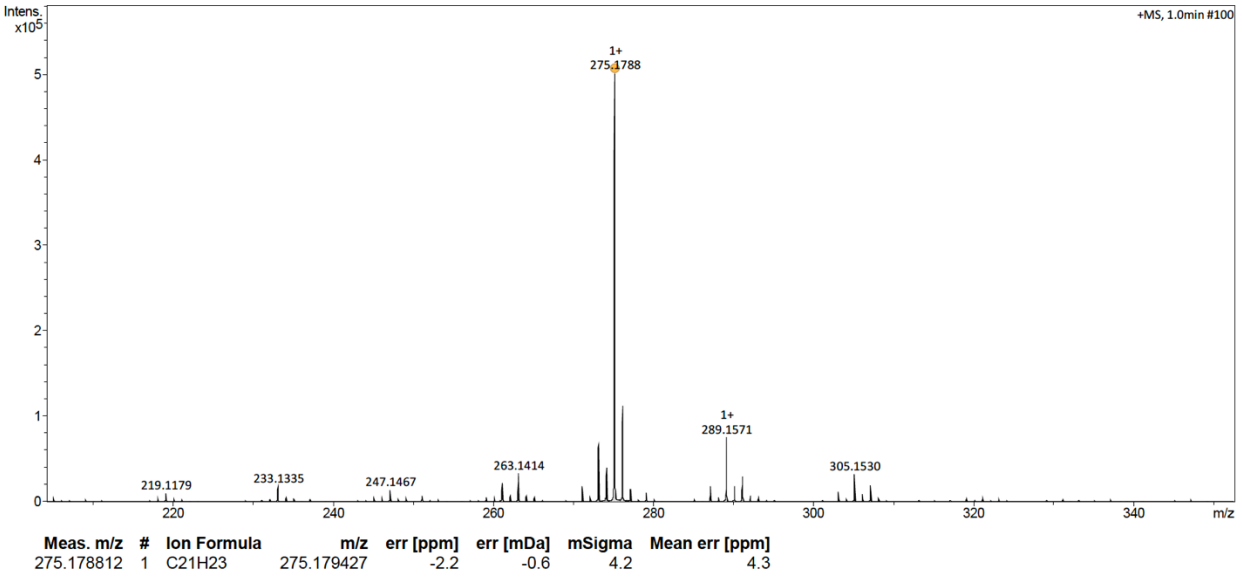
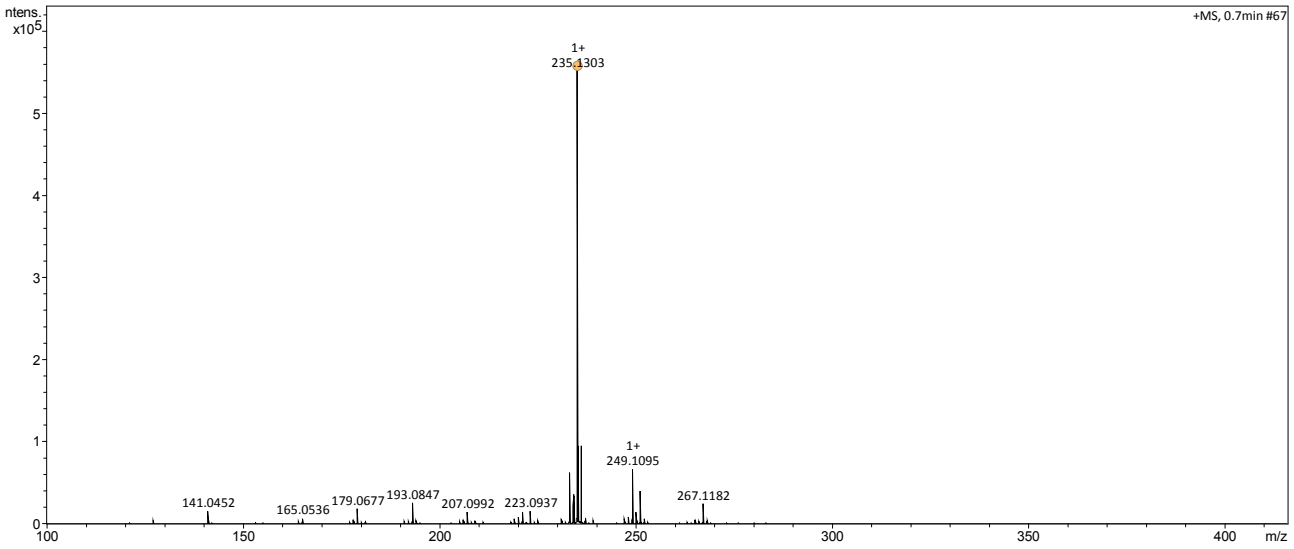
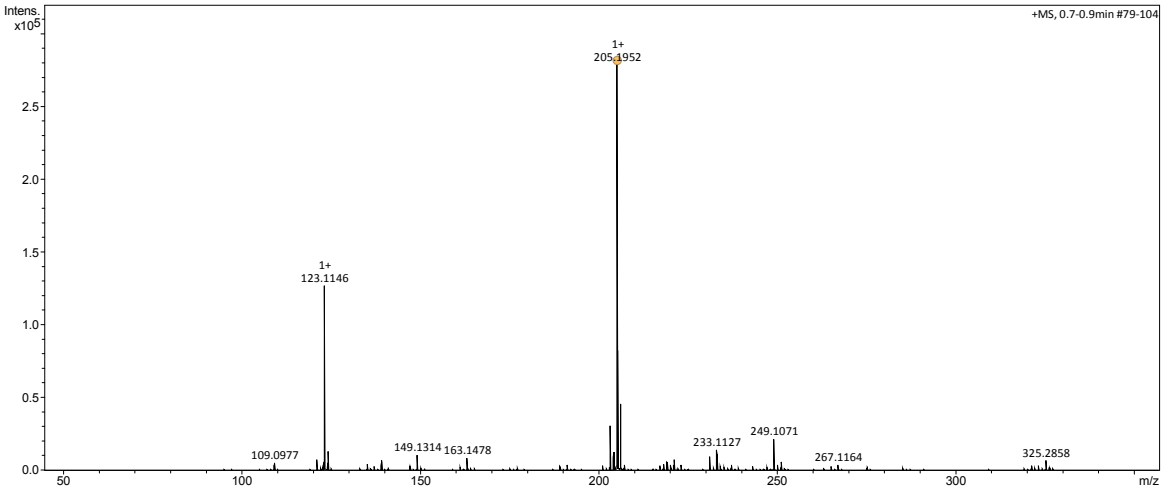


Figure 235. HRMS spectrum of Cp2.



Meas. m/z	#	Ion Formula	m/z	err [ppm]	err [mDa]	mSigma	Mean err [ppm]
235.130282	1	C15H17F2	235.129283	-4.2	-1.0	5.1	-3.2

Figure 236. HRMS spectrum of Cp3.



Meas. m/z	#	Ion Formula	m/z	err [ppm]	err [mDa]	mSigma	Mean err [ppm]
205.195188	1	C15H25	205.195077	-0.5	-0.1	0.6	0.4

Figure 237. HRMS spectrum of Cp4.

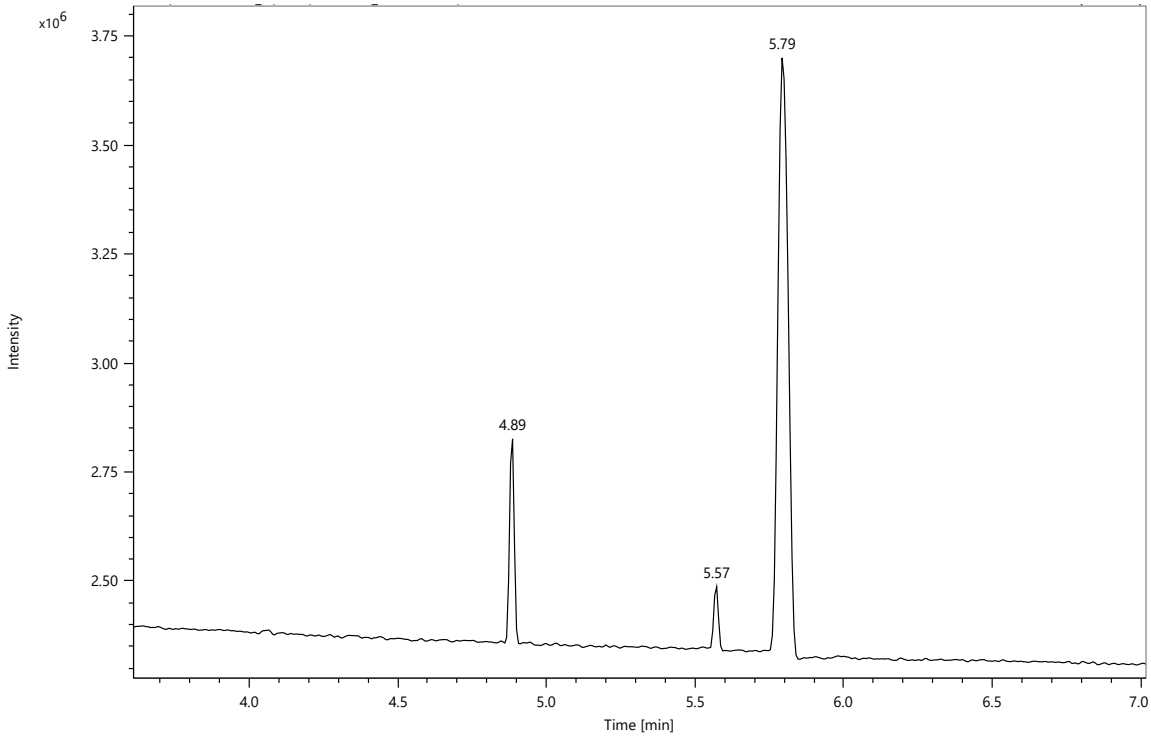
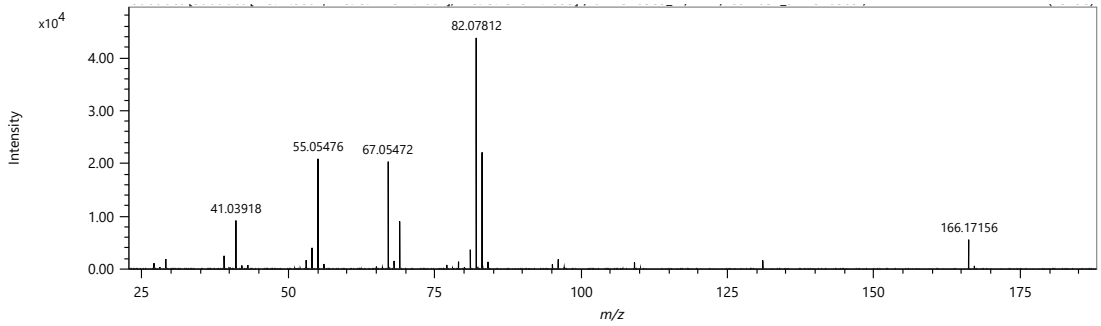


Figure 238. GCMS total ion chromatogram (TIC) of Cp4. Rt: 5.79 min is desired product.



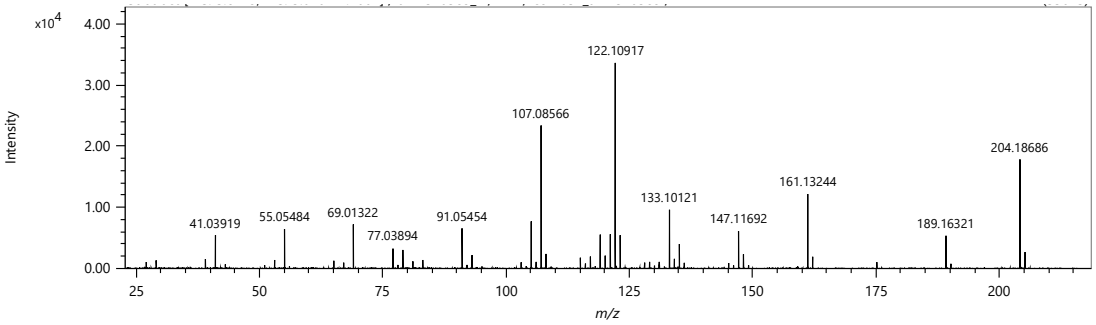
Elemental Composition

Parameters		Elements Set 1:		
Tolerance:	±20.00 ppm	Symbol	C	H
Electron:	Odd/Even	Min	6	7
Charge:	+1	Max	30	30
DBE:	-0.5 - 100.0			

Results

Mass	Intensity	Formula	Calculated Mass	Mass Difference [ppm]	DBE
166.17156	5580.45	C12 H22	166.17160	-0.28	2.0

Figure 239. GCMS fragmentation pattern of Rt: 4.89 min, side product homo-coupled 1,1'-bicyclohexyl.



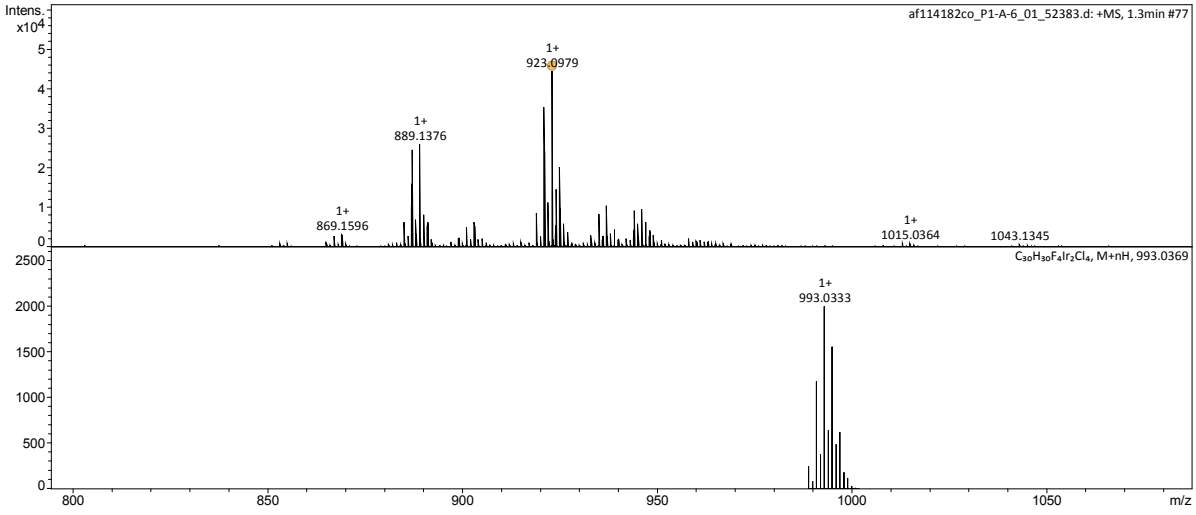
Elemental Composition

Parameters		Elements Set 2:			
Tolerance:	±20.00 ppm	Symbol	C	H	O
Electron:	Odd/Even	Min	6	4	0
Charge:	+1	Max	15	30	2
DBE:	-0.5 - 100.0				

Results

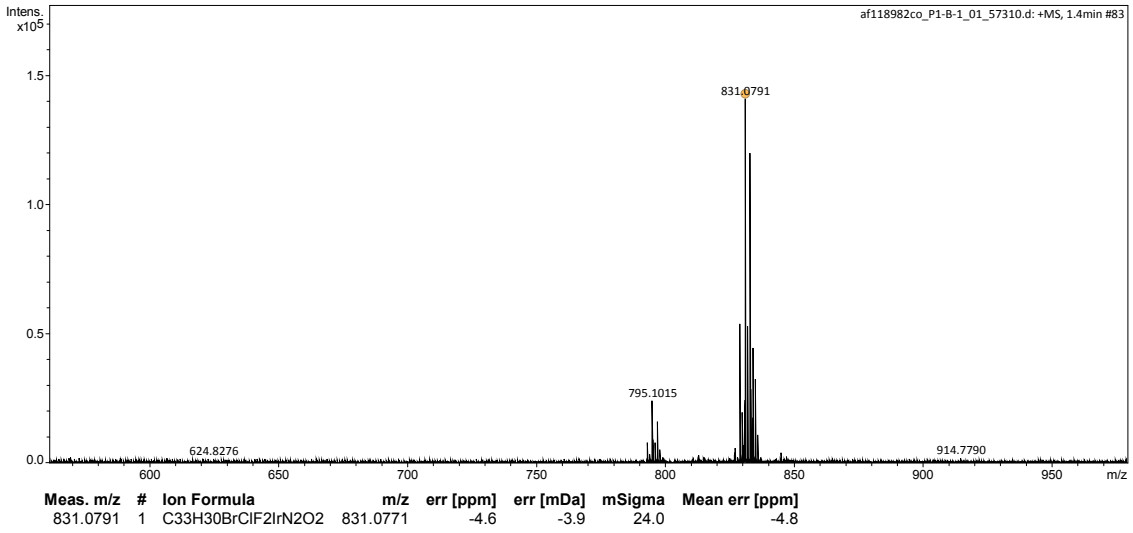
Mass	Intensity	Formula	Calculated Mass	Mass Difference [ppm]	DBE
204.18686	17868.06	C15 H24	204.18725	-1.90	4.0

Figure 240. GCMS fragmentation pattern of Rt: 5.79 min, the desired product.



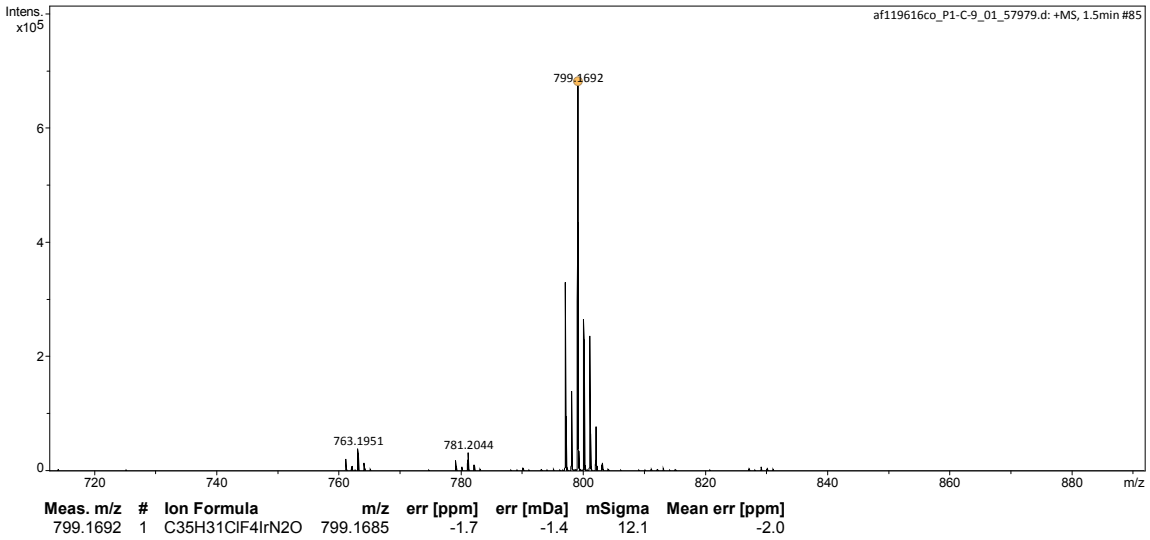
Meas. m/z	#	Ion Formula	m/z	err [ppm]	err [mDa]	mSigma	Mean err [ppm]
923.0979	1	C30H31Cl2F4Ir2	923.0992	-1.0	-0.9	10.6	-2.1

Figure 241. HRMS of IrCp3.



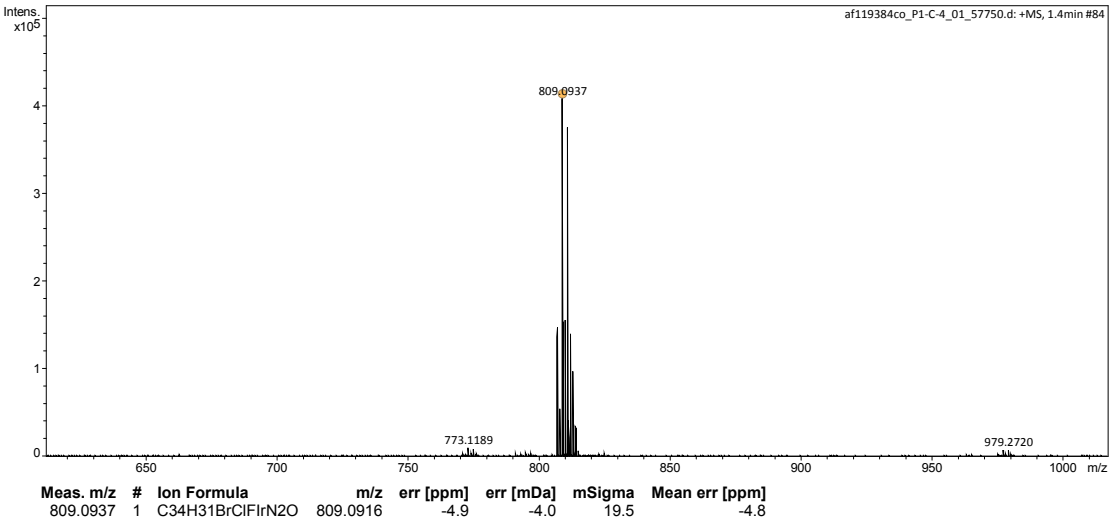
Meas. m/z	#	Ion Formula	m/z	err [ppm]	err [mDa]	mSigma	Mean err [ppm]
831.0791	1	C33H30BrClF2IrN2O2	831.0771	-4.6	-3.9	24.0	-4.8

Figure 242. HRMS of Ir9.



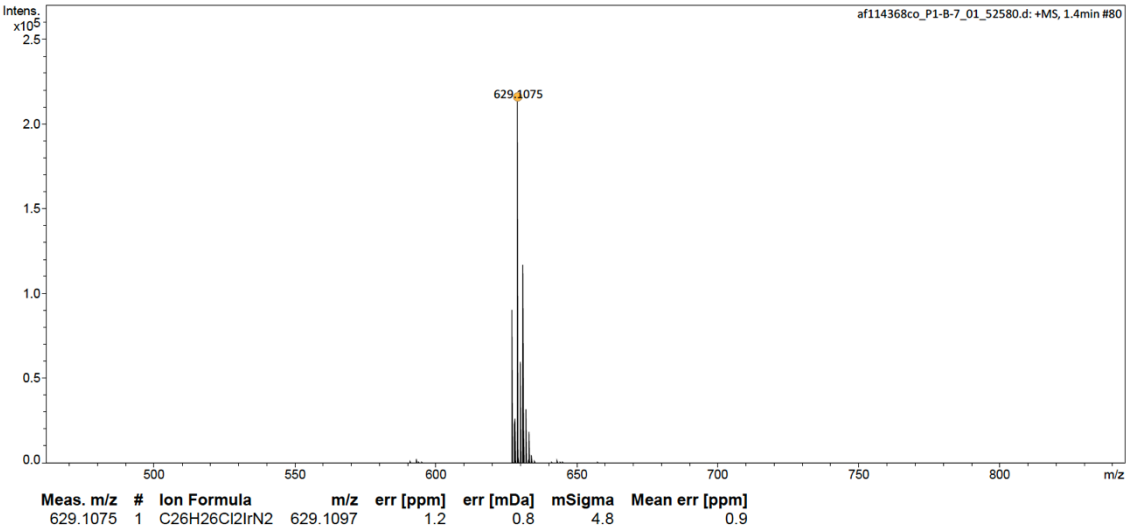
Meas. m/z	#	Ion Formula	m/z	err [ppm]	err [mDa]	mSigma	Mean err [ppm]
799.1692	1	C35H31ClF4IrN2O	799.1685	-1.7	-1.4	12.1	-2.0

Figure 243. HRMS of Ir14.



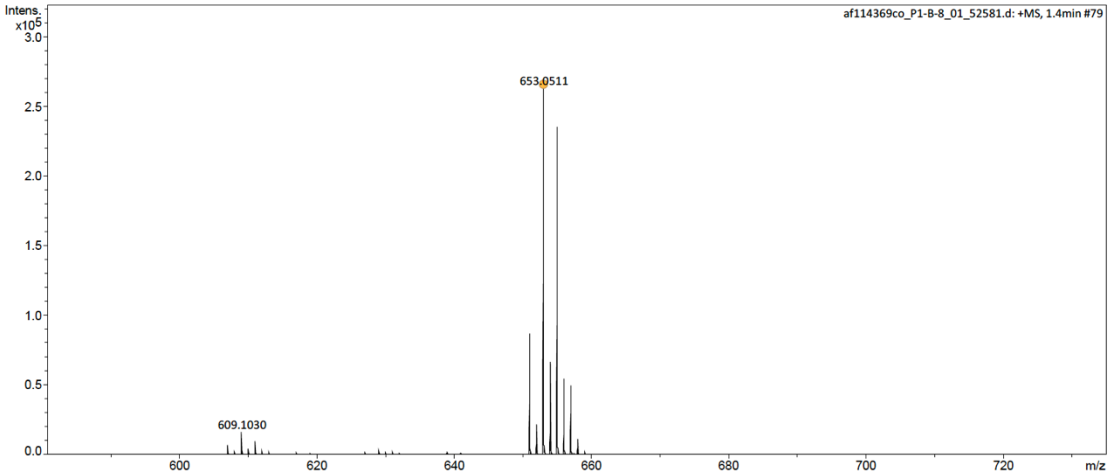
Meas. m/z	#	Ion Formula	m/z	err [ppm]	err [mDa]	mSigma	Mean err [ppm]
809.0937	1	C34H31BrClFIrN2O	809.0916	-4.9	-4.0	19.5	-4.8

Figure 244. HRMS of Ir15.



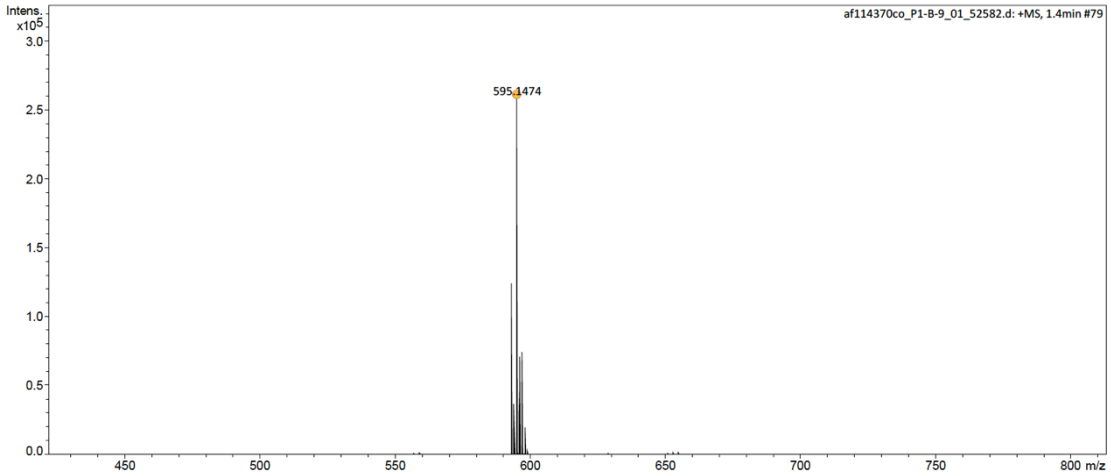
Meas. m/z	#	Ion Formula	m/z	err [ppm]	err [mDa]	mSigma	Mean err [ppm]
629.1075	1	C26H26Cl2IrN2	629.1097	1.2	0.8	4.8	0.9

Figure 245. HRMS of IrCp1K7.



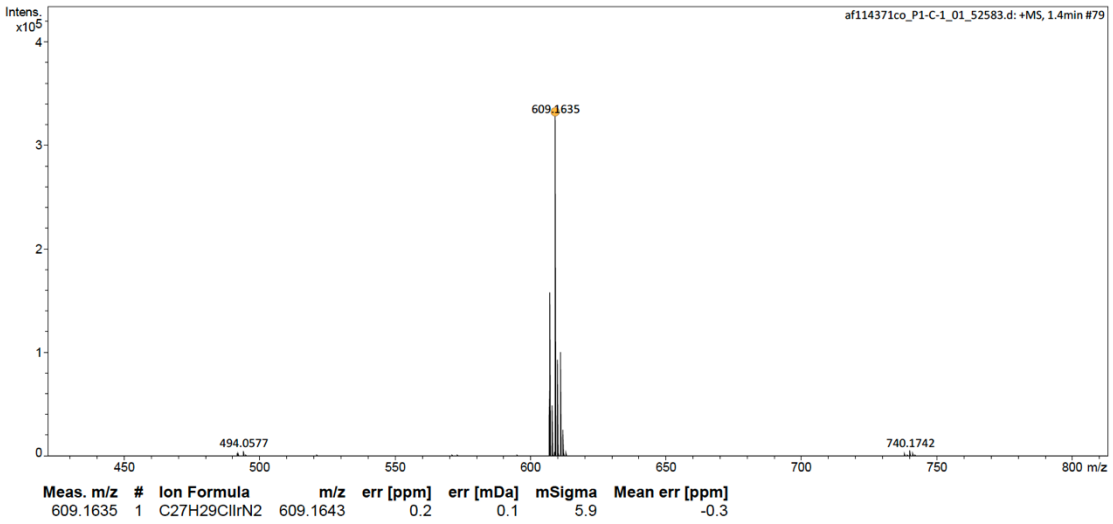
Meas. m/z	#	Ion Formula	m/z	err [ppm]	err [mDa]	mSigma	Mean err [ppm]
653.0511	1	C23H26BrClIrN2O	653.0541	1.6	1.0	14.5	0.9

Figure 246. HRMS of IrCp1L7.



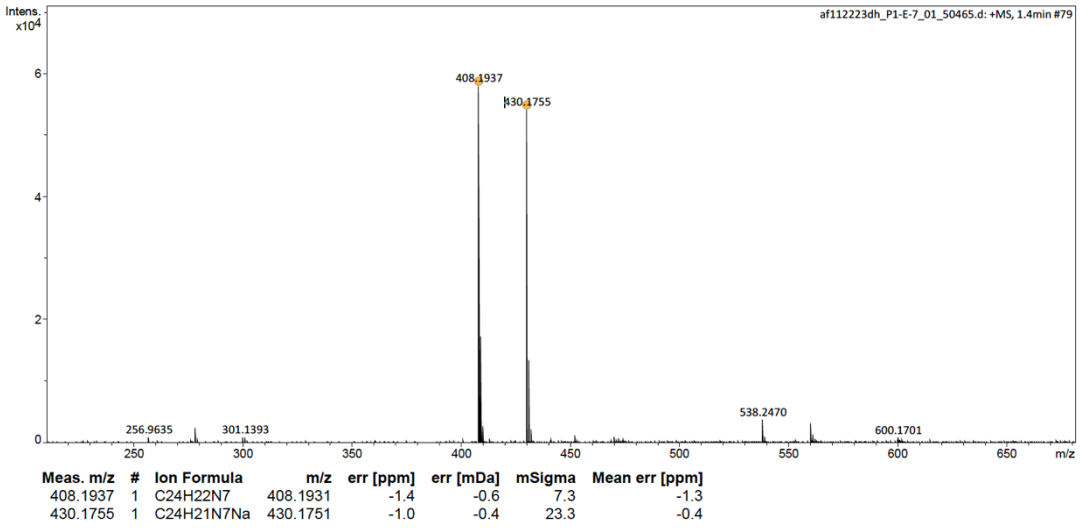
Meas. m/z	#	Ion Formula	m/z	err [ppm]	err [mDa]	mSigma	Mean err [ppm]
595.1474	1	C26H27ClIrN2	595.1486	0.9	0.5	8.4	-0.2

Figure 247. HRMS of IrCp1B7.



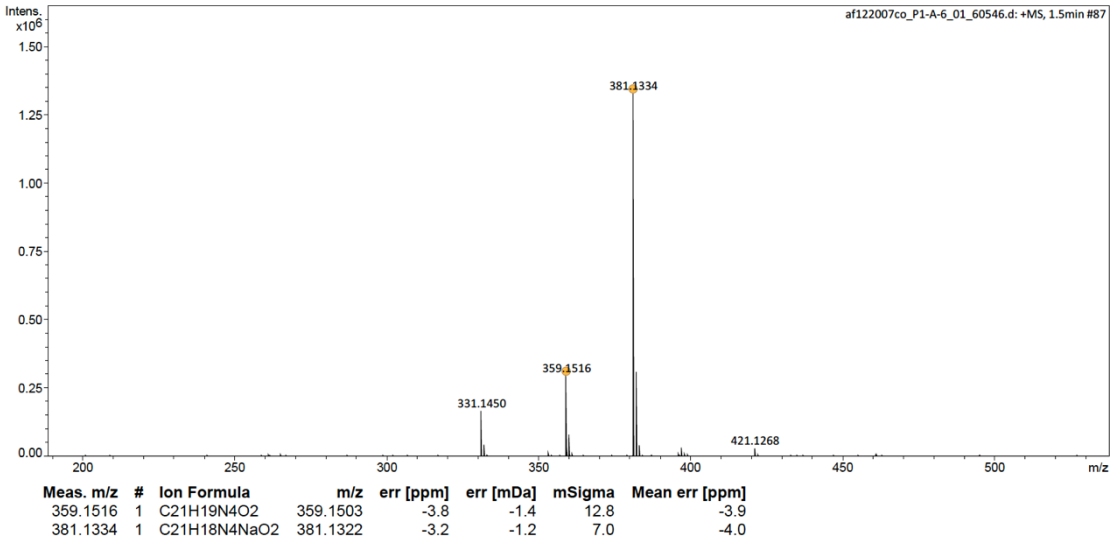
Meas. m/z	#	Ion Formula	m/z	err [ppm]	err [mDa]	mSigma	Mean err [ppm]
609.1635	1	C27H29ClIrN2	609.1643	0.2	0.1	5.9	-0.3

Figure 248. HRMS of IrCp1B8.



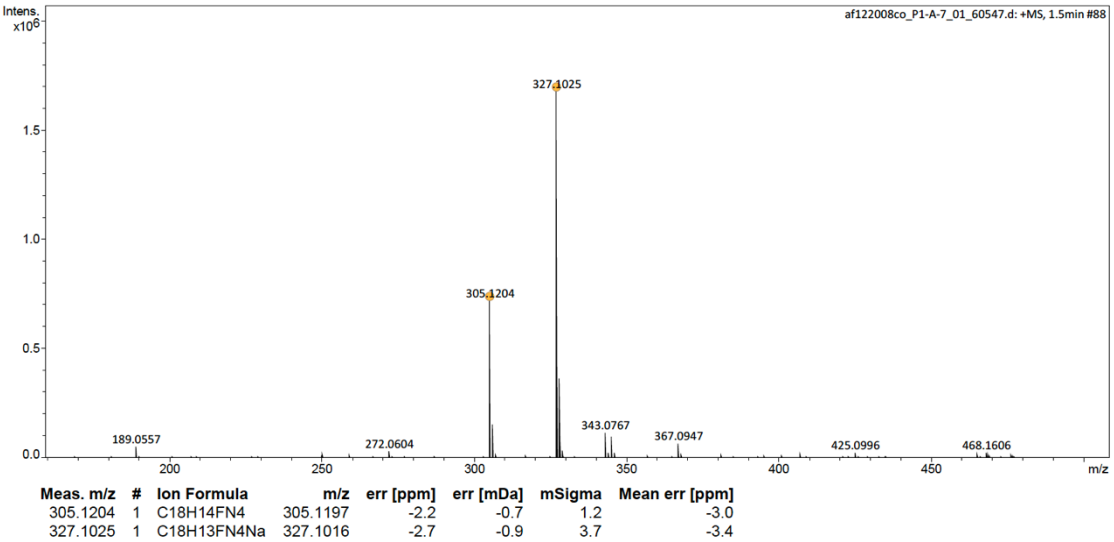
Meas. m/z	#	Ion Formula	m/z	err [ppm]	err [mDa]	mSigma	Mean err [ppm]
408.1937	1	C24H22N7	408.1931	-1.4	-0.6	7.3	-1.3
430.1755	1	C24H21N7Na	430.1751	-1.0	-0.4	23.3	-0.4

Figure 249. HRMS of $(BimH)_3$ ligand.



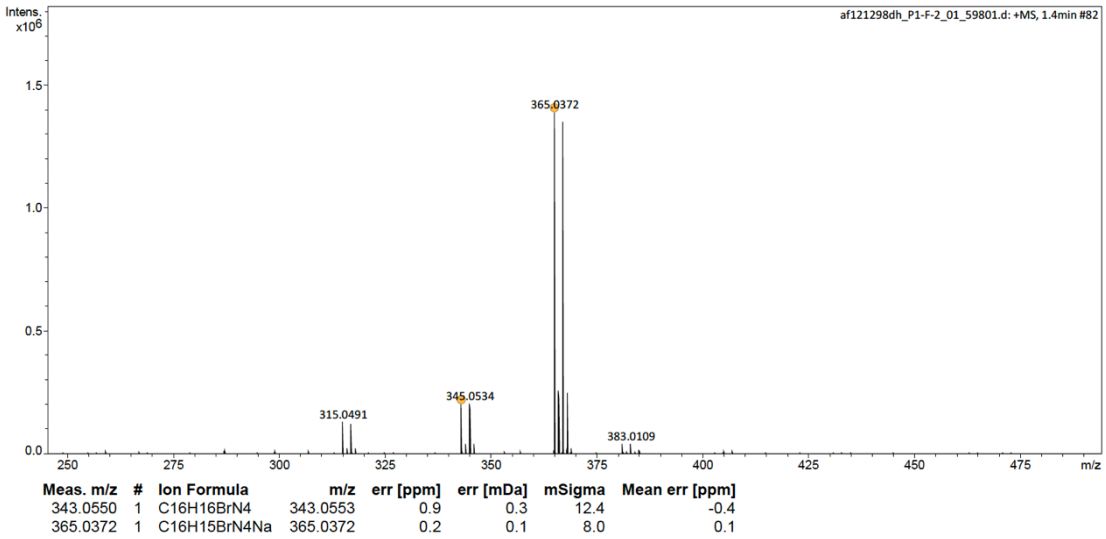
Meas. m/z	#	Ion Formula	m/z	err [ppm]	err [mDa]	mSigma	Mean err [ppm]
359.1516	1	C21H19N4O2	359.1503	-3.8	-1.4	12.8	-3.9
381.1334	1	C21H18N4NaO2	381.1322	-3.2	-1.2	7.0	-4.0

Figure 250. HRMS of M23Y3.



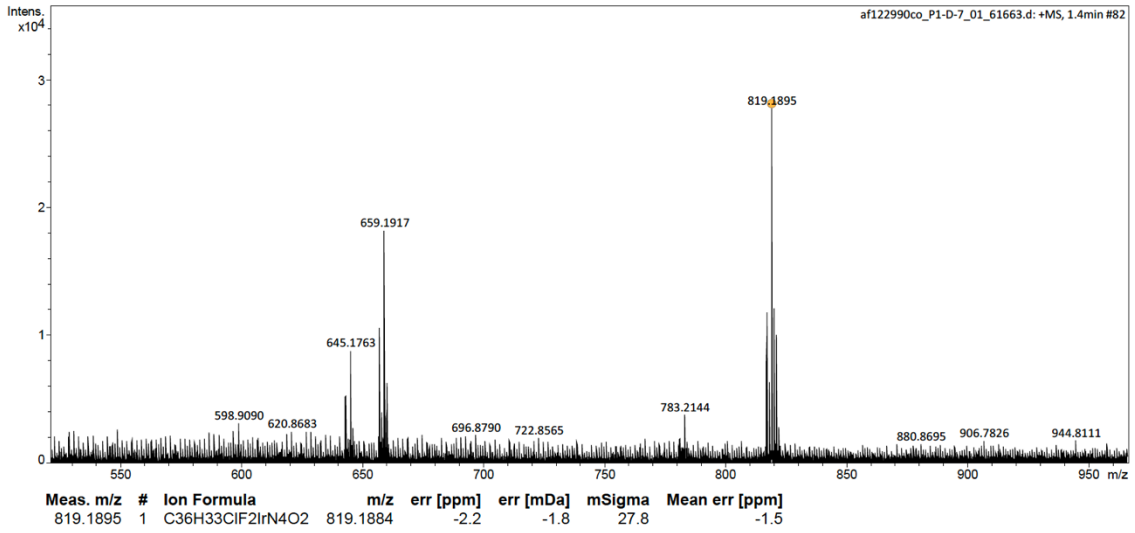
Meas. m/z	#	Ion Formula	m/z	err [ppm]	err [mDa]	mSigma	Mean err [ppm]
305.1204	1	C18H14FN4	305.1197	-2.2	-0.7	1.2	-3.0
327.1025	1	C18H13FN4Na	327.1016	-2.7	-0.9	3.7	-3.4

Figure 251. HRMS of P3A10.



Meas. m/z	#	Ion Formula	m/z	err [ppm]	err [mDa]	mSigma	Mean err [ppm]
343.0550	1	C16H16BrN4	343.0553	0.9	0.3	12.4	-0.4
365.0372	1	C16H15BrN4Na	365.0372	0.2	0.1	8.0	0.1

Figure 252. HRMS of M23Y2.



Meas. m/z	#	Ion Formula	m/z	err [ppm]	err [mDa]	mSigma	Mean err [ppm]
819.1895	1	C36H33ClF2IrN4O2	819.1884	-2.2	-1.8	27.8	-1.5

Figure 253. HRMS of IrCp3M23Y3.

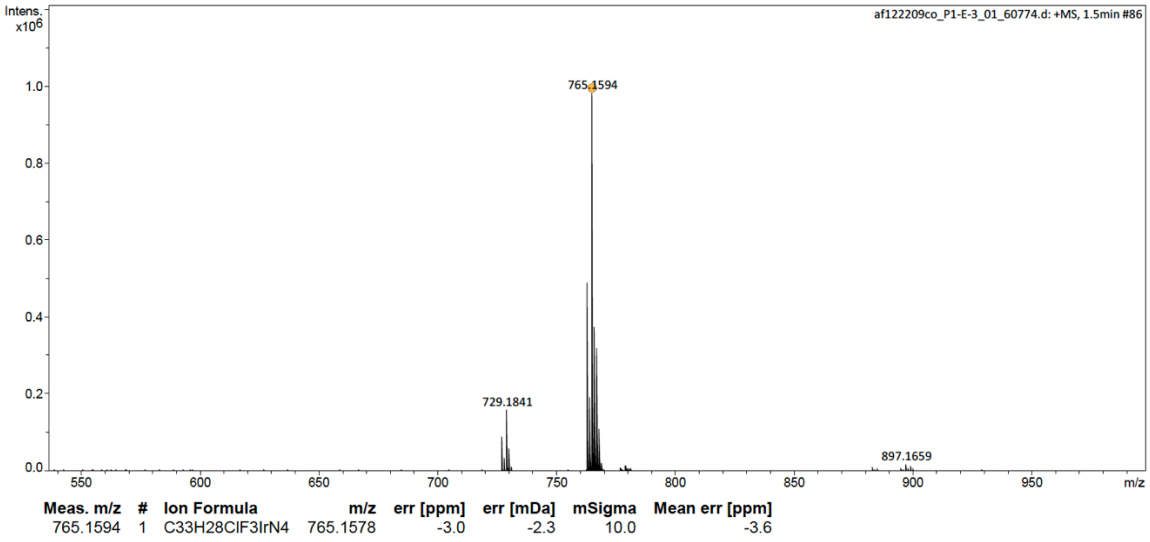


Figure 254. HRMS of IrCp3P3A10.

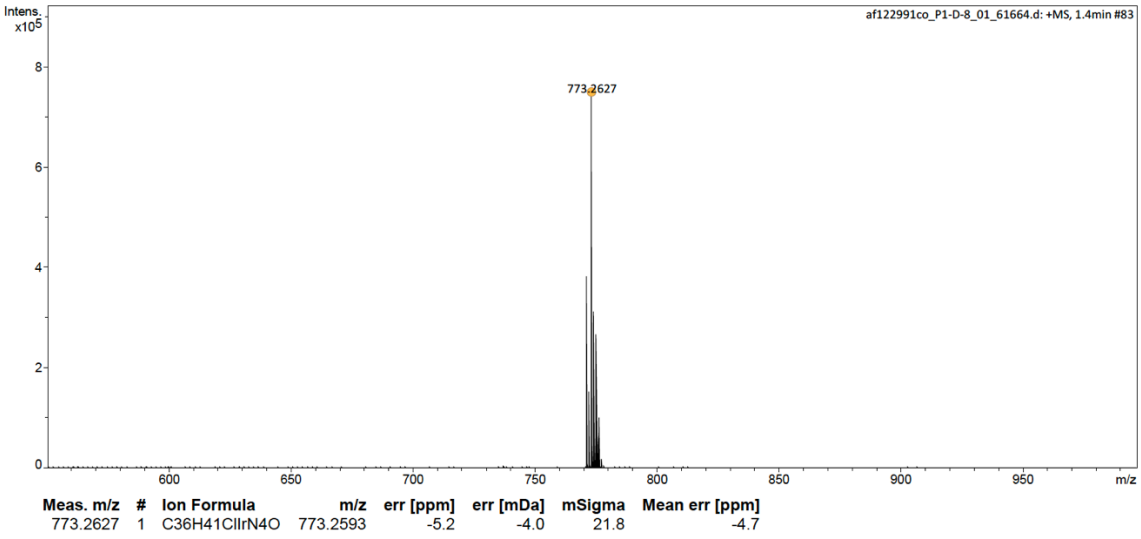


Figure 255. HRMS of IrCp4M23Y2.

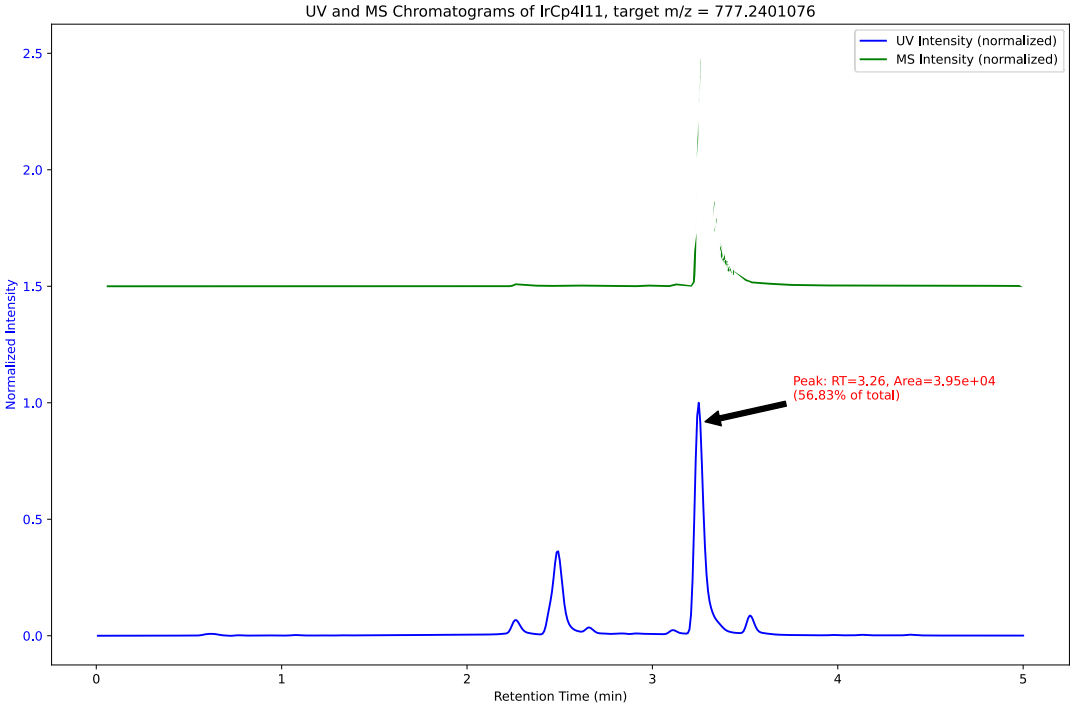


Figure 256. Processed LC-MS spectrum for Ir1 (crude). The lower graph is UV trace at 254 nm, and the upper trace is extracted ion chromatography for the target mass of the complex.

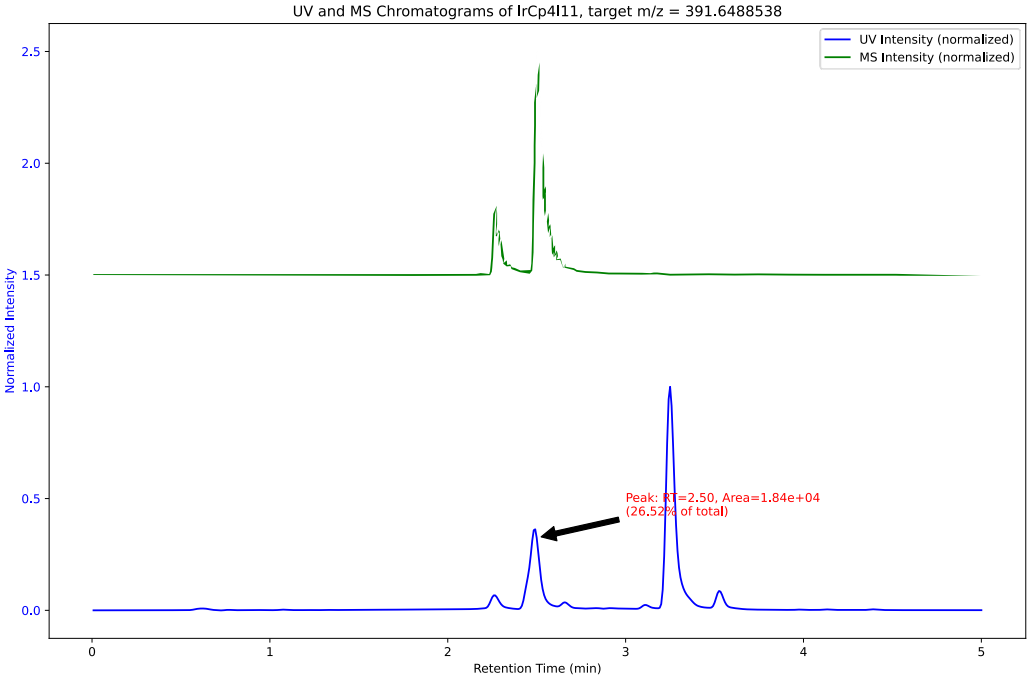


Figure 257. Processed LC-MS spectrum for Ir1 (crude). The lower graph is UV trace at 254 nm, and the upper trace is extracted ion chromatography for the [(M – Cl)+ MeCN]$^{2+}$ ion of the complex.

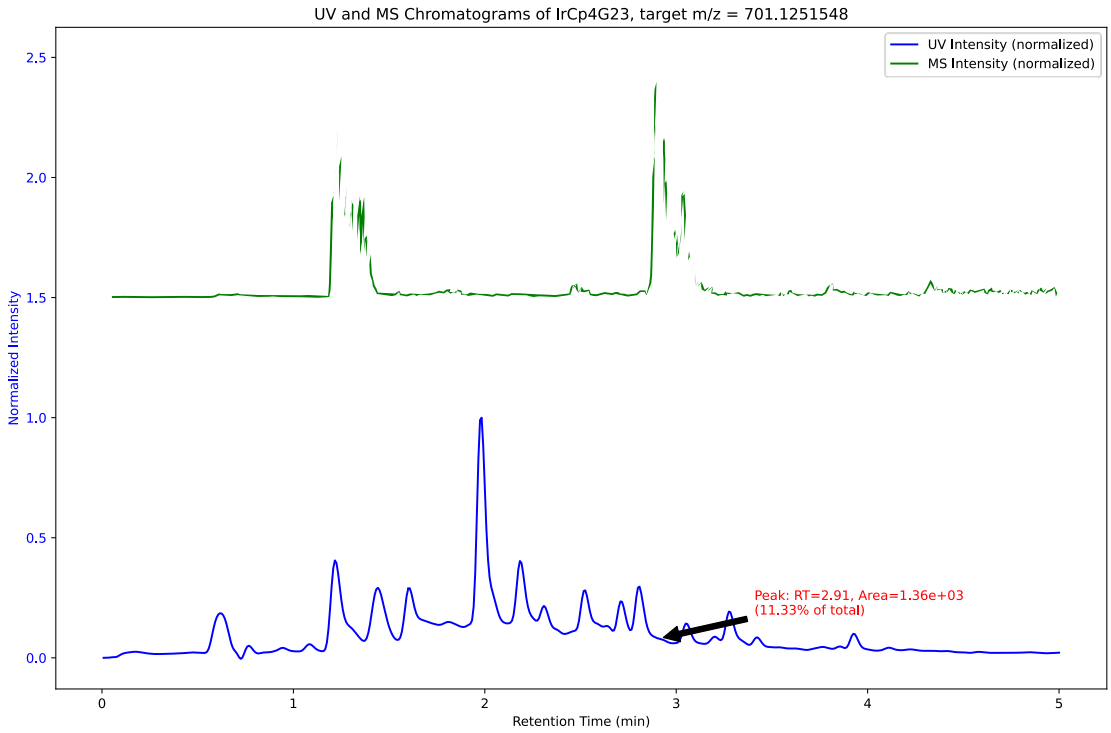


Figure 258. Processed LC-MS spectrum for Ir2 (crude). The lower graph is UV trace at 254 nm, and the upper trace is extracted ion chromatography for the target mass of the complex.

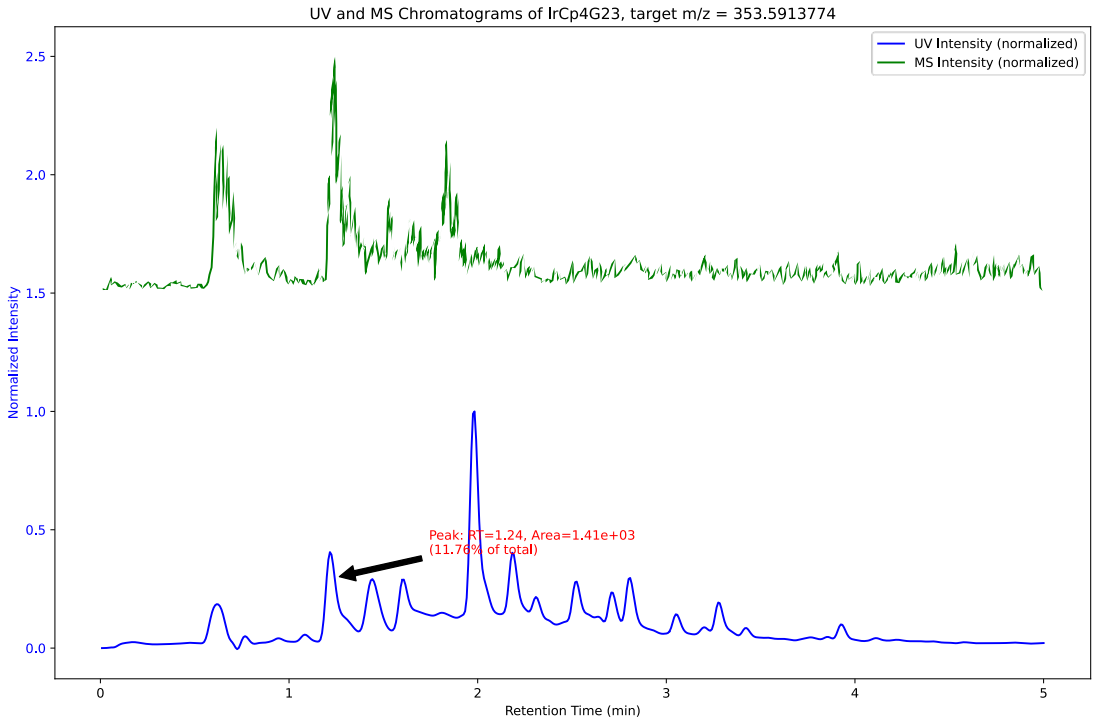


Figure 259. Processed LC-MS spectrum for Ir2 (crude). The lower graph is UV trace at 254 nm, and the upper trace is extracted ion chromatography for the $[(M - Cl) + MeCN]^{2+}$ ion of the complex.

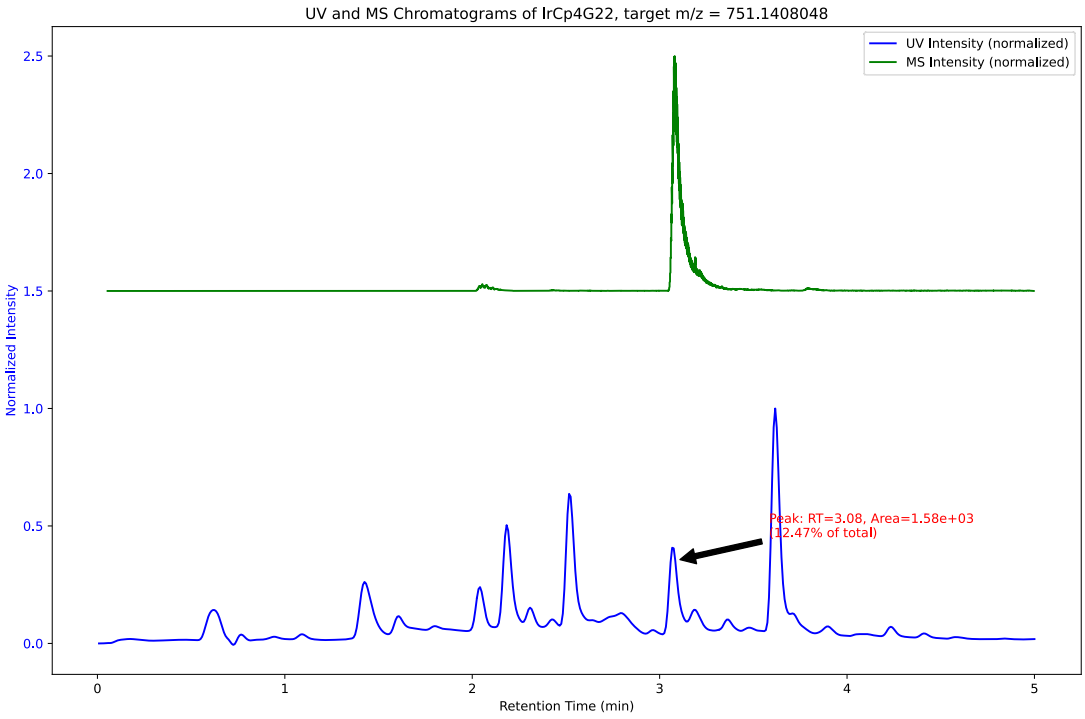


Figure 260. Processed LC-MS spectrum for Ir3 (crude). The lower graph is UV trace at 254 nm, and the upper trace is extracted ion chromatography for the target mass of the complex.

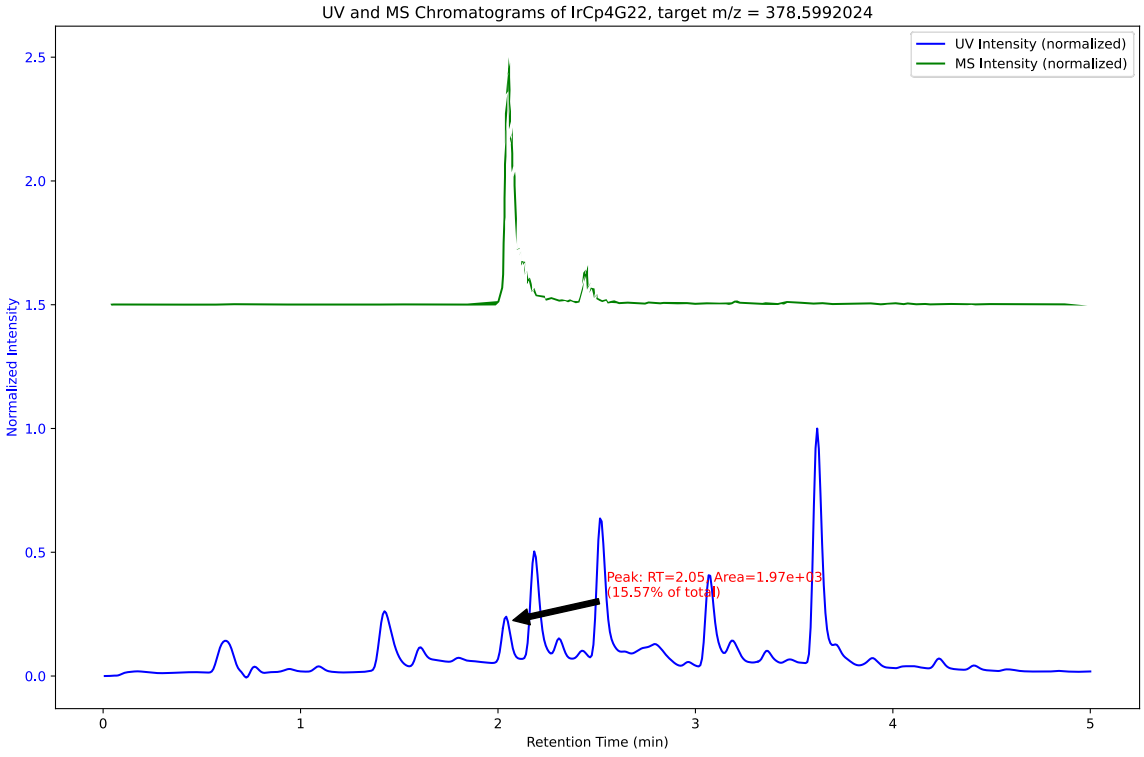


Figure 261. Processed LC-MS spectrum for Ir3 (crude). The lower graph is UV trace at 254 nm, and the upper trace is extracted ion chromatography for the $[(M - Cl) + MeCN]^{2+}$ ion of the complex.

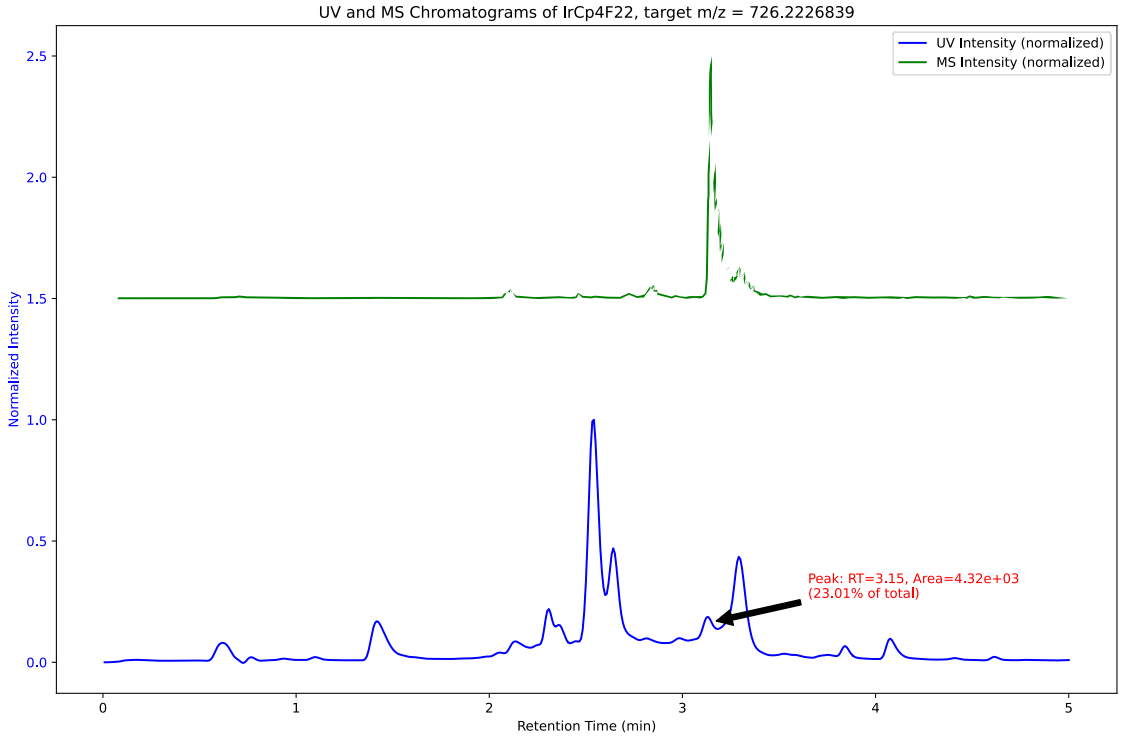


Figure 262. Processed LC-MS spectrum for Ir4 (crude). The lower graph is UV trace at 254 nm, and the upper trace is extracted ion chromatography for the target mass of the complex.

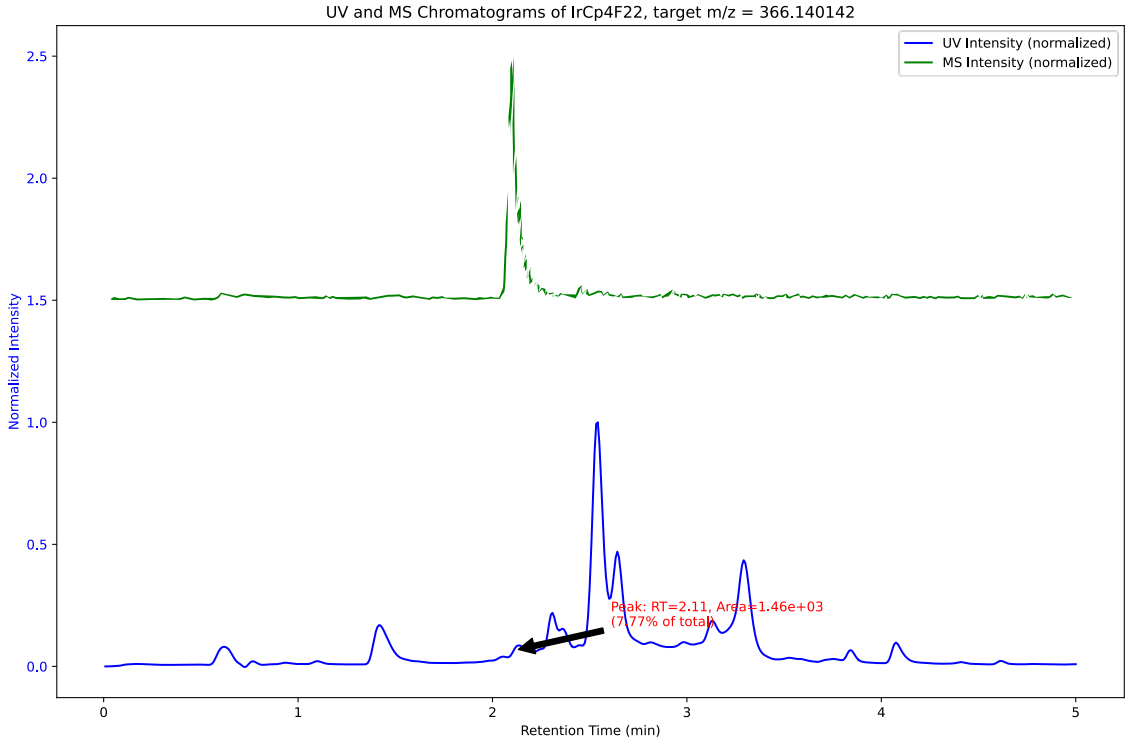


Figure S263. Processed LC-MS spectrum for Ir4 (crude). The lower graph is UV trace at 254 nm, and the upper trace is extracted ion chromatography for the $[(M - Cl) + MeCN]^{2+}$ ion of the complex.

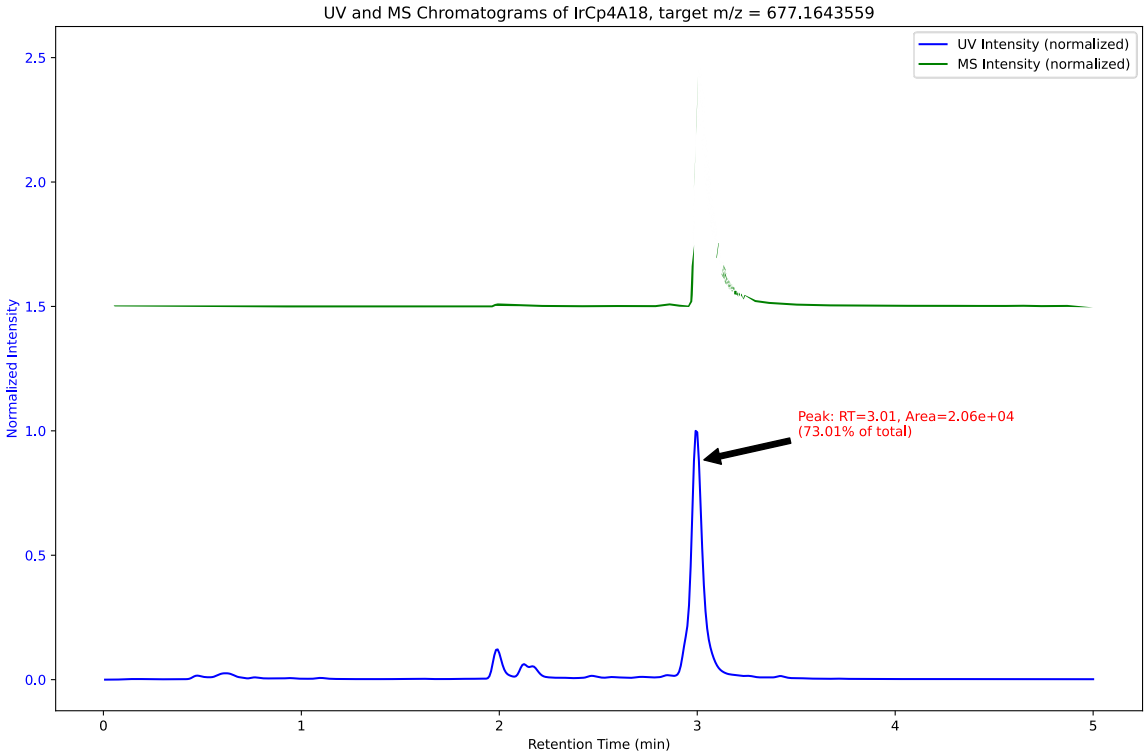


Figure 264. Processed LC-MS spectrum for Ir5 (crude). The lower graph is UV trace at 254 nm, and the upper trace is extracted ion chromatography for the target mass of the complex.

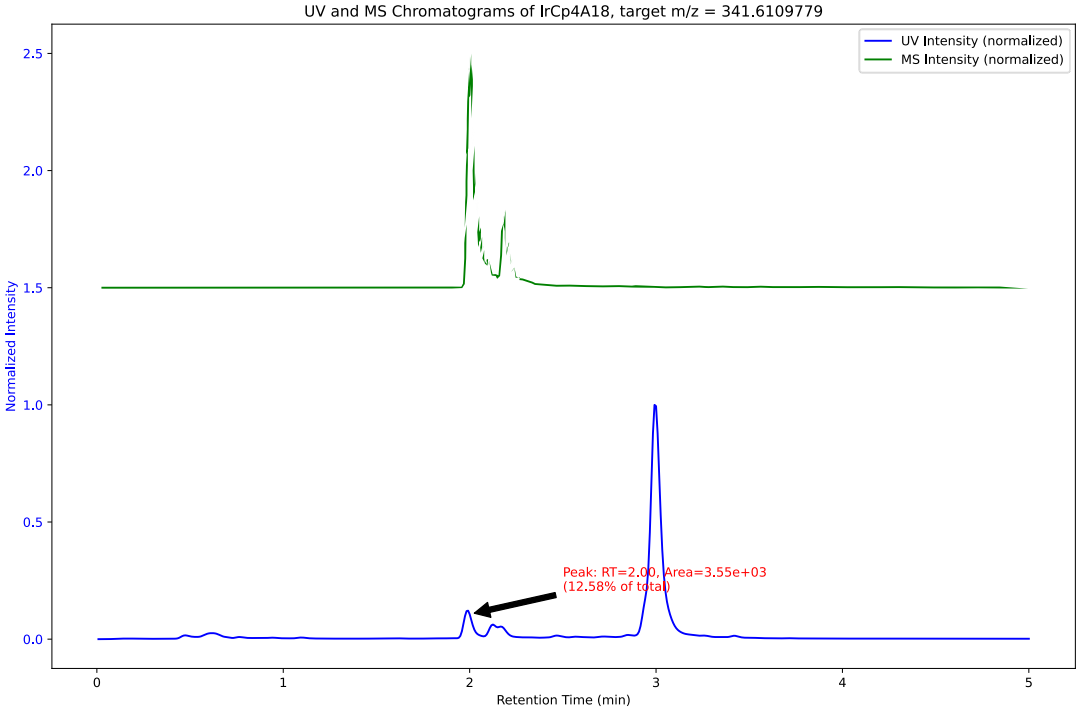


Figure 265. Processed LC-MS spectrum for Ir5 (crude). The lower graph is UV trace at 254 nm, and the upper trace is extracted ion chromatography for the [(M – Cl)+ MeCN]$^{2+}$ ion of the complex.

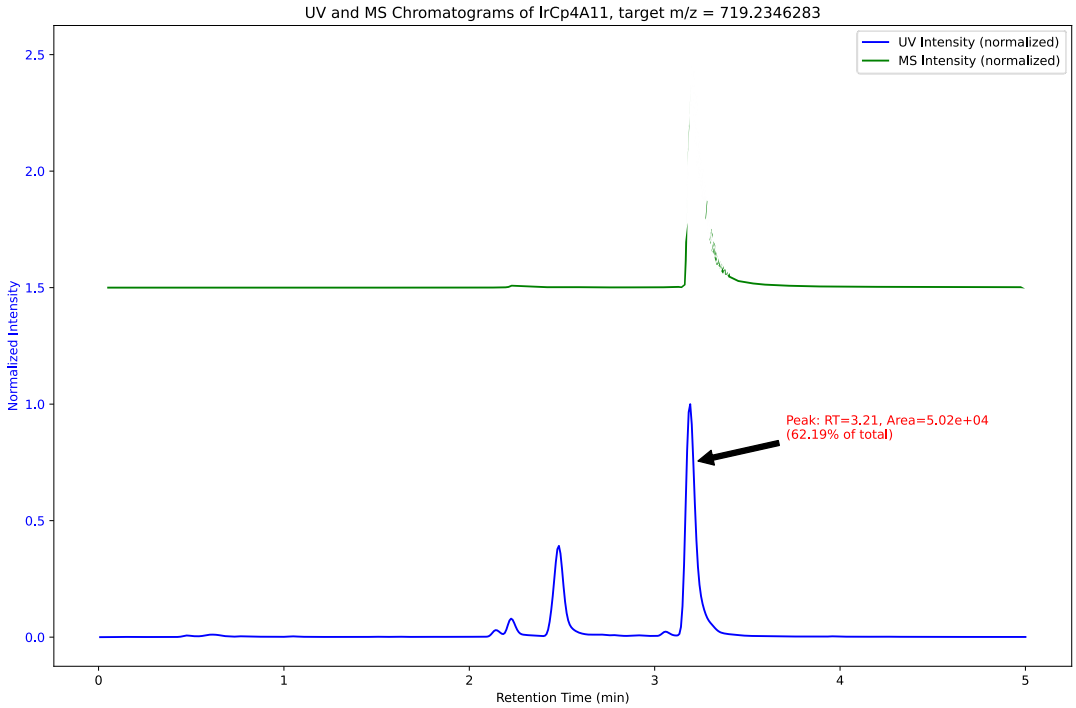


Figure 266. Processed LC-MS spectrum for Ir6 (crude). The lower graph is UV trace at 254 nm, and the upper trace is extracted ion chromatography for the target mass of the complex.

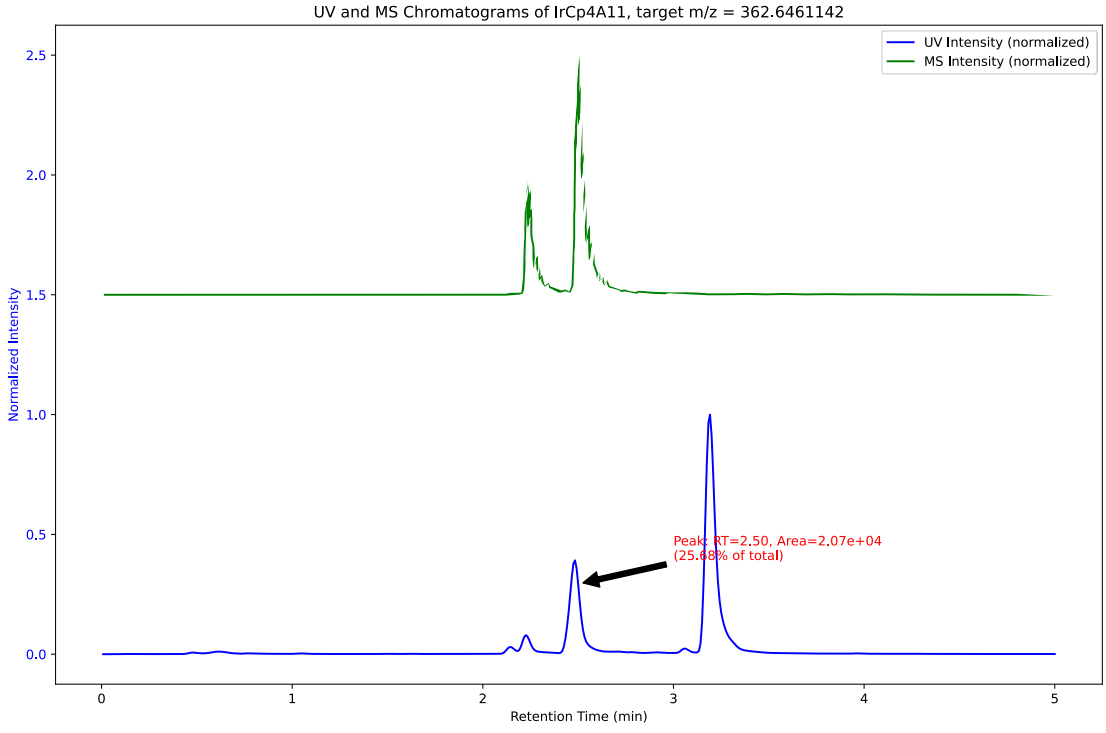


Figure 267. Processed LC-MS spectrum for Ir6 (crude). The lower graph is UV trace at 254 nm, and the upper trace is extracted ion chromatography for the $[(M–Cl)+ MeCN]^{2+}$ ion of the complex.

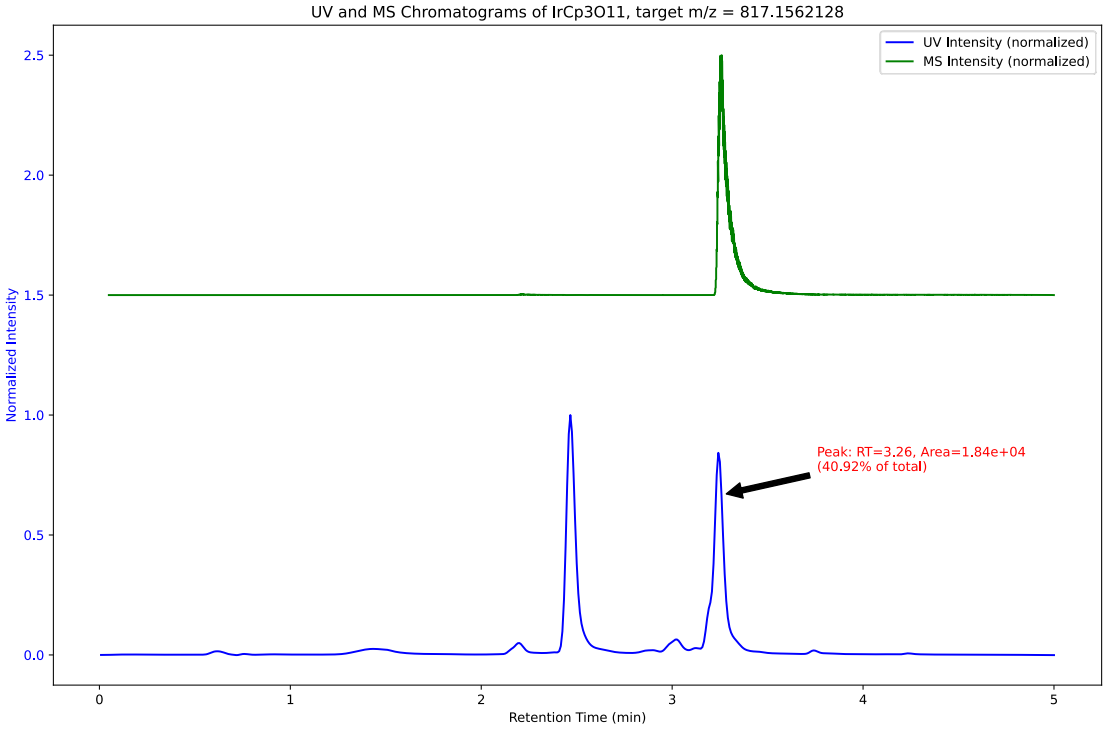


Figure 268. Processed LC-MS spectrum for Ir7 (crude). The lower graph is UV trace at 254 nm, and the upper trace is extracted ion chromatography for the target mass of the complex.

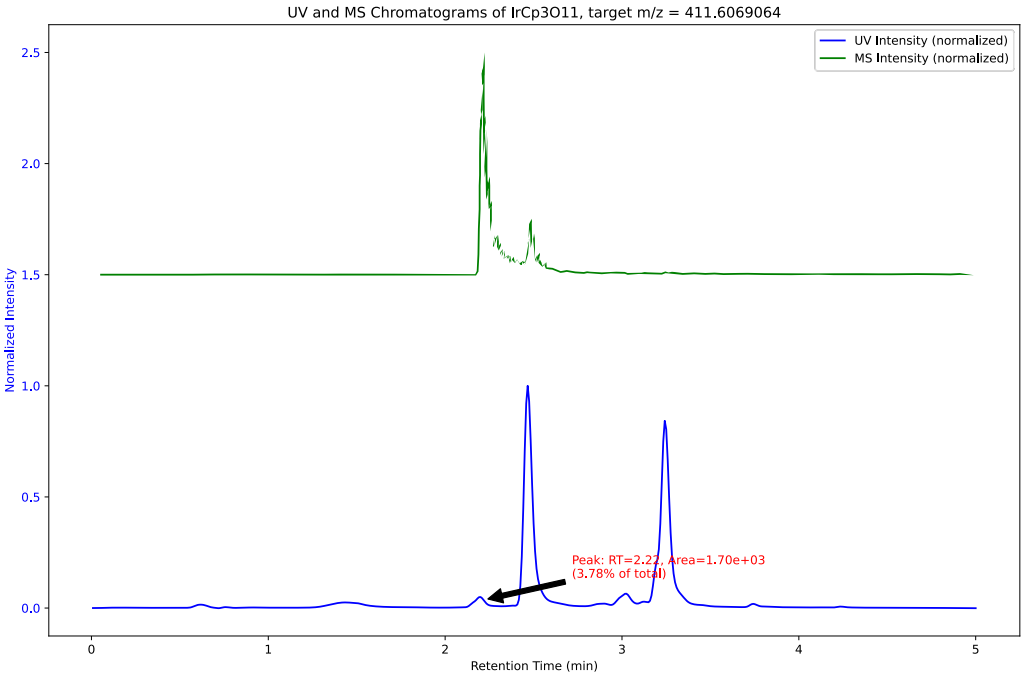


Figure 269. Processed LC-MS spectrum for Ir7 (crude). The lower graph is UV trace at 254 nm, and the upper trace is extracted ion chromatography for the $[(M–Cl)+ MeCN]^{2+}$ ion of the complex.

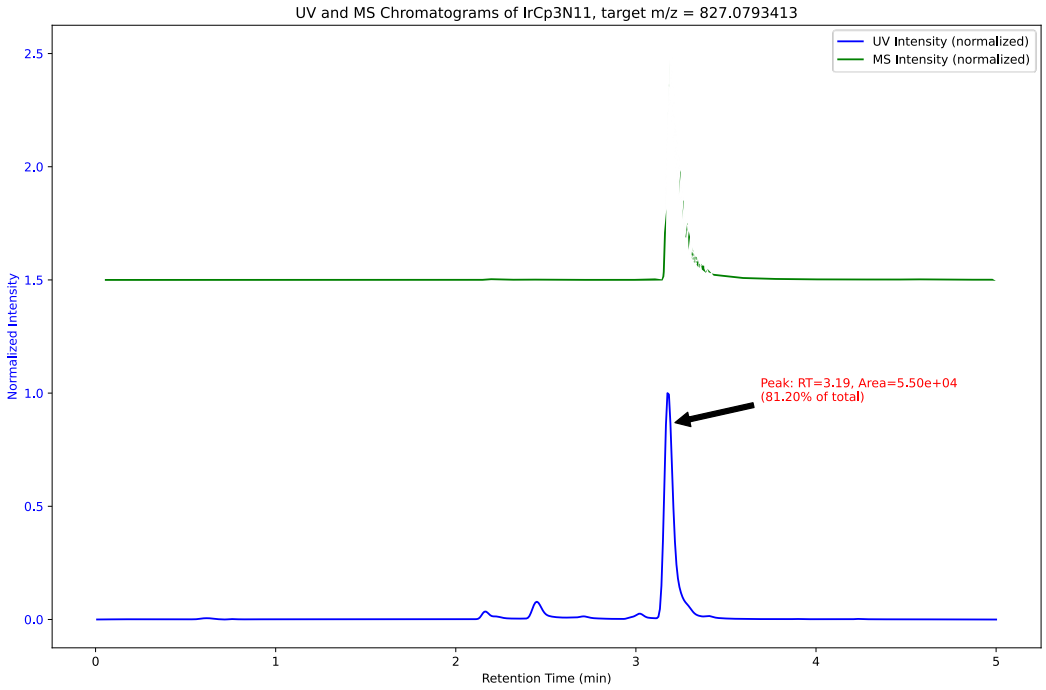


Figure 270. Processed LC-MS spectrum for Ir8 (crude). The lower graph is UV trace at 254 nm, and the upper trace is extracted ion chromatography for the target mass of the complex.

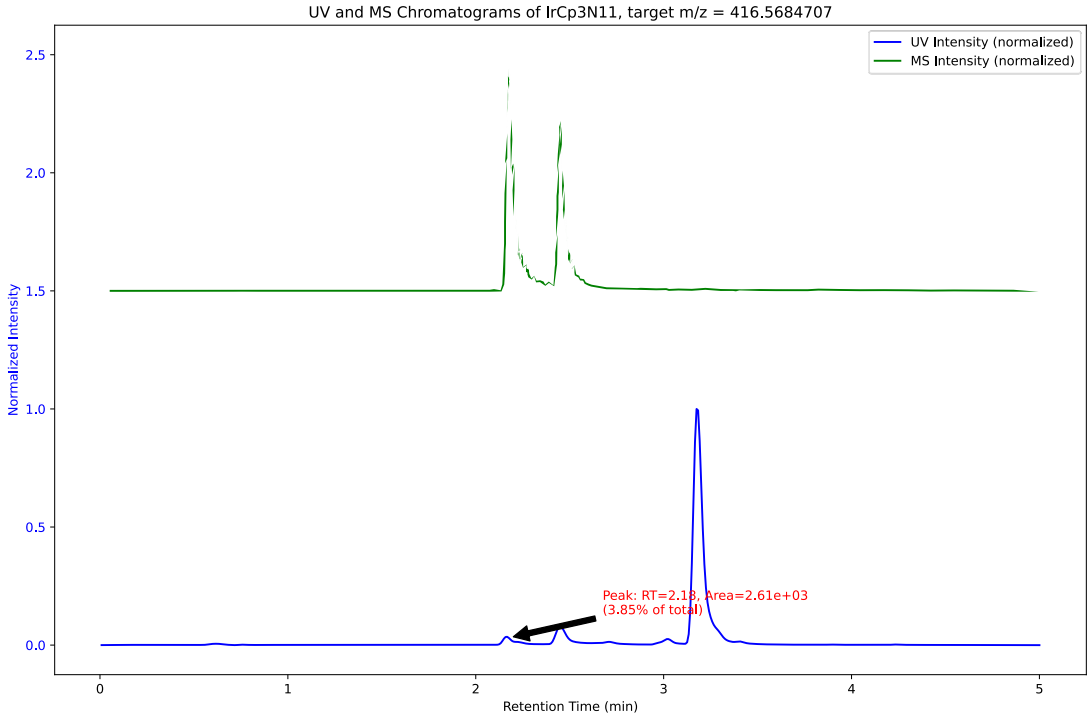


Figure 271. Processed LC-MS spectrum for Ir8 (crude). The lower graph is UV trace at 254 nm, and the upper trace is extracted ion chromatography for the [(M–Cl)+ MeCN]$^{2+}$ ion of the complex.

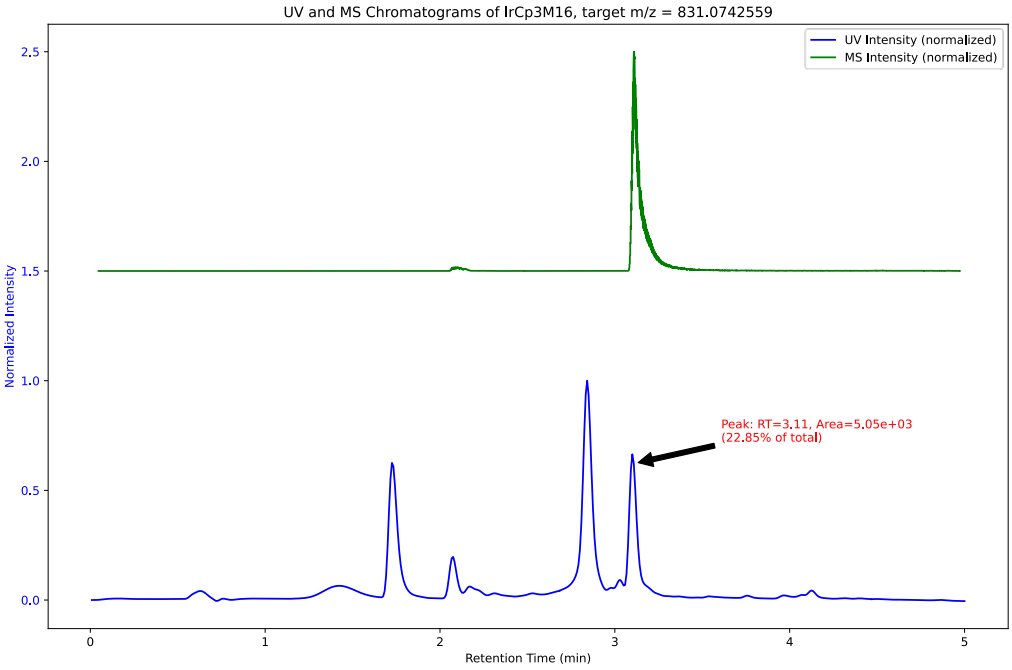


Figure 272. Processed LC-MS spectrum for Ir9 (crude). The lower graph is UV trace at 254 nm, and the upper trace is extracted ion chromatography for the target mass of the complex.

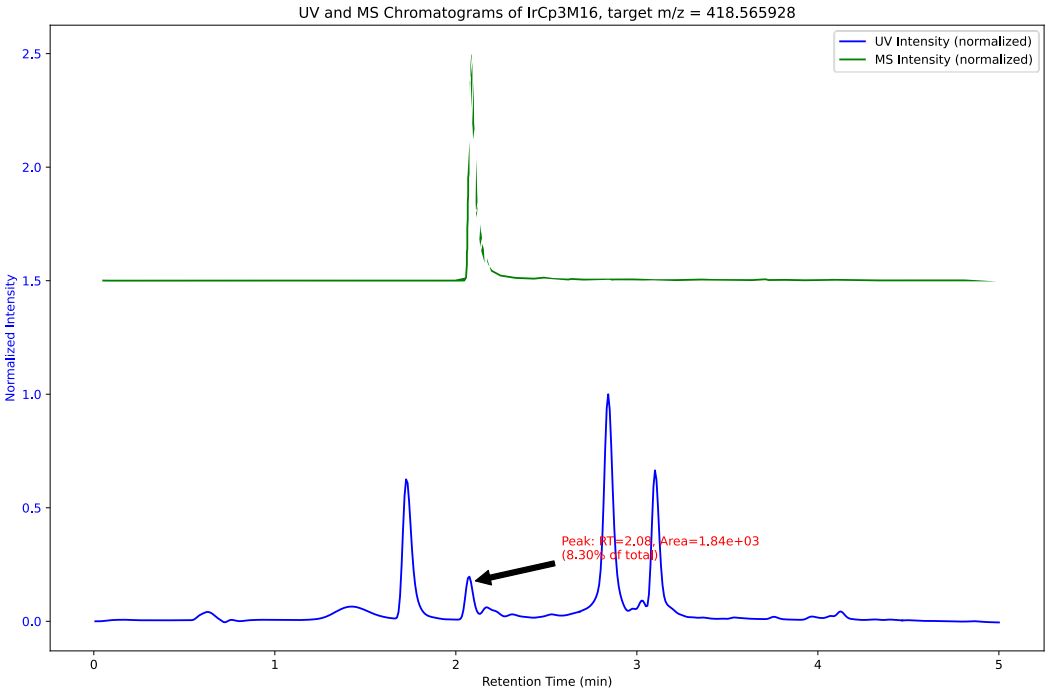


Figure 273. Processed LC-MS spectrum for Ir9 (crude). The lower graph is UV trace at 254 nm, and the upper trace is extracted ion chromatography for the $[(M–Cl)+ MeCN]^{2+}$ ion of the complex.

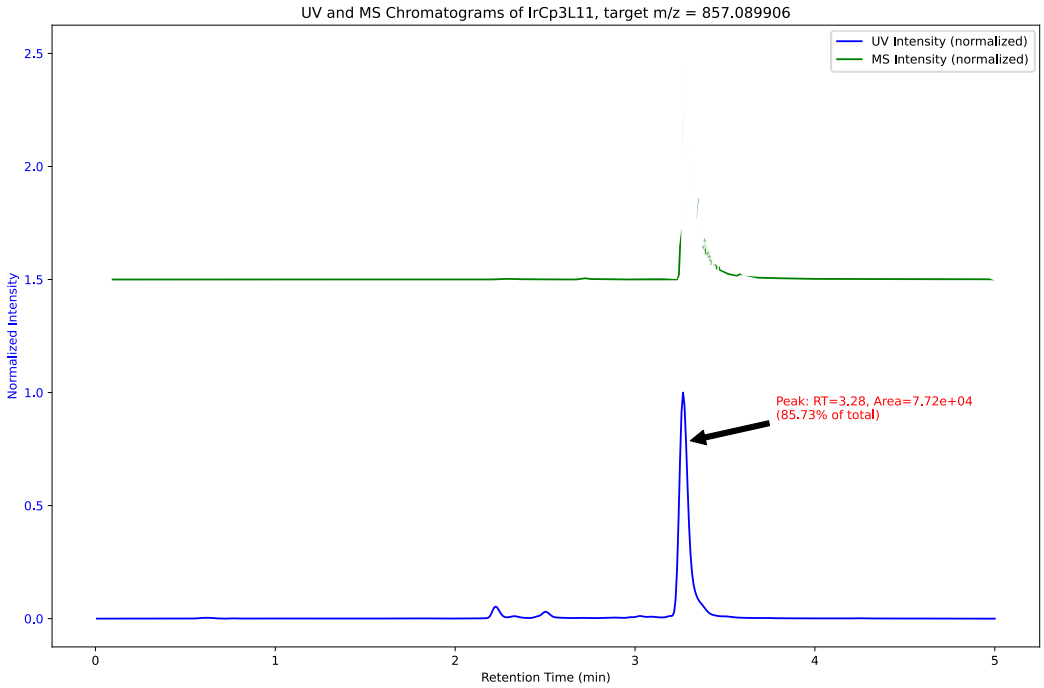


Figure 274. Processed LC-MS spectrum for Ir10 (crude). The lower graph is UV trace at 254 nm, and the upper trace is extracted ion chromatography for the target mass of the complex.

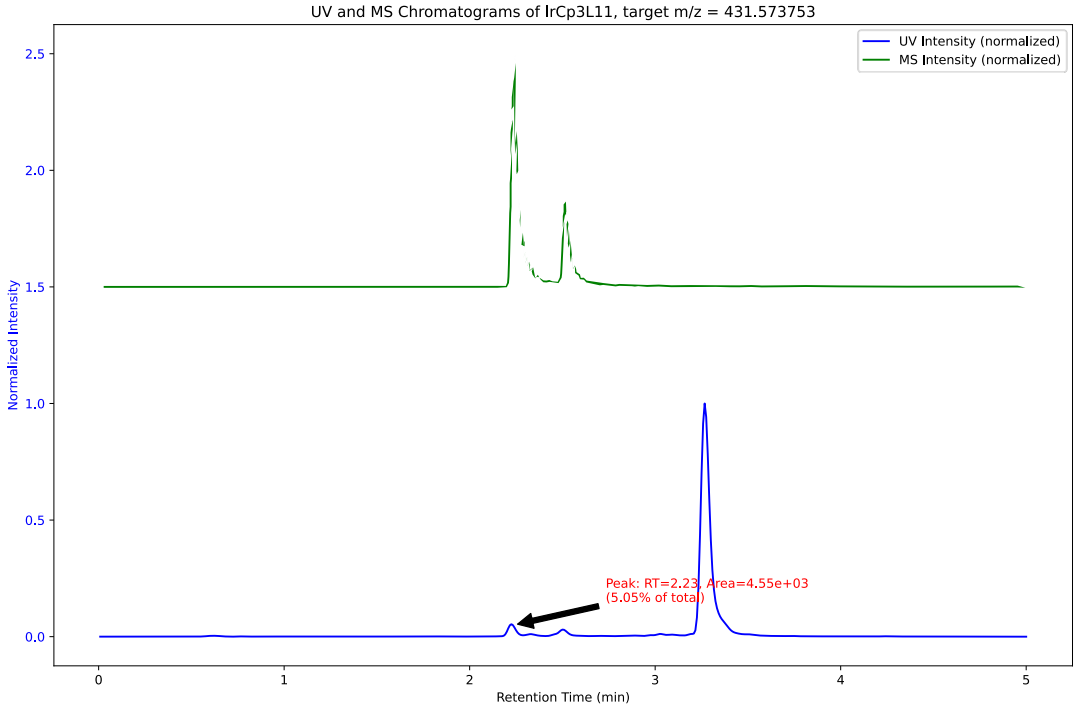


Figure 275. Processed LC-MS spectrum for Ir10 (crude). The lower graph is UV trace at 254 nm, and the upper trace is extracted ion chromatography for the [(M–Cl)+ MeCN]$^{2+}$ ion of the complex.

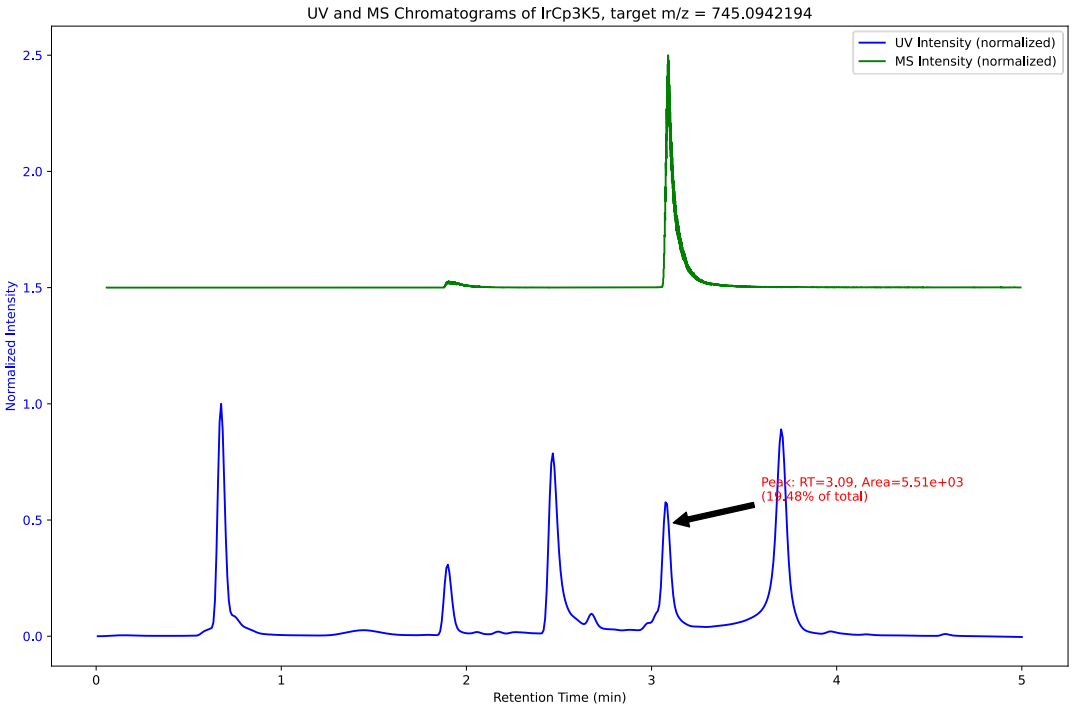


Figure 276. Processed LC-MS spectrum for Ir11 (crude). The lower graph is UV trace at 254 nm, and the upper trace is extracted ion chromatography for the target mass of the complex.

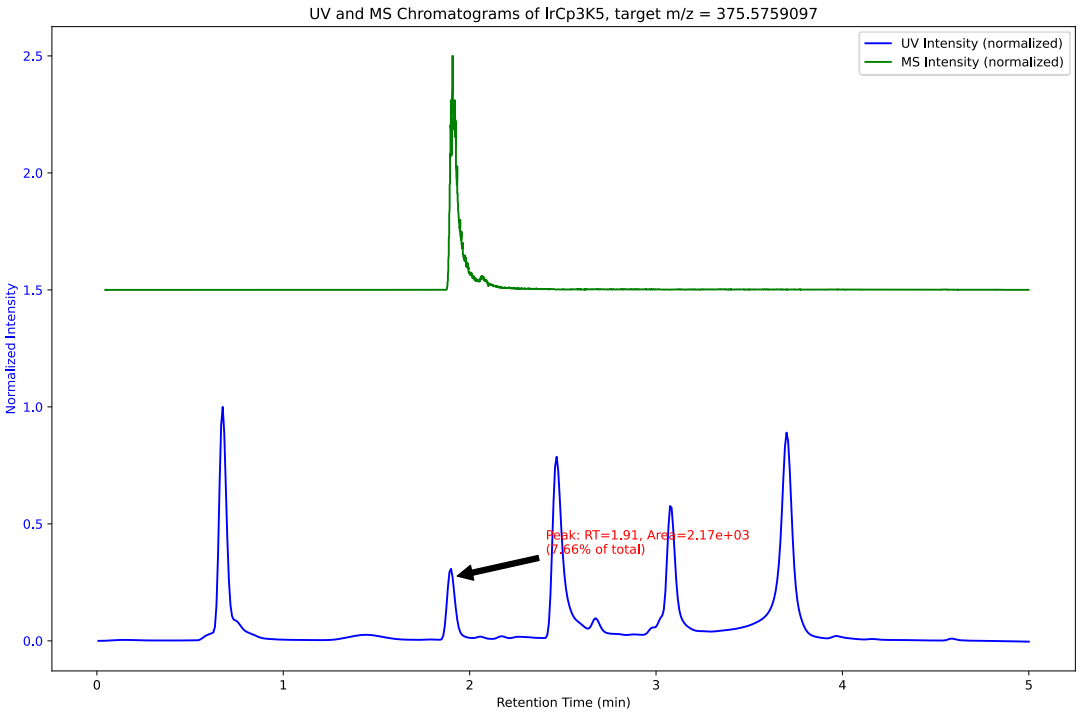


Figure 277. Processed LC-MS spectrum for Ir11 (crude). The lower graph is UV trace at 254 nm, and the upper trace is extracted ion chromatography for the $[(M–Cl)+ MeCN]^{2+}$ ion of the complex.

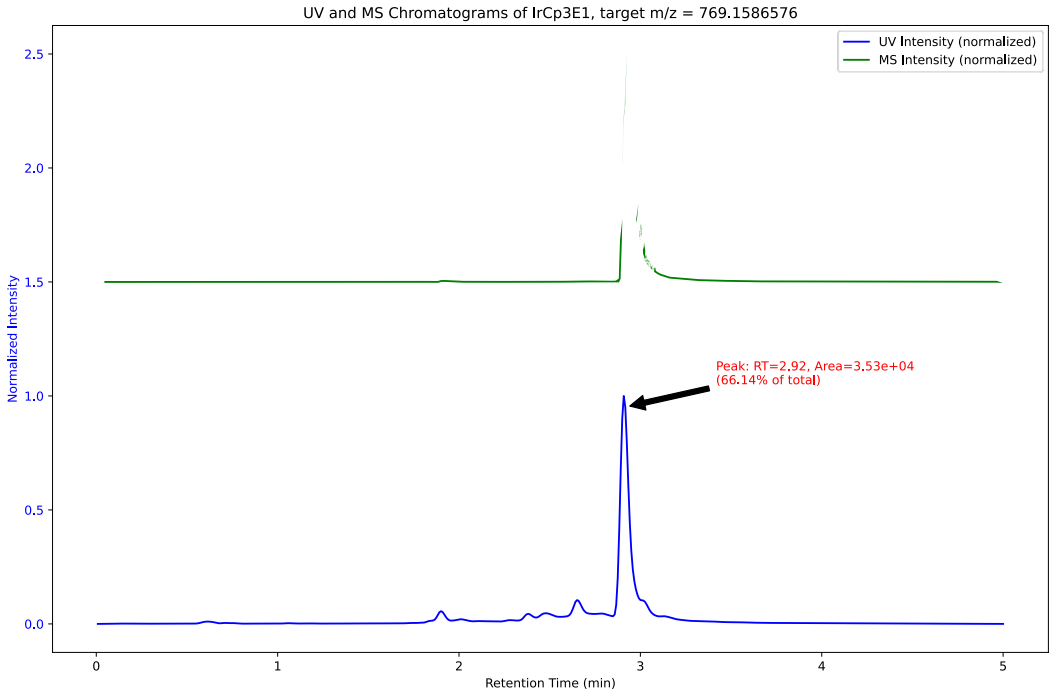


Figure 278. Processed LC-MS spectrum for Ir12 (crude). The lower graph is UV trace at 254 nm, and the upper trace is extracted ion chromatography for the target mass of the complex.

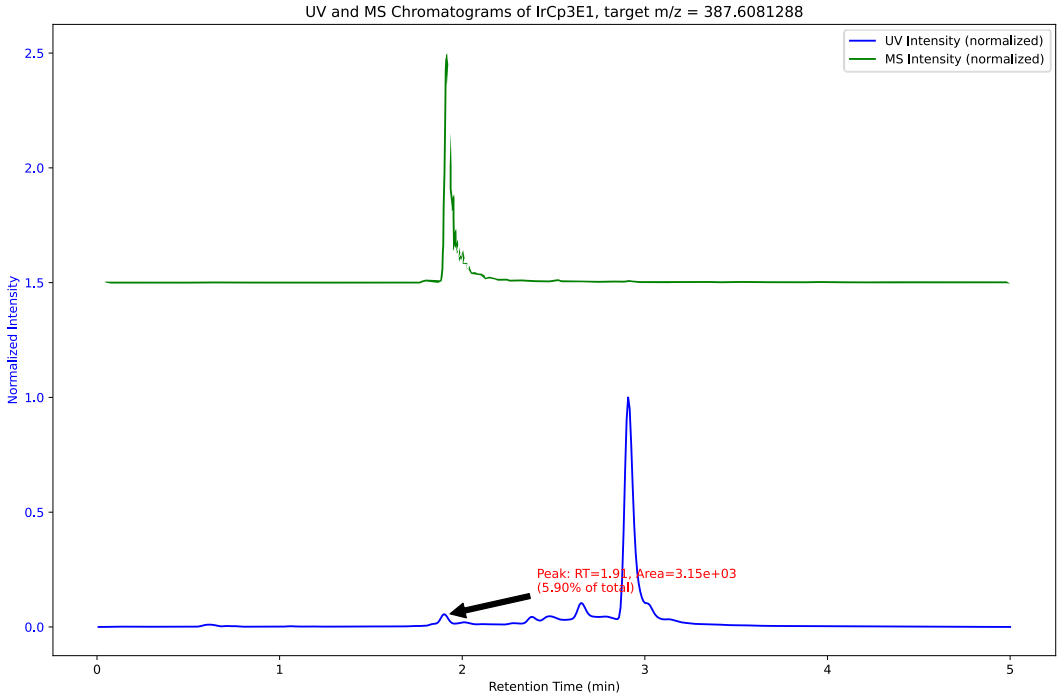


Figure 279. Processed LC-MS spectrum for Ir12 (crude). The lower graph is UV trace at 254 nm, and the upper trace is extracted ion chromatography for the $[(M–Cl)+ MeCN]^{2+}$ ion of the complex.

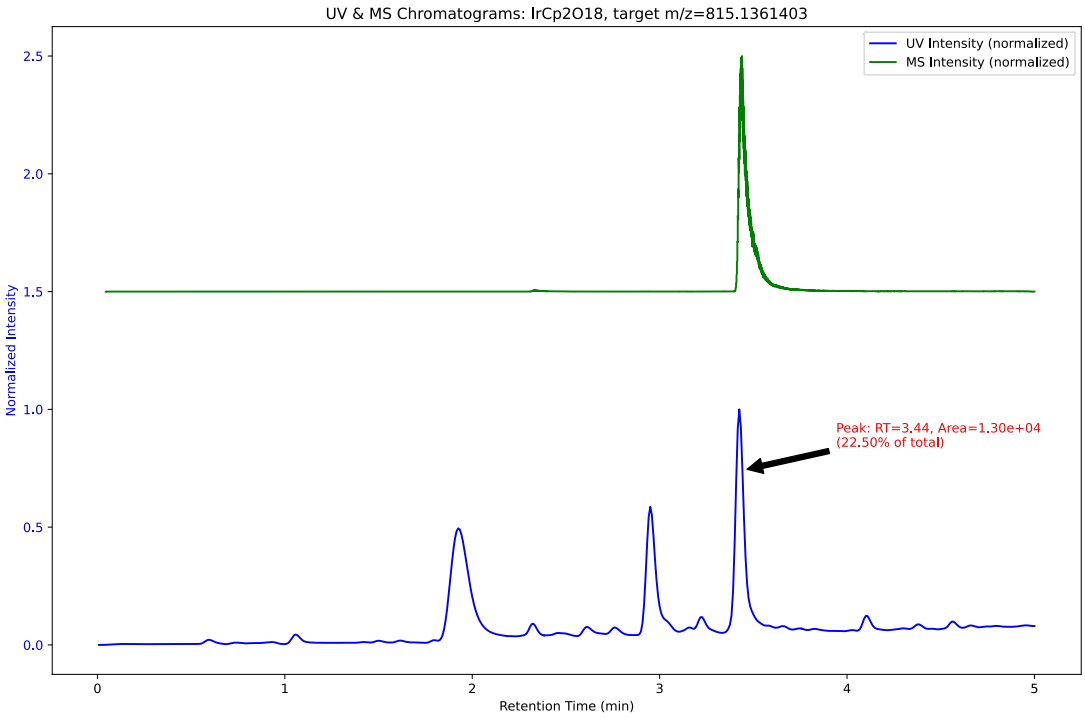


Figure 280. Processed LC-MS spectrum for Ir13 (crude). The lower graph is UV trace at 254 nm, and the upper trace is extracted ion chromatography for the target mass of the complex.

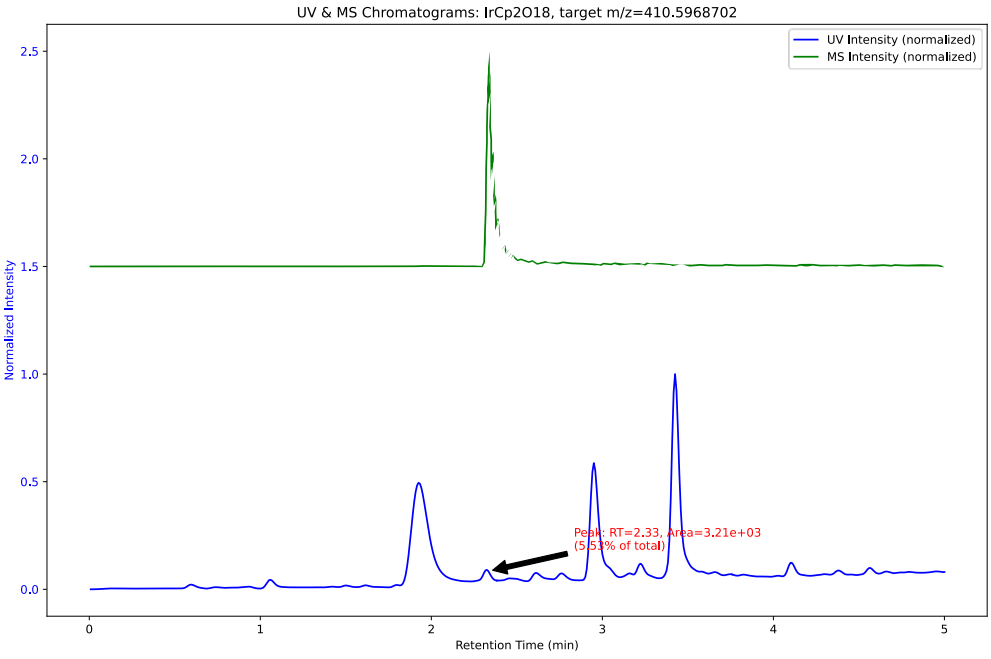


Figure 281. Processed LC-MS spectrum for Ir13 (crude). The lower graph is UV trace at 254 nm, and the upper trace is extracted ion chromatography for the $[(M–Cl)+ MeCN]^{2+}$ ion of the complex.

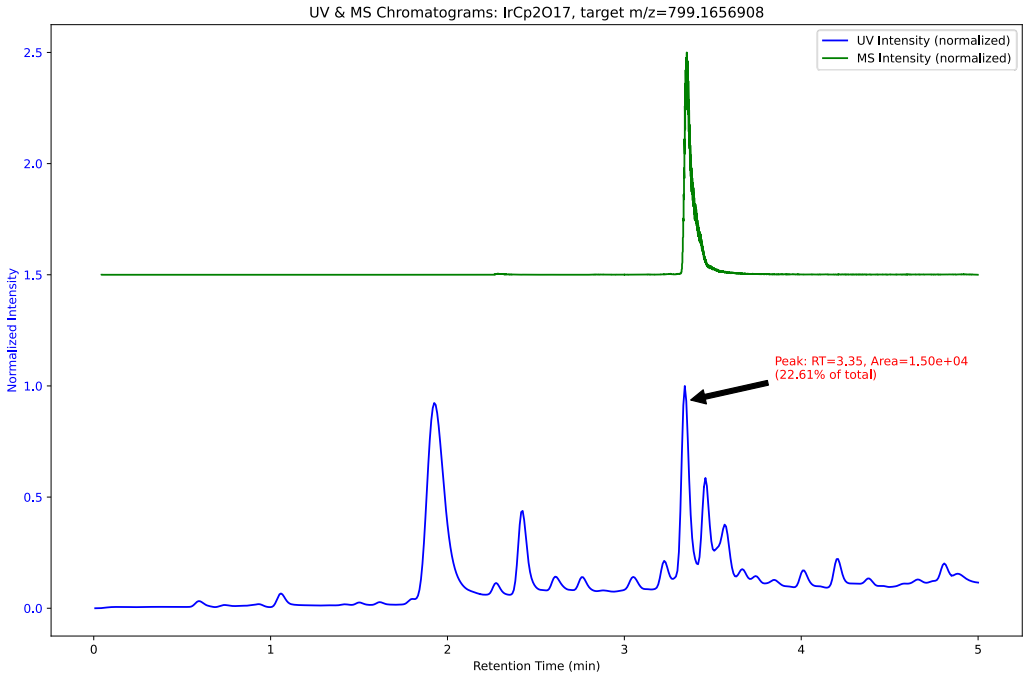


Figure 282. Processed LC-MS spectrum for Ir14 (crude). The lower graph is UV trace at 254 nm, and the upper trace is extracted ion chromatography for the target mass of the complex.

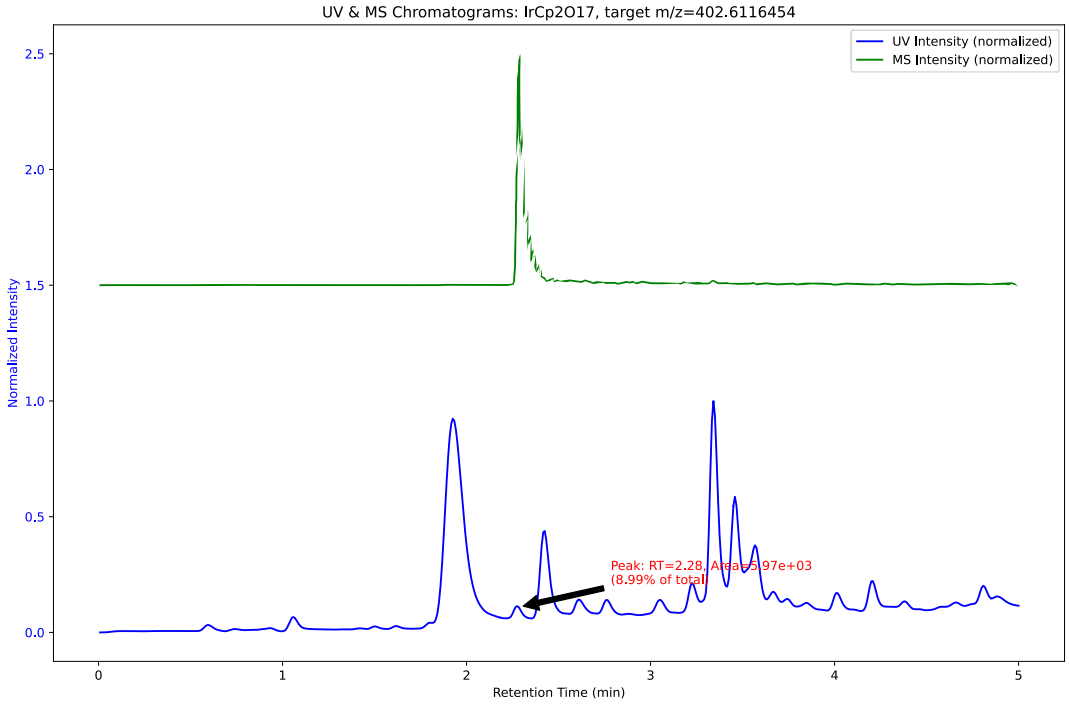


Figure 283. Processed LC-MS spectrum for Ir14 (crude). The lower graph is UV trace at 254 nm, and the upper trace is extracted ion chromatography for the [(M–Cl)+ MeCN]$^{2+}$ ion of the complex.

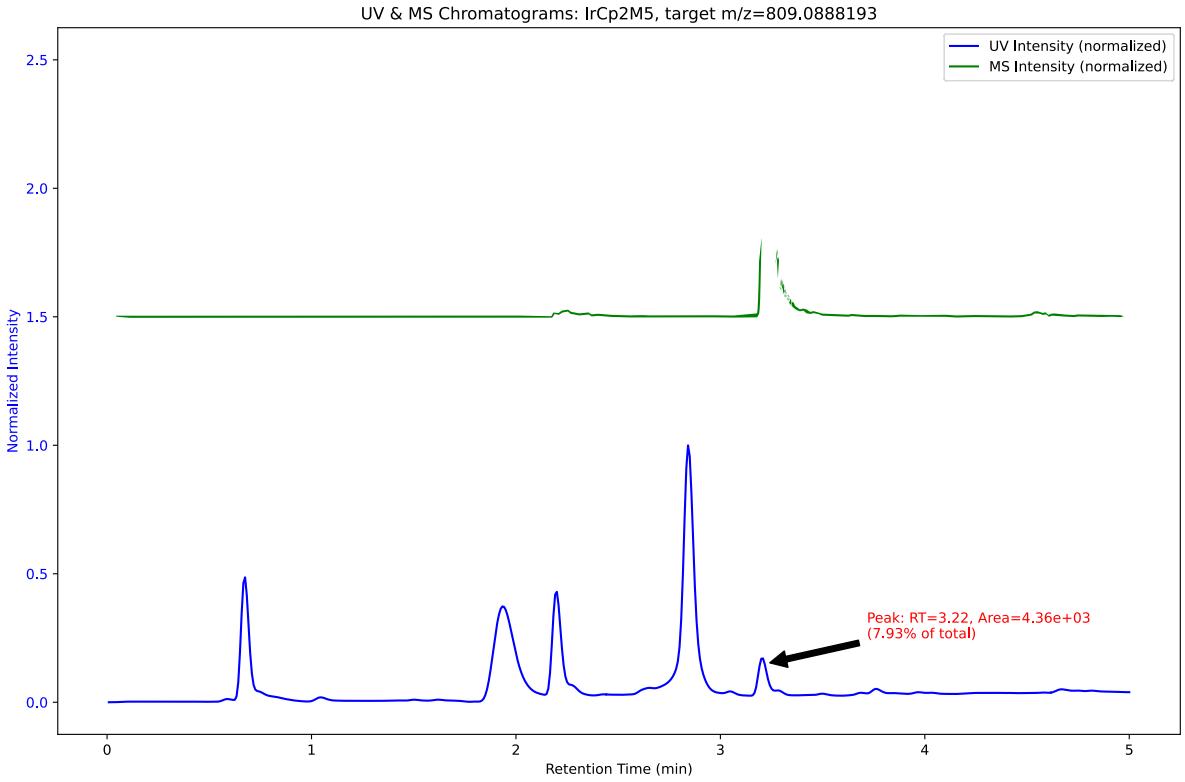


Figure 284. Processed LC-MS spectrum for Ir15 (crude). The lower graph is UV trace at 254 nm, and the upper trace is extracted ion chromatography for the target mass of the complex.

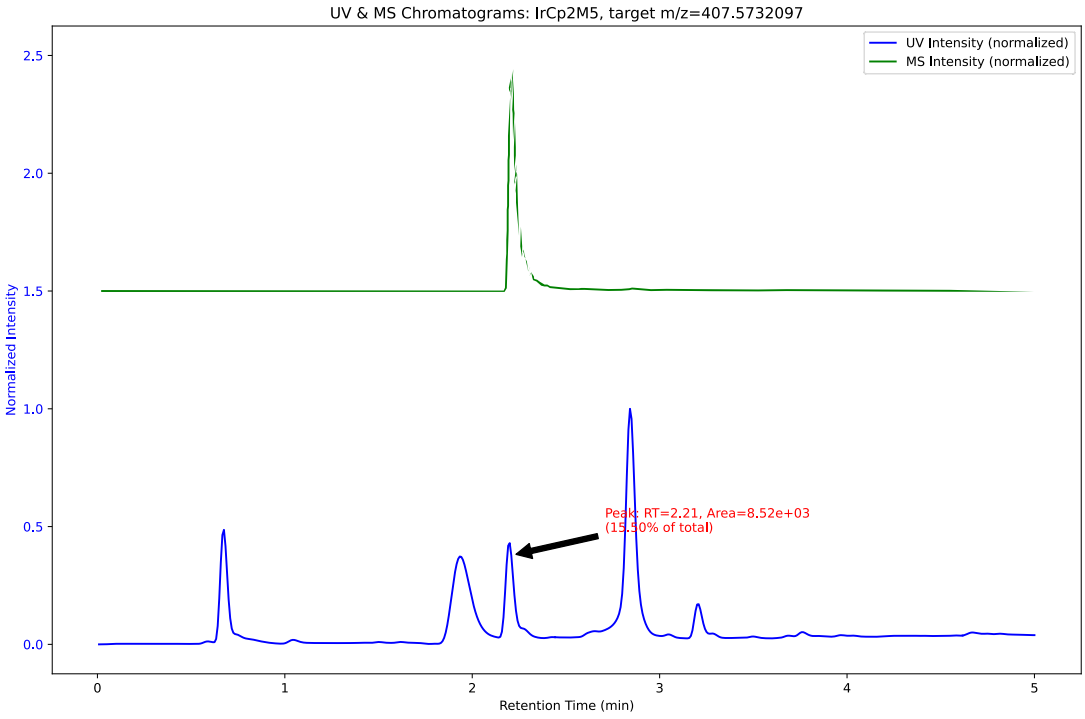


Figure 285. Processed LC-MS spectrum for Ir15 (crude). The lower graph is UV trace at 254 nm, and the upper trace is extracted ion chromatography for the $[(M–Cl)+ MeCN]^{2+}$ ion of the complex.

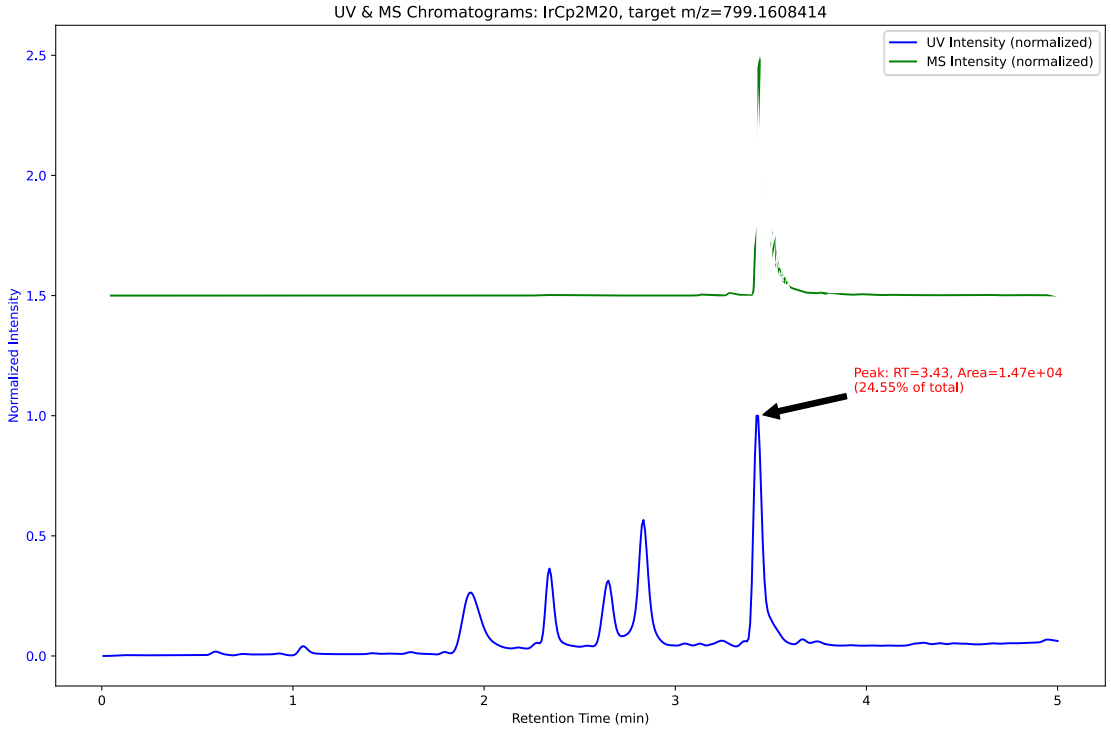


Figure 286. Processed LC-MS spectrum for Ir16 (crude). The lower graph is UV trace at 254 nm, and the upper trace is extracted ion chromatography for the target mass of the complex.

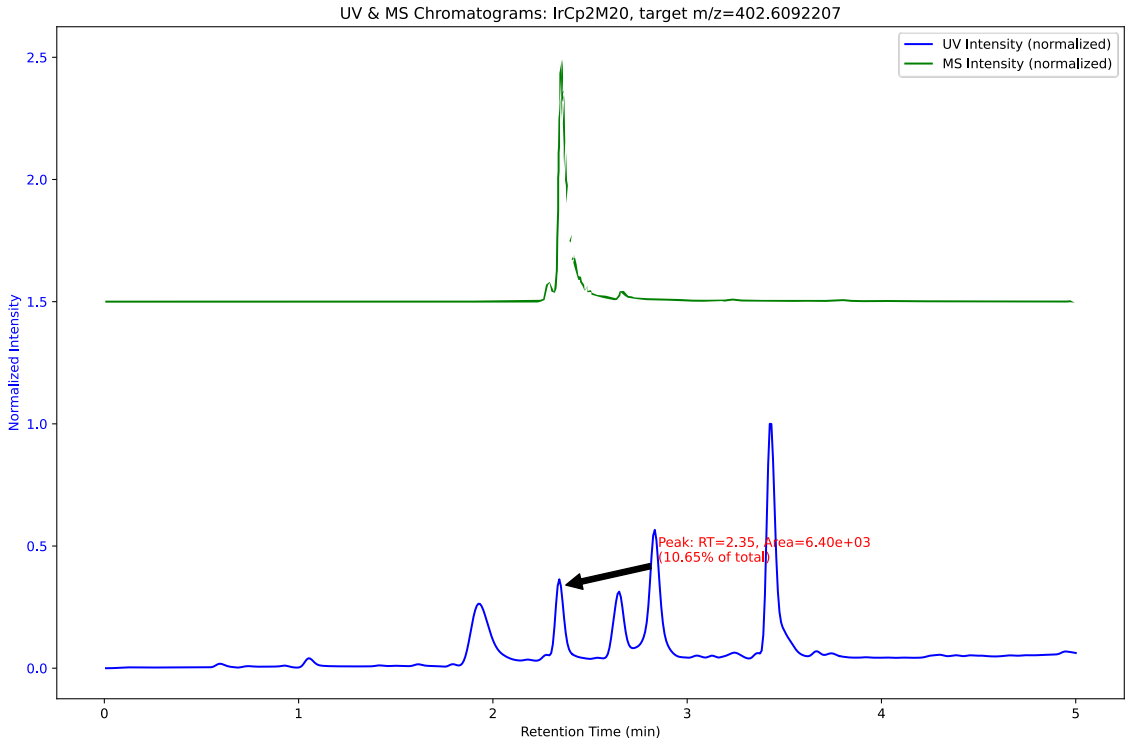


Figure 287. Processed LC-MS spectrum for Ir16 (crude). The lower graph is UV trace at 254 nm, and the upper trace is extracted ion chromatography for the $[(M–Cl)+ MeCN]^{2+}$ ion of the complex.

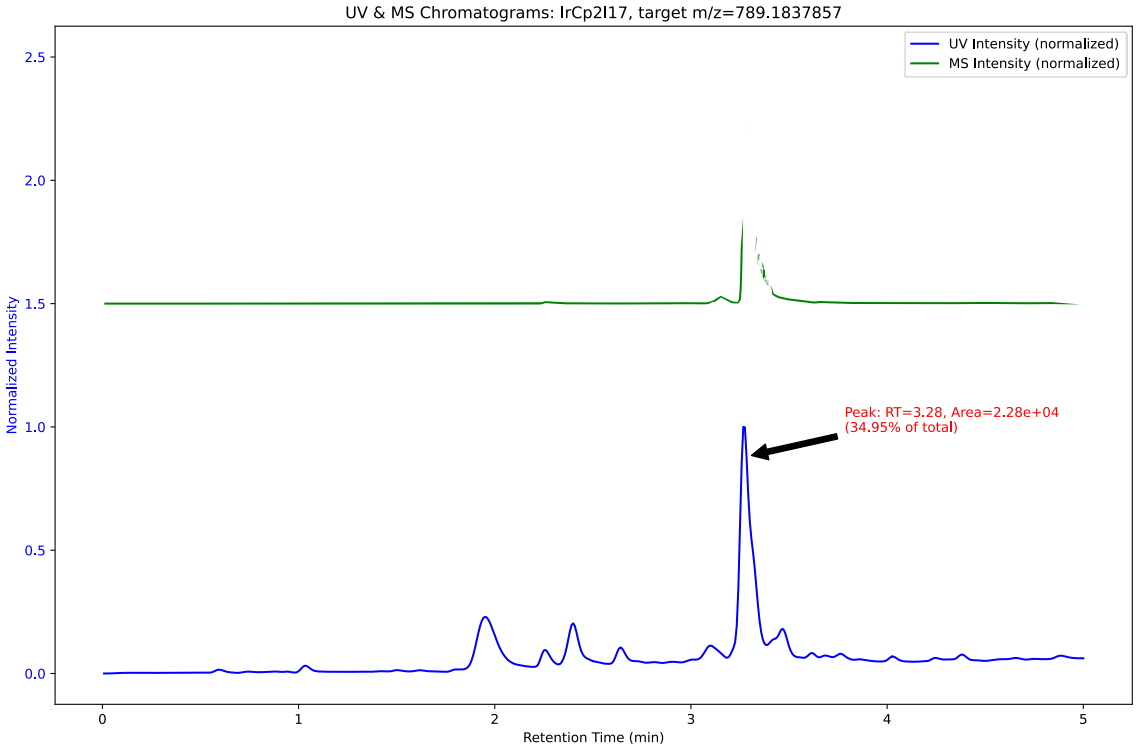


Figure 288. Processed LC-MS spectrum for Ir17 (crude). The lower graph is UV trace at 254 nm, and the upper trace is extracted ion chromatography for the target mass of the complex.

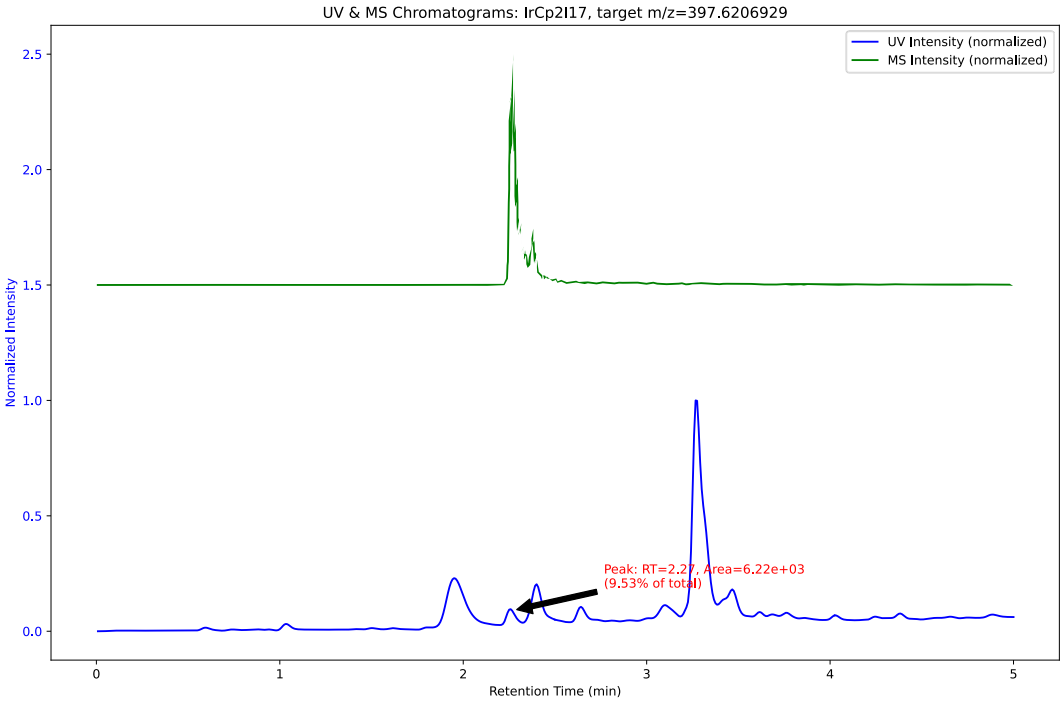


Figure 289. Processed LC-MS spectrum for Ir17 (crude). The lower graph is UV trace at 254 nm, and the upper trace is extracted ion chromatography for the $[(M–Cl)+ MeCN]^{2+}$ ion of the complex.

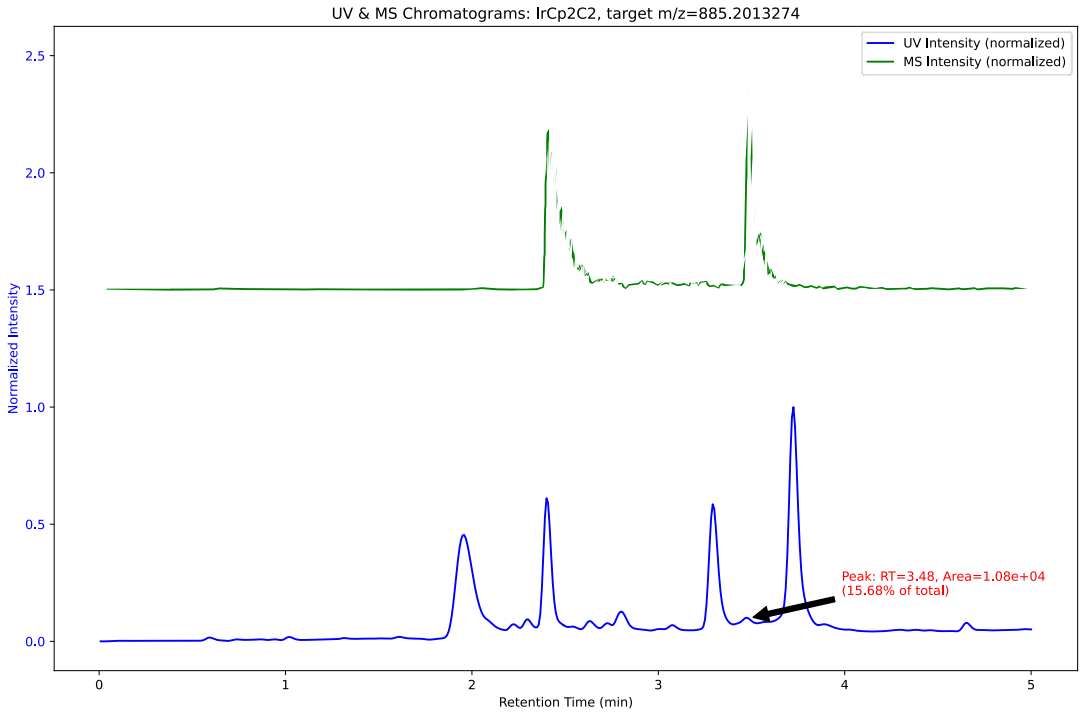


Figure 290. Processed LC-MS spectrum for Ir18 (crude). The lower graph is UV trace at 254 nm, and the upper trace is extracted ion chromatography for the target mass of the complex.

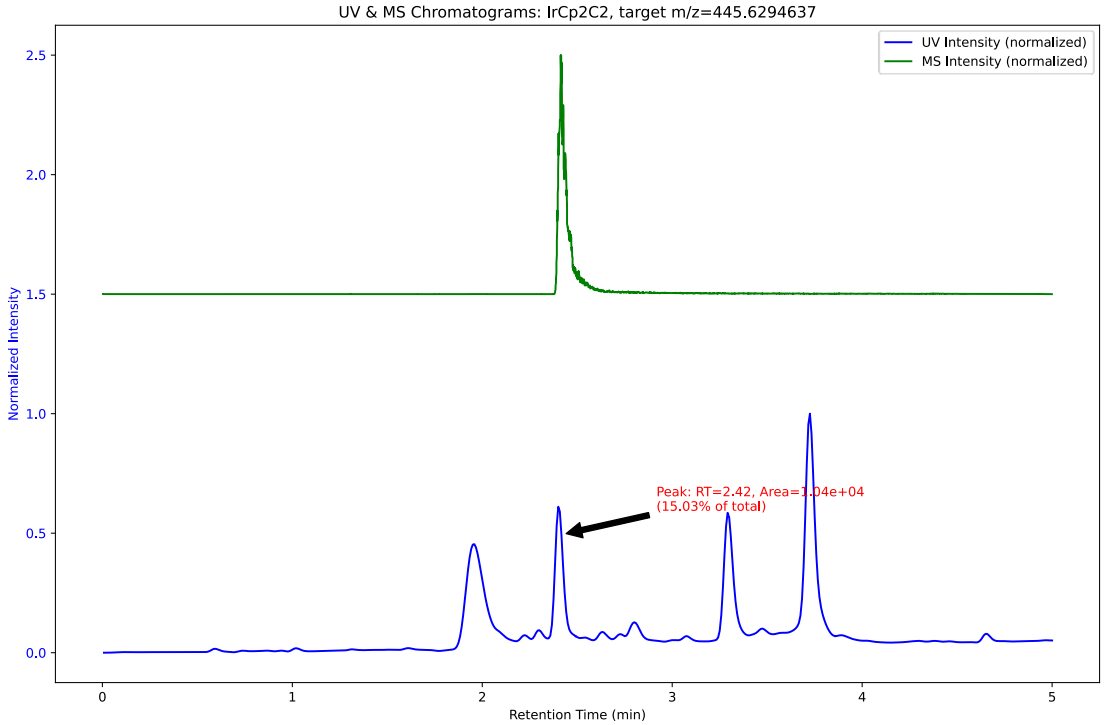


Figure 291. Processed LC-MS spectrum for Ir18 (crude). The lower graph is UV trace at 254 nm, and the upper trace is extracted ion chromatography for the $[(M–Cl)+ MeCN]^{2+}$ ion of the complex.

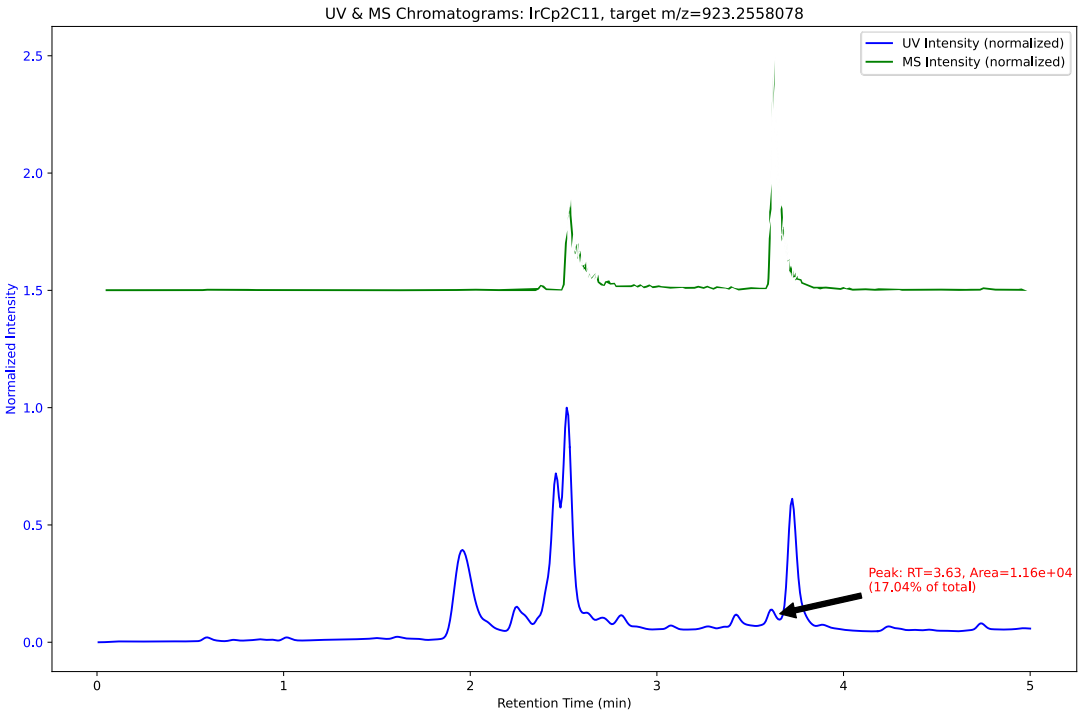


Figure 292. Processed LC-MS spectrum for Ir19 (crude). The lower graph is UV trace at 254 nm, and the upper trace is extracted ion chromatography for the target mass of the complex.

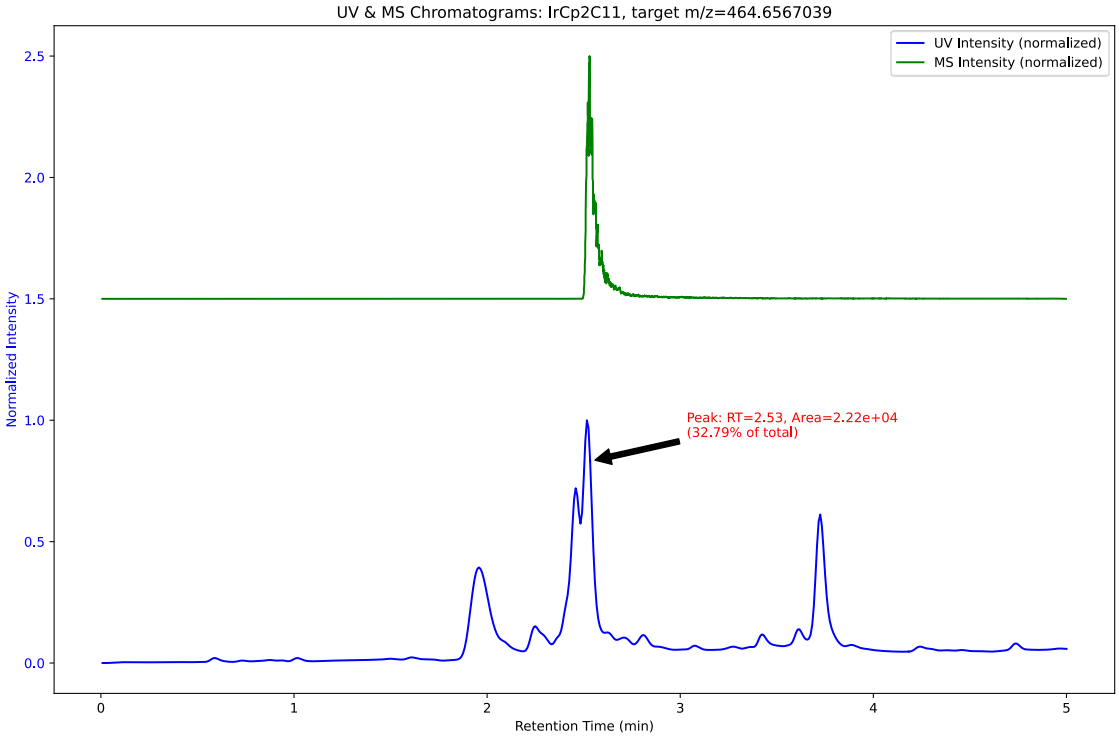


Figure 293. Processed LC-MS spectrum for Ir19 (crude). The lower graph is UV trace at 254 nm, and the upper trace is extracted ion chromatography for the $[(M–Cl)+ MeCN]^{2+}$ ion of the complex.

Chapter 8: Bibliography

1 M. R. J. Salton and K.-S. Kim, in *Medical Microbiology*, ed. S. Baron, University of Texas Medical Branch at Galveston, Galveston (TX), 4th edn., 1996.
2 P. G. Falkowski, T. Fenchel and E. F. Delong, *Science*, 2008, **320**, 1034.
3 R. Sender, S. Fuchs and R. Milo, *PLOS Biology*, 2016, **14**, e1002533.
4 E. Thursby and N. Juge, *Biochem J*, 2017, **474**, 1823.
5 F. A.-Z. Sayed, N. G. Eissa, Y. Shen, D. A. Hunstad, K. L. Wooley and M. Elsabahy, *J. Nanobiotechnology*, 2022, **20**, 536.
6 D. T. Kysela, A. M. Randich, P. D. Caccamo and Y. V. Brun, *PLoS Biol*, 2016, **14**, e1002565.
7 K. D. Young, *Microbiol. and Mol. Biol. Rev.*, 2006, **70**, 660.
8 J. Dworkin, *Mol. Microbiol.*, 2010, **78**, 792.
9 K. D. Young, *Curr. Opin. Microbiol.*, 2007, **10**, 596.
10 N. R. Salama, *Curr. Opin. Microbiol.*, 2020, **54**, 11.
11 R. Coico, *Curr. Protoc. Microbiol.*, 2006, **00**, A.3C.1-A.3C.2.
12 T. J. Silhavy, D. Kahne and S. Walker, *Cold Spring Harb. Perspect. Biol.*, 2010, **2**, a000414.
13 H. Nikaido, *Microbiol. Mol. Biol. Rev.*, 2003, **67**, 593.
14 C. R. H. Raetz and C. Whitfield, *Annu. Rev. Biochem.*, 2002, **71**, 635.
15 K. Sankaran and H. C. Wu, *J. Biol. Chem.*, 1994, **269**, 19701.
16 S. W. Cowan, T. Schirmer, G. Rummel, M. Steiert, R. Ghosh, R. A. Pauptit, J. N. Jansonius and J. P. Rosenbusch, *Nature*, 1992, **358**, 727.
17 A. Arora, D. Rinehart, G. Szabo and L. K. Tamm, *J. Biol. Chem.*, 2000, **275**, 1594.
18 C. Schwechheimer and M. J. Kuehn, *Nat. Rev. Microbiol.*, 2015, **13**, 605.
19 V. Braun, *Biochim. Biophys. Acta*, 1975, **415**, 335.
20 C. W. Mullineaux, A. Nenninger, N. Ray and C. Robinson, *J. Bacteriol.*, 2006, **188**, 3442.
21 F. C. Neuhaus and J. Baddiley, *Microbiol. Mol. Biol. Rev.*, 2003, **67**, 686–723.
22 J. R. Scott and T. C. Barnett, *Annu. Rev. Microbiol.*, 2006, **60**, 397.
23 M. I. Hutchings, A. W. Truman and B. Wilkinson, *Curr. Opin. Microbiol.*, 2019, **51**, 72.
24 P. Ehrlich, *Br. Med. J.*, 1913, **2**, 353.
25 S. Hata, in *Die experimentelle Chemotherapie der Spirillosen: (Syphilis, Rückfallfieber, Hühnerspirillose, Frambösie)*, eds. P. Ehrlich and S. Hata, Springer, Berlin, Heidelberg, 1910, 1.
26 G. Domagk, *Dtsch Med. Wochenschr.*, 1935, **61**, 250.
27 A. Fleming, *Br. J. Exp. Pathol.*, 1929, **10**, 226.
28 E. P. Abraham, E. Chain, C. M. Fletcher, A. D. Gardner, N. G. Heatley, M. A. Jennings and H. W. Florey, *The Lancet*, 1941, **238**, 177.
29 D. C. Hodgkin, *Adv. Sci.*, 1949, **6**, 85.
30 J. Brunel, *J. Hist. Med. Allied. Sci.*, 1951, **VI**, 287.
31 E. E. Hays, I. C. Wells, P. A. Katzman, C. K. Cain, F. A. Jacobs, S. A. Thayer, E. A. Doisy, W. L. Gaby, E. C. Roberts, R. D. Muir, C. J. Carroll, L. R. Jones and N. J. Wade, *J. Biol. Chem.*, 1945, **159**, 725.

32 S. A. Waksman, A. Schatz and D. M. Reynolds, *Ann. N. Y. Acad. Sci.*, 2010, **1213**, 112.
33 H. B. Woodruff, *Appl. Environ. Microbiol.*, 2014, **80**, 2–8.
34 B. Ribeiro da Cunha, L. P. Fonseca and C. R. C. Calado, *Antibiotics (Basel)*, 2019, **8**, 45.
35 E. D. Brown and G. D. Wright, *Nature*, 2016, **529**, 336.
36 R. L. Peck, C. E. Jr. Hoffhine and K. Folkers, *J. Am. Chem. Soc.*, 1946, **68**, 1390.
37 A. A. Adeyemo, O. Oluwatosin and O. O. Omotade, *SpringerPlus*, 2016, **5**, 758.
38 K. M. Overbye and J. F. Barrett, *Drug Discov. Today*, 2005, **10**, 45.
39 S. J. Projan, *Curr. Opin. Microbiol.*, 2003, **6**, 427–430.
40 S. J. Projan and D. M. Shlaes, *Clin. Microbiol. Infect*, 2004, **10**, 18.
41 G. D. Wright, *Nat. Rev. Microbiol.*, 2007, **5**, 175.
42 K. W. K. Tang, B. C. Millar and J. E. Moore, *Br. J. Biomed. Sci.*, 2023, **80**, 11387.
43 M. Naghavi *et al*. *The Lancet*, 2024, **404**, 1199.
44 C. J. L. Murray *et al*. *The Lancet*, 2022, **399**, 629.
45 World Health Organization, Antimicrobial resistance expected to cause 5.2 million deaths in the Western Pacific by 2030, https://www.who.int/westernpacific/news/item/13-06-2023-antimicrobial-resistance-expected-to-cause-5.2-million-deaths-in-the-western-pacific-by-2030, (accessed April 8, 2024).
46 B. Isler, Ş. Keske, M. Aksoy, Ö. K. Azap, M. Yilmaz, S. Ş. Yavuz, G. Aygün, E. Tigen, H. Akalın, A. Azap and Ö. Ergönül, *Clinical Microbiology and Infection*, 2019, **25**, 651.
47 T. P. Van Boeckel, J. Pires, R. Silvester, C. Zhao, J. Song, N. G. Criscuolo, M. Gilbert, S. Bonhoeffer and R. Laxminarayan, *Science*, 2019, **365**, eaaw1944.
48 V. M. D'Costa, C. E. King, L. Kalan, M. Morar, W. W. L. Sung, C. Schwarz, D. Froese, G. Zazula, F. Calmels, R. Debruyne, G. B. Golding, H. N. Poinar and G. D. Wright, *Nature*, 2011, **477**, 457.
49 J. Clardy, M. A. Fischbach and C. R. Currie, *Curr. Biol.*, 2009, **19**, R437.
50 J. M. A. Blair, M. A. Webber, A. J. Baylay, D. O. Ogbolu and L. J. V. Piddock, *Nat. Rev. Microbiol.*, 2015, **13**, 42.
51 S. Kojima and H. Nikaido, *Proc. Natl. Acad. Sci. U.S.A*, 2013, **110**, E2629.
52 Q.-T. Tran, S. Williams, R. Farid, G. Erdemli and R. Pearlstein, *Proteins*, 2013, **81**, 291.
53 Y. Wang, H. Venter and S. Ma, *Current Drug Targets*, 2016, **17**, 702–719.
54 X.-Z. Li, in *Efflux-Mediated Antimicrobial Resistance in Bacteria: Mechanisms, Regulation and Clinical Implications*, eds. X.-Z. Li, C. A. Elkins and H. I. Zgurskaya, Springer International Publishing, Cham, 2016, 131.
55 S. Huber, M. A. Knoll, M. Berktold, R. Würzner, A. Brindlmayer, V. Weber, A. E. Posch, K. Mrazek, S. Lepuschitz, M. Ante, S. Beisken, D. Orth-Höller and J. Weinberger, *Microorganisms*, 2021, **9**, 1023.
56 G. De Pascale and G. D. Wright, *ChemBioChem*, 2010, **11**, 1325.
57 M. S. Ramirez and M. E. Tolmasky, *Drug Resist. Updat.*, 2010, **13**, 151.

58 E. Bordeleau, P. J. Stogios, E. Evdokimova, K. Koteva, A. Savchenko and G. D. Wright, *mBio*, 2021, **12**, e02705-20.
59 J. Szychowski, J. Kondo, O. Zahr, K. Auclair, E. Westhof, S. Hanessian and J. W. Keillor, *ChemMedChem*, 2011, **6**, 1961.
60 A. S. Bayer, T. Schneider and H.-G. Sahl, *Ann. N. Y. Acad. Sci.*, 2013, **1277**, 139.
61 L. Cui, H. Murakami, K. Kuwahara-Arai, H. Hanaki and K. Hiramatsu, *Antimicrob. Agents Chemother.*, 2000, **44**, 2276.
62 L. Cui, X. Ma, K. Sato, K. Okuma, F. C. Tenover, E. M. Mamizuka, C. G. Gemmell, M.-N. Kim, M.-C. Ploy, N. El Solh, V. Ferraz and K. Hiramatsu, *J Clin Microbiol*, 2003, **41**, 5.
63 N. N. Mishra and A. S. Bayer, *Antimicrob. Agents Chemother.*, 2013, **57**, 1082.
64 S.-J. Yang, N. N. Mishra, A. Rubio and A. S. Bayer, *Antimicrob. Agents Chemother.*, 2013, **57**, 5658.
65 C. L. Tooke, P. Hinchliffe, E. C. Bragginton, C. K. Colenso, V. H. A. Hirvonen, Y. Takebayashi and J. Spencer, *J. Mol. Bio.*, 2019, **431**, 3472.
66 T. Naas, S. Oueslati, R. A. Bonnin, M. L. Dabos, A. Zavala, L. Dortet, P. Retailleau and B. I. Iorga, *J. Enzyme Inhib. Med. Chem.*, 2017, **32**, 917.
67 K. J. Forsberg, S. Patel, T. A. Wencewicz and G. Dantas, *Chem. Biol.*, 2015, **22**, 888.
68 E. M. Darby, E. Trampari, P. Siasat, M. S. Gaya, I. Alav, M. A. Webber and J. M. A. Blair, *Nat. Rev. Microbiol.*, 2023, **21**, 280.
69 W. Yang, I. F. Moore, K. P. Koteva, D. C. Bareich, D. W. Hughes and G. D. Wright, *J. Biol. Chem.*, 2004, **279**, 52346.
70 J. Sharma, D. Sharma, A. Singh and K. Sunita, *Can. J. Infect. Dis. Med. Microbiol.*, 2022, **2022**, 1.
71 H. Sati, E. Carrara, A. Savoldi, P. Hansen, J. Garlasco, E. Campagnaro, S. Boccia, J. A. Castillo-Polo, E. Magrini, P. Garcia-Vello, E. Wool, V. Gigante, E. Duffy, A. Cassini, B. Huttner, P. R. Pardo, M. Naghavi, F. Mirzayev, M. Zignol, A. Cameron, E. Tacconelli, and WHO Bacterial Priority Pathogens List Advisory Group, *Lancet Infect. Dis.*, 2025, **25**, 1033.
72 P. Rajput, K. S. Nahar and K. M. Rahman, *Antibiotics*, 2024, **13**, 1197.
73 E. Mühlberg, F. Umstätter, C. Kleist, C. Domhan, W. Mier and P. Uhl, *Can. J. Microbiol.*, 2020, **66**, 11.
74 N. T. U. Inc, Nabriva Therapeutics Announces European Medicines Agency (EMA) Validation of Marketing Authorization Application for Lefamulin, https://www.globenewswire.com/news-release/2019/06/24/1873292/37424/en/Nabriva-Therapeutics-Announces-European-Medicines-Agency-EMA-Validation-of-Marketing-Authorization-Application-for-Lefamulin.html, (accessed March 23, 2026).
75 S. Hu, H. Yu and J. Gao, *Drug Discov Ther*, 2025, **19**, 129–130.
76 O. of the Commissioner, FDA Approves Two Oral Therapies to Treat Gonorrhea, https://www.fda.gov/news-events/press-announcements/fda-approves-two-oral-therapies-treat-gonorrhea, (accessed July 7, 2026).
77 G. Gasser, *Chimia*, 2015, **69**, 442.
78 A. Frei, *Antibiotics*, 2020, **9**, 90.

79 T. C. Johnstone, G. Y. Park and S. J. Lippard, *Anticancer Res.*, 2014, **34**, 471.
80 K. Alimoghaddam, *Int. J. Hematol. Oncol. Stem Cell Res.*, 2014, **8**, 44.
81 E. Kanal, *Magn. Reson. Imaging*, 2016, **34**, 1341.
82 E. National Academies of Sciences, D. on E. and L. Studies and N. and R. S. Board, in *Opportunities and Approaches for Supplying Molybdenum-99 and Associated Medical Isotopes to Global Markets: Proceedings of a Symposium*, National Academies Press (US), 2018.
83 O. of the Commissioner, FDA Approves First Treatment for Children With Menkes Disease, https://www.fda.gov/news-events/press-announcements/fda-approves-first-treatment-children-menkes-disease, (accessed July 9, 2026).
84 Theralase® Technologies Inc., *A Phase II Clinical Study of Intravesical Ruvidar® in Patients With BCG-Unresponsive Non-Muscle Invasive Bladder Cancer ("NMIBC") Carcinoma In-Situ ("CIS") or Patients Who Are Intolerant to BCG Therapy ("Study II")*, clinicaltrials.gov, 2025.
85 C. Biot, G. Glorian, L. A. Maciejewski, J. S. Brocard, O. Domarle, G. Blampain, P. Millet, A. J. Georges, H. Abessolo, D. Dive and J. Lebibi, *J. Med. Chem.*, 1997, **40**, 3715.
86 Zydus Lifesciences Limited, *Phase Ib, Single-center, Randomized, Study to Determine Safety, Tolerability, and Pharmacokinetics of Different Orally Administered Regimens of the Combination ZY19489-Ferroquine in Adult Asymptomatic Plasmodium Falciparum Carriers*, clinicaltrials.gov, 2024.
87 R. Desai, *A Phase 0 Clinical Trial of Oral Gallium Maltolate for Recurrent Glioblastoma*, clinicaltrials.gov, 2026.
88 GE Healthcare, *A Prospective, Multicenter Phase 2/3 Study to Assess the Efficacy and Safety of Mangaciclanol in Adult Patients With Known or Highly Suspected Lesions Referred for Contrast-Enhanced Magnetic Resonance Imaging (MRI) of Central Nervous System (CNS) or Body (LUMINA)*, clinicaltrials.gov, 2026.
89 M. S. Butler, I. R. Henderson, R. J. Capon and M. A. T. Blaskovich, *J. Antibiot.*, 2023, **76**, 431.
90 C. A. Lipinski, F. Lombardo, B. W. Dominy and P. J. Feeney, *Adv. Drug Delivery Rev.*, 1997, **23**, 3.
91 M. A. Cooper, *Nat. Rev. Drug Discov.*, 2015, **14**, 587.
92 A. Frei, J. Zuegg, A. G. Elliott, M. Baker, S. Braese, C. Brown, F. Chen, C. G. Dowson, G. Dujardin, N. Jung, A. P. King, A. M. Mansour, M. Massi, J. Moat, H. A. Mohamed, A. K. Renfrew, P. J. Rutledge, P. J. Sadler, M. H. Todd, C. E. Willans, J. J. Wilson, M. A. Cooper and M. A. T. Blaskovich, *Chem. Sci.*, 2020, **11**, 2627.
93 F. Lovering, J. Bikker and C. Humblet, *J. Med. Chem.*, 2009, **52**, 6752.
94 G. Gasser and N. Metzler-Nolte, *Curr. Opin. Chem. Biol.*, 2012, **16**, 84.
95 C. N. Morrison, K. E. Prosser, R. W. Stokes, A. Cordes, N. Metzler-Nolte and S. M. Cohen, *Chem. Sci.*, 2020, **11**, 1216.
96 A. W. Hung, A. Ramek, Y. Wang, T. Kaya, J. A. Wilson, P. A. Clemons and D. W. Young, *Proc. Natl. Acad. Sci. U.S.A.*, 2011, **108**, 6799.
97 M. Ishikawa and Y. Hashimoto, *J. Med. Chem.*, 2011, **54**, 1539.
98 A. Pandey and E. Boros, *Chem. - Eur. J.*, 2021, **27**, 7340.

99 F. P. Dwyer, E. C. Gyarfas, W. P. Rogers and J. H. Koch, *Nature*, 1952, **170**, 190.
100 M. Patra, G. Gasser, D. Bobukhov, K. Merz, A. V. Shtemenko and N. Metzler-Nolte, *Dalton Trans.*, 2010, **39**, 5617.
101 M. Wenzel and J. E. Bandow, *Proteomics*, 2011, **11**, 3256.
102 M. Wenzel, M. Patra, C. H. R. Senges, I. Ott, J. J. Stepanek, A. Pinto, P. Prochnow, C. Vuong, S. Langklotz, N. Metzler-Nolte and J. E. Bandow, *ACS Chem. Biol.*, 2013, **8**, 1442.
103 M. Patra, M. Wenzel, P. Prochnow, V. Pierroz, G. Gasser, J. E. Bandow and N. Metzler-Nolte, *Chem. Sci.*, 2014, **6**, 214.
104 A. Noor, G. S. Huff, S. V. Kumar, J. E. M. Lewis, B. M. Paterson, C. Schieber, P. S. Donnelly, H. J. L. Brooks, K. C. Gordon, S. C. Moratti and J. D. Crowley, *Organometallics*, 2014, **33**, 7031.
105 C. Wandersman and P. Delepelaire, *Proc. Natl. Acad. Sci. U.S.A.*, 1990, **87**, 4776.
106 D. Zeng, J. Zhao, H. S. Chung, Z. Guan, C. R. H. Raetz and P. Zhou, *J. Biol. Chem.*, 2013, **288**, 5475.
107 A. Frei, M. Amado, M. A. Cooper and M. A. T. Blaskovich, *Chem. Eur. J.*, 2020, **26**, 2852.
108 S. N. Sovari, N. Radakovic, P. Roch, A. Crochet, A. Pavic and F. Zobi, *Eur. J. Med. Chem.*, 2021, **226**, 113858.
109 S. M. Cooper, C. Siakalli, A. J. P. White, A. Frei, P. W. Miller and N. J. Long, *Dalton Trans.*, 2022, **51**, 12791.
110 G. Demirci, Y. Cortat, A. Crochet, E. Calia, S. G. Sprecher and F. Zobi, *Dalton Trans.*, 2026, **55**, 10068.
111 S. S. Mendes, J. Marques, E. Mesterházy, J. Straetener, M. Arts, T. Pissarro, J. Reginold, A. Berscheid, J. Bornikoel, R. M. Kluj, C. Mayer, F. Oesterhelt, S. Friães, B. Royo, T. Schneider, H. Brötz-Oesterhelt, C. C. Romão and L. M. Saraiva, *ACS Bio. Med. Chem. Au*, 2022, **2**, 419.
112 C. C. Romão, S. S. Mendes, C. Rebelo, S. M. Carvalho and L. M. Saraiva, *Dalton Trans.*, 2024, **53**, 11009.
113 E. R. Serrano, P. M. David Gara, J. J. Martínez Medina, F. Prencipe, O. E. Piro, G. A. Echeverría, G. Petroselli, T. Da Ros and G. T. Ruiz, *J. Inorg. Biochem.*, 2026, **276**, 113178.
114 S. Fulgencio, M. Scaccaglia and A. Frei, *ChemBioChem*, 2024, **25**, e202400435.
115 F. Li, J. G. Collins and F. R. Keene, *Chem. Soc. Rev.*, 2015, **44**, 2529–2542.
116 K. Ashwini Kumar, K. L. Reddy, S. Vidhisha and S. Satyanarayana, *Appl. Organomet. Chem.*, 2009, **23**, 409.
117 A. K. Gorle, M. Feterl, J. M. Warner, L. Wallace, F. R. Keene and J. G. Collins, *Dalton Trans.*, 2014, **43**, 16713.
118 P.-Y. Ho, T. W. Rees, M. A. Phillips, E. Jin, E. Christodoulou, A. G. Purkiss, S. Mouilleron, C. K. Hind, M. Kintzel, Y. M. Yip, A. Pasquier, O.-R. Song, I. Gameiro-Ros, S. Warchal, M. Sopena, B. Wu, V. I. Enne, M. Jiang, J. Redmond, M. Howell, J. M. Sutton, S. Kjær, D. Evangelopoulos and J. Hess, ChemRxiv, 2026 .
119 B. James, S. D. Fairbanks, M. Horton, J. A. Thomas, S. McLean and A. M. Varney, *ACS Omega*, 2026, **11**, 37874.

120 S. V. Kumar, S. Ø. Scottwell, E. Waugh, C. J. McAdam, L. R. Hanton, H. J. L. Brooks and J. D. Crowley, *Inorg. Chem.*, 2016, **55**, 9767–9777.
121 P.-L. Lam, G.-L. Lu, K.-M. Hon, K.-W. Lee, C.-L. Ho, X. Wang, J. C.-O. Tang, K.-H. Lam, R. S.-M. Wong, S. H.-L. Kok, Z.-X. Bian, H. Li, K. K.-H. Lee, R. Gambari, C.-H. Chui and W.-Y. Wong, *Dalton Trans.*, 2014, **43**, 3949.
122 F. Li, M. Feterl, Y. Mulyana, J. M. Warner, J. G. Collins and F. R. Keene, *J. Antimicrob. Chemother.*, 2012, **67**, 2686.
123 F. Li, Y. Mulyana, M. Feterl, J. M. Warner, J. G. Collins and F. R. Keene, *Dalton Trans.*, 2011, **40**, 5032.
124 S. McLean, R. Begg, H. E. Jesse, B. E. Mann, G. Sanguinetti and R. K. Poole, *Antioxid. Redox Signal.*, 2013, **19**, 1999.
125 M. Orsi, B. Shing Loh, C. Weng, W. H. Ang and A. Frei, *Angew. Chem. Int. Ed.*, 2024, **63**, e202317901.
126 M. Pandrala, F. Li, M. Feterl, Y. Mulyana, J. M. Warner, L. Wallace, F. R. Keene and J. G. Collins, *Dalton Trans.*, 2013, **42**, 4686.
127 K. L. Smitten, S. D. Fairbanks, C. C. Robertson, J. B. de la Serna, S. J. Foster and J. A. Thomas, *Chem. Sci.*, 2019, **11**, 70.
128 K. L. Smitten, E. J. Thick, H. M. Southam, J. B. de la Serna, S. J. Foster and J. A. Thomas, *Chem. Sci.*, 2020, **11**, 8828.
129 P. Srivastava, M. Shukla, G. Kaul, S. Chopra and A. K. Patra, *Dalton Trans.*, 2019, **48**, 11822.
130 L. Stevens-Cullinane, T. W. Rees, C. Evans, P.-Y. Ho, M. Kintzel, Y. M. Yip, R. Jia, J. Bailey, E. Clifford, R. Alam, S. Maslen, S. Mouilleron, A. Pasquier, O.-R. Song, S. Warchal, J. Redmond, M. Howell, S. Kjær, M. Skehel, M. M. Müller, E. O. Johnson, M. M. Roessler and J. Hess, *J. Am. Chem. Soc.*, 2025, **147**, 44860.
131 A. M. Varney, K. L. Smitten, J. A. Thomas and S. McLean, *ACS Pharmacol. Transl. Sci.*, 2021, **4**, 168.
132 Z. ChunYan, Y. RuJian, W. LiQiang, H. HaiYan, W. JinTao, L. XiangWen, D. XueMin and X. YanShi, *Eur. J. Med. Chem.*, 2022, **240**, 114562.
133 K. L. Smitten, H. M. Southam, J. B. de la Serna, M. R. Gill, P. J. Jarman, C. G. W. Smythe, R. K. Poole and J. A. Thomas, *ACS Nano*, 2019, **13**, 5133.
134 A. Frei, A. D. Verderosa, A. G. Elliott, J. Zuegg and M. A. T. Blaskovich, *Nat. Rev. Chem.*, 2023, **7**, 202.
135 F. Li, E. J. Harry, A. L. Bottomley, M. D. Edstein, G. W. Birrell, C. E. Woodward, F. R. Keene and J. G. Collins, *Chem. Sci.*, 2014, **5**, 685.
136 A. M. Varney, K. L. Smitten, H. M. Southam, S. D. Fairbanks, C. C. Robertson, J. A. Thomas and S. McLean, *ACS Infect. Dis.*, 2024, **10**, 3346.
137 W. R. Miller and C. A. Arias, *Nat. Rev. Microbiol.*, 2024, **22**, 598.
138 A. Y. Chen, P. W. Thomas, A. C. Stewart, A. Bergstrom, Z. Cheng, C. Miller, C. R. Bethel, S. H. Marshall, C. V. Credille, C. L. Riley, R. C. Page, R. A. Bonomo, M. W. Crowder, D. L. Tierney, W. Fast and S. M. Cohen, *J. Med. Chem.*, 2017, **60**, 7267.
139 X. Huang and V. M. Dixit, *Cell Res.*, 2016, **26**, 484.

140 F. Wagenlehner, C. R. Perry, T. M. Hooton, N. E. Scangarella-Oman, H. Millns, M. Powell, E. Jarvis, J. Dennison, A. Sheets, D. Butler, J. Breton and S. Janmohamed, *The Lancet*, 2024, **403**, 741.
141 J. D. C. Ross, J. Wilson, K. A. Workowski, S. N. Taylor, D. A. Lewis, S. Gatsi, W. Flight, N. E. Scangarella-Oman, C. Jakielaszek, D. Lythgoe, M. Powell, S. Janmohamed, J. Absalon and C. Perry, *The Lancet*, 2025, **405**, 1608.
142 B. D. Bax, P. F. Chan, D. S. Eggleston, A. Fosberry, D. R. Gentry, F. Gorrec, I. Giordano, M. M. Hann, A. Hennessy, M. Hibbs, J. Huang, E. Jones, J. Jones, K. K. Brown, C. J. Lewis, E. W. May, M. R. Saunders, O. Singh, C. E. Spitzfaden, C. Shen, A. Shillings, A. J. Theobald, A. Wohlkonig, N. D. Pearson and M. N. Gwynn, *Nature*, 2010, **466**, 935.
143 A. Kolarič, T. Germe, M. Hrast, C. E. M. Stevenson, D. M. Lawson, N. P. Burton, J. Vörös, A. Maxwell, N. Minovski and M. Anderluh, *Nat. Commun.*, 2021, **12**, 150.
144 H. Song, J. T. Kaiser and J. K. Barton, *Nature Chem.*, 2012, **4**, 615.
145 A. E. Friedman, J. C. Chambron, J. P. Sauvage, N. J. Turro and J. K. Barton, *J. Am. Chem. Soc.*, 1990, **112**, 4960.
146 G. W. Kaatz and S. M. Seo, *Antimicrob. Agents Chemother.*, 1995, **39**, 2650.
147 D. N. Brawley, D. B. Sauer, J. Li, X. Zheng, A. Koide, G. S. Jedhe, T. Suwatthee, J. Song, Z. Liu, P. S. Arora, S. Koide, V. J. Torres, D.-N. Wang and N. J. Traaseth, *Nat. Chem. Biol.*, 2022, **18**, 706.
148 G. W. Kaatz, S. M. Seo, L. O'Brien, M. Wahiduzzaman and T. J. Foster, *Antimicrob. Agents Chemother.*, 2000, **44**, 1404.
149 J. R. Aeschlimann, G. W. Kaatz and M. J. Rybak, *J. Antimicrob. Chemother.*, 1999, **44**, 343.
150 B. A. Eijkelkamp, J. R. Morey, M. P. Ween, C. Y. Ong, A. G. McEwan, J. C. Paton and C. A. McDevitt, *PLoS One*, 2014, **9**, e89427.
151 K. M. Papp-Wallace and M. E. Maguire, *Annu. Rev. Microbiol.*, 2006, **60**, 187.
152 S. Friães, C. Trigueiros, C. S. B. Gomes, A. R. Fernandes, O. A. Lenis-Rojas, M. Martins and B. Royo, *Molecules*, 2023, **28**, 7453.
153 Y. Lai, L. Wang, H. Ma, Z. Chen, H. Wu, G. Wen, X. Wu, B. Yu, D. Li, G. Yuan, H. Huang and P. Zhang, *J. Am. Chem. Soc.*, 2025, **147**, 19353.
154 N. Rana, H. E. Jesse, M. Tinajero-Trejo, J. A. Butler, J. D. Tarlit, M. L. von und zur Muhlen, C. Nagel, U. Schatzschneider and R. K. Poole, *Microbiology*, 2017, **163**, 1477.
155 P. V. Simpson, C. Nagel, H. Bruhn and U. Schatzschneider, *Organometallics*, 2015, **34**, 3809.
156 M. Tinajero-Trejo, N. Rana, C. Nagel, H. E. Jesse, T. W. Smith, L. K. Wareham, M. Hippler, U. Schatzschneider and R. K. Poole, *Antioxid. Redox Signal*, 2016, **24**, 765.
157 P. Güntzel, C. Nagel, J. Weigelt, J. W. Betts, C. A. Pattrick, H. M. Southam, R. M. La Ragione, R. K. Poole and U. Schatzschneider, *Metallomics*, 2019, **11**, 2033.
158 A. Liakopoulos, R. M. La Ragione, C. Nagel, U. Schatzschneider, D. E. Rozen and J. W. Betts, *J. Glob. Antimicrob. Resist.*, 2020, **22**, 594.

159 C. Nagel, S. McLean, R. K. Poole, H. Braunschweig, T. Kramer and U. Schatzschneider, *Dalton Trans.*, 2014, **43**, 9986.
160 J. S. Ward, R. Morgan, J. M. Lynam, I. J. S. Fairlamb and J. W. B. Moir, *Medchemcomm*, 2017, **8**, 346.
161 M. Scaccaglia, M. P. Birbaumer, S. Pinelli, G. Pelosi and A. Frei, *Chem. Sci.*, 2024, **15**, 3907.
162 R. Motterlini and L. E. Otterbein, *Nat Rev Drug Discov*, 2010, **9**, 728.
163 E. Kwon, D. Y. Kim, C. A. Gross, J. D. Gross and K. K. Kim, *Protein Sci.*, 2010, **19**, 2252.
164 S. C. Andrews, A. K. Robinson and F. Rodríguez-Quiñones, *FEMS Microbiol. Rev.*, 2003, **27**, 215.
165 S. Hijazi, D. Visaggio, M. Pirolo, E. Frangipani, L. Bernstein and P. Visca, *Front. Cell. Infect. Microbiol.*, 2018, **8**, 316.
166 Y. Kaneko, M. Thoendel, O. Olakanmi, B. E. Britigan and P. K. Singh, *J Clin Invest*, 2007, **117**, 877.
167 E. Banin, A. Lozinski, K. M. Brady, E. Berenshtein, P. W. Butterfield, M. Moshe, M. Chevion, E. P. Greenberg and E. Banin, *Proc. Natl. Acad. Sci. U.S.A.*, 2008, **105**, 16761.
168 C. Bonchi, F. Imperi, F. Minandri, P. Visca and E. Frangipani, *BioFactors*, 2014, **40**, 303.
169 S. Choi, B. E. Britigan and P. Narayanasamy, *ACS Infect. Dis.*, 2019, **5**, 1559.
170 A. Pandey, C. Savino, S. H. Ahn, Z. Yang, S. G. Van Lanen and E. Boros, *J. Med. Chem.*, 2019, **62**, 9947.
171 T. J. Sanderson, C. M. Black, J. W. Southwell, E. J. Wilde, A. Pandey, R. Herman, G. H. Thomas, E. Boros, A.-K. Duhme-Klair and A. Routledge, *ACS Infect. Dis.*, 2020, **6**, 2532.
172 A. Pandey, D. Śmiłowicz and E. Boros, *Chem. Sci.*, 2021, **12**, 14546.
173 A. Marlin, M. Cao, J. E. Hamouche, O. Glaser and E. Boros, *Chem. Sci.*, 2025, **16**, 7039.
174 S. Choi, G. A. Talmon, K. Hearne, J. Woo, V. L. Truong, B. E. Britigan and P. Narayanasamy, *Mol. Pharmaceutics*, 2023, **20**, 4058.
175 Y. Wang, B. Han, Y. Xie, H. Wang, R. Wang, W. Xia, H. Li and H. Sun, *Chem. Sci.*, 2019, **10**, 6099.
176 D. Kumar, J. G. Hirz, S.-R. Choi, J. S. Stevenson, P. Narayanasamy, B. E. Britigan and J. E. Michaud, *J. Antibiot.*, 2026, **79**, 616.
177 G. Centola, D. J. Deredge, K. Hom, Y. Ai, A. T. Dent, F. Xue and A. Wilks, *ACS Infect Dis*, 2020, **6**, 2073.
178 M. Scaccaglia, M. Rega, M. Vescovi, S. Pinelli, M. Tegoni, C. Bacci, G. Pelosi and F. Bisceglie, *Metallomics.*, 2022, **14**, mfac070.
179 R. Wang, T.-P. Lai, P. Gao, H. Zhang, P.-L. Ho, P. C.-Y. Woo, G. Ma, R. Y.-T. Kao, H. Li and H. Sun, *Nat. Commun.*, 2018, **9**, 439.
180 Biological Chemistry of Arsenic, Antimony and Bismuth | Wiley, https://www.wiley.com/en-se/biological-chemistry-of-arsenic-antimony-and-bismuth-p-9780470713907, (accessed June 27, 2026).
181 K. M. Fock, D. Y. Graham and P. Malfertheiner, *Nat. Rev. Gastroenterol. Hepatol.*, 2013, **10**, 495.

182 Y. Hong, Y.-T. Lai, G. C.-F. Chan and H. Sun, *Proc. Natl. Acad. Sci. U.S.A.*, 2015, **112**, 3211.
183 R. Ge, X. Sun, Q. Gu, R. M. Watt, J. A. Tanner, B. C. Y. Wong, H. H. Xia, J.-D. Huang, Q.-Y. He and H. Sun, *J. Biol. Inorg. Chem.*, 2007, **12**, 831.
184 B. Han, Z. Zhang, Y. Xie, X. Hu, H. Wang, W. Xia, Y. Wang, H. Li, Y. Wang and H. Sun, *Chem. Sci.*, 2018, **9**, 7488.
185 T. Ka-Yan Ip, Y. Wang, S. Wang, K. Pu, R. Wang, B. Han, P. Gao, Y. Xie, R. Y. Kao, P.-L. Ho, H. Li and H. Sun, *RSC Med. Chem.*, 2025, **16**, 1829.
186 S. Park and K. Sauer, *Adv Exp Med Biol*, 2022, **1386**, 69.
187 L. Plate and M. A. Marletta, *Mol Cell*, 2012, **46**, 449.
188 D. P. Arora, S. Hossain, Y. Xu and E. M. Boon, *Biochemistry*, 2015, **54**, 3717.
189 J. Li, P. Gao, R. Y.-T. Kao, H. Li and H. Sun, *RSC Med. Chem.*, 2026, **17**, 3313.
190 Y. Xia, X. Wei, P. Gao, C. Wang, A. de Jong, J. H. K. Chen, M. J. Rodríguez-Sánchez, A. Rodríguez-Nogales, P. Diez-Echave, J. Gálvez, F. García, W. Wu, R. Y.-T. Kao, H. Li, R. Cebrián, O. P. Kuipers and H. Sun, *Nat Microbiol*, 2024, **9**, 2600.
191 Galib, M. Barve, M. Mashru, C. Jagtap, B. J. Patgiri and P. K. Prajapati, *J Ayurveda Integr. Med.*, 2011, **2**, 55.
192 S. Medici, M. Peana, V. M. Nurchi and M. A. Zoroddu, *J. Med. Chem.*, 2019, **62**, 5923.
193 S. Wattanaploy, K. Chinaroonchai, N. Namviriyachote and P. Muangman, *Int. J. Low. Extrem. Wounds*, 2017, **16**, 45.
194 Z. M. Rashaan, P. Krijnen, K. A. A. Kwa, C. H. van der Vlies, I. B. Schipper and R. S. Breederveld, *Wound Repair and Regeneration*, 2019, **27**, 257.
195 A. B. da S. Maciel, J. F. Ortiz, B. S. Siqueira and G. F. Zanette, *An. Bras. Dermatol.*, 2019, **94**, 204.
196 S. Silver, *FEMS Microbiol. Rev.*, 2003, **27**, 341.
197 P. Dibrov, J. Dzioba, K. K. Gosink and C. C. Häse, *Antimicrob. Agents Chemother.*, 2002, **46**, 2668.
198 S. A. Anuj, H. P. Gajera, D. G. Hirpara and B. A. Golakiya, *European J. Pharm. Sci.*, 2019, **127**, 208.
199 H. Wang, A. Yan, Z. Liu, X. Yang, Z. Xu, Y. Wang, R. Wang, M. Koohi-Moghadam, L. Hu, W. Xia, H. Tang, Y. Wang, H. Li and H. Sun, *PLoS Biol*, 2019, **17**, e3000292.
200 H. Wang, M. Wang, X. Yang, X. Xu, Q. Hao, A. Yan, M. Hu, R. Lobinski, H. Li and H. Sun, *Chem. Sci.*, 2019, **10**, 7193.
201 H. Wang, M. Wang, X. Xu, P. Gao, Z. Xu, Q. Zhang, H. Li, A. Yan, R. Y.-T. Kao and H. Sun, *Nat. Commun.*, 2021, **12**, 3331.
202 L. Ronga, M. Varcamonti and D. Tesauro, *Molecules,* 2023*,* **28***, 4435*.
203 X.-B. Chen, Q. Ye, Q. Wu, Y.-M. Song, R.-G. Xiong and X.-Z. You, *Inorg. Chem. Commun.*, 2004, **7**, 1302.
204 M. Patra, G. Gasser, A. Pinto, K. Merz, I. Ott, J. E. Bandow and N. Metzler-Nolte, *ChemMedChem*, 2009, **4**, 1930.
205 M. L. Low, L. Maigre, P. Dorlet, R. Guillot, J.-M. Pagès, K. A. Crouse, C. Policar and N. Delsuc, *Bioconjugate Chem.*, 2014, **25**, 2269.

206 X.-Y. Yang, J.-Y. Xu, M. Meng, N. Li, C.-Y. Liu and Q.-Y. He, *Journal of Proteomics*, 2019, **194**, 160.
207 P. Kalaivani, R. Prabhakaran, E. Ramachandran, F. Dallemer, G. Paramaguru, R. Renganathan, P. Poornima, V. V. Padma and K. Natarajan, *Dalton Trans.*, 2012, **41**, 2486.
208 K. L. Smitten, P. A. Scattergood, C. Kiker, J. A. Thomas and P. I. P. Elliott, *Chem. Sci.*, 2020, **11**, 8928.
209 L. Kelland, *Nat Rev Cancer*, 2007, **7**, 573.
210 M. Peyrone, *Justus Liebigs Annalen der Chemie*, 1844, **51**, 1.
211A. Werner, *Zeitschrift für anorganische Chemie*, 1893, **3**, 267.
212 Rosenberg, Barnett, Van Camp, Loretta, Grimley, Eugene B., and Thomson, Andrew J., *J. Biol. Chem.*, 1966, **242**, 1347.
213 S. Ghosh, *Bioorg. Chem.*, 2019, **88**, 102925.
214 B. Rosenberg, L. Vancamp, J. E. Trosko and V. H. Mansour, *Nature*, 1969, **222**, 385.
215 S. Dasari and P. B. Tchounwou, *Eur. J. Pharmacol.*, 2014, **740**, 364.
216 A. Chattaraj, M. P. Syed, C. A. Low and T. K. Owonikoko, *JCO Oncol. Pract.*, 2023, **19**, 278.
217 S. Yamamoto, M. Kato, Y. Takeyama, N. Yukimatsu, Y. Hirayama, T. Otoshi, T. Yamasaki, K. Kuratsukuri and J. Uchida, *Urol. Oncol.:Semin. Orig. Invest.*, 2022, **40**, 194.e7-194.e14.
218 S. Ishida, J. Lee, D. J. Thiele and I. Herskowitz, *Proc. Natl. Acad. Sci. U. S. A.*, 2002, **99**, 14298.
219 A. K. Holzer, G. H. Manorek and S. B. Howell, *Mol. Pharmacol.*, 2006, **70**, 1390.
220 A. K. Holzer, G. Samimi, K. Katano, W. Naerdemann, X. Lin, R. Safaei and S. B. Howell, *Mol. Pharmacol.*, 2004, **66**, 817.
221 D.-W. Shen, L. M. Pouliot, M. D. Hall and M. M. Gottesman, *Pharmacol. Rev.*, 2012, **64**, 706.
222 V. Schiavoni, M. Emanuelli, R. Campagna, M. Cecati, D. Sartini, G. Milanese, A. B. Galosi, V. Pozzi and E. Salvolini, *Journal of Cellular Biochemistry*, 2024, **125**, e30572.
223 E. R. Jamieson and S. J. Lippard, *Chem. Rev.*, 1999, **99**, 2467.
224 J. W. Reishus and D. S. Jr. Martin, *J. Am. Chem. Soc.*, 1961, **83**, 245.
225 A. Eastman, *Chem.-Biol. Interact.*, 1987, **61**, 241–248.
226 A. Eastman, *Biochemistry*, 1986, **25**, 3912.
227 D. Wang and S. J. Lippard, *Nat. Rev. Drug Discov.*, 2005, **4**, 30.
228 T. C. Johnstone, S. M. Alexander, W. Lin and S. J. Lippard, *J. Am. Chem. Soc.*, 2014, **136**, 116.
229 S. Reslova, *Chem.-Biol. Interact.*, 1971, **4**, 66–70.
230 S. Rubino, R. Busà, A. Attanzio, R. Alduina, V. Di Stefano, M. A. Girasolo, S. Orecchio and L. Tesoriere, *Bioorg. Med. Chem.*, 2017, **25**, 2378.
231 E. Ortega, C. Pérez-Arnaiz, V. Rodríguez, C. Janiak, N. Busto, B. García and J. Ruiz, *Eur. J. Med. Chem.*, 2021, **222**, 113600.
232 B. Rayner, A. D. Verderosa, V. Ferro and M. A. T. Blaskovich, *RSC Med. Chem.*, 2023, **14**, 800.
233 Q. Perraud, P. Cantero, M. Munier, F. Hoegy, N. Zill, V. Gasser, G. L. A. Mislin, L. Ehret-Sabatier and I. J. Schalk, *Microorganisms*.

234 G. Tonziello, E. Caraffa, B. Pinchera, G. Granata and N. Petrosillo, *Infect. Dis. Rep.* 2019, **11**, 8208.
235 Y. Yamano, *Clin. Infect. Dis.*, 2019, **69**, S544.
236 T. Sato and K. Yamawaki, *Clin. Infect. Dis.*, 2019, **69**, S538.
237 C. Guo and E. M. Nolan, *J. Am. Chem. Soc.*, 2022, **144**, 12756.
238 C. Guo, K.-K. A. Wang and E. M. Nolan, *ACS Infect. Dis.*, 2024, **10**, 1250.
239 A. Frei, S. Ramu, G. J. Lowe, H. Dinh, L. Semenec, A. G. Elliott, J. Zuegg, A. Deckers, N. Jung, S. Bräse, A. K. Cain and M. A. T. Blaskovich, *ChemMedChem*, 2021, **16**, 3165.
240 A. J. J. Lennox and G. C. Lloyd-Jones, *Angew. Chem. Int. Ed.*, 2013, **52**, 7362.
241 Norio. Miyaura and Akira. Suzuki, *Chem. Rev.*, 1995, **95**, 245.
242 J. K. Kochi and R. V. Subramanian, *J. Am. Chem. Soc.*, 1965, **87**, 4855.
243 A. L. J. Beckwith and A. A. Zavitsas, *J. Am. Chem. Soc.*, 1986, **108**, 8230.
244 M. Vaara, *Microbiol Rev*, 1992, **56**, 395–411.
245 S. J. Kim, J. Jo, J. Kim, K. S. Ko and W. Lee, *Microbiol. Spectr.*, **12**, e03687-23.
246 K. Joyce, S. Saxena, A. Williams, C. Damurjian, N. Auricchio, S. Aluotto, H. Tynan and A. L. Demain, *J. Antibiot.*, 2010, **63**, 530.
247 N. Chowdhury, T. L. Wood, M. Martínez-Vázquez, R. García-Contreras and T. K. Wood, *Biotechnol. Bioeng.*, 2016, **113**, 1984.
248 R. Wilcken, M. O. Zimmermann, A. Lange, A. C. Joerger and F. M. Boeckler, *J. Med. Chem.*, 2012, **56**, 1363.
249 S. J. Blanksby and G. B. Ellison, *Acc. Chem. Res.*, 2003, **36**, 255.
250 M. Gehringer and S. A. Laufer, *J. Med. Chem.*, 2018, **62**, 5673.
251 N. Jahn, S. Brantl and H. Strahl, *Mol. Microbiol.*, 2015, **98**, 651–666.
252 P. Greenspan, E. P. Mayer and S. D. Fowler, *J Cell Biol*, 1985, **100**, 965.
253 H. Strahl, F. Bürmann and L. W. Hamoen, *Nat Commun*, 2014, **5**, 3442.
254 T. A. Larsen, D. S. Goodsell, D. Cascio, K. Grzeskowiak and R. E. Dickerson, *J Biomol Struct Dyn*, 1989, **7**, 477.
255 A.-B. Schäfer, M. Sidarta, I. Abdelmesseh Nekhala, G. Marinho Righetto, A. Arshad and M. Wenzel, *Microbiol. Spectr.*, 2024, **12**, e0327523.
256 F. A. Tanious, J. M. Veal, H. Buczak, L. S. Ratmeyer and W. D. Wilson, *Biochemistry*, 1992, **31**, 3103.
257 J. S. Lenhart, E. R. Brandes, J. W. Schroeder, R. J. Sorenson, H. D. Showalter and L. A. Simmons, *J. Bacteriol.*, 2014, **196**, 2851.
258 A.-B. Schäfer, M. Steenhuis, K. K. Jim, J. Neef, S. O'Keefe, R. C. Whitehead, E. Swanton, B. Wang, S. Halbedel, S. High, J. M. Van Dijl, J. Luirink and M. Wenzel, *ACS Infect. Dis.*, 2023, **9**, 253.
259 O. A. Aning, A. Dvirnas, M. Nyblom, J. Krog, J. Carlson, P. Johansson, T. Ambjörnsson and F. Westerlund, *DNA Repair (Amst)*, 2025, **149**, 103836.
260 P. B. Tchounwou, S. Dasari, F. K. Noubissi, P. Ray and S. Kumar, *JEP*, 2021, **13**, 303.
261 J. D. te Winkel, D. A. Gray, K. H. Seistrup, L. W. Hamoen and H. Strahl, *Front. Cell Dev. Biol.*, 2016, **4**, 29.

262 D. A. Kelkar and A. Chattopadhyay, *Biochim Biophys Acta*, 2007, **1768**, 2011.
263 H. Strahl and L. W. Hamoen, *Proc. Natl. Acad. Sci.*, 2010, **107**, 12281–12286.
264 M. Wenzel, I. N. Celik Gulsoy, Y. Gao, Z. Teng, J. Willemse, M. Middelkamp, M. G. M. van Rosmalen, P. W. B. Larsen, N. N. van der Wel, G. J. L. Wuite, W. H. Roos and L. W. Hamoen, *Proc. Natl. Acad. Sci.*, 2021, **118**, e2002635118.
265 K. Schirner, Y.-J. Eun, M. Dion, Y. Luo, J. D. Helmann, E. C. Garner and S. Walker, *Nat. Chem. Biol.*, 2015, **11**, 38.
266 A. M. Kamal El-Sagheir, I. Abdelmesseh Nekhala, M. K. Abd El-Gaber, A. S. Aboraia, J. Persson, A.-B. Schäfer, M. Wenzel and F. A. Omar, *ACS Bio. Med. Chem. Au*, 2023, **3**, 494.
267 J. Errington, R. A. Daniel and D.-J. Scheffers, *Microbiol. Mol. Biol. Rev.*, 2003, **67**, 52.
268 D. Saeloh, V. Tipmanee, K. K. Jim, M. P. Dekker, W. Bitter, S. P. Voravuthikunchai, M. Wenzel and L. W. Hamoen, *PLoS Pathog.*, 2018, **14**, e1006876.
269 A. Frei, M. Amado, M. A. Cooper and M. A. T. Blaskovich, *Chem. - Eur. J.*, 2020, **26**, 2852.
270 T. Z. Liu, T. F. Lin, D. T. Chiu, K. J. Tsai and A. Stern, *Free Radic. Biol. Med.*, 1997, **23**, 155.
271 P. Cornelis, Q. Wei, S. C. Andrews and T. Vinckx, *Metallomics*, 2011, **3**, 540.
272 D. A. Gray, B. Wang, M. Sidarta, F. A. Cornejo, J. Wijnheijmer, R. Rani, P. Gamba, K. Turgay, M. Wenzel, H. Strahl and L. W. Hamoen, *Nat. Commun.*, 2024, **15**, 6877.
273 J. Checa and J. M. Aran, *J. Inflamm Res.*, 2020, **13**, 1057.
274 A. Frei, A. G. Elliott, A. Kan, H. Dinh, S. Bräse, A. E. Bruce, M. R. Bruce, F. Chen, D. Humaidy, N. Jung, A. P. King, P. G. Lye, H. K. Maliszewska, A. M. Mansour, D. Matiadis, M. P. Muñoz, T.-Y. Pai, S. Pokhrel, P. J. Sadler, M. Sagnou, M. Taylor, J. J. Wilson, D. Woods, J. Zuegg, W. Meyer, A. K. Cain, M. A. Cooper and M. A. T. Blaskovich, *JACS Au*, 2022, **2**, 2277.
275 F. M. MacKenzie and I. M. Gould, *J. Antimicrob. Chemother.*, 1993, **32**, 519.
276 B. W. P. Griffith, *Platinum Met. Rev.*, 2004, **48**, 182.
277 Zhe Liu and Peter J. Sadler, *Acc. Chem. Res.*, 2014, **47**, 1174.
278 F. Chen, J. Moat, D. McFeely, G. Clarkson, I. J. Hands-Portman, J. P. Furner-Pardoe, F. Harrison, C. G. Dowson and P. J. Sadler, *J. Med. Chem.*, 2018, **61**, 7330.
279 P. V. Simpson, C. Schmidt, I. Ott, H. Bruhn and U. Schatzschneider, *Eur. J. Inorg. Chem.*, 2013, **2013**, 5547.
280 G. Liao, X. Peng, T. Li, Z. Ye, X. Xiang and C. Fu, *Polymers*.
281 A. Gupta, P. Prasad, S. Gupta and P. K. Sasmal, *ACS Appl. Mater. Interfaces*, 2020, **12**, 35967.
282 B. F. Hohlfeld, B. Gitter, C. J. Kingsbury, K. J. Flanagan, D. Steen, G. D. Wieland, N. Kulak, M. O. Senge and A. Wiehe, *Chemistry – A European Journal*, 2021, **27**, 6440.

283 B. Das, P. Biswas, A. I. Mallick and P. Gupta, *Chem. Eur. J.*, 2024, **30**, e202400646.
284 D. Moreth, L. Stevens-Cullinane, T. W. Rees, V. V. L. Müller, A. Pasquier, O.-R. Song, S. Warchal, M. Howell, J. Hess and U. Schatzschneider, *J Biol Inorg Chem*, 2024, **29**, 573.
285 B. J. Butuyuyu, J. Liu, Q. Ding, J. Zhang, D. Li, A. Z. Abdulkadir, C.-S. Lee, L. Cai, K. M.-C. Wong, J. S. Kim and P. Zhang, *Inorg. Chem.*, 2025, **64**, 8135.
286 A. Gautam and P. K. Sasmal, *Inorg. Chem.*, 2025, **64**, 2905–2918.
287 Y. Lu, X. Zhang, M. Song, H. Xie, S. Chen, Y. Zhou, J. Jia and H. Tang, *RSC Adv.*, 2025, **15**, 2329.
288 J. Shu, H. Jiang, M. Lin, J. Liang, Y. Zhao, D. Luo, J. Wang and H. Chao, *Eur. J. Med. Chem.*, 2025, **294**, 117758.
289 B. V. Paes, D. N. Costa, I. V. Esarev, S. Boschuk, P. Lippmann, S. Sant'Anna Maranhão, C. Pessoa, I. Ott and H. Beraldo, *J. Inorg. Biochem.*, 2026, **276**, 113179.
290 Y. Li, C. Zhou, M. Liu, L. Yang, X. Chen, X. Feng, C. Zhang, G. Li and L. Xu, *ACS Infect. Dis.*, 2026, **12**, 1409.
291 Y. Zhang, L. Shao, Z. Wang, X. Fang, X. Zhang, G. Fu, L. Xu, G. Li and X. Lü, *J. Inorg. Biochem.*, 2026, **279**, 113274.
292 G. W. Karpin, J. S. Merola and J. O. Falkinham, *Antimicrob. Agents Chemother.*, 2013, **57**, 3434.
293 G. W. Karpin, D. M. Morris, M. T. Ngo, J. S. Merola and J. O. F. Iii, *Med. Chem. Commun.*, 2015, **6**, 1471.
294 S. B. Gajera, J. V. Mehta and M. N. Patel, *ChemistrySelect*, 2016, **1**, 3966.
295 P. Chellan, V. M. Avery, S. Duffy, J. A. Triccas, G. Nagalingam, C. Tam, L. W. Cheng, J. Liu, K. M. Land, G. J. Clarkson, I. Romero-Canelón and P. J. Sadler, *Chem. Eur. J.*, 2018, **24**, 10078..
296 C. M. DuChane, L. C. Brown, V. S. Dozier and J. S. Merola, *Organometallics*, 2018, **37**, 530.
297 C. M. DuChane, G. W. Karpin, M. Ehrich, J. O. Falkinham and J. S. Merola, *Med. Chem. Commun.*, 2019, **10**, 1391.
298 N. Baartzes, A. Jordaan, D. F. Warner, J. Combrinck, D. Taylor, K. Chibale and G. S. Smith, *Eur. J. Med. Chem.*, 2020, **206**, 112694.
299 A. M. Mansour and K. Radacki, *Dalton Trans.*, 2020, **49**, 4491.
300 C. M. Bernier, C. M. DuChane, J. S. Martinez, J. O. I. Falkinham and J. S. Merola, *Organometallics*, 2021, **40**, 1670.
301 X. Liu, M. Shao, C. Liang, J. Guo, G. Wang, X.-A. Yuan, Z. Jing, L. Tian and Z. Liu, *ChemBioChem*, 2021, **22**, 557.
302 B. Balázs, Z. Tóth, I. Kacsir, A. Sipos, P. Buglyó, L. Somsák, É. Bokor, G. Kardos and P. Bai, *Front. Chem.*, 2022, **10**, 868234.
303 A. Marco, G. Vigueras, N. Busto, N. Cutillas, D. Bautista and J. Ruiz, *Dalton Trans.*, 2023, **52**, 13482.
304 M. Sawkmie, V. Banothu, W. Kaminsky and M. R. Kollipara, *J. Coord. Chem.*, 2023, **76**, 1650.
305 K.-W. Jeong, J.-Y. Lee, D.-I. Kang, J.-U. Lee, S. Y. Shin and Y. Kim, *J. Nat. Prod.*, 2009, **72**, 719.

306 R. Liu, X. Li and K. S. Lam, *Curr. Opin. Chem. Biol.*, 2017, **38**, 117–126.
307 S. C. Smith, C. S. Horbaczewskyj, T. F. N. Tanner, J. J. Walder and I. J. S. Fairlamb, *Digital Discovery*, 2024, **3**, 1467.
308 S. Brenner and R. A. Lerner, *Proc. Natl. Acad. Sci.*, 1992, **89**, 5381.
309 A. A. Peterson and D. R. Liu, *Nat. Rev. Drug Discov.*, 2023, **22**, 699.
310 D. Guan, J. Liu, F. Chen, J. Li, X. Wang, W. Lu, Y. Suo, F. Tang, L. Lan, X. Lu and W. Huang, *J. Med. Chem.*, 2024, **67**, 3778.
311L. Li, X. Wang, P. Ding, X. Shen, H. Hu, X. Wang, R. Jin, X. Wu, Y. Zhang, W. Lu, J. Yue, H. E. Xu, W. Yin, Y. Xu and X. Lu, *JACS Au*, 2026, **6**, 1370.
312 A. M. Rowley, G. Yao, L. Andrews, A. Bedermann, R. Biddulph, R. Bingham, J. J. Brady, R. Buxton, T. Cecconie, R. Cooper, A. Csakai, E. N. Gao, M. C. Grenier-Davies, M. Lawler, Y. Lian, J. Macina, C. Macphee, L. Marcaurelle, J. Martin, P. McCormick, R. Pindoria, M. Rauch, W. Rocque, Y. Shen, L. M. Shewchuk, M. Squire, W. Stebbeds, W. Tear, X. Wang, P. Ward and S. Xiao, *J. Med. Chem.*, 2024, **67**, 2049.
313 D. M. Taylor, J. Anglin, S. Park, M. N. Ucisik, J. C. Faver, N. Simmons, Z. Jin, M. Palaniappan, P. Nyshadham, F. Li, J. Campbell, L. Hu, B. Sankaran, B. V. V. Prasad, H. Huang, M. M. Matzuk and T. Palzkill, *ACS Infect. Dis.*, 2020, **6**, 1214.
314 X. Wang, L. Xiong, Y. Zhu, S. Liu, W. Zhao, X. Wu, M. Seydimemet, L. Li, P. Ding, X. Lin, J. Liu, X. Wang, Z. Duan, W. Lu, Y. Suo, M. Cui, J. Yue, R. Jin, M. Zheng, Y. Xu, L. Mei, H. Hu and X. Lu, *J. Am. Chem. Soc.*, 2024, **146**, 33983.
315 Y. Zhou, W. Shen, Y. Gao, J. Peng, Q. Li, X. Wei, S. Liu, F. S. Lam, J. Mayol-Llinàs, G. Zhao, G. Li, Y. Li, H. Sun, Y. Cao and X. Li, *Nat. Chem.*, 2024, **16**, 543.
316 J. Andersson, S. Cowland, M. Vestergaard, Y. Yang, S. Liu, X. Fang, S. Mukund, S. Ghimire-Rijal, C. Carter, G. Chung, T. Jacso, I. Sarvary, P. E. Hughes, A. Gouliaev, M. Payton, B. Belmontes, S. Caenepeel, T. Franch, S. Glad, B. Husemoen and S. J. Nielsen, *Proc Natl Acad Sci U S A*, 2025, **122**, e2425052122.
317 A. Varkaris *et al*., *Cancer Discov.*, 2024, **14**, 240.
318 B. Belmontes *et al*., *Cancer Discov.*, 2025, **15**, 139.
319 S. L. Belyanskaya, Y. Ding, J. F. Callahan, A. L. Lazaar and D. I. Israel, *Chembiochem*, 2017, **18**, 837.
320 A. Welsh, D. Husbands and A. Frei, *Angew. Chem. Int. Ed.*, 2025, **64**, e202420204.
321 K. E. Sandman, P. Fuhrmann and S. J. Lippard, *JBIC*, 1998, **3**, 74.
322 M. S. Lowry, W. R. Hudson, R. A. Pascal and S. Bernhard, *J. Am. Chem. Soc.*, 2004, **126**, 14129.
323 S. DiLuzio, V. Mdluli, T. U. Connell, J. Lewis, V. VanBenschoten and S. Bernhard, *J. Am. Chem. Soc.*, 2021, **143**, 1179.
324 V. Mdluli, S. Diluzio, J. Lewis, J. F. Kowalewski, T. U. Connell, D. Yaron, T. Kowalewski and S. Bernhard, *ACS Catal.*, 2020, **10**, 6977.
325 T. Kench, A. Rahardjo, G. G. Terrones, A. Bellamkonda, T. E. Maher, M. Storch, H. J. Kulik and R. Vilar, *Angew. Chem. Int. Ed.*, 2024, **63**, e202401808.

326 T. Kench, N. Sultana Chowdhury, K. M. Rahman and R. Vilar, *Inorg. Chem.*, 2025, **64**, 5113.
327 D. R. Husbands, Ç. Özsan, A. Welsh, R. J. Gammons and A. Frei, *Nat Commun*, 2025, **16**, 11195.
328 L. Fabbrizzi, *J. Org. Chem.*, 2020, **85**, 12212.
329 M. J. Chow, C. Licona, D. Yuan Qiang Wong, G. Pastorin, C. Gaiddon and W. H. Ang, *J. Med. Chem.*, 2014, **57**, 6043.
330 M. J. Chow, M. Alfiean, G. Pastorin, C. Gaiddon and W. H. Ang, *Chem. Sci.*, 2017, **8**, 3641.
331 C. Weng, L. Shen and W. H. Ang, *Angew. Chem. Int. Ed.*, 2020, **59**, 9314.
332 C. Weng, H. Yang, B. S. Loh, M. W. Wong and W. H. Ang, *J. Am. Chem. Soc.*, 2023, **145**, 6453.
333 C. Weng, L. Shen, J. W. Teo, Z. C. Lim, B. S. Loh and W. H. Ang, *JACS Au*, 2021, **1**, 1348.
334 M. Benz, M. R. Molla, A. Böser, A. Rosenfeld and P. A. Levkin, *Nat Commun*, 2019, **10**, 2879.
335 C. J. Torrance, V. Agrawal, B. Vogelstein and K. W. Kinzler, *Nat Biotechnol*, 2001, **19**, 940.
336 K. Petrželová, O. Bárta, R. Héžová, A. Andrýsková, J. Hošek and P. Štarha, *ChemistryOpen*, 2025, **14**, e202500026.
337 Z. Liu, A. Habtemariam, A. M. Pizarro, S. A. Fletcher, A. Kisova, O. Vrana, L. Salassa, P. C. A. Bruijnincx, G. J. Clarkson, V. Brabec and P. J. Sadler, *J. Med. Chem.*, 2011, **54**, 3011.
338 M. F. Richter, B. S. Drown, A. P. Riley, A. Garcia, T. Shirai, R. L. Svec and P. J. Hergenrother, *Nature*, 2017, **545**, 299.
339 R. Sievers, M. Sellin, S. M. Rupf, J. Parche and M. Malischewski, *Angew. Chem. Int. Ed.*, 2022, **61**, e202211147.
340 N. Hulstaert, J. Shofstahl, T. Sachsenberg, M. Walzer, H. Barsnes, L. Martens and Y. Perez-Riverol, *J. Proteome Res.*, 2020, **19**, 537.
341 C. Nataro, L. M. Thomas and R. J. Angelici, *Inorg. Chem.*, 1997, **36**, 6000.
342 M. P. Johansson and J. Olsen, *J. Chem. Theory Comput.*, 2008, **4**, 1460.
343 C. Maher and K. A. Hassan, *mBio*, 2023, **14**, e01205-23.
344 A. Encinas López, 2015, vol. ch 6., pp. 132.
345 B. S. Matada, R. Pattanashettar and N. G. Yernale, *Bioorg. Med. Chem.*, 2021, **32**, 115973.
346 A. Falanga, R. Bellavita, S. Braccia and S. Galdiero, *J. Pept. Sci.*, 2024, **30**, e3558.
347 R. Jerzy Kopiasz, A. Zabost, M. Myszka, A. Kuźmińska, K. Drężek, J. Mierzejewska, W. Tomaszewski, A. Iwańska, E. Augustynowicz-Kopeć, T. Ciach and D. Jańczewski, *RSC Advances*, 2022, **12**, 26220–26232.
348 J. Faria, S. Ahmed, K. G. F. Gerritsen, S. M. Mihaila and R. Masereeuw, *Arch. Toxicol.*, 2019, **93**, 3397–3418.
349 S. J. Kim, J. Jo, J. Kim, K. S. Ko and W. Lee, *Microbiol. Spectr.*, 2024, **12**, e03687-23.
350 E. Vaisbourd, D. S. Glass, Y. Yang, A. Mayo, A. Bren and U. Alon, *mBio*, 2025, **16**, e02066-25.

351 Z. Liu, A. Habtemariam, A. M. Pizarro, G. J. Clarkson and P. J. Sadler, *Organometallics*, 2011, **30**, 4702.
352 Ç. Özsan, A.-B. Schäfer, A. Akhir, O. A. Aning, S. Fulgencio, R. Maitra, R. Rani, D. Saxena, F. Westerlund, S. Chopra, M. Wenzel and A. Frei, *npj Antimicrob. Resist.,* 2026*,* **4***,* 37.
353 H.-J. Kang and H.-J. Park, *Biochemistry*, 2009, **48**, 7392.
354 M. McCann, J. McGinley, K. Ni, M. O'Connor, K. Kavanagh, V. McKee, J. Colleran, M. Devereux, N. Gathergood, N. Barron, A. Prisecaru and A. Kellett, *Chem. Commun.*, 2013, **49**, 2341.
355 A. Gibney, M. Sidarta, E. Delahunt, P. Mesdom, L. Arrué, S. Kk, O. A. Aning, H. Hjerpe, F. Figueiredo, K. Cariou, V. McKee, P. Johansson, S. Bhattacharya, D. Thompson, M. Wenzel, G. Gasser, F. Westerlund and A. Kellett, *Nat. Commun.*, 2026, **17**, 2309.
356 Y. Seif, J. M. Monk, N. Mih, H. Tsunemoto, S. Poudel, C. Zuniga, J. Broddrick, K. Zengler and B. O. Palsson, *PLoS Comput Biol*, 2019, **15**, e1006644.
357 B. Halliwell, A. Adhikary, M. Dingfelder and M. Dizdaroglu, *Chem. Soc. Rev.*, 2021, **50**, 8355.
358 S. Mukherjee, S. Ghosh, R. D. M, S. Roy, S. S. Roy, M. Acharya, B. K. Kumar and A. Mukherjee, *J. Med. Chem.*, 2025, **68**, 21201.
359 J. Li, L. Guo, Z. Tian, S. Zhang, Z. Xu, Y. Han, R. Li, Y. Li and Z. Liu, *Inorg. Chem.*, 2018, **57**, 13552.
360 W. Ni, X. Shao, X. Di, J. Cui, R. Wang and Y. Liu, *Int. J. Antimicrob. Agents*, 2015, **45**, 8.
361 W. Y. Belay, M. Getachew, B. A. Tegegne, Z. H. Teffera, A. Dagne, T. K. Zeleke, S. A. Wondm, R. B. Abebe, A. A. Gedif, A. Fenta, G. Yirdaw, A. Tilahun and Y. Aschale, *Ther Adv Infect Dis*, 2025, **12**, 20499361251340144.
362 WHO fungal priority pathogens list to guide research, development and public health action, https://www.who.int/publications/i/item/9789240060241, (accessed July 15, 2026).
363 D. W. Denning, *Lancet Infect Dis*, 2024, **24**, e428.
364 E. Puumala, S. Fallah, N. Robbins and L. E. Cowen, *Clinical Microbiology Reviews*, 2024, **37**, e00142-23.
365 M. C. Fisher, F. Burnett, C. Chandler, N. A. R. Gow, S. Gurr, A. Hart, A. Holmes, R. C. May, J. Quinn, T. Soliman, N. J. Talbot, H. M. West, J. S. West, P. L. White, M. Bromley and D. Armstrong-James, *npj Antimicrob. Resist.*, 2024, **2**, 36.
366 N. A. R. Gow, C. Johnson, J. Berman, A. T. Coste, C. A. Cuomo, D. S. Perlin, T. Bicanic, T. S. Harrison, N. Wiederhold, M. Bromley, T. Chiller and K. Edgar, *Nat. Commun.*, 2022, **13**, 5352.
367 R. Rubbiani, O. Blacque and G. Gasser, *Dalton Trans.*, 2016, **45**, 6619–6626.
368 R. Rubbiani, T. Weil, N. Tocci, L. Mastrobuoni, S. Jeger, M. Moretto, J. Ng, Y. Lin, J. Hess, S. Ferrari, A. Kaech, L. Young, J. Spencer, A. L. Moore, K. Cariou, G. Renga, M. Pariano, L. Romani and G. Gasser, *RSC Chem. Biol.*, 2021, **2**, 1263.

369 A. Frei, A. P. King, G. J. Lowe, A. K. Cain, F. L. Short, H. Dinh, A. G. Elliott, J. Zuegg, J. J. Wilson and M. A. T. Blaskovich, *Chemistry*, 2021, **27**, 2021.
370 K.-L. Barry, C. D. Grimmer, O. Q. Munro and M. P. Akerman, *RSC Adv.*, 2020, **10**, 7867.
371 S. Gao, C.-Q. Cao, Z.-J. Liu and Z.-J. Yao, *Inorg. Chem.*, 2024, **63**, 13311.
372 Y. Wu, Y. Deng, G. Tan and J. You, *Nat Commun*, 2025, **16**, 4499.
373 R. Garcia-Rubio, H. C. de Oliveira, J. Rivera and N. Trevijano-Contador, *Front Microbiol*, 2020, **10**, 2993.
374 N. A. R. Gow, J.-P. Latge and C. A. Munro, *Microbiol. Spectr.*, 2017, **5**, FUNK-0035-2016.
375 H. C. Kolb, M. G. Finn and K. B. Sharpless, *Angew. Chem. Int. Ed.*, 2001, **40**, 2004.
376 C. W. Tornøe, C. Christensen and M. Meldal, *J. Org. Chem.*, 2002, **67**, 3057.
377 E. Haldón, M. C. Nicasio and P. J. Pérez, *Org. Biomol. Chem.*, 2015, **13**, 9528.
378 G. C. Tron, T. Pirali, R. A. Billington, P. L. Canonico, G. Sorba and A. A. Genazzani, *Medicinal Research Reviews*, 2008, **28**, 278–308.
379 P. A. Scattergood and P. I. P. Elliott, *Dalton Trans.*, 2017, **46**, 16343.
380 J. D. Crowley and D. A. McMorran, in *Click Triazoles*, ed. J. Košmrlj, Springer, Berlin, Heidelberg, 2012, 31.
381 W. K. C. Lo, G. S. Huff, J. R. Cubanski, A. D. W. Kennedy, C. J. McAdam, D. A. McMorran, K. C. Gordon and J. D. Crowley, *Inorg. Chem.*, 2015, **54**, 1572.
382 W. Stroek and M. Albrecht, *Chem. Soc. Rev.*, 2024, **53**, 6322.
383 R. G. Miller, M. Vázquez-Hernández, P. Prochnow, J. E. Bandow and N. Metzler-Nolte, *Inorg. Chem.*, 2019, **58**, 9404.
384 A. Kafle and S. T. Handy, *Tetrahedron*, 2017, **73**, 7024.
385 S. Bräse, C. Gil, K. Knepper and V. Zimmermann, *Angew. Chem. Int. Ed.*, 2005, **44**, 5188.
386 G. Meng, T. Guo, T. Ma, J. Zhang, Y. Shen, K. B. Sharpless and J. Dong, *Nature*, 2019, **574**, 86.
387 A. K. Pandiakumar, S. P. Sarma and A. G. Samuelson, *Tetrahedron Letters*, 2014, **55**, 2917.
388 Ç. Özsan, A. Welsh, S. Zineddu, D. R. Husbands, K. Robinson and A. Frei, ChemRxiv, 2026.
389 R. Keese and M. Meyer, *Tetrahedron*, 1993, **49**, 2055.
390 C. A. Hunter, C. M. R. Low, C. Rotger, J. G. Vinter and C. Zonta, *Proc. Natl. Acad. Sci.*, 2002, **99**, 4873.
391 G. Yuan, Y. Guan, H. Yi, S. Lai, Y. Sun and S. Cao, *Sci Rep*, 2021, **11**, 10471.
392 R. Wei, C. L. Dickson, D. Uhrín and G. C. Lloyd-Jones, *J. Org. Chem.*, 2021, **86**, 9023.
393 S. Zineddu, A. Welsh, Ç. Özsan, A. K.-H. Chau, D. R. Husbands, K. Robinson, L. Messori and A. Frei, ChemRxiv, 2026.

394 P. Nonejuie, M. Burkart, K. Pogliano and J. Pogliano, *Proc. Nat.l Acad. Sci. U S A*, 2013, **110**, 16169.
395 P. Bellio, L. Fagnani, L. Nazzicone and G. Celenza, *MethodsX*, 2021, **8**, 101543.
396 N. Fatsis-Kavalopoulos, D. L. Sánchez-Hevia and D. I. Andersson, *J. Antimicrob. Chemother.*, 2024, **79**, 2394.
397 M. M. Sopirala, J. E. Mangino, W. A. Gebreyes, B. Biller, T. Bannerman, J.-M. Balada-Llasat and P. Pancholi, *Antimicrob. Agents Chemother.*, 2010, **54**, 4678..
398 O. RAAB, *Zeitschr Biol*, 1900, **39**, 524.
399 H. v. Tappeiner, *Ergebnisse der Physiologie*, 1909, **8**, 698.
400 F. Cieplik, D. Deng, W. Crielaard, W. Buchalla, E. Hellwig, A. Al-Ahmad and T. Maisch, *Crit. Rev. Microbiol.*, 2018, **44**, 571.
401 K. Moghissi, K. Dixon, M. Stringer and J. A. C. Thorpe, *Photodiagnosis and Photodynamic Therapy*, 2009, **6**, 159.
402 D. J. Piacquadio, D. M. Chen, H. F. Farber, J. Fowler Joseph F., S. D. Glazer, J. J. Goodman, L. L. Hruza, E. W. B. Jeffes, M. R. Ling, T. J. Phillips, T. M. Rallis, R. K. Scher, C. R. Taylor and G. D. Weinstein, *Arch Dermatol*, 2004, **140**, 41.
403 N. M. Bessler and Vam Study Writing Committee, *Retina*, 2004, **24**, 512.
404 M. Wainwright, T. Maisch, S. Nonell, K. Plaetzer, A. Almeida, G. P. Tegos and M. R. Hamblin, *Lancet Infect Dis*, 2017, **17**, e49..
405 M. R. Hamblin and H. Abrahamse, *Drug Development Research*, 2019, **80**, 48.
406 J. Karges, *Angew. Chem. Int. Ed.*, 2022, **61**, e202112236.
407 L. K. McKenzie, H. E. Bryant and J. A. Weinstein, *Coordination Chemistry Reviews*, 2019, **379**, 2–29.
408 Y. Feng, W.-Z. Sun, X.-S. Wang and Q.-X. Zhou, *Chem. Eur. J.*, 2019, **25**, 13879.
409 G. E. Giacomazzo, L. Conti, A. Guerri, M. Pagliai, C. Fagorzi, P. S. Sfragano, I. Palchetti, G. Pietraperzia, A. Mengoni, B. Valtancoli and C. Giorgi, *Inorg. Chem.*, 2022, **61**, 6689.
410 Y. Jian, Z. Jin, S. Qi, X. Da, Z. Wang, X. Wang and Q. Zhou, *Chem. Eur. J.,* 2022, **28**, e202103359.
411T. Le Gall, G. Lemercier, S. Chevreux, K.-S. Tücking, J. Ravel, F. Thétiot, U. Jonas, H. Schönherr and T. Montier, *ChemMedChem*, 2018, **13**, 2229.
412 A. A. Mandal, A. Upadhyay, A. Mandal, M. Nayak, M. S. K, S. Mukherjee and S. Banerjee, *ACS Appl. Mater. Interfaces*, 2024, **16**, 28118.
413 A. Mesra-Brahmi, S. Martínez-Olmo, I. Guerrero, X. Fontrodona, J. Poater, A. Verdaguer, M. Auset Vallejo, R. Bresolí-Obach, S. Nonell, R. Núñez and I. Romero, *Inorg. Chem.*, 2026, **65**, 15389.
414 S. Patra, Z. Papadopoulos, J. Sanz-Villafruela, J. Karges and A. Galstyan, *J. Mater. Chem. B*, 2026, **14**, 8271.
415 S. Pierce, M. P. Jennings, S. A. Juliano and A. M. Angeles-Boza, *Inorg. Chem.*, 2020, **59**, 14866.
416 Z. Zhao, H. Li, X. Tao, Y. Xie, L. Yang, Z.-W. Mao and W. Xia, *Chem. Eur. J.*, 2021, **27**, 5453.

417 A. A. Mandal, S. Kumar, S. Singh, A. Mandal, S. Banerjee and P. Dhar, *Chem. Commun.*, 2026, **62**, 2554.
418 D. A. Smithen, S. Monro, M. Pinto, J. Roque III, R. M. Diaz-Rodriguez, H. Yin, C. G. Cameron, A. Thompson and S. A. McFarland, *Chem. Sci.*, 2020, **11**, 12047.
419 B. Das, P. Biswas, A. I. Mallick and P. Gupta, *Chem. Eur. J.,* 2024, **30**, e202400646.
420 L. Wang, S. Monro, P. Cui, H. Yin, B. Liu, C. G. Cameron, W. Xu, M. Hetu, A. Fuller, S. Kilina, S. A. McFarland and W. Sun, *ACS Appl. Mater. Interfaces*, 2019, **11**, 3629.
421 I. Singh, R. Rai, R. Kushwaha, P. Dhar and S. Banerjee, *Dalton Trans.*, 2025, **54**, 11174.
422 R. Devraj Prakashchandra, R. Rai, A. Ali Mandal, P. Dhar, S. Banerjee, T. Sarkar and B. Nagendra Babu, *ChemBioChem*, 2025, **26**, e202400678.
423 A. Galstyan, Y. K. Maurya, H. Zhylitskaya, Y. J. Bae, Y.-L. Wu, M. R. Wasielewski, T. Lis, U. Dobrindt and M. Stępień, *Chem. Eur. J.*, 2020, **26**, 8262.
424 R.-K. Lin, C.-I. Chiu, C.-H. Hsu, Y.-J. Lai, P. Venkatesan, P.-H. Huang, P.-S. Lai and C.-C. Lin, *Chem. Eur. J.,* 2018, **24**, 4111–4120.
425 D. Musib, M. K. Raza, S. Kundu and M. Roy, *Eur. J. Inorg. Chem.*, 2018, **2018**, 2011.
426 C. Al Hageh, M. Al Assaad, Z. El Masri, N. Samaan, M. El-Sibai, C. Khalil and R. S. Khnayzer, *Dalton Trans.*, 2018, **47**, 4959.
427 N. Mukherjee, S. Podder, K. Mitra, S. Majumdar, D. Nandi and A. R. Chakravarty, *Dalton Trans.*, 2018, **47**, 823.
428 M. V. Appleby, P. G. Walker, D. Pritchard, S. van Meurs, C. M. Booth, C. Robertson, M. D. Ward, D. J. Kelly and J. A. Weinstein, *Mater. Adv.*, 2020, **1**, 3417.
429 T. Maisch, S. Hackbarth, J. Regensburger, A. Felgenträger, W. Bäumler, M. Landthaler and B. Röder, *J Dtsch Dermatol Ges*, 2011, **9**, 360–366.
430 Z. Pang, R. Raudonis, B. R. Glick, T.-J. Lin and Z. Cheng, *Biotechnology Advances*, 2019, **37**, 177.
431 J. W. Southwell, R. Herman, D. J. Raines, J. E. Clarke, I. Böswald, T. Dreher, S. M. Gutenthaler, N. Schubert, J. Seefeldt, N. Metzler-Nolte, G. H. Thomas, K. S. Wilson and A.-K. Duhme-Klair, *Chem. Eur. J.*, 2023, **29**, e202202536.
432 R. N. Motz, G. T. Walker, G. J. Norton, M. Raffatellu and E. M. Nolan, *J. Am. Chem. Soc.*, 2026, **148**, 3206.
433 T. Zheng and E. M. Nolan, *J. Am. Chem. Soc.*, 2014, **136**, 9677.
434 S. Zhao, Z.-P. Wang, Z. Lin, G. Wei, X. Wen, S. Li, X. Yang, Q. Zhang, C. Jing, Y. Dai, J. Guo and Y. He, *Angew. Chem. Int. Ed.*, 2022, **61**, e202204139.
435 K. Lewis, *Nat. Rev. Drug Discov.*, 2013, **12**, 371.
436 F. Vincent, A. Nueda, J. Lee, M. Schenone, M. Prunotto and M. Mercola, *Nat. Rev. Drug Discov.*, 2022, **21**, 899.
437 L. L. Silver, *Nat. Rev. Drug Discov.*, 2007, **6**, 41.
438 D. Saxena, R. Maitra, R. Bormon, M. Czekanska, J. Meiers, A. Titz, S. Verma and S. Chopra, *npj Antimicrob. Resist.*, 2023, **1**, 17.

439 K. A. Muñoz and P. J. Hergenrother, *Acc. Chem. Res.*, 2021, **54**, 1322.
440 E. N. Parker, B. S. Drown, E. J. Geddes, H. Y. Lee, N. Ismail, G. W. Lau and P. J. Hergenrother, *Nat. Microbiol.*, 2020, **5**, 67.
441 E. J. Anthony, E. M. Bolitho, H. E. Bridgewater, O. W. L. Carter, J. M. Donnelly, C. Imberti, E. C. Lant, F. Lermyte, R. J. Needham, M. Palau, P. J. Sadler, H. Shi, F.-X. Wang, W.-Y. Zhang and Z. Zhang, *Chem. Sci.*, 2020, **11**, 12888.
442 M. E. Palmer, L. J. Andrews, T. C. Abbey, A. E. Dahlquist and E. Wenzler, *Front. Pharmacol.*, 2022, **13**, 888079.
443 A. E. E. Wandler, M. R. M. Koos, M. Nieger, B. Luy and S. Bräse, *Dalton Trans.*, 2018, **47**, 3689.
444 N. Kutsumura, M. Iijima, S. Toguchi and T. Saito, *Chem. Lett.*, 2011, **40**, 1231.
445 N. Becker and E. M. Carreira, *Org. Lett.*, 2007, **9**, 3857.
446 C. Bandari and K. M. Nicholas, *J. Org. Chem.*, 2020, **85**, 3320.
447 J. Fawcett, P. A. T. Hoye, R. D. W. Kemmitt, D. J. Law and D. R. Russell, *J. Chem. Soc., Dalton Trans.*, 1993, **22**, 2563.
448 O. V. Dolomanov, L. J. Bourhis, R. J. Gildea, J. a. K. Howard and H. Puschmann, *J. Appl. Cryst.*, 2009, **42**, 339.
449 G. M. Sheldrick, *Acta Cryst A*, 2015, **71**, 3.
450 X. Cai, M. Orsi, A. Capecchi, T. Köhler, C. van Delden, S. Javor and J.-L. Reymond, *Cell Rep. Phys. Sci.*, 2022, **3**, 101161.
451 Performance Standards for Antimicrobial Susceptibility Testing, https://cdn.bfldr.com/YLD4EVFU/at/hvshwc8rxbsbnnmtqp9f3886/m100ed35e_sample.pdf (accessed 30.05.2025), (accessed May 30, 2025).
452 Joel Rosenblatt, Nylev Vargas-Cruz, Ruth A. Reitzel, and Issam I. Raad, *Antimicrob. Agents Chemother.*, 2019, **63**, 9.
453 P. Twentyman and M. Luscombe, *Br. J. Cancer*, 1987, **56**, 279.
454 T. Mosmann, *J. Immunol. Methods*, 1983, **65**, 55.
455 M. Stach, N. Maillard, R. U. Kadam, D. Kalbermatter, M. Meury, M. G. P. Page, D. Fotiadis, T. Darbre and J.-L. Reymond, *Med. Chem. Commun.*, 2012, **3**, 86.
458 M. Wenzel, M. Rautenbach, J. A. Vosloo, T. Siersma, C. H. M. Aisenbrey, E. Zaitseva, W. E. Laubscher, W. Van Rensburg, J. C. Behrends, B. Bechinger and L. W. Hamoen, *mBio*, 2018, **9**, e00802-18.
459 J. Schindelin, I. Arganda-Carreras, E. Frise, V. Kaynig, M. Longair, T. Pietzsch, S. Preibisch, C. Rueden, S. Saalfeld, B. Schmid, J.-Y. Tinevez, D. J. White, V. Hartenstein, K. Eliceiri, P. Tomancak and A. Cardona, *Nat. Anal. Methods*, 2012, **9**, 676.
460 A. Ducret, E. M. Quardokus and Y. V. Brun, *Nat. Microbiol.*, 2016, **1**, 16077.
461 S. Syvertsson, N. O. E. Vischer, Y. Gao and L. W. Hamoen, *PLoS One*, 2016, **11**, e0151267.
462 C. Anagnostopoulos and J. Spizizen, *J. Bacteriol.*, 1961, **81**, 741.
463 P. J. Lewis, S. D. Thaker and J. Errington, *EMBO J*, 2000, **19**, 710–718.
464 A. Müller, M. Wenzel, H. Strahl, F. Grein, T. N. V. Saaki, B. Kohl, T. Siersma, J. E. Bandow, H.-G. Sahl, T. Schneider and L. W. Hamoen, *Proc. Natl. Acad. Sci. U.S.A.*, 2016, **113**, E7077

464 B. Seddon and G. H. Fynn, *Journal of General Microbiology*, 1973, **74**, 305–314.
465 N. R. Stokes, J. Sievers, S. Barker, J. M. Bennett, D. R. Brown, I. Collins, V. M. Errington, D. Foulger, M. Hall, R. Halsey, H. Johnson, V. Rose, H. B. Thomaides, D. J. Haydon, L. G. Czaplewski and J. Errington, *J Biol Chem*, 2005, **280**, 39709–39715.
466 S. Handtke, D. Albrecht, D. Zühlke, A. Otto, D. Becher, T. Schweder, K. Riedel, M. Hecker and B. Voigt, *Microb. Cell Fact.*, 2017, **16**, 72.
467 B.-M. Koo, G. Kritikos, J. D. Farelli, H. Todor, K. Tong, H. Kimsey, I. Wapinski, M. Galardini, A. Cabal, J. M. Peters, A.-B. Hachmann, D. Z. Rudner, K. N. Allen, A. Typas and C. A. Gross, *Cell Systems*, 2017, **4**, 291-305.e7.
468 Q. Wei, W. Luo, S. Chiang, T. Kappel, C. Mejia, D. Tseng, R. Y. L. Chan, E. Yan, H. Qi, F. Shabbir, H. Ozkan, S. Feng and A. Ozcan, *ACS Nano*, 2014, **8**, 12725–12733.
469 A. Geißler, H. Junca, A. M. Kany, L. J. Daumann, A. K. H. Hirsch, D. H. Pieper and S. A. Sieber, *Chem. Sci.*, 2024, **15**, 11946–11955.
470 Elisabeth Kugelberg, Tobias Norström, Thomas K. Petersen, Tore Duvold, Dan I. Andersson, and Diarmaid Hughes, *Antimicrob. Agents Chemother.*, 2005, **49**, 3435–3441.